A Multi-Approach Investigation of Late Quaternary Lacustrine Sediments in Southern Jordan

Ahmad I. AlShdaifat

Thesis submitted to The University of Nottingham

For the degree of Doctor of Philosophy

October, 2021

Approximate word count (excluding references): 80,000 words

Abstract

Past lacustrine and wetland sediments from arid regions, sensitive to changes in precipitation and evaporation, are important archives of past environmental variability. This thesis presents new data that contribute to the Quaternary records of Jordan through multi-proxy analyses of sediment archives from two study sites in southern Jordan; the Gharandal Valley and the Dead Sea Basin. Through detailed analyses of the sediments from the two study sites, the depositional environments, environmental conditions, and how these changed, and to some extent their timing were reconstructed.

Sediments from the Gharandal Valley were investigated and collected from five different sedimentary sections (> 30 m sediments) and analyzed for particle size distribution, organic and carbonate content (through LOI), and elemental (through XRF) and minerogenic (through magnetic susceptibility) composition. The results indicated complex tectonic/climate-driven depositional environments prevailed in the valley, during Marine Isotope Stage (MIS) 6, alternating from fluvial in-wash to fluvio-aeolian and wetland deposition following the proposed valley outlet damming.

The GH1 and GH2, the main sections in the valley, record the environmental aggradation from stream-fed wetland depositional conditions where thin wetland beds developed following in-wash events, in the lower parts, into more consistent wetland (wetter) conditions towards the top of the sections. These cycles were identified in 16 fining upward primary associations in the GH1 section and 8 fining upward primary associations in the GH2 section.

The age estimate (MIS6) is consistent with wet phases recorded elsewhere in the Levant and increased monsoon precipitation recorded in southern Arabia suggesting that an influence of the two systems (the northeastern Mediterranean Cyclones and the southern tropical monsoon), which do not reach the valley site today, may have contributed to maintaining the wetland conditions in the valley during glacial stadials and interstadials.

From the eastern side of the Dead Sea Basin (DSB), the lacustrine section DS1 was investigated. The section is primarily comprised of laminated pale and dark laminae and laminated detrital laminae with a thick gypsum-dominated bed. Considering the different nature of the sediments, the DS1 bulk sediments were first analysed using proxies mentioned earlier for the Gharandal Valley. In addition,

the pale laminae were analysed for the carbonate isotope composition ($\delta^{13}C$ and $\delta^{18}O$), mineralogy (through XRD) and carbonate crystal habit (through SEM EDS) analysis.

Through preliminary U/Th dating of aragonite laminae, the DS1 section age was estimated at ca. 40 ka to 37 ka (MIS3). This places the section as part of the Lake Lisan Middle Member (ca. 58 ka to 31ka).

Based on the sediment's lithology and the multi-proxy records, the environmental history of the DS1 section, of enhanced/reduced freshwater input into the lake (P/E ratio) at millennial, centennial and close to annual scales, is recorded in four distinct lithostratigraphic units. The units record relatively high lake levels, then lake level lowering and the deposition of the gypsum bed, a lake re-filling stage and return to stable relatively high lake levels.

The environmental proxies suggest that during Greenland Interstadials (GIs), the lake level was relatively higher than during Stadials (GSs). The gypsum bed, the lowest relative lake level in the record, probably coincides with Heinrich Event 4. At centennial scales, the environmental proxies apparently record lake level changes corresponding to the GIs indicating variable amounts of freshwater reaching the DSB.

An initial assessment of the moisture source was done based on the aragonite initial $^{234}U/^{238}U$ ratios variability and indicated the dominance of the Eastern Mediterranean cyclones in driving the deposition of the DS1 section.

The results of this thesis emphasize southern Jordan's sedimentological and palaeoclimatic heterogeneity and the complexity of the past environmental records that can be recovered. This indicates the need for continued investigations and particularly more dating control, based on more comprehensive and detailed approaches in order to achieve a better assessment of the Quaternary sedimentological and environmental variability in the region.

Acknowledgements

Author's co-authored manuscripts

I have contributed to the writing of the following papers through the course of my PhD programme:

- Jones, M.D., Richter, T., Rollefson, G., Rowan, Y., Roe, J., Toms, P., Wood, J., Wasse, A., Ikram, H., Williams, M., **AlShdaifat, A.**, Pedersen, P.N., Esaid, W., 2021. The palaeoenvironmental potential of the eastern Jordanian desert basins (Qe'an). *Quaternary International*. doi: 10.1016/j.quaint.2021.06.023.

- Jones, M.D., Abu-Jaber, N., **AlShdaifat, A.**, Baird, D., Cook, B.I., Cuthbert, M.O., Dean, J.R., Djamali, M., Eastwood, W., Fleitmann, D., Haywood, A., Kwiecien, O., Larsen, J., Maher, L.A., Metcalfe, S.E., Parker, A., Petrie, C.A., Primmer, N., Richter, T., Roberts, N., Roe, J., Tindall, J.C., Ünal-İmer, E., Weeks, L., 2019. 20,000 years of societal vulnerability and adaptation to climate change in southwest Asia. *Wiley Interdisciplinary Reviews: Water 6*, e1330. doi:10.1002/wat2.1330.

Table of Contents

List of Figures

List of Tables

Chapter 1. Introduction

1.1   Introduction

"The palaeoclimate record shouts to us that, far from being self-stabilizing, the Earth's climate system is an ornery beast which overreacts even to small nudges."

-- (Broecker 1995, p.213)

Understanding past environmental and climatic variability is important to further improve climate projections needed to guide adaptation to global warming (IPCC, 2012; Mischke et al., 2015). Such reconstructions can be recovered from several archives, including, but not limited to: ice cores (e.g. Rasmussen et al., 2014), marine cores (e.g. Cacho et al., 1999; Worne et al., 2019), speleothems (e.g. Vaks et al., 2003; Fleitmann and Matter, 2009), corals (e.g. Moustafa et al., 2000), tree rings (e.g. Büntgen et al., 2016) lake sediments (e.g. Jones et al., 2007; Metcalfe and Davies, 2007; Neugebauer et al., 2016; Parton et al., 2018) and wetland sediments (e.g. Pigati et al., 2014; Ginat et al., 2018; Al-Saqarat et al., 2020), with potential to provide long term (up to glacial/interglacial scale) and short term (decadal to close-to-annual scale) climate proxies.

Semi-arid to arid regions are sensitive to local and regional climate changes, particularly evaporation and precipitation variability (Jones and Richter, 2011; Parton et al., 2018). In addition, climate models predict increased temperatures, and reduced rainfall over the next decades (Figure 1.1) (IPPC, 2014) for much of the region, leading to increased pressures in terms of future water availbility (Alraggad et al. 2017; Salameh, 2008).

The Levant, including present day Jordan, Palestine, Israel, Syria and Lebanon, is presently characterized by freshwater scarcity (Salameh, 2008; Kaniewski et al., 2012; Alraggad et al., 2017) and it is particularly sensitive to changes in water availability, driven by climate changes (e.g. droughts) (Kelley et al., 2015; Jones et al., 2019). Both long term and short term climate changes (Seager et al., 2014) affect the water and food availabilty, which are significant factors in the social and socio-political conditions in the Levant (Kelley et al., 2015).
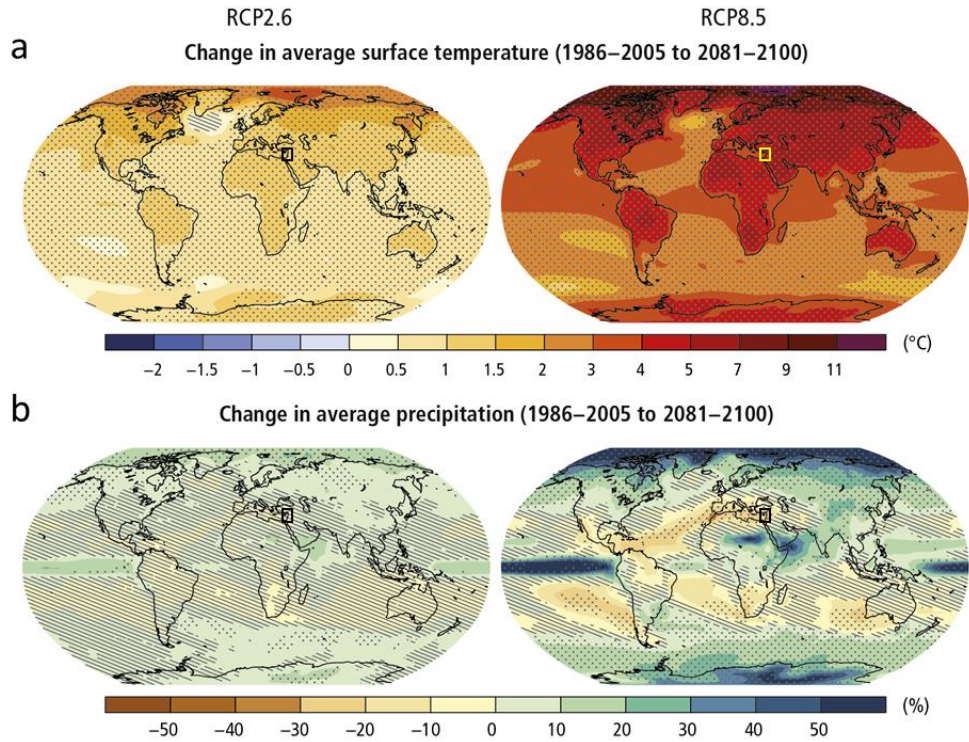
Figure 1.1 CMIP5 multi-model average projections for the years 2081 to 2100 compared to the years 1986 to 2005, (left) RCP2.6, (right) RCP8.5 scenarios. a) Changes in mean surface temperature, b) Changes in mean precipitation. Squares on panels show the Levant location (modified from IPCC, 2014).

Moreover, Jordan, one of the most water-deprived countries worldwide, with ca. 135 m^3 of water per capita per year (Odeh, 2019), is particularly subject to several challenges that are affected by the aforementioned climate changes. Natural population growth accompanied by several refugee influxes over the past few decades (Al-Karablieh and Salman, 2016) have resulted in population size increase from ca. 2 million in 1980 to >10 million in 2020 (DOS, 2020), posing stresses on a limited and depleting freshwater resource (Qdais and Batayneh, 2002; Salameh, 2008). The share per capita per year is expected to decrease to ca. 91 m^3 in the next few decades (Odeh, 2019).

Reconstructing past climate and environmental changes in Jordan is essential in order to draw more comprehensive conclusions regarding present and future climate variability. Evaluating the distribution, age and nature of past water bodies leads to the interpretation of changes in the environment, climate and the hydrological system (Abed et al., 2008).

This thesis investigates two sites from the presently arid southern Jordan, using sedimentary archives from a desert valley (wadi) system and a lacustrine system, in order to provide new data and contribute to the growing body of Quaternary

palaeoenvironmental records from Jordan (e.g. Abu-Jaber et al., 2020; Al-Saqarat et al., 2020; Abu Ghazleh and Kempe, 2021; Jones et al., 2021; Mischke et al., 2021).

1.2   Sediment archives in palaeoenvironmental studies

Sediments can be formed through different processes: physical, biological and chemical. Based on the driving and most dominant process, the resulting sediments can be classified into different types: (1) siliciclastic sediments that primarily comprise clasts (fragments), sourced from local rocks; (2) biochemical and organic sediments; (3) chemical sediments and (4) volcaniclastic sediments (Tucker, 2001). The physical and geochemical characteristics of these sediments record the environmental conditions that facilitated their formation. Accordingly, the sediments' physical (e.g. particle size and sedimentaray structures) and chemical (e.g. elemental, mineral and isotopic) characteristics and composition have been extensively investigated to reconstruct past climate and environmental conditions (e.g. Passega, 1964; Metcalfe et al., 2010; Parton et al., 2013; Baiyegunhi et al., 2017; Lucke et al., 2019b; Parker et al., 2020; Jones et al., 2021). This thesis particularly focuses on wetland and lacustrine environments.

1.3   Past wetlands and lakes

Geomorphological and tectonic settings play a significant role in facilitating and maintaining wetlands and lakes through providing accommodation space and drainage systems to maintain allogenic discharge from the surrounding slopes (Miall, 1996; LeBéon et al., 2012; Parton et al., 2018). The fluvial, and wetland sediments and their composition can be distinguished from lacustrine sediments. This is of great significance for palaeoenvironmental studies, as discerning between palaeo wetland and lacustrine sediments in arid regions, and the site-specific response to local and regional climate changes (Jones et al., 2017; Parton et al., 2018), is crucial for correctly interpreting the past environmental conditions and potentially the climate variability story (Pigati et al., 2014; Engel et al., 2017; Rech et al., 2017). Unlike lakes, wetlands require less moisture availability and can persist under low effective precipitation conditions, during which, shallow emergent groundwater levels can maintain wetlands and marshes in arid regions (Jones and Richter, 2011; Pigati et al., 2011; 2014). However, based on various definitions, lakes can be considered as a type of wetland (Engel et al., 2017).

Generally, both wetland and lake sediments show vertical lithological changes that record the waterbody response to the variable hydrological and hydroclimatic

conditions. However, unlike lake deposits, wetland deposits are usually asymmetrically distributed. Lakes require complete topographic closure, while wetlands do not (Pigati et al., 2014). In arid regions, such as Arabia, it has been reported that shoreline indicators can be found, but not complete shorelines, due to several reasons including erosional processes, dune deposition and vegetation (Engel et al., 2017). These characteristics and others such as microfaunal assemblages have been implemented to assess arid region palaeolakes and palaeowetlands (Pigati et al., 2014; Rech et al., 2017; Parton et al., 2018). However, a specific definition of past lakes, particularly in arid regions is still not confirmed (Parton et al., 2018).

1.3.1 Wetlands as palaeoarchives

Wetlands are temporary continental water bodies that form as a function of environmental conditions and water availability (Sivan and Greenbaum, 2017). In arid regions, desert wetlands are common and form in localities where groundwater approaches the surface providing a water resource. These wetlands comprise several hydrological settings such as marshes, ponds, meadows and others that form in response to fluvial depositional processes (Pigati et al., 2014). These water bodies are archives of environmental variability recorded in their distinct sedimentological, geochemical, faunal and floral compositions, particularly in arid regions (Jones and Richter, 2011; Mischke et al., 2017). Since these water bodies are primarily dependant on water availability, they record changes in the hydrological system and climate (mainly evaporation/precipitation changes) (Sivan et al., 2016). In addition, wetlands driven by groundwater levels can provide data about periods of high groundwater table conditions reflecting changes in past moisture and the magnitude of the climate change that caused groundwater change (Pigati et al., 2011; 2014).

Due to the interactions between groundwater, surface water, geological and biological systems, desert wetland deposits commonly comprise: (1) siliciclastic sediments that are primarily sourced from the nearby areas by surface water flow or aeolian processes from proximal and distal areas, (2) groundwater precipitates that form from de-gassing, (3) organic matter, dark-coloured organic-rich sediments (known as black mat) that originate from aquatic and terrestrial plants remains, and (4) biological remains (Pigati et al., 2014; Ginat et al., 2018). Thus, such records have been used as archives for proxies of past environmental and hydroclimatic changes in deserts where lake sediments (or speleothem records)

are usually lacking (e.g. Williams et al., 2006; Jones and Richter, 2011; Parton et al., 2015a; Jones et al., 2021).

In addition, aeolian/fluvial systems interactions can be significant in the study of palao-water bodies. Aeolian sand deposits are wide-spread worldwide, and have been interpreted as archives of past climatic and environmental changes in Jordan (e.g. Saqqa and Atallah, 2004; Lucke et al., 2019a), Arabia (e.g. Parton et al., 2015a), the Chinese deserts (e.g. Liu et al., 2016), and different regions around the world (e.g. Bullard and Livingstone, 2002; Ben Ameur et al., 2019). In general, aeolian deposition is more dominant when moisture is low. With the increase of moisture availability, the two systems reach a zone of maximum interaction after which the fluvial processes dominate the system (Bullard and Livingstone, 2002). This alternation between the two systems can be a useful signal reflecting changes in moisture availability (Liu et al., 2016). Also, vegetation cover can be a vital determining factor, especially in ephemeral channels, where vegetation in arid regions is often concentrated due to access to groundwater (Bullard and Livingstone, 2002).

The identification of the aeolian signature within a fluvial system depends primarily on the investigation of the sediments' characteristics. Several studies reported alternations between aeolian and fluvial/lacustrine deposition in arid to semi-arid environments based on the sediments' texture, elemental composition and magnetic susceptibility (Parton et al., 2015a; Ben Ameur et al., 2019; Lucke et al., 2019a). These studies reported cycles of wetting and drying and further understanding of the sites-specific responses to local and regional environmental changes. Thus indicating the significance of understanding these interactions in achieving better palaeoclimatic and palaeoenvironmental reconstructions, particularly from semi-arid and arid regions.

1.3.2   Lakes as palaeoarchives

Lakes act as systems that record complex tectonic, environmental and climate variability as continuous archives of local and regional variability in both space and time (e.g. Torfstein et al., 2013b; Roberts et al., 2016). These can be classifed into two primary hydrological systems; open system lakes where an outlet for outflow is present, and closed systems that have no outflow outlet which makes them more susceptible to abrupt lake level changes in response to changes in evaporation and precipitation (E/P) ratios (Talbot, 2005).

Compared to arid region wetlands, lake sediments are capable of providing high resolution palaeoenvironmental reconstructions, probably at decadal to centennial scales based on multi proxy records (Prasad et al., 2004; Kolodny et al., 2005; Dean et al., 2015). Accordingly, these archives have been widely investigated and have provided high resolution environmental records worldwide (Metcalfe et al., 2002; Jones et al., 2007; Neugebauer et al., 2014; Zhang et al., 2021).

Carbonate deposition in lakes is a function of variable factors (Kelts and Hsü, 1978) but is an important deposit for palaeoenvironmental work, which can be reconstructed based on the sediments' mineralogical, geochemical and sedimentological characteristics (e.g. Prasad et al., 2004; Metcalfe and Davies, 2007). The primary types of carbonates that may form include: endogenic inorganic precipitates, biogenic, through allochtonous in-wash, and diagenetic. However, studies on lacustrine sediments from the Dead Sea Basin in Jordan, the sudy area of this project, reported that the carbonates are only formed through endogenic inorganic precipitation (Stein et al., 1997; Landmann et al., 2002), thus this type will be discussed further.

Endogenic inorganic carbonate precipitation can be analysed through different laboratory analyses. For example, using scanning electron microscopic (SEM) analysis, the crystal structure of the carbonate precipitate can indicate its endogenic deposition, where acicular crystal habit indicate aragonite precipitation and euhedral crystals would indicate calcite precipitation (Žigovečki Gobac et al., 2009). This endogenic precipitation of carbonates is a function of the equilibrium amongst the lake's calcium carbonate ($CaCO_3$), carbonic acid (H_2CO_3) calcium ion (Ca^{+2}), and bicarbonate ion (HCO_3^-) composition based on the reaction in equation (1), while the carbonic acid is a function of the reaction between H_2O and CO_2

$$CaCO_3 + H_2CO_3 \longleftrightarrow Ca^{+2} + 2\,HCO_3^- \qquad (1)$$

Accordingly, the carbonate endogenic precipitation is affected by: temperature which drives the CO_2 dissolution where high-temperature waters produce less CO_2, pH which is related to several factors where higher pH waters produces more calcium carbonate precipitate, and the Ca^{+2} and bicarbonate concentrations where higher concentrations yield higher contents of calcium carbonate precipitation (Lindsay, 1979). The endogenic calcium carbonate resulting from the aforementioned factors and processes can be mineralogically different, based on

the water geochemistry and the varying effects of these factors. Common minerals formed are calcite and aragonite, and occasional dolomite.

In lakes, at certain time-intervals, laminated carbonate and detrital lake sequences can be deposited (e.g. Brauer et al., 2008; Ben Dor et al., 2019). If this regularity is seasonal, over a certain period of time, the laminations are considered as varves (couplets) (e.g. Brauer et al., 2008; Roberts et al., 2016; Ben Dor et al., 2019). Varves primarily comprise at least two laminae that are distinguishable by their own characteristics, composition and thickness, reflecting the environmental process driving their deposition, hence climate seasonality (Brauer et al., 2008; Ben Dor et al., 2019).

1.4 Thesis aims, objectives and outline

This study aims to contribute new data and understanding regarding the Quaternary sedimentology of Jordan, through undertaking analyses from two study sites in southern Jordan; the Gharandal Valley and the Dead Sea Basin. The two study sites represent two different hydrological systems; a fluvial/wetland wadi system and a lacustrine system, respectively.

Specifically, this research aims to provide detailed sedimentological and geochemical records from ca. 30 m of sediments from the presently arid Gharandal Valley (modern precipitation <100 mm.yr^{-1}) emphasizing the importance of detailed investigations in better understanding the depositional environments and hydrodynamics of sediments in arid regions, which will contribute to the previous studies that reported inconsistent chronological and environmental interpretations from the Valley (e.g. Henry et al., 2001; Mischke et al., 2017; Al-Saqarat et al., 2020).

Similar methods are then applied on a 4.6 m section of finely laminated (lacustrine) sediments from the eastern (Jordanian) side of the Dead Sea Basin (DSB), accompanied by high resolution multi-proxy (sedimentological and geochemical) environmental records. DSB sediments in Jordan have remained relatively understudied compared to those on the west side of the basin. This research will also contribute to the ongoing debate regarding the tectonic movements along the DSB and their effects on the sediments position on both sides of the basin (e.g. Bartov et al., 2002; 2006; Ferry et al., 2007; Jara-Muñoz et al., 2020; Abu Ghazleh and Kempe, 2021), i.e. whether sediments from the same age are at the same level on both sides of the basin, and if not, if any offsets are consistent in time.

The two records will then be correlated with local and regional archives and put within the broader context of Quaternary climate system variability.

1.4.1 Thesis outline

This thesis is constructed to discuss the palaeoclimatic importance of the Levant and Jordan (Chapter 2), and present the study sites selection and the field and laboratory methodological approaches used in this PhD project (Chapter 3).

Chapter 4 outlines the study sites, their characteristics, previous studies and rationale for further investigations.

Chapter 5 concentrates on the Gharandal Valley study area, where the detailed analyses and results collected from the five sections in the valley are presented in terms of sedimentological and geochemical analyses, interpretation of the associated hydrodynamics and depositional environments.

Chapter 6 presents the combined results from the Gharandal Valley and provides a comprehensive reconstruction of the valley's environmental and hydrodynamic history. This chapter ends with positioning the Gharandal new age estimates within the context of broader Quaternary records.

Chapter 7 focusses on the lacustrine sediments (DS1 section) collected from the DSB. In this chapter, the DS1 section lithology is described in detail with the sediments' bulk sedimentological and geochemical analyses. Then, the DS1 section lithostratigraphic units are discussed. This is followed by presenting the DS1 laminae characteristics and composition in terms of their potential to provide high resolution records. The DS1 chronology is then presented accompanied by an assessment of the tectonic processes. This chapter ends with a discussion of the new DS1 section data within the broader DSB lacustrine records from both sides of the basin and with regional and global Quaternary records.

Finally, Chapter 8 presents combined conclusions from the two study sites, the contribution to Quaternary records of Jordan and recommendations for future work.

Chapter 2. The palaeoclimate importance of the Levant

The Levant, the easternmost part of the Mediterranean (Radaideh and Melichar, 2015) (Figure 2.1), encompasses a region starting from the northern high Lebanon Mountains to the southern Sinai low relief desert. Its unique position between Africa, Arabia and Euroasia gives this small (~800×250 km) region its high importance in understanding the global palaeoclimate and palaeoenvironment records. The Levant also has a long archaeological and human occupation history making it a focal point to study the human and environment interactions and early human dispersals (Al-Nahar and Clark, 2009; Jones et al., 2017; Hershkovitz et al., 2018).
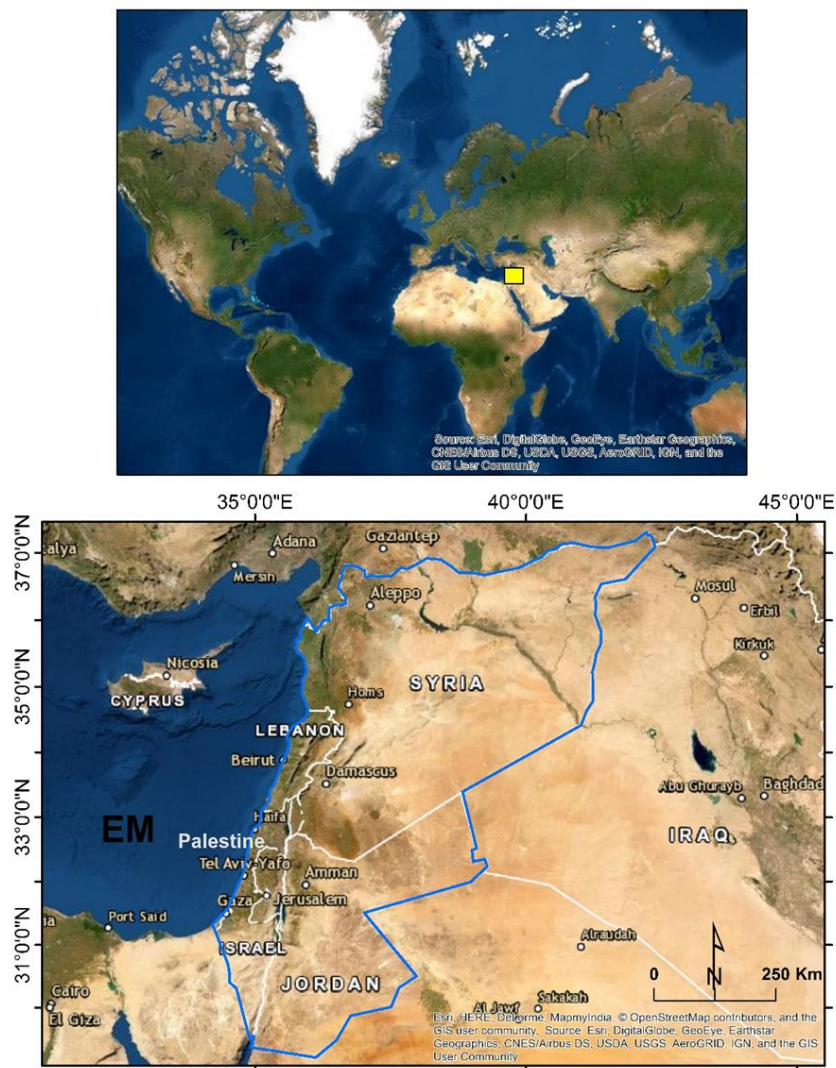
Figure 2.1 Map of the Levant in the global context (yellow square) (top) and in its regional context (blue polygon) (bottom). **EM**: Eastern Mediterranean Sea.

2.1 Regional tectonic and physiographic settings of the Levant and Jordan

The tectonic evolution of the Levant has involved long periods of deformation (Alawabdeh et al., 2016). Following the thermal activation of the northeastern Afro-Arabian plate (~300 to 25 Ma), the Levant experienced tectonic uplifting which resulted in the formation of a crustal dome of about 3000×1500 km centred on both sides of the current Red Sea. This feature reactivated older tectonic structures resulting in their truncation and eventually forming the Oligocene Regional Truncation System (RTS) (Avni, 2017). Late to Early Miocene rifting resulted in the formation of the Red Sea-Suez Rift, and the plate boundary known as the Dead Sea Transform (DST), which is the main factor controlling the recent tectonic activity in the Levant (Diabat et al., 2004; Alawabdeh et al., 2016). As a result of multiple tectonic events, the Arabian plate and the Sinai plate were separated from the African plate and the Bitlis-Zagros zone was formed alongside several large-scale srike-slip faults and the Red Sea opening (Radaideh and Melichar, 2015).

The present day Levant therefore encompasses various physiographic features (Figure 2.2) comprising mountains, plateaus and lowlands. The main features from North (Lebanon) to South (Jordan), comprise: the Lebanon Mountains (Figure 2.2 a) which are the highest mountains in the Levant and they extend about 120×40 km with a highest peak of ca. 3083 m above sea level (asl); the central mountain chain, ca. 800-1200 m asl, that extends from southern Lebanon to the central Negev (Figure 2.2 b); the Jebel (mountain) Druze and the northeastern basalt plateau that extend from the Golan Heights in Syria to the Al-Harra basalt field in northeastern Jordan (Figure 2.2 c); the ca. 800 km Central Depression which extends through the Levant to the northern end of the Gulf of Aqaba (Figure 2.2 d) and comprises the Dead Sea, a segment of the DST (see above), the lowest depression on Earth at ca. -420 m asl (Avni, 2017). The Jordan Plateau lies east of the Central depression and extends north-south, ca. 300 km long and 60-180 km wide (Figure 2.2 e).
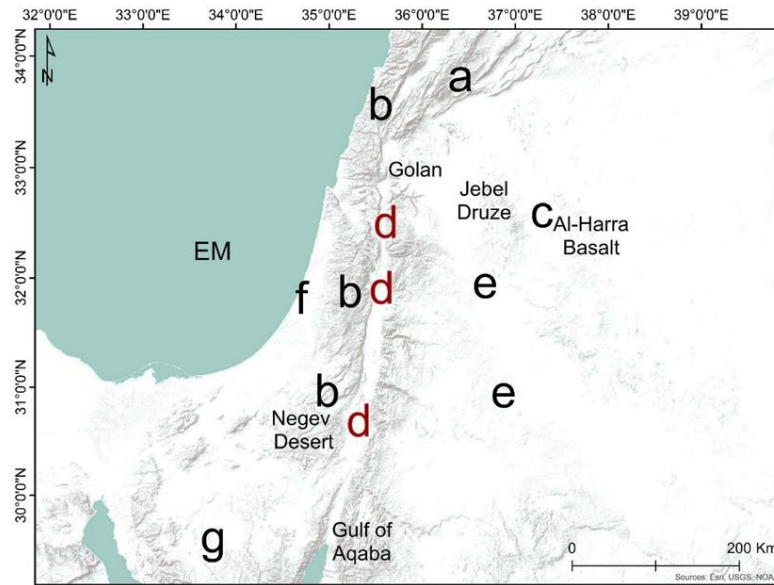
Figure 2.2 Main physiographic features of the Levant overlay topographic map. **a**. the Lebanon Mountains, **b**. the Central Mountain Chain, **c**. Jebel Druze and the northeastern basalt plateau, **d**. the Central Depression, **e**. the Jordan Plateau, **f**. the Western Coastal Plain, **g**. the Sinai Peninsula and the northern tip of the Red Sea (Data from Avni, 2017). Also showing the main landmarks mentioned in the text. **EM**: Eastern Mediterranean.

2.1.1   Tectonic and hydrologic settings of Jordan

The DST (see above) is the main tectonic structure controlling the tectonic settings of Jordan (Diabat et al., 2004; Diabat, 2013; Al Hseinat et al., 2020). The plateau is an eastward tilted feature comprising highlands with summits of ca. 1700 m asl and it is subdivided into several depressions. In the south, the plateau is bounded by an escarpment separating the Upper Cretaceous to Eocene rocks of the Central Plateau from the southern Cambrian to Lower Cretaceous sandstone lowlands (Bender, 1974; Abed, 2017; Cordova and Ames, 2017). To the south and west, the strata are truncated by the RTS and the Precambrian basement complex is exposed. Separate tectonic features are formed as a result of N-S and E-W faults (Figure 2.3 b) preserving Eocene strata and Oligocene conglomerates. An Oligocene uplift of southern Jordan is indicated by the exposure of the Precambrian basement in and around Aqaba in the south. The northeastern parts of the country are divided into the northeastern Al-Harra Basalt plateau and Al-Hammad (northeastern limestone) (Cordova and Ames, 2017). The western highlands start from the Ajlun highlands, and display a gradual elevation increase towards the south.

The current topographical features have evolved since the Late Miocene due to the rejuvenation of tectonic uplift caused by the Dead Sea Transform (DST), were

wadis were formed flowing westward, draining water from the eastern highlands towards the western rift, the Dead Sea Basin (DSB) and Wadi Araba (Alawabdeh et al., 2016; Avni, 2017).

In response to this tectonic setings, Jordan's hydrology is dominated by endorheic basins that as well as the western rift, spread across the Central Plateau (Cordova and Ames, 2017) and the northeastern Deserts (Jones et al., 2021) (Figure 2.3 a). The main endorheic basins (locally known as "Qa'", plural "Qe'an") are Qa' Al-Azraq in the northeastern desert, Qa' Al-Jafr and Qa' Al-Mudawwara in the south (Abed, 2017). Several smaller physiographic structures can be found in northern and southern Jordan, that primarily resulted from the ongoing strike-slip DSTF movement creating pull apart basins and accommodation spaces (Atallah et al., 2002; Le Béon et al., 2010).

2.2   Contemporary climate settings of the Levant

The Levant's physiographic features, topography, and location within the hemispheric atmospheric system control its climate variability (Enzel et al., 2008; Kushnir et al., 2017). The Levant experiences two main seasons: wet and cold season through the months October to April, and hot and dry in summer during June to September. A North-South decreasing precipitation trend is present in the Levant. For example, precipitation varies from ca. 800 mm.yr^{-1} in the northern Levant and over the highlands to reach <50 mm.yr^{-1} in the southern and eastern Jordanian deserts.

The Levant wet season

During this season, the Mediterranean Sea acts as a precipitation moisture source where sub-monthly transient cyclones and anticyclones deliver moisture over the surrounding regions (Seager et al., 2014). The Mediterranean winter transients are primarily formed in the basin and track from west to east (Kushner, et al., 2017). The generation of low pressure systems in the Mediterranean is affected by sea surface temperatures, where the sea surface temperature is warmer than the cold air coming from Europe, during winter and autumn seasons. This instability enhances the formation of low-pressure centres.
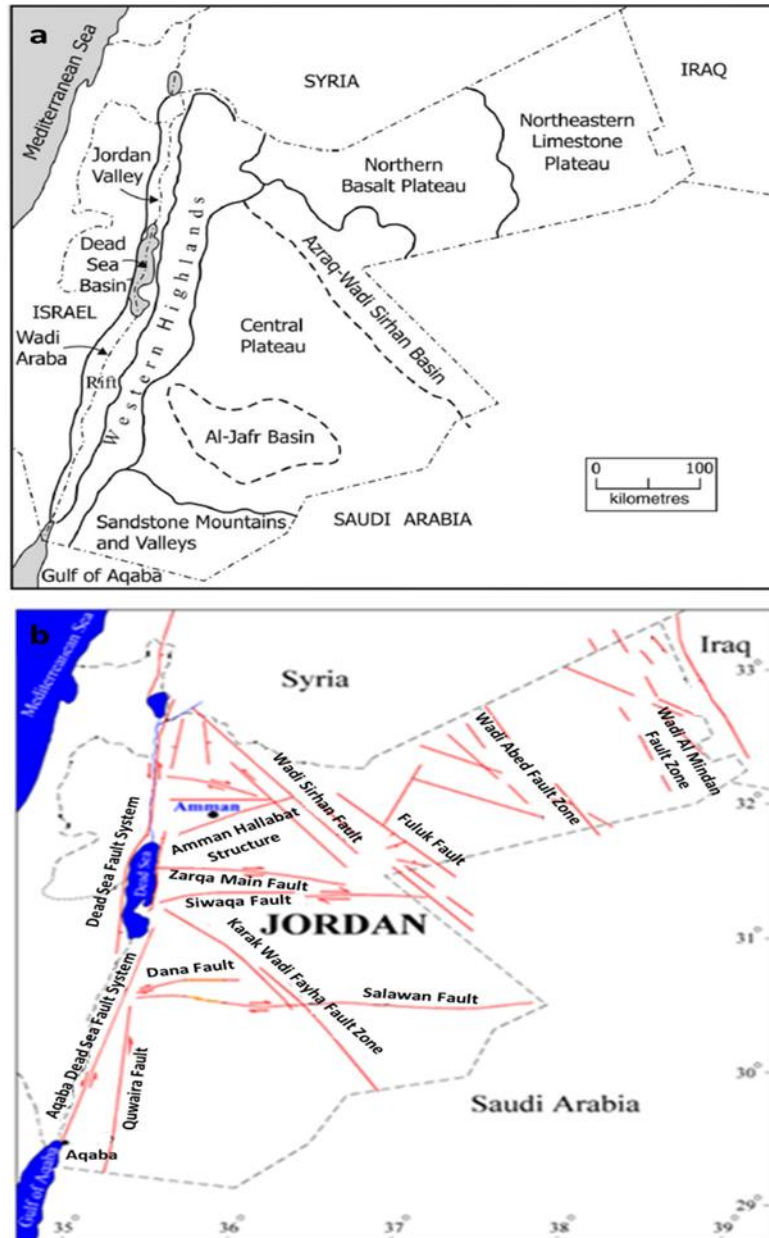
Figure 2.3 a) Regions of Jordan (from Cordova and Amis, 2017), b) Tectonic map of Jordan (modified after Diabat and Masri, 2005).

At the broader scale, the North Atlantic Oscillation (NAO), can influence the Levant climate. During the deepening of the Icelandic Low and strengthening of Azores High (positive NAO phase), the western Mediterranean experiences reduced precipitation, but the Levant receives slightly enhanced precipitation (Romanski et al., 2012; Kushnir et al., 2017). This has been attributed to a shift in the Mediterranean Sea deep water formation from the Adriatic Sea to the Aegean Sea, similar to the observations for the EM intense winter during the year 1991/1992 (Romanski et al., 2012).

13

Saaroni et al. (2010) evaluated the period from November to March over 50 years and reported that an average of 45 annual EM Low days persist in the Eastern Mediterranean. The number, track and intensity of these lows primarily control the enhanced/reduced wetness in the Levant (Kushner et al., 2017). The Sharav cyclones, also known as Khamaseen cyclones (Abed et al., 2008), are primarily active during spring, as a result of the spring temperature gradient between the Mediterranean sea and Africa. These cyclones move along the southern coast of the Mediterranean. However, their potential in generating precipitation over the Levant is limited due to the low moisture content of the Saharan air masses. The outcome of these, on average 10 cyclones a year, is usually hot and dry weather and sand storms (Kushnir et al., 2017).

Even though precipitation over the Levant is primarily controlled by the extratropical EM cyclones, an influence of the tropical cyclones is also present during the cold season. Cloud bands termed "African Tropical Plumes" (ATPs) (Figure 2.4), last for about 12 to 24 hours in the southern Levant, where they provide intense rain that originates from distal sources of tropical Africa and the tropical Atlantic. These plumes track >2000 km over North Africa (Rubin et al., 2007; Kushnir et al., 2017).
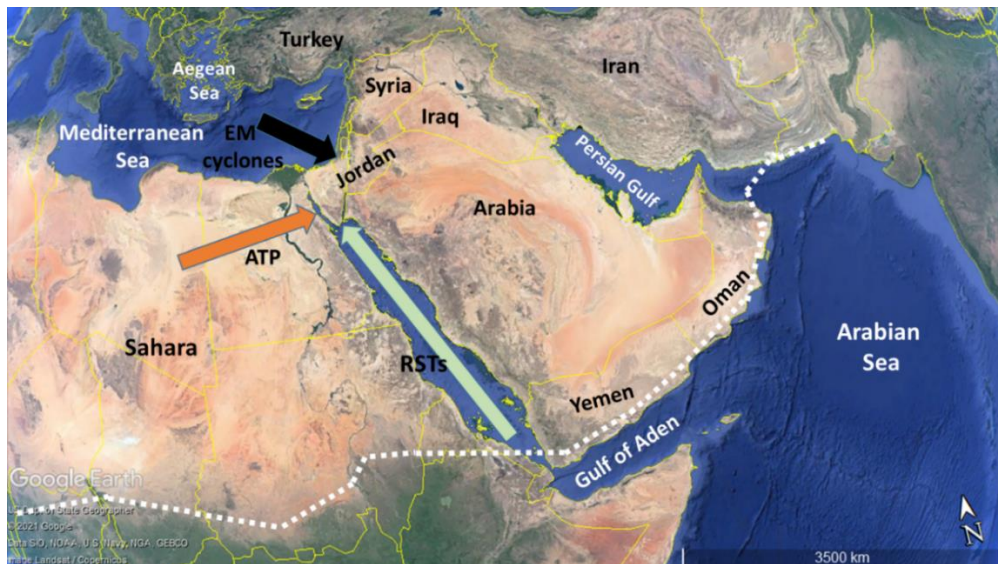
Figure 2.4 Google Earth image showing the primary present-day moisture sources reaching the Levant. **EM:** Eastern Mediterranean. **ATP:** African Tropical Plumes, **RST:** Red Sea Trough. EM cyclones are the dominant winter precipitation source while the ATPs are active during the wet season, and the RSTs are active during transitional seasons. The latter two systems deliver moisture over the southern Levant. Dashed white line delineates the approximte modern northern limit of the summer monsoon precipitation. (data from Catlett et al. (2017); Torfstein et al. (2015)).

During transitional seasons, the EM cyclones are weakened, facilitating the generation of a southern trough. The Red Sea Trough (RST) (Figure 2.4) is a trough overlying the Red Sea and acts as a corridor that facilitates the transport of thermally unstable air masses from the Arabian Sea and tropical Africa northward into the southeastern Mediterranean. This process generates the so called, Active Red Sea Troughs (ARSTs), capable of reaching into the southern Levant to deliver precipitation (Kahana et al., 2002). In certain instances, when these troughs are synchronous with mid-tropospheric troughs from Europe, through the Nile and Mediterranean respectively, this association is capable of delivering torrential precipitation and storms in the southern Levant (Kushnir et al., 2017). ARSTs were the driving mechanism of more than 38% of the autumn floods in the southern Negev during the period 1965-1994 (Kahana et al., 2002).

The Levant warm season

The distinctive characteristic of the Levant warm season is its stability and minor daily variations. This stability is attributed to the nature of the active synoptic systems. A trough related to Hadley Cell, generated in the lower troposphere extends from the Persian Gulf into Iraq, Syria, and Turkey and into the Aegean Sea. This trough is an extension of the Indian summer monsoon. The Indian summer monsoon generally controls two systems that affect the summer temperature in the Levant, namely, mid to upper level subsidence and lower level advection (etesian winds). These systems sustain the dry summer stability in the Levant, where no monsoon precipitation currently reaches as far north as the Levant (Lionello et al., 2006; Kushnir et al., 2017).

2.2.1 Contemporary climate of Jordan

The general climatic pattern of Jordan follows the general Levant climate settings. A dry, hot summer with dust storms, and north to northwesterly winds, from June to September, and a semi-dry cold windy winter season from October to April. The months of April and May are marked by Khamaseen cyclones (Abed et al., 2008). Precipitation over the highlands of northern and central Jordan provides Mediterranean humid conditions (ca. > 500 mm.yr^{-1}) which decreases southward and eastward (Figure 2.5) and transitions to semi-arid and arid conditions with precipitation less than 50 mm.yr^{-1} in the eastern and southeastern deserts (Abed et al., 2008).

Considering the aforementioned synoptic controls over the Levant's climate variability, the region represents a distinct setting linking the tropical southern

monsoon systems and the northwestern extratropical EM rainfall regime. These synoptic scale systems and their temporal and spatial variability, that is primarily controlled by the orography and physiographic features of the Levant, result in a sharp decreasing trend in precipitation from north to south and from west to east (Enzel et al., 2008), which in turn created different microenvironments and biogeographic zones within the Levant and even within the individual countries (see section 2.3.4).
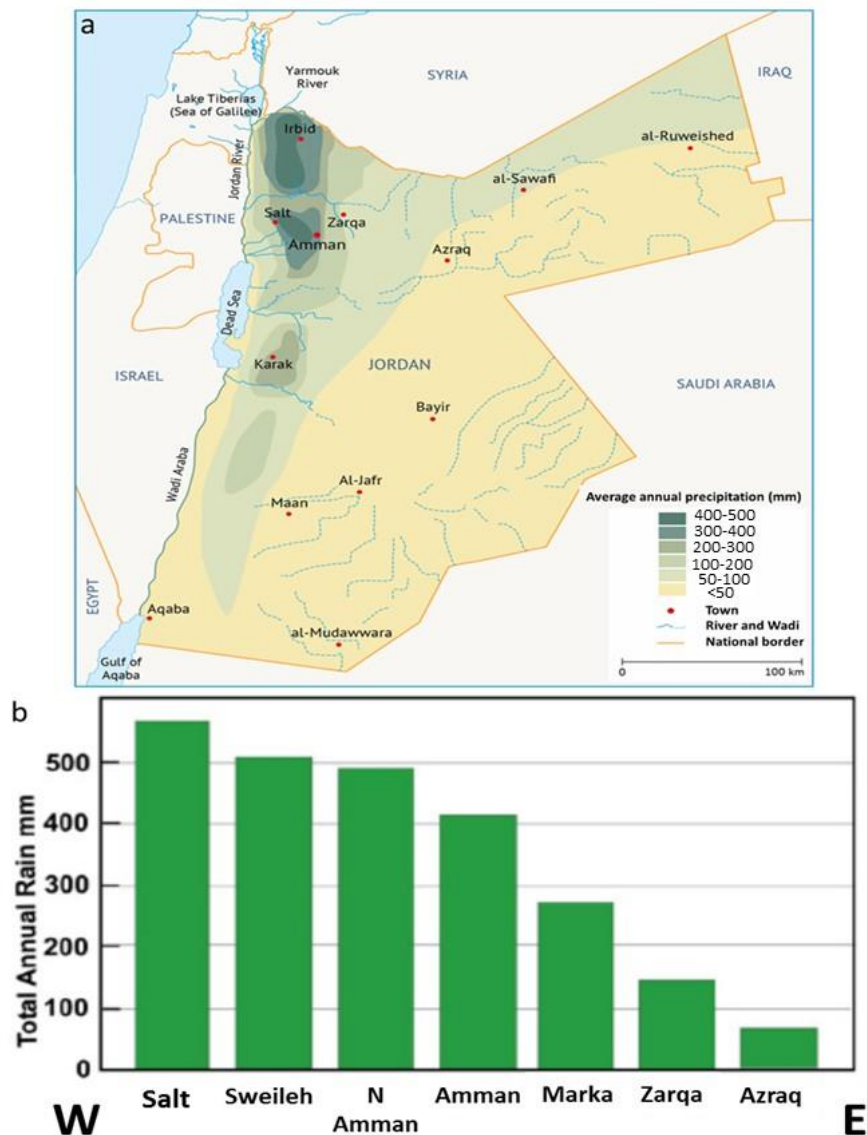
Figure 2.5 a) Mean Annual Precipitation over Jordan (from MWI open files, 2014). b) West-East total annual rainfall trend (from Abed et al., 2008).

2.3 Jordan

2.3.1 Location and general topography

Jordan lies between 35°30' to 38°80' E and 29°30' to 32°50' N, with a topographic gradient varying from more than 1700 m asl in the southwestern highlands (SM) to ca. 1500 m asl in the northern Ajlun mountains (AJ), to the low relief central plateau and the less than -420 m asl western Dead Sea basin (DS) (Figure 2.6).
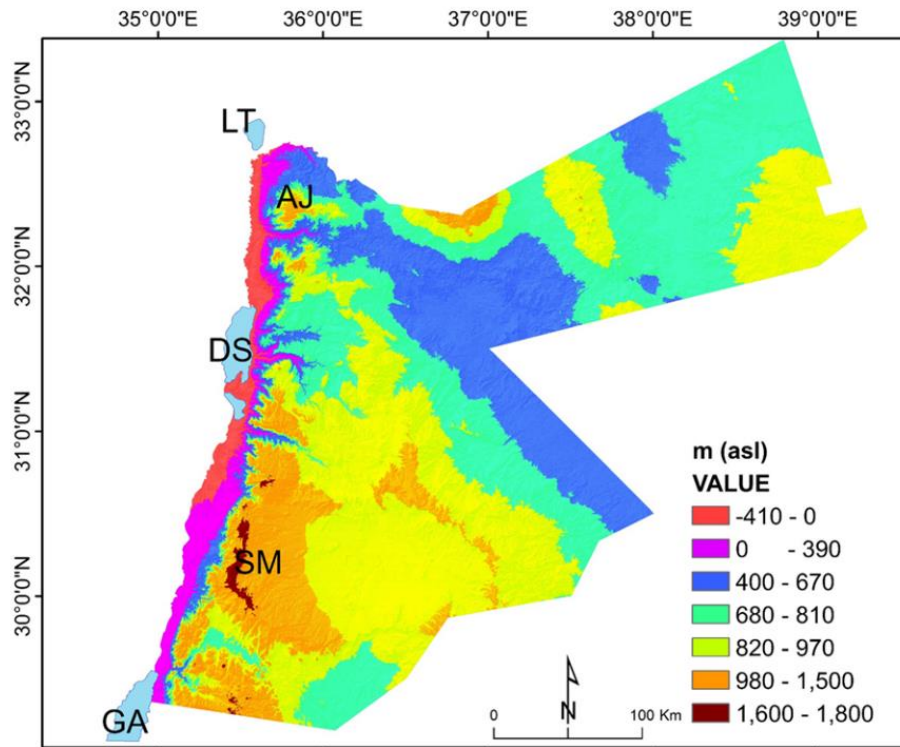
Figure 2.6 SRTM v3 (30m pixel) Digital Elevation Model (DEM) of Jordan illustrating the topographic variation across the country. **GA**: Gulf of Aqaba, **DS**: Dead Sea, **LT**: Lake Tiberius, **AJ**: Ajlun highlands, **SM**: Southwestern highlands.

2.3.2 General geological settings of Jordan

The general geological units of Jordan are divided depending on tectonic activities and the location within the country (Abed, 2017). The oldest Precambrian unit is found at the southernmost limit of the country, near Aqaba and south of Wadi Araba, comprising granite, granodiorite, porphyry and metamorphic rocks. The sandstone formations exposed in the south along the Rift Valley escarpment, Wadi Araba, around Wadi Ram and Petra, include two main groups; the Ram and Kurnub. These units date to the Palaeozoic and Triassic-Jurassic periods, respectively. The Upper Cretaceous and Eocene periods are represented by the sedimentary deposits comprising marine rocks, i.e. marls and limestone, phosphorites and travertine found in the Western Highlands and the Central

Plateau. The youngest unit dates to the Plio-Pleistocene period and it is found mainly in the incised wadis and the tectonically evolved pull apart basins (Bender, 1974; Abed, 2017).

2.3.3   Land cover

Land cover in Jordan follows the climatic variability where <9 % of the country comprise agricultural lands and green surfaces (e.g. forests) and they are primarily over the highlands, either near water resources (e.g. dams), or in areas where groundwater level is shallow. The main agricultural activities are concentrated in the highlands and the Jordan Rift Valley to the north of the present-day Dead Sea (Al-Zu'bi, 2007). Deserts dominate the rest of country covering ca. 90 % of the total area (Figure 2.7) (Ababsa, 2013).
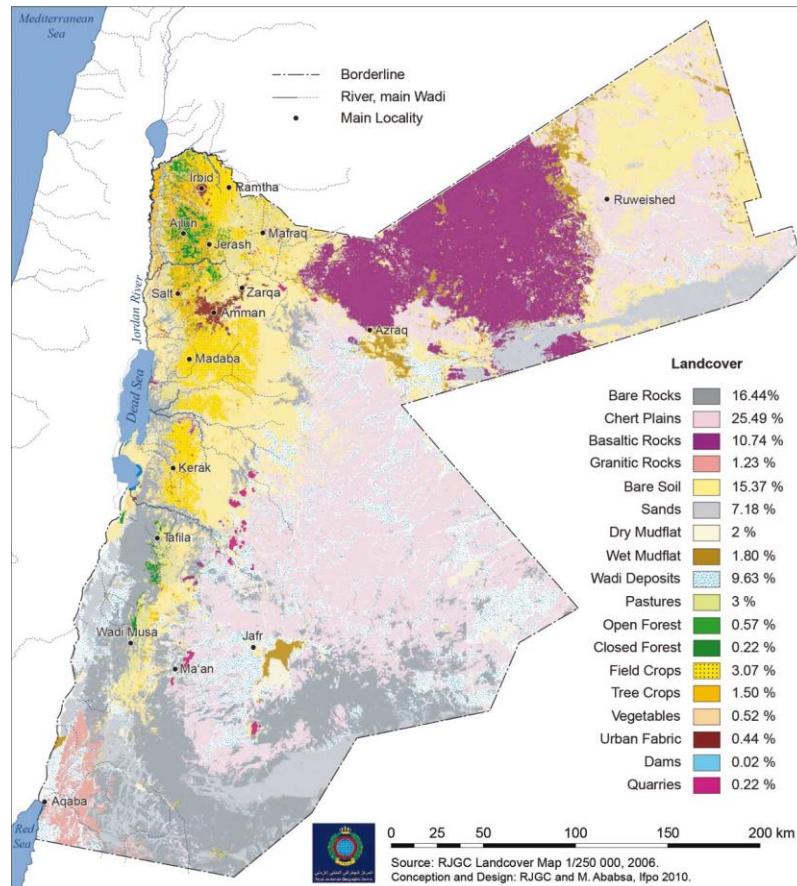
Figure 2.7 Jordan land cover map based on landsat images. The map shows that green surfaces are concentrated in the northwestern parts and over the southern highlands. Also showing the eastern and southern bare lands and deserts (from Ababsa, 2013).

2.3.4   Bioclimatic zones

In response to Jordan's location, orography and climatic settings, particularly summer dryness and droughts, the country comprises diverse flora that include ca. 2500 species (Palmer, 2013). Accordingly, four primary bioclimatic regions can be defined in Jordan (Davies and Fall, 2001; Litt et al., 2012; Palmer, 2013).

The Mediterranean floral region is primarily in the highlands that reach up to >700 m asl where the mean annual precipitation is 300-600 mm.yr^{-1},. Soil types in this region are yellow Mediterranean soil (*Rendzina*) and *Terra Rossa.* This region is primarily characterized by forest and shrub-land assemblages with Aleppo pine (*Pinus halepensis Mill.*) and wild Phoenician Juniper (*Juniperus phoenicea L.*) as the main forest types in the north, and in the south, respectively. In addition, this region comprises *Quercus calliprinos* (Evergreen oak) that can be found in the northern and southern parts of Jordan (e.g. Figure 2.8 a) (Palmer, 2013).

The Irano-Turanian (Steppe) region is found surrounding the Mediterranean region at altitudes of 500-700 m asl with precipitation of ca. 150-300 mm.yr^{-1} and primarily calcareous soils (Palmer, 2013). The typical flora include *Artemisia herba-alba* and *Noaea mucronata*, primarily in the south and north, respectively (e.g. Figure 2.8 b).

The Saharo-Arabian floral region is primarily present across the flat semi-arid and desertic lands where altitudes range from ca. 520 m asl in Al-Azraq to areas of 700 m asl with mean annual precipitation of 100-150 mm.yr^{-1} to 50 mm.yr^{-1} in the eastern and southern deserts. This region is dominated by the rocky plateau and the basaltic deserts with poor soil (e.g. Figure 2.8 c). The vegetation in this region is generally sparse and can be found in Wadis where flood events bring water through the catchments. The main species include *Retama raetam*, *Tamarix spp.*, Acacia spp., and *Phoenix dactylifera* L.

The Sudanian floral region is defined as representing the penetration of tropical elements and includes the Dead Sea area and Wadi Araba to Aqaba. The soil is predominantly alluvial and it is found at diverse altitudes reaching <-400 m asl in the Dead Sea area. The mean annual precipitation is 50-100 mm.yr^{-1}. This region is characterized by *Acacia* woodlands and *Ziziphus-Balanites*. The region vegetation comprises date palm (*Phoenix dactylifera* L.), and willow (*Salix acmophylla* Boiss.), Black Poplar (*Populus euphratica* Oliv.), and Saline (hydrophytic), primarily surrounding the Dead Sea (e.g. Figure 2.8 d) (Davies and Fall, 2001; Litt et al., 2012; Palmer, 2013).
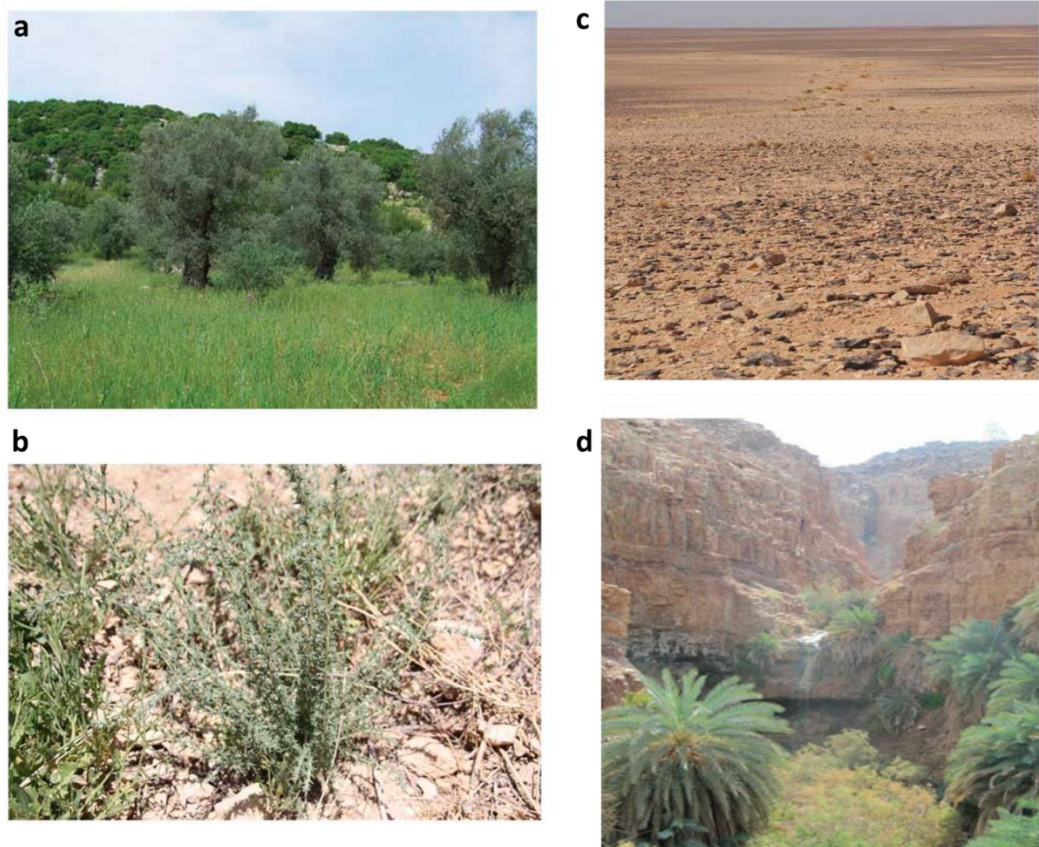
Figure 2.8 Primary vegetation types of Jordan's four bioclimatic zones. a) Olive and arable cultivation and Quercus calliprinos, b) Artemisia herba-alba, c) Sparse vegetation in the basaltic desert east of Jordan, d) Date palm vegetation in a Wadi near the Dead Sea following intense precipitation (From Palmer, 2013).

2.4   Middle-late Quaternary to Holocene records of the Levant and Jordan

This section discusses the middle-late Quaternary to Holocene records from the Levant with a focus on records from Jordan. It outlines the literature, hypotheses regarding changing moisture sources and gaps in current understanding.

The Quaternary records from the Levant, and particularly the southern Levant, are still poorly investigated (Abed and Yaghan, 2000; Enzel et al., 2008; Torfstein et al., 2015; Guillemot et al., 2019; Jones et al., 2021). Only few studies, based on terrestrial archives provide long records that span glacial/interglacial cycles while the majority of the records are short or discontinuous, in terms of geological time scales (Guillemot et al., 2019).

The discussion here presents the key Quaternary records of the Levant from the southernmost records of the Red Sea to the northern records of Lebanon (Figures

2.9 and 2.10). The effect of the present (and time-constant (Enzel et al., 2008)) north-south precipitation trend is also highlighted.

The Red Sea corals and coral reefs records represent a rich palaeoenvironmental source. Lazar and Stein (2011) reported fresh water fluxes into the Red Sea based on coral reef recrystallization (aragonite to calcite) documented at ca. 140 ka. Near the Gulf of Aqaba (RSC in Figure 2.9 a), the corals are mainly of Holocene age (ca. 6.5 cal ka BP onwards) based on ^{14}C dating (Moustafa et al., 2000). Moustafa et al. (2000) recovered $\delta^{18}O$ and $\delta^{13}C$ records from corals (Porites spp.). The authors reported that seasonal $\delta^{18}O$ values were greater than in modern corals. The authors attributed this to   temperature seasonality and salinity reduction during the mid Holocene summer seasons due to the northern migration of monsoon summer precipitation into the northern Red Sea (Moustafa et al., 2000).

Farther north, in Wadi Araba (WAT in Figure 2.9 a), Livnat and Kronfeld (1985), based on U/Th dating, identified spring travertines where no similar deposition occurs today, primarily during interglacials MIS7, MIS5 and corresponding to interstadials during the last glacial (a in Figure 2.10) suggested that these periods were characterized by higher effective moisture availability in Wadi Araba.
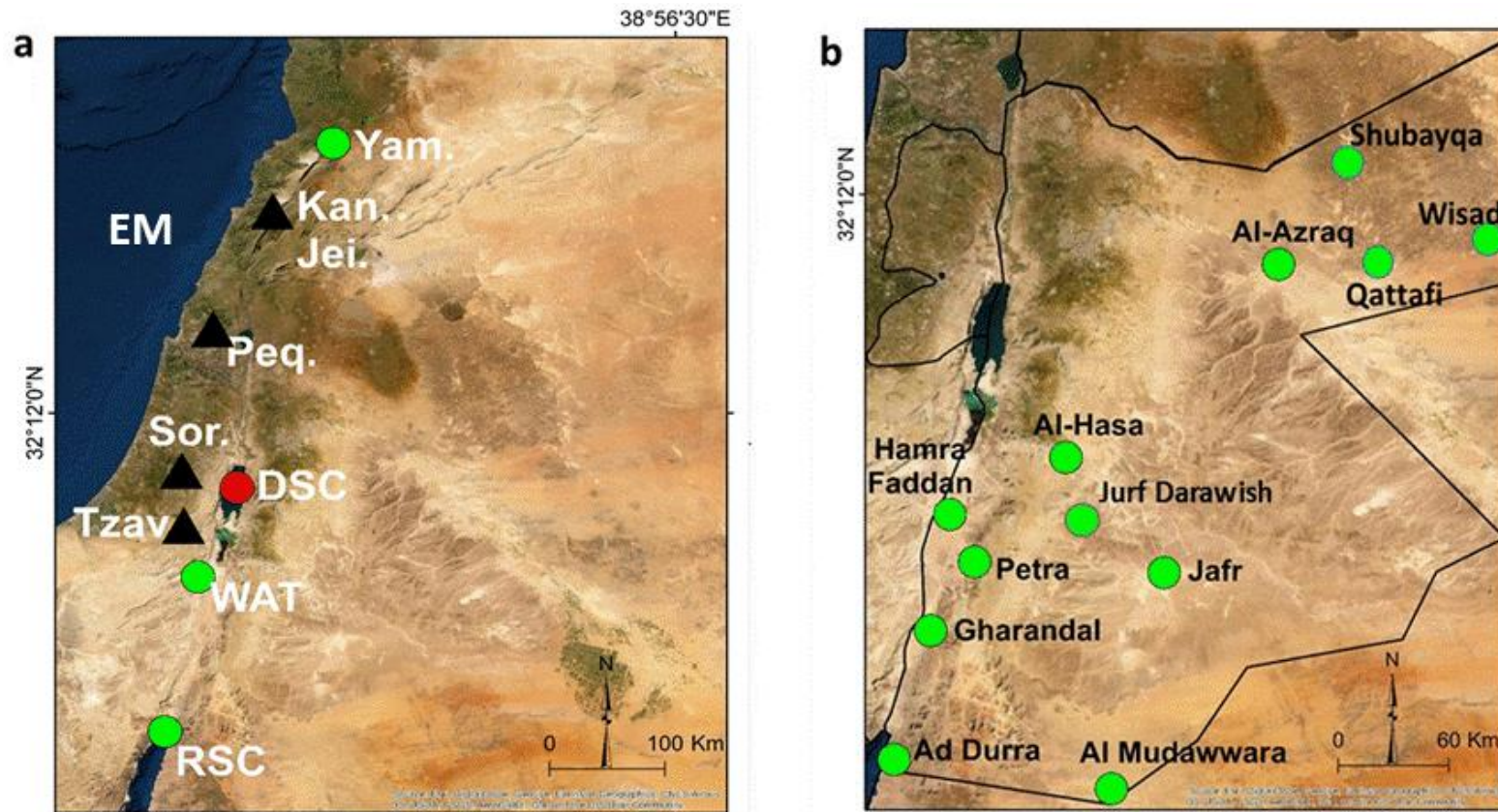
Figure 2.9 a) Map of the Levant showing the key records discussed in text. **Kan. Jei:** Kanaan and Jeita Caves, **Yam:** Yammouneh Basin, **Peq:** Peqiin Cave, **Sor:** Soreq Cave, **Tzav:** Tzavoa Cave, **WAT:** Wadi Araba travertine, **DSC:** Dead Sea Basin records, **RSC:** Red Sea corals. b) Map of Jordan showing locations of key Quaternary records discussed in 2.4.2. **EM**: Eastern Mediterranean Sea. **Speleothems** (Black triangles). **Dead Sea**: Red circle. **Other records**: Green circle.
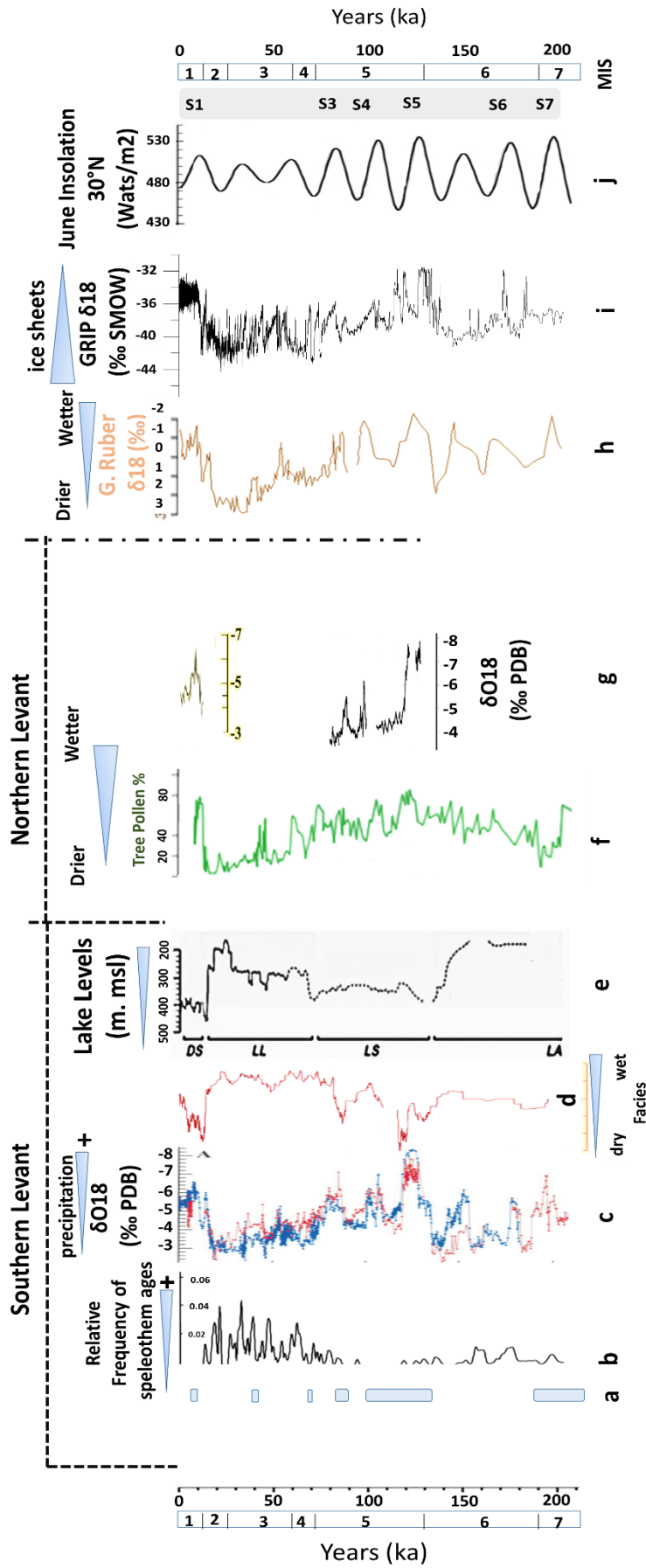
Figure 2.10 Comparison of the selected key palaeoclimatic records in the Levant mentioned in the text. **a)** Wadi Araba Travertines (Livnat and Kronfeld, 1985), **b)** Tzavoa Cave speleothem growth (Vaks et al., 2006), **c)** Soreq (blue) and Peqiin (red) δ18O records, ((Bar-Matthews et al., 2003**), d)** DSDDP 5017-1 core facies analysis, (Torfstein et al., 2015), **e)** DSB lakes levels, DS: Dead Sea, LL: Lake Lisan, LA: Lake Amora, (Waldmann et al, 2010), **f)** Yammouneh Basin, (Gasse et al., 2011), **g)** Kanaan Cave and Jeita Cave records (Verheyden et al., 2017), **h)** East Mediterranean Sea, (Kallel et al., 2000), **i)** Oxygen isotope record of Greenland Ice Core Project (GRIP) ice core (in ‰) (Johnsen et al., 1997), **j)** June Insolation 30°N. MISs: (Lisiecki and Raymo, 2005).

23

To the south of the DSB, speleothem growth in Tzavoa cave (Tzav. in Figure 2.9 a) indicates deposition during different time periods (Figure 2.10 b) where MIS6 is characterized by higher frequency of speleothem ages compared to MIS5. The last glacial period (MISs 4 to 2) is characterized by speleothem growth, while no speleothem deposition is recorded during the Holocene, which led Vaks et al. (2006) to suggest higher moisture availability and wetter conditions, compared to the present day, prevailed during these periods of speleothem deposition when precipitation above the modern amounts must have prevailed (Vaks et al., 2006). Dry conditions in the record corresponding to events at ca. 150-144 ka (MIS6), 141-140 ka, 117- 96 ka, 92-85 ka (MIS 5), 25-23 ka and 13 ka were reported suggesting conditions similar to present-day or drier (Vaks et al., 2006).

The Dead Sea Basin (DSC in Figure 2.9 a) comprises the longest lacustrine records in the Levant and represents the main hydrological and hydroclimatic archive in the southern Levant (Kaufman et al., 1992; Neugebauer et al., 2014). Based primarily on U/Th and ^{14}C chronologies, the lacustrine deposits date back to the early Pleistocene Lake Amora Formation with a basal age of >700 ka and a top age of ca. 140 ka. Lake Amora is followed by Lake Samra (ca. 140 ka to 70 ka), which is then followed by Lake Lisan (ca. 70 ka to 14 ka) and Lake Damya (ca. 14 ka to 12 ka) and ending with the Holocene Dead Sea (Abed, 1985a; 1985b; Waldmann et al., 2010; Torfstein and Enzel, 2017). The DSB lake level changes record the catchment hydrology and hydroclimate (Enzel et al., 2008), thus the reconstructed lake levels have been compared to other local and regional climatic records and showed good agreement with climate changes recorded in Northern Hemisphere (NH) ice cores (Kolodny et al., 2005; Torfstein et al., 2013b; Neugebauer et al., 2016) (Figure 2.10 d and e).

Lake Amora (ca. >700 ka to 140 ka) and Lake Samra (ca. 140 ka to 70 ka) levels are not yet well reconstructed (Waldmann, 2017), however, the current literature indicates high variability in the lake levels corresponding to global climate events (Waldmann et al., 2010; Neugebauer et al., 2014; Waldmann, 2017). During MIS6 (ca. 190 ka-130 ka) Lake Amora primarily deposited alternating aragonite and detrital laminae (indicative of high lake levels and fresh water input in the DSB (Stein et al., 1997; Bartov et al., 2002; Ben Dor et al., 2019), while the subsequent Lake Samra was primarily dominated by detrital and halite deposits (low lake levels). This observed lithological change indicates that wetter conditions prevailed during MIS6, compared to lower effective moisture conditions during MIS5 (Torfstein, 2017; Waldmann, 2017). These observations were also

confirmed by lithological investigations of a deep core recovered from the DSB central deep basin (DSDDP 5017-1) (Neugebauer et al., 2014) where halite and detrital deposits characterize the Samra formation. The later Lake Lisan (ca. 70 ka to 14 ka) is better investigated based on sedimentary exposures along the DSB margins (Kaufman et al., 1992; Bani Sakhir, 1996; Abed and Yaghan, 2000; Torfstein et al., 2013a). Lake Lisan reconstructed levels show that the DSB hydrology was directly affected by changes in the NH climate, primarily driven by ice sheet formation or break down, from glacial/interglacial scales to decadal and close-to-annual scales, where the highest lake level was achieved at ca. 26 ka to 24 ka during the Last Glacial Maximum (LGM) (see Chapter 4; 4.4.2). The reconstruction of the DSB lake levels generally indicates that glacials were characterized by higher P/E ratios and effective moisture availability in the wider catchment, while interglacials were the opposite (Machlus et al., 2000; Bartov et al., 2002; Torfstein et al., 2013b; Ben Dor et al., 2018).

In Soreq Cave (Sor. in Figure 2.9 a), the speleothem $\delta^{18}O$ and $\delta^{13}C$ records (Figure 2.10 c) are the longest in the Levant and cover several G/IG cycles (Bar-Matthews et al., 2003; 2017). The characteristics of the isotope records signify specific conditions for glacials and interglacials in the DSB, During glacials, the MIS6 $\delta^{18}O$ values fluctuated from -6 to -3 ‰ while the $\delta^{13}C$ values fluctuated from -12 to -10 ‰ suggesting dominance of C_3 vegetation. Overall, MIS6 was generally characterized by higher moisture compared to the last glacial.

During interglacial MIS5 the values are highly variable and three wet phases are recorded at ca. 128 ka to 120 ka (MIS5e), 109 ka to 100 ka (MIS5c) and 86 ka to 83 ka (MIS5a). On the other hand, the $\delta^{13}C$ record shows that during interglacials the values were -13 ‰ to -10 ‰ indicating dominant C_3 vegetation with an exception for the MIS5e period where the values change to ca. 0‰ associated with light $\delta^{18}O$ excursions (representative of precipitation amount) suggesting deluge events and high water flux into the cave. During the interglacials, particularly between sapropel deposition events, the $\delta^{18}O$ values were ca. 2-3 ‰ higher indicating increased aridity.

During MISs 4 to 2, the $\delta^{18}O$ values fluctuated from -5 to -2 ‰ and the $\delta^{13}C$ values fluctuated from -11 to -7 ‰ suggesting mixed C_4/C_3 vegetation, or the response to colder temperatures or reduced precipitation. During MIS3, wetter events are recorded at ca. 56 ka to 50 ka and 36 ka associated with Dansgaard–Oeschger (D-O) interstadials. Bar-Matthews et al. (1999) reported $\delta^{18}O$ peak at ca. 25 ka

corresponding to arid conditions, followed by another peak starting at ca. 21 ka and reaching a maxima at ca. 19 ka corresponding to the LGM. At 17 ka, an abrupt decline in the $\delta^{18}O$ was recorded corresponding to the deglaciation.

During the Holocene, light $\delta^{18}O$ values are recorded from ca. 10 ka to to 6.5 ka. Light $\delta^{13}C$ values of ca. -5 ‰ are observed at ca. 9.4 ka to 7 ka associated with light $\delta^{18}O$ values, similar to conditions during MIS5e, suggesting similar conditions of deluge events (Bar-Matthews et al., 2003; 2017). From 8.5 to 7 ka, low $\delta^{18}O$ values of -6.5 ‰ and high $\delta^{13}C$ values of -5 to -4 ‰ are recorded. This change is synchronous to early Holocene floods, related to sapropel S1 deposition in the EM. A short-lived phase is recorded from 8.2-8 ka represented by sharp decline (-4 to -11 ‰) in $\delta^{13}C$ values and a slight increase of 1‰ in $\delta^{18}O$ which can be related to a sudden cooling and decrease in rainfall. At 7 ka, the isotopic values become similar to those of present day (Bar-Matthews et al., 1999).

To the north, the Peqiin Cave (Peq. in Figure 2.9 a) speleothem $\delta^{18}O$ and $\delta^{13}C$ records (Bar-Matthews et al., 2003; 2017) indicated continuous speleothem deposition for the last 240 ka (Figure 2.10 c) suggesting continuous water availability in the unsaturated zone and annual precipitation of >300 mm, the threshold for speleothem deposition in the DSB (Vaks et al., 2013).

The Peqiin isotopic records are similar to the Soreq records and show similar climatic fluctuations. However, the Peqiin records suggest that the $\delta^{18}O$ values are ca. 1‰ enriched, compared to the Soreq values, at ca. 150 to 140 ka, 128 to 110 ka, and at 7.5 to 5 ka. The records also show lighter $\delta^{18}O$ values, compared to the Soreq records, by ca. 1‰ at ca. 100 to 94 ka, 89 to 60 ka, and at 45 to 26 ka. These differences are attributed to the local conditions of the two caves in terms of $\delta^{18}O$ gradient, vegetation cover and temperature (Bar-Matthews et al., 2003).

In Lebanon, northern Levant, palaeo-records recovered from speleothems dated by U/Th dating (Verheyden et al., 2008; 2017; Nehme et al., 2018) and lacustrine sediment cores dated using AMS ^{14}C dating and magnetic chronostratigraphy (Gasse et al., 2011) provided discontinuous environmental data spanning several G/IG cycles. From Kanaan Cave, located ca. 5 km to the east from the Mediterranean coastline (Kan. Jei. in Figure 2.9), speleothem $\delta^{18}O$ and $\delta^{13}C$ records were recovered spanning ca. 130 ka to 80 ka (Verheyden et al., 2017) (Figure 2.10 g). The record indicates wet conditions prevailed in Lebanon at the transition from the glacial MIS6 to the interglacial MIS5 at ca. 130 ka with indications of active vegetation. This period is followed by $\delta^{18}O$ enrichment from

ca. 126 ka to 120 ka probably as a result of moisture source change or severe drought conditions. Two other wet intervals were identified from ca. 108 ka to ca. 100 ka and from ca. 93 ka to 90 ka characterized by light $\delta^{18}O$ values. However, the record suggests generally humid conditions prevailed over Lebanon, hence northern Levant, during interglacial MIS5 and late MIS6 (Verheyden et al., 2017).

Based on a long core recovered from the Yammouneh Basin (Yam. in Figure 2.9 a) representing the longest record from the northern Levant, several G/IG cycles have been investigated (Gasse et al., 2011; 2015; 2017). Based on sedimentological, geochemical and pollen analyses, the record (Figure 2.10 f) indicated that during interglacials MIS7, MIS5 and MIS1, the northern Levant was under high effective moisture conditions when a productive water body was present in the Yammouneh Basin associated with expansions of wooded vegetation indicating wetter conditions prevailed (Gasse et al., 2017). MIS7 was characterized by large fluctuations, where the mid MIS7 was generally wet while the late MIS7 was drier than the mid MIS7. The glacial MIS6 was initiated with arid conditions, followed by higher precipitation availability from ca. 175-170 ka corresponding to Sapropel (S) S6 deposition. Another wet period was indicated after ca. 150 ka. During MIS5, three wetting phases were identified during MIS5-5, 3 and 1 corresponding to MIS5 Sapropel fomation in the Mediterranean Sea (S5, 4 and 3). The sapropel formation occurs during both glacials and interglacials suggesting periods of wetter conditions. These MIS5 wet phases were punctuated by drier steppic vegetation conditions. The wet periods during interglacials coincided with insolation maxima conditions and reduced ice sheets in the Northern Hemisphere. On the other hand, during glacials (MISs 4 and 2) the interglacial forests were replaced by steppic vegetation in the basin associated with erosional processess and increase in detrital carbon in the record. The period of MISs 4 to 2 was generally dry associated with aeolian deposition, lake dessication and steppic vegetation, with harshest conditions during MIS2. During the MIS3 period, only two wet periods were identified at ca. 60 ka and 45 ka. For the transition into the Holocene, a wetting period is indicated from ca. 16 ka to 8.5 ka characterized by woodland expansions in the basin and a trend towards lighter $\delta^{18}O$ values (Gasse et al., 2017).

In addition, speleothem $\delta^{18}O$ and $\delta^{13}C$ records from Jeita Cave (Kan. Jei. in Figure 2.9 a) spanning the Holocene indicate that the early Holocene was a wet phase from ca. 9 ka to ca. 6 ka (Figure 2.10 g). This period was followed by a drying trend, indicated by reduced speleothem growth, from ca. 6 ka to 4 ka. At ca. 4 ka

a return to wetter conditions is recorded and followed by a dry phase at ca. 3 ka to 1 ka indicated by a progressive decrease in soil activity and enriched $\delta^{13}C$ values (Verheyden et al., 2008; 2017).

Thus, the Lebanon records generally suggest that interglacials in the northern Levant were characterized by high moisture availability, while glacials were drier. Nonetheless, the degree of dryness and/or water availability fluctuated from one period to the other, probably reflecting the varied effects and degree of impact of local and global climatic conditions on moisture availability and the sites' specific responses to these changes. While, records from the southern Levant (see also section 2.4.2) suggest different climate and environmental conditions prevailed during the Quaternary where the DSB lake levels suggest wet glacials and dry interglacials, while other records (e.g. Soreq Cave) agree with the northern Levant records that suggest higher effective moisture availability during interglacials probably affected by changes in the track and intensity of the moisture sources (see 2.4.2).

2.4.1   Quaternary records, and gaps, of Jordan

This section presents the spatial and temporal extent of the Quaternary records from Jordan. It also presents the gaps in the records and justifies the need for further investigations.

Quaternary sediments are widespread in Jordan (Moumani et al., 2003; Cordova and Ames, 2017; Jones et al., 2021) making the country a focus of growing interest for studies with regard to palaeoclimate and the reconstruction of palaeoenvironmental conditions (Catlett et al., 2017; Ginat et al., 2018; Abu-Jaber et al., 2020; Al-Saqarat et al., 2020; Jones et al., 2021). Nevertheless, detailed information about the timing, climatic and environmental settings of such deposits is sparse and lacking (Jones and Richter, 2011; Cordova and Ames, 2017). The available Late Quaternary sedimentary record from Jordan, however, suggests complex climatic and environmental variations through time (Mischke et al., 2017; Abu-Jaber et al., 2020; Jones et al., 2021), where the Quaternary lake and wetland sediments associated with prehistoric artefacts in the Jordan desert are proof for different hydrodynamics in the region that is presently hyper-arid with scarce surface and groundwater resources (Al-Nahar and Clark, 2009; Jones and Richter, 2011; Al-Saqarat et al., 2020).

Quaternary records of Jordan comprise fluvio/wetland and lacustrine sediments that can be found across different geomorphic features such as in endhoric basins

(Qe'an) (Davies, 2005; Jones et al., 2021) and in tectonically evolved (e.g. pull-apart) basins (e.g. Al-Saqarat et al., 2020). In addition, extensive lacustrine sediments are found across the DSB (e.g. Kaufman et al., 1992; Abed and Yaghan, 2000) (Figure 2.9 b).

Starting from the southernmost records, where aridity presently prevails, fluvial-paludal sediments crop out east of the Gulf of Aqaba , at elevations of ca. 10-110 m asl, at the Ad Durra site, which presently receives ca. 50 mm.yr^{-1} rainfall (Figure 2.9 b). Poorly preserved ostracods of *Candona neglecta* and *Ilyocypris sp.* were found in the sediments but no age estimates were recovered (Abbas et al., 2016; Ginat et al., 2018).

In addition, a large palaeolake was reported in the Qa' Mudawwara area located ca.100 km east of the Gulf of Aqaba (Figure 2.9 b), and today receiving mean annual rainfall of ca. 50 mm.yr^{-1}. The surrounding wadis join to enter the Qa' as a series of clay pans. The Qa' lowest point, occupied by a large sebkha, is found in Saudi Arabia, whilst in Jordan, the lowest Qa' elevation is at ca. 673 m asl (Petit-Maire et al., 2010) and the highest at ca. 860 m asl (Catlett et al., 2017). Petit-Maire et al. (2010) recorded the presence of coquina layers at the upstream of a clay pan at altitudes of 718–720 and 700 m asl, from which, macrofossil (bivalves and gastropods) were recovered. *Cerastoderma glaucum* species, which tolerates salinity ranges of 3 ‰ and 60 ‰, was dominant. The gastropods comprised the salt tolerant *Hydrobia sp.*, and the fresh to oligohaline *Melanoides tuberculata*. Based on the sediments and the macrofossil assemblages location at elevations of 20 m higher than the clay beds, Petit-Maire et al. (2010) estimated a surface area of the proposed palaeolake to be > 2000 km^2 and ~40m deep. Freshwater bodies are thought to have existed from 170 ka to 150 ka (MIS 6) and from 125 ka to 77 ka (MIS 5) based on ostracods and Alpha-counting U/Th dating of eleven shells. The authors suggested that the proposed water bodies received water from both EM winter and monsoon summer rains (Petit-Maire et al., 2010). This suggests generally wet interglacial MIS5 prevailed in southern Jordan, in agreement with the northern Levant wet interglacials and the soreq records (see above).

Catlett et al. (2017), reported physical, chemical, and mineralogical composition and radiocarbon age estimates (4 samples) at ca. 29 ka BP to 21 ka BP from a 2.35 m sediment core from Kharbat Ratiya in Qa' Mudawwara. The sediment core was primarily composed of reddish siliciclastic sediments with <50% sand content

with ca. 30 to 40% clay and silt contents. Based on XRD analysis, the authors reported the presence of quartz, kaolinite and calcite. The calcite $\delta^{13}C$ and $\delta^{18}O$ values were in the range of 0.16 to 2.58 ‰ and 0.52 to 4.59 ‰, respectively. The nature of the sediments and their low organic carbon content (0.06 to 0.17%) led the authors to suggest that the record represents a dry evaporative playa possibly similar to present-day conditions in the area, where the slight variability in the sediments composition probably reflect small changes in precipitation and erosion. The authors proposed that the playa was flooded with stream water that overflowed through the drainage network. The authors suggested that the synchronous of this erosional and depositional phase in the area with high lake levels in the DSB and wetter conditions in central Jordan suggests that the main moisture source was the EM cyclones rather than a southern intensified source (Figure 2.9 b).

Two previous studies reported OSL age estimates of 112±9 ka (MIS 5) and 32.5±0.8 ka (MIS 3) (Mischke et al., 2017) and 125 ka to 75 ka (MIS 5) (Al-Saqarat et al., 2020) from the fine-grained sediments of the Gharandal Valley (Figure 2.9 b) and reported wetter conditions, compared to the present, persisting during these periods (see Chapter 4; 4.3.6). In Wadi Araba, Le Béon et al. (2012), at a location ca. 15 km north of the Gharandal Valley, suggested a humid alluviation and hydrological activation period at ca. 163±19 ka (MIS 6) based on [10]Be cosmogenic dating of alluvial surfaces near Al-Risha town.

More recently, Abu Jaber et al. (2020) reported the presence of a lake, covering an area of ca.30 km^2 and ca. 50 m deep at its deepest, in the presently arid Petra region to the northeast of the Gharandal Valley (Figure 2.9 b). The authors argued that this lake existed from ca. 70 ka to 9 ka (MISs 4 to 1) based on 18 OSL age estimates from 5 localities, the characteristics of the sediments and fossil assemblages (e.g. gastropods) providing evidence of significantly wetter conditions and an open lake system with short residence time as suggested by the carbonates $\delta^{18}O$ and $\delta^{13}C$ weak covariance, during the late Pleistocene to Holocene in the area (Abu-Jaber et al., 2020).

In the Qa' Jafr (Figure 2.9 b), covering ca. 13500 km^2 (Rech et al., 2017), surface deposits consist of fluvial, aeolian, and lacustrine sediments. Mudflat sediments are found in the north of the basin, while, the surroundings comprise fluvial gravels, sandy limestones, marls, lacustrine limestones, and gypsum. Davies (2005) analysed a 31 m sediment core from the Qa', at 847 m asl. The results

showed that the Jafr sediments record various episodes of deposition. $CaCO_3$ cementation, fibrous gypsum bands, and peaks of sulphur and strontium indicated that periods of elevated moisture were followed by fluctuating events of intense evaporation. Based on two ^{14}C age estimates of charcoal, the age of wet phases was estimated at 24±0.2 ka and 16±0.1 ka (MIS 2) (Davies, 2005).

Mischke et al. (2015) recovered ostracod shells of *Candona neglecta, Ilyocypris* cf. *bradyi, Pseudocandona* sp., and *Heterocypris salina* with charophyte algae from the Jafr marls alongside two ^{14}C age estimates of biogenic carbonates at 42.4±0.3 ka and 33.9±0.2 ka (MIS 3). The authors suggested that wetland conditions prevailed in Qa' Jafr area probably during MIS3 (Mischke et al., 2015).

McLaren et al. (2004) dated a sequence of alluvial fans, fluvial terraces and aeolian sediments near the Hamra Faddan area (Figure 2.9 b). Through ^{14}C and OSL age estimates, aeolian sediments were dated to ca. 13.7 cal ka BP, indicating a dry period with reduced moisture availability. Early Holocene perennial meandering stream deposits suggested that enhanced effective moisture (wetter) conditions dominated from about 9.5–8 cal ka BP. Arid climatic conditions were indicated by a wind-blown unit after 7.4 cal ka BP. In addition, four OSL age estimates, at 22±1 ka to 21±2 ka and at 14±1 ka to 12±1 ka, were recovered from sedimentary sections of fine-grained deposits in the Hamra Faddan area (Al-Shdaifat, 2015; Ginat et al., 2018). A shallow wetland environment was suggested for the Hamra Faddan area based on the sediments' characteristics and ostracod species, primarily of *Candona neglecta, Pseudocandona sp.*, and *Ilyocypris sp.* (Al-Shdaifat, 2015; Ginat et al., 2018).

In Wadi Hasa, in west-central Jordan (Figure 2.9 b) running westwards to the southeastern margin of the Dead Sea, with a catchment of about 2520 km^2, Clark (1984) documented Late Quaternary lacustrine deposits and argued for the presence of a 'Pleistocene Lake Hasa' that existed from 70-20 ka based on ^{14}C age estimates of charcoal and organic matter. The author suggested that the lacustrine deposits represented a palaeolake over 15 km long and about 200 m deep. Pleistocene Lake Hasa was interpreted to have dried at about 20 ka (Schuldenrein and Clark, 2001). However, Winer (2010) studied the Hasa sediments' organic material and microfossils (gastropods, ostracod and bivalves) and based on stratigraphic relationships and radiocarbon/amino acid racemization of ostracods and ^{14}C age estimates of charcoal and organic matter, identified several time stratigraphic units, at >100 ka, ca. 70-45 ka, ca. 32-27 ka and ca. 14-

12 ka, constraining periods of enhanced wetness and wetland conditions in the Wadi (Winer, 2010).

In Jurf Darawish (Figure 2.9 b), Moumani et al. (2003) proposed the presence of a lake, based on sedimentological analyses and the presence of ostracod, charophytes and gastropods, that prevailed at 111±14 ka, 57±4 ka and 39±3 ka based on three OSL age estimates.

In the DSB, exposed Quaternary lacustrine sediments are extensive, nonetheless studies from the eastern DSB are scarce. Based on 7 ^{14}C age estimates, Landmann et al. (2002) investigated two laminated lacustrine sediments from the southern and northern DSB and reported that a lake level decrease and gypsum deposition occurred at ca. 36 cal. ka BP and at ca. 17 cal. ka BP to 15 cal. ka BP. The authors suggested that the lake level decrease was the result of reduced EM cyclones, however, considering the lake levels during these periods, the moisture availability was higher compared to the present-day conditions. Abed and Yaghan (2000) investigated a section from the DSB and used varve counting and lithological characteristics of the lacustrine deposits and suggested a dry LGM prevailed in the DSB at ca. 23 ka to 15 ka, representing the driest period prior to the final lake level decline. The authors argued that the gypsum in the section was deposited under drier (reduced moisture) conditions, compared to the wet interglacials. More recently, Ghazleh and Kempe (2021), based on lake shoreline terraces and U/Th dating, suggested that the lake stromatolites from the DSB for the past ca. 80 ka record periods of both enhanced and reduced moisture avilability. The authors reported that the highest lake level achieved was ca. 0 m asl during MIS5 (at 87 ka to 75 ka BP). The authors suggested drier conditions during MIS4 and MIS2, compared to MIS5 and MIS3, nonetheless the authors reported relatively wetter conditions and lake level rise during the LGM followed by a lake level drop at ca. 11 ka (Abu Ghazleh and Kempe, 2021).

In the northeastern Jordanian desert, several localities in the Badia (Jones et al., 2021) and across Qa' Al-Azraq (Figure 2.9 b) are filled with Quaternary sediments (Jones et al., 2011; Cordova et al., 2013). The Al-Azraq Oasis lies in the lower reaches of Al-Azraq Basin and is fed by springs. This basin presently receives <100 mm.yr^{-1} precipitation (Ibrahim and El-Naqa, 2018). Jones and Richter (2011) investigated sediments from Ayn (spring) Qasiyya in Al-Azraq Basin and provided a record of environmental changes spanning the last glacial to interglacial (ca. 60000 yr.). The authors reported environmental changes between drier and wetter

conditions, where the wettest period was prior to the LGM, while a marsh environment prevailed during the LGM. The authors also suggested a drought period, probably similar to present-day conditions and dry springs, from 16 ka to 10.5 ka. The authors also emphasized the role of groundwater recharge and spring discharge in maintaining the environment at most times, even under harsh climate conditions, and reported that the harshest conditions in the area prevailed during the North Atlantic Bölling–Allerod (Jones and Richter, 2011) rather than during the LGM as reported for the southern Levant by other authors (e.g. Abed and Yaghan, 2000; Bar-Matthews et al., 2003).

Also, from the Azraq Basin, Cordova et al. (2013) recorded climatic fluctuations from lake to marsh and periods of dryness for a sedimentary sequence from Qa' Al-Azraq spanning ca. 160 ka to 15 ka, with wet periods primarily corresponding to MIS5a and early MIS4. However, the authors also reported wet periods (marsh environment) during times that are asynchronous to other regional records during late MIS3 and early MIS2. More recently, Jones et al. (2021) reported the first age estimates and sedimentological and geochemical data for sediments from three Qe'an (Wisad, Qattafi and Shubayqa) located in the Jordanian eastern Badia (Figure 2.9 b), spanning the last 15,000 years, the Pleistocene-Holocene transition. The results indicated the significance of these Qe'an as potential palaeoenvironmental archives for environmental changes in the Badia in relation to the archaological sites and the changing environmental conditions.

As mentioned earlier (Chapter 1; 1.3), distinguishing between lakes and wetlands is essential especially when dealing with arid to semi-arid environments (Pigati et al., 2014; Parton et al., 2018). Thus, the previously mentioned palaeolakes of Hasa, Mudawarra and Jafr were recently reinterpreted as wetlands by Rech et al. (2017). The authors argued against the assumption of a large perennial lake in Mudawwara, as the occurrence of such a lake at a site where the present evaporation is about 2000 $mm.yr^{-1}$ would imply an estimated inflow of 4000 $MCM.yr^{-1}$. Also, no shorelines have been detected and the coquina beds were constrained to one side of the area, thus making it hard to define the exact environment of the Qa' Mudawwara. The authors also questioned the ages recorded by Petit-Maire et al. (2010) and whether the bivalve shells were a closed system with respect to uranium (Rech et al., 2017). More recently, Mischke et al. (2021) revisited the Jerf Ed Darawish sediments and reported new OSL age estimates, ostracod valves primarily of *Ilyocypris*, *Potamocypris*, and *Pseudocandona,* gastropod shells and charophytes and reported that the

sediments represent an in-stream wetland rather than a lake with wet conditions prevailing at ca. 90 to 70ka (MIS5), 68 to 59 ka (MIS4) that was followed by a more vegetated plain during MIS3. The authors also reported artefacts from sediments dated at 85 to 65ka indicating human presence in the area (Mischke et al., 2021).

Overall, the aforementioned Quaternary records of Jordan are sparse, in space and time, contradictory in terms of spatial and temporal relationships, and no high resolution long term records exist (Figure 2.11), making it challenging to develop a comprehensive understanding of Quaternary climate variability of Jordan.

A particular discrepancy in southern Jordan records are studies on the DSB lake sediments. Quaternary records for the western DSB basin lakes and speleothems are extensive (Bartov et a., 2002; Vaks et al., 2006; Landmann et al., 2010; Bar-Matthews et al., 1993; and references therein). On the other hand, there are only two records from sedimentary exposures and terraces with radiometric ages from the eastern (Jordanian side) DSB. However, records from both sides of the basin are contradictory and debates are present regarding periods of enhanced/reduced moisture availability over the DSB and lake level changes. Thus, improving the Quaternary records from Jordan will add significant information and allow a better understanding of this important region's hydrodynamics and environmental variability.
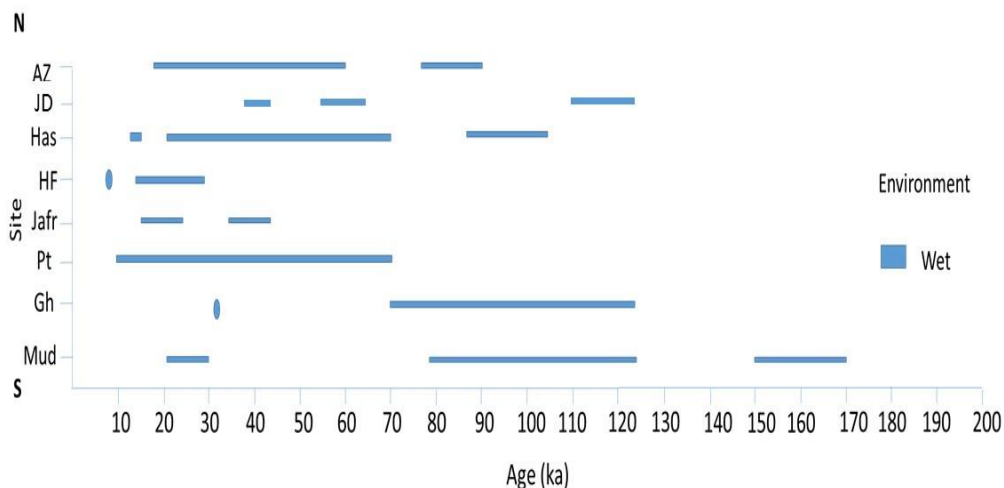
Figure 2.11 Synthesis of the Quaternary records from Jordan. **Mud:** Qa' Mudawwara (Petit-Maire et al. (2010); Catlett et al. (2017)), **Gh:** Gharandal (Mischke et al. (2017); Al-Saqarat et al. (2020)), **Pt**: Petra (Abu Jaber et al. (2020)), **Jafr**: (Davies (2005); Mischke et al. (2015)), **HF**: Hamra Faddan (McLaren et al. (2004); Al-Shdaifat (2015); Ginat et al. (2018)), **Has**: Wadi Hasa (Clark (1984); Schuldenrein and Clark (2001); Winer (2010)), **JD**: Jurf Darawish (Moumani et al., 2003), **AZ**: Qa' Al-Azraq ((Jones and Richter (2011); Cordova et al. (2013)). For locations refer to Figure 2.9 b.

2.4.2 Quaternary synoptic scale and moisture sources

The previously discussed records suggest that an anti-phase is present between the northern and southern Levant, and even within Jordan, during certain time periods; e.g. the LGM, MIS3 and MIS6. Generally, northern Levant records suggest wet interglacials and dry glacials where the main moisture source is suggested to have been the EM cyclones reaching the northern Levant, while during glacials, the expansion of the Eurasian ice sheets reduced the cyclones intensity and depth into the Northern Levant (Gasse et al., 2017). On the other hand, the expansion of ice sheets resulted in a deflection of the EM cyclones track to the south and resulted in intensified cyclones reaching the DSB which explains the high lake levels in the DSB during glacials and the lower lake levels during interglacials (Enzel et al., 2008; Torfstein and Enzel, 2017). Nonetheless, Abed and Yaghan (2000) and Ghazleh and Kempe (2021), based on records from the Jordanian side argue that interglacials were wetter over the DSB and higher lake levels were achieved.

Considering the northern and southern Levant, an anti-phase relationship can be deduced based on two different inferences, of precipitation amounts in the north and lake levels in the south, while when considering only precipitation amounts from the northern and southern speleothem records (e.g. Bar-Matthews et al., 2003; Verheyden et al., 2017) this proposed anti-phase, during LGM for example,

does not seem to be present where both records indicate lowered precipitation amounts. This was also suggested by Miebach et al. (2017) who reported palynological data for the period ca. 28 to 22.5 ka cal BP from Lake Tiberius (Sea of Galilee) indicating the dominance of steppe vegetation and semi-arid to arid conditions during MIS2, which has been also suggested by Abed and Yaghan (2000). Accordingly, this needs further, well dated and resolved multi-proxy records from the Levant to contribute to this debate.

In addition, this understanding of EM cyclones role in providing precipitation over the Levant during the Quaternary does not fully explain the moisture sources for Quaternary wetlands and lakes in the southern Levant, located to the south of the DSB where the EM cyclones do not reach today. Enzel et al. (2008) argue that EM cyclones track and depth during past times was similar to the present-day and could have reached as deep as the northern Negev Desert and not farther south, thus other hypotheses have been presented to explain the moisture reaching the presently arid southern Levant.

For instance, Enzel et al. (2008) argue that the ATPs (winter precipitation) (see 2.2) are responsible for wetter periods in the Negev Desert during periods of the Quaternary. Presently, the effect, depth and frequency of these cyclones are not well studied in the Levant (Kushnir et al., 2017). While others (e.g. Petit-Maire et al., 2010) suggested combined northern (EM cyclones) and southern moisture sources reaching the southern Levant during different times in the Quaternary. Furthermore, in southern Jordan, Catlett et al. (2017) argued that EM cyclones were the main moisture source reaching as far south as the Mudawwara area during LGM, as the ARST convective storms would have decreased or stopped due to the low temperature during the glacial period which in turn stabilizes the RST, however, studies from Arabia (e.g. Parton et al., 2015a) reported a northward intrusion of the monsoon precipitation into Arabia during the glacial MIS6 corresponding to the monsoon intensity at ca. 160 to 150 ka.

In addition, the suggested southern monsoon moisture source during peak interglacials (e.g. during MIS5e; Kiro et al., 2020) or the Holocene optimum (e.g. Moustafa et al., 2000; Waldmann et al., 2010) probably suggest that summer seasons were more rainy.

Thus, the main moisture sources during the Quaternary are still a debate and more records from the southern Levant (e.g. southern Jordan) will contribute important information regarding these discrepancies.

2.5   Chapter conclusions

The location of the Levant and its physiography provide it with unique climatic settings where the northern and central Levant receive precipitation primarily from the EM cyclones, while the southern Levant, where Jordan is located, receives rare precipitation from southern tropical origins.

These characteristics have given the Levant, and Jordan in particular, high significance as a focal point for Quaternary environmental and climate reconstruction studies. However, Quaternary records from Jordan are scarce, sporadic and contradictory to some extent. In Jordan, no long well dated records are present and the available records suggest complex climatic and environmental conditions prevailed during the Quaternary. To address this gap in our understanding, this thesis presents records from two sites. The methods used are set out in Chapter 3.

Chapter 3. Methodology

3.1 Introduction

This chapter presents the study areas' selection and methods used for fieldwork, sampling, laboratory analyses and interpretation of the results. All analyses have been conducted by the author unless otherwise stated.

3.2 Selection of the study areas

As discussed in Chapter 2 (2.4.1), Quaternary deposits in Jordan can be found in different geomorphic features spread over different localities. Accordingly, the two study sites discussed here were chosen to represent two different hydrological systems.

3.2.1 The Gharandal Valley

The Gharandal Valley is one of the main locations in Jordan where sedimentary sequences of apparent Quaternary age are found. By the time this project started, one previous preliminary study had reported 2 OSL age estimates (ca. 112 ka and 32 ka) from the Valley (Mischke et al., 2017) with ostracod data indicating that different hydrodynamics prevailed in the valley during different times in the past. Thus, this study area was chosen as it comprises thick (ca. 30 m) sedimentary sequences of fluvial/wetland deposits and could provide significant information about the Quaternary environmental variability of southern Jordan.

3.2.2 The Dead Sea Basin (DSB) lacustrine Sequence (DS1)

The DSB comprises extensive Quaternary deposits that date back to >740 ka (Torfstein, 2017). These lacustrine sequences are subdivided into different formations, each representing a separate lacustrine environment with its distinct history and limnology.

Due to the scarcity of records from the eastern side of the basin, a need to improve the eastern records is apparent due to contradictory results from both sides of the basin (Torfstein et al., 2013a; Abu Ghazleh and Kempe, 2021) (see Chapter 2, 2.4). Accordingly, the DS1 section was chosen at the eastern side of the DSB to provide new data and contribute to understanding the apparent discrepancies between records from either side of the basin.

The two chosen study sites comprise sediments that are primarily comprised of siliciclastic, carbonates and/or evaporite deposits. As discussed in Chapter 1 (1.2), the physical and geochemical compositions of these sediments can provide

significant information regarding the specific depositional environments, hydrodynamics and the prevailing climatic conditions.

Thus, the methodological approach in this research was drawn to investigate the aforementioned variables and to produce detailed proxy records for the Gharandal Valley and the lacustrine DS1 section sediments.

3.3 Fieldwork and sampling

The fieldwork focused on lithological investigations of the sections and sampling during August, 2018 and January, 2019, in the Gharandal Valley and the Dead Sea Basin, respectively. Sections were cleaned and the surface material was removed.

Considering the nature of the sedimentary sequences, the sampling was conducted following two different approaches.

3.3.1 The Gharandal Valley

A month of extensive fieldwork was undertaken during August, 2018. Five sections (Figure 3.1) were chosen, two of these (GH1 and GH2) were sampled at high resolution (continuously at ca. 2 to 10 cm resolution), while, three sites (GH3, GH4 and GH5) were sampled based on lithological changes and thickness of beds. In all cases, samples of ca. 30 to 200g were collected in plastic bags.

Due to the steep cliffs of the Gharandal Valley GH1 and GH3 sections, the sampling of sediments was done laterally from bottom to top. Sub sections (e.g. Figure 3.2) were cleaned, the sedimentary beds were assigned based on lithological variations and described in terms of texture, colour and sedimentary structures (if present). Lateral distances between the sub-sections were ca. 0.7 m to 1.5 m, depending on the steepness of the cliff.
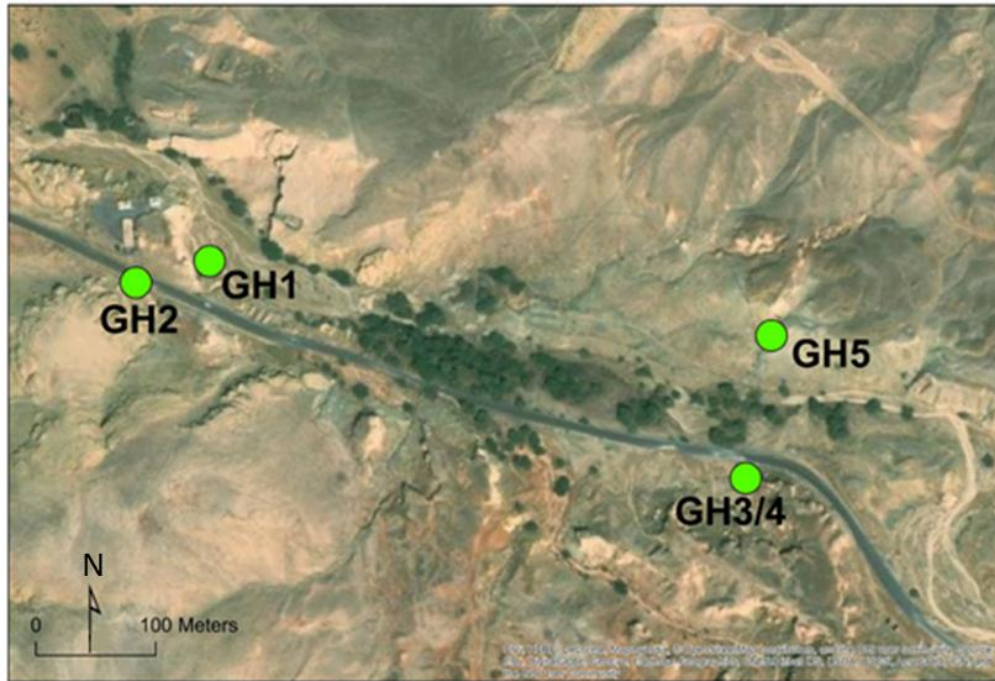
Figure 3.1 Google Earth Image of the Gharandal Valley showing the locations of the sedimentary sections chosen for this project.
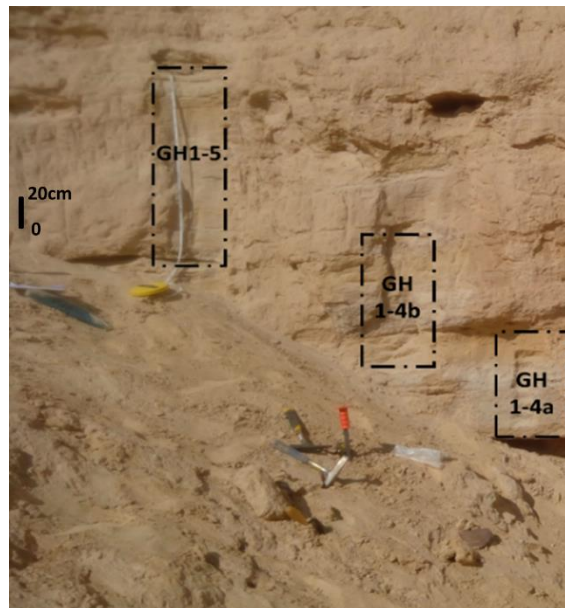
Figure 3.2 Sub-sections of the GH1 sedimentary sequence, showing the steep cliff.

Inspite of the steepness of the GH2 sequence, a complete section was cleaned from bottom to top using a pick and a diesel-fuelled hammer (Figure 3.3). The section was described similar to the GH1 section, and sampled continuously at intervals of 2-10 cm covering the complete, ca. 13.25 m, section. The GH3, 4 and 5 sections were sampled at intervals of 10-30 cm, based on the lithological variations of the beds.

A total of 548 bulk sediment samples were collected from the five sedimentary sections. The samples were labelled and transported into plastic boxes for air shipping to the School of Geography at the University of Nottingham under a DEFRA licence.

Figure 3.3 The GH2 sedimentary sequence (ca. 13.25 m) and sampling process.

3.3.2   The Dead Sea Basin (DSB) Sequence (DS1)

The DS1 section was sampled during a field trip in January, 2019. Considering the laminated nature of the sediments (Figures 3.4), a custom made 5 x 5 x 35 cm sampling box was used, following a sampling method used for laminae sampling from sections developed by Prof. Achim Brauer (pers. comm.). The 4.6 m section was sampled in 16 box samples. The samples were wrapped with thick aluminium foil to preserve the original lamination and to keep the samples from breaking. The samples were then transported into thick plastic boxes and air shipped to the School of Geography, University of Nottingham.

Figure 3.4 DS1 section laminated sediments sampling. Shown is the lower part of the section and the custom made sampling box (5 x 5 x 35 cm) used for the sampling procedure.

3.4   Sedimentary facies analysis

Field observations of both fluvial/wetland and lacustrine sediments can be used in order to differentiate vertical sedimentary facies to provide a first order reconstruction of the sedimentation processes and hydrodynamics in a specific basin (Miall, 1977; 1996; Dercourt and Paquet, 1985; Zieliński and Goździk, 2001; Makhlouf and El-Haddad, 2006; Alçiçek et al., 2007). A sedimentary facies is assigned to reflect the physical, chemical and palaeontological characteristics of a sedimentary deposit (Dercourt and Paquet, 1985; Makhlouf and Abed, 1991; Makhlouf and El-Haddad, 2006). For fluvial, primarily clastic sediments, the classification into gravel, sand and fines done in the field, accompanied by the sedimentary structures, can be used to assign specific facies that represent the vertical changes in the depositional conditions and hydrodynamics (e.g. Miall, 1977; 1996; Khalifa, 2005; Makhlouf and Abed, 1991). In some instances, mixed compositions can be observed, where gravel beds may contain sand or when sand beds may contain gravel-sized clasts. These beds can be identified based on the

dominant particle size composition to further distinguish them from the underlying and overlying beds (Miall, 1996).

The first order identification of the sedimentary lithofacies, based on field observations from the two study sites, was then confirmed based on the sediments' granulometric and geochemical compositions using a second order, quantitative multivariate statistical approach (e.g. Jungmann et al., 2011; He et al., 2019; Oyedotun, 2020) . This approach was used by He et al. (2019) to reclassify core lithology-based sedimentary facies. In their study of the Precipice Sandstone and Evergreen Formation in Australia, they simplified 20 core lithology-based sedimentary facies into 10 facies reflecting their common characteristics by applying the Principal Component Analysis - Linear Discriminant Analysis (PCA-LDA) approach.

PCA is applied to identify the main parameters governing the covariance in the sediments granulometric and chemical composition. The validity of applying PCA for the dataset was tested using Detrended Correspondence Analysis (DCA). The DCA was applied and based on the primary axis length of < 2 SD, the linear PCA was chosen here. Redundant features, and features that are not distinctive, are removed. The features representing the main drivers of the variance are then used for the LDA to increase value discrimination. It packs each group tightly by projecting its distinct values (inner-scatter matrix) while other values from different groups are aligned far away. LDA particularly decreases the feature space dimensionality. The PAleontological Statistics Software (PAST, v. 4.03 (Hammer et al., 2001)) was used to run the PCA and LDA analyses. This step was conducted to confirm the field-based lithofacies and to statistically derive the primary drivers of the different lithofacies. Following this, the sediments were then classified based on the sedimentary structures, where present, following lithofacies codes in the literature (e.g. Miall, 1996).

3.5   Markov-chain analysis of depositional cycles

In general, the concept of sedimentation cyclicity implies that any subsequent state (lithofacies) is dependent, to some extent, on the initial state (Tewari et al., 2009). A Markov chain defines a sequence of events, in which the occurrence of a state may be dependent on the previous one (Powers and Easterling, 1982). Accordingly, Markov chain analysis has been used in the investigation of lithostratigraphic vertical relationships where the presence of a Markovian characteristic implies order in the system (e.g. Staňová et al., 2009; Tewari et al.,

2009; He et al., 2019). The facies transitions were conducted following the Walker method (Ndiaye, 2007) (Figure 3.5).
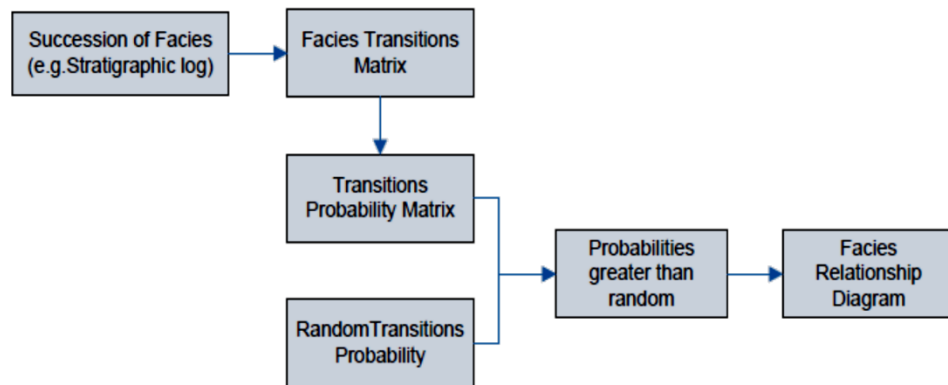
Figure 3.5 Walker method for facies transitions flow diagram (from Ndiaye, (2007)).

The input data is the observed upward lithologic transitions in a stratigraphic sequence regardless of the thickness (embedded matrix) to reduce the analytical errors. From this input data, a facies transition matrix can be generated. A first step is to test the input data for randomness through the application of a Chi-square (x^2) test with the null hypothesis that the data is random. If the x^2 computed values is higher than the critical x^2 value then the data is not random (the null hypotheis is rejected).

These transitions (transition matrix) are then calculated as probabilities (probability matrix) and as a random probability matrix calculated to a computed random sequence. In the latter step, the probabilities are caluclated based on the assumption that all transitions are random.

Following this, the observed and random matrices are used to generate a matrix of higher than random probabilities. The latter matrix is then used to generate a Facies Relationship Diagram (FRD) which is used for the interpretation of the cylicity model.

The Markov-chain analysis was conducted using Strati-Signal software (Ndiaye, 2007) to test the vertical relationships, particularly amongst the Gharandal Valley deposits where variable and more complex depositional units were observed in the field, compared to the DS1 section.

3.6   Laboratory Methods

The laboratory work is subdivided based on the different nature of the sediments from the two study areas.

3.6.1 Chronology

Accurate chronology is an important tool in the study of palaeoenvironments, as determining the age of the sediments will set the environmental proxies within a known period, allow for further correlation with local and regional records from similar time periods, and possible links with recorded climatic events.

Different methods can be used to date sediments (wetlands and lakes), whilst the most common are ^{14}C radiocarbon dating (e.g. Metcalfe et al., 2002; Rech et al., 2017), U/Th dating (e.g. Haase-Schramm et al., 2004; Dean et al., 2015), and Optically Stimulated Luminescence (OSL) dating (e.g. Mischke et al., 2017; Abu-Jaber et al., 2020; Al-Saqarat et al., 2020).

3.6.1.1 Optically Stimulated luminescence (OSL) Dating

In this research, OSL dating was implemented for the Gharandal Valley sediments due to the nature of the sediments and richness of quartz. Mischke et al. (2017) attempted radiocarbon (^{14}C) dating on four organic-rich samples from the Gharandal Valley. Nonetheless, they stated that the samples were not in stratigraphic order and attributed this to contamination with younger organic carbon which resulted in much younger ages for some samples than obtained using OSL (Mischke et al., 2017). Thus, OSL dating for the Gharandal Valley sediments seems more reliable. However, even OSL dating from the Gharandal Valley is not straight forward, where Al-Saqarat et al. (2020) reported OSL age estimates that are not in stratigraphic order, thus, understanding the valley hydrodynamics and the nature of the sediments is significant in order to contruct a robust OSL chronology (see Chapter 5).

The OSL dating presented here was conducted at the luminescence dating laboratory at the China University of Geosciences, Wuhan, by Dr. Mahmoud Abbas.

Samples were collected using opaque tubes, ca. 25 cm long, hammered into the clean sections and covered directly afterwards to avoid any exposure to light. The samples were then air shipped to the luminescence dating laboratory at the China University of Geosciences. In the subdued red light in the laboratory, the samples were opened and ca. 3-4 cm from both sides of the tubes were removed to ensure that the rest of the sample was protected and not been subjected to daylight or any light source during sampling or transportation. The rest of the tube samples were used for further analysis. Pretreatment with 10% HCL for three days was conducted to remove the carbonate material, and two weeks pretreatment with

38% H_2O_2 to remove the organic material. The particle size fractions of 90-125 µm were used for hydrofluoric acid (HF) etching for 40 minutes in order to dissolve feldspars. In addition, the samples were pretreated with 10% HCl to remove any acid-soluble fluoride precipitate (Lai and Wintle, 2006). The quartz grains purity was confirmed through infrared stimulated luminescence (IRSL) (Lai et al., 2009; Yu and Lai, 2014) and the results showed that none of the samples had any notable amount of feldspars.

Then, the pretreated particles were mounted on stainless steel disks (1 cm diameter), on the centre part (~0.5 cm diameter), using silicone oil. An automated RisØ TL/OSL-DA-20 reader, equipped with blue diodes (ʌ=470±20nm) and IR laser diodes (ʌ=830nm), was used for the OSL measurements. The luminescence was stimulated by blue LEDs at 130 °C for 40s, and detected using 7.5 mm thick U-340 filter (detection window 275-390nm) in front of the photomultiplier tube (Yu and Lai, 2014). Neutron activation analysis (NAA) was used to measure the U, Th, and K concentrations. For each sample, the cosmic-ray dose rate was estimated as a function of depth, geomagnetic latitude and altitude (Lai and Wintle, 2006).

The determination of the equivalent Dose (De) was done using single aliquot regenerative-dose (SAR) protocol (Murray and Wintle, 2000; Lai, 2006; Yu and Lai, 2014) through the use of an automated RisØ TL/OSL-DA-20 reader. 6 aliquots were measured for each sample to generate 6 growth curves. Then, using more aliquots, the values of standardized natural signal (LN/TN) were measured, under similar measuring conditions of the SAR protocol (Lai et al., 2013). All De values were less than 100 Gy.

3.6.1.2 U/Th Dating

U/Th dating is used in this research to recover the age estimates of the lacustrine sediments from the DS1 section. This method was chosen based on previous research on DSB sediments. The general U concentrations of >2 ppm of previously studied lacustrine sediments from the DSB (Kaufman et al., 1992; Haase-Schramm et al., 2004; Torfstein et al., 2013b) have allowed the application of U/Th dating to retrieve age models from these sediments. Nonetheless, dating of these carbonates can be problematic; the U-Th isotopic system is influenced by the presence of initial hydrogenous Th and detrital Th and U. Based on previous work (Haase-Schramm et al., 2004) on the Lisan Formation carbonates, hydrogenous Th is present and can be attributed to the formation of Th-hydroxyl complexes following the stabilisation of Th in the lake water, assuming a pH value

similar to the present Dead Sea (pH~6.1). However, since the early attempts at implementing U-series dating on Lake Lisan sediments (e.g. Kaufman et al.,1992), these problematic contributions have been addressed and corrected for, for example using isochron methods and trace element evaluation (Haase-Schramm et al., 2004), and single sample calculations (Haase-Schramm et al., 2004) and including the use of small (100 mg) samples to allow targeting of clean carbonates (Torfstein et al., 2013b).

This project follows similar methodological approaches to the previous studies. Following discussions with Dr. Diana Sahy at the British Geological Survey (BGS), and based on the relatively high U concentrations reported for the sediments from the DSB, ca. 15 mg of clean carbonates were targeted for the U/Th dating analysis in an attempt to reduce the potential contributions of detrital Th and U. As an addition to methods used by previous researchers, prior to sub-sampling for U/Th dating, Scanning Electron Microscopy (SEM EDS) analysis was conducted on the selected sediments to ensure clean carbonates are used (see section 3.6.3.1).

Clean aragonite laminae were identified using SEM EDS analyses, placed in glass vials and transported to the Geochronology and Tracers Facility of the NERC Isotope Geosciences Laboratory at the British Geological Survey (BGS). The samples preparation was done by the author and Dr. Diana Sahy while the analysis was conducted by Dr. Diana Sahy. Following dissolution in 8M HNO_3, samples were centrifuged to isolate any detrital silicates, which were dissolved in 29 M HF and 16M HNO_3 mixture, (1:4) dried down, re-dissolved in 8M HNO_3 and re-combined with the respective acid-soluble carbonate fractions. Samples were spiked with a mixed ^{229}Th–^{236}U isotopic tracer. The tracer is calibrated against gravimetric solutions of CRM112a U and Ames laboratory high purity Th, left to equilibrate overnight on a hotplate at 100ºC, and dried down. In order to remove any organic matter, samples were refluxed in a mixture of 10 M $HClO_4$ and 16 M HNO_3 (1:5) overnight at 100ºC and the dried down over 24h, increasing the temperature to 150ºC for the final 10h to ensure evaporation of the $HClO_4$. Through Fe co-precipitation, U and Th were pre-concentrated, and separated using Edwards et al. (1987) HCl-based anion exchange procedure on EichromAG-1 ×8 resin. Th and U fractions were oxidized twice in 16M HNO_3 with a small amount of 30% H_2O_2 and dissolved in 1 ml 0.1M HCl + 0.035 M HF for mass spectrometry. Prior to mass spectrometry measurements, all fractions were filtered using 0.45 µm pore-size syringe filters to remove any particles and prevent blockages in the sample uptake system. Isotope ratio measurements were done

on a Thermo Neptune Plus multi-collector ICP-MS, according to the Crémière et al. (2016) protocols. U–Th age calculations were performed using an in-house Excel spreadsheet with the ^{230}Th and ^{234}U decay constants of Cheng et al. (2013), and a detrital correction based on (^{232}Th/^{238}U) = 1.2 ± 0.6,(^{230}Th/^{238}U) = 1.0 ± 0.5, and (^{234}U/^{238}U) = 1.0 ± 0.5 (all uncertainties quoted at the 2σ level). Following this, a Dead Sea lacustrine sediments-specific correction for detrital Th was applied following the work of Haase-Schramm et al. (2004).

3.6.2 Methods applied on sediments from the two study areas

3.6.2.1 Laser particle size analysis

Particle size is directly related to the dynamic conditions of transportation and deposition, therefore, the grain size distribution of the siliciclastic components is a vital characteristic and can be implemented to infer climatic changes and environmental evolution over space and time. Grain size characteristics have been extensively implemented by researchers to reconstruct the modern (Passega, 1964; Passega and Byramjee, 1969; Hazermoshar et al., 2016) and palaeo (Basanta K. Sahu, 1964; Passega and Byramjee, 1969; Skaberne, 1996; Saffarini and Amireh, 2016) hydrodynamics and depositional processes in different settings around the world.

From each sample, 30g were sieved using -1ϕ (2 mm) sieve and a shaker to separate the fine (<-1ϕ (2mm), sand, silt and clay) fraction from the coarser (>-1ϕ (2mm), gravel) fraction.

After sieving, the coarse fraction (>-1ϕ (2mm)) was sieved again using -2 (4mm) and -1ϕ (2mm) sieves and the gravel fraction was calculated as weight percent of the total sample weight. Additionally, ca. 3 g of the fine fraction (<-1ϕ (2mm)) of each sample were put in a 50 ml centrifuge tube. In a fume cupboard, hydrogen peroxide (100vol H_2O_2) was added just to cover the sample and to wait for an initial fizzing. After the fizzing subsided, hydrogen peroxide was added up to the 30ml mark. The samples were then heated in a water bath at 80°C for 5 hours to remove any organic material. The samples were then left to cool down. Following this, the samples were topped up with distilled water to ensure equal volumes. The mixture was then washed at least three times with distilled water using a centrifuge (3000 rpm for 5 minutes) until the peroxide was removed. The final step was to add about 15ml of 10% Calgon (sodium hexametaphosphate and sodium bicarbonate) to the sediments, with a shake to ensure that the samples are well dispersed in the solution. The samples were then analysed at the laboratories of the School of

Chapter 3 Methodology

Geography at the University of Nottingham using a Beckman Coulter LS 13 320 particle size analyser providing grain size data for a size range from 0.041 to 2000μm. Before the instrument measurement run, ultrasonic disintegration was applied for ca. 30 seconds.

A preliminary representation of the particle size analysis results can be done using cumulative curves and frequency curves (Visher, 1969; Mycielska-DowgiałŁo and Ludwikowska-Kedzia, 2011; Baiyegunhi et al., 2017; Amireh, 2016). The frequency curves provide a representation of the sediments' grain-size fraction proportions in the sample, while the cumulative curve is a representation of the particle size distributions as cumulative curves on a probability scale (Visher, 1969; Francke et al., 2013; Amireh, 2015).

The results of the laser particle size analysis were then entered into Gradistat software. Gradistat is a particle size distribution and statistics package developed by Blott and Pye (2001). It provides geometrical and logarithmic statistics using Folk and Ward (1957) and moment graphical methods. Based on the work of Folk and Ward (1957), the primary statistical parameters to describe particle size distribution are as follows:

1) Mean grain size (M_z), a descriptive parameter that measures the arithmetic average size of all the particles in a given sample, 2) Sorting, a measure of a range of grain sizes in a sample and the degree of the corresponding scatter around the mean size, 3) Skewness (Sk), a measure of the degree of symmetry of the grain size distribution, and 4) Kurtosis (K_G), a measure of the grain size frequency curve peakedness. In addition, the main particle modes were extracted.

It has been reported in several studies (Folk and Ward, 1957; Basanta K. Sahu, 1964; Blott and Pye, 2001; Makhlouf et al., 2010; Mycielska-DowgiałŁo and Ludwikowska-Kedzia, 2011; Amireh, 2015; Saffarini and Amireh, 2016) that each depositional environment has, to certain limits, its distinctive dynamics and energy conditions that can be inferred from the corresponding grain size characteristics. However, various, and to some extent controversial, interpretations of grain size data have been reported (Mycielska-DowgiałŁo and Ludwikowska-Kedzia, 2011). Thus, a more comprehensive understanding of the particle size distribution and statistical parameters is needed to draw more comprehensive conclusions and interpretations. In addition, kurtosis and skewness generally represent the transport medium magnitude and the separation of the particle size populations, where, for example, the sediments may show positive or negative skewness

based on the dominant particle size fraction. Accordingly, in order to draw a broader understanding of the particle size distributions signal, variability within the different sediments, depositional environment and modes of transportation, the CM diagram (Passega and Byramjee, 1969; Mycielska-DowgiaŁŁo and Ludwikowska-Kedzia, 2011) is used here.

The CM diagram is a widely used method to reflect the sediments' transport medium (Passega, 1964; Madukwe, 2016; Baiyegunhi et al., 2017; Venkatesan et al., 2017). Passega (1964) was the first to establish a relationship between the sediment texture and the agent of transportation. As fine particles might be transported independently of the coarse particles through several agents, it is more reliable to define the transportation agent of a specific sediment based on its content of coarse particles. Thus, Passega (1964) proposed a logarithmic diagram composed of two parameters; C and M, the one percentile and the median diameter, respectively, to define the different agents contributing to the sediments transportation. The general diagram pattern is spread over 6 points; Q, N, O, P, R and S (Figure 3.6). The points are assigned based on the size of the C parameter where the largest grain size transported by graded suspension corresponds to point Q and the largest grain size transported by uniform suspension is at point R, thus the segment QR represents graded suspension deposition. The QR segment reflects well sorted sediments that plot nearest to the C=M line. Point P represents sediments deposited by rolling that adds coarser sediments to point Q. Point O represents coarser sediments compared to point P where an increase in rolled sediments occur (segment PO). Point N represents the coarsest C parameter where sediments are transported by rolling. Thus, segment NO represents material almost entirely transported by rolling. The finest C is at point S where segment RS represents uniform suspension deposition (Passega, 1964). Further refining of the CM pattern was introduced by Passega and Byramjee (1969) with values of C and M used to identify diagram zones reflecting the different hydrodynamic processes. The original Passega diagram was applied mainly to the study of marine environments, but the following attempts to refine and apply this diagram to fluvial environments with known conditions, have shown that this diagram is a useful tool in the study of fluvial depositional environments (Royse, 1970; Mycielska-DowgiaŁŁo and Ludwikowska-Kedzia, 2011; Kittel, 2014).
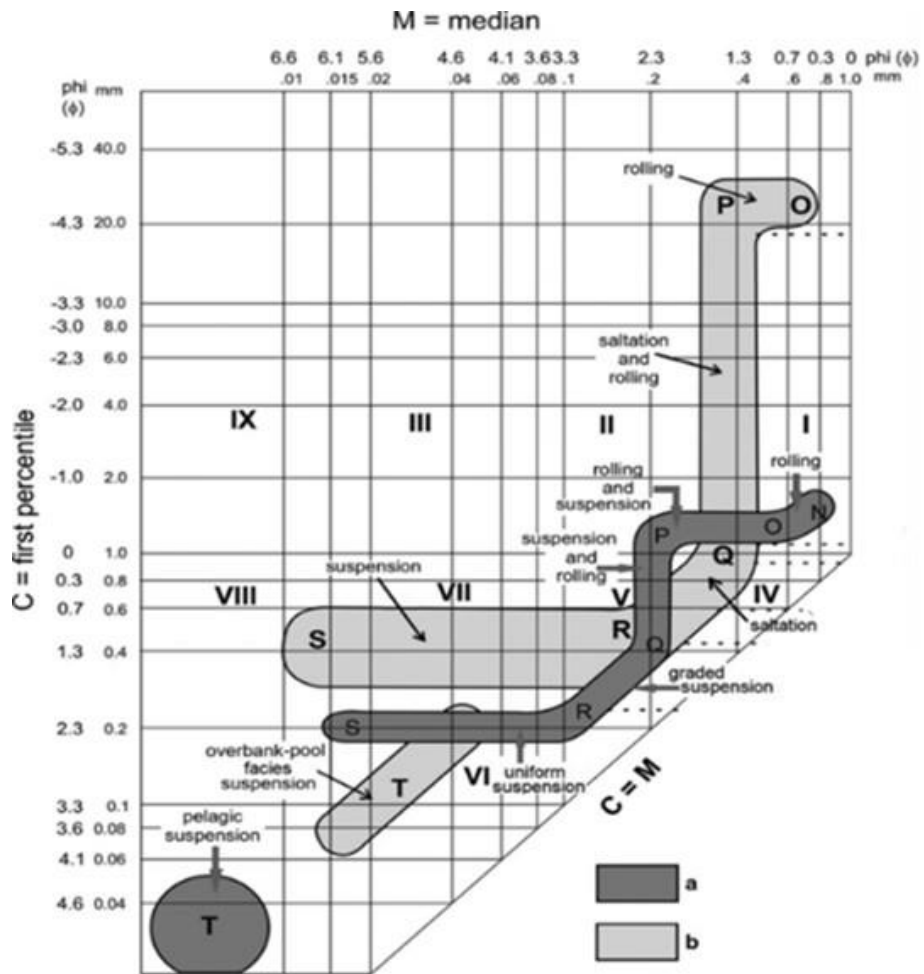
Figure 3.6 Complete CM pattern of tractive current deposits. a) Dark grey shaded area based on Passega (1964) and Passega and Byramjee (1969); b) Light grey shaded area based on LudwikowskaKędzia (2000). I, II, III, IX: rolled grains; IV: High turbulence deposit; V: Low turbulence deposit; VI: Graded suspension; VII: Uniform suspension; VIII: Finest uniform suspension (after Passega and Byramjee, 1969) (modified from Mycielska-DowgiaŁŁo and Ludwikowska-Kedzia, 2011).

3.6.2.2 Magnetic Susceptibility (κ)

Bulk magnetic susceptibility (κ) analysis measures the concentration of magnetic minerals in bulk sediments (Thompson and Oldfield, 1986; Dearing, 1994). Since most of these minerals are allochthonous and associated with catchment erosional and in-wash processes, the variability in (κ) values can be considered as a proxy of enhanced/reduced erosional processes. Accordingly, quantitative K measurements have been widely used in the estimation of catchment disturbance and in-wash processes, primarily corroborated with the elemental composition of the sediments (e.g. Metcalfe et al., 2000; Jones and Richter, 2011; Ben Ameur et al., 2019; Parker et al., 2020).

Following Dearing (1994), the κ analysis was performed on air dried ca.10 cm^3 bulk sediments (<-1φ (2mm) particle size), and gently ground using a porcelain mortar, placed in a non-magnetic10 cm^3 plastic box. The plastic boxes were full at all times during the measurements. The measurements were done in the laboratories of the School of Geography at the University of Nottingham using the Bartington MS2B single sample dual frequency sensor at 0.1 sensitivity range (0.46 kHz) and each measurement was run for an average of 16 seconds.

Prior to the analysis, all metal objects were kept away from the sensor. The instrument was then turned on and switched to the 0.1 sensor. A drift test was then conducted, during which, the sensor records air measurements for 30 minutes. To measure the κ (*10^{-6} SI) for sediments, an air reading is measured first and then the sample is placed in the instrument and the measurement is done. A drift correction is applied when using the 0.1 sensitivity sensor, which requires recording another air reading after the sample measurement. The mean of air measurements before and after the sample measurement is subtracted from the (nth) sample measurement (R_n) by the following equation:

$$R_k = R_n - n * (R_{Final} - R_0)/N$$

Where: R_k is the Corrected value, R_{Final} is the final air reading, N is the total number of measurements after the initial zero (including R_{Final}) and R_0 is the first air reading.

This drift correction is done automatically using Multisus. Software as it records the time of each measurement and the drift is then applied linearly as a function of time (Dearing, 1994).

3.6.2.3 Carbonate and organic matter content (Loss on Ignition (LOI))

Loss on Ignition (LOI) is a sequential analysis method that has been used extensively in estimating the amount of organic matter and carbonate content of sediments (Dean, 1974; Heiri et al., 2001). Here standard methods were applied (Dean, 1974; Heiri et al., 2001). Dry crucibles were weighed at first to an accuracy of ±0.1mg (W_{cruc}), then 1cm^3 of sub-sample was added to the crucible and weighed (W_{wet}). The crucible was then put into an oven at 105°C to dry over-night and the weight of the dried sample was measured (W_{105}). The dried sample was then put in a muffle furnace at 550°C for 4 hours to combust the organic matter. The weight of the sample after this step is (W_{550}). The carbonate content was then depleted after placing the sample back in the muffle furnace at 925 °C for 2 hours (W_{925}).

The organic (LOI$_{550}$) and carbonate (LOI$_{925}$) contents were calculated following the equations of Dean (1974):

$$LOI_{550}\ (\%) = (W_{105} - W_{550}) / (W_{105} - W_{cruc}) *100$$

$$LOI_{925}\ (\%) = (W_{550} - W_{925}) / (W_{105} - W_{cruc}) *100$$

Despite LOI being a cheap and easy method to estimate the organic and inorganic carbon in sediments, it should be presented with caution due to effects of sediments clay composition which could skew the results based on the temperatures used. The LOI results at best represent qualitative rather than quantitative variability within the sediments (Santisteban et al., 2004).

Here, LOI results are used to show general variability within the Gharandal sediments and locations with elevated organic content. In addition, the results are used to show the general variability within the DS1 sediments and locate parts of the section marked with higher carbonate content to locate laminae for further U/Th dating and stable isotope analyses.

3.6.2.4   X-Ray Fluorescence (XRF) analysis

XRF spectrometry is based on detecting and estimating the X-ray photons generated by different atoms and then converting them into concentrations (Weltje and Tjallingii, 2008). XRF analysis is a simple analysis, regarding sample preparation and to retrieve sediments bulk geochemical major and trace elements, however, there are a few disadvantages, for example, the results can be influenced by sediments' particle size variations and water content (Oyedotun, 2018).

For the XRF analysis in this research, bulk sediment samples <2mm were used. Considering the dry nature of the Gharandal sediments, the samples were air dried for 24 hours before analysis, while, the moister DS1 sediments were dried at 105° overnight. Following this, the samples were gently ground using an agate mortar and pestle. The loose powder samples were then loaded into sample cups with a thin film covering the base. The samples were prepared by the author and the cups were ca. 3/4 full and analysed for major and trace elements in the laboratories of the School of Geography at the University of Nottingham by Teresa Needham, using a PANalytical Epsilon3XL X-ray fluorescence spectrometer with high resolution Si drift detector (typically 145 eV@5.9keV/1000cps). This spectrometer can detect elements range from F to U with a concentration range from ppm to 100%. The instrument uses a built-in 4096 multi-channel analyser

(MCA) and Epsilon 3 software for qualitative and quantitative analysis with a precision of 0.05 ppm.

Since the original elemental composition is crucial for understanding the variability within the sediments and to assign the correct sedimentary lithofacies, the results of the XRF analysis were not summed up to 100% in order to preserve the original variability within the samples.

Elemental composition of the sediments is significant in understanding the geochemical variability within a sedimentary sequence, and hence depositional and environmental history of the deposits (Cox et al., 1995; Aristizábal et al., 2005; Metcalfe et al., 2010; Jones et al., 2015; Hazermoshar et al., 2016; Hossain et al., 2017; Yang and Du, 2017; Ben Ameur et al., 2019; Amireh, 2020). In addition, important implementations of the elemental composition of the sediments are evaluating provenance (e.g. Roser and Korsch, 1988; Ryan and Williams, 2007; Pandey and Parcha, 2017), maturity (e.g. Pettijohn et al., 1972), and the quantitative estimation of the sediments' weathering intensity (e.g. Nesbitt and Young, 1982; Fedo et al., 1995; Meunier et al., 2013; Hossain et al., 2017) and catchment in-wash (Metcalfe et al., 2010). However, geochemical estimates of weathering intensity has to be presented with caution, and paired with an understanding of the catchment geology and hydrology (Cox et al., 1995; Fedo et al., 1995; Duzgoren-Aydin et al., 2002; Garzanti et al., 2010).

Considering that weathering processes affect the geochemical composition of the sediments, weathering intensity is an important indicator of their depositional environment and climate variability. Accordingly, several researchers have proposed different chemical weathering indices using the sediments' elemental compositions (e.g. Nesbitt and Young, 1982; Cox et al., 1995; Fedo et al., 1995). Generally, the chemical weathering indices aim to quantify the compositional alteration of primarily mobile elements in the sediments (such as Na, Ca and K), where deposition in humid (positive moisture balance) environments results with different indices values compared to arid and dry climates (Duzgoren-Aydin et al., 2002; Amireh, 2020).

Numerous chemical weathering indices have been developed (e.g. Yang et al., 2006; Garzanti and Resentini, 2016b; Malick and Ishiga, 2016; Hossain et al., 2017), however, amongst the most widely used are the Chemical Index of Alteration (CIA) (Nesbitt and Young, 1982) and the Plagioclase Index of Alteration (PIA) (Fedo et al., 1995). Similar to other indices, CIA and PIA are calculated using

molecular ratios, in which, a calculation of the CaO^* (CaO content in the silicate fraction) is required. However, it has been suggested that these indices are not suitable for catchments rich with carbonates (Fedo et al., 1995), such as the Gharandal Valley (Ibrahim, 1993) and the DSB catchment areas. Thus, a different index is used to reflect the sediments' compositional maturity, namely, the Index of Compositional Variability (ICV). The ICV was introduced by Cox et al. (1995) based on the fact that clay minerals and non-clay minerals comprise various contents of aluminium. The ICV measures the abundance of aluminium relative to other major cations in the sediment, and silica is excluded in order to reduce its dilution effect.

The ICV is calculated as weight percent of $[(Fe_2O_3 + K_2O + CaO + MgO + MnO + TiO_2) / Al_2O_3]$ (Cox et al., 1995). In general, compositionally immature sediments, containing a high proportion of non-clay silicate minerals will show high ICV values (>1), while, compositionally mature sediments will show low (<1) ICV values. The immature sediments are usually an indicator of tectonically active settings and may also indicate first cycle sediments (Cox et al., 1995). Hossain et al. (2017) showed that ICV is well correlated with CIA, where sediments with ICV values of ca. 1 correspond to ca. 60% CIA (low chemical weathering), while lower ICV values correspond to higher CIA values indicating moderate to intense weathering intensity, where the lower the ICV value, the higher the CIA value (towards more intense chemical weathering) (Hossain et al., 2017). Thus, ICV variability may indicate alternating degrees of source chemical weathering.

These chemical proxies are implemented in this research to draw a more comprehensive understanding of the geochemical variability within the sediments.

3.6.3 The DSB (DS1) Sequence

3.6.3.1 Scanning Electron Microscopy with Energy Dispersive Spectroscopy (SEM EDS) Analysis

SEM EDS analysis is implemented in this research as a method used for the identification of the purity of the DS1 carbonates.

Based on the LOI_{925} composition and on visual identification, thick (ca, 2-4 mm) pale laminae were identified through the DS1 section. The laminae were then sub-sampled (ca. 4-10 mg) and analysed using an FEI Quanta 650 SEM (60Pa pressure and 20.00 kV) equipped with Inca EDS software, at the Nanoscale and Microscale Research Centre (NmRC) at the University of Nottingham. The analysis was conducted by the author and by Dr. Elisabeth Steer.

20 samples were analysed focusing on identifying clean carbonate, particularly aragonite, crystals, represented by their acicular crystal habit. Where needed, to further identify aragonite crystals or detrital contamination, EDS spectra were used and elemental maps were generated. Laminae with EDS spectra indicating an absence of detrital contamination (i.e. lacking Fe and Ti with dominance of Ca) were then chosen for the U/Th dating.

3.6.3.2 X-Ray Diffraction (XRD) Analysis

Powder XRD analysis was implemented in order to confirm the aragonite purity; i.e. the mineral phases percentages in the samples. The XRD was conducted as a pre analysis for the stable isotope ratios analysis. Thus, the laminae prepared for the stable isotope analyses (see section 3.6.3.3 for procedure) were first analysed for their mineralogical composition using a PANalytical MPD-X-ray diffractometer, in the laboratories of the School of Chemistry at the University of Nottingham, by Dr. Stephen Argent. The analysis was conducted using XPERT-PRO diffractometer system. The settings were 30mA/40kV with CuKα radiation of λ = 1.5406 Å. The diffractograms were generated using PW3050/60 goniometer. Continuous scanning from 15° to 80° 2θ range, with a step size of 0.01 was carried out.

The minimum 2θ value of 15° was assigned based on initial runs that showed no significant intensities are observed at <15° 2θ. The mineral phases were then identified and refined using the Profex v.4.2.3 software (Doebelin and Kleeberg, 2015).

3.6.3.3 Stable isotope analyses

Oxygen and carbon isotope ratios have been used extensively in palaeoclimate and palaeolimnological reconstruction studies (e.g. Kolodny et al., 2005a; Swann et al., 2005; Jones et al., 2007; Dean et al., 2015). However, lacustrine sediments' isotopic ratios are influenced by several environmental factors and understanding these factors is essential in understanding the isotopic signal (Leng and Marshall, 2004; Roberts et al., 2010). The Dead Sea, and hence its predecessor lakes, represents an evaporative closed lake system, where the water balance (inflow vs evaporation), is the primary control over isotopic compositions. The inflow is characterized by lighter isotopic values, while the evaporation processes result in the enrichment of heavy isotopes (Gat, 1984). This means that, the isotopic balance follows the hydrological processes, where rising lake level stages are marked with less enriched isotopic ratios (Gat, 1984; Kolodny et al., 2005). It has been suggested that excursions, short term variations from longer term values (e.g. ca. 4.5‰ ± 1‰ for $\delta^{18}O$ and -2.1‰ to +3.7‰ for $\delta^{13}C$ for the Lake Lisan Middle Member (Kolodny et al., 2005) ca. 58ka to 31ka (Machlus et al., 2000; Bartov et al., 2002)), in the DSB lakes' endogenic carbonates isotopic ratios reflect seasonal evaporation/precipitation (E/P) variability and amount effects (Kolodny et al., 2005).

Accordingly, this research measures the $\delta^{18}O$ and $\delta^{13}C$ of four (ca. 5 cm) continuous laminated blocks through the DS1 section in order to investigate the short term isotopic behaviour of the endogenic carbonates, and hence, response to short-term hydrological changes. Thus, the blocks are sampled from parts where no significant variations in the lithology are observed; i.e. no thick clastic laminae or gypsum beds, and from parts following a clear lithological variation; i.e. following a thick clastic lamina, in order to understand the isotopic system behaviour and how it is affected by the hydrological changes in the catchment area. The four sediment blocks (see above) (e.g. Figure 3.7) were chosen at 63 cm, 1.59m, 3m and 4m above the section base. From each block, 15 individual laminae and 5 mixed laminae (3 laminae each) were used for the analysis.

Figure 3.7 Clean continuous laminated sediment block at 63.5 to 68.5 cm above the DS1 section base.

For the oxygen and carbon isotope analyses, 80 ca. 1 to 4 mm pale (aragonite) laminae were sampled. The amount of sample required for the analysis was determined through the equation [Sample required (mg) = 1000/ (TIC*8.33)]. The removal of organic material was done through the standard procedures of the BGS as follows:

The sample was placed in a 200mg beaker and ca. 50ml of 5% sodium hypochlorite was added and mixed to immerse the sample. The mixture was left overnight. Then, the beaker was topped up to 200ml with deionised water and left until the sample settled. Following to this, the water was decanted, with caution not to lose the sediments, and topped up again with deionised water up to 200ml. This decanting step was done ca. 5 times until a neutral pH was reached. Then, the water was decanted and the beakers were dried overnight at 40°C. After the samples were dried, a soft spatula was used to transfer the sediments into an agate pestle and mortar where they were gently ground to fine powder. Finally, the powder samples were transferred into vials and labelled. The prepared samples were then delivered to Prof. Melanie Leng at the Stable Isotope Facility at the BGS.

In the BGS laboratories, the sample material was ground in agate and the equivalent of 10 mg of carbonate was reacted with anhydrous phosphoric acid *in vacuo* for 72 hours at a constant 25°C (Ca and Mg carbonates including dolomite should react within this time). The CO_2 liberated was separated from water vapour under vacuum and collected for analysis. Measurements were made on a VG

Optima mass spectrometer. Overall analytical reproducibility for these samples is normally better than 0.2‰ for δ^{13}C and δ^{18}O (2□). Isotope values (δ^{13}C, δ^{18}O) are reported as per mil (‰) deviations of the isotopic ratios (^{13}C/^{12}C, ^{18}O/^{16}O) calculated to the VPDB scale using a within-run laboratory standard calibrated against NBS standards (McCrea, 1950; Craig, 1957).

3.7   Chapter conclusions

The methodology of this PhD project has been described, explaining the drivers for choosing the study areas and explains the analytical approach based on the different nature of the sedimentary sequences investigated. These sequences and their settings are described in detail in the following chapters.

Chapter 4. Study Sites

4.1   Introduction

This chapter presents the study sites of this PhD project. It outlines their distinct geomorphological, geological and contemporary climate settings. It also outlines the previous studies and the need for further investigations.

4.2   The Dead Sea Transform Fault

The two study sites for this PhD project are located within the Dead Sea Rift (DST) (see also Chapter 2; 2.1). The DST extends from Aqaba in southern Jordan to southern Turkey in the north (Figure 4.1). In Jordan, the DST extends for about 375 km on a NNE direction from the Gulf of Aqaba in the south to Lake Tiberius (Galilee) in the north with an average displacement of ca. 5 to 10 mm/yr (Freund et al., 1968; Galli, 1999; Klinger et al., 2000); i.e. a total lateral displacement of 107 km since the Miocene (Al Hseinat et al., 2020). This process produced several pull-apart basins: Wadi Araba (where the Gharandal Valley is located), the Dead Sea (where the lacustrine DS1 section is located), and the Jordan valley (Figure 4.1) (Girdler, 1990; Atallah and Al-Taj, 2004; Abed, 2017). These three structures are of the oldest structures within the DST (Garfunkel et al., 1981).
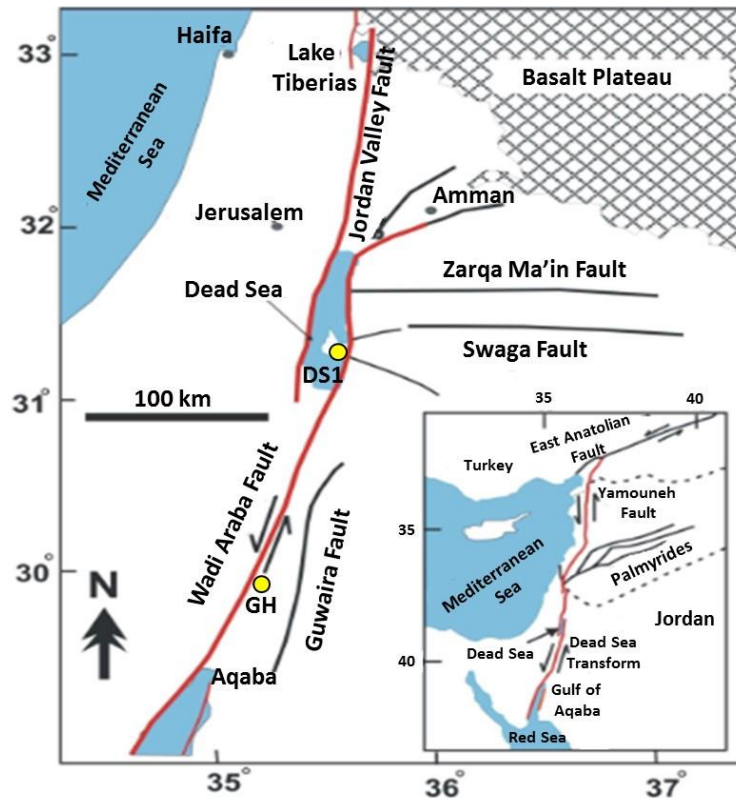
Figure 4.1 The Dead Sea Transform Fault (DST) and associated faults in Jordan. The Wadi Araba Fault and the Jordan Valley Fault overlap forming the pull-apart basin of the current Dead Sea. Inset shows the complete length of the DST from the Gulf of Aqaba in the south to the East Anatolian Fault in the north (after Abed, 2000) (modified from Abu Ghazleh, 2011). **DS1**: Location of the DSB section of this project. **GH**: Location of the Gharandal Valley.

4.3 The Gharandal Valley study site

This section outlines the contemporary climate settings of Wadi Araba and the Gharandal Valley. Following this, a description of Wadi Araba, with a focus on the Gharandal Valley study area, in terms of location, morphotectonic and geological contexts is presented. Finally, the sediments of the Gharandal Valley, the previous studies, and the sedimentary sequences chosen for this PhD project are discussed.

4.3.1 Wadi Araba contemporary climate settings

Along any W-E cross section through the present day Levant, Wadi Araba is the driest area (ca. 31 mm.yr^{-1} precipitation) (Figure 4.2) (Kushnir et al., 2017; Saqqa and Atallah, 2004) (see Chapter 2; 2). Wadi Araba's aridity is attributed to its position in the rain shadow of the Eastern and Western highlands. The contribution of the Eastern Mediterranean (EM) cyclones in bringing moisture into southern Wadi Araba is limited due to the orography-dependent, north-south decreasing, precipitation trend (Kahana et al., 2002; Saqqa and Atallah, 2004; Enzel et al.,

2008). Nonetheless, similar to what is observed in the southern Negev Desert on the western side of the rift, two tropical synoptic systems contribute to bringing moisture, during the wet (winter) season, into the southern Wadi Araba, namely, the Red Sea Trough (RST), and the African Tropical Plumes (ATPs) (Kahana et al., 2002; Kushnir et al., 2017) (see Chapter 2; 2.2).

The long-term average annual air temperature in Wadi Araba is ca. 17 °C in winter and ca. 30 °C in summer. However, summer daily maximum temperature reaches up to 48°C (Makhlouf et al., 2010), while the winter minimum drops to less than 0 °C (Saqqa and Atallah, 2004). Due to the daytime to night-time air temperature difference of >30 °C and low precipitation, plant growth in the Wadi is sparse (Abed, 2002; Saqqa and Atallah, 2004). Nonetheless, the highlands along the eastern flanks of the Wadi receive an average annual precipitation of ca. 200 mm.yr^{-1} (Makhlouf et al., 2010). Considering the location of the highlands on the eastern flanks of Wadi Araba, the precipitation falling over these highlands is drained westward through valleys, such as Gharandal Valley, making this precipitation an important source of surface runoff through these E-W drainage networks and also as a groundwater recharge resource. Based on long-term meteorological data (1955–1985), from two stations in northern (Ghor Safi Station) and southern Wadi Araba (Aqaba Airport Station), 95km and 65km from the Ghrandal Valley, respectively (1 and 2 in Figure 4.2), Saqqa and Atallah (2004) concluded that the Wadi is presently arid to hyper-arid. They calculated a mean annual potential evapotranspiration of ca. 2500 mm in the south and ca. 2200 mm in the north. The winter relative humidity ranges from 53% in the south to 62% in the north, while during summer it reduces to 40% and 30% in the south and north, respectively.
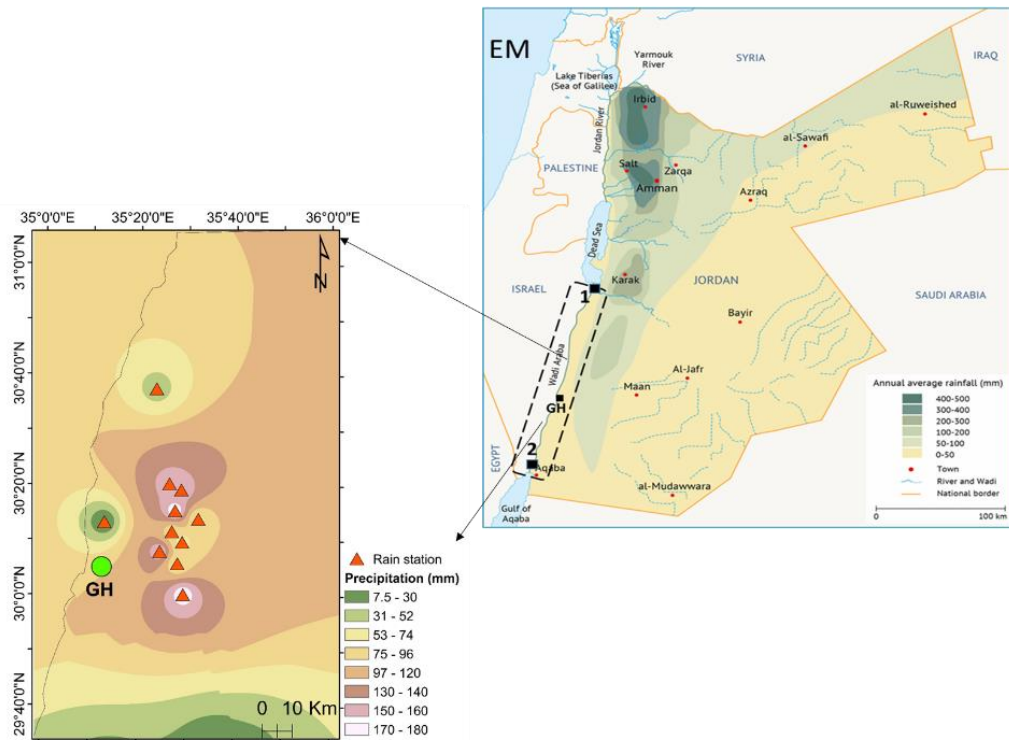
Figure 4.2 Mean annual precipitation over Jordan (from the Ministry of Water and Irrigation, Jordan, open files). Meteorological stations: (1) Ghor Safi Station, (2) Aqaba Airport Station. **EM**: Eastern Mediterranean Sea. Inset shows the east west precipitation gradient, relative to the Gharandal Valley (GH). Data from Jordan Meteorological Department, 2018.

4.3.1.1 Wind systems and dust storms

Due to the elevation difference between the Wadi Araba floor and the surrounding highlands, >1000 m in some places, and the resulting pressure variations, wind speed along the Wadi is not constant and varies through the year. Events with high wind speed are not restricted to specific months, however, they are common during April to June, and February to March (Figure 4.3), where four main wind systems are observed in the Wadi originating from the NW, NE, SW and SE (Saqqa and Atallah, 2004). The strongest are the northerly systems, representing ca. 70% of the total winds (Abed, 2002), while, the southerly winds comprise ca. 8% of the total winds (Abed and Al-Hawari, 1991). In general, the present average annual wind speed ranges from 4 to 7 m/s, while the maximum can reach up to 19 m/s 36 knots/h. On the other hand, the easterly and westerly winds are less effective in the Wadi due to obstruction caused by the surrounding highlands (Saqqa and Atallah, 2004).

Generally, high amounts of mineral dust reach the Levant from different sources based on the origin and track of the air masses affecting the region. The Levant receives mineral dust primarily from the North African Sahara and the Arabian

Deserts. The Sahara is the largest source of aeolian dust in the world, from which ca. 70 Mt reach the Levant annually, from Libya, Tunisia and Algeria, transported with winter and spring Eastern Mediterranean (EM) cyclones that move over North Africa (Dayan et al., 2008). Additionally, the southern RSTs can bring dust from the Arabian Desert into the Levant (Kushnir et al., 2017).

Based on long-term meteorological data (1955–1985) in Wadi Araba, Saqqa and Atalla (2004) reported that dust storms occur primarily during early spring and can prevail through the entire summer season, mainly affecting the southern Wadi Araba (Figure 4.3). The authors reported that the sources of the sand dunes near the Gharandal Valley are mainly the nearby eastern highlands where sandstone formations are located in the Wadi Araba (see Figure 4.4 c).
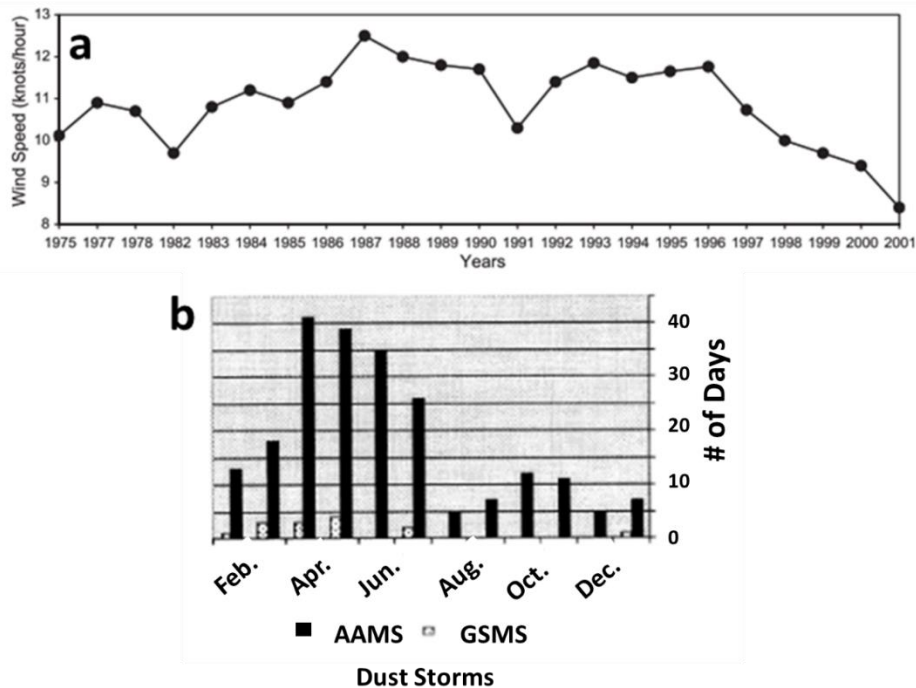
Figure 4.3 a) Time series 1975 – 2001, showing annual wind speed average for Aqaba Airport Meteorological Station (AAMS) and Ghor Safi Meteorological Station (GSMS). b) Annual recurrence of dust storms in Wadi Araba (Records for 30 years between 1955 and 1985 (from Saqqa and Atallah, 2004)).

4.3.1.2 Floods in Wadi Araba

The main hydrological process in Wadi Araba is flash flooding following rare, intense, rain events (Saqqa and Atallah, 2004; LeBéon et al., 2012). Thus understanding this process is important in reconstructing the past hydrodynamics, where stream alluviation or entrenchment is dependent on flood frequency and erosion, reflecting the catchment fluvial response to climatic variability and tectonic movements (Niemi and Smith, 1999; Saqqa and Atallah, 2013). Fewer

rainstorms occur in the southern Wadi Araba compared to the north. Nonetheless, high intensity localized rainstorms are likely to happen in southern Wadi Araba, when the southern RSTs troughs are synchronous with a mid-tropospheric trough from Europe, through the Mediterranean and the Nile (Kahana et al., 2002). Based on long term data from 1965 to 1994, Kahana et al. (2002) studied the major flood events in the Negev Desert. The authors concluded that there is a variable influence of the main synoptic systems on the temporal and spatial distribution and intensity of major floods. The ARST caused 38% of the total floods in the Negev, the EM cyclones were responsible for 33%, and the ATPs were responsible for 10% of the total floods (Kahana et al., 2002). Today, similar to the Negev desert, these rain storms are the main drivers of Wadi Araba hydrological events, primarily as floods draining water from the eastern highlands through E-W valleys into Wadi Araba.

4.3.2   Morphotectonic settings

Wadi Araba is a linear (Niemi and Smith, 1999) 175 km N-S (Ibrahim, 1993) and 10 to 15 km E-W wide morphotectonic depression (Atallah, 2002). It is generally oriented NNE-SSW and it represents a significant portion of the Dead Sea Transform (DSTF) (Figure 4.4) (Atallah and Al-Taj, 2004; Makhlouf et al., 2010). Wadi Araba extends from the present day Dead Sea in the north at ca. -400 m asl to the Gulf of Aqaba in the south (Figure 4.4) where it reaches an elevation at sea level. The highest elevation along the Wadi floor is the Ar-Risha hill (Figure 4.4 b) at ca. 250 m asl. The subsidence of the Wadi floor is a result of the tectonic motion along the DSTF which also elevated the neighbouring highlands (flanks) to the east and west (Niemi and Smith, 1999). The Wadi Araba is tectonically active and intensively faulted, either by major faults cutting through the Wadi floor or by localized faults, at or close to the eastern highlands (Atallah, 2002; Ibrahim, 1993).

These tectonic activities are reflected by the low sinuosity of the highland fronts and the ratio of valley floor width to valley height, indicating tectonically active fronts (Atallah, 2002). An average of 4–10 mm.yr^{-1} (Garfunkel et al., 1981; LeBéon et al., 2012) left lateral slip rate has been reported for Wadi Araba for the last 20 Ma, including the Quaternary. In southern Wadi Araba, the slip movement is usually the result of high magnitude earthquakes, for example, 1 cm.yr^{-1} slip rate occurs almost every 200 to 400 years accommodating earthquakes of magnitude (M) = 6.5 (Galli, 1999).

Accordingly, Wadi Araba, is mainly comprised of two geomorphological features: (1) the eastern highlands (flanks) that reach up to 2000 m asl, characterized by steep westward slopes and gently dipping eastern fronts that are generally dissected by E-W trending wadis, and (2) the low relief rift covered with Quaternary alluvial fans, playas, sand dunes and fluvial/alluvial sediments (Atallah, 2002; Le Béon et al., 2012). In the southeastern part of Wadi Araba, two strike-slip faults overlap producing several pull apart basins, such as the Gharandal Valley pull apart basin. In addition, tectonically tilted structures can be spotted in the Gharandal Valley indicating tectonic activity in the area (Figure 4.5).

Alongside the slip movements, vertical tectonic movements, of Late Pleistocene and recent age (Galli, 1999), are also observed as a result of the epeirogenic movement along the DSTF (Bender, 1974). The Pleistocene Risha Formation gravels, located ca. 15 km north of the Gharandal Valley, record evidence of at least 80 m uplift (Ibrahim, 1993) and a fan located near the Risha gravels is raised ca. 20 m above the Wadi Araba fault surface (Le Béon et al., 2012). These tectonic processes alongside rock outcrops are important factors in defining the morphological characteristics of Wadi Araba (e.g. Saqqa and Atallah, 2013). Fluvial systems relief is generally influenced by tectonic fall, while the stream flow and dynamics can be adjusted by tectonic uplift.

The nature of the sedimentary sequences in Wadi Araba is mainly controlled by the geological formations and their distribution. Accordingly, the Quaternary sediments in the wadi are widespread (Ginat et al., 1998; Le Béon et al., 2012) and are well preserved due to its aridity (Niemi and Smith, 1999; Le Béon et al., 2012; Mischke et al., 2017) and record the interactions between the geomorphological controls, climatic variations, and vegetation zones during times of sediment deposition (Saqqa and Atallah, 2004).
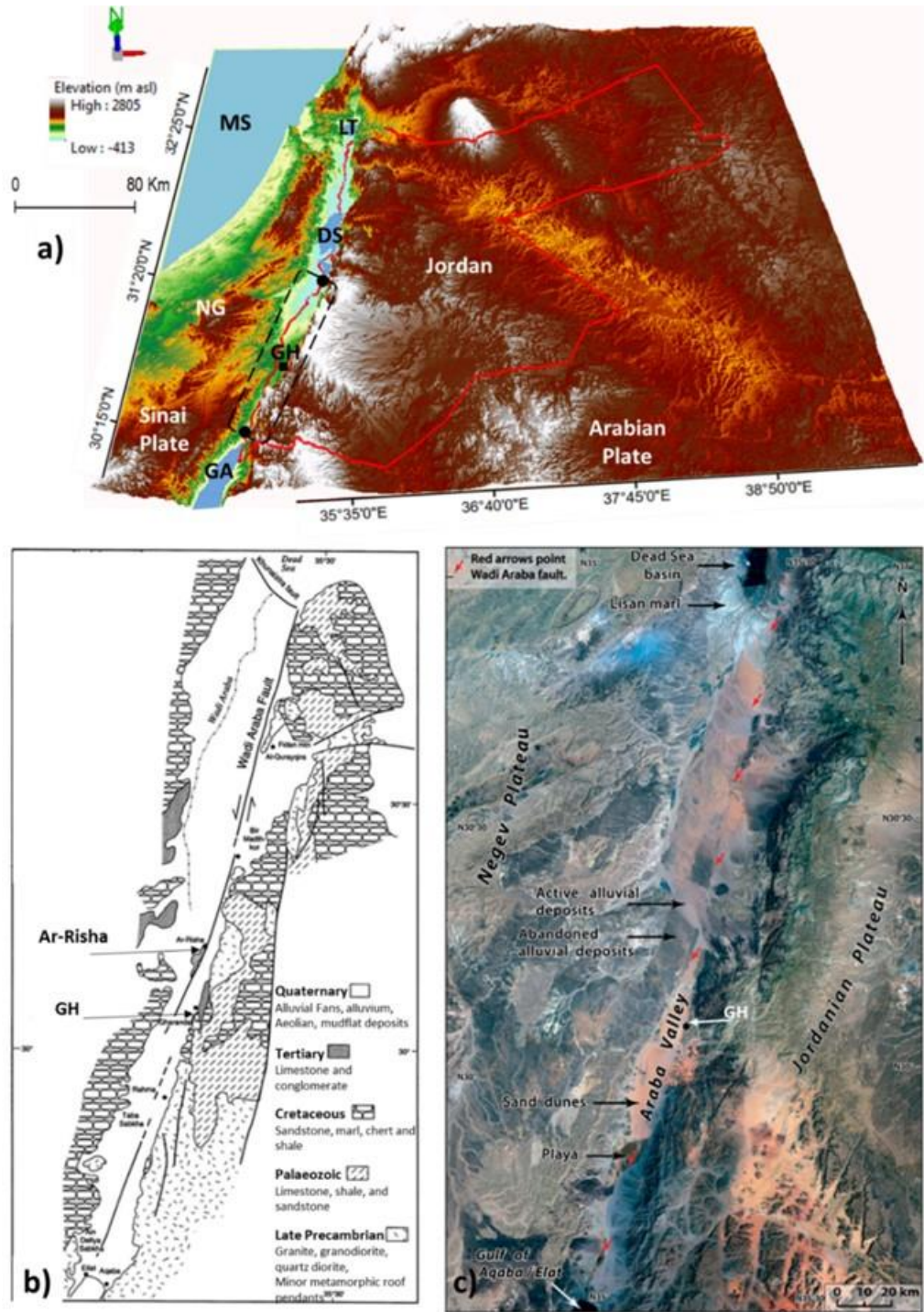
Figure 4.4 a) SRTM v3 (30m pixel) Digital Elevation Model (DEM) of Jordan and the surrounding countries showing the Gharandal Valley (**GH**) location relative to the Mediterranean Sea (**MS**), **LT**: Lake Tiberius, **DS**: the Dead Sea, **NG**: the Negev Desert and **GA**: Gulf of Aqaba (Red Sea). b) Generalized geological map of Wadi Araba (modified after Niemi and Smith, 1999). c) Landsat7 satellite image of Wadi Araba, showing the types of Quaternary sediments covering the Wadi floor (modified from Le Béon et al., 2012).

Figure 4.5 Tilted structure in the Gharandal Valley. Photo taken in 2018.

4.3.3   The Gharandal Valley study area general description

The Gharandal Valley study area (30.0854°N, 35.2075°E) is located in the southeastern part of Wadi Araba near the southwestern border of Jordan, about 65 km to the north of the Gulf of Aqaba (Figures 4.4 and 4.6). Following the Wadi Araba general climate settings, rare winter flash floods flow through the wadis from east to west and bring sediments to the sporadically vegetated Wadi floor (Niemi and Smith, 1999; Saqqa and Atallah, 2004) (e.g. Figure 4.6 b).
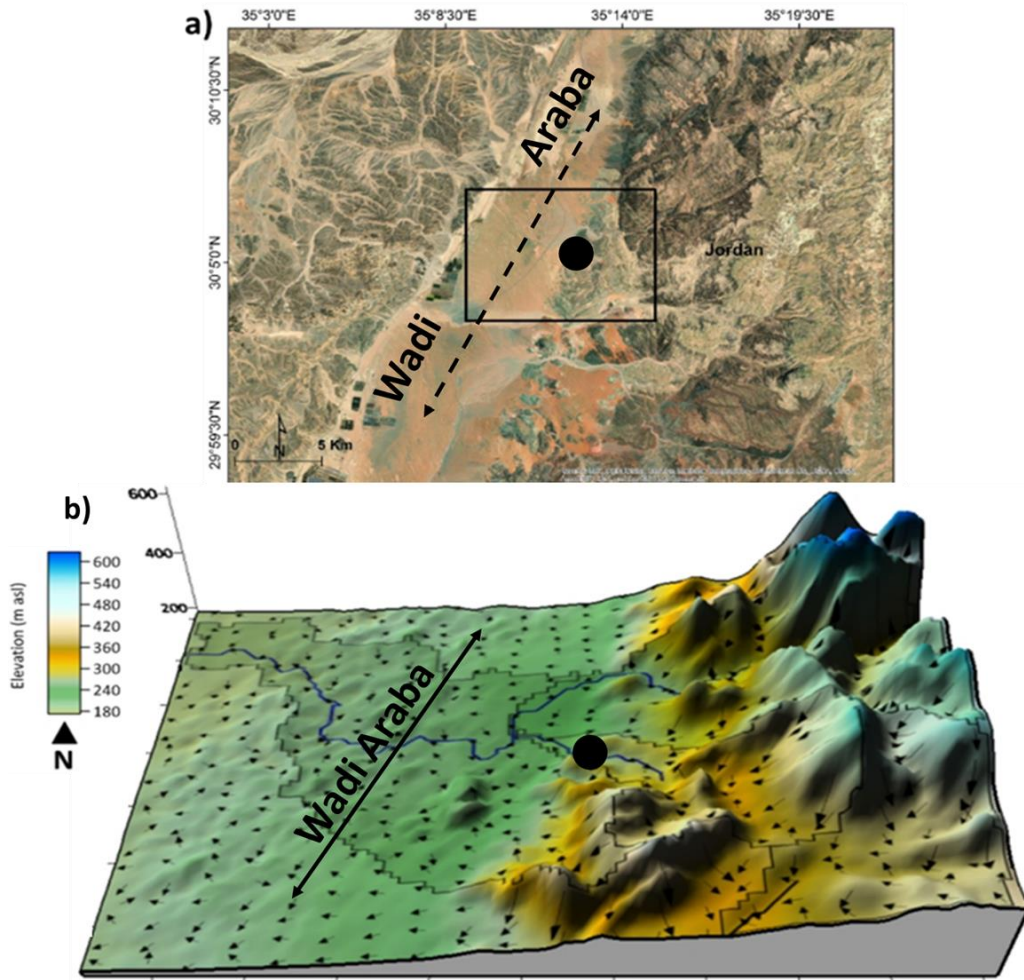
Figure 4.6 a) Location of the Gharandal Valley study area (black circle) in the south-eastern part of Wadi Araba. Black polygon: the specific area represented in b. b) 3D surface representation of the area around the Gharandal Valley showing the highlands at the eastern flanks of Wadi Araba and the low relief floor to the west. Blue lines represent the potential major streams and black arrows indicate the flow direction, based on the SRTM v3 (30m pixel) DEM.

4.3.4 Geological settings
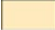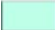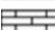
From the southern end of Wadi Araba to about 50 km to the northeast, granite and quartz diorite Precambrian igneous rocks (Aqaba complex) outcrop along the eastern highlands. The Aqaba complex is overlain by Cambrian conglomerates and arkosic sandstone. Farther north, just south of the Gharandal Valley, outcrops of Cambrian to Silurian quartzose sandstones (Nubian Sandstone) are observed (Bender, 1974; Niemi and Smith, 1999; Abed, 2017). Cretaceous, Paleogene and Neogene limestone bedrock outcrops in and around the Gharandal Valley.

The Gharandal Valley present-day catchment comprises the following geological formations as identified in the Gharandal Valley geological map prepared by the

Jordan Natural Resources Authority (Ibrahim and Rashdan, 1988). Starting from the oldest formations, the Neocomian to Early Cenomanian Kurnub Sandstone (KS) Formation is found over the eastern highlands and consists of white, red, pink and yellow fine to medium sandstone, siltstone and clay with abundant quartz. The Palaeocene to Eocene Gharandal (GN) and Thulaythat (TT) Members of the Umm Rijam Chert Limestone (URC) Formation, comprise green and brown yellow marl and gypsum and yellow marl and nummulites respectively. The Pliocene Wadi Bustan (WB) member of the Dana Conglomerate (DC) Formation, comprises sandy marls and pebble to cobble conglomerate. The Late Pleistocene Lisan Marl (LM) Formation comprises yellow fine sandstone, green grey marl with rootlets, claystone, and gypsum with pebble conglomerate. Recent (probably Holocene) Alluvium and Wadi Sediments (Al) are sands and gravels which were deposited through the present day drainage (Figure 4.7 and Table 4.1).

Generally, the limestone is often fossiliferous and interbedded with chert, shale, and phosphate (Atallah, 2002). The dune field to the south of the Gharandal Valley is believed to have formed due to erosion of the sandstone formations (Ibrahim, 1993). Figure 4.7 also shows the presence of several major and minor faults in the area surrounding the Gharandal Valley indicating the importance of the tectonic settings in the modification of the depositional system over time (e.g. Le Béon et al., 2010; Saqqa and Atallah, 2013). One fault is located near the Gharandal Valley outlet affecting the URC Formation, the DC formation and the LM Formation exposures in the valley (Ibrahim and Rashdan, 1988; Ibrahim, 1993).

Lithology

Figure 4.7 Detailed lithological and structural map around the Gharandal Valley study area (black shaded polygon). Blue lines: minor faults, orange lines: major faults (data from the NRA Wadi Gharandal 3050 III 1:50000 geological map (Ibrahim and Al-Rashdan, 1988)). See Table 4.1 for the geological formations and ages of the lithologies.

Table 4.1 Geological formations of the lithologies illustrated in Figure 4.7. Data from the NRA Wadi Gharandal 3050 III 1:50000 geological map.

Formation (local name)	Lithology	Age
Mudflat (Alm)	Mudflat	Recent
Alluvium and Wadi Sediments (Al)	Sand and gravel	Recent
Alluvial Fan (ALF)	Sand and gravel	Recent
Lisan Marl (LM)	Marl. Sand stone, clays, evaporites, gypsum, conglomerate	late Pleistocene
Fluvial gravels (Plg)	Clasts in a sandy matrix	Pleistocene
Sand (ALS)	Sandstone	Pleistocene
Dana Conglomerate (DC)	Sandy marl with conglomerate	Pliocene
Thulaythat Member (TT)	Marl and Gypsum	Palaeocene to Eocene
Gharandal Member (GN)	Chalky marl and nummulites	Palaeocene to Eocene
Umm Rijam Chert Limestone (URC)	Chalek, Chert, Marl and sandy marl	Palaeocene to Eocene
Muwaqqar Chalk Marl (MCM)	Marly siltstone and Gypsum	Maastrichtian to Palaeocene
Belqa (BQ)	Chalk and sandstone	Coniacian to Santonian
Wadi Sir Limestone (WSL)	Limestone, Dolomite, Sandstone, Siltstone	Turonian
Fuhais Hummar Shuaib (FHS)	Mudstone, Siltstone, Limestone and Gypsum	Cenomanian to Lower Turonian
Naur Limestone (NL)	Sandstone, siltstone, Dolomite and Marl	Cenomanian to Lower Turonian
Kurnub Sandstone (KS)	Sandstone, Siltstone and Clay	Neocomian to Early Cenomanian
Disi Sandstone (DI)	Sandstone	Middle Cambrian to Early Ordovician
Umm Ishrin Sandstone (IN)	Sandstone and Siltstone	Early to Middle Cambrian
Abu Khushayba Sandstone (AK)	Sandstone	Late Early Cambrian
Qusayb Rhyolite (QB)	Rhyolitic sills with carbonate and microgranite	Early Cambrian
Musaymir Effusive (MR)	Lithic Tuffs	Early Cambrian
Salib Arkosic Sandstone (SB)	Clast supported conglomerate and Arkosic sandstone	Early Cambrian

4.3.5   The Gharandal Valley sediments

Within the Gharandal Valley (Figures 4.7 and 4.8), thick, up to 16 m fluvial and lacustrine sedimentary sequences have been reported (Ibrahim and Rashdan, 1988; Henry et al., 2001; Mischke et al., 2017; Al-Saqarat et al., 2020). The sedimentary exposures can be traced along the valley slopes to a distance of about 1 km to the east of the present-day outlet. However, the presence of the Gharandal base limits the area available to study to ca. 500 m to the east of the outlet. The sedimentary sequences are thicker and more consistent along the right valley slope and closer to the valley outlet.

The slope aspect in and around the Gharandal Valley study area is generally orientated towards the west and northwest emphasizing the significance of the Wadis in bringing the surface water from the eastern highlands. These Wadis are also important in recharging the groundwater in the area, where people get their water from wells penetrating the alluvial groundwater aquifer (Makhlouf et al., 2010).

Present day flash floods mainly deposit coarse sediments and gravels in currents flowing from east to west (Ibrahim and Rashdan, 1988; Makhlouf et al., 2010). However, this depositional system does not explain the presence of exposures up to > 16 m of generally fine-grained sediments with carbonate concretions and root casts at some locations (e.g. Figure 4.9 a).

Thus, the Gharandal thick sedimentary sequences probably record periods of valley hydrodynamics that are different than the present state. Presently, a spring (Figures 4.8 and 4.9 b) is discharging along the lower reaches of the valley where palm trees are growing. This emphasizes the importance of the shallow GW level in the area and its possible contribution to the depositional processes. Few studies, discussed in the next section, have attempted to date and investigate these sediments in order to provide insights about their depositional environments and palaeoclimate implications.
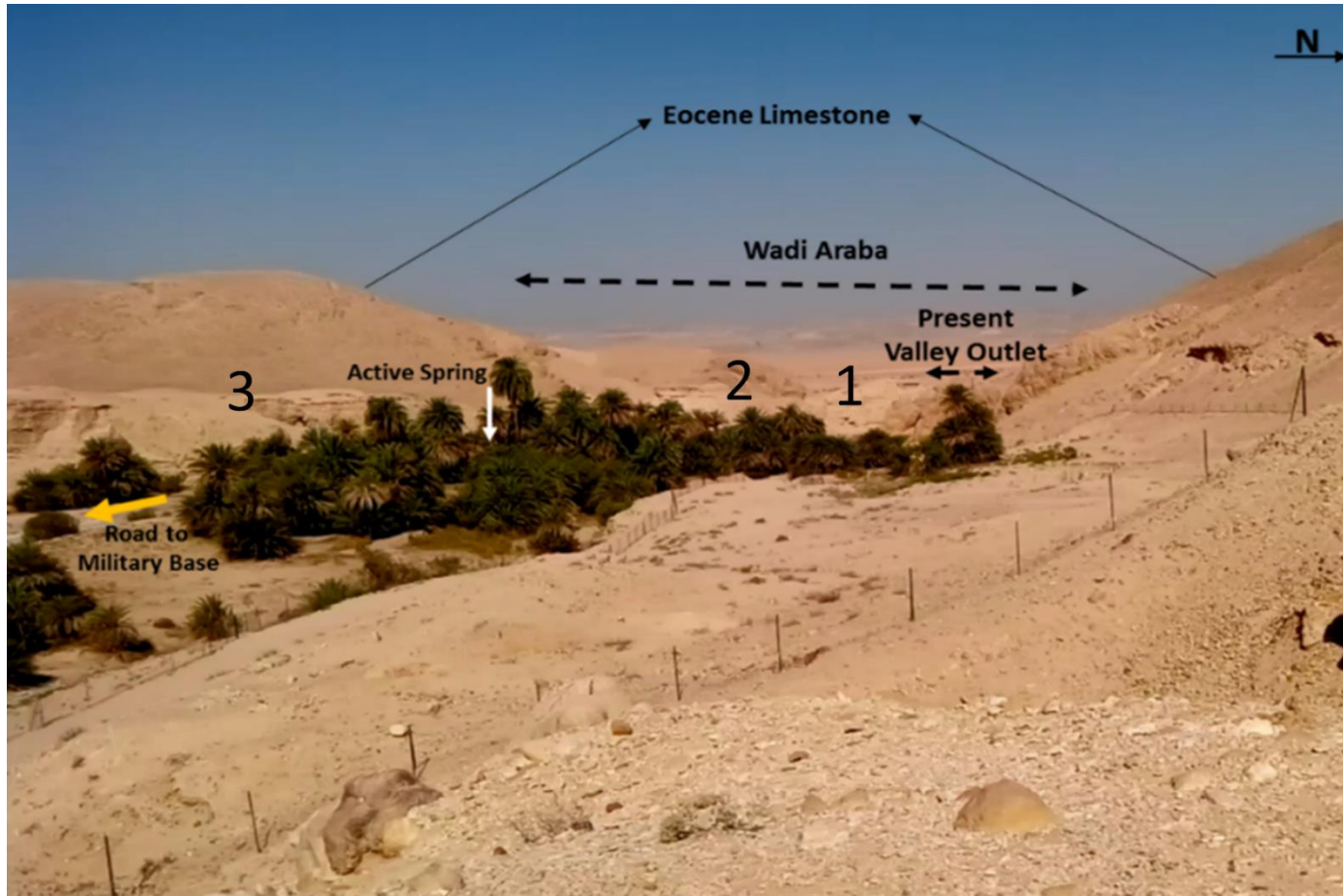
Figure 4.8 Westward view of the Gharandal Valley showing the spatial distribution of the sedimentary deposits (e.g. 1, 2, 3), the present day valley outlet, vegetation (Palm trees) and the location of an active spring (Photo taken at a location next to the GH5 section discussed later in the next chapters).

Figure 4.9 a) The Gharandal Valley sediments near the present-day valley outlet. b) Active spring in the Valley. Photos taken in 2018.

4.3.6   Previous studies

The fine-grained sediments in the Gharandal Valley were attributed to the Lisan Formation (late Pleistocene) and considered as lacustrine sediments (Ibrahim and Rashdan, 1988), however, the Lisan Formation is named after Lake Lisan that existed in the Dead Sea Basin (ca. 70 to 14 ka) (Bartov et al., 2002; Torfstein and Enzel, 2017) with a maximum altitude of ca. -168 m asl, thus making it impossible for the Gharandal sediments, located ca. 80 km to the south of the maximum extent of Lake Lisan (Kaufman et al., 1992) and at altitudes of 250 m to 270 m asl, to be part of this formation (Henry et al., 2001; Al-Masaeed, 2014). In addition, the Lisan sediments are characterized by laminated (mm-thick) carbonate and clastic

laminae (Neugebauer et al., 2014), while the Gharandal sediments do not show this lithological sequence.

In their survey of historic sites in Wadi Araba, Henry et al. (2001) reported the presence of fine-grained sandstone and clay lacustrine sediments in the Gharandal Valley, from which apparently Middle and early Upper Palaeolithic (ca. 150 to 30 ka) artefacts were collected and hence they assumed that the sediments were of late Pleistocene age. Other artefacts of apparent Acheulean age were also reported near the Gharandal Valley (Al-Nahar and Clark, 2009).

The two thick sequences near the valley outlet (1 and 2 in Figure 4.8), separated by the road leading eastward to the Gharandal base, were the focus of three previous studies. As part of an investigation of Quaternary sites in southern Jordan and Israel, Röhl (2015) collected 37 bulk sediment samples from ca. 15 m of sediments in the Valley, and based on laser particle size distribution analysis, the author reported that the sediments particle sizes and granulometric parameters (e.g. sorting and skewness) vary widely and that the sediments comprise both fluvial and aeolian deposits, with an increase in particle size towards the top of the sequences, where the sand is enriched in silica (Al-Masaeed, 2014). Mischke et al. (2017) also investigated the Gharandal Valley sediments. In their study the authors considered the two sequences near the valley outlet to represent one continuous sequence with an overlap at ca. 6 m above the base of the section located north of the road (1 in Figure 4.8). This study was the first to report OSL and ^{14}C age estimates from the sediments. The authors collected samples from the exposure south of the road (2 in Figure 4.8) and reported two OSL ages of 112±9 ka and 32±4 ka and four ^{14}C ages of 38 to 25 ka cal BP. The upper two ^{14}C ages agreed with an OSL age of 32±4 ka, while the lower two ^{14}C ages were not in stratigraphic order with the OSL age of 112±9 ka (Table 4.2). The authors attributed this to contamination of the younger carbonates and to the fact that the ages are beyond the limit of the dating method. Accordingly, the authors suggested two periods of sedimentation occurred at 112±9 ka and 32±4 ka. In addition, based on bulk sediment samples from the lower ca. 7 m of the section located north of the road, the authors reported the presence of ostracod shells in 5 of 13 samples collected, where species of *Ilyocypris cf. bradyi*, *Scottia pseudobrowniana*, *Candona neglecta*, and *Heterocypris salina* were found. The dominance of *I. cf. bradyi*, and the presence of *S. pseudobrowniana* and *H. salina* led the authors to conclude that the interpretation of an ancient lake is not confirmed and suggested that an in-stream wetland environment of small ponds

and swamps probably existed in the Gharandal Valley at two periods during MIS5 and MIS3 (Mischke et al., 2017).

More recently, Al-Saqarat et al. (2020) revisited the Gharandal Valley sediments and provided new OSL age estimates from the sediments. They investigated the sequences near the valley outlet, however, following the assumption of Mischke et al. (2017), the authors also considered the two sections to represent one continuous sequence from bottom to top. The authors also reported OSL ages from two different sections (Sites 2 and 3) located at ca. 500 m to the east of the valley outlet. In their study, seven stratigraphically inconsistent ages for their Site1 were reported. The lower part of their Site 1 (which represents the section north of the road) age estimates were 138±11 ka, 117±9 ka, and 95±8 ka and the top part (the section south of the road) age estimates were 120±8 ka, 104±11 ka, 70±6 ka and 36±3 ka (Table 4.2). These results showed that the OSL age estimate of 32±4 ka and all the ^{14}C ages reported by Mischke et al. (2017) for this sequence are stratigraphically inconsistent. The authors also reported OSL age estimates of 115±8 ka and 69±6 ka for their Site 2 and 74±7 ka for their Site 3 (Table 4.2). Two artefacts were recovered from their Site 3 which were assigned to Middle Palaeolithic (minimum age of 74±7 ka).The authors reported the presence of wetland deposits and fluvial in-wash beds. Accordingly, based on these age estimates and field observations the authors concluded that the Gharandal Valley sediments record a palustrine wetland environment that persisted from ca. 125-70 ka and resulted from a positive water balance in southern Jordan and a landslide dam structure that blocked the valley outlet supporting the previous conclusions of Mischke et al. (2017). Regarding the wetland demise, the authors suggested that after ca. 70 ka a period of fluvial aggradation and then dam removal occurred and valley dissection occurred at ca. 36 ± 3 ka.

Table 4.2 Published OSL age estimates for the Gharandal Valley sediments. (from Al-Saqarat et al., 2020; Mischke et al., 2017)

Al Saqarat et al., 2020								
Sample ID	Depth (m)	K (%)	Th (ppm)	U (ppm)	Water content (%)	Total dose rate (Gy/kyr)	Equivalent dose, De (Gy)	OSL age (ka)
GH11	12.3	0.17±0.02	3.8±0.38	1.61±0.08	20±5	0.68±0.05	93.2±2.96	138±11
GH12	11.1	0.17±0.02	4.55±0.46	2.07±0.1	20±5	0.81±0.06	95±3.15	117±9
GH13	10.6	0.49±0.05	7.07±0.71	3.79±0.19	20±5	1.74±0.13	144.53±6.17	95±8
GH14	1.6	0.2±0.02	2.61±0.26	1.36±0.07	20±5	0.71±0.04	85.09±2.82	120±8
GH15	1.2	0.29±0.03	2.5±0.25	2.22±0.11	20±5	0.95±0.07	98.2±7.52	104±11
GH16	0.8	0.35±0.04	3.84±38	2.56±0.13	20±5	1.14±0.07	79.85±4.95	70±6
GH17	0.6	0.64±0.06	8.38±0.84	2.77±0.14	1±0.5	2.07±0.15	75.59±2.51	36±3
GH21	9.2	0.04±0.01	1.97±0.2	0.76±0.04	20±5	0.34±0.02	38.59±0.83	115±8
GH22	0.4	0.31±0.03	5.14±0.51	2.11±0.11	20±5	1.11±0.07	77.11±3.67	69±6
GH31	0.8	0.68±0.07	4.32±0.43	4.88±0.24	20±5	1.85±0.14	137.32±4.07	74±7
Mischke et al., 2017								
JED-20	2.4	0.56	3.3	1.3	11	1.13±0.031	36±4	32±4
JED-21	5.5	0.1	2.1	0.9	11	0.53±0.015	59±4	112±9

However, discrepancies between the studies are present, particularly regarding the age estimates of the sediments. Figure 4.10 shows the reported OSL age estimates from the two studies for the sections near the valley outlet. It shows that the samples were collected from different locations in the sedimentary exposures. However, Al-Saqarat et al. (2020) argued that the inconsistent age estimates of Mischke et al. (2017) are due to dosemitry miscalculations, while the authors did not provide an explanation for the two stratigraphically inconsistent age estimates in their study and were attributed to uknown reasons. In addition, Mischke et al. (2017) and Al-Saqarat et al. (2020) considered the two sedimentary sequences

near the valley outlet to represent one continuous sequence, thus, no studies reported any sedimentary descriptions or analyses for the upper ca. 10 m of the section north of the road. This needs further investigation to establish if the two sequences really record synchronous depositional events. Furthermore, the discrepancies in the age estimates and interpretations could be the result of dosimetry miscalculations due to the lack of understanding of the sedimentological and geochemical characteristics of the sediments.

Considering the present-day environmental processes at and around the Gharandal Valley, where both fluvial and aeolian deposition are active (Ibrahim and Rashdan, 1988; Saqqa and Atallah, 2004), a more comprehensive understanding of the sediments granulometric and geochemical characteristics is needed in order to identify the associated hydrodynamics and aerodynamics within the broader depositional environment of the sediments. Understanding these processes, their interaction with GW deposition (Pigati et al., 2014) and climate/tectonics in the valley (Le Béon et al., 2010; Saqqa and Atallah, 2013) is essential in resolving the nature of the depositional environments and the associated hydrological processes which could also add significant data for the correct OSL dosimetry calculations, particularly about the samples' depth and moisture content, where the latter is a significant factor in OSL age estimations (Duller, 2008). Thus, this study will provide these detailed characteristics of the deposits at high resolution sampling intervals and contribute to resolving the age and nature of the Gharandal Valley sediments.

For this PhD. project, five sedimentary sections were chosen, representing the main sequences in the valley (see 3.3.1). GH1 and GH2 sections are the main sections near the present-day valley outlet, while GH3 and GH4 (Site 2 of Al-Saqarat et al., 2020) were sampled from one continuous sequence located ca. 450 m to the east of the outlet and GH5 (Site 3 of Al-Saqarat et al., 2020) is located at ca. 500 m to the east of the outlet. The latter three sections were chosen in order to investigate any spatial sedimentological and depositional relationships within the valley (Figure 4.11).
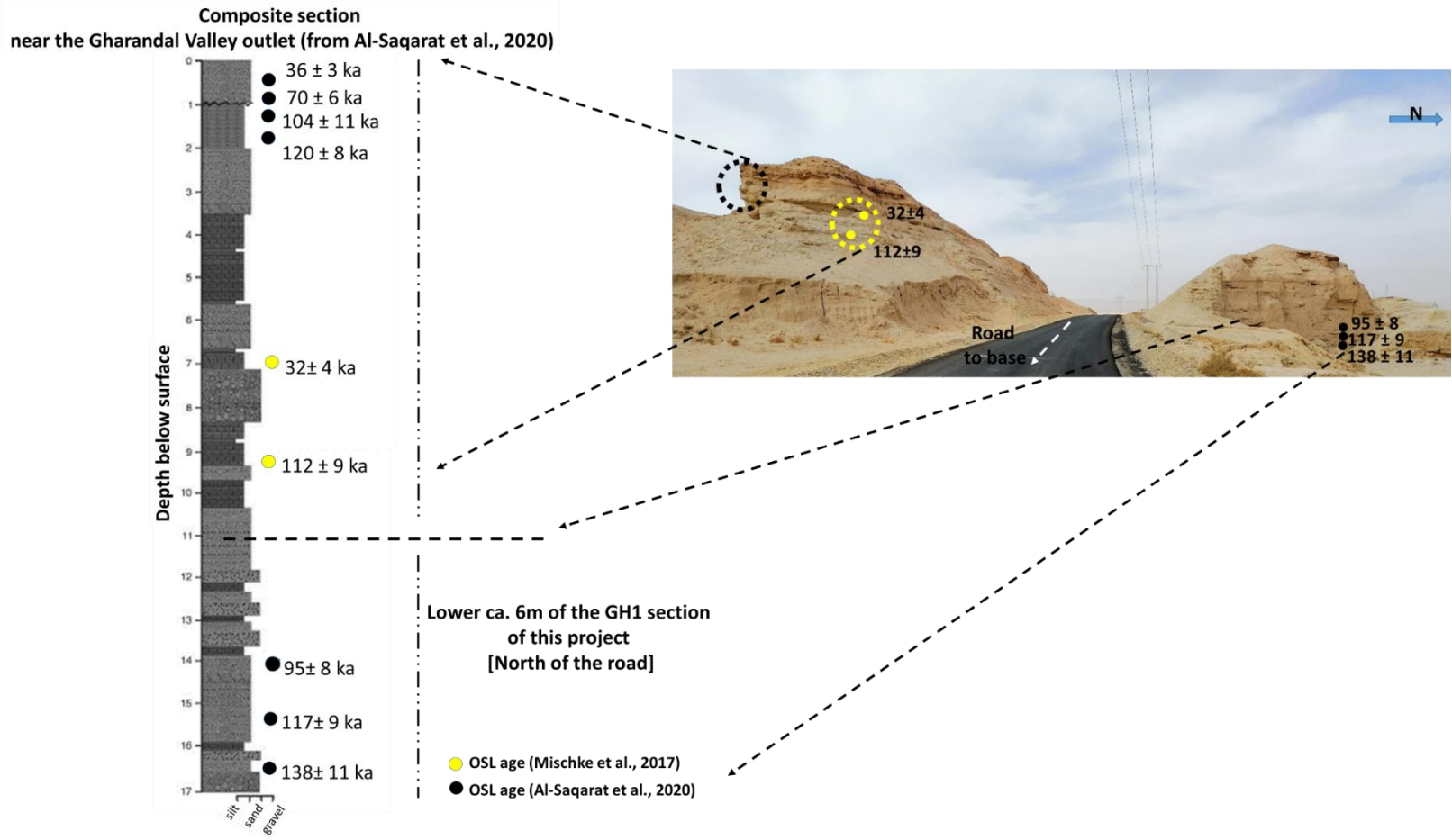
Figure 4.10 OSL age estimates and their locations in the sections near the Gharandal valley outlet reported in Mischke et al. (2017) (yellow colour) and Al-Saqarat et al. (2020) (black colour). Ages are in ka.
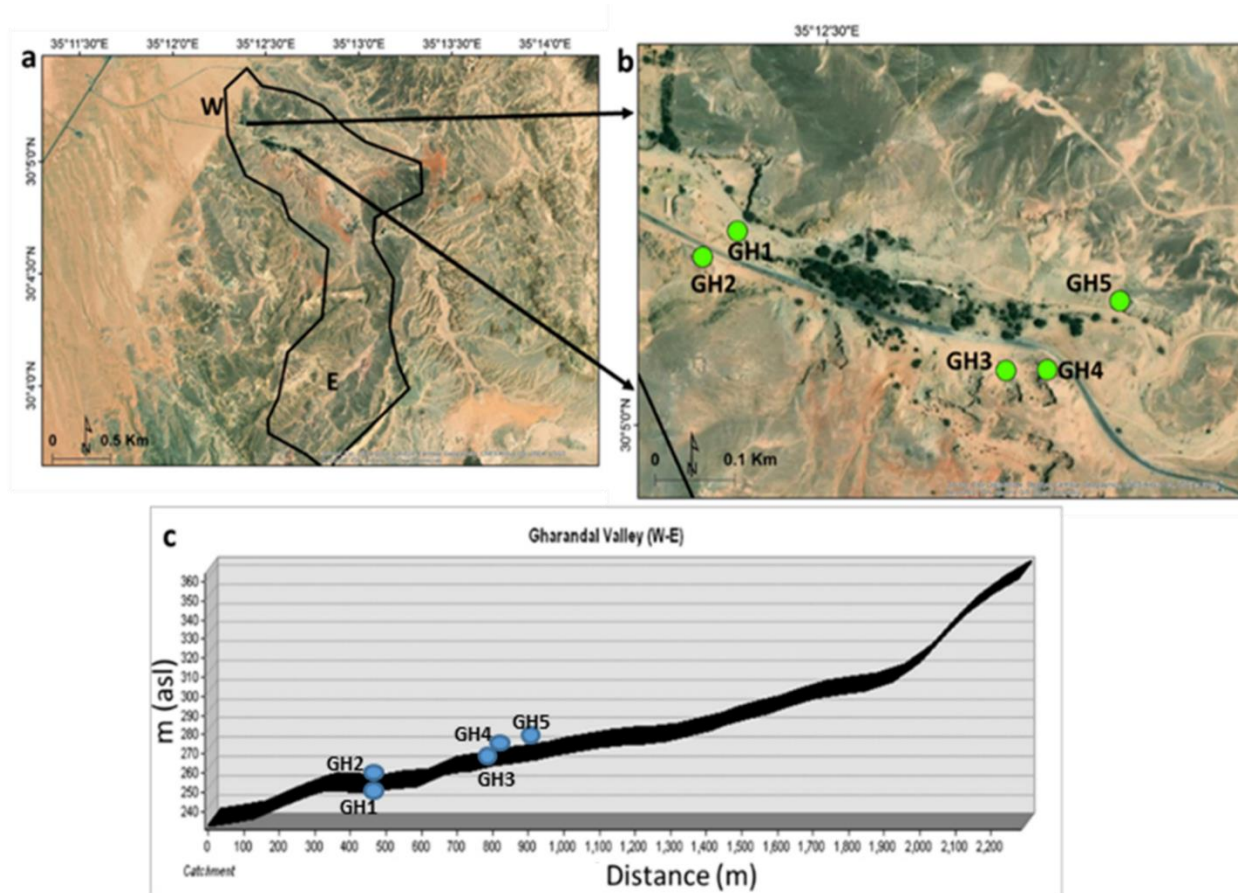
Figure 4.11 a) Google Earth image of the Gharandal Valley. Black polygon: the present day catchment area built using hydrological tools in ArcMap 10.3.1 using SRTM v3 (30m pixel) Digital Elevation Model. W, E show the extension of the elevation profile in (c). b) Google Earth Image showing the locations of the Gharandal Valley study area sequences studied in this project.

4.4   The Dead Sea Basin (DSB)

The Dead Sea pull-apart basin has formed at the overlap between two major plates along the Dead Sea Transform (DST), where the Arabian Plate (Jordan) moves north, while the Sinai Plate moves south (Atallah and Al-Taj, 2004). This movement has resulted in different geological outcrops on both sides of the DSB, where the rocks along the eastern side are older (Precambrian to Eocene) (Abed, 1985b) than on the western side, where Precambrian and Palaeozoic rocks are absent (Figure 4.12). The geological formations along the eastern side of the basin are more varied comprising sandstone formations, sandy limestone and dolomite, limestone, marl, chalk and conglomerate. This variability in the catchment drives the allogenic siliciclastic sediments deposition and their compositions (see Chapter 1; 1.2).

Alongside the slip movements, vertical displacement of the rift floor has been occurring since its formation; this displacement does not occur at the same rate throughout the basin and the rate of the subsidence/uplift is still a matter of debate (Freund, 1965; Neev and Emery, 1967; Freund et al., 1968; Atallah et al., 2002; Bartov et al., 2002; 2006; Ferry et al., 2007; Abu Ghazleh and Kempe, 2021).
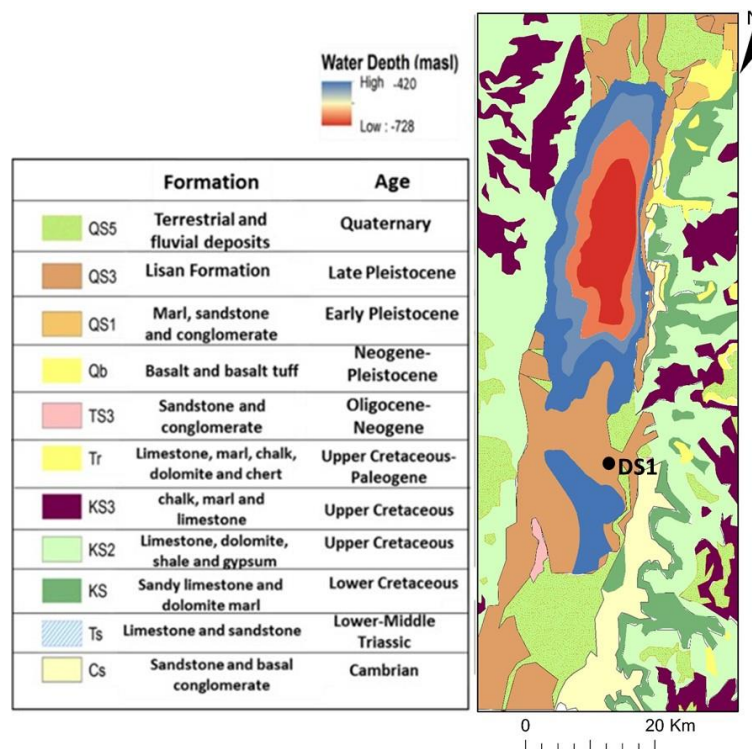
Figure 4.12 Geological map of the Dead Sea area. Showing outcrops along the eastern side are older than strata on the western side. Also showing the location of the DS1 section of this project. The map was generated based on geological data from Abu Ghazleh, (2011) and the Dead Sea bathymetry data from Neugebauer et al. (2014).

4.4.1 The Dead Sea Basin (DSB) hydrology

The Dead Sea (DS), and probably its precursors (Bartov et al., 2002; Torfstein, 2017), is a deep, large terminal lake located in the lowest point on Earth's surface (Abu-Jaber, 1998; Al-Weshah, 2000; Gertman and Hecht, 2002), presently at ca. -420 m asl..

The lake level fluctuations in the DS are a function of the evaporation/precipitation and runoff (including the inflow from subsurface springs) balance (Abu-Jaber, 1998; Al-Weshah, 2000; Salameh and Al Farajat, 2007; Enzel et al., 2008). The Dead Sea receives its fresh water input from its ca. 43000 km^2 catchment (Salameh and Al Farajat, 2007) primarily through northern tributaries (e.g. the Jordan River), western highlands and groundwater discharge, and from the eastern highlands that drain into the Dead Sea (Figure 4.13) (Al-Weshah, 2000). The main precipitation sources are the wet season (winter) EM cyclones affecting the northern and central parts of the basin, and ATPs with occasional ARSTs during autumn affecting the southern parts of the basin (Kahana et al., 2002; Kushnir et al., 2017) (see Chapter 2; 2.2).

The DSB is bounded by western and eastern highlands reaching up to 1200 m asl. The DSB catchment orographic gradient of precipitation between the highlands and the lower rift is ca. 30 mm /100 m (Salameh and Al Farajat, 2007). For example, higher annual precipitation is recorded in Amman Airport and Rabba stations compared to Es Safi station in the southern DSB (Figure 4.13 b) (Alraggad et al., 2017). The average annual precipitation over the present Dead Sea is ca 100 mm.yr^{-1} (Alraggad et al., 2017), while over the northern highlands of the DSB catchment it can reach up to >800 mm.yr^{-1}, and the southern arid to hyper-arid zone receives <50 mm.yr^{-1} precipitation (Kahana et al., 2002; Salameh and Al Farajat, 2007) (Figure 4.13). The DSB summer temperature reaches up to 40°C, with a mean temperature of ca. 15°C in January, over the present-day Dead Sea. The wind over the Dead Sea reaches a maximum speed of >10 m/s and occurs primarily during the winter season. During winter, the winds are northerly (55%) with southerly winds (26%), while during summer, the northerly winds increase (69%) compared to the southerly winds (8%). During both seasons, Eeastern Mediterranean breeze winds occur representing ca. 12% with an average speed of ca. 3.5 to 4 m/s (Hect and Isaac, 2003). The relative humidity over the DS ranges from 50 to 70%. The Dead Sea lake evaporation is >1500 mm.yr^{-1} (Stein et al., 1997; Abu-Jaber, 1998).
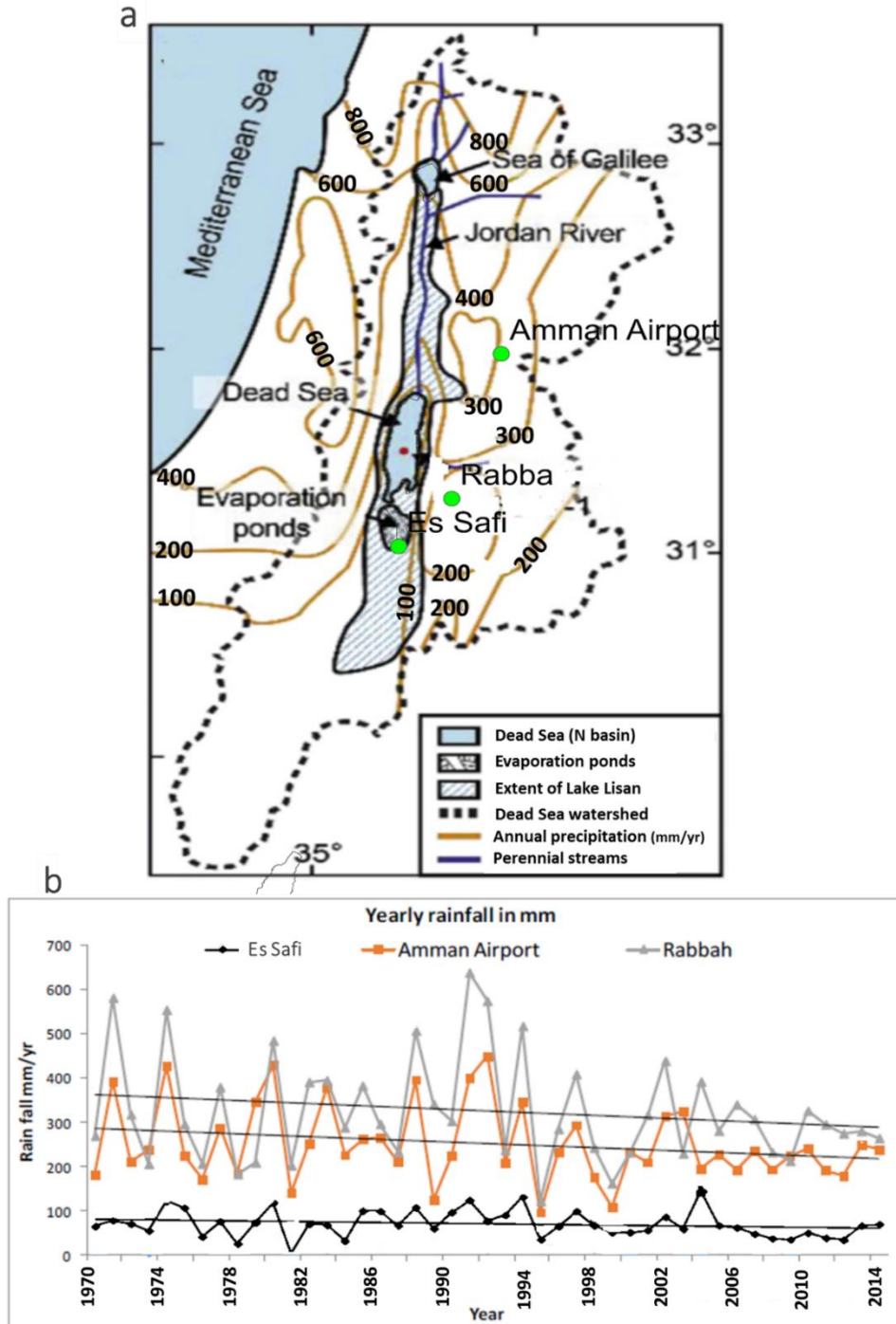
Figure 4.13 a) Schematic map showing the present-day Dead Sea catchment. Also shown are the precipitation isohyets (modified after Ben Dor et al. (2018)), b) Average annual precipitation for the period 1970 to 2014 for three stations (locations on a) (modified from Alraggad et al. (2017)).

The present-day Dead Sea levels have fluctuated significantly through time (Al-Weshah, 2000; Gertman and Hecht, 2002; Abou Karaki and Closson, 2012). Major falls in lake level have been recorded since the 1970s following the extensive exploitation of freshwater resources in the DSB catchment for domestic and agricultural uses (Figure 4.14), with the exception of two lake level rise events

following the major rainy years of 1980 and 1992 (Gertman and Hecht, 2002). The annual water inflow from the Jordan River decreased from ca. 1870 million cubic meter (MCM) in the 1920s to ca.190 MCM in early 1990s (Salameh, 1996) which led to decreased freshwater input into the DS and consequently the evaporation exceeded the water input (Gertman and Hecht, 2002).

The Dead Sea water is enriched with magnesium, calcium, bromide and potassium, and relatively poor in sulphate, sodium and carbonate (Abu-Jaber, 1998; Al-Weshah, 2000; Gertman and Hecht, 2002). In the Dead Sea, the bromide/chloride ratio is 1:35 compared to the ratio of 1:1000 in oceans, with a pH value of 6.1 to 6.7 (avg. 6.4), lower than the pH in oceans (8.2) (Abed, 1985b). In addition, the Dead Sea water salinity of 345 g/l is the highest worldwide, ca. 10 times the oceans' salinity (Abed, 1985b; Al-Weshah, 2000). Thus, the vertical stability of the Dead Sea is a function of temperature and salinity variability.
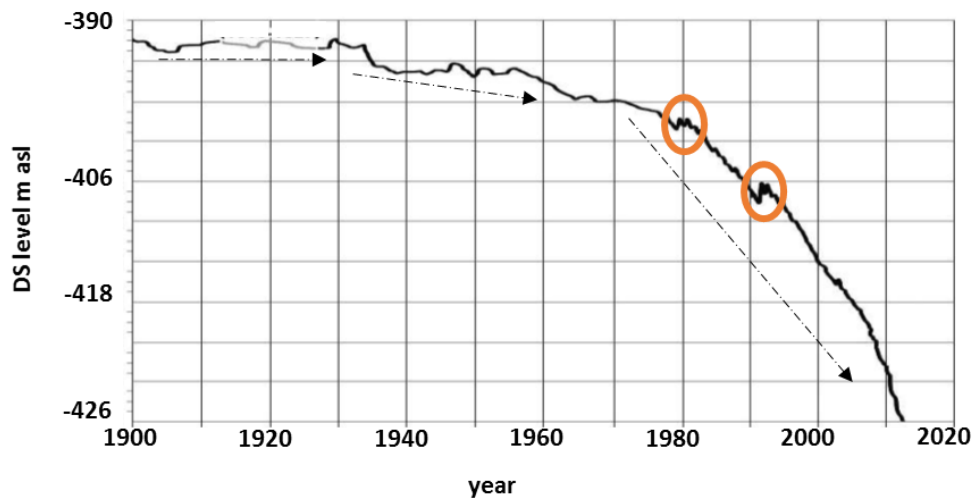
Figure 4.14 The Dead Sea (DS) level record from the year 1900 to 2012. The dashed arrows show the post-1970 rapid decline in the DS levels. Circles indicate the two level-rise events (modified from Abou Karaki and Closson, 2012).

Prior to the 1970s, the Dead Sea was under meromictic conditions for centuries (Gertman and Hecht, 2002) when the input of freshwater was sufficient to sustain an upper, ca. 40 m deep and 30% saline, epilimnion layer and a lower, ca. 34 % saline hypolimnion layer (Abed, 1985b), while post the 1970s, the Dead Sea started a holomictic period. A meromictic period refers to a lake period with a stable stratification throughout the year in which no lake overturn occurs during winter, while, a holomictic period refers to a lake period where stable stratification is maintained during summer with a lake overturn during winter due to the reduced freshwater input and the increase in the upper water layer salinity (Gertman and

Hecht, 2002). This holomictic period was interrupted following the high rainfall events in 1980 and 1992 and the addition of substantial amounts of freshwater establishing meromictic conditions for short periods of time in the DS (Figure 4.15) (Gertman and Hecht, 2002).
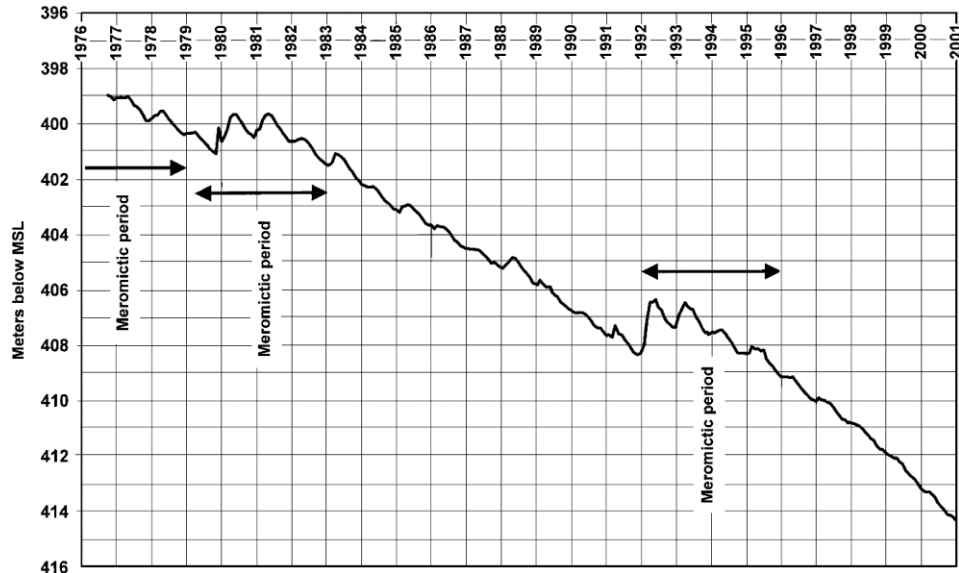
Figure 4.15 The post-1970 Dead Sea level record showing the formation of two meromictic periods from ca. 1980 to 1983 and from 1992 to 1995 (modified from Gertman and Hecht, 2002).

The water bodies that occupied the DSB in past times comprise mixtures of Ca-chloride brines to freshwater lakes (Lazar et al., 2014). They originated from evaporated seawater, that occupied the early DSB. These waters interacted with the surrounding carbonate outcrops, resulting in the formation of Ca-Chloride brines depositing the Sedom salts (>740 ka). Following the Sedom lagoon disconnection from the Mediterranean Sea, several brackish to fresh-water lakes filled the DSB. The interaction between these water bodies and freshwater input from the drainage area, i.e. precipitation, have contributed to changes in their size and composition (Waldmann et al., 2007).

Being a terminal lake, the DS hydrology and lake levels are sensitive to climate variability and short-term, seasonal, climate events (e.g. intense floods and droughts). Similarly, the water bodies that occupied the DSB during past times and left sedimentary exposures in the surroundings of the present-day Dead Sea; i.e. Lake Amora (~740-140 ka) (Torfstein et al., 2009), Lake Samra (~135 to 70 ka) (Waldmann et al., 2010), Lake Lisan (~70-14 ka BP) (Bartov et al., 2002) and Lake Damya (~14-12 ka BP) (Abed and Yaghan, 2000) record both short term,

close to annual (Prasad et al., 2004), and long term, glacial/interglacial (Torfstein et al., 2013a), hydroclimate fluctuations in the DSB.

The geographical location (Abed, 1985b; Landmann et al., 2002) altitude (Machlus et al., 2000) and lithology (Bani Sakhir, 1996; Abed and Yaghan, 2000; Kolodny et al., 2005) of the DS1 sedimentary sequence investigated in this project (Figure 4.12) suggest that it is part of the Lisan Formation which is discussed further below.

4.4.2   Lake Lisan

4.4.2.1   Introduction

Lake Lisan, a brackish (Abed, 1983) to fresh water lake, occupied the DSB between ca. 70 ka and ca.14 ka (Bartov et al., 2002; Torfstein and Enzel, 2017). One study suggested earlier onset of Lake Lisan at ca. 87 ka BP (Abu Ghazleh and Kempe, 2021). Lake Lisan levels fluctuated between more than -400 m asl (Torfstein et al., 2013a), and its highest level, ca. -164 m asl, at ca. 26 ka (Bartov et al., 2002), reflecting hydrological and climatic changes in the DSB watershed (Kaufman et al., 1992; Abed and Yaghan, 2000; Bartov et al., 2002; Landmann et al., 2002). Lake Lisan levels fell dramatically after 14.5 ka. Between ca. 14 ka to 12 ka, the Damya Lake formed, followed, during the Holocene, by the Dead Sea (Abed and Yaghan, 2000). Nonetheless, one study suggested Lake Lisan levels reached ca. 0 m asl during the onset of its filling at ca. 87 ka BP to 75 ka BP and another high lake level of ca. -56m asl at ca. 79 ka BP (Abu Ghazleh and Kempe, 2021).

At its maximum extent, Lake Lisan extended from Lake Tiberius, ca. 60 km north of the present-day Dead Sea, to ca. 35 km south of the present-day Dead Sea, a total lake length of ca. 200 km (Kaufman et al., 1992) (Figures 4.16 and 4.17). This maximum extent was associated with the highest lake level of ca. -164m asl at ca. 26 ka (Bartov et al., 2002). This level, ca. >200 m higher than the present-day Dead Sea level (<-400m asl), was attributed to a substantial increase in freshwater input that allowed the lake to overcome a tectonic sill (at ca. -280 m asl, Sill in Figure 4.16 b), and join Lake Tiberius and Lake Lisan (Bartov et al., 2002). During the LGM, Hazan et al. (2005) also recorded a high stand for Lake Tiberius, at ca. 24 ka to 26 ka, synchronous with the high stand of Lake Lisan, further supporting the joining of the two lakes.
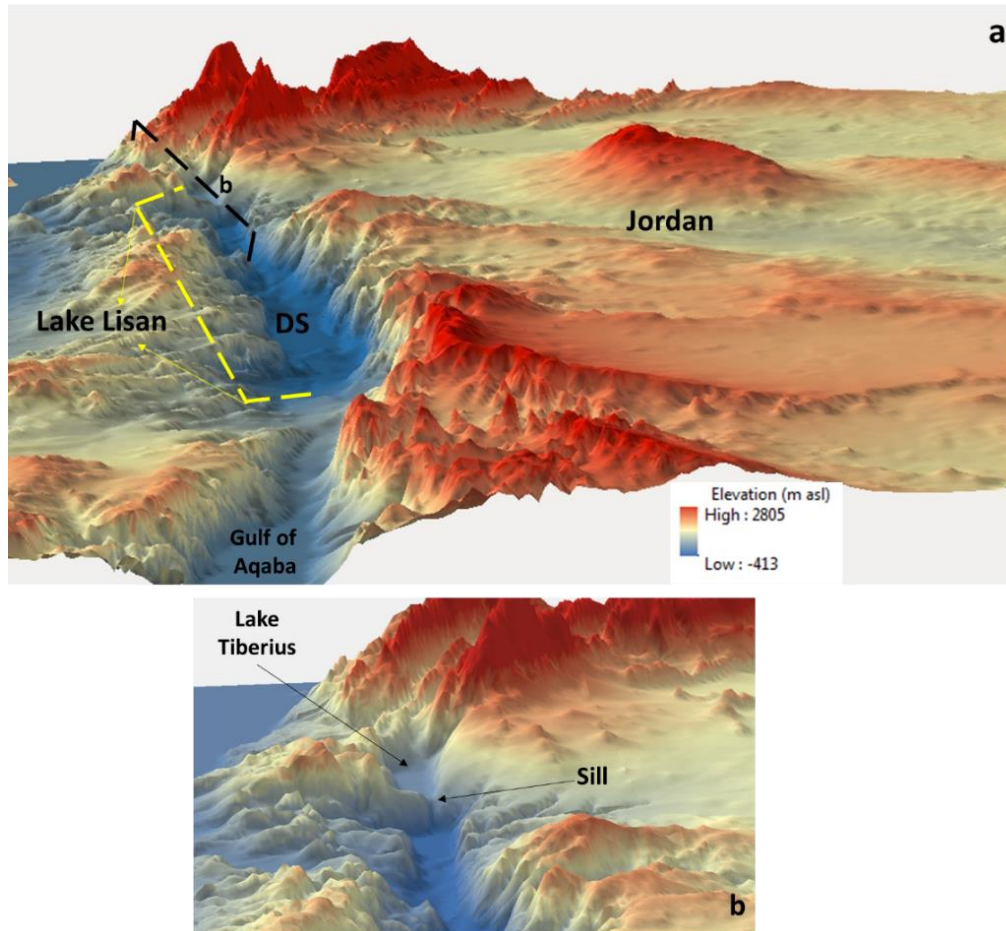
Figure 4.16 a) 3D representation of the DSB topography, showing the maximum extent of Lake Lisan at ca. 26ka (yellow dashed line). b) Close-up view of the northern part of the basin showing the tectonic sill separating the DS and Lake Tiberius. **DS**: present-day Dead Sea. Created using SRTM v3 (30m pixel) Digital Elevation Model (DEM). Vertical scale is exaggerated.

Lake Lisan limnological and hydrological history is archived in its deposits (known as the Lisan Formation) (Kaufman et al., 1992; Bani Sakhir, 1996; Abed and Yaghan, 2000; Bartov et al., 2006; Neugebauer et al., 2014). Several studies have investigated the Lisan Formation and provided data about tectonics in the DSB, lake levels, hydrological variations, and long term climatic fluctuations and relations with global climatic events. These studies mainly focused on exposed sedimentary sequences (Kaufman et al., 1992; Bartov et al., 2002; Haase-Schramm et al., 2004; Torfstein et al., 2013b), terraces (Lisker et al., 2009; Abu Ghazleh and Kempe, 2021) and sediment cores (Neugebauer et al., 2014; Ben Dor et al., 2019). Also, the geochemistry of the sediments has been addressed (e.g. Stein et al., 1997; Landmann et al., 2002; Lazar et al., 2014).

Most of these studies, however, were conducted on the western margins of the DS basin (the Israeli side), while few studies investigated the eastern (Jordanian

side) sediment sequences (Figure 4.17). From the eastern side of the DSB, only two studies reported radiometric ages of exposed Lisan sediments (LSM1, LSM2, Landmann et al., 2002) and terraces (Abu Ghazleh and Kempe, 2021), while other studies only reported laminae counting and stratigraphic correlation with dated sequences from the western DSB (e.g. Abed and Yaghan, 2000; Ferry et al., 2007). This indicates the importance of investigating the eastern side of the DSB to contribute new data on the Lisan Formation exposures and to correlate with well-dated records from the western side.
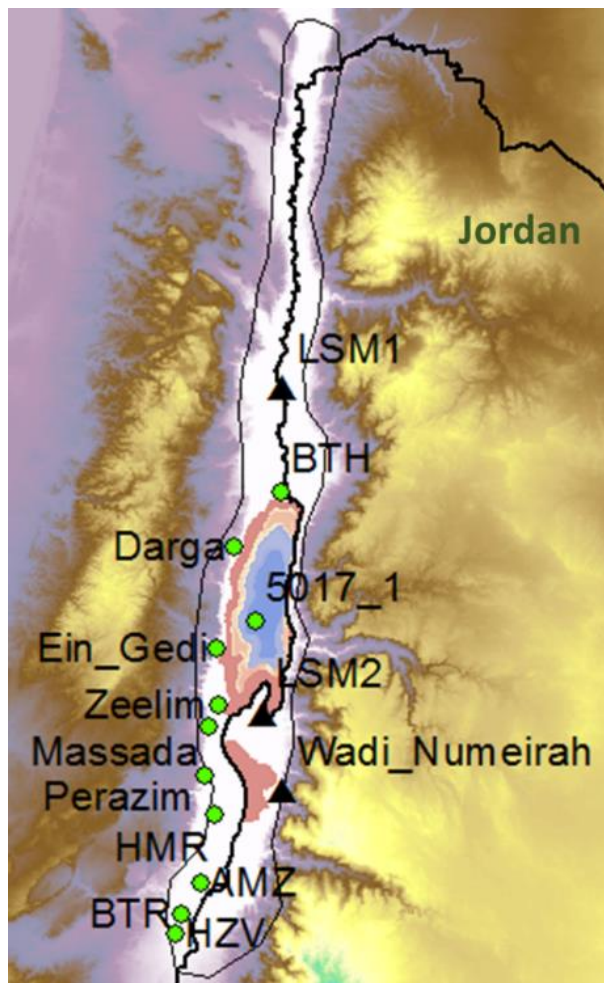
Figure 4.17 Locations of main previous studies on both sides of the DSB. **Green circle**: location on the western DSB margin. **Black triangle**: location on the eastern DSB margin. **Black polygon**: maximum extent of Lake Lisan (Kaufman et al., 1992). Data sources; BTR, HZV, Darga, BTH (Kaufman et al., 1992), Perazim (Machlus et al., 2000), Masada, Zeelim (Bartov et al., 2002; Haase-Schramm et al., 2004; Torfstein et al., 2013a), Ein Gedi (Migowski et al., 2006), LSM1, LSM2 (Landmann et al., 2002), Wadi Numeirah (Abu Ghazleh, 2021), 5017_1 ICDP core (Neugebauer et al., 2014).

4.4.2.2   Tectonic processes effects on Lake Lisan sediments

As discussed earlier, terminal lake levels are affected by short-term and long-term evaporation and precipitation variations (Abu-Jaber, 1998; Gertman and Hecht, 2002; Kolodny et al., 2005; Xiao et al., 2018). Nonetheless, the DSB is an active tectonic pull-apart basin where continuous tectonic subsidence/uplift have been occurring since its formation (Joffe and Garfunkel, 1987; Atallah and Al-Taj, 2004; Diabat et al., 2004; Bartov et al., 2006; Ferry et al., 2007; Lisker et al., 2009). Thus, the sediment archives can also record the different tectonic processes in the basin alongside the climatic changes in the catchment, the correct reconstruction of the sediments' history therefore requires proper identification of these processes and accounting for their varied effects (e.g. Bartov et al., 2006) since tectonic subsidence can affect lake level lowering. For example, it has been suggested (Neev and Emery, 1967) that the final decline of Lake Lisan may have been the result of tectonic subsidence of the northern and southern DS basins accompanied by the uplift near the central parts of the DSB rather than climate.

Generally, the DSB is governed by two primary tectonic regimes affecting its edges and the inner basin (Bartov et al., 2006). The margins are affected by an E-W extension due to flexure, while the inner basin is extensional on a N-S axis, resulting in different tectonic subsidence and uplift rates across the basin for the last ca. 70ka (Sagy et al., 2003; Bartov et al., 2006; Ferry et al., 2007) (Figure 4.18). Bartov et al. (2006) investigated the tectonic settings of the Massada Plain and the Lisan Peninsula, an elongated structural dome (Figure 4.18). They concluded that in the Massada plain, three tectonic episodes are recorded during the last 40 kyr, at 35-32 kyr, at 24-26 kyr and at 15-12 kyr. Thus, they calculated a subsidence rate of 0.3 m/kyr for the last ca. 40 kyr (Bartov et al., 2006). However, the Lisan Peninsula, which presently separates the northern and southern DSB segments, is an exception, where an uplift rate of ca. 2.3 m/kyr, for the last 34 kyr, is recorded as a result an underlying salt diapir buried at ca. 100m (Bartov et al., 2006; Al-Zoubi and ten Brink, 2001).

On the eastern side of the DSB, Ferry et al. (2007) reported a vertical displacement rate of 0.2 mm/yr for the last 47.5 ka for a Lisan Formation sedimentary sequence located about 35 km to the north of the present-day Dead Sea northern boundary. However, this study did not report any radiometric age estimates; it was based on stratigraphic correlation with other dated western Lisan sequences.

It has been suggested that the basin escarpments have not been significantly affected by the tectonic settings and that stromatolites along the western (Lisker et al., 2009) and eastern (Abu Ghazleh and Kempe, 2021) escarpments record the original lake levels. This assumption has resulted in reconstructed lake level curves at levels ca. 80 m (Lisker et al., 2009) and 150 m (Abu Ghazleh, 2021) higher than lake levels reconstructed from the inner basin exposed sedimentary sequences (e.g. Torfstein et al., 2013b). Lisker et al. (2009) attributed the 80 m difference at 35.6 ka, between their reconstructed lake levels and the inner basin reconstructed lake levels, to a subsidence rate of 2 m/ka for the last 75 ka. However, this subsidence rate is higher than the rates measured in the inner basin, at least for the last 70ka, and may not be representative of the true subsidence rates (Torfstein et al., 2013b).

Figure 4.18 Northward view of the DS showig the major tectonic structures along the Dead Sea pull-apart basin and locations of Massada Plain and Lisan Peninsula overlay Google Earth Pro. 2021 image, data from Bartov et al. (2006).

Nonetheless, a recent study that investigated the fossil lake shorelines at 8 sites in the DSB using high resolution drone topography and U-series dating, reported that the subsidence/uplift rates are not similar either N-S or E-W (Jara-Muñoz et al., 2020). The authors estimated an uplift rate at a shoreline on the eastern escarpment, near the Lisan Peninsula, of 0.19 m/ka for the last 50 ka, while all the fossil shorelines on the western escarpment indicated subsidence rates in the range of 0.09 to 0.44 m/ka (Jara-Muñoz et al., 2020).

These studies indicate the significance of tectonic activity in the DSB and show that for a particular sediment exposure or a shoreline terrace, the location and the understanding of the tectonic activity (i.e. subsidence/uplift effect) are significant prior to any basin-wide stratigraphic correlation between Lake Lisan sections.

4.4.2.3 Lake Lisan sediments

Based primarily on sedimentary exposures in the DSB near the Perazim Valley, Massada and LSM2 (see Figure 4.17 for locations), the sedimentary record of Lake Lisan, the Lisan Formation, is composed of three main stratigraphic members. The lower member (ca. 70-58.5 ka) dominated by alternating inorganic aragonite and clastic laminae (*aad*) sequences, the middle member (ca. 58.5-31 ka) dominated by alternating gypsum, laminated silt, sands and *aad* sequences and the upper member (ca. 31-14.5 ka) characterized again by *aad* sequences (Abed and Yaghan, 2000; Machlus et al., 2000; Stein, 2001; Bartov et al., 2002; Haase-Schramm et al., 2004; Kolodny et al., 2005). The three members correspond to MISs 4, 3 and 2, respectively, reflecting the effect of global climate changes on the DSB.

Based on the 5017_1 ICDP deep core lithology (for location see Figure 4.17) (Neugebauer et al., 2014; Ben Dor et al., 2019), the facies in the Lisan Formation comprise: (1) the *aad* facies, with sub-types, namely green *aad* that is recognized by the presence of green organic matter overlying the detrital laminae and mixed aragonite laminae of *aad* where alternating clastic, gypsum and aragonite laminae is observed. These sub-types can only be properly distinguished through micro-facies analysis. The *aad* sequences also comprise disturbed laminations, probably following mass wasting events, i.e. slumping and turbidites, which can be triggered by floods, dramatic lake level changes and tectonic events such as earthquakes (Neugebauer et al., 2014; Ben Dor et al., 2019); (2) the laminated detritus (*ld*) facies, mostly common in the Lisan middle member (ca. 58.5-31 ka) (Machlus et al., 2000; Ben Dor et al., 2019), this facies is distinguished from the *aad* facies by a lower frequency of aragonite laminae with higher abundance of clastic laminae. In addition, a halite facies is also present in the sediments recovered from the core (Neugebauer et al., 2014). Figure 4.19 illustrates the deposition of the different facies and the controlling hydroclimatic conditions during high and intermediate water balance conditions showing the importance of freshwater input in maintaining *aad* deposition (Ben Dor et al., 2019), where the alternations between the lithological facies is representative of the Lake Lisan limnological changes; i.e.

the lake's response to local and regional climate changes (Stein, 2001; Prasad et al., 2004; Ben Dor et al., 2019).
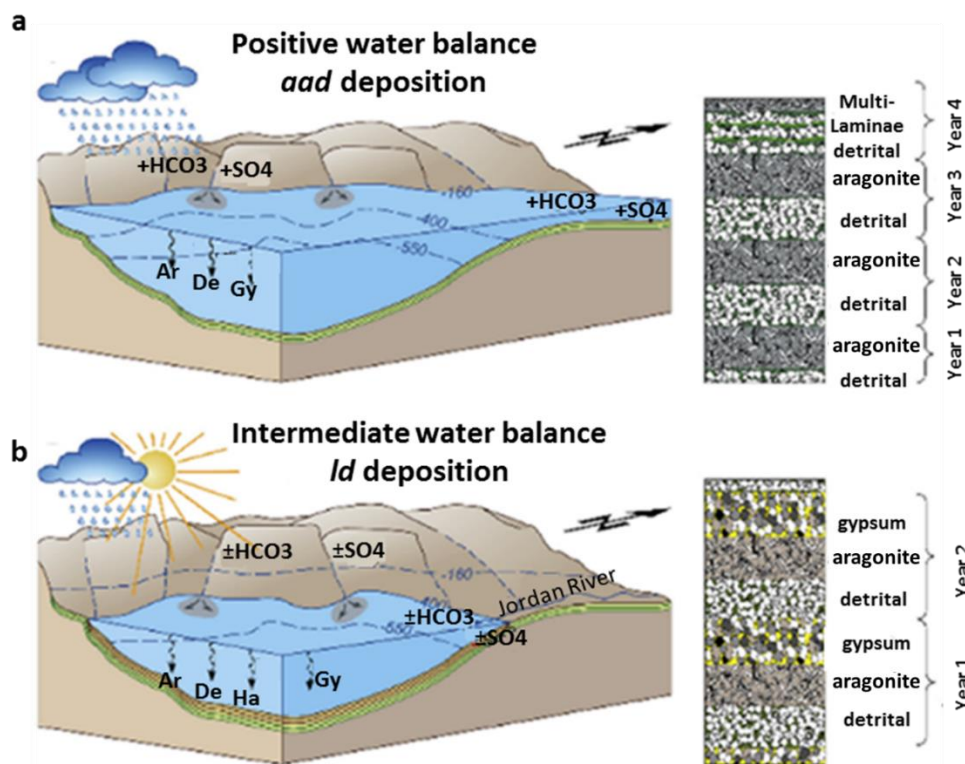
Figure 4.19 Schematic representation of the depositional processes in the DSB during variable hydroclimatic conditions. a) During positive water balance, aragonite (Ar) precipitation of during summer, and deposition of allochtonous detrital material (De) during winter ('*aad*' facies), b) Under moderate conditions, laminated detritus ('*ld*' facies) and alternating aragonite, detritus and gypsum deposition (from Ben Dor et al. (2019)). **Ar**: aragonite, **De:** detrital, **Gy:** gypsum, **Ha:** halite.

Lake Lisan, similar to the present Dead Sea, had very low HCO_3 content thus almost all bicarbonates required for the carbonate deposition were supplied through freshwater input (Stein et al., 1997). Based on present-day chemical composition of the water input into the Dead Sea, the deposition of ca. 0.5 mm carbonate laminae in Lake Lisan must have required the addition of a ca. 4.57 $m.yr^{-1}$ layer of freshwater to the lake, which significantly exceeds the lake's evaporation, e.g. evaporation of >1500 $mm.yr^{-1}$ for the Dead Sea (Stein et al., 1997).

The freshwater input into the lake supplies significant amounts of bicarbonate and sulphate and forms a less saline upper water body overlying the bottom brine. Following the input of freshwater, the lake reaches a stratified structure with sufficient Ca and bicarbonate content to deposit the aragonite. Gypsum deposition occurs during low lake stands when mixing, or overturn,occurs between the upper

less saline, $SO4^{-2}$ rich, low Sr/Ca water body and the underlying Ca^{2+} rich, high Sr/Ca brine. The clastic deposits occur during low lake stands when the freshwater input brings allogenic siliciclastic sediments from the catchment into the lake (Stein et al., 1997; Abed and Yaghan, 2000; Stein, 2001).

The inorganic precipitation of carbonates in Lake Lisan is primarily governed by the Mg/Ca ratio and salinity of the upper water layer (Stein et al., 1997; Landmann et al., 2002) which are inherited from several sources: (1) the hypersaline lakes that predated Lake Lisan, (2) saline springs discharging into the DSB, (3) freshwater input and (4) freshwater springs in the catchment, where an Mg/Ca ratio of ca. 2 is required for the deposition of aragonite (Katz, 1973). The Dead Sea water Mg/Ca ratio is 4.36 and the saline water springs in the DSB area have an Mg/Ca ratio of 2.74 indicating their tendency to precipitate aragonite rather than calcite, while in an opposing trend, Lake Tiberius precipitates calcite corresponding to its Mg/Ca ratio of 1.25 (Stein et al., 1997).

4.4.2.4 The Lisan gypsum beds

Gypsum is present in the Lisan sediments in many forms, as crystals, thin laminae and thick beds (Stein et al., 1997; Abed and Yaghan, 2000; Torfstein et al., 2013b; Neugebauer et al., 2014). The most significant gypsum formations are the thick gypsum beds of tens of centimetres observed in the exposed sedimentary sequences (Landmann et al., 2002; Torfstein et al., 2013b). However, prior to interpreting the environmental implications of these gypsum beds, an understanding of the drivers of their formation and their relation to climate-induced events is required.

Like the present-day Dead Sea, Lake Lisan was low in SO_4. Thus, the freshwater that supplied the bicarbonate for Lisan aragonite precipitation must have also supplied the SO_4 required for the gypsum deposition. However, in order to explain the formation of thick (tens of centimetres) gypsum beds, high amounts of Ca^{2+} must have been provided by the lower brine (Stein et al., 1997). As discussed by Stein et al. (1997), during positive water balance periods, the upper water layer of Lake Lisan mass increases, thus restricting the contribution of Ca^{2+} from the lower brine into the locations of gypsum precipitation near the upper water layer. In the upper water layer, Ca^{2+} and bicarbonate are depleted to form the aragonite, while the SO_4 is being stored in the upper water layer in large amounts. During negative water balance periods, when complete or partial mixing of the upper and lower water layers occur, the lower brine supplies the required Ca^{2+}, combined with the

existing high mass of SO_4, thick gypsum beds are then formed in the lake. Thus, the gypsum thick beds of Lake Lisan have been considered to represent severe lake level drops and negative water balance conditions where partial or complete mixing of the two water layers took place (Stein et al., 1997; Abed and Yaghan, 2000; Torfstein et al., 2013b).

These gypsum beds, are considered as stratigraphic markers that can be traced laterally for long distances (Torfstein et al., 2013a). Based on stratigraphic correlation of five sedimentary sequences along the western DSB, and U/Th dating, Torfstein et al. (2013a) constrained the age estimates of the main gypsum beds within the Lisan Formation by dating aragonite laminae below and above these beds. Six gypsum stratigraphic anchor points were identified. The regression age estimates of the gypsum beds were estimated for the bottom and the top of each unit. These units comprise: the Lower Gypsum Unit with a top age from (57.94±3.44 ka to 57.12±3.5 ka) and a bottom age from (60.42±3.44 ka to 58.2±0.82 ka); the Small Gypsum Unit with a top age from 54.4±0.82 ka to 51.89±3.44 ka and a bottom age from 55.14±3.5ka to 52.85±3.44ka; the Curled Gypsum Unit with a top age from 45.2±3.44 ka to 45.81±3.5 ka and a bottom age from 46.47±3.44 ka to 46.12±3.5 ka; the Broken Gypsum Unit with age ranges from 36.83±3.44 ka to 39.9±0.81 ka for the bottom of the unit while no ages were reported for the unit top; the Upper Gypsum Unit with a top age range from 17.24±3.44 ka to 15±0.81 ka and a bottom age from 22.54±3.44 ka to 17.4±0.81 ka; and the Additional Gypsum Unit between 13.06±2.2 ka for the top of the unit and 15.21±3.44ka to 13.6±2.2 ka for the bottom of the unit.

Due to the close connection between the ages of the gypsum beds and the Heinrich Stadials (icebergs discharge into the North Atlantic), Torfstein et al. (2013a) tuned the ages of the gypsum beds to match the Heinrich events (H6 to H1). The gypsum beds and the tuned ages are listed in Table 4.3. Based on these estimates, tuned ages and previous Lake Lisan level reconstructions, Torfstein et al. (2013a) provided a revised lake level curve (see 4.4.2.6). However, no age estimates for the gypsum beds themselves have been retrieved in order to confirm these tuned ages.

In addition, due to the lack of well dated Lisan sequences from the eastern DSB, a basin (W-E) correlation with Torfstein et al. (2013a) stratigraphic marker beds has not been reported. This correlation, can add significant information about the

tectonic settings and help in refining the lake level curves from both sides of the DSB.

Table 4.3 Gypsum anchor units tuned ages. **GU**: Gypsum unit. Uncertainties: average residual value of radiometric ages around linear regression curves. (Data from Torfstein et al., 2013a).

Gypsum Unit	Lower GU		Small GU		Curled GU		Broken GU		Upper GU		Additional GU	
	Top	Bot.	Top	Bot.	Top	Bot.	Top	Bot.	Top	Bot.	Top	Bot.
Tuned age (ka)	58.5	61	54	56	47.5	49	38.3	39.7	15.5	17.1		14.5
Uncertainty	1	1	0.5	0.5	0.5	0.5	0.5	0.5	0.5	0.5		0.5

4.4.2.5 Lake Lisan sediments geochemical composition

The pale laminae in the Lisan sedimentary sequences are assumed to have been deposited as endogenic aragonites in the upper water layer of the lake and not to have undergone any diagenetic alteration, while the clastic laminae reflect catchment disturbance and in-wash (Bani Sakhir, 1996; Stein et al., 1997; Abed and Yaghan, 2000; Landmann et al., 2002; Kolodny et al., 2005). Thus, the variability in the chemical composition of the different facies in the Lisan Formation reflect the lake's limnological history.

The most abundant minerals in the Lisan sediments are aragonite, gypsum, halite, calcite, and quartz. In addition, poorly defined Mg-calcite is present (Bani Sakhir, 1996; Abed and Yaghan, 2000). However, considering that the catchment area around the DSB contains abundant carbonate formations, Ca content may be influenced by detrital contributions, thus, since Sr is primarily associated with aragonite in the Lisan sediments (Landmann et al., 2002; Neugebauer et al., 2016), aragonite precipitation can be indicated by elevated values of Sr/Ca (Begin et al., 2004; Neugebauer et al., 2016). The siliciclastic fraction can be identified by the Ti/Ca ratio, considering that Ti is an allochthonous element and has been associated with catchment erosion and in-wash (e.g. Metcalfe et al., 2010), while the gypsum deposition can be represented by the SO_3/Ca ratio (Neugebauer et al., 2016).

4.4.2.6 Lake Lisan reconstructed level curves

Several studies have attempted to reconstruct absolute lake level curves for Lake Lisan using different approaches. Some studies used direct level indicators such as fan deltas (e.g. Bartov et al., 2007) and sequence stratigraphy (e.g. Bartov et al., 2002), while other studies estimated relative lake levels based on the sedimentology from exposed outcrops in the DSB, based on the assumption that

the sedimentological changes in the sediments indicate the relative depth of water (e.g. Migowski et al., 2006).

Regardless of the previously discussed tectonic influence on the Lisan sediments (see 4.4.2.2), some studies (e.g. Landmann et al., 2002; Migowski et al., 2006; Abu Ghazleh and Kempe, 2021) did not account for the tectonic correction in their lake level reconstructions. While others such as Bartov et al. (2006) re-evaluated their previously published lake curve (Bartov et al., 2002) and applied a subsidence correction of 0.3 m/ka (Figure 4.20). Similarly, Torfstein et al. (2013b) re-evaluated their previously published data and corrected the gypsum beds altitudes (Torfstein et al., 2013a) by applying a subsidence correction of 0.3 m/ka. These corrections showed that a subsidence of ca. >10 m can be calculated for deposits at ca. 40 ka near the Massada site (Figure 4.18), thus indicating the need to account for this tectonic influence in order to achieve a basin-wide understanding of Lake Lisan limnological changes. These discrepancies are well illustrated in a synthesis of the reconstructed Lake Lisan levels (Figure 4.21). Discrepancies in the records exist, which can be attributed, but not limited to factors such as dating problems (e.g. Haase-Schramm et al., 2004), and adjustments for tectonic effects (e.g. Bartov et al., 2006; Lisker et al., 2009; Abu Ghazleh, 2021).
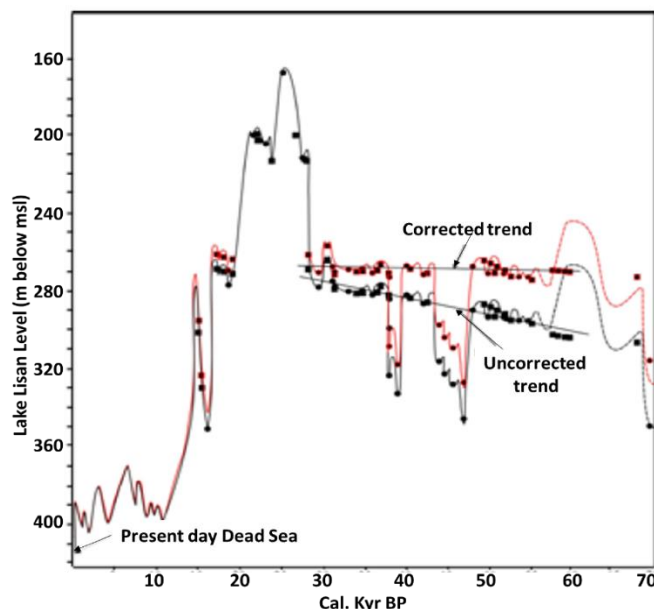
Figure 4.20 Bartov et al. (2006) Corrected Lake Lisan level curve. Tectonic subsidence rate of (0.3 m/ka) is used. Also showing the uncorrected lake level curve of Bartov et al. (2002). This indicates the significance of the tectonic processes influence on the vertical placement of the lake levels. (Modified after Bartov et al. (2006))
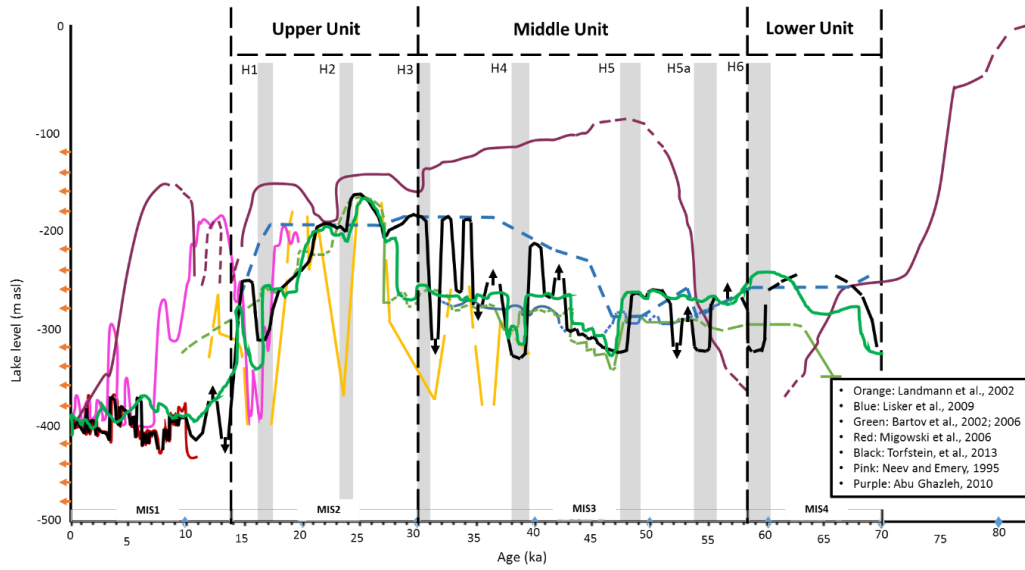
Figure 4.21 Synthesis of the reconstructed lake levels for Lake Lisan. Data sites; orange (LSM1, 2), blue (Perazim), Green (Massada), Red (Ein Gedi), Purple (Wadi Numeira). For locations and references refer to Figure 4.17. Also showing the Lisan Members (Upper, Middle and Lower). MISs based on (Lisiecki and Raymo, 2005).

From the seven reconstructed lake level curves shown in Figure 4.21, only two were based on sites from the Jordanian side: the orange (Landmann et al., 2002) and purple (Abu Ghazleh and Kempe, 2021) curves, dated using ^{14}C and U/Th dating methods, respectively. The orange curve follows almost similar trends to those obtained on the western side, however, it indicates lower lake levels. The purple curve does not show good correlation with the other records, probably due to the fact that this record was established based on terraces along the eastern escarpment and suggests that the lake level reached up to zero m asl at ca. 87 ka BP (Abu Ghazleh and Kempe, 2021).

Torfstein and Enzel (2017), based on the literature from the western DSB, attempted to refine and combine the reported relative and absolute lake level curves to generate a unified absolute lake level curve for Lake Lisan. Generally, the hydrological changes in the DSB indicate that glacial periods were characterized by higher lake levels, compared to low interglacial lake levels. The lake level fluctuations during MIS4 are still not well constrained, but they generally show higher levels compared to MIS3. The middle Lisan period during MIS3 is less stable compared to MIS2, with up to 100 m millennial-scale lake level fluctuations (Stein and Goldstein, 2017; Torfstein and Enzel, 2017). During MIS3, short-term high lake levels are recorded at 57, 53.5, 50.4, 49, 42.4, 40.5, 36.7, 34.5, 33 and 30ka. While, the highest lake level of ca. -164 m bsl was achieved

during the MIS2 period (see above) (Bartov et al., 2002; Stein and Goldstein, 2017; Torfstein and Enzel, 2017).

Nonetheless, a basin wide W-E correlation of lake levels or sediment altitudes, based on well dated stratigraphic anchor points, has not been reported yet. Identifying these stratigraphic relationships and the altitude ranges across the DSB is important especially when considering millennial-scale fluctuations, as small-scale offsets in altitude and/or age estimates could result in different interpretations. Not correcting for the tectonic effects could result in vertical offsets in the reconstructed lake levels by as much as tens of meters, which could be interpreted as hyperaridity (Torfstein and Enzel, 2017). For example, the lake level curve of Landman et al. (2002) (orange line in Figure 4.21) shows a high vertical offset with the lake level curves reconstructed from the western DSB.

Given the active tectonic setting of the basin, and the importance of relative lake level reconstructions in understanding the palaeohydrology and palaeoclimate of the region, understanding any differences in altitude in lake deposits of the same age either side of the Dead Sea fault system is important to refining these interpretations.

4.4.2.7 Lake Lisan sediments as proxies of short term climatic variability

The aragonite and clastic laminae in the published Lisan *aad* sequences are presumed to be varves that reflect annual or close to annual deposition (Prasad et al., 2009; Ben Dor et al., 2019). It is assumed that the aragonite and/or gypsum laminae were deposited during summer (dry season), depending on lake salinity, while the clastic laminae were deposited during winter (wet season) and flooding events (Abed and Yaghan, 2000). However, considering Lisan laminae as varves is not straight forward and requires detailed investigations (López-Merino et al., 2016; Ben Dor et al., 2019). One method to investigate the varve nature of sediments is by comparing the laminae count with radiometric ages. This was attempted by Prasad et al. (2009) who investigated a laminated section spanning ca. 17.4 ka to 22 ka from the Massada section and combined laminae counting and radiometric ages and concluded that the laminated aragonite and detrital facies (*aad*) in the section represent varves (Prasad et al., 2009). Other studies (e.g. Migowski et al., 2006; López-Merino et al., 2016) reported that the consideration of Lisan sediments as varves should be corroborated by detailed micro-facies identification of the laminae and the sub-laminae, especially for the deposition during relatively low lake levels where there is not enough supply of

freshwater to maintain seasonal aragonite deposition, i.e. *ld* facies (Ben Dor et al., 2019). Accordingly, the high lake level facies, particularly *aad*, deposits are considered varves, yet this is usually corroborated by age estimates to produce floating varve chronologies from different Lisan sequences (Prasad et al., 2009; Neugebauer et al., 2016; Ben Dor et al., 2018).

The identification of varves within the Lisan sediments is crucial for understanding short-term, annual, and decadal to centennial, hydrological and hydroclimatic changes in the DSB and the southern Levant. Several studies (e.g. Machlus et al., 2000; Bartov et al., 2002; Landmann et al., 2002; Waldmann et al., 2007; Torfstein et al., 2013a,b) have focused on resolving long-term, up to glacial/interglacial, climate variability during the period of Lake Lisan, however, resolving short-term climatic and hydrological variability has not been widely exploited. Few studies have attempted to focus on the lithological variations in the sediments, particularly *aad* sequences (e.g. Ben Dor et al., 2018), while other studies focused on the isotopic composition of the aragonites (Kolodny et al., 2005).

Lithological variations of the Lisan sediments

Considering that the hydrological changes in the DSB watershed have been associated with EM cyclones, the lake level fluctuations (rise and fall) reflect either enhanced or reduced EM precipitation, which is primarily determined by the track, depth and frequency of the EM cyclones into the Levant (Kahana et al., 2002; Enzel et al., 2008). Thus, to understand EM cyclone seasonality, attempts to reconstruct short-term climate variability, based on the lithological variability and characteristics of the *aad* laminae, have been carried out on sediment exposures (Prasad et al., 2004) and on the ICDP deep core (e.g. Ben Dor et al., 2018; 2019). For example, Ben Dor et al. (2018) investigated two sections from the ICDP core at ca. 27 ka and 18ka, by micro-facies analysis of 708 and 701 varves, respectively, and showed that the clastic laminae in the *aad* varves are comprised of sub-laminae reflecting flooding events and their frequency in the DSB watershed. Lake level rise is characterized by a higher frequency of clastic sub-laminae, i.e. higher flood frequency, compared with lake level falls, reflecting the intra-annual, enhanced and reduced, EM precipitation over the DSB watershed.

Oxygen and Carbon isotope ratios

Another proxy to estimate short-term hydrological, primarily P/E ratio, changes in the DSB catchment is the variability in the isotopic ratios, namely $\delta^{18}O$ and $\delta^{13}C$, of the Lisan aragonites (Gat, 1984; Kolodny et al., 2005). Lake carbonate oxygen isotope composition is primarily controlled by the water isotopic composition and temperature at time of deposition (Leng and Marshall, 2004) , which, in the case of Lake Lisan, refers to the upper (less saline) water layer (Gat, 1984). Nonetheless, for a lake in a specific regional context, a careful consideration and understanding of the complete hydrological and climatic system is required prior to the interpretation of the isotopic compositions (Jones and Imbers, 2010).

The present-day Dead Sea water isotopic composition short-term changes are a function of several factors, including water input, evaporation, E/P ratio and the mixing depth of the upper, less saline, water layer (Gat, 1984), while the lake steady-state ($\delta_{L,ss}$), considering the Dead Sea a terminal lake, is a function of the input water and evaporating water isotopic compositions. Thus, the $\delta_{L,ss}$ depends on the humidity, the lake water activity, the isotopic composition of water vapour in the atmosphere and the water/vapour fractionation factor. The $\delta_{L,ss}$ is dependent primarily on climate-related factors and independent of the incoming or evaporating water fluxes (Gat, 1984). Accordingly, it is important to differentiate between short-term (i.e. close to annual) $\delta^{18}O$ fluctuations and long-term steady state composition, around which the short-time oscillations occur (Kolodny et al., 2005).

Considering the Dead Sea (DS) as analogous to Lake Lisan (LL), LL reached considerably higher lake levels, and the upper water layer was generally more dilute due to enhanced precipitation over the region (Bartov et al., 2002; Kolodny et al., 2005; Enzel et al., 2008; Torfstein et al., 2013b; Torfstein and Enzel, 2017). This dilution of the upper water layer is based on the assumption that the Sedom Formation is the source of salt in the DSB, which has not changed through time; thus the lake volume in the DSB is inversely proportional to its salinity. Considering a maximum LL level of ca. -164m asl (Bartov et al., 2006), compared to the DS level of ca. -400m asl, ca. >230m in lake level difference is recorded corresponding to a substantial increase in the lake volume. Thus, it has been reported that LL salinity was 0.5 to 0.3 the salinity of the present DS (Begin et al., 2004; Kolodny et al., 2005). This indicates higher water activity (saturation vapour pressure) for

LL compared to the DS in the range of 0.88 to 0.94, for 0.5 to 0.3 salinity ratio of LL/DS, respectively (Kolodny et al., 2005).

Short-term $\delta^{18}O$ oscillations in the present-day Dead Sea waters during the period 1953-1983 (Figure 4.22) show two major excursions, from the DS $\delta^{18}O_{L,SS}$ of ca. +4.4 ±0.2‰, are observed with excursions to ca. +2.8 ‰ ($\delta^{18}O$= +1.6 ‰) during the rainy year 1968-1969 and the rainy year of 1980 (Gat, 1984; Kolodny et al., 2005). Based on the DS hydrograph (Figure 4.15) the effect of the $\delta^{18}O$ excursion during the year 1968-1969 was not as significant as during the year 1980, even though a lake level rise is recorded. This probably reflect the more stable lake limnology and levels prior to the freshwater exploitation and the sharp lake level lowering since the 1970s.
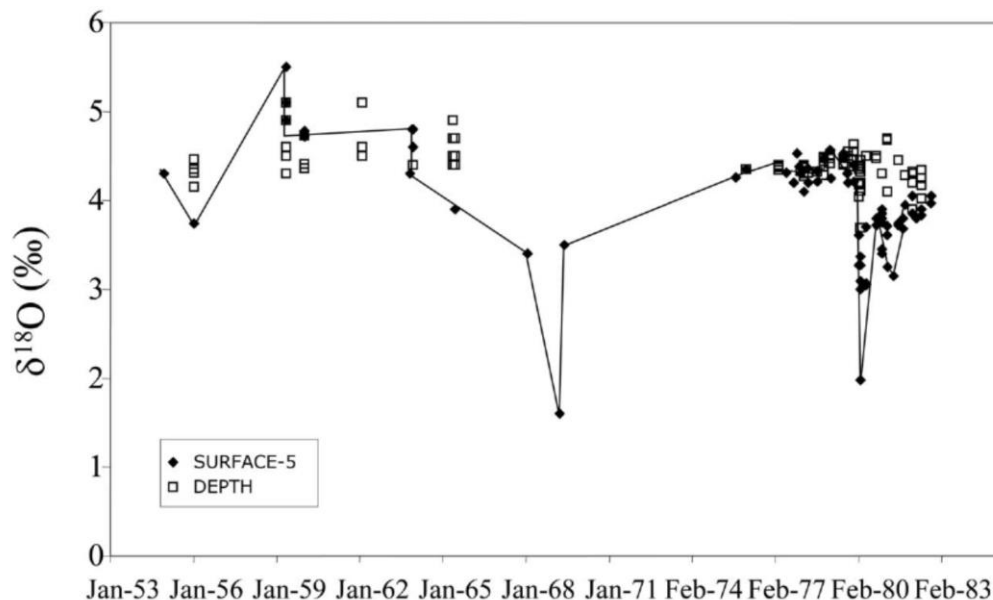
Figure 4.22 Dead Sea $\delta^{18}O$ variation over the period 1953 to 1983. The figure indicates that the deep water layer values are stable over time, while the upper water layer values vary following either enhanced precipitation or drought conditions. (From Kolodny et al., 2005).

Similarly, Kolodny et al. (2005) observed short-term, possibly annual, aragonite $\delta^{18}O$ excursions for LL aragonites in the Perazim Valley and Massada. The lower LL member values range from +2.9 to +6.6‰ (avg. +4.6±0.7 ‰), the middle member values range from +1.6 to +6.8‰ (avg. +4.6±1 ‰) and the upper member values from +4.2 to +6.5‰ (avg. +5.6 ±0.5 ‰). Aside from the long-term $\delta^{18}O$ steady state values, achieved at ca. 500 years (3 to 5 times the residence time of 100 years for LL), Kolodny et al. (2015) recognised short-term $\delta^{18}O$ steady state values, possibly as responses of changing and stabilizing environmental conditions around the DSB. Through high resolution laminae analysis, Kolodny et

al. (2005) observed three short-term $\delta^{18}O$ steady states (avg. values) over approx. 200 years (Figure 4.23 a), where large excursions in the $\delta^{18}O$ values are recorded at different times of LL. For example, Figure 4.23 a shows a continuous laminae by laminae analysis of ca. 200 laminae from the Massada section at ca. 30 Kyr BP, the values show relatively low excursions from the average values with only one extreme excursion of ca. 3‰ ($\delta^{18}O$= +1.8 ‰) in lamina #185 from the avg. value of ca. +5.2 ‰ and the long-term steady state of ca. +4.6 ‰. This excursion was attributed to a short-lived event of substantial increase in freshwater input and increased precipitation (Kolodny et al., 2005). These large $\delta^{18}O$ excursions from the average values (or steady state values) are representative of large flood events in the DSB catchment that are linked to changes in E/P ratio rather than temperature changes. As argued by Kolodny et al. (2005), a change of ca. 3 ‰ in $\delta^{18}O$ in a decade would require a temperature variation of ca. 15°C, while, if the upper less saline water layer is diluted to ca. 87% of the maximum salinity, the $\delta^{18}O$ value is reduced from ca. +4.5 ‰ to ca. +2.4 ‰. Thus, the aragonite $\delta^{18}O$ values do not only reflect changes in LL conditions, but also fluctuations of the input water $\delta^{18}O$ values (climatic conditions in the DSB catchment), i.e. increased precipitation and/or drought. In addition, Kolodny et al. (2005) provided a lamina by lamina $\delta^{18}O$ record of 50 laminae from the Perazim Valley at ca. 35 Kyr BP (Figure 4.23 b). This record follows a drop in lake level represented by a halite layer and a thick clastic layer. It shows a drop of ca. 3 ‰ that is followed by an increase of ca. 4 ‰ reflecting the lake filling up stage after a period of low lake stand (Kolodny et al., 2005).

Similar to the aragonite $\delta^{18}O$ composition, the carbonate $\delta^{13}C$ values can also be used to identify short and long-term variations in lake sediments (e.g. Kolodny et al., 2005; Dean et al., 2015). During transitions between different carbon-cycles, inorganic carbon isotopes are fractionated prior to their deposition with the lake authigenic carbonates (Leng and Marshall, 2004). However, the interpretation of lake sediment $\delta^{13}C$ is not straight forward and requires a comprehensive understanding of lake productivity, producers and changing sources (Wang et al., 2013).
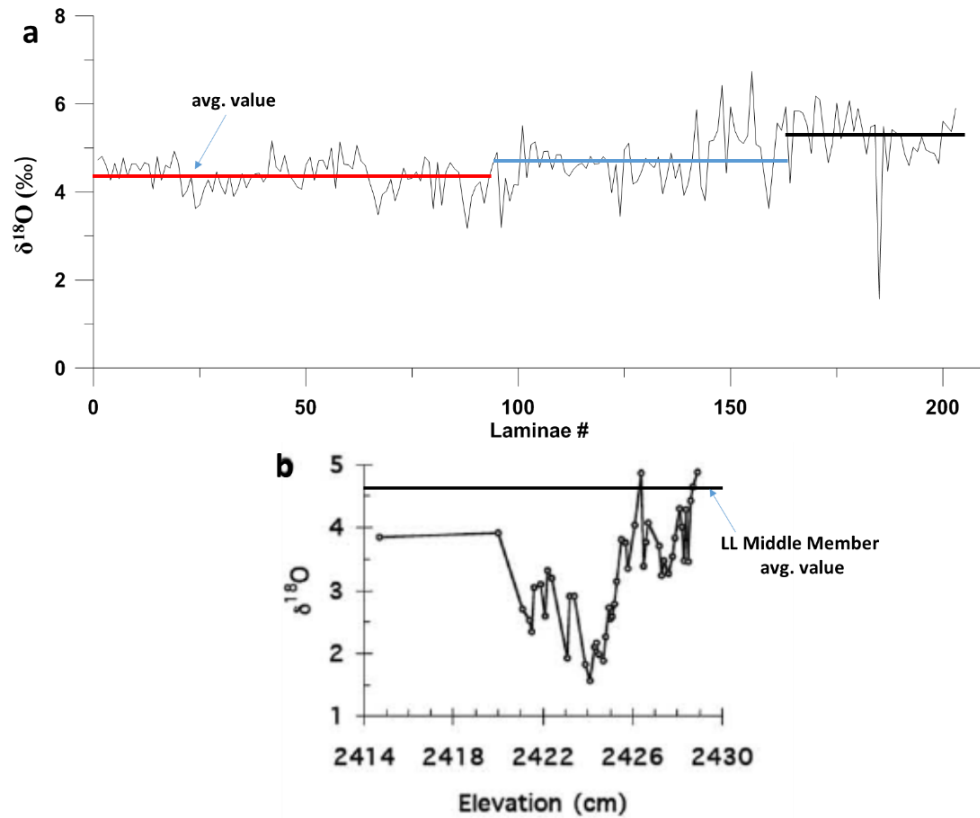
Figure 4.23 a) $\delta^{18}O$ composition of a of 200 aragonite laminae sequence from Massada at ca. 30 Kyr B.P. b) Detailed 50 aragonite laminae sequence from the Perazim Valley after a lake level decrease at ca. 35 Kyr B.P. (data from Kolodny et al., 2005).

Considering the "*sterility*" of the present-day DS and the similarity between its sediments and LL sediments, and the lack of bioturbation in the Lisan Formation laminated sediments, it has been suggested that LL sediments were *"sterile"* as well, except for the northern and southernmost parts of the lake where water input was supplied (Stein et al., 1997). Based on observations of the present DS, aragonite deposition has been associated with CO_2 degassing processes that is not mediated by biologic uptake of TCO_2, even though the deposition of aragonite during LL time was ca. six times the present-day DS deposition. Barkan et al. (2001) showed that when the partial pressure of CO_2 in the DS lake is very high during the aragonite deposition, total alkalinity and total carbon of the upper mixed water layer decreased, while $\delta^{13}C$ increased with time (Barkan et al., 2001). In addition, a trend towards less-enriched $\delta^{13}C$ values in a lake could be attributed to runoff through humid, well vegetated, catchment areas, where isotopically light plant material decomposition prevail, compared to enriched $\delta^{13}C$ values of a dry, sparsely vegetated, catchment (Talbot, 1990). Based on the latter consideration,

LL sediments and stromatolites $\delta^{13}C$ values have been used as a proxy of catchment erosion (runoff) (e.g. Abu Ghazleh, 2011).

Nonetheless, following an extremely rainy year in 1992 and the dilution of the upper water layer of the DS, Oren and Gurevich (1995) observed a dense spring bloom of *Dunaliella prava,* unicellular green algae, in the upper ca. 5-10 m of the DS waters that was visible by red colouration of the water. Considering this observation, and the fact that the LL epilimnion was more dilute than the DS epilimnion, such dense blooms may have occurred during the LL high stands. Accordingly, such spring blooms would have participated in CO_2 removal during the summer and this process would have ultimately been reflected in $\delta^{13}C$ enrichment of the precipitated aragonite (Kolodny et al., 2005).

Considering these two observations and the fact that the $\delta^{13}C$ values of LL show a wider range compared to the $\delta^{18}O$ values, avg. -1.2±1.9 ‰ and avg. +4.7±0.7 ‰, respectively, it has been suggested that $\delta^{13}C$ varies under a different time constant compared to $\delta^{18}O$ (Figure 4.24) (Kolodny et al., 2005). Thus until better understanding of LL productivity and contribution in the enrichment of the $\delta^{13}C$ is achieved, especially during high lake stands, $\delta^{13}C$ use an environmental proxy is limited (e.g. Kolodny et al., 2005).
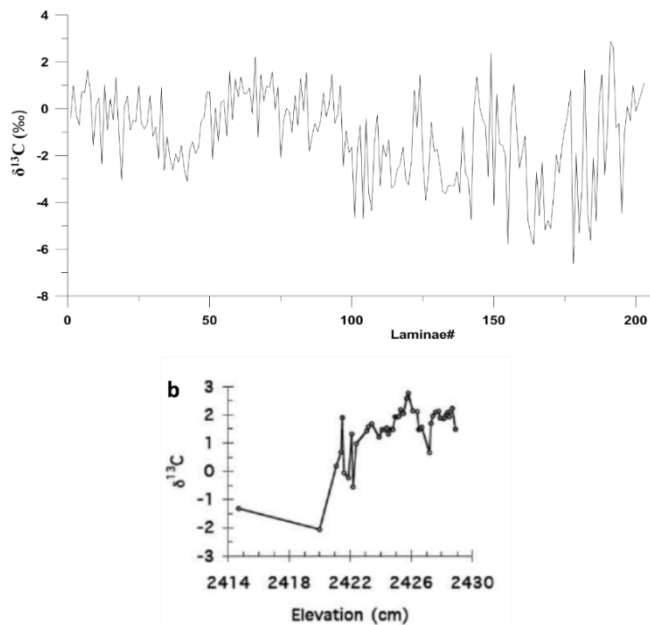
Figure 4.24 a) $\delta^{13}C$ composition of a 200 aragonite laminae sequence from Massada at ca. 30 Kyr B.P. b) Detailed 50 aragonite laminae sequence from the Perazim Valley after a lake level decrease at ca. 35 Kyr B.P. (data from Kolodny et al., 2005).

4.5   Chapter conclusions

In this chapter, the context of the two study sites (Gharandal Valley and the Dead Sea DS1 section) has been described and current literature and uncertainties, about the deposits age estimates and palaeoenvironmental interpretations, discussed.

The potential of the two study sites has been highlighted. The following chapters present the detailed results from the Gharandal Valley (Chapters 5 and 6) and DS1 section (Chapter 7).

Chapter 5. Gharandal Valley sedimentary sequences

5.1   Introduction

This chapter consists of three main sections that present the GH1, GH2 and then the GH3/4 and GH5 sedimentary sequences' locations, thicknesses, lithologies and age estimates. Following this, the sedimentary lithofacies are discussed in terms of their distinct sedimentological and geochemical characteristics. Finally, the identification of the sediments' depositional environment is explained and the interpreted environmental and climatic history of the sedimentary sequences is presented. The overall findings for Gharandal are summarised in Chapter 6.

5.2   GH1 sedimentary sequence

5.2.1   General description

The GH1 section (Figures 4.11 and 5.1) is located near the present-day outlet of the Gharandal Valley, to the north of the road leading eastwards to the Gharandal base. This site comprises about 16 m of sediments starting from the valley floor, with a basal elevation of 243 m asl. The base of the sequence, as observed on the valley floor, is composed of pebbles and gravels (Figure 5.1b) overlain by medium to coarse sand beds, silty beds with carbonate concretions and carbonate-rich silty beds. This stratigraphic sequence is repeated through the section, but with varied order and colour in some places, where the silt and carbonate concretions are found overlying beds of sand and small gravels. The thicknesses of the beds also vary, in some parts of the sequence, thicker small gravels, sand or silt beds are present compared to other parts (e.g. Figure 5.2 a). Also, starting from about 7m from the base, weak horizontally bedded sand is present at a few locations. Reddish colour root casts are also present, mainly accompanying some of the carbonate rich layers (identified in the field by HCL fizzing). Between 9.39 m to 12.4 m from the base of the section, thin (mm to cm) dark colour layers occur in places. The lithological investigation of this site indicates the presence of different hydrodynamics and depositional processes, compared to the present, which allowed the deposition of this section.The palaeocurrent direction is oriented 140/320 as measured on a weak cross bedding structure at ca. 2 m above the base of the section (Figure 5.2 b), similar to the present day generally E-W flow direction in the valley (Ibrahim and Rashdan, 1988; Ibrahim, 1993; Makhlouf et al., 2010; Mischke et al., 2017).

In order to investigate the granulometric and geochemical characteristics of the GH1 sediments, 295 bulk sediment samples were collected contiguously at

intervals of 2-10 cm representing the complete sequence from bottom to top, as explained in 3.3.1.
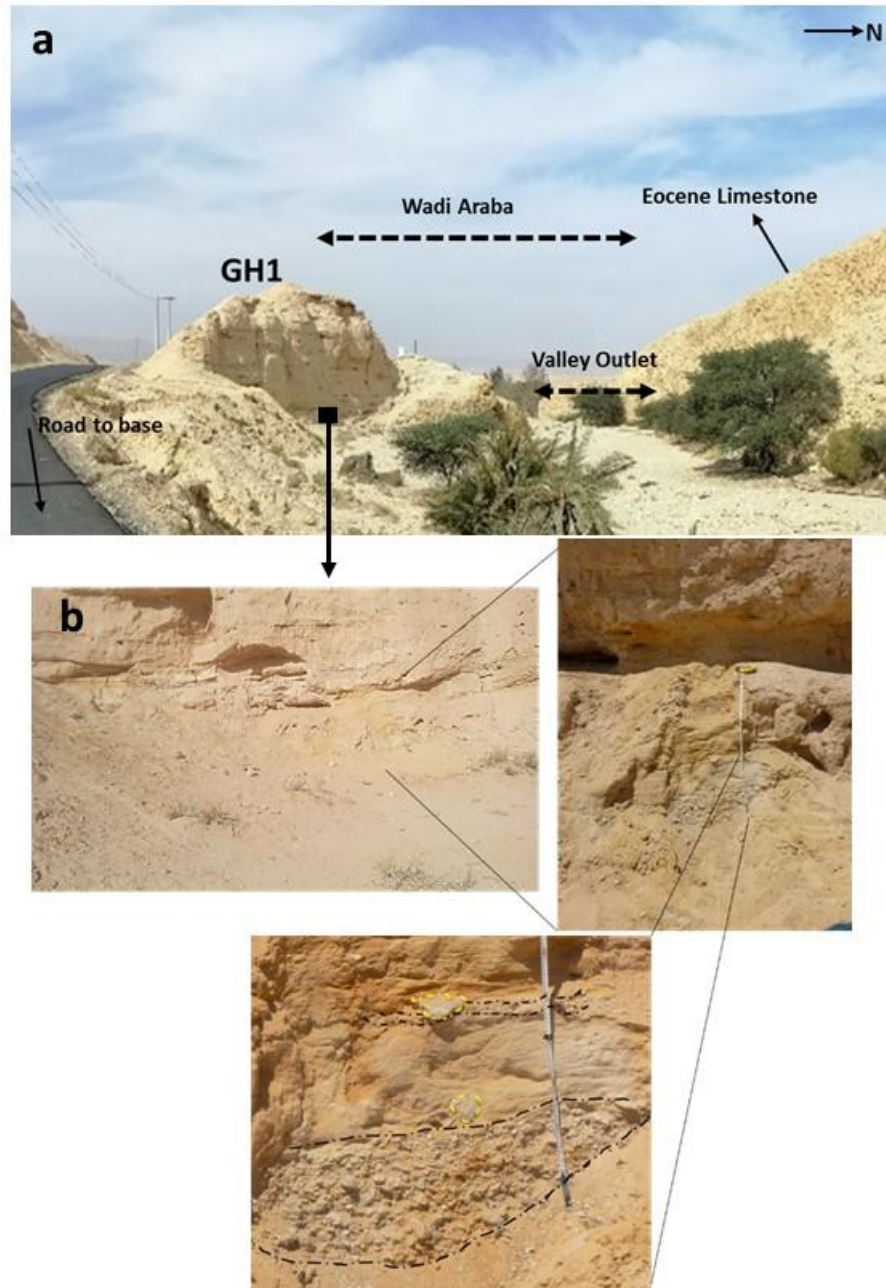
Figure 5.1 a) Location of the GH1 section at the present-day valley outlet towards Wadi Araba. b) Image of the GH1 section base showing the basal gravel unit overlain by a thick sand unit and encircled with yellow dashed-polygons are two cobbles.
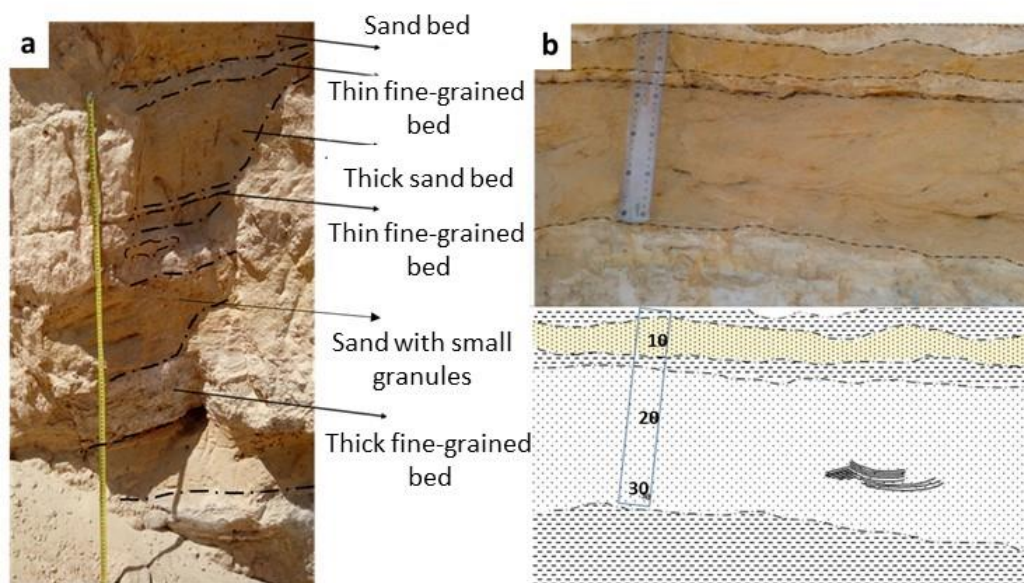
Figure 5.2 a) Beds with different lithologies and thicknesses in GH1-4b sub-section (3.3 to 3.8 m above base), b) Gh1-2 sub-section weak ripple cross bedding at 2.05 m from base. Orientation 140/320.

5.2.2 Chronology

As discussed in Chapter 4 (4.3.6), two stratigraphically consistent OSL ages were reported for the lower part of the GH1 section of this project (Site 1 in Al-Saqarat et al., 2020), at 138±11 ka and 117±9 ka, for samples collected during fieldwork in 2018 at ca. 0.40 m and ca. 1.3 m above the GH1 section base, respectively (Samples Gh11 and GH12 in Table 4.2), suggesting MIS6 to MIS5 (ca.190-130 to ca.130-70ka, respectively) age (Lisiecki and Raymo, 2005) for the deposition of the lowermost part of the GH1 section.

5.2.3 Sedimentary lithofacies analysis

The detailed lithological field descriptions of the GH1 section sediments, as explained in Chapter 3 (3.4), identified six distinct first order sedimentary lithofacies based on particle size, presence of sedimentary structures and bioturbation. These lithofacies were basically identified as gravel-dominated and sand with gravels (G1, G2), sand-dominated (S1, S2) and silt (fine)-dominated lithofacies (F1 and F2). In order to confirm the field-based lithofacies, the PCA-LDA approach was implemented. The data set used for the PCA analysis included the GH1 sediments XRF elemental composition, particle size distribution, LOI results and magnetic susceptibility (see 3.4). The PCA results (Figure 5.3) indicate that there are few primary characteristic features for the grouping of the gravel facies, the sand-dominated facies and the fines-dominated facies.

The first three eigenvectors explain 60 % of the variance. Based on the loadings, which reflect the contribution of each feature in the variance of the samples, the alignment of the fine grained sediments (r^2=>0.8; P<0.05 with PCA1), CaO (r^2=0.8; P<0.05 with PCA1), allogenic markers Al_2O_3 (r^2=0.7; P<0.05 with PCA1), Fe_2O_3 (r^2=0.7; P<0.05 with PCA1), and Ti (r^2=0.6; P<0.05 with PCA1), (κ) (r^2=0.6; P<0.05 with PCA1) and the organic content (LOI_{550}) (r^2=0.9; P<0.05 with PCA1), at the opposite segment from SiO_2 (r^2= -0.8; P<0.05 with PCA1), medium sand (r^2=0.9; P<0.05 with PCA1) and coarse sand (r^2=0.6; P<0.05 with PCA1) shows that the sediments record the environmental history of the GH1 section as represented by the different lithofacies. PCA 2 (12%) correlates positively with the allogenic markers Ti (r^2=0.6; P<0.05) and Fe_2O_3 (r^2=0.5; P<0.05) and the coarse sand content (r^2=0.4; P<0.05), pebble and granule content (r^2=0.2; P<0.05). PCA3 (8%) correlates positively with the fine particles fraction and the allogenc markers. Thus, K, SiO_2, Al_2O_3, CaO, Fe_2O_3, Ti, organic content, clay, very coarse silt, granules, pebbles, fine sand, medium sand and coarse sand contents were used as the input for the LDA analysis.
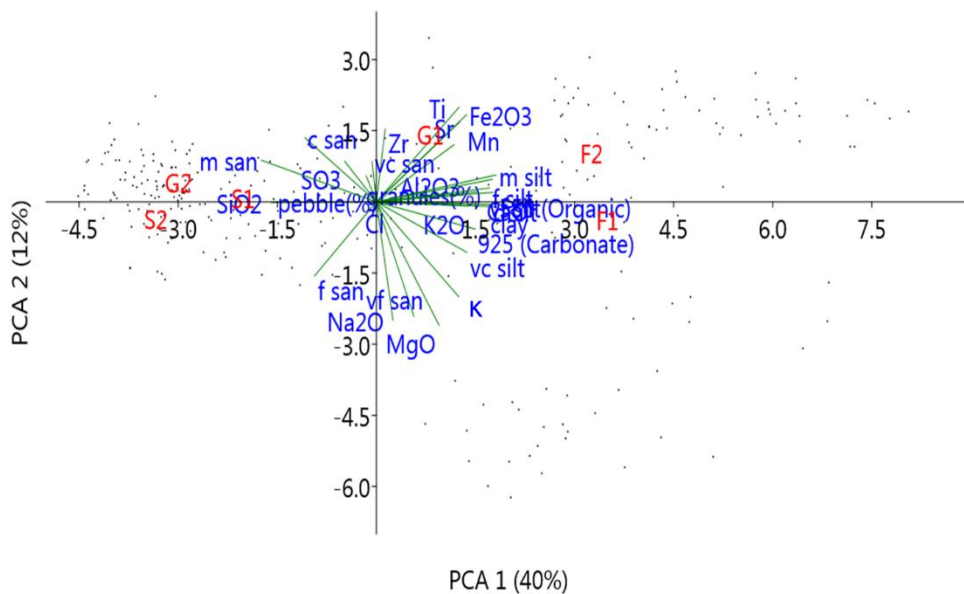
Figure 5.3 PCA results of the GH1 sediments chemical and granulometric composition showing the contribution of each element to the variance. G1 and G2: field-based gravel lithofacies, S1 and S2: field-based sand lithofacies, F1 and F2: field-based fines lithofacies.

The LDA plot (Figure 5.4 a) confirmed the 3 distinct lithofacies groups, representing the gravel, sand-dominated and fines-dominated lithofacies. Based on the LDA classification (Figure 5.4 b), the analysis showed that 87.3% of the samples were correctly classified based on the field-observations and the input data while, the field-based G2 (sand with gravel) lithofacies was reclassified with the sand lithofacies (the variance is more driven by the sand content variability), where all the samples containing less than 15 wt. % granules (< -2phi) were reclassified as pebbly sand.

Finally, the resulting fluvial lithofacies were re-classified following fluvial lithofacies coding of previous research, e.g. Miall (1996), using the sedimentary structures, and representing the lithofacies groups described above (Table 5.1). The lithofacies associations are discussed individually in the next sections in terms of their distinct sedimentological and geochemical characteristics and interpretations.
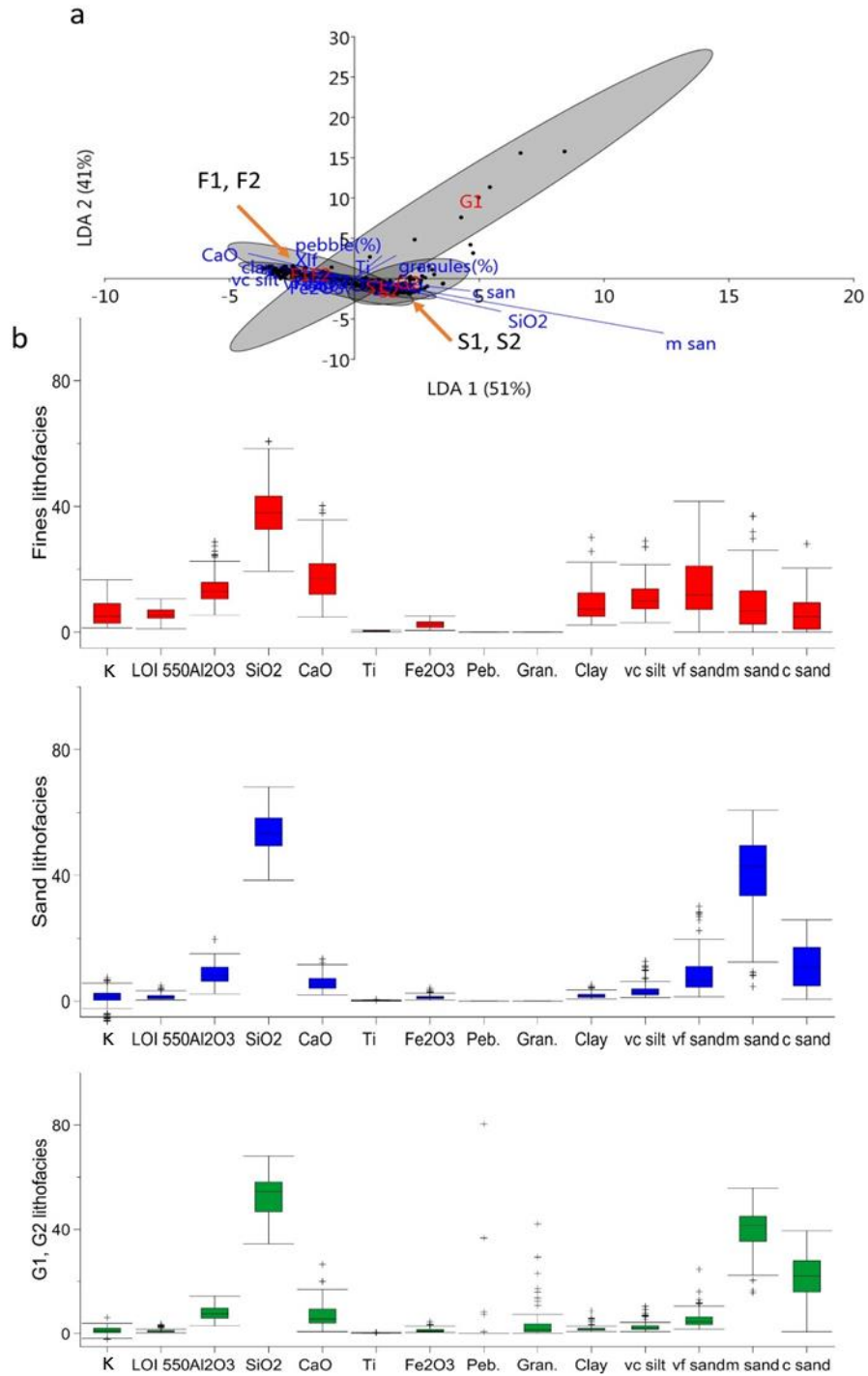
Figure 5.4 a) GH1 sediments LDA plot. F1, F2: fine-dominated facies, S1, S2: sand-dominated facies, G1, G2: gravel-dominated facies. b) Box plots of the composition (%) of the sediments of each facies (outliers are data located at 1.5 times the interquartile range). v.c.: Very coarse. c.: Coarse. f.: Fine. Peb: Pebble. Gran: Granule.

Table 5.1 GH1 section lithofacies analyses results and definitions.Values in the PCA-LDA facies are minimum to maximum/average.

Field-based facies	Particle size	Sedimentary structures	Bioturbation	Gravels
G1	Granules and pebbles in sandy matrix	None	None	yes
G2	Granules in a sandy matrix	None	None	yes
S1	Fine to coarse sand	Yes	Yes	no
S2	Fine to coarse sand	None	None	no
F1	Silt to clay	none	Yes	no
F2	Silt to clay	yes	Yes	no

PCA-LDA facies	LOI550	Al2O3	SiO2	CaO	Fe2O3	K	Clay	vf sand	m sand	Pebbl.	Gran.	c sand
Gravel and Sand with granules	0.2 to 3.7/1.15	2.89 to 14/7.8	34.4 to 68/52	0.73 to 26/7.2	0.4 to 4.5/1.3	-2.2 to 6.1/1.2	0.8 to 8.6/1.9	1.6 to 24/5.6	15 to 55/39	0 to 80/2	0 to 42/4.2	0.68 to 39/21.6
Sand dominated	0.4 to 4.9/1.4	2.4 to 19.6/8.6	38 to 68/53.5	2.1 to 13.4/5.9	0.3 to 4.07/1.3	-6.3 to 7.5/1.3	0.7 to 5/1.8	1.4 to 30/9	4.7 to 60.7/40.7	0	0	0.4 to 25/11.4
Fines dominated	1.1 to 10.6/5.6	5.5 to 28.6/13.6	19.4 to 60.6/38	4.7 to 40.3/17.6	0.5 to 5.2/2.5	1.3 to 16.6/6	2.3 to 30/9	0 to 41/15	0 to 36.9/8.8	0	0	0 to 28/6

Facies code	Facies	Sedimentary structure
Gh	Granules and pebbles, clast supported, crudely bedded gravels	Crude horizontal bedding, imbrication
Ss	Sand, fine to very coarse, may be pebbly	none
Sm	Sand, very fine to coarse	Massive or faint lamination
Sr	Sand, very fine to coarse	Ripple, cross lamination
Fm	Mud, silt	massive
Fl	Sand, silt, clay	Fine lamination, simple ripples

5.2.4   Fluvial deposition of the GH1 sediments

In fluvial environments, siliciclastic sediment transportation depends on the transportation agent (water flow) characteristics (Miall, 1996). Gravel-sized sediments are transported through high energy flows, where the variability in gravel facies textures reflect changes in current unsteadiness and transport rates (Miall, 1996), and sands are generally transported by traction currents as saltation and bed load (Miall, 1996; Mycielska-DowgiałŁo and Ludwikowska-Kedzia, 2011; Amireh, 2015).

Fluvial deposition in the GH1 section is represented by four distinct lithofacies: the high energy flood deposition gravel lithofacies (Gh); the mass flow deposition pebbly sand lithofacies (Ss); the medium energy mass flow or fast moving flow deposition Sm lithofacies and the Sr lithofacies associated with sand migration downstream to form sedimentary structures (e.g. cross bedding). These lithofacies are distinguishable based on their sedimentological structures, granulometric and chemical compositions reflecting the associated depositional energy and hydrodynamic variability.

5.2.4.1   Gravel Lithofacies (Gh)

Lithofacies Gh represents the gravel beds that contain gravel-sized material (pebbles and granules) up to >-2 phi (4 mm) (Miall, 1996).

The Gh beds are located in the lower part of the GH1 sequence (from the base to 3 m). The main bed of this lithofacies is the basal bed, with an exposed thickness of ca. 25 cm. However, the basal contact of this bed is not exposed and it may be thicker. This bed is generally comprised of poorly sorted granules and pebbles. The gravels are crudely horizontally bedded with a fining upward trend and imbrication (Figure 5.5).

The upper beds are about 4 cm to 10 cm thick, and they are located at 0.42 – 0.46 m, 2.78– 3.02 m above the sequence base. They are also poorly sorted granules and pebbles, however, they do not show any bedding structures.
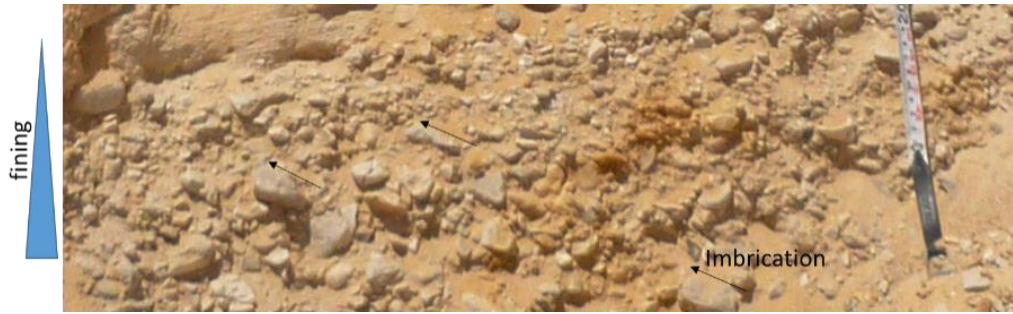
Figure 5.5 GH1 section base bed gravels showing fining upward trend and imbrication in an east-west direction.

The gravel fraction (>-1phi (2mm))

The particle size analysis of the Gh samples showed that there are different percentages and sizes of granules and pebbles in the different beds (e.g. Figure 5.6). The pebbles wt. % is highest in the basal unit and shows a decreasing trend towards the upper beds (Figure 5.7). However, the granules wt. percentages do not show a clear trend.

Figure 5.6 Loose sediments of the gravel fraction in the Gh lithofacies beds of the GH1 section. a) Base bed, b) Bed at 0.44 m from base, c) Upper bed at 3 m above base.
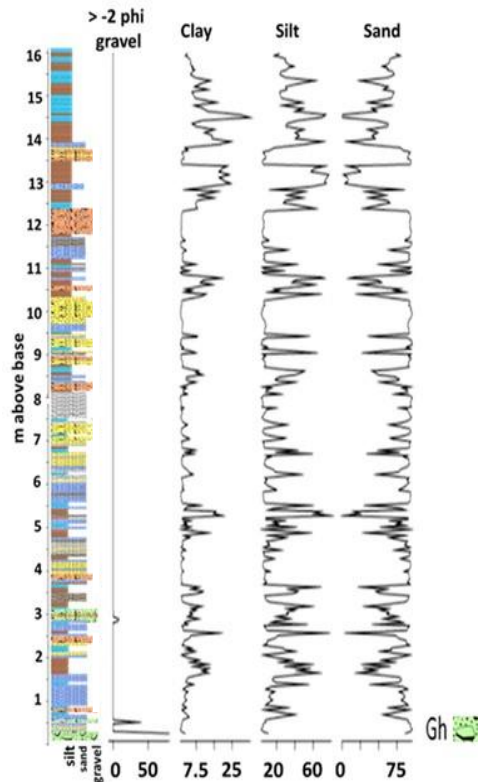
Figure 5.7 Stratigraphy of the GH1 section showing the location of the Gh lithofacies beds marked by the content (wt. %) of gravel-sized clasts (> -2 phi). Also indicated is the association of the Gh beds with elevated sand contents. Clay, silt and sand in vol. %.

The sand and fines (silt and clay) fractions

The particle size distribution results of the Gh lithofacies sediments show that the samples are mainly composed of sand-sized material, with total sand volume percentages (vol. %) ranging from 56.3 to 90.1 vol. %. The silt content ranges from 8.1 to 35.04 vol. %, while the clay content ranges from 1.6 to 8.6 vol. % (Figure 5.8). The samples are unimodal to polymodal with main particle modes of 1911, 356, 391, 169, 429, and 356 µm for the Gh samples from the base bed to the upper beds, respectively (Figure 5.8 b). The samples are poorly to very poorly sorted with sorting values ranging from 1.4 to 3.03 phi. The samples are fine skewed to very fine skewed, with skewness values of 0.16 to 0.44 phi. In terms of kurtosis, the first three samples from bottom are very leptokurtic (1.51 to 2.05 phi). The samples at 2.85-2.95 m from base are platykurtic, 0.73 and 0.9 phi, respectively, while, the sample at ca. 3 m from base is mesokurtic (0.98 phi). The (κ) values are in the range of 1.4 to 3.9 ($*10^{-6}$ SI) (Figure 5.8 d).

PCA is usually used to investigate the common covariance in a dataset and to summarize its variation, however, a minimum of 40 samples have been suggested

in order to achieve eigenvectors and values stability in a PCA for environmental studies (Shaukat et al., 2016), but the Gh facies sample size is small (6 samples), so Pearson correlation coefficients, using the PAST software, were used to extract the interrelations between the different parameters.

A positive (p<0.05) correlation is observed between the pebbles wt. % and coarse sand vol. %. The fines (clay to very coarse silt) are generally positively correlated with each other and negatively correlated with the granules, pebbles and sand vol. %.

The chemical composition results show that the most abundant elements in the composition are silica (SiO_2)> calcium oxide (CaO)> aluminum oxide (Al_2O_3) (Figure 5.8 e). However, the Al_2O_3 content shows two trends, relatively lower content of 7.9 and 6.6 wt. %, in the base unit and the unit at 0.44 m from base, respectively, and 10.78 to 12.3 wt. % in the upper units. Significant positive correlations (r^2 >0.5; P<0.05) exist for Ti with CaO, Al_2O_3 and Fe_2O_3 and SO_3. Positive correlations are also present for K_2O with CaO wt. %, Sr and Ti wt. %. The Gh samples Index of Compositional Variability (ICV) values range from 2.6 to 1.6, avg. 1.8.
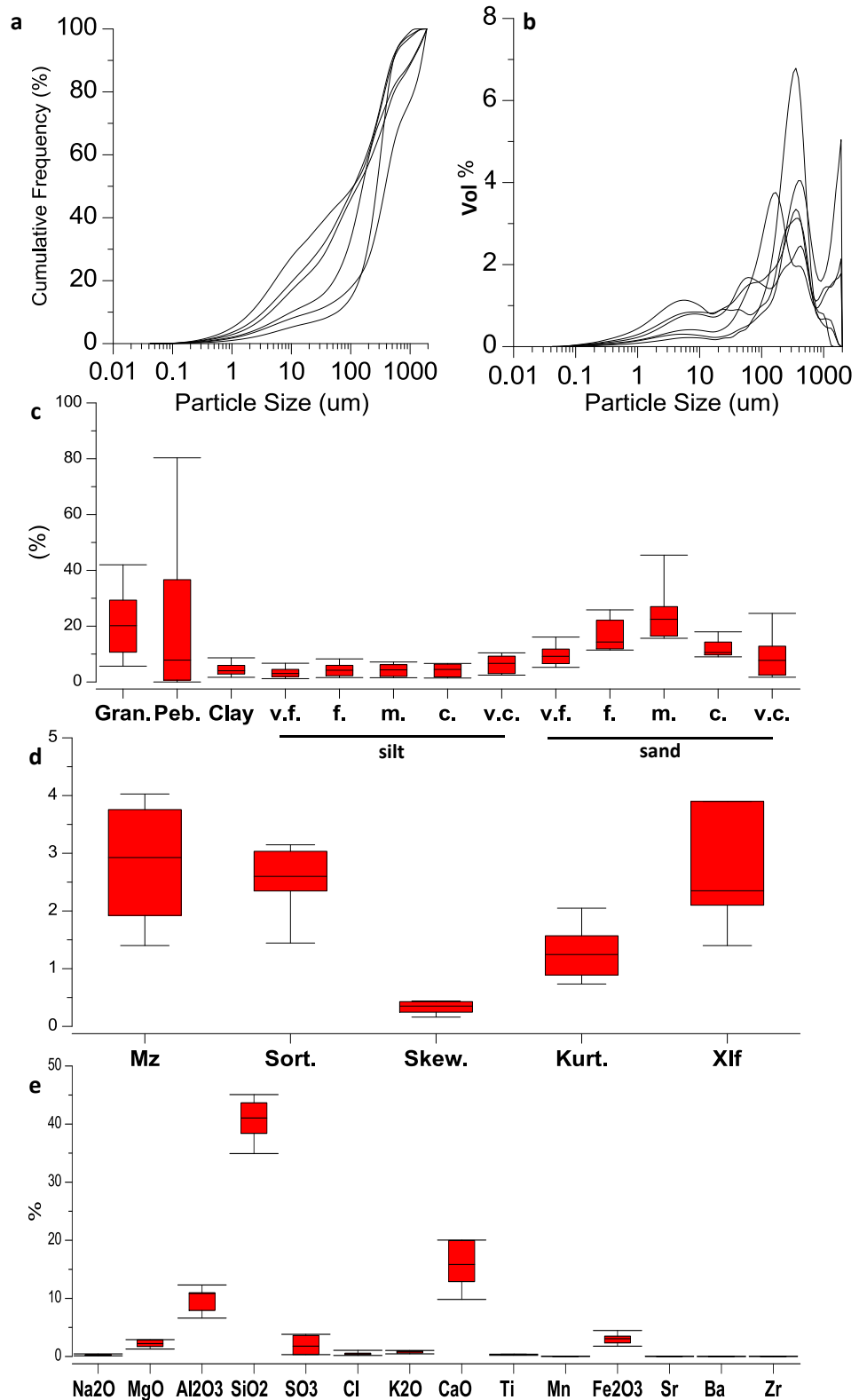
Figure 5.8 a) Cumulative frequency curves of the GH1 section *Gh* facies sediments. b) Particle size distribution curves of the Gh facies sediments. c) Particle size distribution results. d) Granulometric statistical parameters (in phi units) and K values (*10^{-6}SI). e) Elemental composition of the Gh facies sediments. Elements in wt. %. vf. Very fine. f. Fine. m. Medium. c. Coarse. vc. Very coarse. Mz: Mean paticle size. Sort: Sorting. Skew: Skewness. Kurt: Kurtosis.

Gh lithofacies interpretation

In the Gh facies, the pebbles and granules can be attributed to the geological outcrops in the catchment area of the Gharandal Valley (Chapter 4, 4.3.4), such as the Dana Conglomerate Formation which contains sub-rounded clasts of pebble to cobble conglomerate (Ibrahim, 1993). Based on the granulometric characteristics, there is a significant difference in clast (>-1 phi, 2 mm) content and ranges between the beds (e.g. Figure 5.6), where the base bed and the bed at 0.44 m from the base contain larger clasts than the upper beds. These variations in clast sizes may reflect changes in flow velocity and shear stress (Miall, 1996). Changes in kurtosis, the measure of the peakedness of the grain size frequency curves, from very leptokurtic for the lower beds to platykurtic and mesokurtic towards the upper beds, are also indicators of changing flow characteristics (Hanamgond and Chavadi, 1998), showing alternating episodes of either fine or coarse sediment deposition. The higher kurtosis values for the lower two beds suggest that the sediments were sorted elsewhere, probably in the parent rocks, and dumped rapidly through high energy deposition (Folk and Ward, 1957).

In addition, changes in the geochemical composition can be affected by the hydraulic sorting, affected by the transfer medium energy, where more sand added indicates higher energy conditions varying with lower energy depositing fines.

The sediments' geochemistry can be attributed to the abundance of limestone and clays in the catchment area and the short distance to the depositional site (Ibrahim and Rashdan, 1988). The association between (к), Al_2O_3 and Fe_2O_3 indicates that K is controlled by the addition of clays. Ti has been suggested to reflect basin in-wash processes (e.g. Metcalfe et al., 2010; Jones et al., 2015) and its positive correlation with Fe_2O_3 in the Gh sediments suggests that it reflects variations in catchment erosion. Similar to the trends in the granulometric composition, the base bed and the bed at 0.44 m above base show lower Ti, Fe_2O_3, and Al_2O_3 contents, compared to the upper beds. The Ti composition is 0.29 and 0.2 wt. % for the lower beds and 0.39 to 0.37 wt. % for the upper beds. The Fe_2O_3 content shows that for the lower beds, the values are 2.7 and 1.7 wt. %, while the upper beds values are 4.47 to 3.5 wt. %. These variations in the granulometric and chemical composition indicate that more than one type of transfer energy and duration are recorded in the deposits (Miall, 1996; Amireh, 2015).

Accordingly, in order to extract any specific associations within the Gh lithofacies beds, the complete set of granulometric and geochemical parameters was used

for hierarchical clustering, dendrogram, analysis using Ward's method, based on Euclidean distance measures (Figure 5.9). The cluster analysis showed two main associations within the Gh facies samples. The first and key split is the separation of the two bottom beds from the rest. This is followed by the joining of samples at 3 m and 2.85 m from base, while the sample at 2.95 m joins the association after a short distance and then it is followed by the sample at 2.79 m from base. This agrees with the previous discussion and indicates that at least two types of hydrodynamics are recorded.
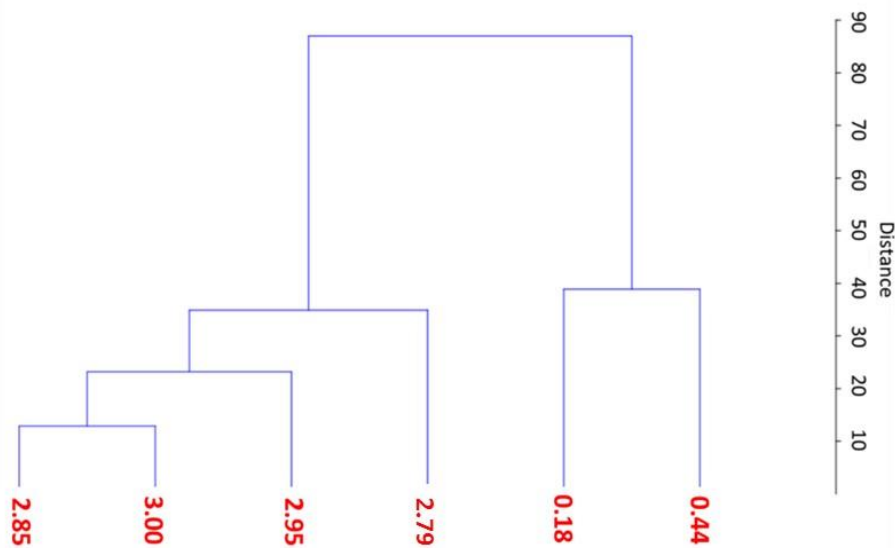
Figure 5.9 Hierarchical clustering, dendrogram of the Gh facies in the GH1 section (numbers in red are elevation above base in m).

Based on the previous discussion and considering the active tectonic settings of the pull-apart basin of the Gharandal Valley area, valley incisions may result from tectonic uplift processes (Miall, 1996; Le Béon et al., 2010; Saqqa and Atallah, 2013). Considering that the base bed of the GH1 section contains higher amounts of gravel (>-2 phi) clasts compared to the other beds, and lower K and allogenic markers content, the deposition of the base bed may be associated with a tectonic incision, rather than high energy floods driven solely by moisture availability. The coarser mean particle size (Mz) of 1.4 phi (medium sand) compared to finer mean particle sizes in the upper beds of 2.6 to 4 phi (fine sand to very coarse silt) and the variability in K and other allogenic markers may indicate a short-lived event that rapidly deposited the coarse sediments, compared to the upper beds. The second bed at 0.44 m from base may reflect a low energy but longer-lived flood

event compared to the base unit, while the other beds reflect high energy and longer duration flood events probably more affected by moisture availability.

It has been suggested that the accumulation of the Gharandal sediments was the result of the valley outlet damming (Mischke et al., 2017; Al-Saqarat et al., 2020) but no analyses have been done to confirm this. The results presented here agree with this suggestion as indicated by the base unit and the unit at 0.44 m which probably suggest their association with, or predating (Al-Saqarat et al., 2020), the damming of the valley initiating sediment accumulation. Nonetheless, this needs further detailed studies of trace elements to confirm (e.g. Ryan and Williams, 2007; Amireh, 2020).

5.2.4.2   Ss (pebbly sand) lithofacies

This lithofacies is dominated by fine to very coarse sand with small amounts of granules (Miall, 1996) and is found at different locations through the GH1 section (Figure 5.11). A small (c. 5 cm) bed is found at 0.73 m from base and it is followed by several beds that vary in thickness. From ca. 2.25 m to ca. 7.25 m above base, 6 (ca. 5-10 cm) beds are present, and from 8.13 m to ca. 13.7 m above base, 9 beds are found with thicknesses ranging from 5 to 54 cm.

The gravel fraction (>-1phi, 2mm)

The gravel-sized clasts of the Ss lithofacies samples show variable contents ranging from 0.6 to 12.6 wt. %. However, the results show no particular stratigraphic trend and this can be attributed to the variability in the transport agent velocity and type (Miall, 1996). The clasts size range and percentage indicate that the transport is different compared to the Gh lithofacies deposition (e.g. Figure 5.9). Accordingly, this lithofacies may indicate sufficient mass flow deposition capable of moving the granules into the wadi (Figure 5.10).

Figure 5.10 Loose sediments of the gravel fraction in the Ss lithofacies of the GH1 section. a) At 6.98 m above the section base. b) At 7.28 m above the section base. c) At 12 m above the section base.

Sand and fines fraction (<-1phi, 2mm)

The results show that the fluvial Ss sediments are primarily dominated by very fine to very coarse sand with high contents of medium and coarse sand (Figure 5.11 and Figure 5.12). The total sand content ranges from 72 to 96 vol. %, the silt content ranges from 4 to 22.6 vol. % and the clay content ranges from 0.8 to 5.5 vol. %. The sediments are unimodal, where only 3 samples show bimodality, with a main particle size mode ranging from 213 to 542 μm. The samples are poorly to very poorly sorted, with one moderately sorted sample, within the range of 0.8 to 2.8 phi. The sediments are generally fine to very fine skewed (0.1 to 0.67 phi), and leptokurtic to very leptokurtic (0.6 to 2.6 phi).

Similar to the Gh lithofacies, the Ss samples (33 samples) were analysed using Pearson correlation coefficients to extract the interrelations between the different parameters.

The Ss sediments results show that there are positive (P<0.05) correlations between the silt and clay fractions. The very fine sand fraction positively correlates (P<0.05) with coarse and very coarse silt. The coarse sand fraction negatively correlates with the fines, while the very coarse sand shows positive correlations with the granules fraction and the coarse sand. The (κ) values range from 0.3 to 7.1 (Figure 5.12).
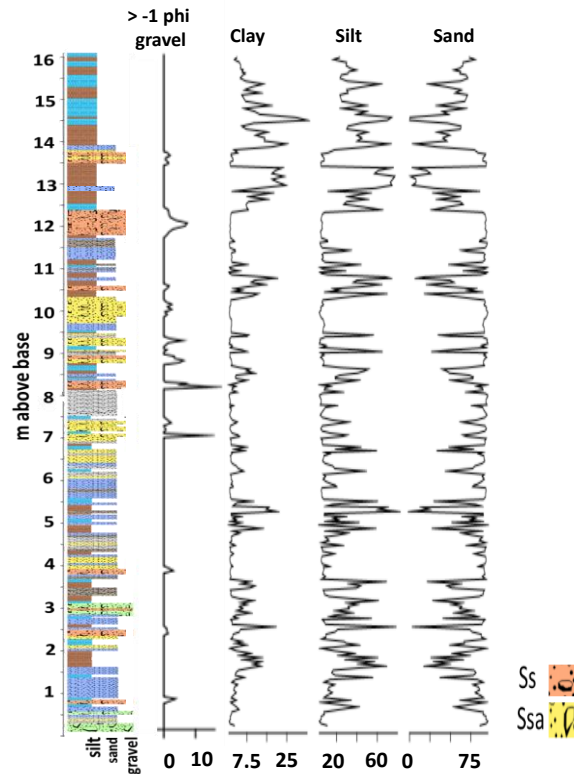
Figure 5.11 Stratigraphy of the GH1 section showing the location of the Ss lithofacies beds marked by the content (wt. %) of granules (2-3 mm). Also indicated is the association of the Ss beds with elevated sand contents. Clay, silt and sand in vol. %. Ss: fluvial pebbly sand lithofacies. Ssa: fluvio-aeolian Ss lithofacies bed (see 5.2.5).

The chemical composition results show that the most abundant elements in the Ss fluvial sediments composition are $SiO_2 > CaO > Al_2O_3$ (Figure 5.12 e). The SiO_2 content is within the range of 63.6 to 34.4 wt. % with an average of 51.6 wt. %. The CaO content shows a wide range from 26.5 to 0.7 wt. % and an average of 8 wt. %. The Al_2O_3 content is in the range of 14.3 to 3.9 wt. % with an average of 8 wt. %. The correlation amongst the chemical elements generally shows several positive (P<0.05) and negative correlations. Positive (P<0.05) correlations are found between Al_2O_3, Ti and Fe_2O_3 with soluble and mobile elements such as MgO and CaO suggesting the allogenic sources of these elements.
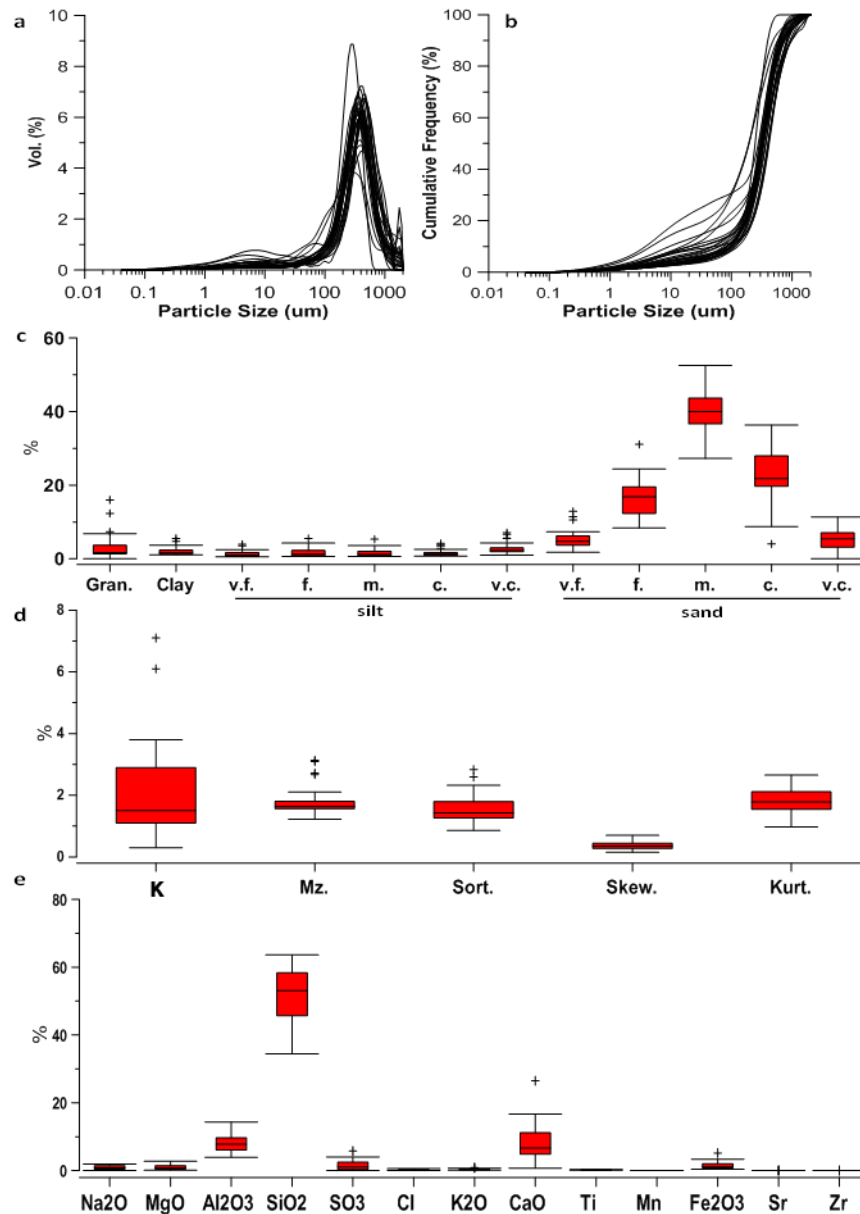
Figure 5.12 a) Cumulative frequency curves of the GH1 section *Ss* facies sediments. b) Particle size distribution curves. c) Particle size distribution results. d) Granulometric statistical parameters (in phi units) and (κ) values (*10^{-6}SI). e) Elemental composition. Elements in wt. %. vf. Very fine. f. Fine. m. Medium. c. Coarse. vc. Very coarse. Mz: Mean paticle size. Sort: Sorting. Skew: Skewness. Kurt: Kurtosis.

In terms of sediment source maturity, the Ss fluvial sediments ICV values range from 0.78 to 3 showing that the sediments comprise both mature (ICV<1) and immature (ICV>1) sediment sources and possibly variable source weathering intensities (Cox et al., 1995).

Ss lithofacies interpretation

The presence of granules (>2 mm) suggests energy hydrodynamics sufficient to transfer gravel-sized material from the slopes into the wadi, however, the depositional energy of the Ss deposition is different from that of the Gh lithofacies. The granules content can be attributed to the geological outcrops in the catchment area (Ibrahim, 1993). Generally, the sorting, skewness and kurtosis values show narrower ranges compared to the Gh lithofacies, probably indicating different hydrodynamics.

The K also indicates variable degrees of hydrodynamics. The positive correlations between (κ), Fe_2O_3 (r^2=0.5; P<0.05) and Ti (r^2=0.4; P<0.05) suggest its association with catchment material. The highest (κ) values of 7 and 6 are associated with higher than average contents of clay (3 and 2 vol. %, avg. 1.9 vol. %) and silt (14 and 9 vol. %, avg. 8 vol. %) compared to the other Ss sediments. These samples also show higher than average composition of CaO (13.11 %, avg. 8 %), Ti (0.33 %, avg. 0.2 %), and Fe_2O_3 (5 %, avg. 1.5 %). These beds are at ca. 12.34, part of the thickest Ss bed of ca. 54 cm and at 12.84 m above base, probably recording a significant mass flow event. Positive (P<0.05) correlations between Al_2O_3, Ti and Fe_2O_3, and MgO and CaO indicate the allogenic sources of the elements which can be attributed to the local area geology (Ibrahim, 1993). The negative correlation between Al_2O_3 and SiO_2 (r^2= -0.2) also suggest variable hydrodynamics depositing the sand and fines.

Accordingly, the Ss lithofacies samples probably record periods of mass flow events with more consistent flow and probably longer duration compared to the Gh events.

5.2.4.3 Sm and Sr (sand) lithofacies

The sand lithofacies (Sm and Sr) beds are generally dominated by very fine to coarse sand (Miall, 1996). The differentiation between the two lithofacies is based on the presence of sedimentary structures. The Sr lithofacies sediments show horizontal laminations or cross bedding structures, generally faint, while, the Sm lithofacies sediments are massive and do not show any sedimentary structures.

Both lithofacies are found at different levels in the section, with varying thicknesses, starting from 0.25 m up to 13.8 m above the section base (Figure 5.13).

The Sm lithofacies sediments are primarily composed of very fine to very coarse sand with high contents of medium sand (Figures 5.14 and 5.15). The total sand content ranges from 71 to 94 vol. %, the silt content ranges from 4 to 42 vol. % and the clay content ranges from 0.7 to 9.1 vol. %. The sediments are unimodal to bimodal and only 3 samples show polymodality. The main particle size modes are in the range of 111 to 1954 µm (mean 464 µm; Std. 462 µm). The samples are poorly to very poorly sorted within the range of 1.06 to 4.1 phi. The sediments are generally fine to very fine skewed (0.015 to 1.08 phi), and platykurtic to very leptokurtic (0.7 to 2.6 phi) (Figure 5.15).

The Sr lithofacies sediments also primarily contain very fine to very coarse sand with high contents of medium and fine sand. The total sand content ranges from 85.6 to 95.3 vol. %, the silt content ranges from 3.3 to 12.6 vol. % and the clay content ranges from 0.9 to 1.8 vol. %. The sediments are unimodal with only one sample showing bimodality, with a main particle size mode of 213 to 410 µm (mean 291.5 µm, Std. 57 µm). The samples are moderately to poorly sorted within the range of 0.81 to 1.43 phi, with a tendency towards more moderately sorted sediments compared to the Sm samples. The sediments are generally fine to very fine skewed (0.13 to 0.45 phi), and leptokurtic to very leptokurtic (1.13 to 2.03 phi). The samples (κ) values range from 0.6 to 7.5 (avg. 3.1; std. 1.8) and from 0.8 to 5.8 (avg. 2.4; std. 1.7) ($*10^{-6}$SI), for the Sm and Sr samples, respectively (Figure 5.15).
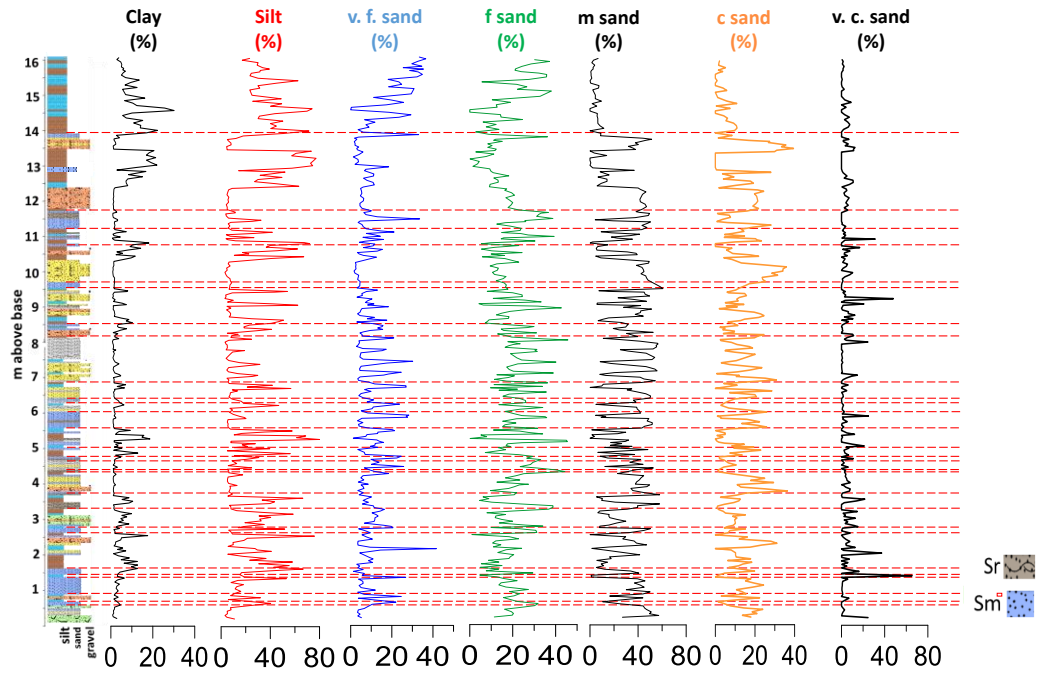
Figure 5.13 Stratigraphy of the GH1 section showing the location of the Sm and Sr lithofacies beds marked by the horizontal lines showing the elevated contents (wt. %) of sand. Also observed is the general association of the Sm beds with the Ss and Gh beds and less commonly with the fine (wetland) lithofacies, while the Sr beds are generally associated with the Sm and fine lithofacies beds. Clay, silt and sand in vol. %. Sm: massive sand lithofacies. Sr: sand lithofacies with sedimentary structures.
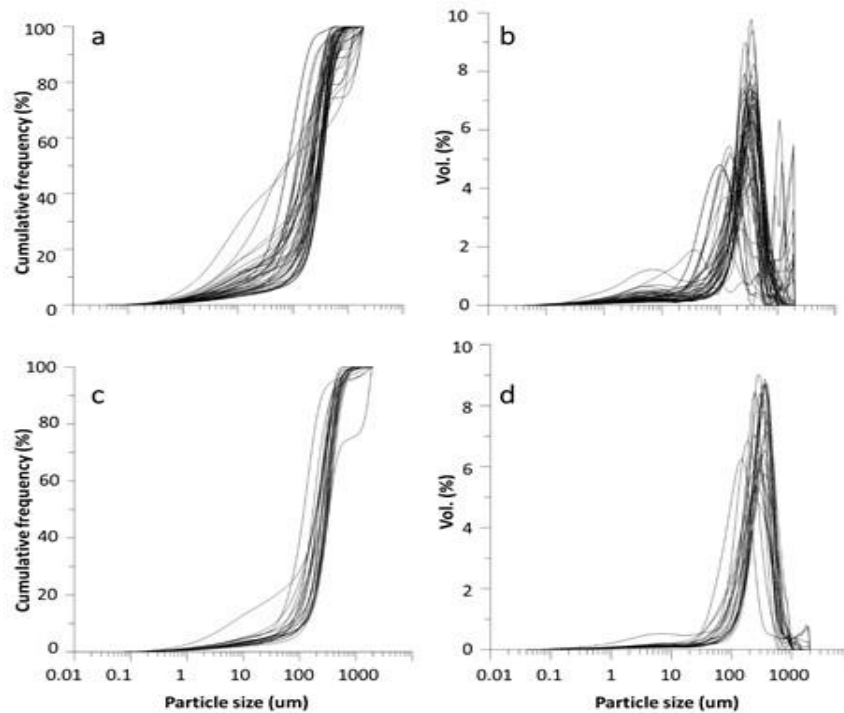
Figure 5.14 a, c) Cumulative frequency curves of the GH1 section Sm and Sr fluvial sediments, respectively, b, d) Particle size distribution curves of the Sm and Sr fluvial sediments, respectively. Showing the trend towards unimodality for the Sr sediments indicating the variable transport energy conditions.

127
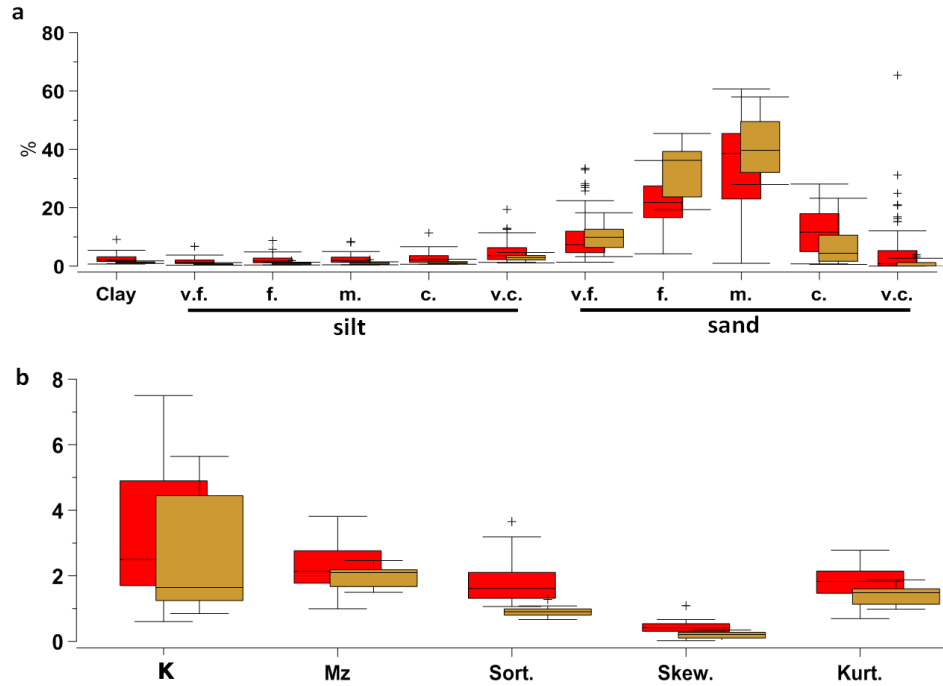
Figure 5.15 a) Particle size distribution results of the GH1 section Sm sediments (red) and the Sr sediments (gold) b) Granulometric statistical parameters of the Sm sediments (red) and the Sr sediments (gold) (in phi units) and (κ) values (*10[-6] SI). Outliers are data located at 1.5 times the interquartile range.

Due to the larger number of the Sm and Sr samples (>40), compared to the Gh and Ss lithofacies samples, PCA analysis was used to extract the interrelations between the parameters. The PCA results of the granulometric composition (Figure 5.16) show that the first two eigenvectors explain 87% of the total variance within the samples. The results indicate that the variance in the Sr sediments is more driven by medium and fine sand content, while the Sm deposits variance is more driven by alternation between coarser and finer fractions, implying the different behaviour of the two lithofacies. The first eigenvector PCA 1 (57.4%) correlates positively (P<0.05) with medium sand content (r^2=0.98) and with coarse sand content (r^2=0.6). PCA 2 (29.7%) correlates with the fine and very fine sand contents (r^2=0.93 and 0.45).
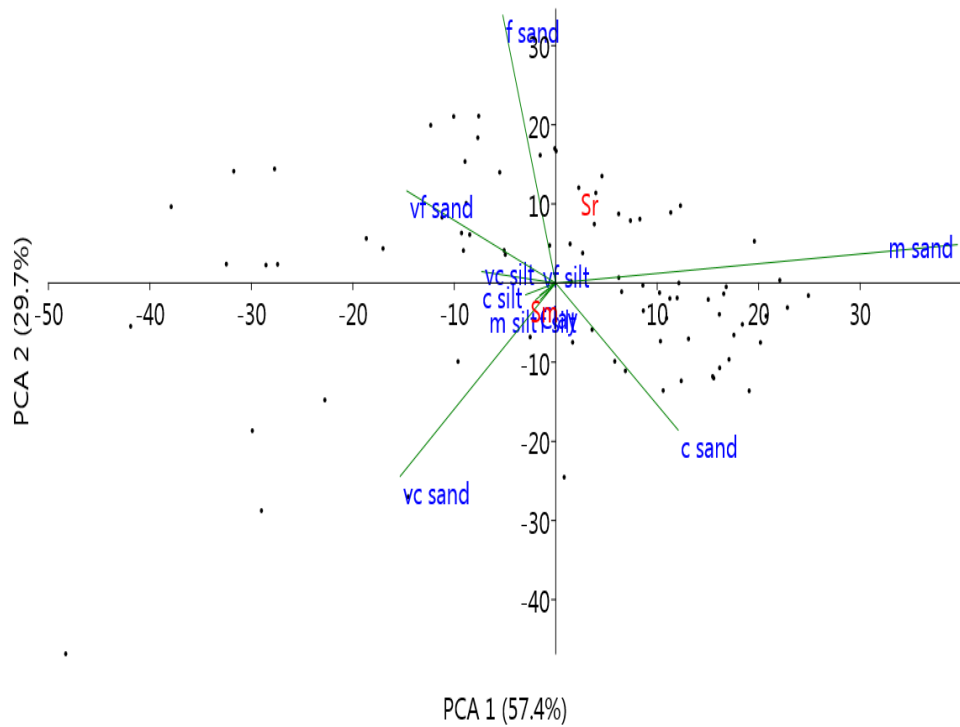
Figure 5.16 Principal Component Analysis of the granulometric parameters of the GH1 section Sm and Sr facies showing the first two eigenvectors.

In terms of the elemental composition, the Sm and Sr lithofacies sediments are primarily dominated by SiO_2> Al_2O_3> CaO, while all the other elements show values of less than 10 wt. % (Figure 5.17 a). The SiO_2 content is within the range of 61.7 wt. % to 33.8 wt. % with an average of 49 wt. % and 68 to 50 wt. % with an average of 58.7 wt. %, for the Sm and Sr samples respectively. The CaO content ranges from 14.7 to 3 wt. % with an average of 7.4 wt. % and 12.1 to 2 wt. % and an average of 5.5 wt. %, for the Sm and Sr samples respectively. The Al_2O_3 content is in the range of 28.6 to 2.7 wt. % with an average of 10.6 wt. % and 13 to 2.3 wt. % with an average of 7.5wt. %, for the Sm and Sr samples respectively.
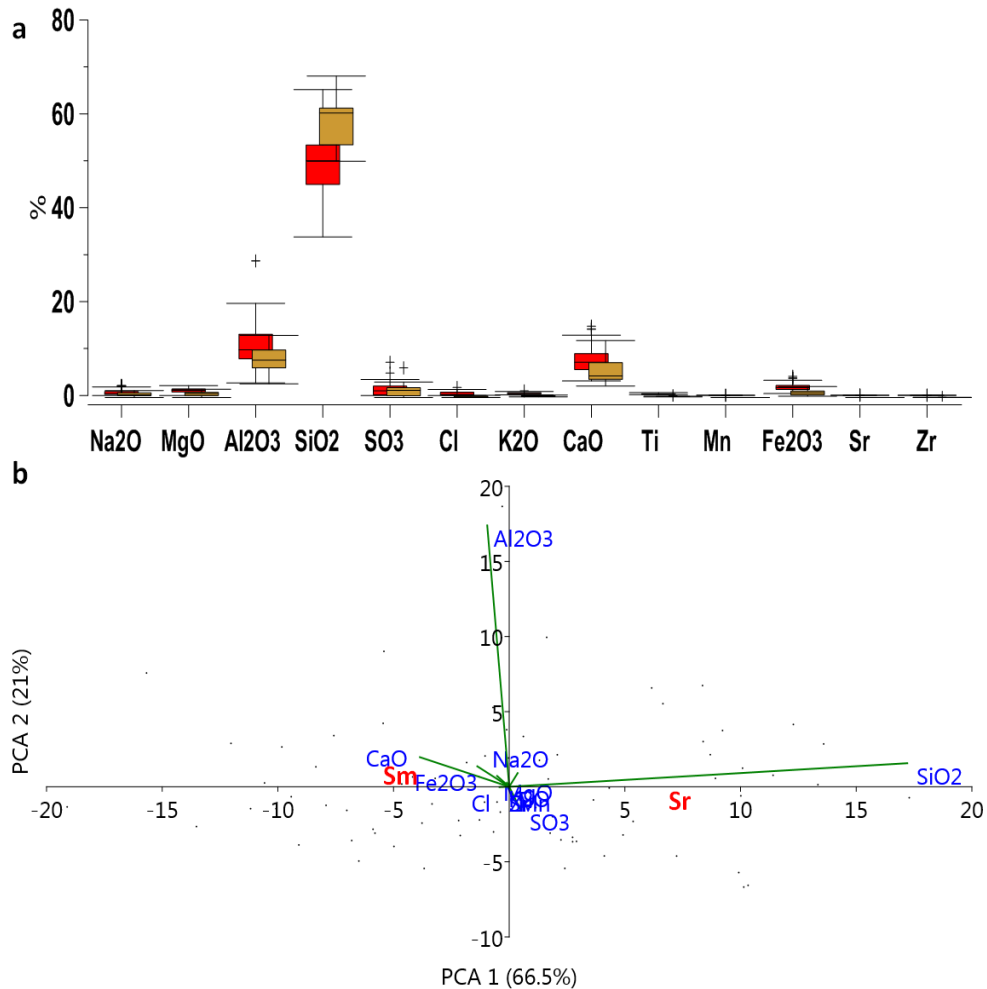
Figure 5.17 a) chemical composition of the GH1 section Sm sediments (red) and the Sr sediments (gold). Outliers are data located at 1.5 times the interquartile range. b) Principal Component Analysis of the chemical composition of the GH1 section Sm and Sr facies showing the first two eigenvectors.

The PCA analysis of the geochemical composition of the Sm and Sr lithofacies (Figure 5.17 b) shows that the first two eigenvectors explain 87.5% of the total variance in the samples. SiO_2 content correlates positively (P<0.05) with PCA 1 (r^2=0.95) while Al_2O_3 correlates positively with PCA2 (r^2=0.96), and PCA 3 (6.7%) correlates positively with CaO (r^2=0.8) indicating that these elements are the typical characteristics of these lithofacies. Positive correlations are present amongst the allogenic elements Fe_2O_3 and Ti (r^2=0.7; P<0.05). The CaO content correlates positively with the allogenic elements, however, 4 samples from the Sm lithofacies show a different behaviour with respect to the CaO/Ti covariance (Figure 5.18), possibly suggesting authigenic deposition. The bed where this relationship is noted is located at ca. 3.25 - 3.4 m above the section base and it is overlain and underlain by fine-sediment lithofacies (see section 5.2.3).
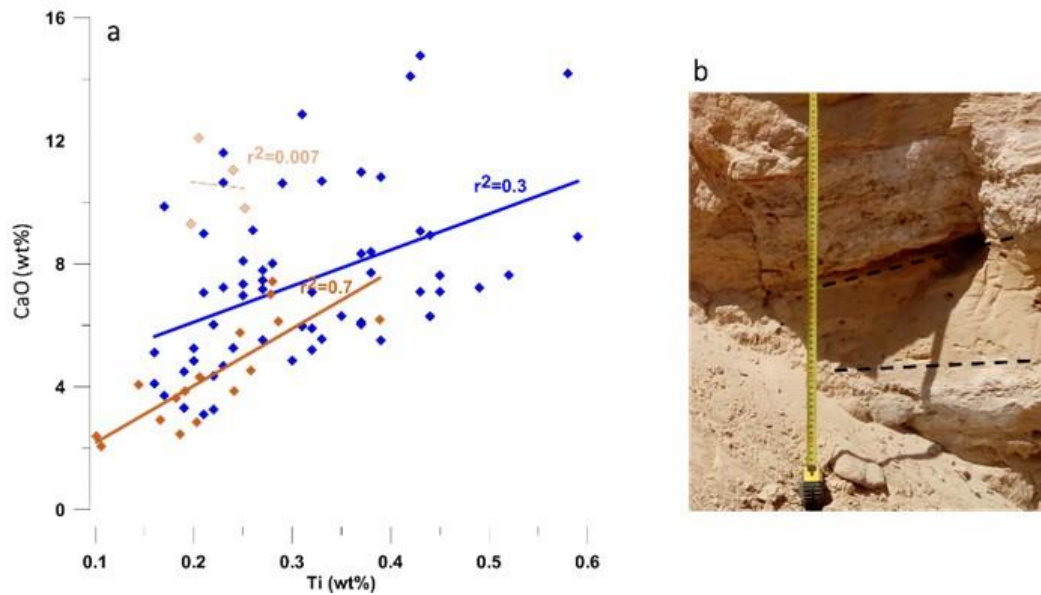
Figure 5.18 a) CaO/Ti bi-plot of the GH1 section Sm (blue) and Sr sediments (gold), b) location of the four samples showing weak negative correlation between CaO and Ti (light gold line in a).

Based on the ICV values, the Sm sediments show a dominance of compositionally immature sediments (>1 ICV) compared to the generally mature Sr sediments (<1 ICV) (Cox et al., 1995). The ICV values range from 3.2 to 0.4 with an average of 1.22 and from 2.6 to 0.56 with an average of 1.2 for the Sm and Sr sediments, respectively.

Sand lithofacies interpretation

In general, the absence of clasts (>-1 phi, 2mm) suggests more consistent transportation energy for the sand lithofacies compared to the Ss and Gh lithofacies where clasts are present. In addition, the granulometric PCA results show that the primary eigenvectors correlate with the sand fractions (see above) which further differentiate the sand lithofacies from the higher energy Ss and Gh lithofacies. The sand lithofacies record hydrodynamic variability responsible for the sand fractions deposition, suggesting lower energy and longer duration events compared to floods or rapid sediments dumping (Miall, 1996). However, some apparent hydrodynamic variations are found within the sand lithofacies.

Both Sm and Sr lithofacies deposits are characterized by high contents of medium sand, however, the Sr facies show enrichment in fine sand and lower contents of very coarse sand. Also, the Sr granulometric statistical parameters show a narrower range for the Mz, skewness, sorting and kurtosis, compared to the Sm

lithofacies (see Figure 5.15 b). These variations indicate the variability within the sandy facies, where the Sr facies suggest more uniform supply of sediments and less hydrodynamic variability in transport energy as also indicated by the main particle size modes and their lower standard deviation for the Sr sediments (Mycielska-DowgiaŁŁo and Ludwikowska-Kedzia, 2011).

The PCA results of the elemental composition show that the fluvial deposition of Sm and Sr facies is primarily characterized by SiO_2, Al_2O_3, and CaO which record the variability in catchment erosion and addition of coarser/finer material controlled by the local area geology. This agrees with the granulometric interpretation where a differentiation between additions of coarser/finer material is recorded. In addition, the association of the Sm beds with the higher energy Ss and Gh beds (see Figure 5.13) also suggests that the massive sand beds were probably deposited in relation to mass flows while moving downstream or probably with fast moving flow picking up the sediments along its path. On the other hand, the association of the Sr beds, showing sedimentary structures, primarily with the fine-grained beds and the Sm beds (see Figure 5.13) suggests that these sediments were deposited through lower energy flows, probably as sand in-wash and migration into the fine-grained beds that redeveloped once the conditions permitted.

Thus, these beds record periods of fluvial in-wash under different valley hydrodynamics following the mass flow or flood deposition and controlled by the decreasing energy of the flow or as sand migration downstream.

5.2.4.4 Fluvial depositional environments characterization

In order to distinguish the characteristic depositional environment and transport modes of the different lithofacies, the fine fraction (sand to clay) samples were plotted on a CM diagram (see 3.6.2.1) to reflect the proposed mode of transportation (Passega and Byramjee, 1969; Mycielska-DowgiaŁŁo and Ludwikowska-Kedzia, 2011) (see Figure 5.19).

For the Gh gravel lithofacies, the results show that the base bed behaves differently compared to the other beds. The sorting reduces with decreasing mean grain size (Mz) indicating an environment with a coarser fraction (e.g. sand) sorting processes where the supply of poorly sorted (finer fractions) also occur (Mycielska-Dowgiałło and Ludwikowska-Kędzia, 2011). In addition, based on the CM diagram (black diamonds in Figure 5.19), the base bed shows rolling as the primary mode of transportation, while the other beds show dominance of both

rolling and saltation as the primary types of transportation reflecting the variable hydrodynamics associated with the high energy gravel deposition.

The Ss (pebbly sand) fluvial sediments also record variable depositional hydrodynamics (see above). These suggested variable hydrodynamics are also observed when plotting the Ss facies fine fraction (sand to clay) samples on the CM diagram suggesting that the samples were probably deposited by saltation in a high to low turbulence environment (gold diamonds in Figure 5.19) (Passega and Byramjee, 1969; Malgorzata and Ludwikowska-Kedzia, 2011).

In addition, the sand deposits (Sm and Sr) CM diagram results (green diamonds (Sm) and blue diamonds (Sr) in Figure 5.19) show that the sand fluvial samples reflect two distinct transportation processes. The Sm sediments of fast moving flows are characterized by rolling, saltation and suspension processes, while the Sr sediments are primarily deposited from suspension, supporting the previously discussed hydrodynamics of the deposition of these beds (see above).

The previous discussion of the fluvial deposition in the GH1 section and the CM diagram results suggest alternating periods of hydrodynamics in the valley in response to either climate variability (moisture availability), tectonic activity, or both where the clasts and siliciclastic sediments are deposited through rolling in flood events, to saltation in high energy fluvial channels, then to saltation in high and low turbulence fluvial channels deposition and the deposition of finer material in low turbulence currents.
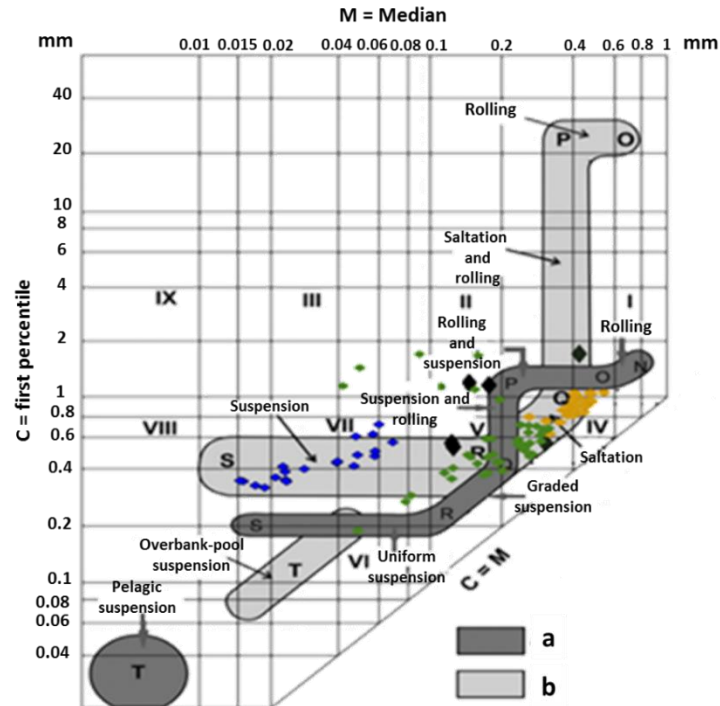
Figure 5.19 Complete CM pattern of tractive current deposits for the GH1 section fluvial sediments. a (dark shaded) Based on Passega (1964) and Passega and Byramjee (1969); b (light shaded) Based on Ludwikowska Kędzia (2000). I, II, III, IX: rolled grains; IV: High turbulence deposit; V: Low turbulence deposit; VI: Graded suspension; VII: Uniform suspension; VIII: Finest uniform suspension (after Passega and Byramjee, 1969) (Modified from Malgorzata and Ludwikowska-Kedzia, 2011). Lithofacies: **Black**: Gh, **gold**: Ss, **Green**: Sm, **Blue**: Sr.

5.2.5 Fluvio-aeolian deposition of the GH1 sediments

As discussed in Chapter 1 (section 1.3.1), it is important to consider the fluvial/aeolian deposition interaction in arid regions. However, discerning between the two systems is not straight forward at either recent (Belnap et al., 2011) or past time-scales (Ben Ameur et al., 2019). The identification of aeolian deposition can be accomplished based on multi-proxy analyses of the sediments, where few studies have reported criteria that can be an indicator of aeolian processes. In southern Jordan, the source of the sands forming the sand dunes to the south of the Gharandal Valley is considered to be the sandstone formations covering the eastern highlands (Ibrahim, 1993) (see Chapter 4, Figures 4.4 and 4.7). Saqqa and Atallah (2004) studied these dunes and sheet-like sands and reported that their particle size is within the range of 200 to 350 μm and 100-500 μm, respectively. Lucke et al. (2019a) investigated the modern dust and Holocene aeolian deposits in Petra, located about 30 km to the northeast of the Gharandal Valley and under similar, present day, climatic conditions. The Petra sediments

are affected by the surrounding sandstone formations, locally known as the "Abu Khushayba Sandstone Formation", "Umm Ishrin Sandstone Formation", "Disi Sandstone Formation" and "Kurnub Sandstone Formation", which are the same sandstone formations spread over the highlands to the east and south of the Gharandal Valley. The authors reported that medium sand dominates the granulometric composition of these reference sand formations, and that the main particle size mode is ca. 415 µm, accompanied by SiO_2 enrichment. Samples from Holocene aeolian sediments showed modes of 132 to 415 µm similar to current dust samples from the area and also associated with low (κ) values. Amireh (2015) also studied the granulometric composition of these sandstone formations and reported that the "Abu Khushayba Sandstone Formation" is unimodal, moderately sorted with a fine sand main mode. The "Umm Ishrin Sandstone Formation" is unimodal with a main particle size mode of medium sand, the "Disi Sandstone Formation" is unimodal with a main particle mode of medium sand, and the "Kurnub Sandstone Formation" is unimodal with a main particle size mode within the medium sand range.

In Tunisia, Ben Ameur et al. (2019) investigated a sediment core from an inland Sebkha and indicated alternating cycles of fluvial and sandstorm deposition based on the sediments' granulometric characteristics and (κ). The authors showed that sandstorm events coincide with peaks in sand content (mean particle size), trend towards better sediment sorting and low (κ) values, indicating that the K values are depleted due to the addition of quartz (fine to medium sand) and the decrease in heavy minerals during sandstorm events (Ben Ameur et al., 2019). Furthermore, in southeastern Arabia, Parton et al. (2013) investigated a sedimentary sequence of aeolian and fluvio/lacustrine sediments spanning MIS3. The aeolian deposition in the sequence was characterized by better sorted sediments, lower K values, unimodal particle distributions and decreased organic content compared to the fluvio/lacustrine deposits (Parton et al., 2013).

The criteria mentioned earlier are used to identify the specific sediments representing aeolian or fluvio-aeolian deposition, suggesting sediment deposition either directly from aeolian processes or reworked/washed into the valley through runoff. Thus, samples showing associations of SiO_2 enrichment, depletion in all other elements, and peaks of sand content, main modes within the medium sand size range, trend towards better sorting and troughs in (κ) values were selected and corroborated by sediment particle size frequency and cumulative curves.

18 samples from the Ss sediments and 46 samples from the Sm and Sr sediments through the GH1 section, marked by low (<1) (κ) values, met these criteria. The samples will be referred to as Ssa, Sma and Sra to denote the aeolian/fluvial deposition (Figure 5.20).
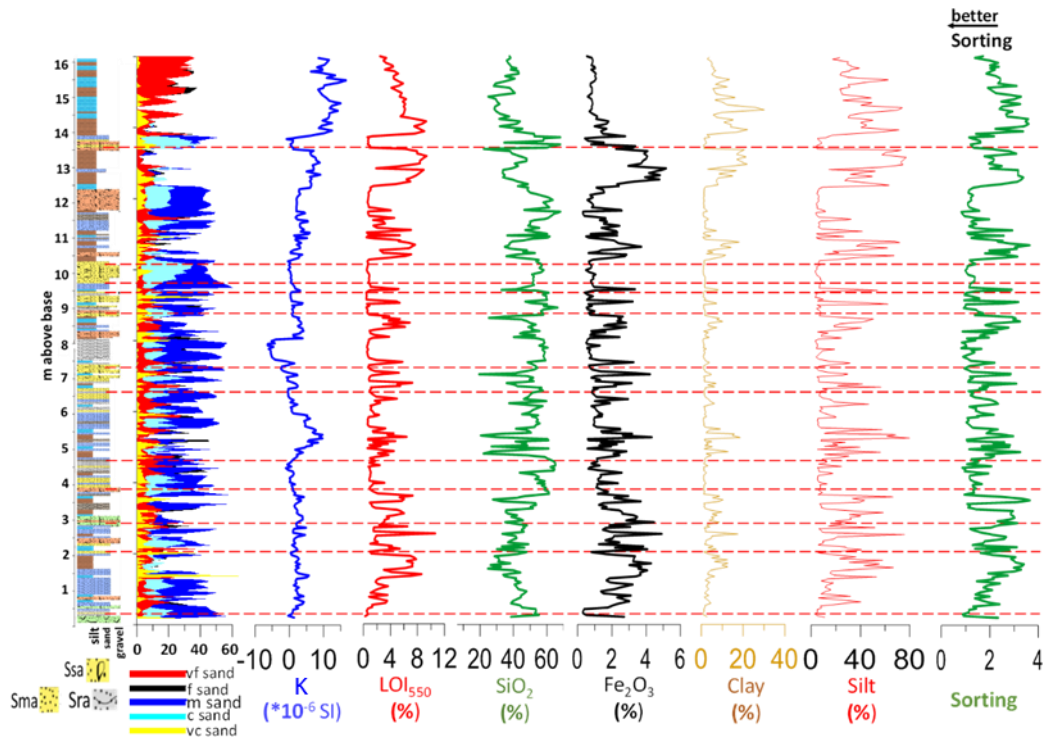
Figure 5.20 Stratigraphy of the GH1 section showing the location of the Ssa, Sma and Sra lithofacies beds (marked by the horizontal red lines) based on the criteria discussed in text. Also shown the silt, clay, and Fe_2O_3, and LOI_{550} contents indicating reduced catchment in-wash. Sand, silt, and clay in vol. %. SiO_2, Fe_2O_3, and LOI_{550} in %. Sorting (phi), κ (*10^{-6} SI). Ssa: fluvio-aeolian pebbly sand, Sma: fluvio-aeolian massive sand. Sra: fluvio-aeolian sand lithofacies with sedimentary structures.

The laser particle size distribution results showed that the SSa sediments are primarily dominated by medium sand content (Figures 5.21 and 5.22). The total sand content ranges from 84.5 to 96 vol. %, the silt content ranges from 3 to 13.5 vol. % and the clay content ranges from 0.8 to 2 vol. %. One sample shows coarse sand content higher than medium sand, and another sample shows higher contents of very coarse sand probably affected by the mass flow siliciclastic content. The sediments are generally unimodal (282 to 450 µm) with a dominant mode of 410-450 µm, with only 2 bimodal samples (Figure 5.21). The samples are moderately to poorly-sorted within the range of 0.9 to 1.57 phi. The sediments are symmetrical to very fine skewed (0.03 to 0.47 phi), and leptokurtic to very leptokurtic (0.6 to 2.32 phi) (Figure 5.22). The Ssa samples show different granulometric characteristics compared with the Ss fluvial samples. The Ssa

sediments are generally unimodal with a narrower range of main particle modes and tend to be better sorted (see 5.2.4.2).

The Sma sediments are mainly dominated by medium sand with elevated contents of coarse sand, while the Sra sediments also dominated by medium sand content, have elevated contents of fine sand (Figure 5.22). The total sand content ranges from 84.8 to 96 vol. % and from 84 to 96 vol. % (with one sample containing 79 vol. %), the silt content ranges from 3.2 to 13.3 vol. % and from 3.1 to 19 vol. %, while the clay content ranges from 0.8 to 2 vol. % and from 0.75 to 2.4 vol. %, for the Sma and Sra sediments, respectively. The sediments are generally unimodal (main mode ranges from 340 to 450 μm and 257 to 410 μm (with one sample showing a main mode of 147 μm) for the Sma and Sra sediments, respectively) (Figure 5.21). The samples are moderately to poorly sorted within the range of 0.87 to 1.87 phi and from 0.83 to 1.66 phi for the Sma and Sra sediments, respectively. The sediments are generally symmetrical to very fine skewed (0.11 to 0.53 and 0.03 to 0.41 phi for the Sma and Sra sediments, respectively), and mesokurtic to very leptokurtic (0.78 to 2.32 and 0.93 to 2 phi for the Sma and Sra sediments, respectively) (Figure 5.22).

The Sma and Sra sediments generally show narower ranges of main particle modes compared to the Sm and Sr fluvial sediments. They also tend to be better sorted. These differences are less notable for the Sr and Sra sediments probably attributed to the lower depositional energy of these facies compared to the Sm sediments.
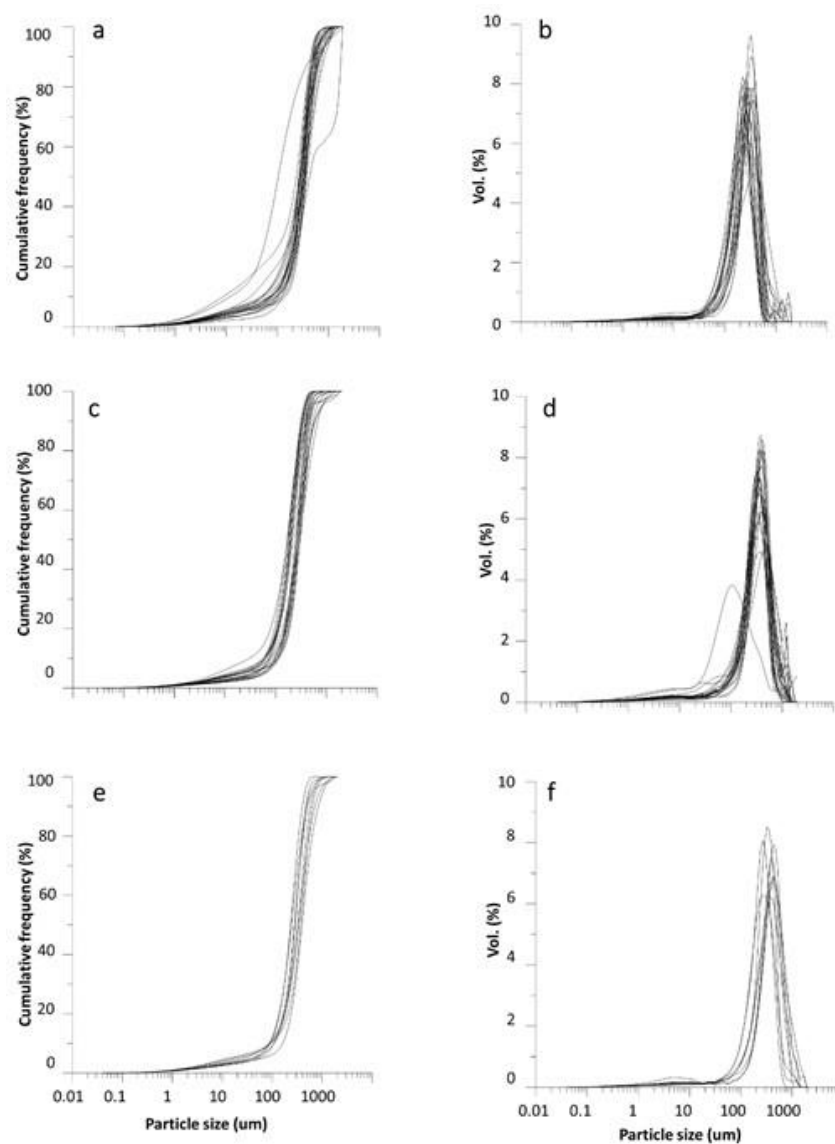
Figure 5.21 a, c, e) Cumulative frequency curves of the GH1 section Sma, Sra and Ssa fluvio-aeolian sediments, respectively. b, d, f) Particle size distribution curves of the Sma , Sra and Ssa fluvio-aeolian sediments, respectively.
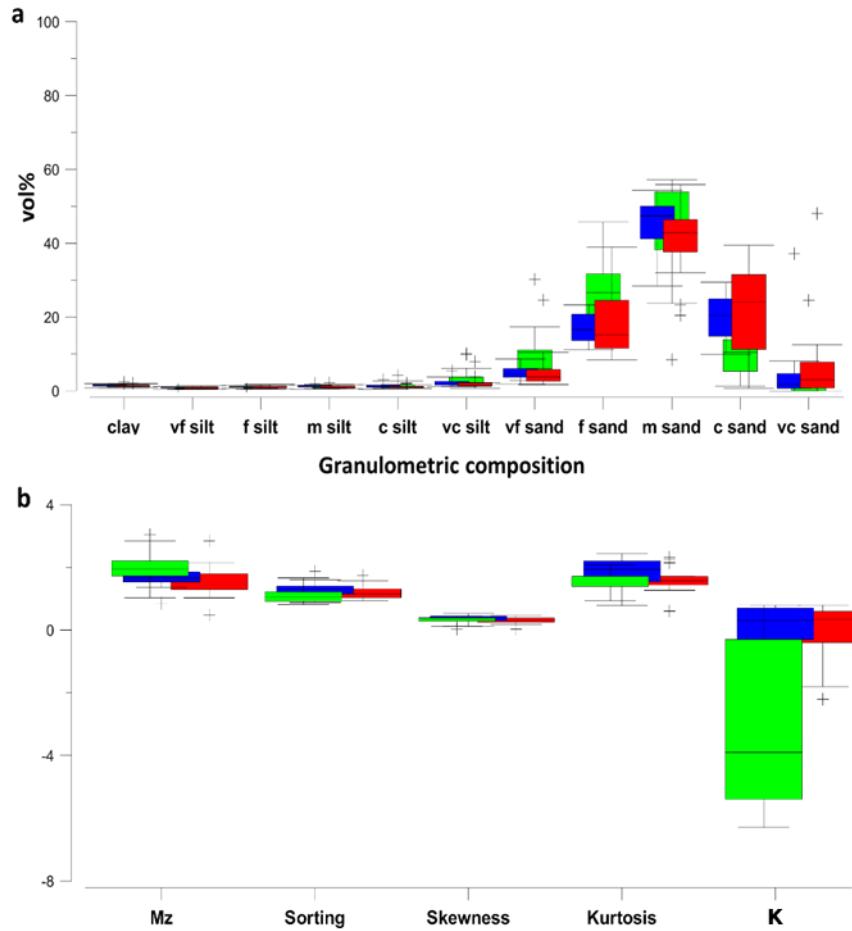
Figure 5.22 a) Box plots of the granulometric composition of the GH1 section Sra (green), Sma (blue) and Ssa (red) sediments. b) Granulometric statistical parameters (in phi units) and κ values. Outliers are data located at 1.5 times the interquartile range.

PCA analysis of the granulometric composition of the fluvio-aeolian sediments (Figure 5.23) show that the first two eigenvectors explain 83.4 % of the variance within the samples, where PCA1 (51.6%) correlates positively with the very fine sand content (r^2=0.9; P<0.05), the fine sand content (r^2=0.92; P<0.05), and the very coarse silt content (r^2=0.74; P<0.05). While, PCA2 (31.8%; P<0.05) correlates positively with the medium sand content (r^2=0.8; P<0.05).
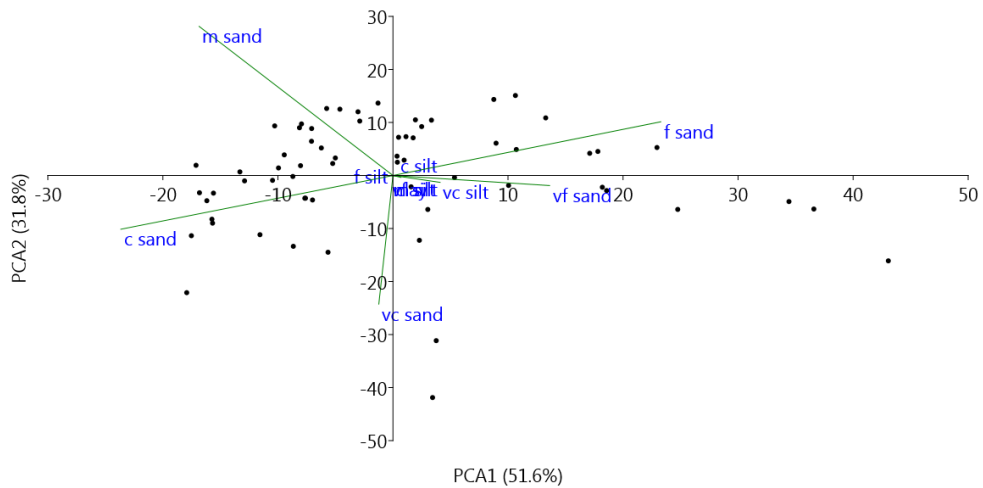
Figure 5.23 Principal Component Analysis of the granulometric parameters of the GH1 section fluvio-aeolian (Ssa, Sma and Sra) sediments showing the first two eigenvectors.

In terms of the sediments' elemental composition, the fluvio-aeolian sediments are generally enriched in silica (Figure 5.24), with silica (SiO_2) contents of 46.7-68 wt. %, 48-68 wt. % and 53-66 wt. % for the Ssa, Sma and Sra sediments, respectively.

PCA analysis of the elemental composition of the fluvio-aeolian sediments (Figure 5.25) shows that the first two eigenvectors explain 89.6% of the total variance within the samples, where PCA1 (69.8%) correlates positively with the SiO_2 content ($r^2=0.99$; $P<0.05$) and shows negative correlations with all the other elements, while, PCA2 (19.8%) correlates positively with the Al_2O_3 content ($r^2=0.98$; $P<0.05$), the Ti content ($r^2=0.65$; $P<0.05$) and the Fe_2O_3 content ($r^2=0.6$; $P<0.05$).
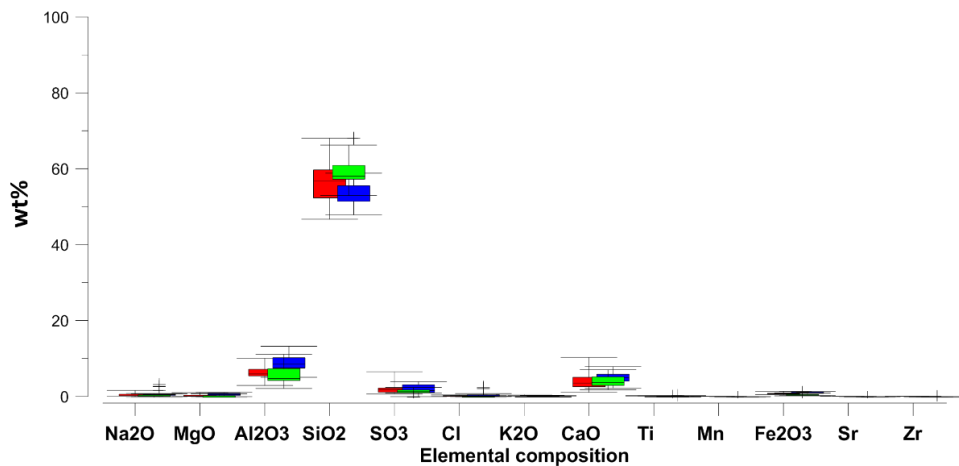
Figure 5.24 Box plots of the chemical composition of the GH1 section Sra (green), Sma (blue) and Ssa (red) sediments. Outliers are data located at 1.5 times the interquartile range.
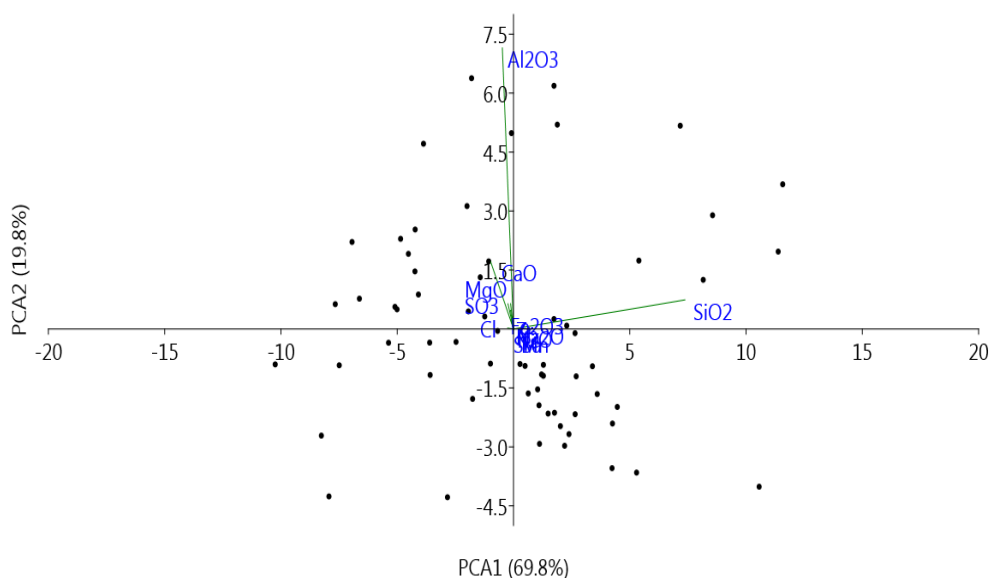
Figure 5.25 Principal Component Analysis of the elemental composition of the GH1 section fluvio-aeolian (Ssa, Sma and Sra) sediments.

The Ssa sediments ICV values range from 0.39 to 2.47 with a mean value of 0.98. The Sma samples ICV values range from 0.49 to 1.6 with a mean value of 1.4, while, the Sra samples ICV values range from 0.6 to 1.8 with an average of 1.6. This indicates that the sediments comprise both mature and immature sediment sources, with a dominance of mature sources (Cox et al., 1995; Hossain et al., 2017).

Fluvio-aeolian sediments interpretation

Aeolian and fluvial systems interactions depend on moisture availability, where the aeolian deposition will be more dominant when moisture is low. With the increase of moisture availability, the two systems reach a zone of maximum interaction after which the fluvial processes dominate the system (Bullard and Livingstone, 2002). As evident from the granulometric parameters PCA analysis (see above), the variation, primarily in the sand contents, characterizes the fluvio-aeolian deposition, which is primarily controlled by wind energy (Ben Ameur et al., 2019; Liang et al., 2013). In addition, the chemical elements PCA analysis (see above) also shows that alternation between silica addition and allogenic elements addition drives the variance in the geochemical composition of the sediments. These associations reflect the system behaviour, where the addition of silica is probably associated with lower moisture availability and sandstorms (e.g. Ben Ameur et al., 2019), while the allogenic elements (e.g. Ti and Fe_2O_3) associated with basin

141

disturbance and in-wash (e.g. Metcalfe et al., 2010), are more active during periods of higher moisture availability, reflecting the signal of catchment in-wash, probably following a dry period (e.g. Ben Ameur et al., 2019; Liang 2013).

In order to investigate the associations within the geochemical and granulometric compositions, PCA analysis was conducted using the main parameters previously extracted (Figure 5.26). The results emphasized the system behaviour, where the first three eigenvectors explain 82.4 % of the total variance. PCA1 (41%) correlates positively with the fine fractions, very coarse silt (r^2=0.9; P<0.05), very fine sand (r^2=0.95; P<0.05), fine sand (r^2=0.7; P<0.05) and with the Ti content (r^2=0.56; P<0.05). The second eigenvector PCA2 (28.8%) correlates positively with Al_2O_3 (r^2=0.9; P<0.05), Ti (r^2=0.7; P<0.05) and Fe_2O_3 (r^2=0.8; P<0.05), while the third eigenvector PCA3 (12.5%) correlates with SiO_2 (r^2=0.9; P<0.05). These associations probably reflect the fluvial/aeolian interactions where the fine grains are associated with moisture availability and may indicate distant sources of the aeolian fraction (e.g. Dayan et al., 2008). The second eigenvector probably reflects the dominance of the fluvial system and addition of allogenic elements, while the third eigenvector's association with silica probably reflects periods of low moisture and sandstorms. This is also supported by the negative covariance between SiO_2 and Ti (r^2=-0.2).

In addition, the magnetic susceptibility values of the fluvio-aeolian sediments are positively correlated with Ti (r^2=0.2) and negatively correlated with SiO_2 (r^2=-0.15). This also supports the association of silica with sandstorms bringing quartz-rich sediments into the system.
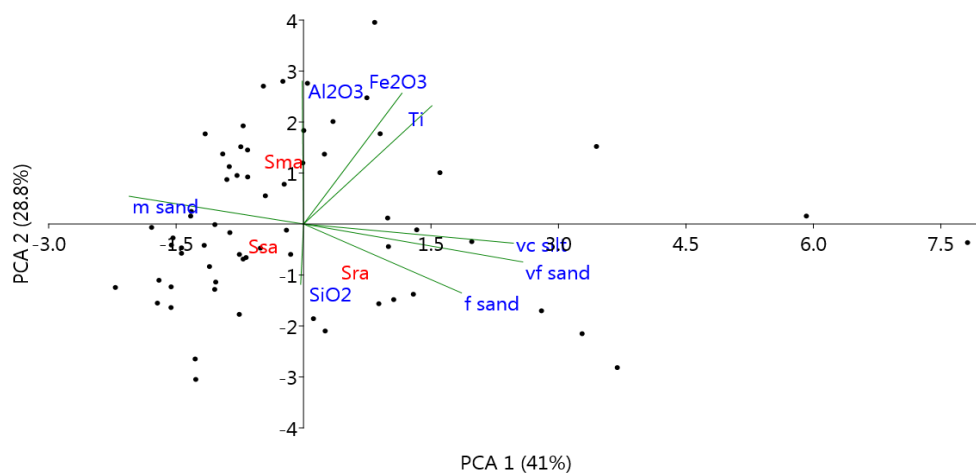
Figure 5.26 Principal component analysis of the GH1 section fluvio-aeolian granulometric and chemical main variance drivers.

Thus, the fluvio-aeolian deposition of the GH1 sediments probably reflect periods of low moisture availability, during which an activation of the aeolian system took place. The differentiation between proximal and distal aeolian sediments and sources requires a more detailed geochemical study of the sediments, however, the contribution of the proximal sandstone formations around the Gharandal Valley is reflected by the dominance of medium-sized particles main modes (Ibrahim, 1993; Saqqa and Atallah, 2004; Amireh, 2015; Lucke et al., 2019a).

5.2.6 Wetland (fine-grained) lithofacies (Fm and Fl)

Fine sediments are primarily the deposits of low energy suspension, with bed thicknesses ranging from less than one centimetre to several metres (Miall, 1996). The fine lithofacies (Fl and Fm) beds are generally dominated by very fine, fine sand, silt and clay (Miall, 1996). The differentiation between the two lithofacies is based on the presence of sedimentary structures. The Fl lithofacies sediments include faint horizontal laminations at some locations, while, the Fm lithofacies are massive.

Both lithofacies are found at different levels in the section, with varying thicknesses, starting from 0.62 m above the base up to the top of the sequence (at 16.2 m). However, thick units (ca. 0.5 m to 2 m) are only present starting from 12.25 m above the section base (Figure 5.27). These beds are also distinguished by their content of LOI_{550} of up to 10.6%, compared to the other lithofacies with values up to a maximum of 4.9 %. Only three other samples from the massive sand beds show LOI_{550} content of ca. 7.5%, however, these samples are located either below or above the fine-grained beds.
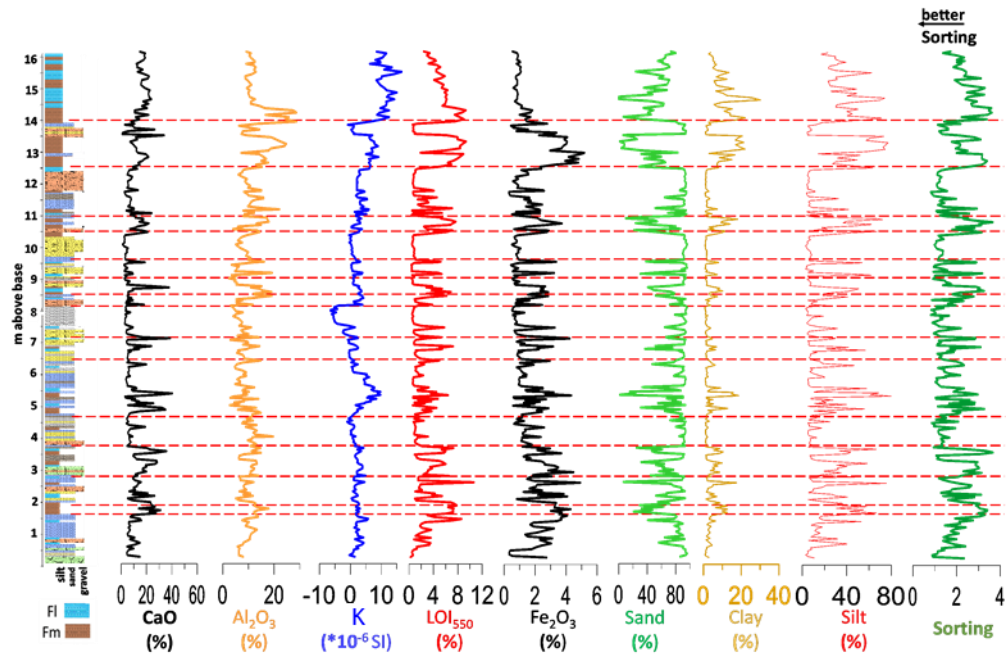
Figure 5.27 Stratigraphy of the GH1 section showing the location of the Fl and Fm (wetland) lithofacies beds marked by the horizontal red lines showing peaks of clay and silt. Also observed is the general association of the wetland beds with elevated content of CaO, Al_2O_3, and LOI_{550}, and (κ). Clay and silt in vol. %. Fm: massive wetland lithofacies. Fl: wetland lithofacies showing faint lamination.

The fine lithofacies sediments are mainly dominated by very fine to fine sand with high contents of fines (silt and clay) (Figures 5.28 and 5.29), compared to the other lithofacies in the section. The total sand content ranges from 0 to 87 vol. %, the silt content ranges from 10 to 80 vol. % and the clay content ranges from 2.3 to 30 vol. %. The samples generally show fine main particle modes in the range of 230 to 5.1 μm (mean 90 μm; Std. 66.8 μm) (Figure 5.28). Only few samples, out of the total 111, show main modes > 410 μm. These samples are located either below or above sand-dominated Sm or Sr beds and probably reflect the transition into the wetland conditions and the effect of these beds on the granulometric composition. The samples are poorly to very poorly sorted within the range of 1.3 to 3.6 phi. The sediments are generally coarse to very fine skewed (-0.2 to 0.67 phi), and platykurtic to very leptokurtic (0.69 to 2.15 phi) (Figure 5.28).

The PCA analysis of the granulometric composition (Figure 5.29) shows that the first three eigenvectors explain 90% of the variance. The first eigenvector PCA1 (56%) correlates with the clay content (r^2=0.3; P<0.05) and fine silt (r^2=0.3; P<0.05), while PCA2 (25%) correlates with the medium sand content (r^2=0.6; P<0.05), and PCA3 (9%) correlates with the fine sand content (r^2=0.5; P<0.05).
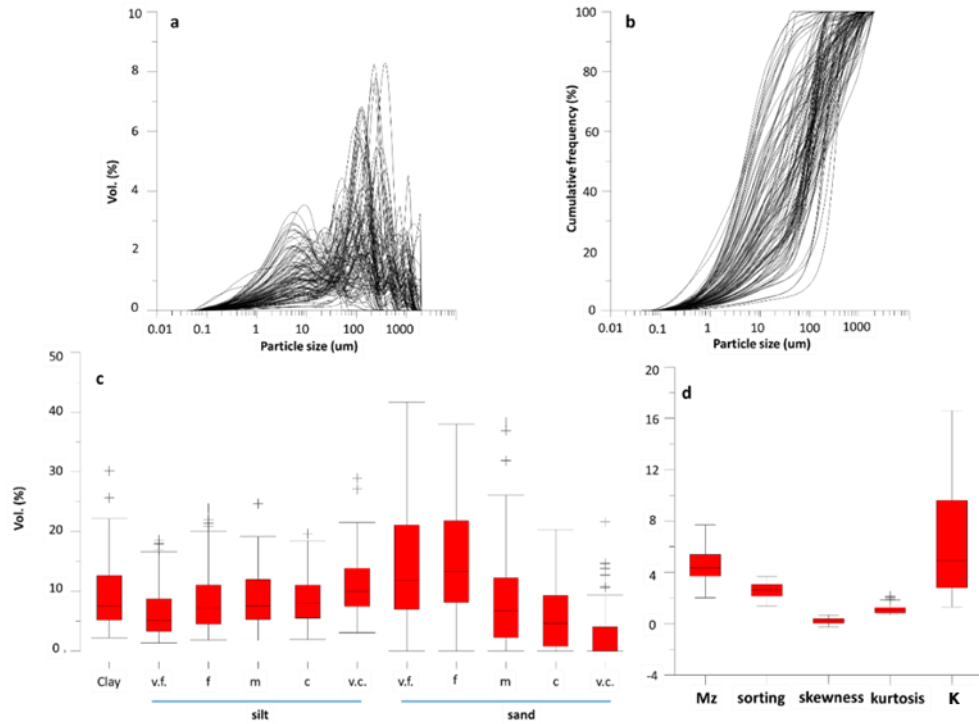
Figure 5.28 a) Particle size distribution curves. b) Cumulative frequency curves. c) Box plots of the granulometric composition of the GH1 section fine-dominated (wetland) sediments d) Granulometric statistical parameters (in phi units) and (κ) values (*10^{-6} SI). Outliers are data located at 1.5 times the interquartile range.
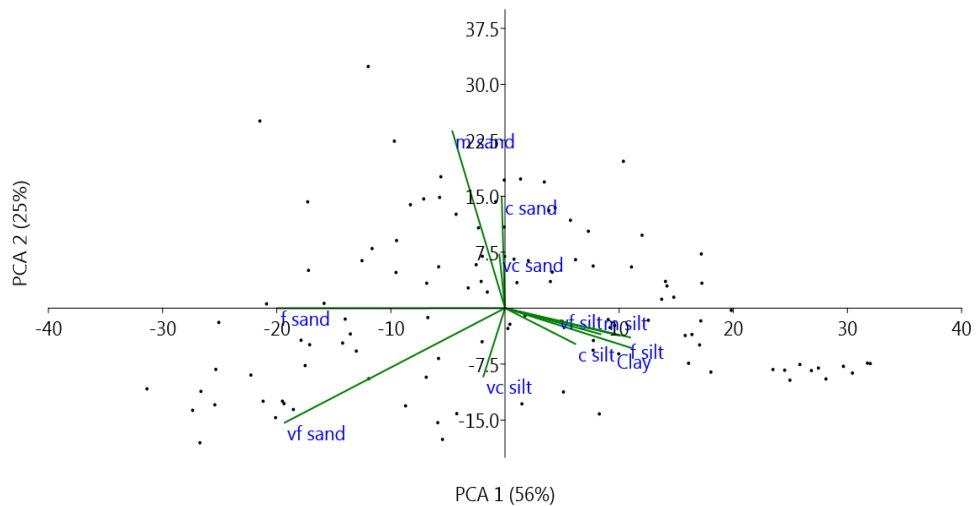
Figure 5.29 Principal Component Analysis of the GH1 section wetland lithofacies granulometric composition showing the first two eigenvectors.

The Fm and Fl sediments show high contents of silica (SiO_2). However, they also show enrichment in calcium oxide (CaO), Na_2O and MgO and OC (LOI_{550}) (Figure 5.30). Higher content of Al_2O_3 is also observed in comparison with the sandy facies (see above). The SiO_2 content is within the range of 19.3 wt. % to 51.5 wt. % with

an average of 37.4 wt. %, the CaO content shows a range from 4 to 41 wt. % and the Al_2O_3 content is in the range of 5.5 to 28.63 wt. % with an average of 13.4 wt. %.
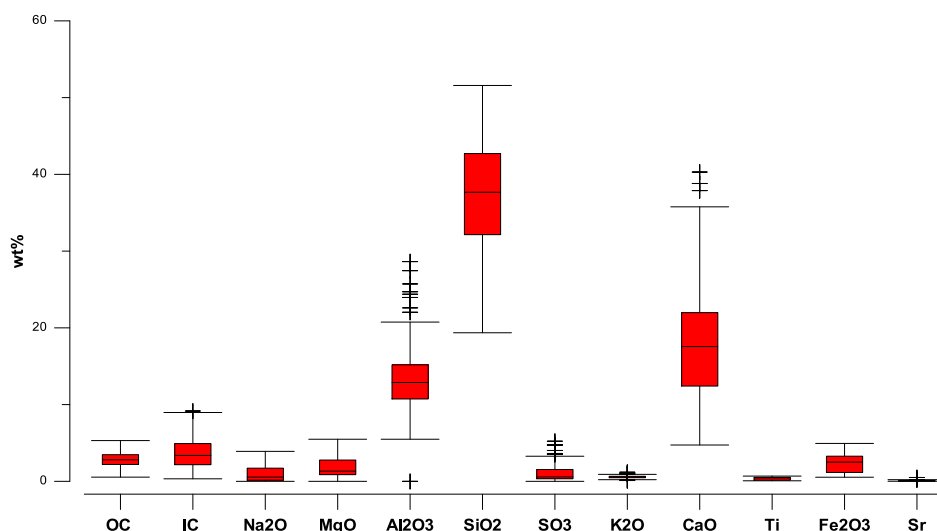
Figure 5.30 Box plots of the chemical composition of the GH1 section fine-dominated (wetland) sediments (outliers are data located at 1.5 times the interquartile range).

The Fl and Fm lithofacies elemental composition shows a different geochemical behaviour compared to the sand and gravel lithofacies. The positive correlation of Ti with Fe_2O_3 (r^2=0.8; P<0.05) suggest its association with catchment in-wash. The SiO_2 content correlates positively with Al_2O_3 (r^2=0.4; P<0.05) and with Ti (r^2=0.3; P<0.05) suggesting its association with catchment in-wash and not with sandstorms (aeolian). On the other hand, the K correlates negatively with Ti and Fe_2O_3, r^2= -0.7 and -0.54 (P<0.05), respectively, and positively with Na_2O, MgO, (r^2= 0.6 and 0.65; P<0.05, respectively) and clay content (r^2= 0.4; P<0.05). The CaO content also correlates negatively with Ti (r^2= -0.13; P<0.05).

The PCA analysis of the geochemical composition of the Fl and Fm facies (Figure 5.31) shows that the eigenvectors (PCA 1 and 2) explain 89.8 % of the total variance in the samples. PCA1 (78.8%) correlates positively with SiO_2 and Al_2O_3 Ti and Fe_2O_3 content (r^2=0.9, 0.5; P<0.05) and negatively with CaO and Sr (r^2=-0.9, -0.4; P<0.05), while Al_2O_3,Ti and Fe_2O_3 correlate positively with PCA2 (11%) with r^2= 0.8, 0.3, 0.33; P<0.05.

To further understand the deposition of the carbonate (Ca) fraction, the bi-plot of CaO vs. Ti (Figure 5.32) shows a general negative covariance, however, two

different regression lines are recovered based on the sampled levels within the sequence: the black regression line for the sediments located between 13.9 m above sequence base to the top of the sequence, and the red regression line representing the samples located between 0.62 m to 13.9 m above the sequence base.
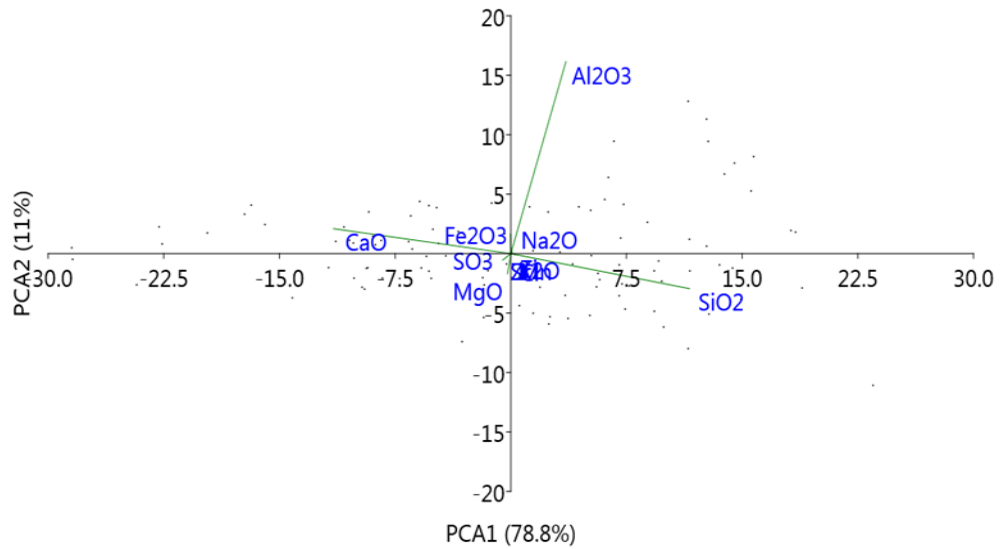
Figure 5.31 Principal Component Analysis of the GH1 section wetland sediments geochemical composition.
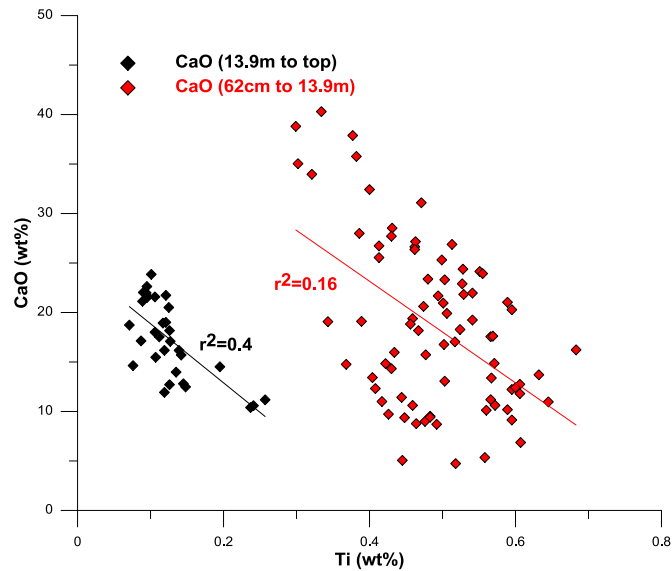
Figure 5.32 CaO/Ti bi-plot of the GH1 section wetland deposits.

In addition, using the Index of Compositional Variability (ICV) (Cox et al., 1995), the Fm and Fl sediments show a dominance of compositionally immature

sediment sources (>1 ICV) with ICV values ranging from 6.7 to 0.54 with an average of 2.

Wetland sediments interpretation

Generally, the fine-grained (wetland) sediments are deposited from suspension or from standing water pools (Miall, 1996). The Fl and Fm lithofacies are enriched with fine sand, silt and clay; the Fl sediments (with faint laminations) probably indicate deposition from suspension or slow currents, while the massive nature of the Fm beds probably suggests deposition in water pools or a shallow water environment.

The samples from the base to 13.9 m indicate more fluvial deposition as observed from the PCA and the CaO/Ti plots, where fines are deposited after a decrease in the medium energy. However, the samples from 13.9 m to the top of the section show a trend where a stable range of sorting rate is accompanied by a variable Mz. This behaviour is representative of low hydrodynamic environments where small variations in the transport medium energy are present (Mycielska-Dowgiałło and Ludwikowska-Kędzia, 2011), which supports the suggested deposition of this part of the section as deposition in standing water bodies.

The geochemical properties of the wetland deposits are different from the other lithofacies in the section, where SiO_2 is associated with catchment erosion, positive covariance with Ti, suggesting the reduction or shutdown of sandstorms during the deposition of the wetland beds and wetter conditions. The PCA results showed that the deposition of these beds is primarily mirrored by variations of CaO, Al_2O_3 and SiO_2. (κ) association with Na_2O and MgO and its negative correlation with Ti and allogenic markers, especially in the topmost 2 m of the section suggest that magnetic susceptibility in this part of the sequence is primarily associated with the accumulation of fines and ferromagnetic minerals in standing water bodies as also suggested by elevated LOI_{550} values (up to 9%) (e.g. Parton et al., 2013; Lucke et al., 2019b).

This is also supported by the steeper regression line (black line in Figure 5.32) which suggests endogenic deposition of CaO in a standing water body, where Ti is depleted reflecting reduced catchment erosion from 13.9 m to the top of the section. This is also supported by a positive correlation between the organic mineral Mn and the organic content (r^2=0.4; P<0.05) in this part of the section, while negative covariance (r^2= -0.1) is recorded in the other parts of the section.

The red regression line, from 0.62 m to 13.9 m from the base, may indicate *in-situ* deposition of CaO accompanying allogenic addition of CaO during periods of catchment erosion and detrital input.

To investigate the modes of transportation and deposition, the wetland deposits were also plotted on the CM diagram (Figure 5.33). The diagram shows that the deposition was primarily through suspension to graded and uniform suspension and over-bank pool deposition, where the Fm sediments (red colour) show a trend towards lower energy deposition and pool (standing water) deposition.
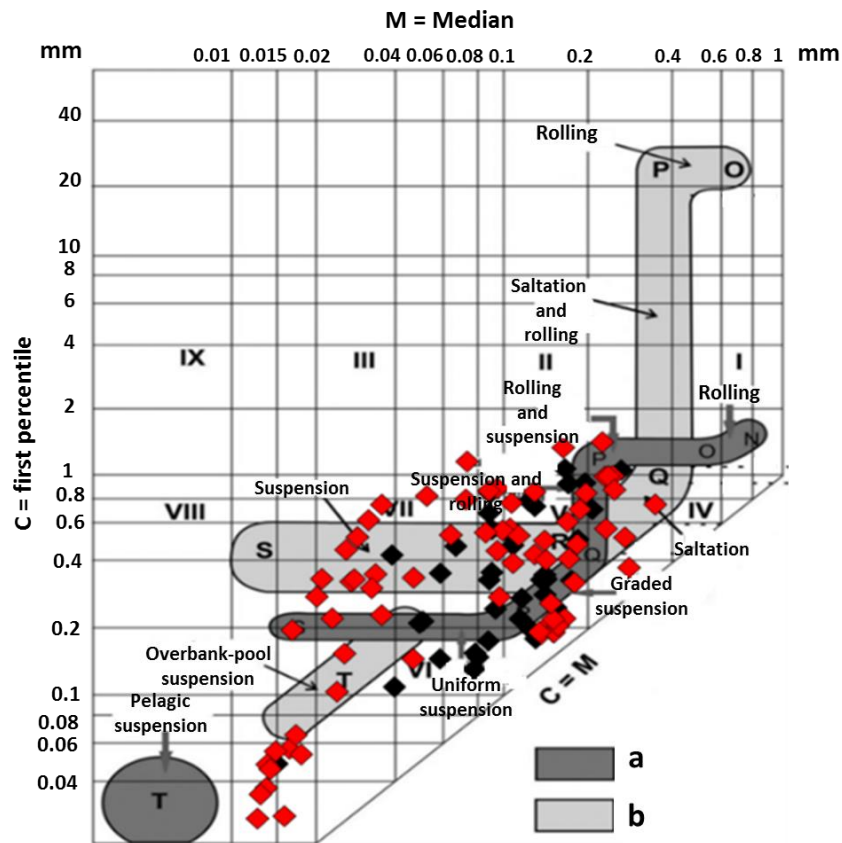
Figure 5.33 Complete CM pattern of tractive current deposits of the GH1 section fine-grained (wetland) sediments. Fm beds (red) and Fl beds (black). a: Dark grey colour based on Passega (1964) and Passega & Byramjee (1969); b: Light grey colour based on Ludwikowska Kędzia (2000). I, II, III, IX: rolled grains; IV: High turbulence deposit; V: Low turbulence deposit; VI: Graded suspension; VII: Uniform suspension; VIII: Finest uniform suspension (after Passega and Byramjee, 1969) (modified from Malgorzata and Ludwikowska-Kedzia, 2011).

Accordingly, the Fm and Fl lithofacies sediments in the GH1 sequence are suggested to primarily represent wetland sediments that were deposited from low turbulence suspension, graded and uniform suspension, and in standing water pools. From the base to ca. 12.6 m, thin wetland beds are present, while from 12.6

m to ca. 13.9 m more consistent wetland deposition is indicated (Figure 5.27) with catchment erosion. These parts of the section records wetland conditions developed following water fluxes.

The most significant wetland bed of ca. 2 m is present from ca. 13.9 m to 16 m over the base suggesting deposition in standing water body, or high groundwater recharge, and enhanced moisture availability (possible precipitation in the valley).

5.2.7 Depositional and environmental history of the GH1 sedimentary sequence

The GH1 section records 16 fining upward (aggradation) cycles that start with flood (in the lower 3 m of the section) or mass flow events, followed by sand deposition and wetland beds. Occasionally, the sand migrates downstream into the wetland beds (Sr lithofacies) followed by the redevelopment of the wetland beds. However, within these fining upward cycles, cyclic associations are observed between sand deposition and wetland deposition. These cyclic associations dominate the section suggesting that the mass flow events are the rare events, contrary to the present day conditions of primary flood deposition. This suggests more stable climatic conditions with less frequent floods.

The GH1 section, from the base to ca. 13.9 m above the section base, indicate deposition in periods of wetting and drying as reflected by the presence of carbonate concretions. The elevated LOI_{550} values in the wetland beds through this part of the sequence suggest shallow marsh environments. The role of the spring discharge is also distinguished from the sedimentation cycles, where the wetland beds develop following basin in-wash, which causes groundwater recharge, and hence enhanced spring discharge. The green colour of the wetland beds in some locations suggests reducing (anoxic) conditions, while the evidence of oxidation is also present as ferruginous staining in some wetland beds and sandy beds through the section (Pigati et al., 2014).

In addition to the discussed hydrodynamic variability, the results of the GH1 sediments indicate significant fluvio-aeolian deposition in the valley. Aeolian deposition in deserts is significant in wetland formation as it may accumulate and contribute to the deposition of fine materials in desert wadis. Williams et al. (2006) showed that during dry periods, aeolian sediment accumulation contributed to the formation of wetlands in the Australian desert. Aeolian deposition increases infiltration, decreases surface runoff and increase base flow. Accordingly, the aeolian deposition of the GH1 section may have played a role in modifying the

hydrological system in the Gharandal Valley accompanied by the vegetation during marshy environment periods.

In order to show the valley response and the cyclicity of wetter and drier conditions, the main granulometric and elemental parameters observed in the different lithofacies were combined and used for PCA analysis. The Al_2O_3, SiO_2, CaO, Ti and Fe_2O_3 contents were used alongside the clay, very fine silt, fine sand, and medium sand contents. In addition, the OC (LOI_{550}), sorting and K were used. These represent the allogenic in-wash elements, the indicators of fluvio-aeolian deposition and wetland conditions development. The PCA results (Figure 5.34) show that the first two eigenvectors explain 72 % of the variance. PCA 1 (60%) correlates with all the features except for the silica, fine and medium sand contents (r^2= -0.8; -0.8 and -0.6, respectively). These associations probably reflect periods of enhanced moisture, either as catchment in-wash or wetland conditions development, (elevated PCA 1 values) that alternate with lower moisture availability and possible activation of the aeolian system (lower PCA 1 values). Accordingly, the PCA 1 and the GH1 section stratigraphy are shown in Figure (5.35) alongside the organic content, the SiO_2/Al_2O_3 ratio and (κ) values. The proxies show good correlation and changes corresponding to the sediments' composition and facies variation. The ratio SiO_2/Al_2O_3 reflects changes in wind energy (enhanced aeolian deposition) relative to fluvial deposition (high Al_2O_3). This element ratio was chosen based on the PCA results of the different sedimentary lithofacies, where both elements were shown to drive the variance within the sediments. It has also been used to reflect the intensity of aeolian deposition elsewhere around the world (e.g. Itambi et al., 2009; Liang et al., 2013).
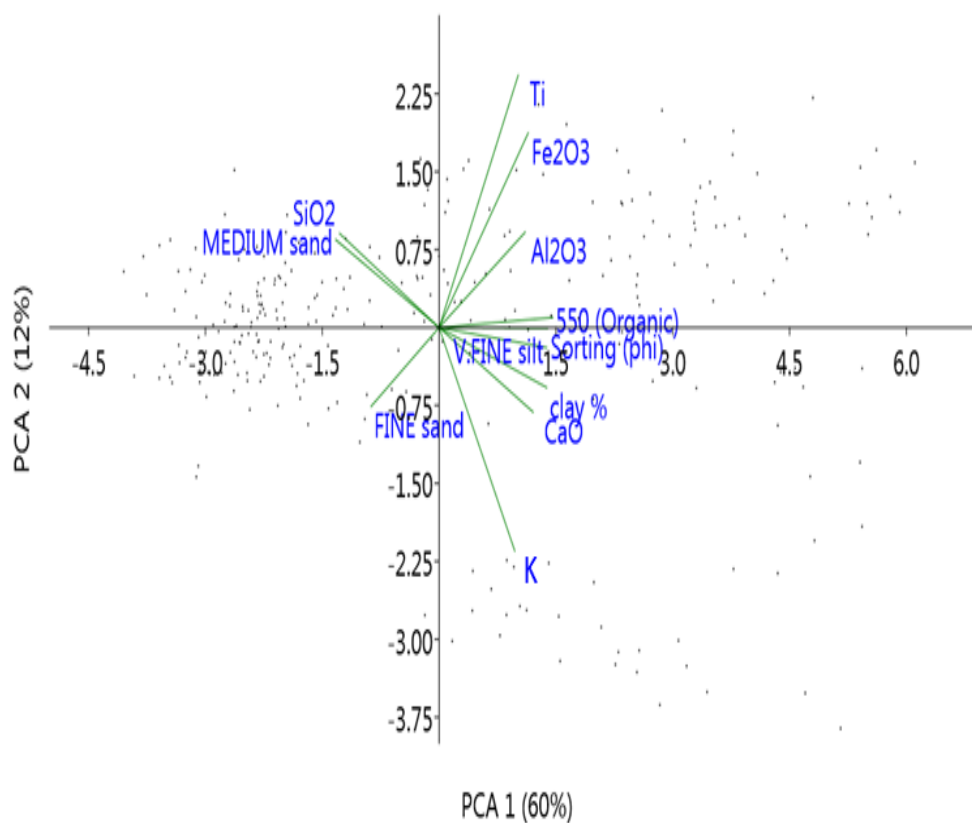
Figure 5.34 Principal component analysis results of the whole GH1 section environmental proxies showing the first two eigenvectors.
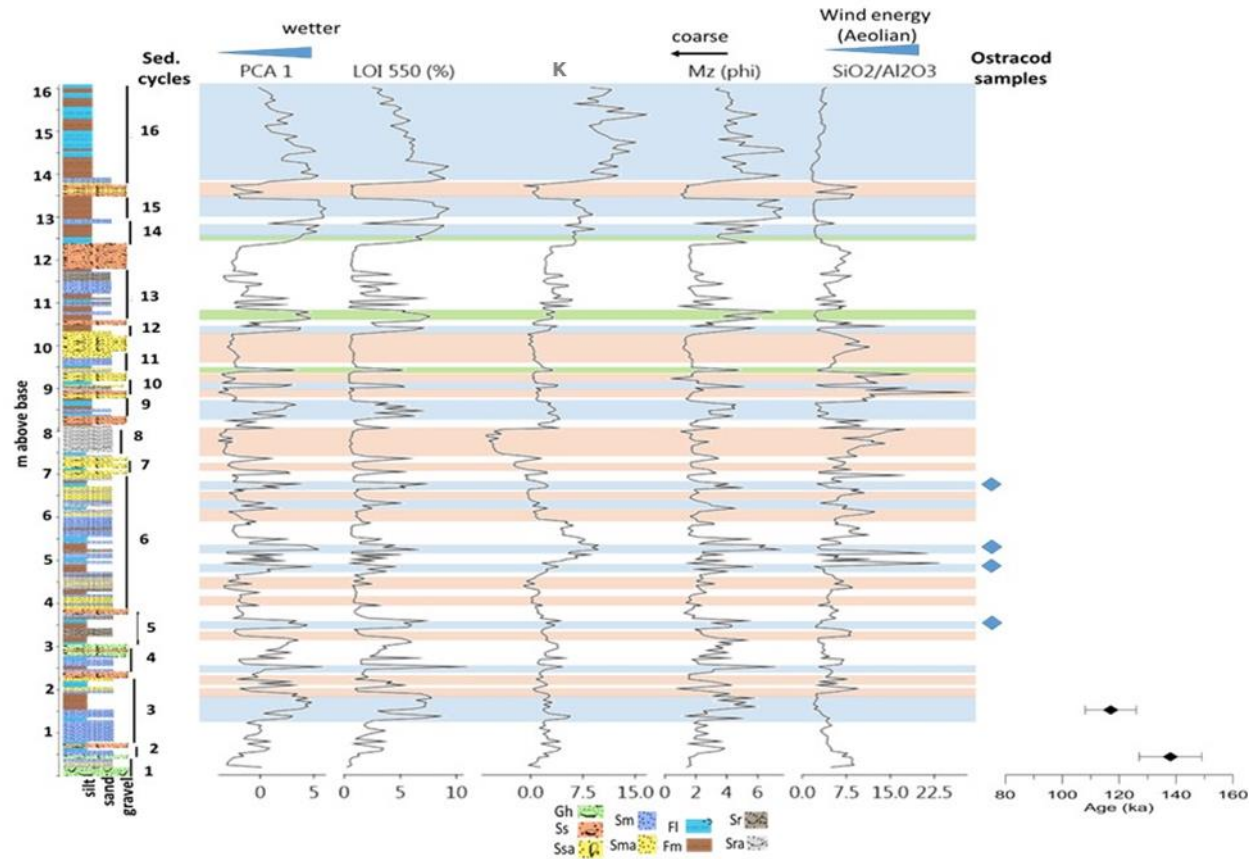
Figure 5.35 GH1 sedimentary sequence stratigraphy showing the 16 depositional cycles alongside the environmental proxies. OSL age estimates (from Al-Saqarat et al., 2020). Blue diamonds: locations of ostracod shells (from Mischke et al., 2017). Blue: wetland conditions. Green: organic-rich shallow marsh. Orange: suggested aeolian processses activation. Gh: gravel lithofacies, Ss: Pebbly sand lithofacies, Sm: massive sand lithofacies, Sr: sand lithofacies with sedimentary structures, Fl, Fm: wetland lithofacies, Ssa, Sma, Sra: fluvio-aeolian lithofacies.

The lower 13.8 m of the GH1 section (sedimentary cycles 1 to 15) probably reflect shallow wetland conditions driven by water fluxes, groundwater changes and spring discharge, deposited during periods of wetting and drying. This agrees with the work of Mischke et al., (2017) (see Chapter 4, 4.3.6). The dominance of *Ilyocypris bradyi* species (Mischke et al., 2017), primarily found in springs, streams and moving water in the southern Levant (Mischke et al., 2014) indicates that the interpretation of a stable standing water body is not supported, at least in the lower 7 m of the section. Indeed, the basal ca. 7 m of the section (sedimentary cycles 1 to 6) shows alternating periods of fluvial in-wash, fluvio-aeolian events, and thin, ca. 5 to 25 cm, possible shallow marshy wetland beds. The locations of the ostracod samples of Mischke et al. (2017) are shown on Figure 5.35 and it indicates their association with thin wetland beds suggesting the presence of possible shallow marshy wetland beds, marked by elevated LOI_{550} contents.

From 13.8 m to the top of the section (at 16.2 m), a change in the valley hydrodynamics is recorded in the sedimentary cycle 16. Re-establishment of the spring discharge and the shutdown of the aeolian deposition, possibly as a response to moisture availability (Bullard and Livingstone, 2002), facilitated the deposition of the thickest wetland bed of ca. 2 m. In desert regions, even a slight increase in groundwater recharge may result in significant increase in the spring discharge (e.g. Jones and Richter, 2011). This part of the section suggests deposition under significantly wetter conditions, compared to the present-day, in a standing water environment fed by localised precipitation or high groundwater recharge conditions, where less fluvial deposition in the upper 2m of the section also suggests more consistently wetter conditions. Based on the available age control, this change corresponds to the MIS5 period (see 5.2.2) (Al-Saqarat et al., 2020). Nonetheless, the environmental proxies record the valley's response and aggradation into more stable wetland conditions towards the top of the section.

The GH1 section provides significant insights regarding the Gharandal Valley hydrodynamics response to climate/tectonic-driven changes. The upward transitions from one lithofacies to the other reflects the cyclicity in the deposition of the GH1 sequence and the site-specific response to changing local and regional hydrodynamics and aerodynamics. However, high energy events (floods) transporting significant amounts of gravels (>2mm) are only observed in the basal 3 m of the section, while mass flows, sufficient to move granules at some times, are recorded from 3 m to ca. 13.9 m from the base, followed by a shift in the system environmental proxies to a more stable wetland environment from 13.9 m

to the top of the section at 16.2 m. Constraining the age of the section will add significant data regarding timing of these cyclic changes and the site response to changes in regional and global climatic conditions.

5.3   GH2 sedimentary sequence

This section presents the second main sedimentary sequence in the Gharandal Valley (Figure 4.11 and Figure 5.36). The GH2 section is located to the south of the GH1 section and the road leading to the base.

5.3.1   General description of the GH2 sedimentary sequence

This sequence comprises about 13 m of sediments from its bottom (at 250 m asl) to the top. Using a compressor and a pick, the author was able to clean a section from the bottom to the top of the sequence as explained in the methodology (Chapter 3; 3.3.1). This sequence starts with a ca. 0.3 m thick bed of whitish and reddish, medium sand with carbonate concretions (Figure 5.36 c). Through the section, sedimentary structures are observed accompanying few sandy beds (e.g. Figure 5.36 c, d). Similar to Site 1, small gravels (ca. -1 to -2 phi; 2 to 4 mm) are found in sand beds at various locations, however, no clasts >-2 phi are present.

Thick silty carbonate-rich beds (identified by HCL response) are also spotted especially through the uppermost 3 m of the section showing massive structures. Dark to black-coloured thin layers are located at 4 locations through the section, at 1.7 m, 7.5 m, 8.3 m and 9.9 m.

The section generally shows several fining upward associations where carbonate-rich beds develop following sand with small gravels beds and sand beds in the lower ca. 4 m of the section, while from 4 m to the top of the section the sedimentary associations show more consistent fine-grained carbonate-rich beds with sand-rich beds suggesting periods of alternating fluvial in-wash and wetland deposition.

155
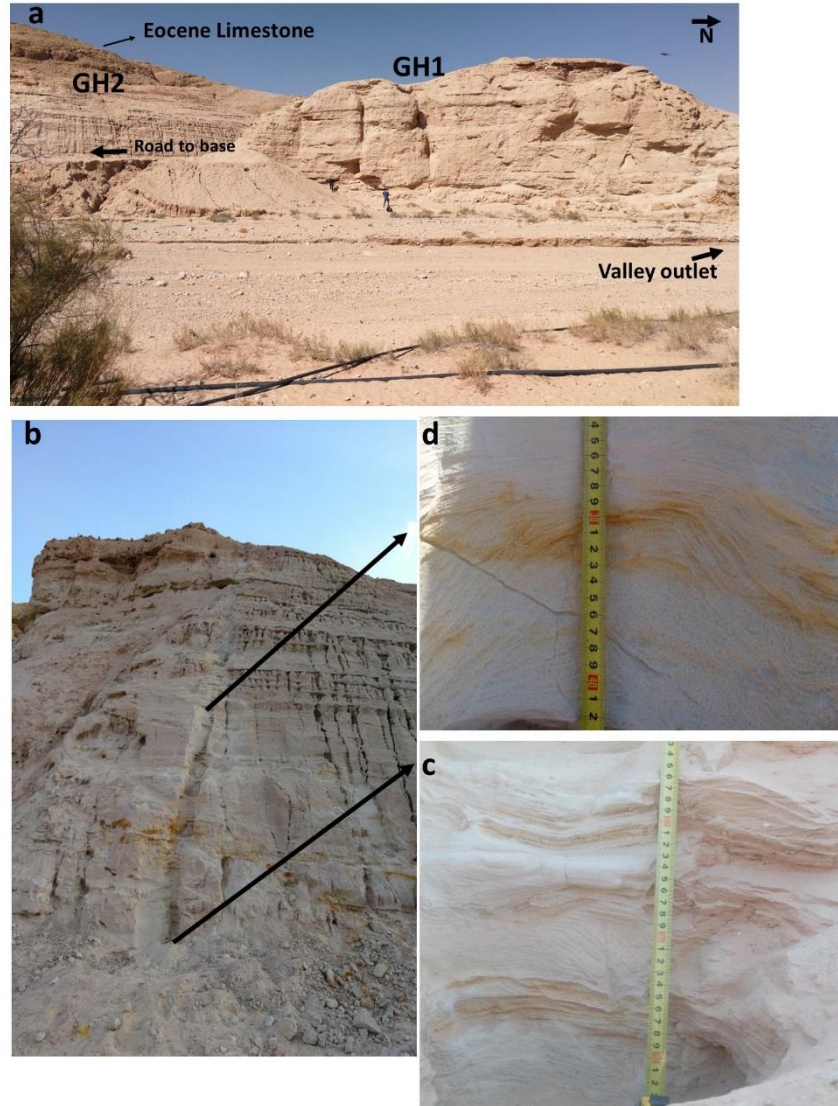
Figure 5.36 a) Westward view from the Gharandal Valley showing the main sections GH1 and GH2, b) The Gharandal GH2 section (ca. 13.2 m) located south of the road leading to the base, also observed the complete section cleaned from base to top, c) Image of the GH2 section base showing the basal sand bed and the planar and cross bedding structures (Sr lithofacies), d) Image showing hummocky cross bedding structure in the section (Sr lithofacies).

5.3.2 Chronology

The chronology of the GH2 section was estimated through four OSL ages following the method explained in Chapter 3 (section 3.6.1.1). The four samples were collected during fieldwork in 2018 at 0.3 m, 5.55 m, 9.15 m and 10.15 m above the section base (Figure 5.37). The OSL signal is dominated by the fast component in the GH2 samples as observed in the OSL growth curves, where the OSL signals decrease during the first second of stimulation (Figure 5.38). A linear or exponential function was used to fit the growth curves of the four OSL samples and yielded De (equivalent dose) values of <100 Gy.

A major uncertainty in dose rate calculation is the sediment's long-term moisture content (Toms et al., 2005; Briant et al., 2006; Preusser et al., 2008; Fiebig et al., 2009). The water trapped in sediment pores absorbs higher amounts of radiation compared to air, and thus the effective dose is higher for sediments with low moisture content (Preusser et al., 2008).

Fluvial sediments are primarily saturated with water directly after deposition, however, in tectonically active areas, or in areas where the water table is not stable, the sediments may stay at elevations higher than the water table for a significant period of time, which will affect the long term water content (Preusser et al., 2008). The present day moisture content for the beds from which the OSL samples were collected is low (<1%) (see Figure 5.37). Previous studies estimated 20±5% (Al-Saqarat et al., 2020) and 11% (Mischke et al., 2017) long term water content for OSL samples from sediments in the Gharandal Valley. The results of this project indicate the complex sedimentological and environmental variability within the valley (see 5.2.7). In addition, the cosmic ray dose rate is calculated as a function of sample depth within the section (e.g. Al-Saqarat et al., 2020) while also accounting for the average overburden density of the sediments. The sensitivity of the Gharandal sediments OSL age estimates to moisture content, overburden density and depth was examined and showed significant effects on the estimated ages that increases with the sediment age. For example, using the published dosimetry data of Mischke et al. (2017), the results suggest that the authors used an average overburden density of ca. 1.6 g/cm^3, similar to the calculated average bulk density based on LOI results of 221 samples from the GH2 section in this project. By modifying the sample depth based on the GH2 section and changing the water content from 11% to 20±5%, the published OSL age estimate of 112±9ka changes to ca. 133±12ka. While, when changing the average burden density to 2.5 g/cm^3 and keeping the water content of 11%, the age changes from 112±8ka to 127±11 ka and to 142±12ka when changing the water content to 20±5% as well. This was also observed for OSL age estimates recovered from the Jurf Ed Darawish area to the north of the Gharandal Valley.
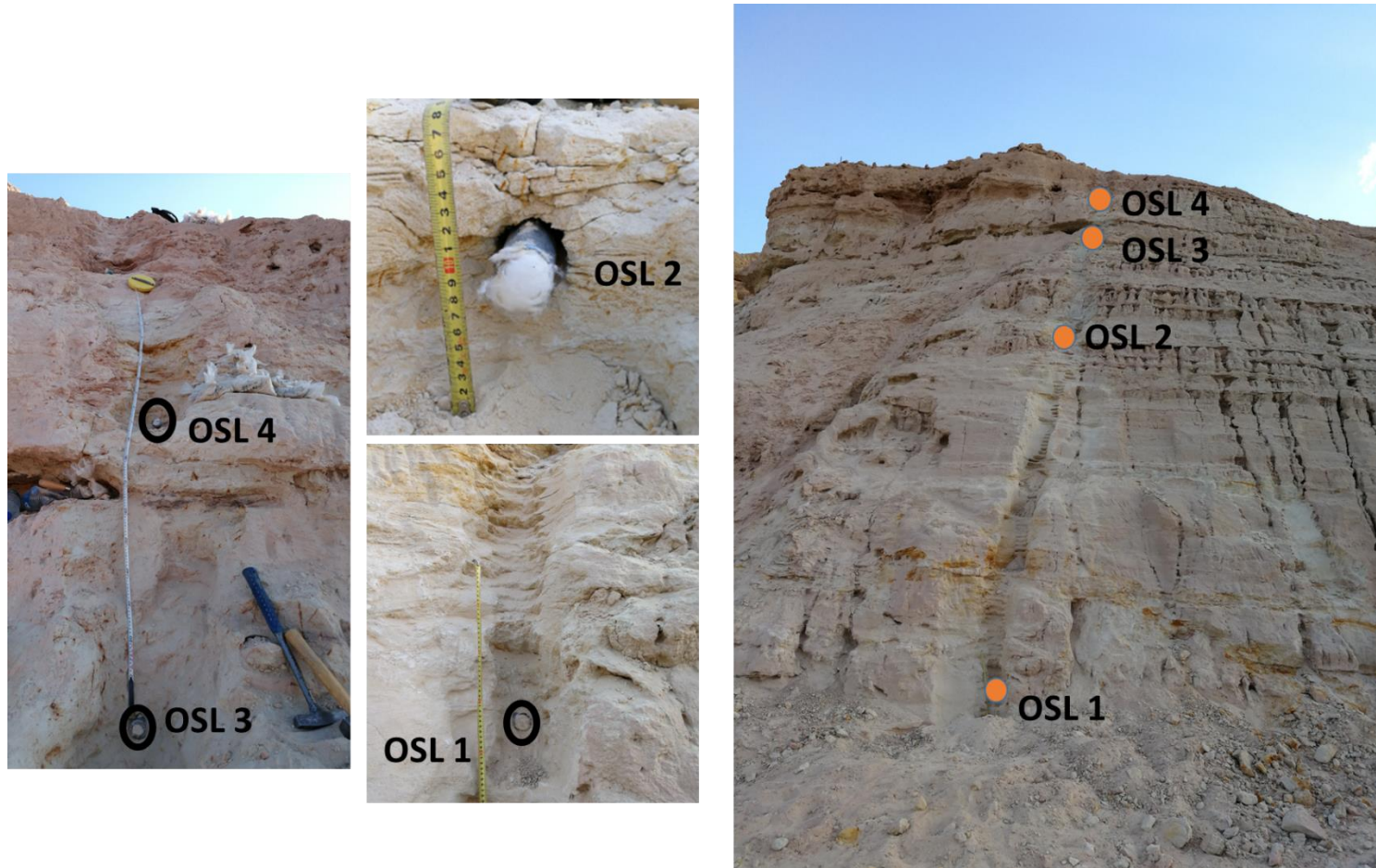
Figure 5.37 Photo showing the GH2 section and locations of the OSL samples.
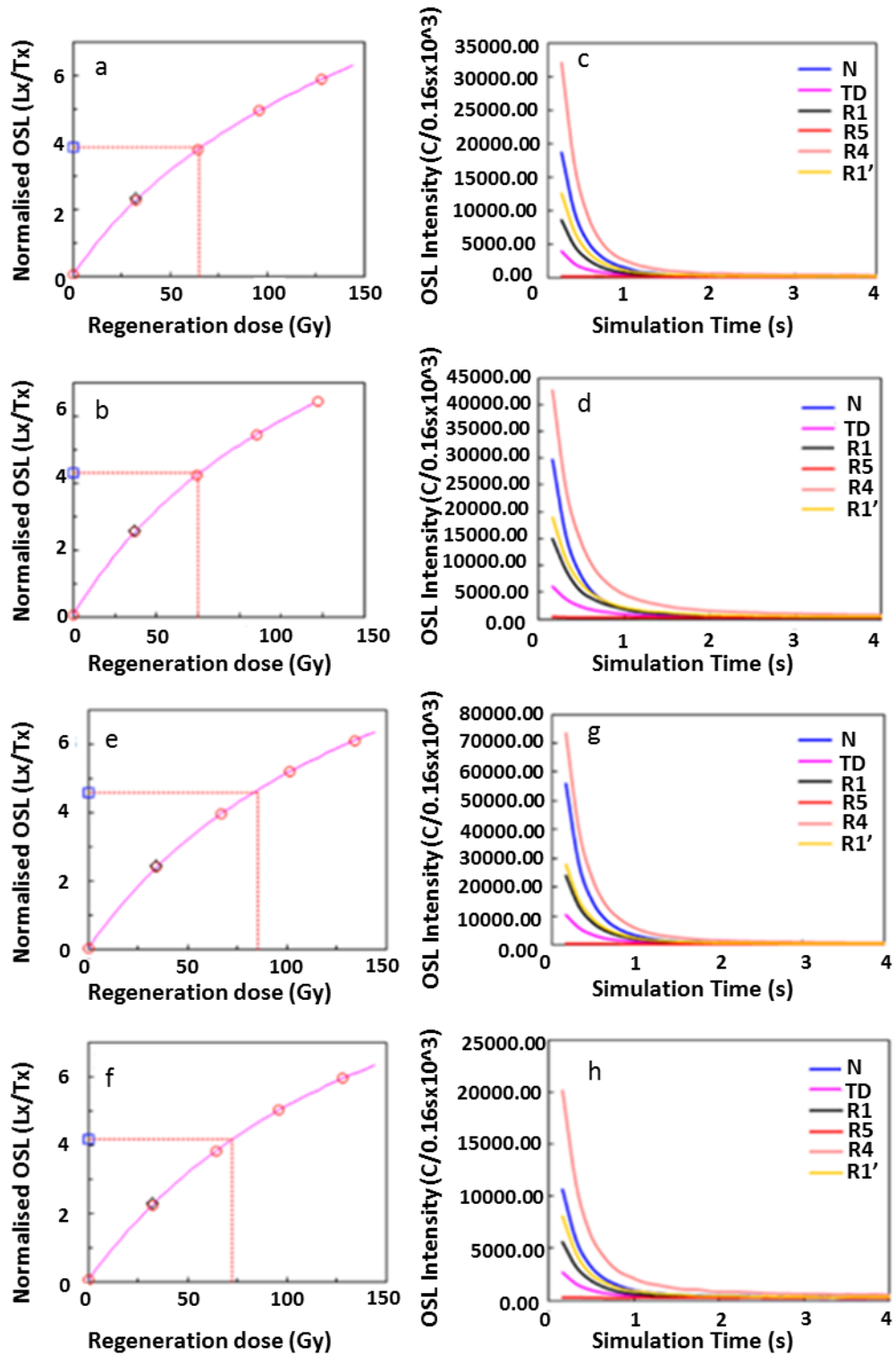
Figure 5.38 Results of optically stimulated luminescence (OSL) analyses, showing growth curves (a, b, e and f) and decay curves (c, d, g and h) for samples OSL1 to 4, respectively. The growth curves show dose response (Lx/Tx). The decay curves of the natural dose (N), regeneration dose (R), and test dose (TD = 12.4 Gy) show the OSL signals decreasing rapidly during the first second of stimulation, indicating that the OSL signal is dominated by the fast component in these samples.

Mischke et al. (2021) recalculated the previously published OSL age estimates of Moumani et al. (2003) and reported a significant change in the OSL age estimate when using different long-term average water content. In the originally published data, Moumani et al. (2003) asusmed a long-term average water content of ca. 2%, while Mischke et al. (2021) recalculated the ages using 25% water content which changed the age estimates from 111±14 ka to 146±19 ka, from 57±4 ka to 75±6 ka and from 39±3 ka to 51±5 ka (Mischke et al., 2021) indicating the sensitiviy of these age estimates to changing the long-term average water content.

On the other hand, the published dosimetry data of Al-Saqarat et al. (2020) suggest that the authors used an average overburden density of 2.5 g/cm^3. When applying the calculated average overburden density of 1.6 g/cm^3 while keeping an assumed long-term average water content of 20±5%, the oldest age reported by Al-Saqarat et al. (2020), from the sedimentary exposure where the GH2 section is located, changes from 120±8 ka to 116±8 ka, while when also changing the water content to 11%, the age estimate changes to 106±6ka.

This sensitivty is also observed for the GH2 OSL age estimates, where using different dosimetry calculations results with variable age estimates. For example, when applying the dosimetry calculations used by Al-Saqarat et al. (2020) of 20±5 water content and 2.5 g/cm^3 overburden density, the GH2 OSL age estimates show high stratgraphic inconsistency (Table 5.2). When applying the accurate overburden density with 20±5% long-term average water content, the results also show high variability (Table 5.2).

Table 5.2 GH2 section OSL age estimates based on different dosimetry assumptions.

	Overburden average density: 2.5 g/cm^3 Long-term water content: 20±5%				Overburden average density: 2.5 g/cm^3 Long-term water content: 11%			
Sample	GH3-5	GH3-6	GH3-7	GH3-8	GH3-5	GH3-6	GH3-7	GH3-8
OSL age	68	172	198	189	60	154	181	173
Uncertainty	7	13	19	17	6	12	16	14
	Overburden average density: 1.6 g/cm^3 Long-term water content: 20±5%				Overburden average density: 1.6 g/cm^3 Long-term water content: 11%			
Sample	GH3-5	GH3-6	GH3-7	GH3-8	GH3-5	GH3-6	GH3-7	GH3-8
OSL age	66	161	186	179	59.13	145.92	170.87	164.76
Uncertainty	6	12	18	16	6.15	11.36	15.70	14.03
	Overburden average density: 2.5 g/cm^3 Long-term water content: 3±1%				Overburden average density: 1.6 g/cm^3 Long-term water content: 3±1%			
Sample	GH3-5	GH3-6	GH3-7	GH3-8	GH3-5	GH3-6	GH3-7	GH3-8
OSL age	54.77	141.79	167.49	161.03	53.70	134.30	158.67	153.44
Uncertainty	4.90	8.98	15.14	13.51	4.78	8.43	14.54	13.06

Considering the present aridity of the Gharandal Valley, the estimation of the average long term water content is considered based on the stratigraphic, sedimentological and geochemical characteristics of the sediments in an attempt to retrieve more robust age estimates.

Sample OSL 1, at 0.3 m above the section base, was collected from a horizontally bedded bed with carbonate concretions located near the OSL collection site and followed by a fine-grained (wetland) bed with LOI_{550} content of ca. 5.5 % compared to the underlying and overlying beds with contents of ca. 0.4 to 1.3 %. The results indicate that this overlying fine-grained bed shows higher (κ) (ca. $3 *10^{-6}SI$) and Fe_2O_3 (ca. 1%) and lower silica contents (ca. 46%), compared to the surrounding beds, suggesting a period of water flow, accordingly, the estimated long term average water content for this bed is 20±5%. Sample OSL2, at 5.55 m above the section base, is collected from a bed that is also characterized by relatively elevated magnetic susceptibility (ca. $4.3 *10^{-6}SI$) and Fe_2O_3 (ca. 1%) and relatively higher LOI_{550} contents (ca. 5.3%) compared to the other beds in the section. The sample was collected following a ca. 20 cm fine sediment-dominated bed (wetland deposit) which suggests the presence of water flow, thus, the estimated long term water content for this sample is 20±5%.

On the other hand, the beds from which samples OSL3 and OSL4 were collected, at 9.15 m and 10.15 m above the section base, respectively, are primarily characterized by low magnetic susceptibility (ca. -0.3 to $0.1 *10^{-6}SI$), LOI_{550} (ca. 0.7%) and Fe_2O_3 (ca. 0.64 to 0.4%) with high silica (ca. 70 to 60%) and sand (ca. 90 to 95%) content. These samples are suggested to have been deposited under the influence of aeolian deposition and probably lower moisture availability, compared to OSL1 and OSL2 samples. Accordingly, the estimated long term water content is 3±1 % for the two samples.

Following the estimation of the long term water content of the sediments, it is important to assess the reliability of the OSL results (Briant et al., 2006). One method to do so is by investigating the equivalent dose (D_e) and the dose rate relationship, where reliable samples are expected to provide similar OSL age estimates, regardless of the difference in their D_e or dose rate; i.e. reliable samples, from a specific section, should plot along a straight line starting from the origin of the D_e - dose rate bi-plot (Briant et al., 2006). By plotting the GH2 section OSL samples on a D_e - dose rate bi-plot (Figure 5.39), samples OSL 2, 3 and 4 plot along the straight line from the origin and are tightly clustered, while sample

OSL1 plots away from the line. Thus, samples OSL 2, 3 and 4 can be considered as reliable, while OSL1 is an outlier, as also observed by its higher contents of K, Th and U, compared to the other 3 samples, and will not be considered as a reliable age for this section.

This observation can be further confirmed by the OSL age estimates of the samples. The results are summarized in Table 5.3 and the age estimates are listed with ±1σ. Sample OSL1 shows a younger, stratigraphically inconsistent, age, while OSL 2, 3 and 4 show a stratigraphically consistent upwards trend starting from the age of OSL2 (161±12ka) through OSL3 (159±14ka) to OSL4 (154±13ka).

These new age estimates suggest that the GH2 sequence, and particularly the upper ca. 8 m, was primarily deposited during Marine Isotope Stage (MIS) 6 which lasted from ca.190 to 130 ka (Lisiecki and Raymo, 2005) with a mean depositional age of 158±7 ka.
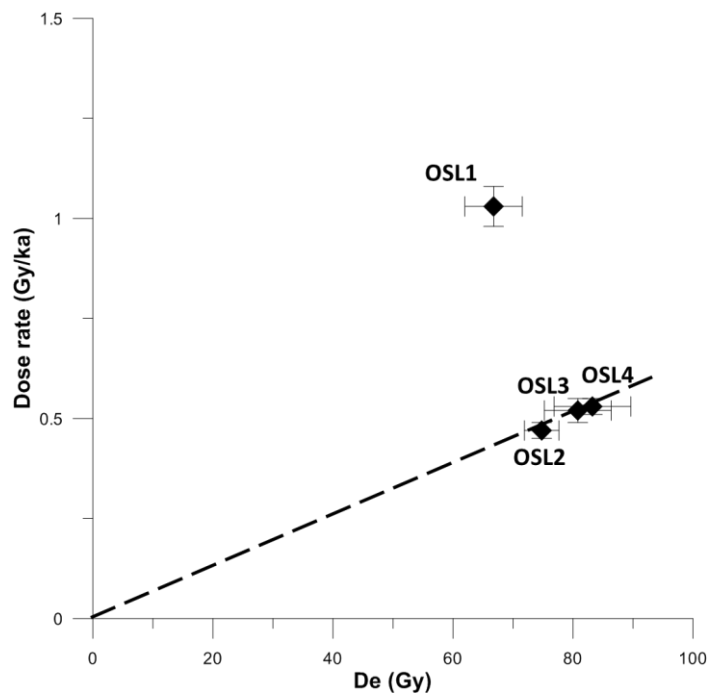
Figure 5.39 Bi-variation of equivalent dose (De) and dose rate for the GH2 section OSL samples. The gradient of the line drawn from the origin through data points represents sample age, where, the shallower the gradient, the older the age estimate. Observed in the figure is the outlier OSL1 sample.

Table 5.3 Summary of OSL results of the GH2 section. All uncertainties are ± 1σ. [b] 12 aliquots were measured for each sample to measure the natural dose, and [a] 6 aliquots to measure the equivalent dose De.

Sample ID	Elevation (m above base)	K (%)	Th (ppm)	U (ppm)	Water Content (%)	Total dose Rate (Gy/ka)	Aliquot number	Equivalent dose, De (Gy)	OSL age (ka)
OSL 4	10.15	0.034±0.03	2.31±0.23	0.78±0.04	3±1	0.53±0.03	6[a]+12[b]	80.8±5.6	**154±13**
OSL 3	9.15	0.043±0.004	1.88±0.2	0.93±0.05	3±1	0.52±0.2	6[a]+12[b]	83.24±6.4	**159±14**
OSL 2	5.55	0.042±0.004	2.6±0.26	1.03±0.05	20±5	0.46±0.03	6[a]+12[b]	74.8±2.9	**161±12**
OSL 1	0.3	0.262±0.026	6.49±0.65	2.07±0.1	20±5	1.01±0.07	6[a]+12[b]	66.77±4.79	**66±7**

5.3.2.1 GH2 section chronology in the context of previous studies

Two previous studies reported OSL age estimates from the sedimentary exposure where the GH2 section is located (see Chapter 4; 4.3.6).

Al-Saqarat et al. (2020) reported 4 OSL age estimates in an upward stratigraphic order, of 120±8 ka, 104±11 ka, 70±6 ka and 36±3 ka (see 4.3.6). These ages were recovered ca. 2m stratigraphically above the GH2 OSL ages. Also, Mischke et al. (2017) reported two OSL age estimates of 112±9 ka and 32±4 ka (see 4.3.6). These samples are stratigraphically within the GH2 OSL age estimates, however as discussed above these samples probably need to be reevaluated.

Accordingly, the discussion of the GH2 section age estimates will focus on the MIS6 period as recovered from the OSL age estimates for this project.

5.3.3 Sedimentary lithofacies analysis

The detailed field-based lithological investigations of the GH2 sediments identified four primary sedimentary lithofacies based on particle size, presence of sedimentary structures and bioturbation. The lithofacies included sand with gravels (G1), sand-dominated (S1 and S2) and silt (fines)-dominated (F1). Thus, to confirm the field-based lithofacies, the data set used for the PCA analysis included the GH2 sediments XRF elemental composition, particle size distributions, magnetic susceptibility and LOI results. The PCA results (Figure 5.40) indicate that there are few main determining features for the grouping of the different lithofacies. Combining the complete dataset shows that the fine sediments are characterized by the LOI_{550}, (κ), the allogenic elements such as Fe_2O_3 and Ti, CaO content and the fine sediments (clay and silt), while the sand lithofacies are dominated by the silica, medium and coarse sand content. The sand with small gravels are differentiated based on their content of granules.

The first three eigenvectors explain 70% of the total variance. PCA1 (43%) correlates positively with all the components except for the SiO_2, medium sand,

coarse sand, very coarse sand and granules content. Significant correlations are for LOI_{550}, Fe_2O_3 (κ), clay, and CaO contents ($r^2 = 0.8$, 0.84, 0.8, 0.7 and 0.7; $P < 0.05$). PCA 2 (18%) correlates positively with SiO_2, Al_2O_3 and clay ($r^2 = 0.2$, 0.8, 0.7 ; $P < 0.05$), while PCA 3 (9%) correlates positively with granules and coarse sand content ($r^2 = 0.5$, 0.6; $P < 0.05$).

The main determinants (SiO_2, Al_2O_3, CaO, LOI_{550}, Fe_2O_3 (κ), clay, very fine sand, medium sand, very coarse sand and granules content) were used for the LDA analysis (Figure 5.41).

The LDA plot (Figure 5.41) confirms that there are 3 distinct facies groups. The LDA analysis indicated that 89% of the samples are correctly classified based on the field-observations and the input data. Some of the sandy facies were reclassified as fine facies based on the facies determinants and their contents of fine-grained particles.
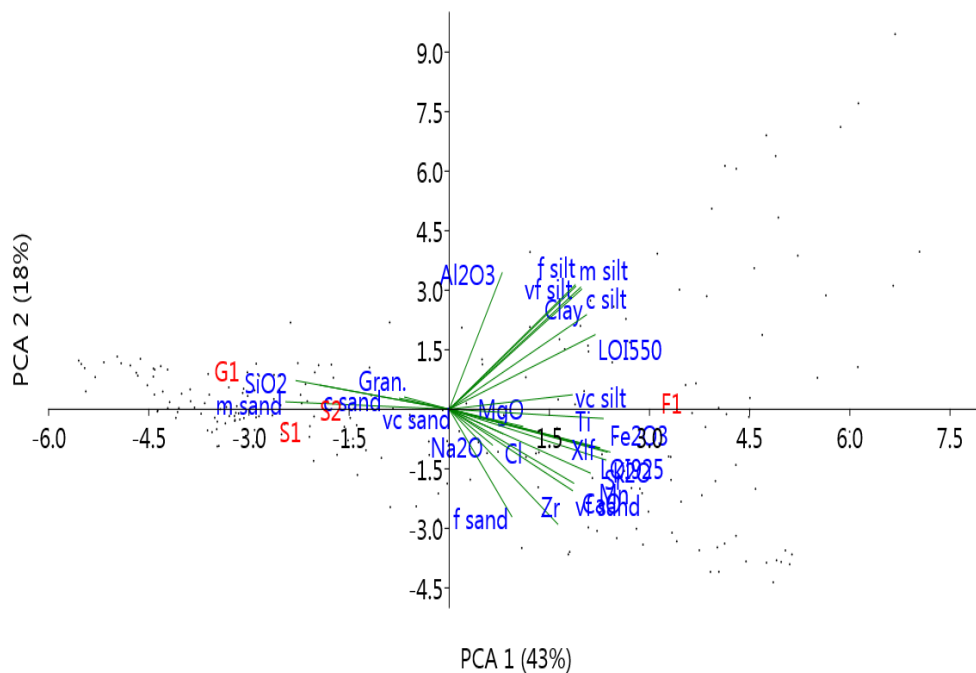
Figure 5.40 PCA results of the GH2 sediments granulometric composition (a) and geochemical composition (b). F: fine-grained lithofacies, S: sand lithofacies, G: sand with small granules lithofacies.
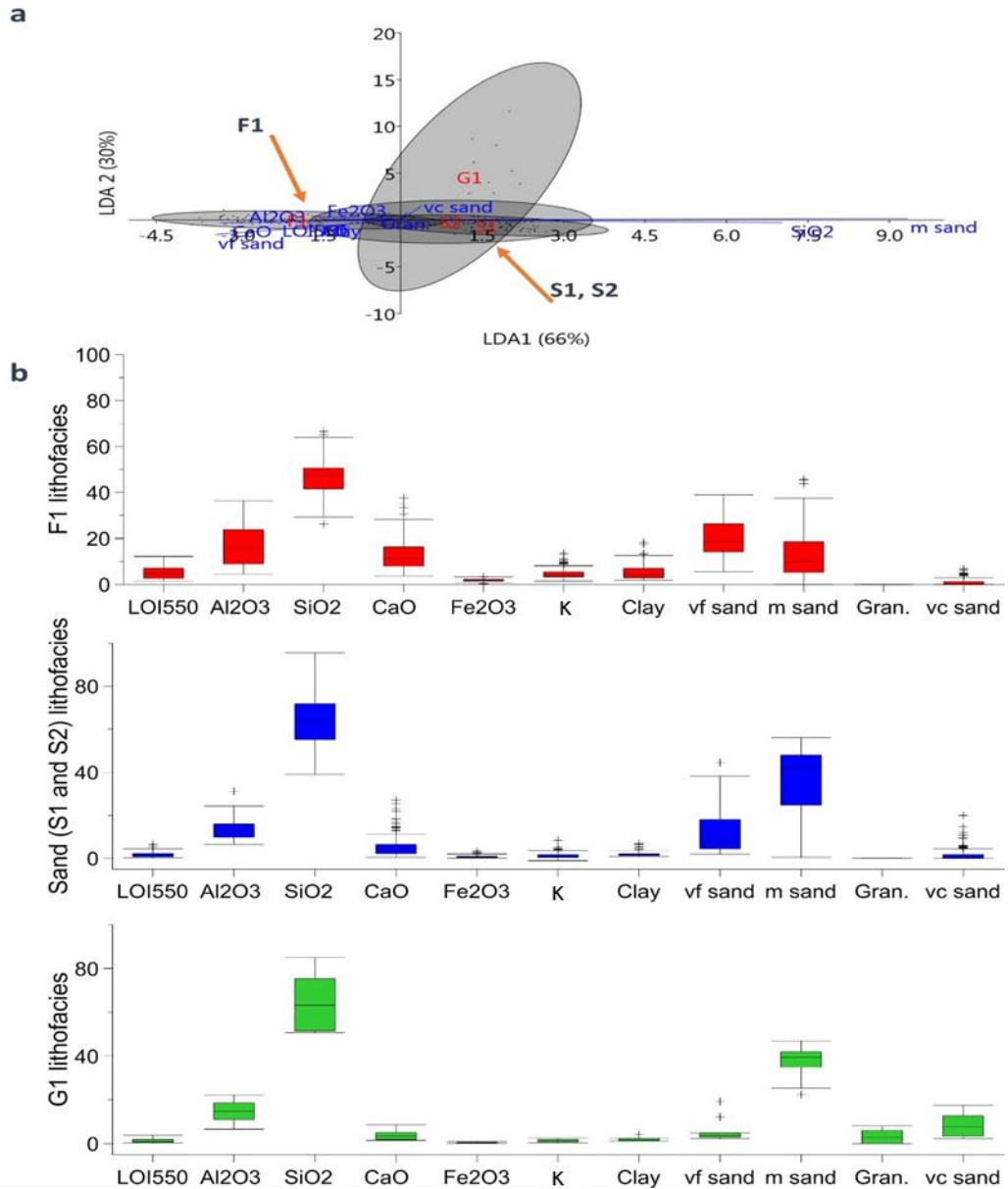
Figure 5.41 a) GH2 sediments LDA plot. F1: fine-dominated facies, S1, S2: sand-dominated facies, G1: sand with granules facies. b) Box plots of the facies sedimentological and chemical composition (outliers are data located at 1.5 times the interquartile range). v.c.: Very coarse. c.: Coarse. f.: Fine. Gran: Granule.

Finally, the resulting three main lithofacies were re-classified following the fluvial facies coding in the literature (e.g. Miall, 1996), based on the presence of sedimentary structures (Table 5.4). The sand with granules facies was classified as pebbly sand similar to the GH1 lithofacies classification as they contain <15 % granules (Figure 5.41 b).

The lithofacies associations are discussed individually in the next sections in terms of their distinct sedimentological and geochemical characteristics and interpretations.

Table 5.4 GH2 section facies analyses results and definitions. Values in the PCA-LDA facies are minimum to maximum/average.

Field-based facies	Particle size	Sedimentary structures	Bioturbation	Gravels
G1	Sand with granules	None	None	yes
S1	Fine to coarse sand	Yes	Yes	no
S2	Fine to coarse sand	None	None	no
F1	Silt to clay	None	Yes	no

PCA-LDA facies	LOI550	Al2O3	SiO2	CaO	Fe2O3	κ	Clay	vf sand	m sand	Gran.	vc sand
Sand with granules	0.3 to 1.9/0.9	6.5 to 18/13	50.6 to 85/68	1.4 to 8.6/3.6	0.13 to 0.417/0.3	0.3 to 2.1/0.9	1.2 to 2.4/1.5	2.4 to 19.2/5.5	22.4 to 47/37	2 to 8/4.2	2.4 to 17.5/9.5
Sand dominated	0.2 to 4.42/1.7	6 to 31/13.6	36 to 95/62.8	0.4 to 27/5.6	0.104 to 3.26/0.77	-1.1 to 5.2/1.3	0.84 to 7/1.9	1.9 to 44.4/11.3	0.4 to 56/36	0	0 to 19/1.8
Fines dominated	1.3 to 12.2/5.3	4.5 to 36.2/17.4	26 to 63/45	4 to 37/13.7	0.26 to 3.27/1.86	1.9 to 13.5/5.6	1.8 to 18.3/5.6	5.4 to 38.9/20	0 to 43.7/12.36	0	0 to 6/0.7

Facies code	Facies	Sedimentary structure
Ss	Sand, fine to very coarse, may be pebbly	none
Sm	Sand, very fine to coarse	Massive or faint lamination
Sr	Sand, very fine to coarse	Ripple, cross lamination
Fm	Mud, silt	massive

5.3.4   Fluvial deposition of the GH2 sediments

The fluvial deposition in the GH2 section is recorded by 3 distinct lithofacies. Similar to the GH1 section lithofacies, these include: The mass flow deposition of pebbly sand lithofacies (Ss); the medium energy or fast moving flow deposition of massive sand (Sm) lithofacies and the Sr lithofacies associated with sand migration downstream to form sedimentary structures (e.g. cross bedding).

5.3.4.1   Ss (pebbly sand) lithofacies

This lithofacies is similar to the Ss lithofacies of the GH1 section (see 5.2.4.2), however, some differences in the bed thicknesses and composition do exist.

Unlike the Ss lithofacies beds in the GH1 section with thicknesses up to 54 cm, in the GH2 section, this lithofacies is found through the section from the base to 3.67 m. Two ca. 5 cm beds are found at 0.43-0.49 m and at 0.55-0.61 m from the base followed by a ca. 10 cm bed at 2.42-2.54 m. A thicker ca. 15 cm bed is at 3.27-3.45 m from base followed by a ca. 10 cm bed at 3.57-3.69 m above base.

The gravel fraction (>-1phi)

The granules content of the Ss lithofacies varies from 2 to 8 wt. %, compared to 0.6 to 16 wt. % in the Ss of the GH1 section (see 5.2.4.2). In addition, the size range of the granules in the GH2 section (Figure 5.42) is generally smaller than in the GH1 section (see Figure 5.10).

The ca. 15 cm bed at 3.27-3.45 m above base contains the highest granules content probably indicating higher mass flow deposition compared to the other beds. Similar to the Ss lithofacies deposition in the GH1 section, here, this lithofacies suggests mass flow deposition (Figure 5.43).

Figure 5.42 Loose sediments of the gravel fraction in the GH2 section Ss lithofacies beds. a) at 0.55-0.61 m from the section base, b) at 2.42-2.48 m. c) at 2.48-2.54 m. d) at 3.27-3.45 m.
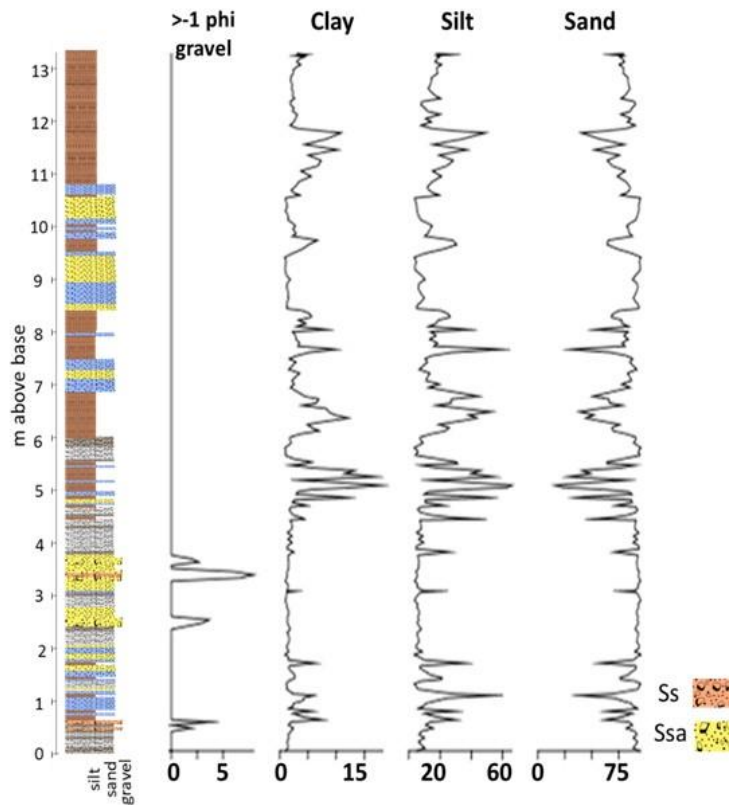
Figure 5.43 Stratigraphy of the GH2 section showing the location of the Ss lithofacies beds marked by the content (wt. %) of granules (> -1 phi). Also indicating their association with elevated sand contents. Clay, silt and sand in vol. %. Ss: fluvial pebbly sand lithofacies. Ssa: fluvio-aeolian Ss lithofacies bed (see 5.3.5).

Sand and fines fraction (<-1phi)

The granulometric analysis results show that the sediments are primarily dominated by very fine to very coarse sand with high contents of medium sand (Figure 5.44). The total sand content for the Ss fluvial sediments ranges from 81 to 93 vol. %, the silt content ranges from 5.3 to 15.6 vol. % and the clay content ranges from 1.3 to 2.4 vol. %.

The composition shows lower clay and silt content compared to the GH1 Ss beds content of up to 5.5 vol. % and 22 vol. %, respectively.

The fluvial Ss sediments are unimodal to trimodal with a main mode of 410 to 450 µm (Figure 5.44). The samples are poorly to very poorly sorted within the range of 1.4 to 2.6 phi. The sediments are generally fine skewed (0.19 to 0.3 phi), and leptokurtic to very leptokurtic (1.2 to 1.9 phi) with K values from 0.3 to 2.1 (Figure 5.44). The granulometric statistical parameters and K values show narrower ranges compared to the GH1 Ss sediments (see 5.2.4.2). Positive (P<0.05) correlations are present amongst the silt, clay, very fine and fine sand fractions.
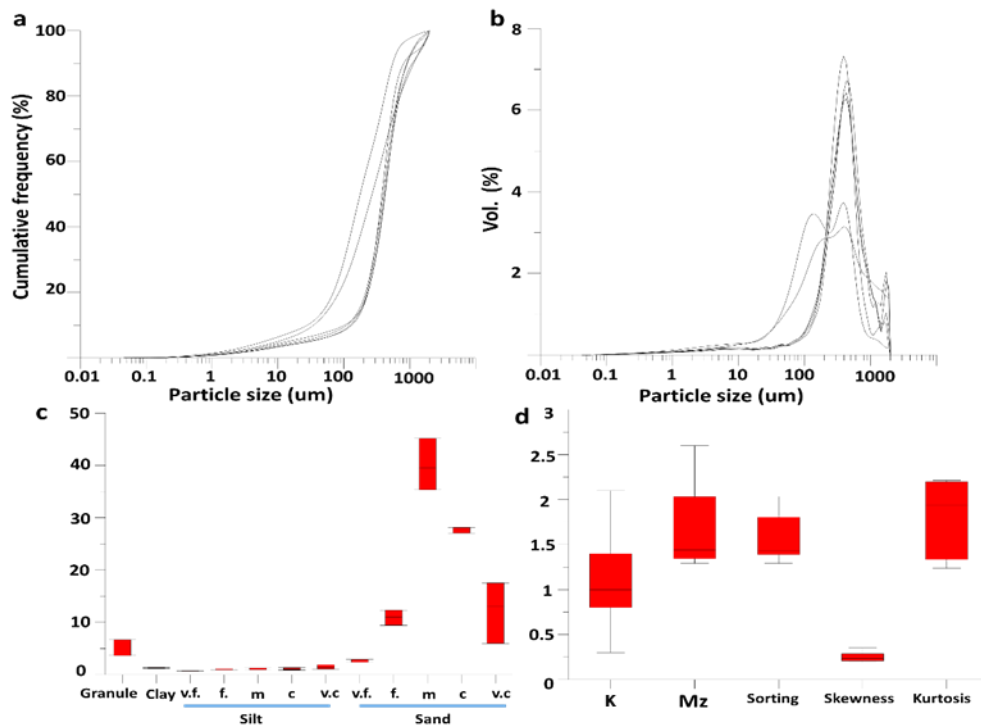
Figure 5.44 a) Cumulative frequency curves of the GH2 section Ss fluvial sediments. b) Particle size distribution curve of the Ss fluvial sediments. c) Box plots of the Granulometric composition of the Ss sediments. d) Box plots of the granulometric statistical parameters (in phi units) and (κ) values (*10^{-6}SI).

The geochemical analyses results show that the most abundant elements in the Ss sediments are SiO_2> Al_2O_3 > CaO (Figure 5.45 and Table 5.4). The SiO_2 content is within the range of 50 to 72 % with an average of 62 %. The CaO content shows a range from 1.6 to 8.6 % and an average of 2.6 %. The Al_2O_3 content is in the range of 6.6 to 18.5 % with an average of 13.5 %. Immobile elements such as Ti and Fe_2O_3 show positive correlations with soluble and mobile elements such as MgO and CaO, suggesting their association with allogenic processes. In addition, Al_2O_3, Ti and Fe_2O_3 correlate positively with the fine grained particles (clay, silt, very fine and fine sand), while SiO_2 correlates positively with the medium and coarse sand.

The ICV values generally indicate compositionally mature sources with values <1 (Cox et al., 1995; Hossain et al., 2017), except for the fluvial sample at 3.33-3.39 m from the base which shows >1 ICV due to its low content of Al_2O_3.

These beds show slight differences from the Ss sediments in the GH1 section. Higher amounts of silica are recorded in the GH2 sediments (max. 72.5%) compared with the GH1 Ss sediments (63 %). In addition, the Fe_2O_3 and (κ) values are significantly lower in the GH2 sediments (max. 0.39 % and 2.1 (10^{-6} SI), respectively) compared to the GH1 Ss sediments (5 % and 7 (10^{-6} SI), respectively).
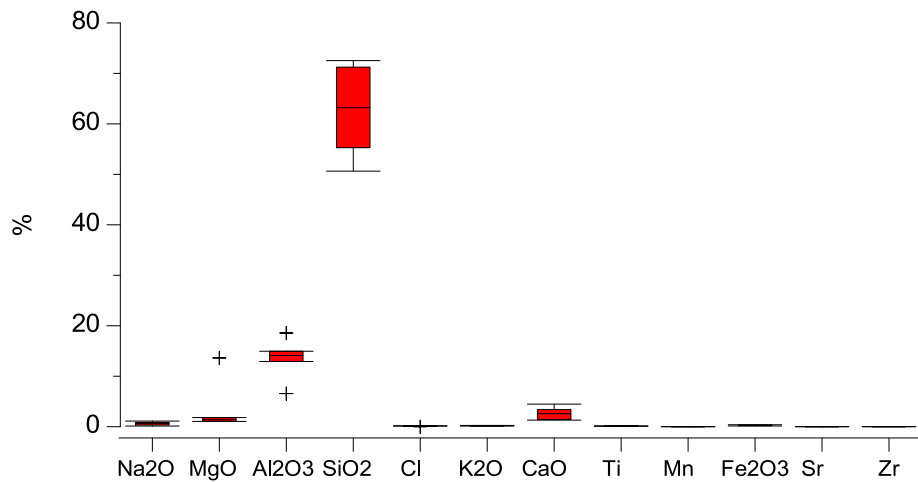
Figure 5.45 Box plots of the GH2 section Ss sediments elemental composition (outliers are data located at 1.5 times the interquartile range).

Ss lithofacies interpretation

Similar to the Ss deposition in the GH1 section (see 5.2.4.2), the Ss deposition in the GH2 section indicate periods of mass flow deposition transporting gravel-sized material into the valley. The results indicate that the highest energy mass flow event is at ca. 3.4 m above the section base depositing a larger amount and larger sizes of granules.

As previously identified, the association of K with Ti and Al_2O_3 suggests its validity as an indicator of catchment processes. The mass flow event at ca. 3.4 m is associated with lower amounts of clay, silt and very fine sand. The sediments are trimodal and show lower Ti and Al_2O_3 values compared to the other beds, suggesting a shorter duration event with rapid deposition of the sediments. The other beds indicate longer duration or lower energy mass flow events depositing higher amounts of fines.

However, differences in the flow energy, duration and composition can be observed between the GH1 and GH2 Ss (mass flow) deposition. In the GH2 section, the Ss deposits comprise lower percentages and smaller granule sizes, compared to the GH1 section. This is associated with narrower ranges of mean particle size (Mz), sorting, skewness and kurtosis and lower (κ) values. This is probably affected by the section location in the valley. The GH2 section is closer to the valley side, while the GH1 section is a mid-valley section that may have been more affected by the incoming mass flows compared to the valley sides.

5.3.4.2 Sand lithofacies (Sm and Sr)

The sand fluvial lithofacies (Sm and Sr) beds are generally dominated by very fine to coarse sand. The differentiation between the two lithofacies is based on the presence of sedimentary structures. The Sr sediments (17 samples) show bedding structures (horizontal bedding, cross bedding, hummocky cross bedding) (see Figure 5.36), both clear and faint, while, the Sm sediments (43 samples) do not show any sedimentary structures (massive sand beds). Both lithofacies are found at different levels through the GH2 section, with varying thicknesses, starting from the sequence base up to 10.72 m above the base.

The total sand contents range from 70 to 94 vol.% and from 71 to 94 vol. %, the silt contents range from 4.7 to 28.7 vol. % and from 5 to 26.6 vol. %, while the clay contents range from 1.2 to 4.2 vol. % and from 1 to 2.5 vol. %, for the Sm and Sr sediments respectively.

Variability is observed within the lithofacies, particularly in the fine, medium, and coarse sand contents (Figure 5.46). The Sm lithofacies contain higher fine and coarse sand compared to the Sr lithofacies, probably reflecting the transport medium energy and composition where the Sm beds are thought to have been deposited by fast moving flows. The Sr lithofacies are primarily dominated by medium sand (Figures 5.46 and 5.47).

The Sm and Sr sediments of the GH2 section do not show significant differences compared to the GH1 section Sm sediments (see 5.2.4.3).
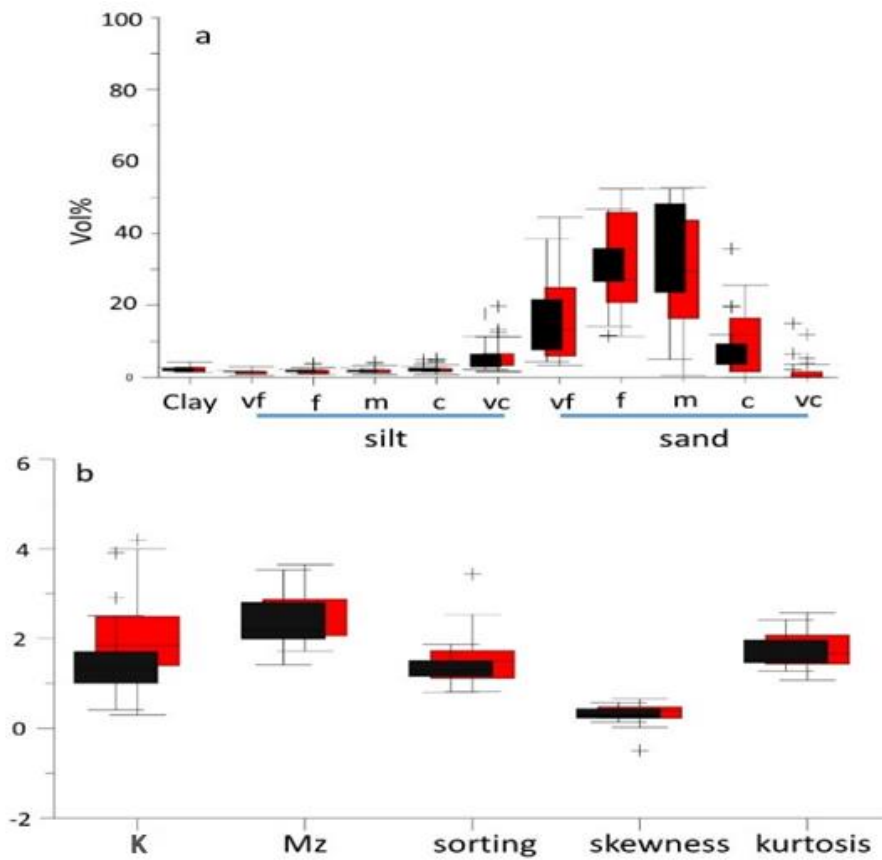
Figure 5.46 a) Particle size distribution of the GH2 section sand lithofacies showing the variability in the sand fractions. b) Granulometric statistical parameters (in phi units) and (κ) values (*10^{-6} SI). Sm sediments: red colour. Sr sediments: black colour. Outliers are data located at 1.5 times the interquartile range.
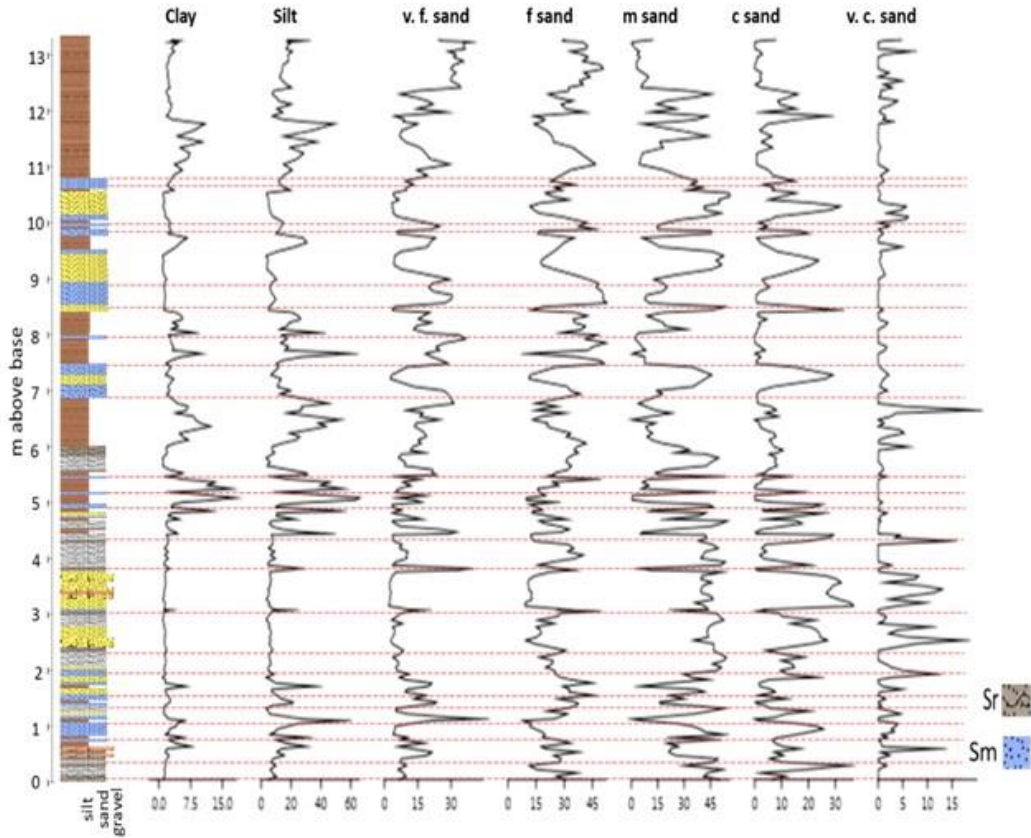
Figure 5.47 Stratigraphy of the GH2 section showing the location of the Sm and Sr lithofacies beds marked by the horizontal red lines showing contents (wt. %) of medium and fine sand. Also observed is the association of the Sm beds with higher fine and coarse sand contents at some locations. The Sr beds are marked by higher medium sand contents. Clay, silt and sand in vol. %. Sm: massive sand lithofacies. Sr: sand lithofacies with sedimentary structures.

The Sm sediments are unimodal (main mode: 101 to 450 µm; mean: 277 µm; Std. 119 µm) to bimodal, with only 1 sample showing trimodality (Figure 5.48). The samples are moderately to very poorly sorted within the range of 0.8 to 3.4 phi. The sediments are generally fine to very fine skewed with 3 symmetrical samples (0.02 to 0.66 phi), and mesokurtic to very leptokurtic (1.08 to 2.6 phi). The K values range from 0.3 to 4.2 with an average of 2 (Figure 5.46 b).

The Sr sediments are unimodal (main mode: 101 to 542 µm; mean: 252 µm; Std. 132 µm) to bimodal (Figure 5.48). The samples are moderately to poorly sorted (0.8 to 1.86 phi), fine to very fine skewed (0.13 to 0. 56 phi), and leptokurtic to very leptokurtic (1.27 to 2.41 phi) (Figure 5.46 b).
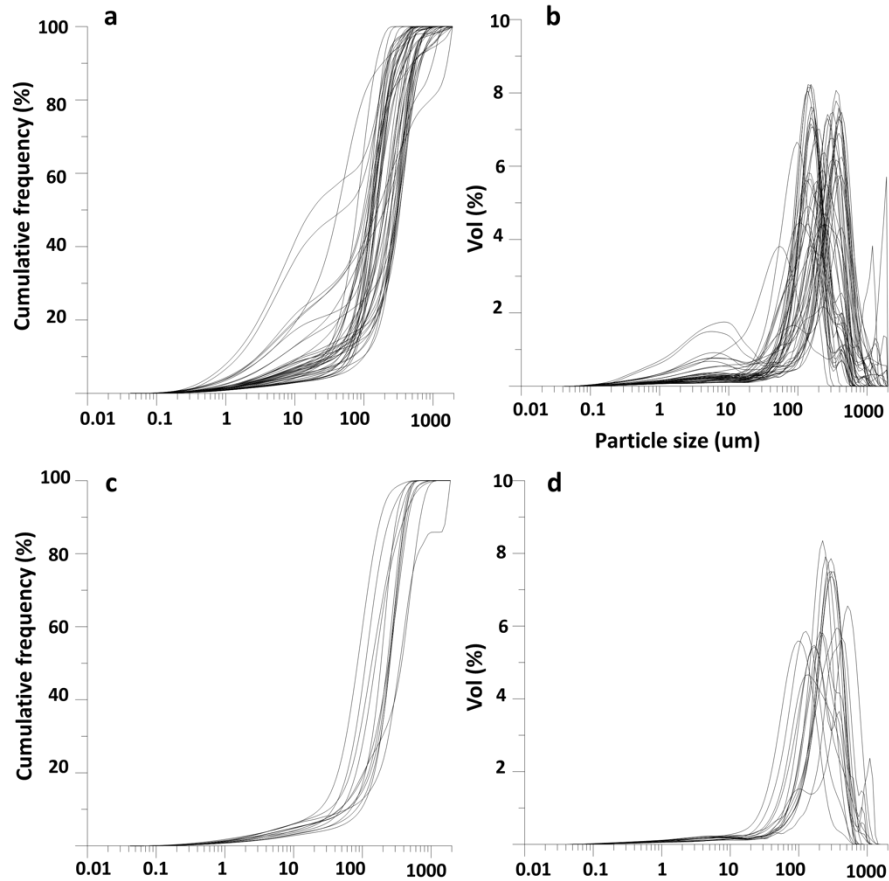
Figure 5.48 a, c) Cumulative frequency curves of the Sm fluvial sediments and Sr fluvial sediments, respectively, b, d) Particle size distribution curves of the Sm facies sediments and Sr fluvial sediments, respectively.

PCA analysis of the Sm and Sr sediments indicated that 70.2% of the total variance within the samples is derived from the first component which significantly correlate with medium sand (r^2 =0.94; P<0.001) and coarse sand contents (r^2 =0.7; P<0.001). The second eigenvector which explains 20% of the total granulometric variance, strongly correlates with fine sand content (r^2 =0.75; P<0.001) (Figure 5.49). This indicates the variable depositional energy conditions of the two lithofacies which also drives the granulometric composition and the sediments' characteristics.
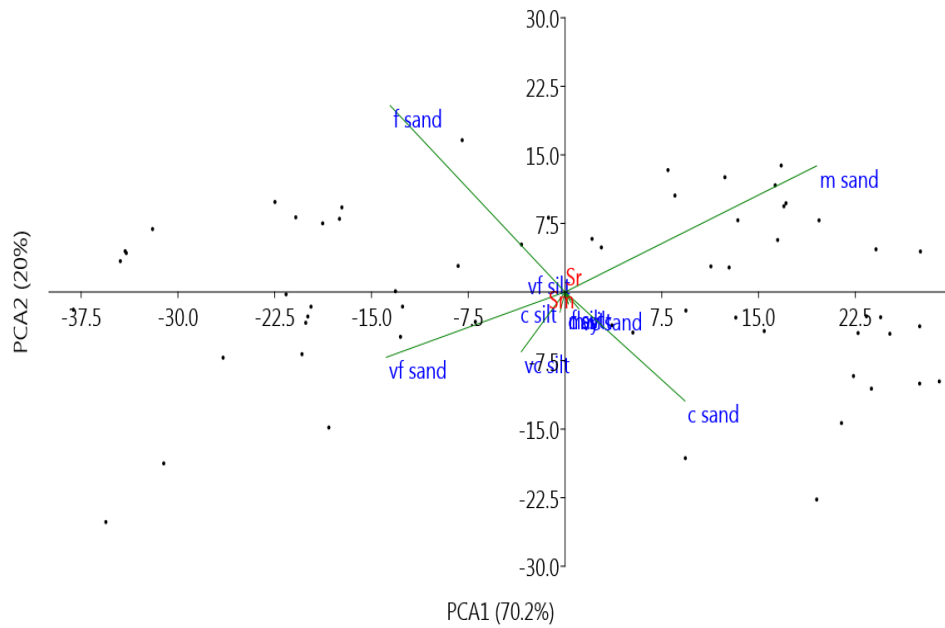
Figure 5.49 Principal Component Analysis of the granulometric parameters of the GH2 section Sm and Sr facies showing the first two eigenvectors.

The Sm and Sr sediments are primarily dominated by $SiO_2 > Al_2O_3 > CaO$ (Figure 5.50). The SiO_2 content is within the range of 40.8 wt.% to 81.4 wt.% with an average of 57.7 wt.% for the Sm sediments, and 50.7 to 81.4 wt.% with an average of 65.2 wt.% for the Sr sediments. The CaO content shows a range from 2.2 to 25 wt. % with an average of 7 wt. % for the Sm sediments and 1.3 to 13.8 wt. % and an average of 4.7 wt. % for the Sr sediments. The Al_2O_3 content is in the range of 6.5 to 23 wt. % with an average of 14.4 wt. % for the Sm sediments and 8.6 to 23 wt. % with an average of 15 wt. % for the Sr sediments (Figure 5.50).
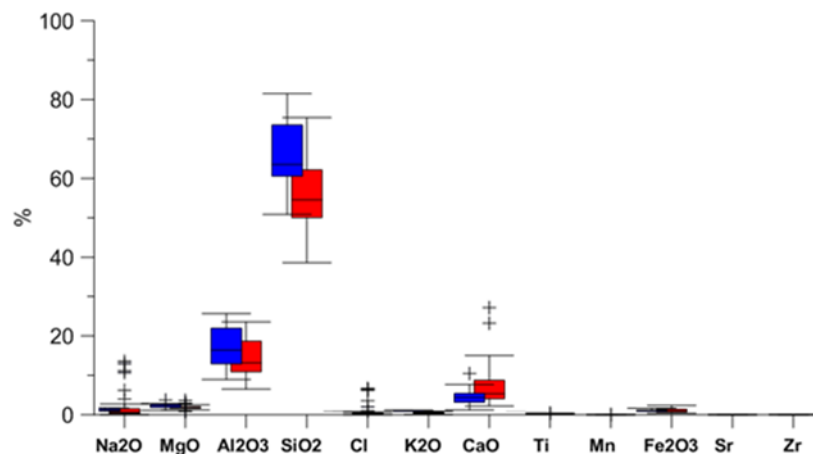
Figure 5.50 Box plots of the elemental composition of the GH2 section Sm sediments (red colour) and the Sr sediments (blue colour). Outliers are data located at 1.5 times the interquartile range.

The PCA analysis of the Sm and Sr sediments' elemental composition (Figure 5.51) shows that the primary eigenvector (PCA 1) explains 68% of the total variance and correlates positively with SiO_2 ($r^2=0.98$; $P<0.05$). The second eigenvector (PCA 2) explains 19.5% of the total variance and correlates positively with Al_2O_3 ($r^2=0.93$; $P<0.05$).
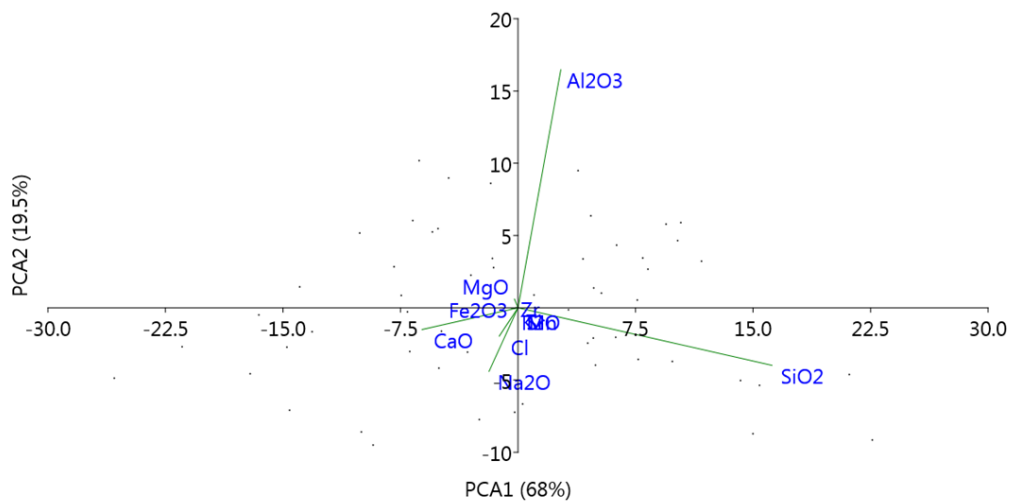
Figure 5.51 Principal Component Analysis of the chemical composition of the GH2 section Sm and Sr lithofacies showing the first two eigenvectors.

Based on the PCA analysis and the positive correlations between K, the fine particle size fractions, and allogenic markers (Fe_2O_3 and Ti; $r^2= 0.5$ and 0.4, respectively), the results reflect a system where higher energy conditions deposit coarser sediments (PCA1), while lower or longer duration events transport the fines (PCA 2). Considering that Ti is representative of catchment erosion and detrital in-wash, two possible origins for the carbonates in the sandy sediments can be retrieved from a CaO/Ti bi-plot (Figure 5.52), an allogenic origin related to factors affecting the catchment erosion, reflected by the positive correlation between CaO and Ti (Sm lithofacies), and a possible endogenic origin reflected by the weak covariance for the Sr sediments and some of the Sm sediments.

The endogenic deposition of the CaO in the Sr sediments probably suggests the role of groundwater in the deposition of the wetland beds. The sand beds are generally associated with the wetland (fine-grained) beds (Figure 5.47) where following the sand migration downstream, the wetland beds redevelop and the sand beds are similarly deposited under the influence of moisture availability. The Sm sediments showing endogenic CaO deposition are located at ca. 9.47 m, 9.7 m to 9.83 m, 9.98 m to 10.09 m and 10.56 m to 10.66 m above the section base.

All the beds are either preceded or followed by wetland beds (see Figure 5.47). In addition, all the beds showing CaO endogenic deposition have higher LOI$_{550}$ values compared to the other sand beds. This distinguishes the Sm and Sr beds of the GH2 section from the GH1 sand beds, where in GH1 section the sand beds show dominance of allogenic CaO origin (see Figure 5.18).

In terms of the sediment source maturity, the Sm (massive sand) sediments show a particular trend where samples with <1 ICV values are found from 0.75 m to 7.45 m above base. From 7.96 m above base to 10.7 m above base, the samples show >1 ICV values. The Sr (sand beds with sedimentary structures) sediments show <1 ICV values, except for two samples at 0.29 m from base and at 2.34 m from base.
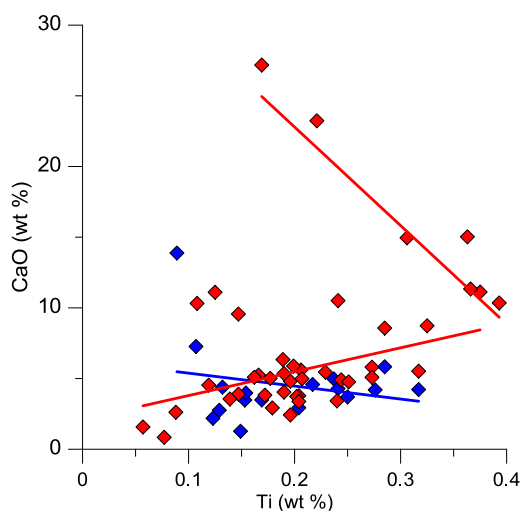
Figure 5.52 CaO /Ti bi-plot of the GH2 section Sm (red) and Sr (blue) sediments. Negative correlations suggest endogenic CaO deposition. The red line with negative covariance represents the Sm samples that suggest possible endogenic CaO deposition.

Sandy lithofacies interpretation

Similar to the Sm and Sr lithofacies in the GH1 section, here, the two lithofacies record periods of water flows as sand in-wash and sand migration downstream. Nonetheless, as discussed above, differences between the sand beds nature in the two sections are observed.

In the GH2 section, the Sm and Sr beds record variable energy conditions. Both Sm and Sr fluvial sediments are characterized by high contents of very fine to very coarse sand with elevated contents of medium sand, nonetheless, the Sr sediments have higher contents of medium sand and lower contents of coarse sand. Also, the Sr granulometric statistical parameters show narrower ranges for

Mz, skewness, sorting and kurtosis along with more dominant unimodal size distributions and lower K values. These variations suggest a more uniform supply of sediments and less hydrodynamic variability in transport energy (Mycielska-Dowgiałło and Ludwikowska-Kedzia, 2011) for the Sr sediments, compared to the massive sands (Sm). These variations are also detected in the geochemical composition of the Sm and Sr sediments where the Sr sediments show higher contents of silica and Al_2O_3, reflecting the variability in catchment erosion, wind energy and addition of coarser/finer material.

As discussed above, the sand beds are generally associated with wetland deposition. The CaO/Ti bi-plot indicates possible endogenic CaO deposition in the Sr beds and some Sm beds (Figure 5.52). The nature of these endogenic beds in the section, as carbonate concretions and thin carbonate-rich layers in reddish sand beds, may indicate their deposition as water-table carbonates reflecting the role of the shallow groundwater level in the area (Ibrahim, 1993) in the depositional processes, similar to water-table carbonates recorded in similar settings worldwide (e.g. Pigati et al., 2014). The carbonate concretions within the beds at some locations also suggest deposition during periods of wetting and drying.

These observations suggest that the sand deposition in the GH2 section record periods of fast moving flows depositing coarse sand fractions and lower energy events that cause the finer-grained sand migration downstream during periods of moisture availability allowing for the wetland conditions to redevelop.

5.3.4.3 Fluvial depositional environments characterization

Similar to the GH1 section (see 5.2.4.4), the Ss, Sm and Sr samples were plotted on a CM diagram to reflect the proposed mode of transportation (Passega and Byramjee, 1969; Mycielska-DowgiałŁo and Ludwikowska-Kedzia, 2011).

The CM diagram (Figure 5.53) indicates different modes of transportation for the Ss, Sm and Sr lithofacies supporting the above discussion of variable hydrodynamics.

The Ss sediments (Gold diamonds in Figure 5.53) primarily plot in the rolling and high turbulence transport suggesting mass flow deposition consistent with the above discussion of the granulometric and geochemical results. The Sm and Sr sediments (black and red diamonds in Figure 5.53, respectively), in accordance with the previous discussion, suggest variable transport modes. The Sm sediments show a mode range from saltation in high turbulence to low turbulence

flows reflecting the changes from fast moving water to lower energy conditions depositing the coarse/fine material, while the Sr sediments primarily plot as low turbulence flow deposits. This confirms the observation of sand migration downstream (Sr) and its deposition where wetland conditions developed. It also distinguishes the deposition of the GH2 sand beds from the GH1 beds. In the GH1 section (see Figure 5.19), the Sm beds are primarily transported as saltation and rolling, while the Sr sediments are transported through low turbulence flows. This supports the previous discussion suggesting that the sand deposition in the two sections was through variable hydrodynamics probably affected by the sections' locations and the characteristics of the flow, or possibly deposition during different periods of valley hydrodynamics.
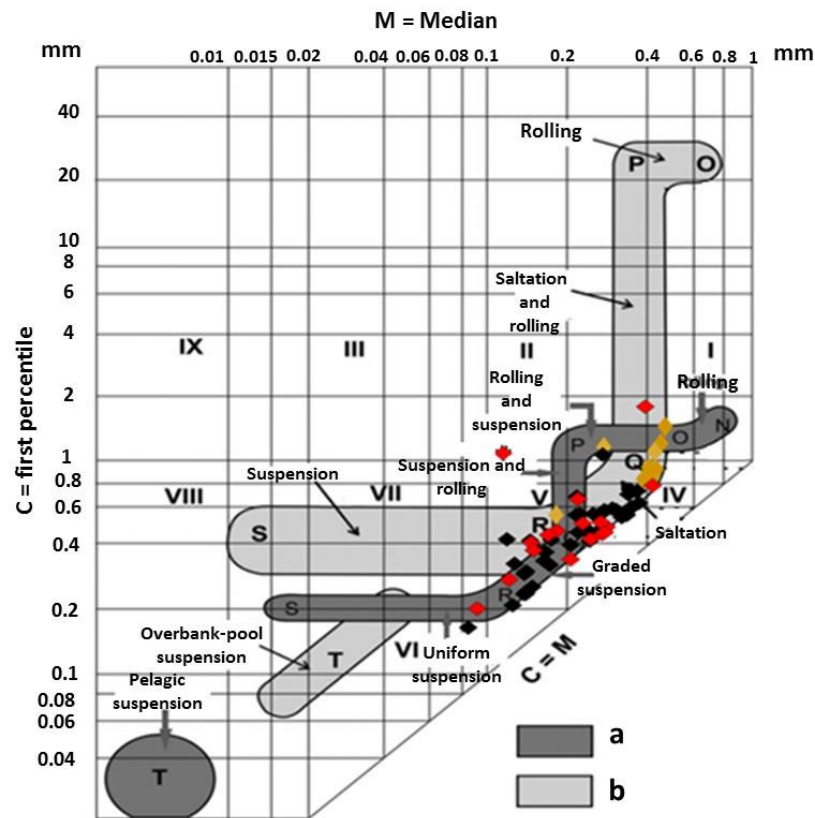
Figure 5.53 Complete CM pattern of tractive current deposits for the GH2 section fluvial sediments. **Ss** (gold), **Sm** (black), and **Sr** (red) sediments. a: based on Passega (1964) and Passega & Byramjee (1969); b: based on Ludwikowska Kędzia (2000). I, II, III, IX: rolled grains; IV: High turbulence deposit; V: Low turbulence deposit; VI: Graded suspension; VII: Uniform suspension; VIII: Finest uniform suspension (after Passega and Byramjee, 1969) (Modified from Malgorzata and Ludwikowska-Kedzia, 2011.

5.3.5 Fluvio-aeolian deposition of the GH2 sediments

As discussed previously5.2.5), samples showing characteristics of possible fluvio-aeolian deposition in the GH2 section were identified in the three lithofacies Ss, Sm, and Sr (Figure 5. 54).

From the Ss samples, 3 samples are marked by high contents of medium sand and have a similar main particle size mode of 450 µm (Figure 5.55). A coarse second mode is present in two samples probably affected by the fluvial component of the Ss deposition. The total sand content ranges from 93 to 94.1 vol. %, the silt content from 4.5 to 6.3 vol. % and the clay content from 1.2 to 1.3 vol. % (Figure 5.56 a). The (κ) values are all ≤1 (Figure 5.56 b). The sediments are poorly sorted (1.16 to 1.5 phi), fine skewed (0.15 to 0.28 phi), and very leptokurtic (ca. 1.8 phi). These sediments tend to be better sorted compared with the Ss fluvial sediments.
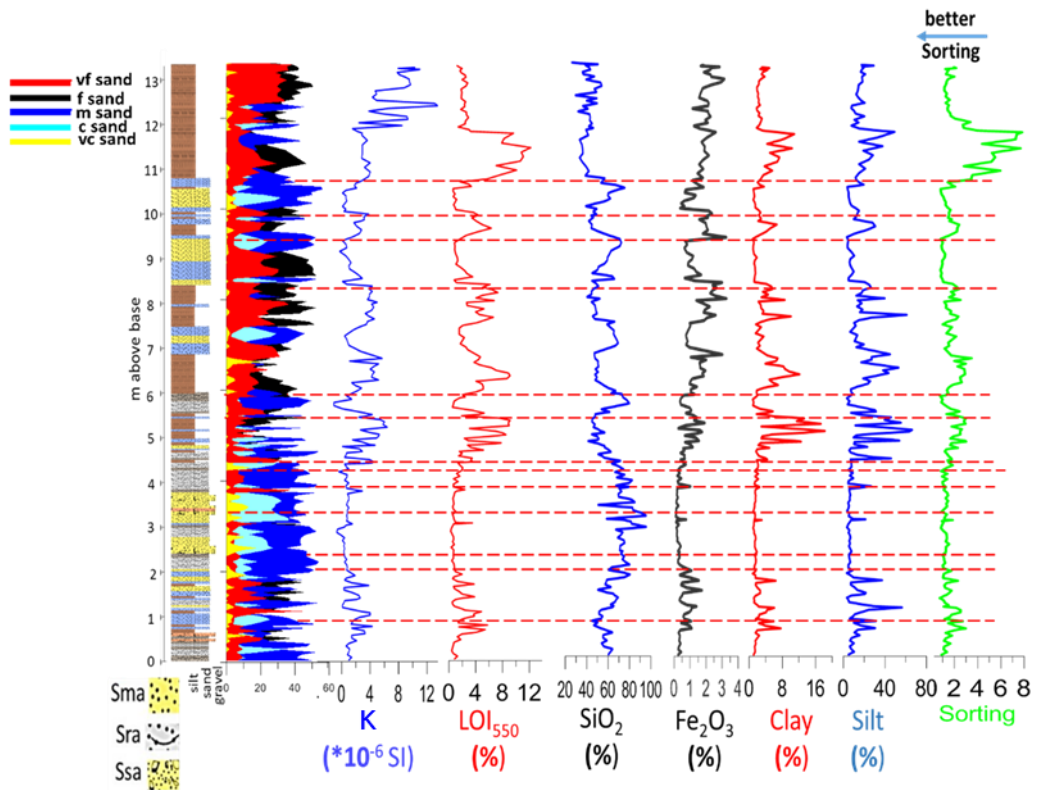
Figure 5.54 Stratigraphy of the GH2 section showing the location of the Ssa, Sma and Sra lithofacies beds marked by the horizontal lines, based on the criteria discussed in text. Also shown the silt, clay, and Fe2O3, and LOI550 contents indicating reduced catchment in-wash. Sand, silt, and clay in vol. %. SiO2, Fe2O3, and LOI550 in %. Sorting (phi), (κ) (*10-6SI). Ssa: fluvio aeolian pebbly sand, Sma: fluvio-aeolian massive sand lithofacies. Sra: fluvio aeolian sand lithofacies with sedimentary structures.

The Sma sediments are generally unimodal with dominant main particle modes in the medium sand size range (260 to 450 µm), while two samples show main modes of 161 and 141 µm (Figure 5.55 c and d), and are primarily dominated by medium sand content (Figure 5.56 a). The total sand content is in the range from 83 to 96 vol. %, the silt content is within the range from 3.2 to 13.4 vol. %, while the clay content ranges from 0.8 to 3.5 vol. % (Figure 5.56 a). The sediments' (κ) values range from -0.3 to 1 with an average of 0.46 (*10^{-6} SI). These sediments show a narrower range of main particle modes an a trend towards more unimodality compared to the Sm fluvial sediments.

The Sra sediments are unimodal with a main particle size mode of 257 to 450 µm (Figure 55 e and f), the medium sand content is more dominant compared to the other fluvio-aeolian sediments. The total sand content ranges from 88.3 to 96 vol. % (Figure 5.56 a). The silt content ranges from 3.3 to 9.5 vol. % and the clay content ranges from 0.8 to 2 vol. %. The sediments are moderately to poorly sorted, fine to very fine skewed and leptokurtic to very leptokurtic with K values range from -1.1 to 1 with an average of 0.31 (Figure 5.56 b). Similar to the Sma sediments, these show a trend towards more unimodality, better sorting and a narrower range of main particle modes compared with the Sr fluvial sediments.
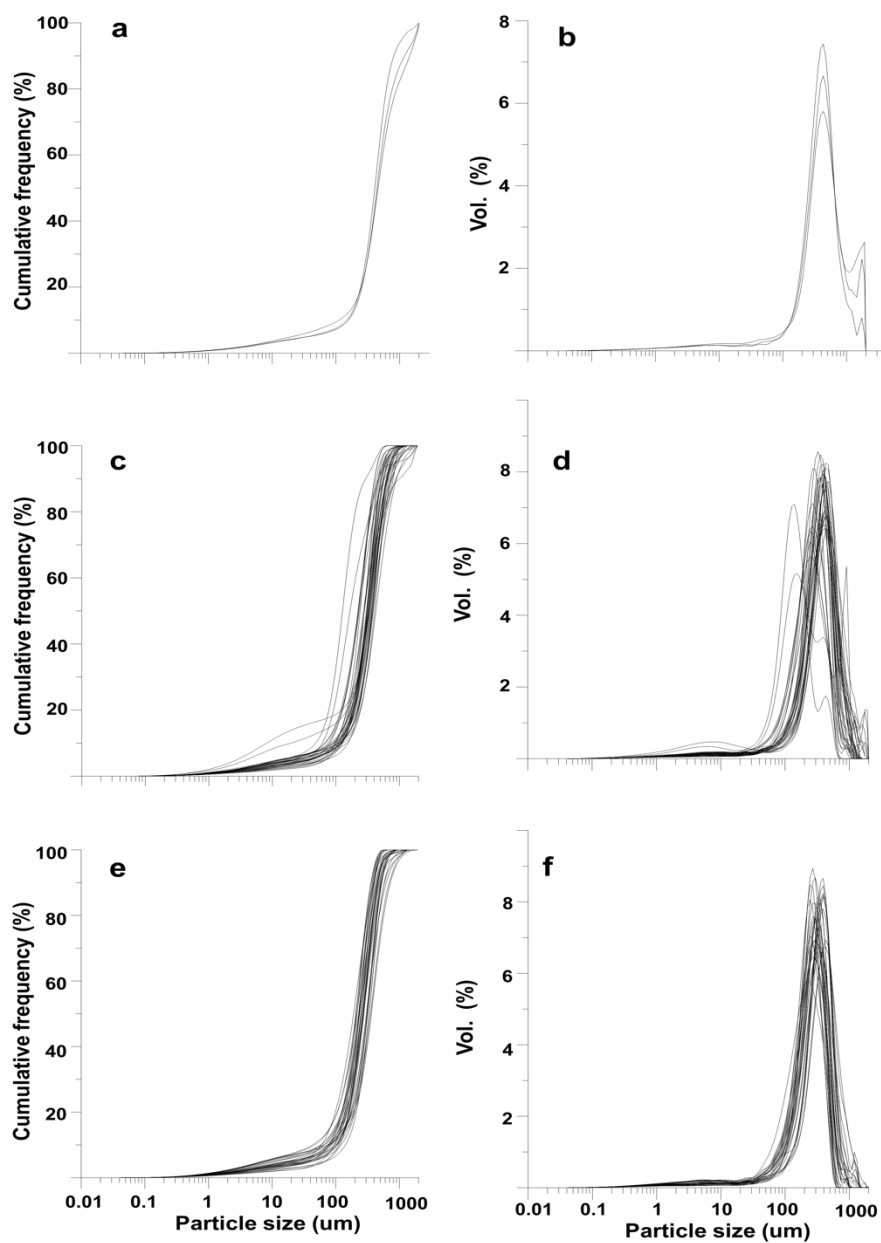
Figure 5.55 a, c, e) Cumulative frequency curves of the GH2 section Ssa , Sma and Sra fluvio-aeolian sediments, respectively. b, d, f) Particle size distribution curves of the Ssa , Sma and Sra fluvio-aeolian sediments, respectively.
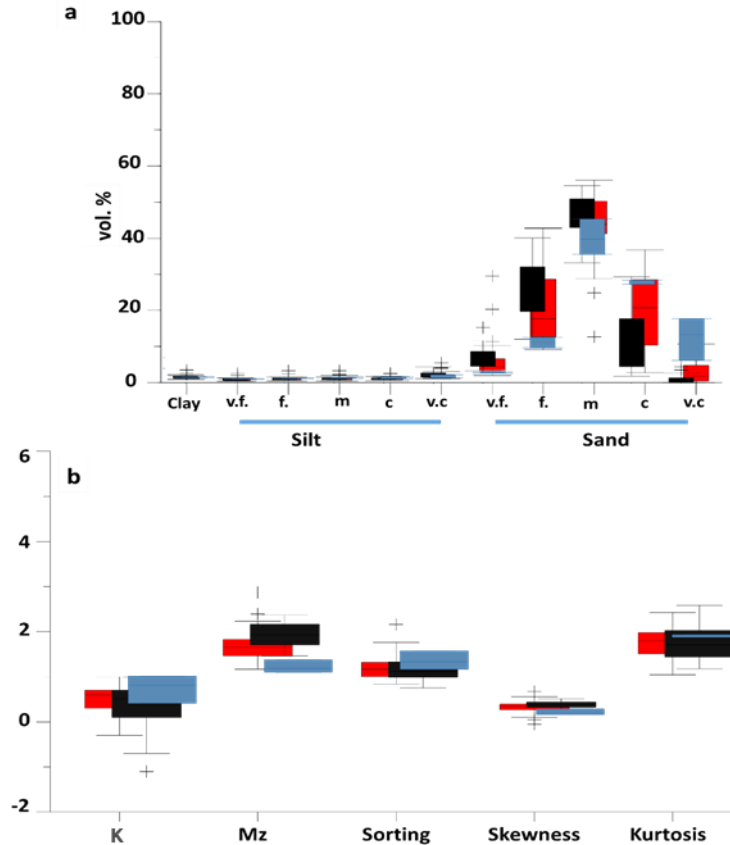
Figure 5.56 a) Box plots of the granulometric composition of the GH2 section Sra (black), Sma (red) and Ssa (blue) sediments. b) Granulometric statistical parameters (in phi units) and (κ) values (*10^{-6}SI). Outliers are data located at 1.5 times the interquartile range.

The fluvio-aeolian sediments are primarily dominated by silica, where the Ssa sediments have 75 to 85 wt. %, while the Sma and Sra silica content ranges from 57 to 95.5 wt. % and 55.8 to 95.6 wt. %, respectively.

PCA analysis of the granulometric and elemental compositions (Figure 5.57) shows that, for the granulometric composition, PCA1 (71%) correlates positively with the coarse sand content (r^2=0.96) and medium sand content (r^2=0.4), and PCA2 (24%) correlates positively with the very fine sand content (r^2=0.5), while for the elemental composition, PCA1 (81.9%) correlates positively with SiO_2 (r^2=0.99) and negatively with all other parameters, PCA2 (13.2%) correlates positively with Al_2O_3 (r^2=0.94).

The Sma, Sra and Ssa sediments generally show ICV values <1, this indicates that the sediments comprise primarily mature sediment sources (Cox et al., 1995; Hossain et al., 2017).
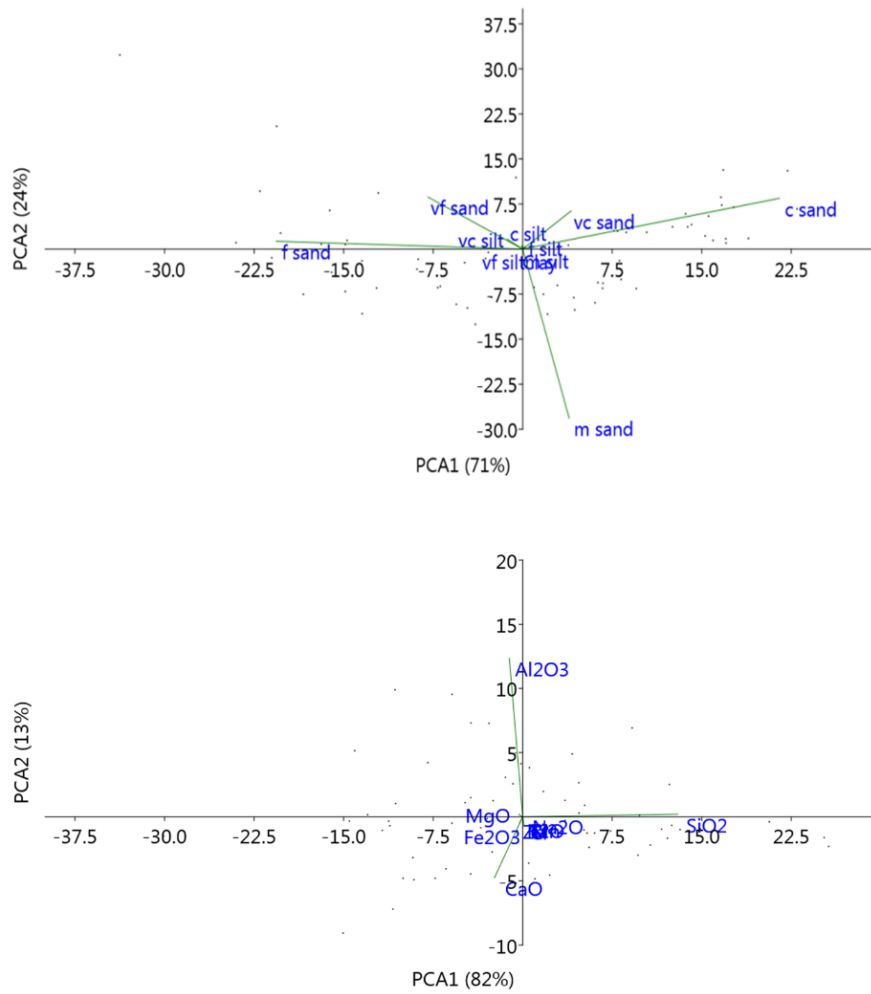
Figure 5.57 Principal component analysis of the GH2 fluvio-aeolian sediments. Top: granulometric composition, bottom: elemental composition.

Fluvio-aeolian sediments interpretation

Similar to the fluvio-aeolian deposition of the GH1 section (see 5.2.5), the PCA results of the granulometric and elemental composition of the GH2 section fluvio-aeolian sediments reflect the system behaviour. The granulometric composition shows the system response to variable energy conditions depositing coarse and medium sand alternating with lower energy depositing the finer sediments. This is also observed in the elemental composition where there is a separation between the additions of silica (through wind processes), possibly alternating with catchment in-wash.

PCA analysis was also conducted using the main parameters previously extracted from the granulometric and elemental composition to assess their association with the different depositional conditions (Figure 5.58). The results indicate that the first

three eigenvectors explain 77 % of the variance. PCA 1 (36%) correlates positively with the silica, medium and coarse sand contents (r^2= 0.6, 0.57, and 0.6, respectively; P<0.05). PCA 2 (25%) correlates positively with Al_2O_3, Ti and medium sand (r^2= 0.6, 0.5, and 0.5, respectively; P<0.05). PCA3 (16%) correlates positively with the coarse sand content (r^2= 0.7, P<0.05). These associations probably record system behaviour, where similar to the GH1 fluvio-aeolian deposition, here, these sediments record periods of enhanced/reduced moisture availability during which catchment in-wash/sandstorms are more dominant depositing fines/coarse material. The higher contents of silica in the GH2 fluvio-aeolian sediments (max. 96 %) compared to the GH1 fluvio-aeolian sediments (max. 68 %) probably suggest higher energy aerodynamics.

The association of the (κ) with the fluvio-aeolian deposition can be observed by the positive correlation of (κ) with Al_2O_3 (r^2= 0.3; P<0.05), and its negative correlation with silica and medium sand (r^2= -0.2 and -0.2, respectively; P<0.05). This suggests its association with basin in-wash and its reduction due to quartz addition.

Accordingly, based on the above discussion, and similar to the GH1 deposition, the fluvio-aeolian deposition of the GH2 sediments probably record periods of low moisture availability, and aeolian system activation, where the contribution of the proximal sandstone formations around the Gharandal Valley is reflected by the dominance of medium-sized particles main modes (Ibrahim and Rashdan, 1988; Saqqa and Atallah, 2004; Lucke et al., 2019b).
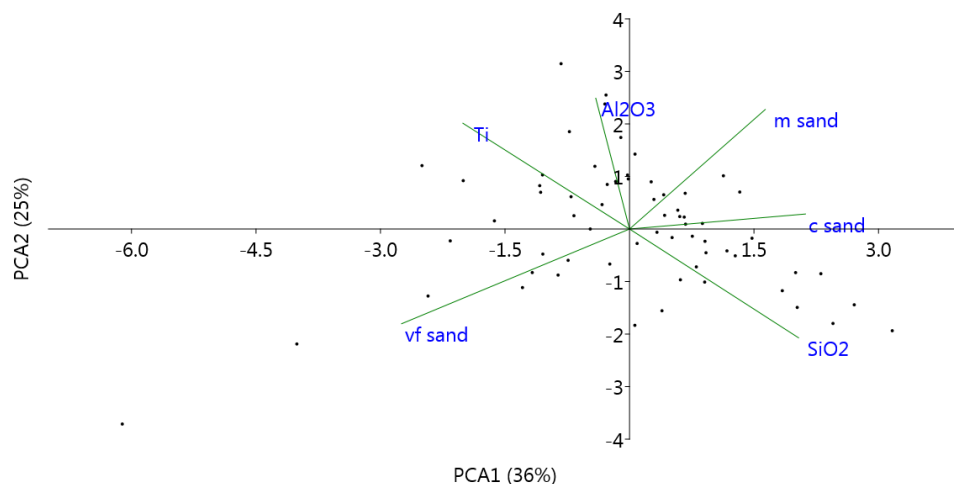
Figure 5.58 Principal component analysis of the GH2 section fluvio-aeolian granulometric and chemical primary variance drivers.

5.3.6 Wetland (fine-grained) lithofacies (Fm)

The wetland sediments in the GH2 section are primarily comprised of fine (clay, silt very fine and fine sand) sediments. The Fm beds are found at different levels in the section, with varying thicknesses, starting from 0.61 m above the base up to the top of the sequence (at 13.25 m). However, thick units (ca. 0.5 m to 2 m) are only present starting from 6 m above the section base (Figure 5.59).

The total sand content ranges from 15 to 90 vol. % with an average of 68 vol. %, the silt content ranges from 7.5 to 66 vol. % with an average of 26 and the clay content ranges from 1.8 to 18 vol. % with an average of 5.5 vol. %. The samples are poorly to very poorly sorted within the range of 1.15 to 7.8 phi. The sediments are generally fine to very fine skewed (-0.7 to 0.66 phi), and platykurtic to very leptokurtic (0.69 to 2.5 phi). The (κ) values of the sediments range from 1.1 to 13.5 (Figure 5.60).
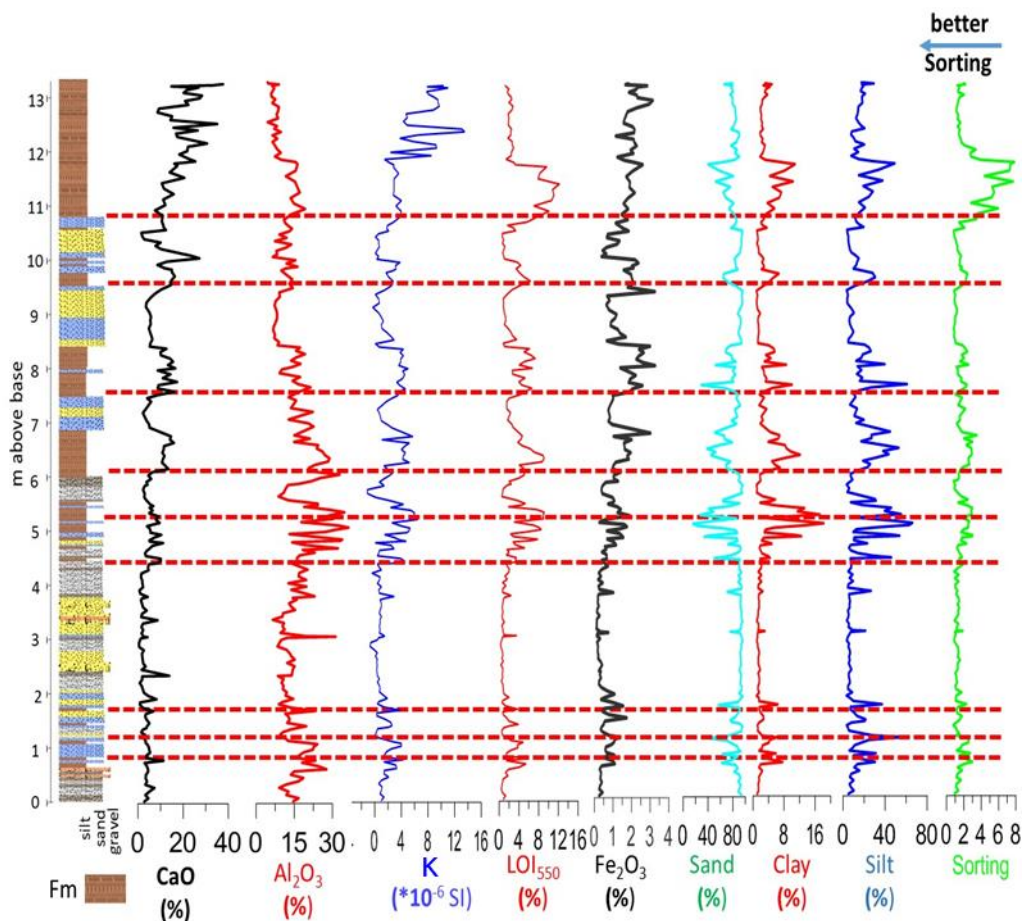
Figure 5.59 GH2 section stratigraphy showing the location of the Fm (wetland) beds, marked by the content (wt. %) peaks of clay and silt. Also observed is their association with elevated content of CaO, Al_2O_3, and LOI_{550}, and (κ). Clay and silt in vol. %. Fm: massive wetland lithofacies.

Figure 5.60 a) Particle size distribution curves of the GH2 section fine sediments. b) Cumulative frequency curves of the fine sediments. c) Box plots of the granulometric composition of the fine sediments. d) Granulometric statistical parameters (in phi units) and (κ) values. Outliers are data located at 1.5 times the interquartile range. v.f.: Very fine. f.: Fine. m.: Medium. c.: Coarse. v.c.: Very coarse. Mz: Mean particle size. Sort. Sorting. Skew.: Skewness. Kurt.: Kurtosis.

PCA analysis of the granulometric composition (Figure 5.61) shows that the first eigenvector PCA1 (52%) correlates with the very fine sand content (r^2=0.9; $P<0.05$). The second eigenvector (33%) correlates with the clay, very fine silt, fine silt, medium silt, coarse silt and very coarse silt ($r^2>0.6$; $P<0.05$). The results indicate different hydrodynamics compared to the other lithofacies, where the variance is explained by the variability in the fine sediments rather than the sand.
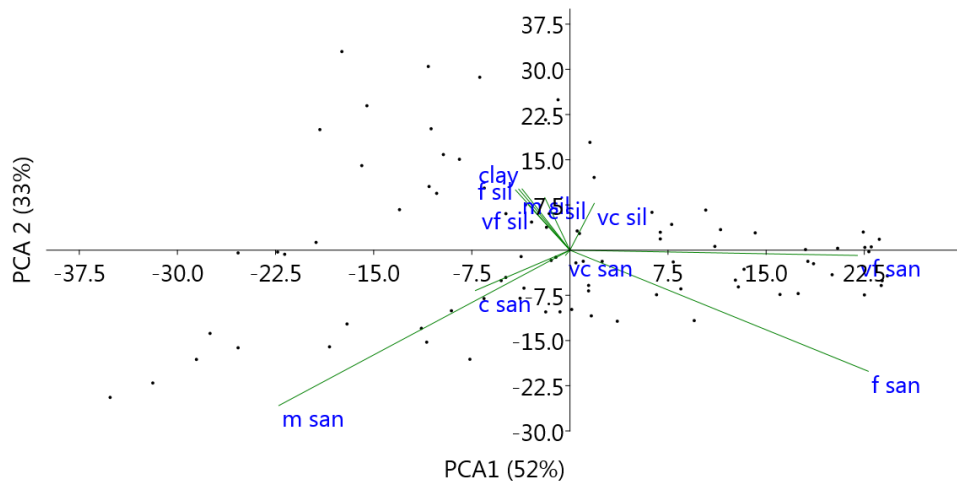
Figure 5.61 Principal Component Analysis of the GH2 section Fm wetland sediments granulometric composition showing the first two eigenvectors.

This observed difference is also recorded in the geochemical composition of the sediments. The wetland beds show enrichment in calcium oxide (CaO) and aluminum oxide (Al_2O_3) (Figure 5.62). The SiO_2 content is within the range of 26 wt. % to 64 wt. % with an average of 46 wt. %, the CaO content shows a range from 1 to 38 wt. % with an average of 13.8 wt. %, and the Al_2O_3 content is in the range of 4.5 to 36.25 wt. % with an average of 17 wt. %. The samples also show higher LOI_{550} (OC) content up to 12.2% with an average of 5%, compared to the other lithofacies with a maximum value of 5.6% and an average of 1.5% (Table 5.4). Positive correlations are present between Ti and Fe_2O_3 (r^2= 0.6; P<0.05).
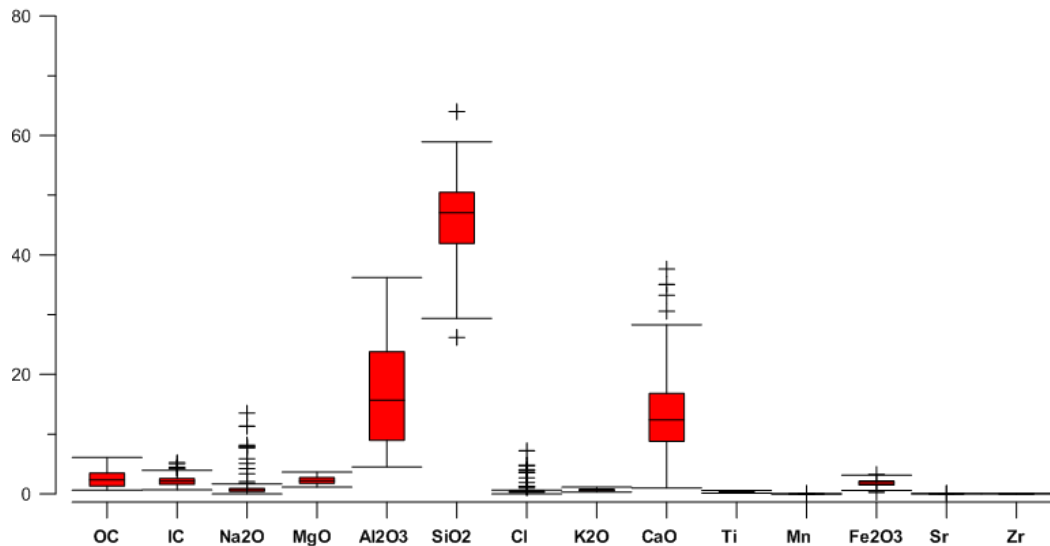
Figure 5.62 Box plots of the chemical composition of the GH2 section wetland sediments (outliers are data located at 1.5 times the interquartile range). OC: $LOI_{550.}$ IC: LOI_{925}.

The negative Ti/CaO correlation in the bi-plot (Figure 5.63) indicates the dominance of endogenic deposition of CaO in the wetland beds. However, three behaviuors based on the samples' levels in the section can be deduced. Samples from the section base to 5.5 m above base, where only thin (ca. 5 cm) wetland beds are found, the covariance (red line in Figure 5.63) suggest dominance of endogenic carbonate deposition. From ca. 5.5 m to ca. 10m above base, where thicker wetland beds exist (ca. 1 m) the covariance (black line in Figure 5.63) suggest an influenc of allochtonous deposition. From ca. 10.7m to the top of the section, the covariance (green line in Figure 5.63) suggests dominance of endogenic deposition. The ICV values indicate three trends through the section. From 0.63 m to 6.6 m above the section base, the ICV values are all <1, from 6.5m above base to 10.8m, the ICV values alternate between >1 and <1 probably reflecting the variability in the degree of source chemical weathering, and a third trend is observed starting from 10.8 m to the top of the section, where the ICV values are all >1 reaching a maximum value of 9.3 at the top of the section (at 13.22-13.25 m).
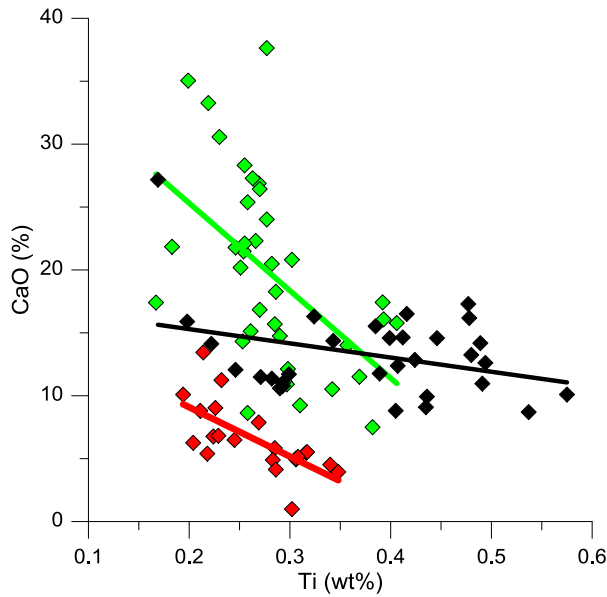
Figure 5.63 CaO/Ti bi-plot of the Fm fine deposits in the GH2 section. Negative covariance suggests endogenic carbonate deposition. Red: from the section base to ca. 5.5m. Black: ca. 5.5 m to ca. 10m above base. Green: ca. 10.7m to the top of the section.

Wetland sediments interpretation

Similar to the deposition of the wetland beds in the GH1 section (see 5.2.6), the Fm beds here represent low energy deposition and the development of wetland conditions through the section. The Fm lithofacies in the GH2 section are enriched in very fine, fine sand, silt and clay. In the GH2 section, the hydrological conditions that facilitated the wetland conditions correlate well with the change in facies, where more stable and consistent wetland conditions are recorded towards the top of the section.

From the section base to ca. 6 m, wetland deposition is recorded as thin beds (<20 cm). The elemental and magnetic record of the sediments in this part show that the K correlates with allogenic markers Fe_2O_3, Al_2O_3 and Ti (r^2= 0.5, 0.2, 0.55; P<0.005) indicating its association with catchment in-wash. On the other hand, the silica correlates negatively with the allogenic markers and positively with Zr and the fine sediments suggesting that it is probably associated with dust deposition, however, the wind energy is less than during the deposition of the fluvio-aeolian beds probably due to the higher moisture availability. Through this part of the section, the wetland deposition is primarily driven by stream influx and fluvial processes. The development of the thin wetland beds was probably due to groundwater recharge facilitating the formation of shallow marshy environments.

These wetland conditions are followed by fluvial and fluvio-aeolian deposition probably indicating alternation between fluvial activation and arid episodes.

From ca. 6 m to 8.5 m above the section base, more frequent wetland conditions prevailed. The environmental records indicate persistent association of K with the allogenic markers observed by positive correlations. However, a change in the moisture availability can be deduced from the change in the silica association. In this part of the section, the silica is positively correlated with the Al_2O_3 ($r^2 = 0.7$; $P<0.005$), and a possible reduction in wind energy. This change to higher moisture availability is recorded in the deposition of thick wetland beds (up to 70 cm).

A return to persistent wetland conditions is recorded from ca. 10.8 m to the top of the section. Nonetheless, the environmental proxies record variable valley hydrodynamics. From ca. 10.8 to 11.8 m, the section records the most dominant wetland conditions and highest LOI_{550} content (ca. 8 to 12%). In this part of the section, the increases in (κ) show negative correlations with the allogenic markers (e.g. with Fe_2O_3, $r^2 = -0.25$) and positive correlation with Al_2O_3 ($r^2 = 0.4$), suggesting its association with the accumulation of fines, possibly in standing water bodies, or high groundwater recharge as also suggested by elevated LOI_{550} contents rather than recharge through stream fluxes.

Towards the top of the section, ca. 11.8 m to 13.2 m, the environmental proxies indicate lower catchment in-wash and the association of silica with allogenic markers. The (κ) is also associated with catchment in-wash where positive correlations are recorded with Ti and Fe_2O_3 ($r^2 = 0.5$, 0.6; $P<0.005$) suggesting a return to a fluvial dominated system in the valley, however the conditions were probably wetter than during the deposition of the fluvio-aeolian beds. This part probably indicates the termination of the wetland conditions associated with rapid reduction in LOI_{550} values from ca. 9.5 % to ca. 1%.

To assess the modes of transportation of the wetland sediments, the samples were plotted on a CM diagram (Figure 5.64). The plot shows that the main transportation modes are primarily through suspension to graded and uniform suspension deposition in water pools, consistent with the above discussion.
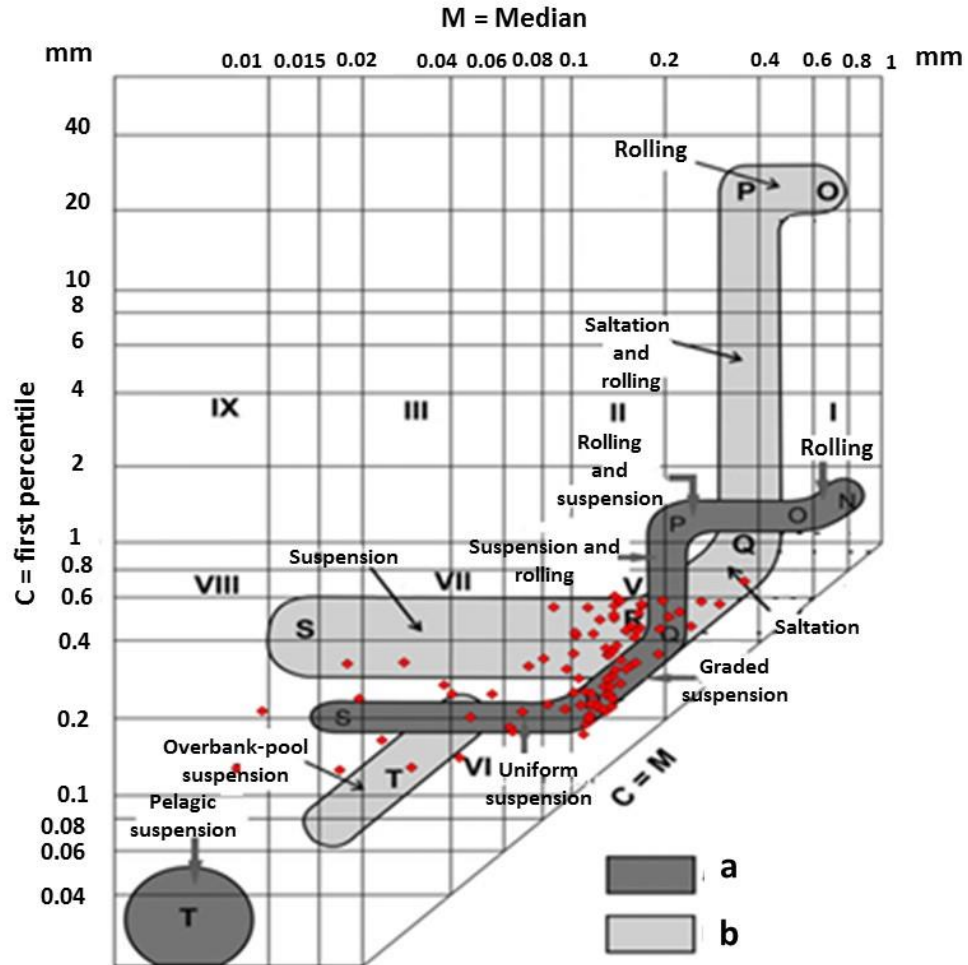
Figure 5.64 complete CM pattern of the GH2 section wetland sediments Fm (red). a: based on Passega (1964) and Passega & Byramjee (1969); b: based on Ludwikowska Kędzia (2000). I,II,III, IX: rolled grains; IV: High turbulence deposit; V: Low turbulence deposit; VI: Graded suspension; VII: Uniform suspension; VIII: Finest uniform suspension (after Passega and Byramjee, 1969) (modified from Malgorzata and Ludwikowska-Kedzia, 2011).

5.3.7 Depositional and environmental history of the GH2 sedimentary sequence

Similar to the GH1 section, the GH2 section records variable valley hydrodynamics of fluvial, fluvio-aeolian and wetland deposition driven by the valley's hydrological and hydrodynamic conditions. These conditions are recorded in the stratigraphic sequence and the sediments' composition. Unlike the GH1 section, gravel-dominated beds are absent in the GH2 section.

Similar to the GH1 section, the main variables recovered from all the lithofacies were combined to show the complete GH2 section environmental variability. The PCA results (Figure 5.65) indicate that the first two eigenvectors explain 71 % of the total variance. PCA1 (50%) correlates with all the features except for the silica

and medium sand contents (r^2= -0.8 and -0.78; P<0.05), respectively. Similar to the GH1 section, this eigenvector probably records the alternation between wetter and drier conditions in the valley where the catchment in-wash and wetland conditions are represented by higher PCA1 values. Accordingly, Figure 5.66 shows the GH2 section with the environmental proxies PCA1, LOI_{550}, (κ), Mz, and the wind energy proxy SiO_2/Al_2O_3.
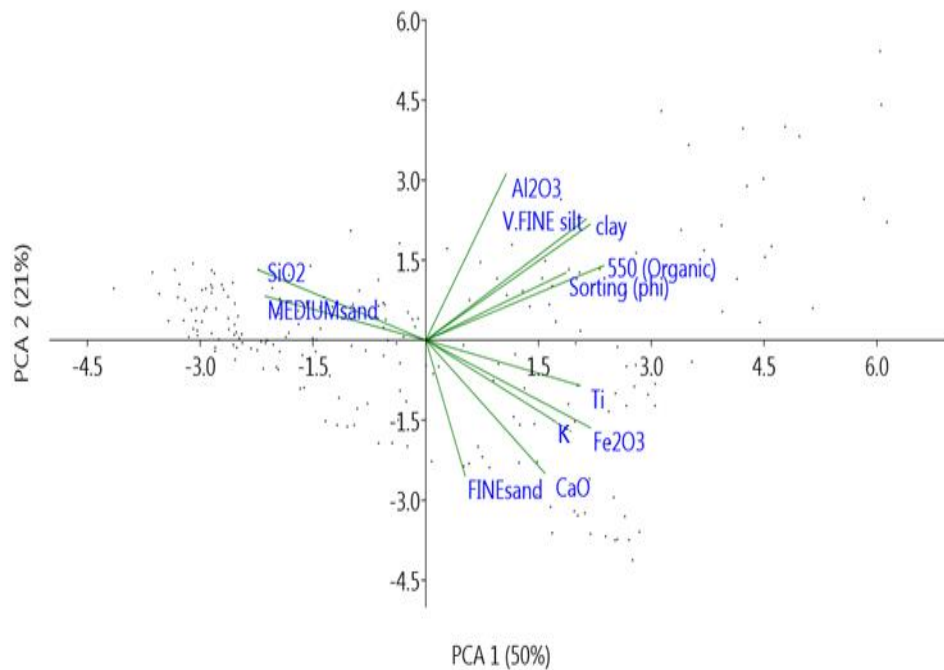
Figure 5.65 Principal Component analysis of the main drivers of the GH2 lithofacies variance showing the first two eigenvectors.

As observed in Figure 5.66, the GH2 section records 8 sedimentary cycles (upward transitions). Based on the OSL age estimates, the GH2 section records the depositional history of the Gharandal Valley during MIS 6. The three OSL age estimates show ages, in an upward stratigraphic trend, of 161±12 ka (at 5.55 m above base), 159±14 ka (at 9.15 m) and 154±13 ka (at 10.15 m) with a mean depositional age of 158±7 ka. For the lower ca. 5.5 m of the section, the first 4 sedimentary cycles start with a mass flow (Ss) bed that fines upward into a sand bed (Sm or Sr), based on the flow nature and the decrease in energy, which is then overlain by the development of a fine-grained wetland bed. Within these main associations, cyclicity is observed where alternations between Sm and Sr beds are present. In this part of the section, fluvio-aeolian deposition is recorded indicating periods of aridity and deposition of medium sand particles sourced from the local catchment. Wetland conditions developed in this part probably driven by

stream influxes and groundwater where carbonate concretions and black mat conditions (observed in the field as dark colour beds) are found. The observed alternations between wet and dry conditions are also observed as oxidation in the sand beds. From 5.5 m to 8.5 m above base (sedimentary cycles 5 and 6), more consistent wetland conditions are recorded, nonetheless, the proxy records (see above) suggest continued deposition driven by stream influxes and groundwater changes. However, wetter conditions can be inferred from the proxies, the lack of significant mass flow events and the thickness of the wetland beds. An OSL age estimate of 161±12 ka is recovered in this part at 5.5 m above base.

A return to more fluvial conditions is recorded from ca. 8.5 m to 10.8 m above base, sedimentary cycle 7 and the lower part of sedimentary cycle 8, where thick sand beds (in-wash) are recorded accompanied by periods of fluvio-aeolian deposition and possible sandstorms. In this part, two OSL age estimates of 159±14 and 154±13 ka were recovered at 9.15 m and 10.15 m.

Following this period, the record shows the most significant wetland conditions where all the proxies indicate wetter conditions and possible deposition in standing water conditions driven by enhanced moisture availability, or high groundwater recharge, rather than stream influxes (see above). Towards the top of the section, the upper part of sedimentary cycle 8, the proxies indicate the termination of the wetland conditions and progressive low energy fluvial deposition.

The section records the valley response to complex hydrological conditions and wetland deposition that progresses upwards with a trend towards wetter conditions followed by return to more fluvial conditions. Considering the high age uncertainties, the variance-weighted mean and standard error of the ages suggest that the wetter conditions prevailed at 158±7 ka, consistent with wetter conditions recorded in the southern Levant and Arabia driven by monsoon precipitation (Petit-Maire et al., 2010; Parton et al., 2015a) and periods of enhanced eastern Mediterranean cyclones reaching the region (Bar-Matthews et al., 2003) (see Chapter 6).
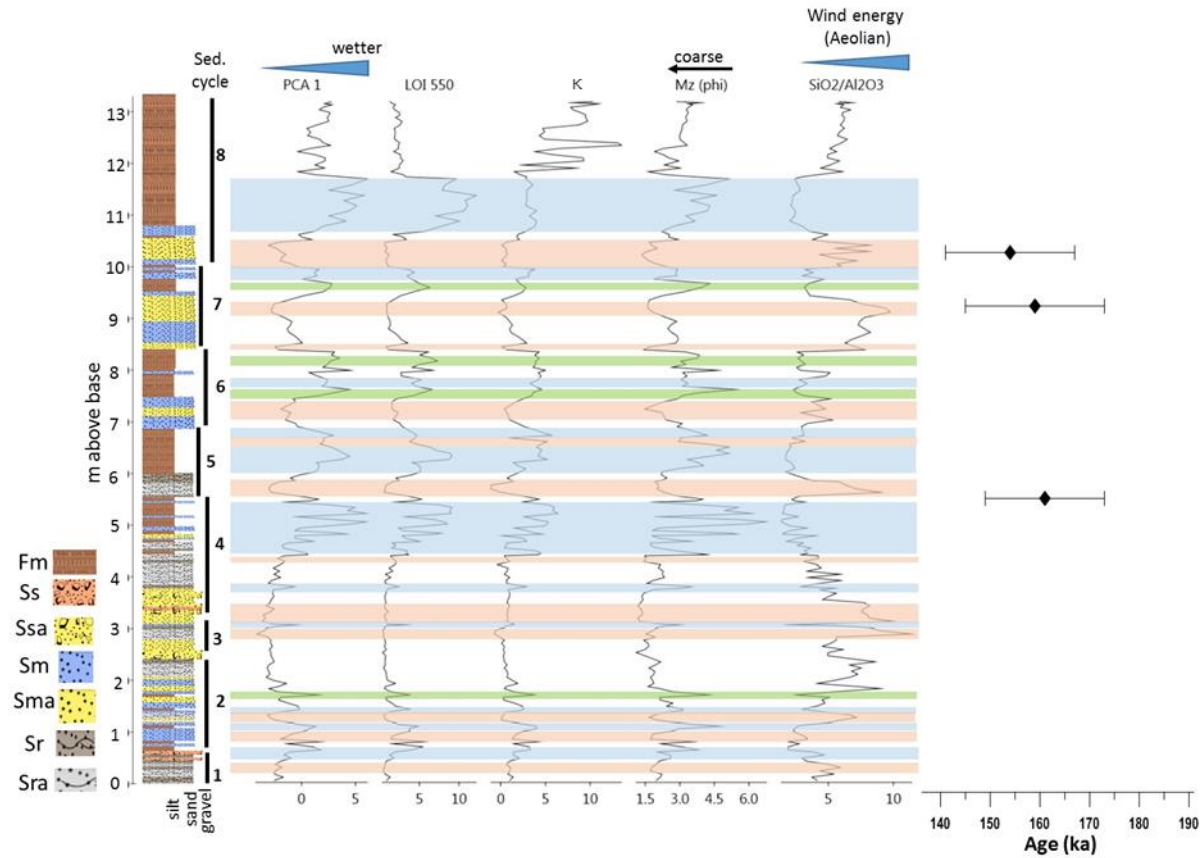
Figure 5.66 GH2 section stratigraphy showing the 8 depositional cycles alongside the environmental proxies and OSL age estimates. **Blue**: wetland condition. **Green**: organic-rich shallow marsh. **Orange**: suggested aeolian processses activation. **Ss**: Pebbly sand lithofacies, **Sm**: massive sand lithofacies, **Sr**: sand lithofacies with sedimentary structures, **Fm**: wetland lithofacies, **Ssa, Sma, Sra**: fluvio-aeolian lithofacies.

5.4   GH3/4 and GH5 sedimentary sequences

5.4.1   Introduction

This section focuses on the GH3, GH4 and GH5 sedimentary sequences (Figure 4.11). Their location, lithology and chronology are described. Following to this, their distinct sedimentary lithofacies are discussed in terms of sedimentological and geochemical characteristics. Finally, the identification of depositional environments and the associated environmental history is presented.

5.4.2   GH3 and GH4 sequences

5.4.2.1   General description

Sections GH3 and GH4 (Figure 5.67 a) are parts of a thick, ca. 10 m, sedimentary sequence (Al-Saqarat et al., 2020) located ca. 500 m to the east of the present-day outlet of the Gharandal Valley, along the road leading to the Gharandal base (see Figure 4.11). The complete section is unconformably overlain by ca. 2 m fluvial gravel deposits (Al-Saqarat et al., 2020).

Due to the steep cliffs, only the basal 4.6 m of the section were accessible and represent the GH3 section, at a basal elevation of 252 m asl. In addition, to constrain the top of the sequence, the uppermost 0.7 m sediments underlying the fluvial gravel bed were sampled (GH4 section) at a basal elevation of 261 m asl.

The sequence starts with a horizontally-bedded sand bed, with carbonate concretions and oxide stains, overlain by a massive sand bed with small granules. The massive sand bed is overlain by fine to medium sand beds and silty carbonate-rich thin beds, up to the top of the cleaned section (at 4.6 m), with reddish and dark colour oxide nodules in some locations, accompanying the carbonate-rich beds and carbonate concretions, while, thin (few cm) dark to black colour beds are located at 0.3 m, 2.6 m, and 3.4 m above the section base. The sediments lithology is similar to some parts of the GH1 and GH2 sediments implying a possibly similar depositional environment. Thus, based on the lithological variations, 24 samples were collected at intervals of 5 to 30 cm for sedimentological and geochemical analyses.

Section GH4 (Figure 5.67 b), ca. 0.7 m, is mainly comprised of fine to medium sand-sized sediments with carbonate concretions in the upper 0.2 m. Based on the lithological variations, 3 samples were collected for sedimentological and geochemical analyses.
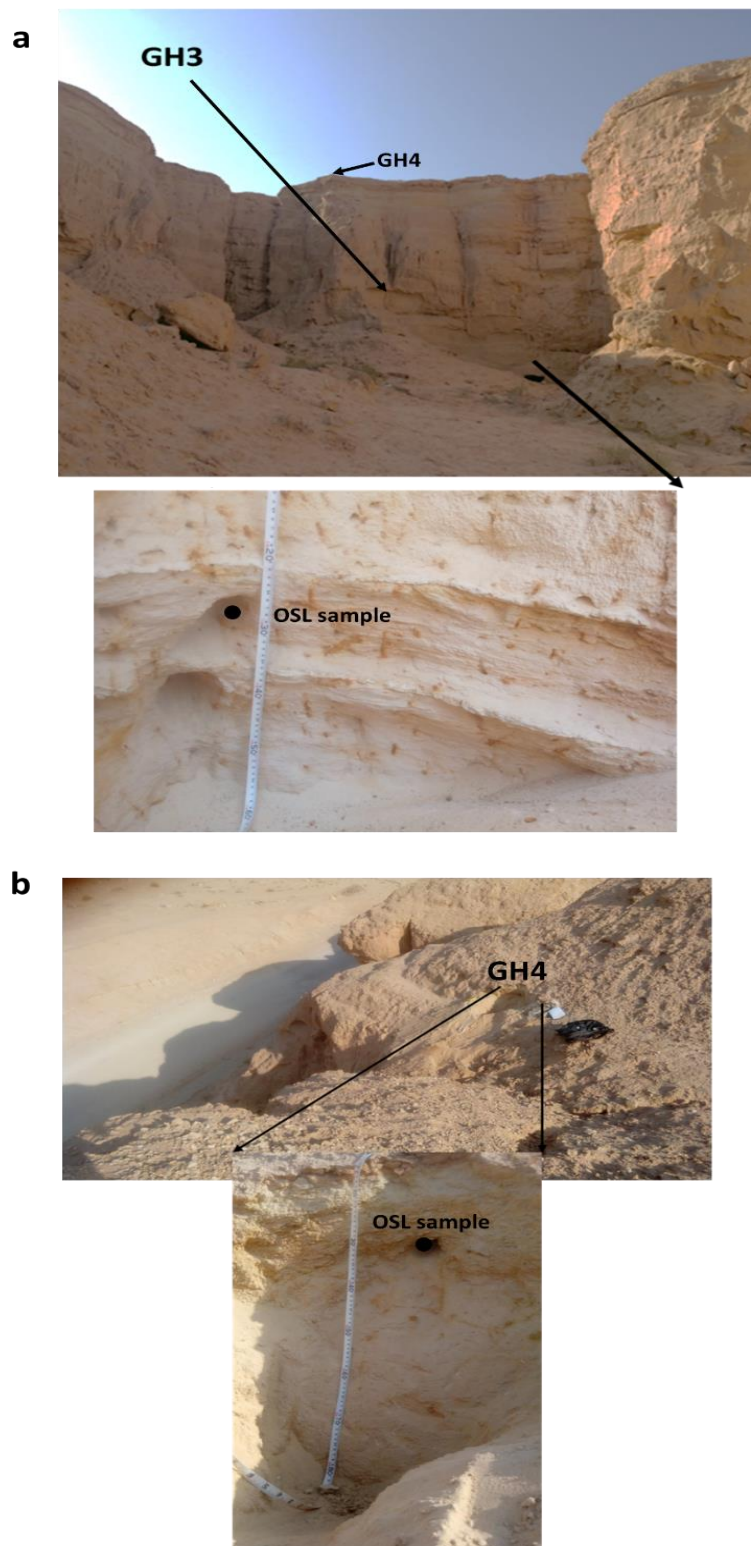
Figure 5.67 a) Outcrop where section GH3 is located showing the steep cliffs with inset showing the basal sand bed, b) Section GH4 location with inset showing the section. OSL sample: sampling locations of Al-Saqarat et al. (2020).

5.4.2.2 Chronology

The chronology of the GH3 and GH4 sections was estimated through 2 OSL ages (Al-Saqarat et al., 2020) (Figure 5.67) at ca. 0.4 m above the base of the GH3 section (at 115±8ka) and at ca. 0.5 m above the base of the GH4 section (at 69±6ka) (Samples GH21 and GH22 in Table 4.2).

5.4.2.3 Sedimentary lithofacies analysis

As discussed in 5.2.3, the sedimentary lithofacies analysis is conducted through three steps. However, the small number of samples for the GH3 and GH4 sections (27 bulk sediment samples) does not allow the application of the PCA-LDA approach (Shaukat et al., 2016). Thus, the sedimentary lithofacies identification is based on the field-based facies and refined using the characteristics obtained for the GH1 and GH2 sedimentary lithofacies.

The GH3 and GH4 sediments show variable lithofacies, comparable to those identified in the GH1 and GH2 sections. Based on the granulometric characteristics, two samples contain granules (2-4 mm; -1 to -2 phi) (<15wt. %) in sand beds, and thus are classified as pebbly sand (Ss) lithofacies (see 5.2.4.2).

18 samples are sand dominated (>86 vol. %), with generally low silt and clay contents, while, the 7 fines-dominated samples are characterized by higher clay and silt contents (>2 and >22 vol. %, respectively) and lower sand content (<76 vol. %). This is further indicated by the chemical composition of the sediments, where the sand-dominated sediments are enriched in silica (43 to 69.5 %), while the fines-dominated sediments show higher CaO (7 to 14.5 %), Al_2O_3 (7.2 to 19 %) and LOI_{550} (2.8 to 8.4%).

The sand-dominated sediments were then reclassified based on the presence of any sedimentary structures. Two samples were collected from horizontally-bedded beds, and thus were classified as Sr lithofacies (samples collected showing sedimentary structures), while the rest of the samples were classified as massive sand (Sm) lithofacies (see 5.2.4.3).

The fluvio-aeolian sediments were identified based on the criteria discussed earlier (see 5.2.5). Samples enriched in silica, with medium sand content, a trend towards better sorting, their main size mode in the range of medium sand and low κ values were considered as fluvio-aeolian deposits. Thus, the two Ss samples were reclassified as associated with fluvio-aeolian deposition (Ssa), 9 Sm samples

were reclassified as (Sma) and one Sr sample was reclassified as Sra (Figure 5.68).
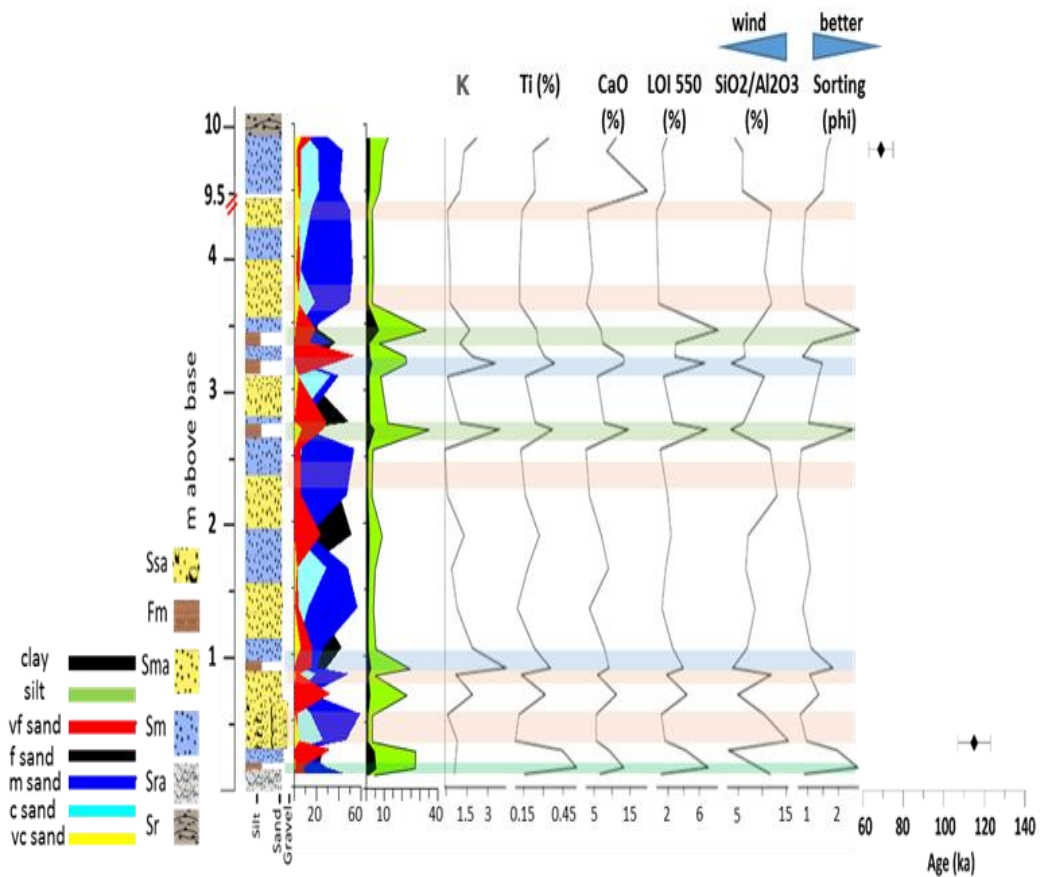
Figure 5.68 GH3/4 sedimentary section stratigraphy and the key environmental indicators. Ssa, Sma: fluvio-aeolian lithofacies. Sm: Massive sand lithofacies. Sr: Sand lithofacies with sedimentary structures. Fm: wetland lithofacies. Orange bars: suggested aeolian deposition. Green bars: organic-rich beds. Blue box: suggested wetland environment. Ages are based on OSL.

5.4.2.4 Fluvial and fluvio-aeolian deposition in the GH3 and GH4 sections

The fluvial deposition in the GH3 and GH4 sections is recorded in the Ss, Sm and Sr deposits indicating catchment in-wash and variable transport energy and modes, which reflect the catchment hydrology in response to local hydroclimatic conditions.

Fluvial deposits

The clasts in the pebbly sand (Ssa) sediments indicate that the deposition required a higher energy environment compared to the sand beds. However, the granules in the GH3 section (<-2 phi) and amount (<15 wt. %), compared to the gravel beds in GH1 section (>-2 phi size and up to 85 wt. %), probably indicate lower energy in-wash events. Nonetheless, in the GH3/GH4 section, these beds record

199

relatively high values of Fe_2O_3 (2.8 and 5.7 %) associated with low content of fine grained particles (0.9 % clay and ca. 3.4 % silt) and Al_2O_3 probably reflecting rapid dumping of the flow composition associated with aeolian deposition reflected by elevated medium sand contents and relatively lowered K values.

The results show that the fluvial sediments (Sm and Sr) are primarily dominated by fine to coarse sand with high contents of fine and medium sand (Figure 5.69 c, f, and 5.70 b). The GH3 sediments show higher contents of fine sand, while the GH4 samples have more coarse sand. The total sand content of the fluvial sediments ranges from 75 to 91 vol. %, the silt content ranges from 5 to 22 vol. % and the clay content ranges from 1 to 2.5 vol. %. The sediments are unimodal (main mode: 194 to 542µm) with one sample showing bimodality and one sample showing trimodality (the top sample in GH4) (Figure 5.69). The samples are generally poorly sorted, with one moderately sorted sample, within the range of 0.94 to 1.7 phi. The sediments are symmetrical to very fine skewed (-0.03 to 0.5 phi), leptokurtic to very leptokurtic (1.4 to 2.1 phi) with κ values from 1 to 2.2 (Figure 5.70 a). The results show that positive ($P<0.05$) correlations are present amongst the silt, clay, very fine and very coarse sand fractions. In addition, positive ($P<0.05$) correlation is found between the very coarse sand and medium sand contents.

The SiO_2 content is dominant in these sediments within the range of 43 to 60 wt. %. The CaO content shows a range from 7.5 to 11 wt. % with one sample showing 19 wt. %, while the Al_2O_3 content is in the range of 7 to 13 wt. % (Figure 5.70 c).

Within the fluvial sediments, the K is positively correlated with Ti, Fe_2O_3, and Al_2O_3 (r^2=0.67, 0.34 and 0.5, respectively; $P<0.05$). The silica is associated with Al_2O_3 (r^2=0.4; $P<0.05$) and shows a weak positive correlation with K and Fe_2O_3 (r^2=0.03). The CaO shows a weak positive correlation with Fe_2O_3 and Ti (r^2= 0.01 and 0.05) probably suggesting endogenic deposition. The ICV values for the sediments generally indicate compositionally immature sources with values >1 (Cox et al., 1995; Hossain et al., 2017).
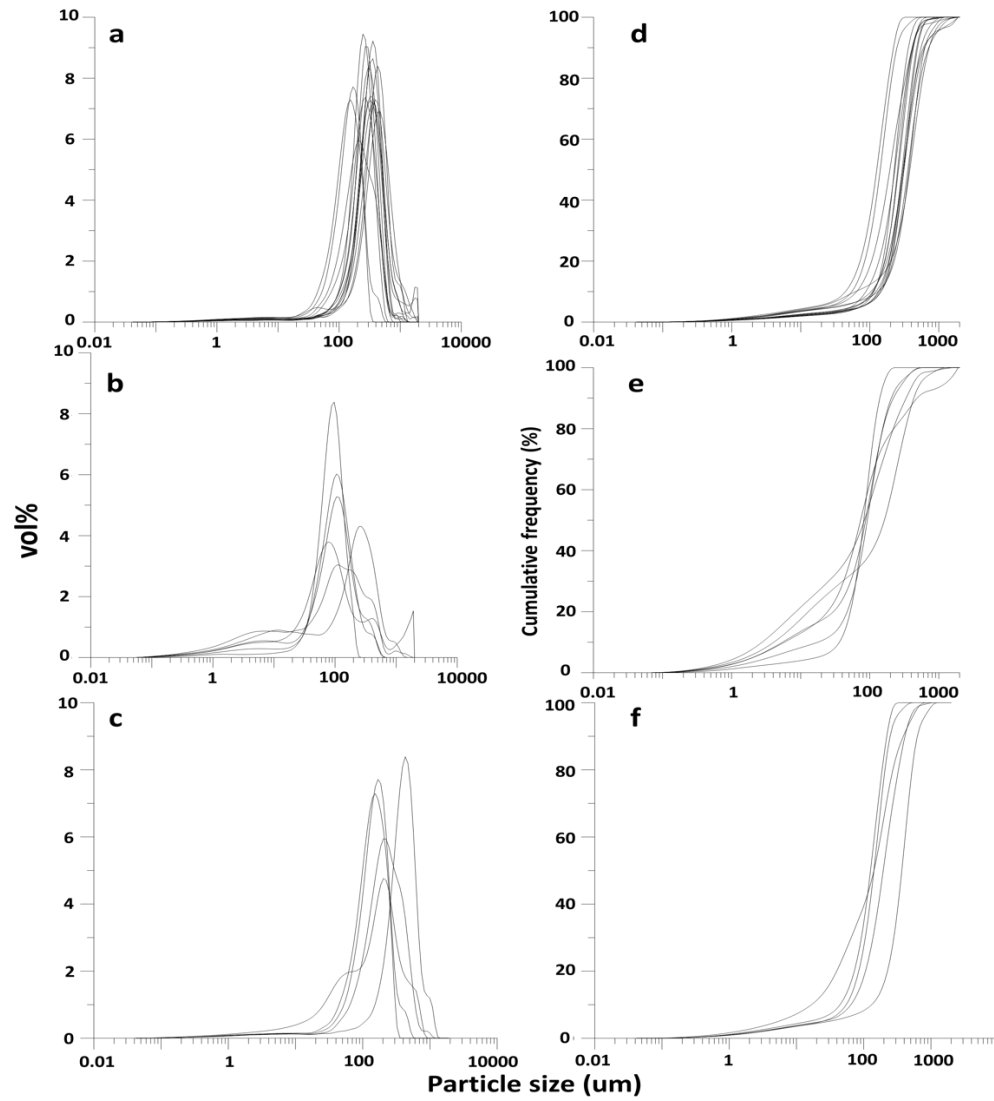
Figure 5.69 a, b, c) GH3/4 section particle size distribution frequency curves; d, e, f) Cumulative frequency curves of the fluvio-aeolian, wetland and fluvial sediments, respectively.
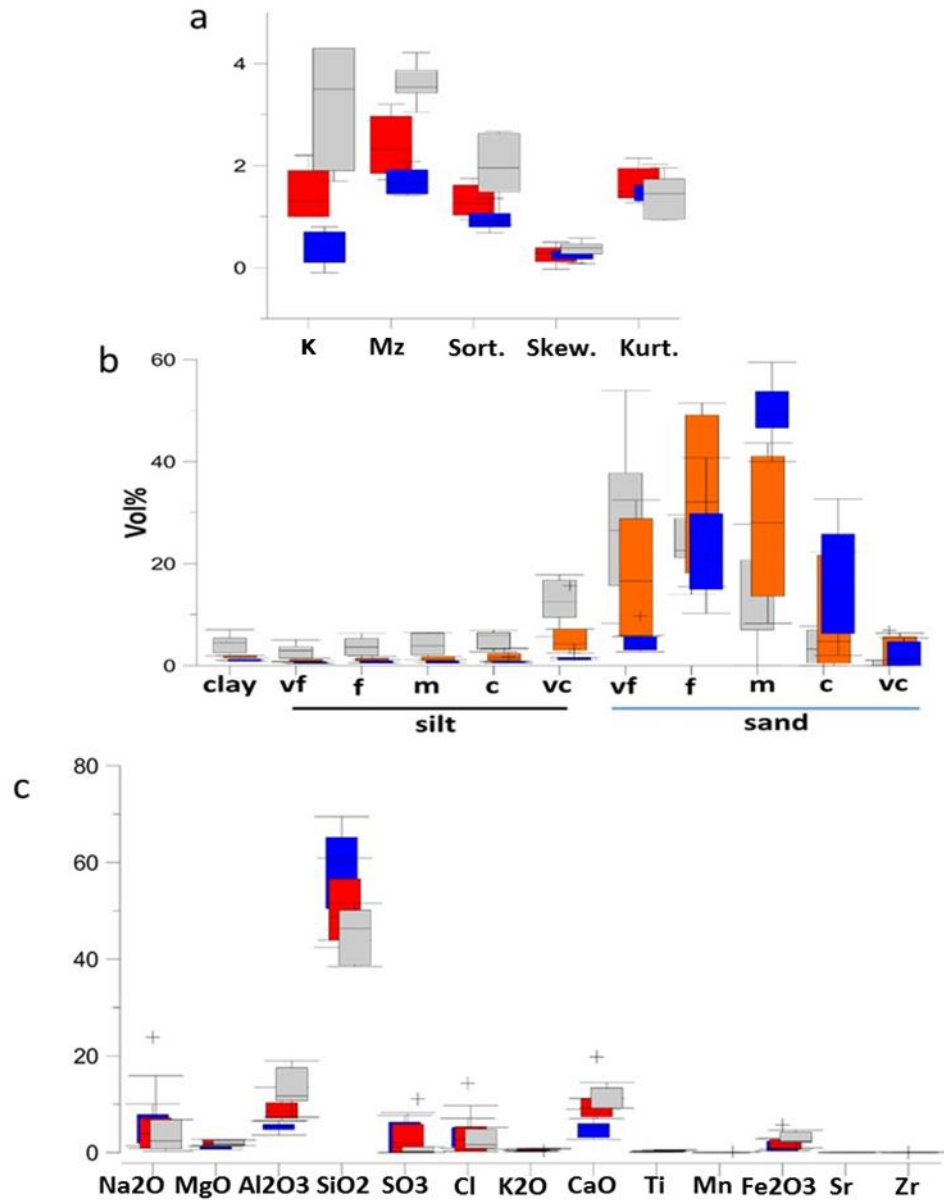
Figure 5.70 a) GH3/4 section box plots of the Granulometric composition, b) Granulometric statistical parameters (in phi units) and (κ) values (*10^{-6} SI), c) Box plots of the elemental composition in wt. % of the fluvio-aeolian Sma and Sra (blue), fluvial Sm and Sr (red) and wetland deposits Fm (grey). Outliers are data located at 1.5 times the interquartile range.

Fluvio-aeolian deposits

The fluvio-aeolian sediments from the GH3/4 section comprise total sand content range from 90 to 96 vol. %, the silt content ranges from 3.1 to 8.1 vol. % and the clay content ranges from 0.8 to 1.5 vol. %, with dominance of medium and fine sand (Figure 5.70 a). The sediments are unimodal (main mode: 340 to 450 µm) (Figure 5.69 a and d). The samples are moderately to poorly sorted within the range of 0.7 to 1.7 phi, very fine to fine skewed (0.09 to 0.4 phi), and leptokurtic to

very leptokurtic (1.2 to 1.9 phi) with (κ) values from -0.1 to 0.8 (Figure 5.70 b). The granulometric analysis shows that positive ($P<0.05$) correlations are present amongst the silt, clay, and very fine sand fractions. The fines show negative correlation with the fine to medium sand and positively with the coarser fraction probably reflecting the system behaviour. The medium and fine sand fraction show positive correlation among them and negative correlation with the other granulometric fractions, probably suggesting their different system.

The geochemical analyses results show that the most abundant element in the fluvio-aeolian sediments is silica (SiO_2) with a range of 46 to 69 wt. %. The rest of the elements are all <10 wt. %, except for one sample that shows 24 wt. % of Na_2O and 14 wt. % of Cl sampled at 1.35 m above the section base (Figure 5.70 c).

The SiO_2 is correlated negatively with all the other elements. Ti is positively correlated with Fe_2O_3 ($r^2=$ 0.3; $P<0.05$) and negatively with silica ($r^2=$ -0.25, $P>0.05$). The CaO content correlates positively ($P<0.05$) with Fe_2O_3 and Ti ($r^2=$ 0.5 and 0.68, respectively), while κ correlates positively ($P<0.05$) with Fe_2O_3 ($r^2=$ 0.66, $P<0.05$) but shows negative correlation with SiO_2 ($r^2=$ -0.58; $P<0.05$).

5.4.2.5 Wetland deposits of the GH3 and GH4 sections

The fine wetland sediments (Fm lithofacies) are primarily composed of very coarse silt to medium sand, with elevated contents of very fine and fine sand (Figure 5.69 b, e). The total sand content ranges from 59 to 76 vol. % with high contents of very fine and fine sand, the silt content ranges from 22 to 35 vol. % and the clay content ranges from 2 to 5.5 vol. % (Figure 5.70 b). The sediments are generally unimodal (main mode: 101 to 340µm) to bimodal (Figure 5.69 b and e). The samples are generally poorly to very poorly sorted, within the range of 0.9 to 2.7 phi. The sediments are symmetrical to very fine skewed (0.07 to 0.58 phi), and mesokurtic to very leptokurtic (0.9 to 1.96 phi) with κ values from 1.9 to 4.3 (Figure 5.70 a). The results show positive ($P<0.05$) correlations amongst the silt, clay, and very fine sand fractions. In addition, negative ($P<0.05$) correlations are found amongst the fine to very coarse sand fractions and the fines (silt and clay). These beds also show higher content of LOI_{550} of 3 to 8.4%, compared to the other beds with values of 0.2 to 4%.

The SiO_2 contents of the Fm lithofacies range from 38 to 51 wt. %, with CaO content from 9 to 14.5 wt. % and Al_2O_3 content in the range of 7 to 19 wt. % (Figure

5.70). The results show positive (P<0.05) correlations are present between Ti and Fe_2O_3, (κ) (r^2=0.5 and 0.84, respectively).

Unlike most of the CaO content in the GH1 and GH2 sections wetland sediments, the CaO content of the GH3 wetland sediments shows a positive correlation with Ti (r^2= 0.4) probably suggesting that some of the CaO is from allogenic sources. The silica is also correlated negatively with CaO, Ti and Fe_2O_3 and positively with Zr (r^2=0.5), probably suggesting that aeolian deposition was not completely shut down during the deposition of the thin wetland beds in the GH3 section., and hence lower moisture availability compared to the deposition of the thick wetland beds in the GH1 and GH2 sections.

5.4.3   GH5 sedimentary sequence

5.4.3.1   General description

GH5 section is located about 450 m to the east of the present day valley outlet at a basal elevation of ca. 269 m asl (Figures 4.11 and 5.71), at the opposite valley side to the GH4 section. It is a distinct sequence from the surroundings due to its contents of in-situ, Middle-Palaeolithic (minimum depositional age of 74±7 ka) lithic artefacts (Al-Saqarat et al., 2020), (Figure 5.71 b). Here, 1.2 m of sediments were cleaned, at a basal elevation of 269 m asl, described and sampled.

From the section base to about 0.45 m, the section is mainly comprised of fine sand and gravels near the section base, varied colours of carbonate-rich layers, and embedded flints. Root casts (possible reeds (Henry et al., 2001)) mainly occur in the upper 0.5 m, and a 4 cm dark to black colour bed is located at 0.6 m above the base. The section is overlain by a fluvial gravel unit. From this section, 5 samples were collected for sedimentological and geochemical analyses (Figure 5.72).

5.4.3.2   Chronology

The chronology of the GH5 section was estimated through 1 OSL age (Sample GH31 in Table 4.2) at an OSL age estimate of 74±7ka (Al-Saqarat et al., 2020).
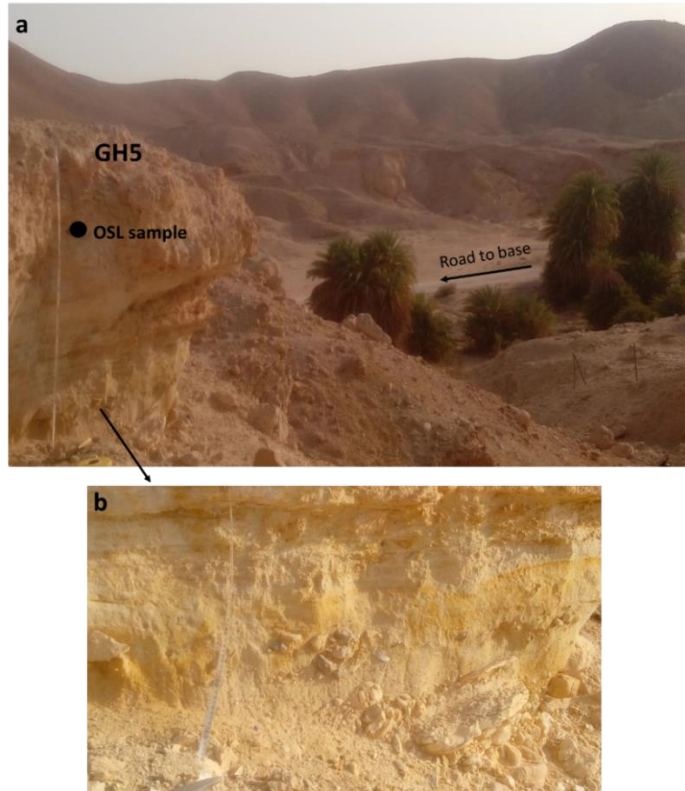
Figure 5.71 a) GH5 section and view into Gharandal Valley showing the palm trees. b) The lower part of the section where lithic artefacts are embedded.
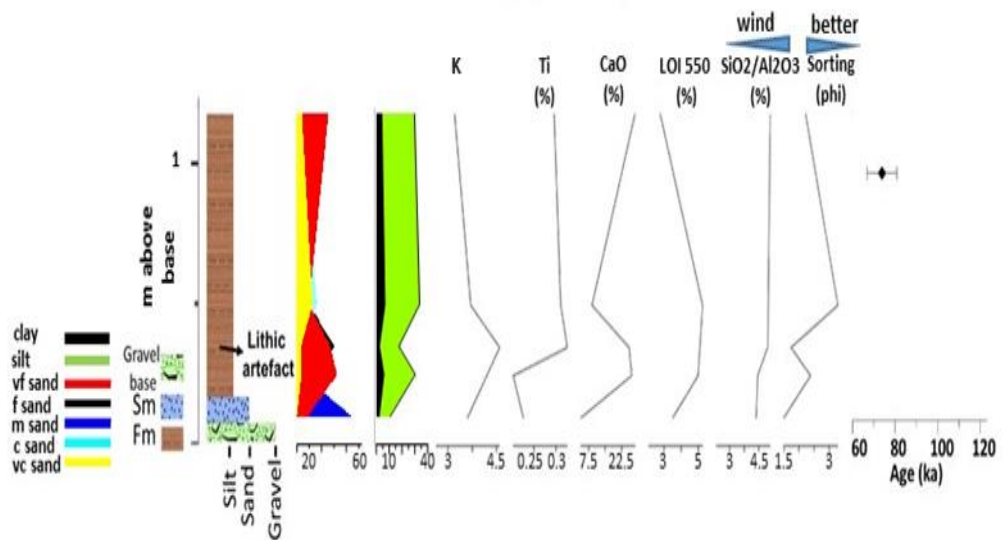
Figure 5.72 GH5 section stratigraphy and the key environmental indicators. Fm: wetland lithofacies. Sm: Massive sand bed. Age is based on OSL.

5.4.3.3 Sedimentary lithofacies Analysis

The sedimentary lithofacies were identified similar to the procedure followed for GH3/4 sections. The GH5 section generally comprises fine sediments overlying a fluvial gravel-rich base. Based on the granulometric characteristics, 1 sample from

the base is considered as massive sand lithofacies (Sm) as it contains the lowest clay and silt contents with high sand content (87.2 vol. %). The other 4 samples are primarily fine-dominated (wetland Fm) lithofacies (Figure 5.73). This is further indicated by the chemical composition of the samples, where the Sm sample comprises the highest amount of silica (43 wt. %) and the lowest content of CaO (3.8 wt. %).

The results show that the Fm sediments are primarily very coarse silt and very fine to fine sand. The total sand content for the sediments ranges from 64 to 87 vol. %, the silt content ranges from 10 to 34 vol. % and the clay content ranges from 2 to 6.5 vol. %. The samples are poorly to very poorly sorted within the range of 2.3 to 3.9 phi. The sediments are generally fine skewed to very fine skewed (0.7 to 0.5 phi), and platykurtic to very leptokurtic (0.7 to 2 phi) with relatively high κ values from 3.2 to 4.6 (Figure 5.73), compared to values reaching <0 in the other sedimentary sections. Positive ($P<0.05$) correlations are present amongst the clay, very fine to medium silt contents, and within these fractions and the coarse and very coarse sand contents.

The chemical composition results show that the most abundant elements in the sediments are the SiO_2> CaO> Na_2O> Al_2O_3 (Figure 5.73 e). The SiO_2 content is within the range of 21 to 43 wt. %. The CaO content shows a wide range from 4 to 28.6 wt. %, the Na_2O content is in the range of 0.3 to 14 wt. %, while, the Al_2O_3 content is in the range of 5 to 12.6 wt. %.

Positive correlations are present between Ti and Fe_2O_3 ($r^2= 0.65$), and between SiO_2 and Ti ($r^2= 0.9$) and Fe_2O_3 ($r^2= 0.7$) suggesting that silica is probably associated with catchment erosion and not aeolian deposition. The CaO is correlated with Fe_2O_3 ($r^2= 0.3$) probably suggesting that some of the CaO is allogenic. The Na_2O shows negative correlations with CaO ($r^2= -0.9$), Ti ($r^2= -0.3$), Fe_2O_3 ($r^2= -0.84$) and SiO_2 ($r^2= -0.4$), while it is positively correlated with Sr ($r^2= 0.8$) and Cl ($r^2= 0.99$) suggesting its possible endogenic deposition.
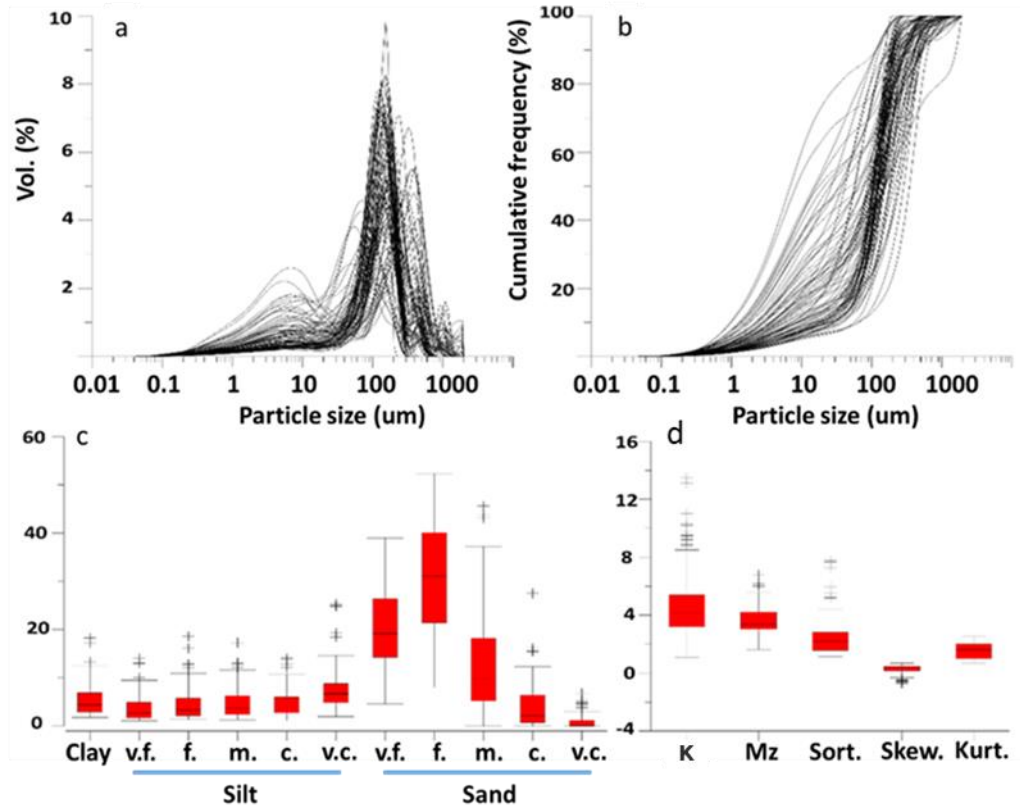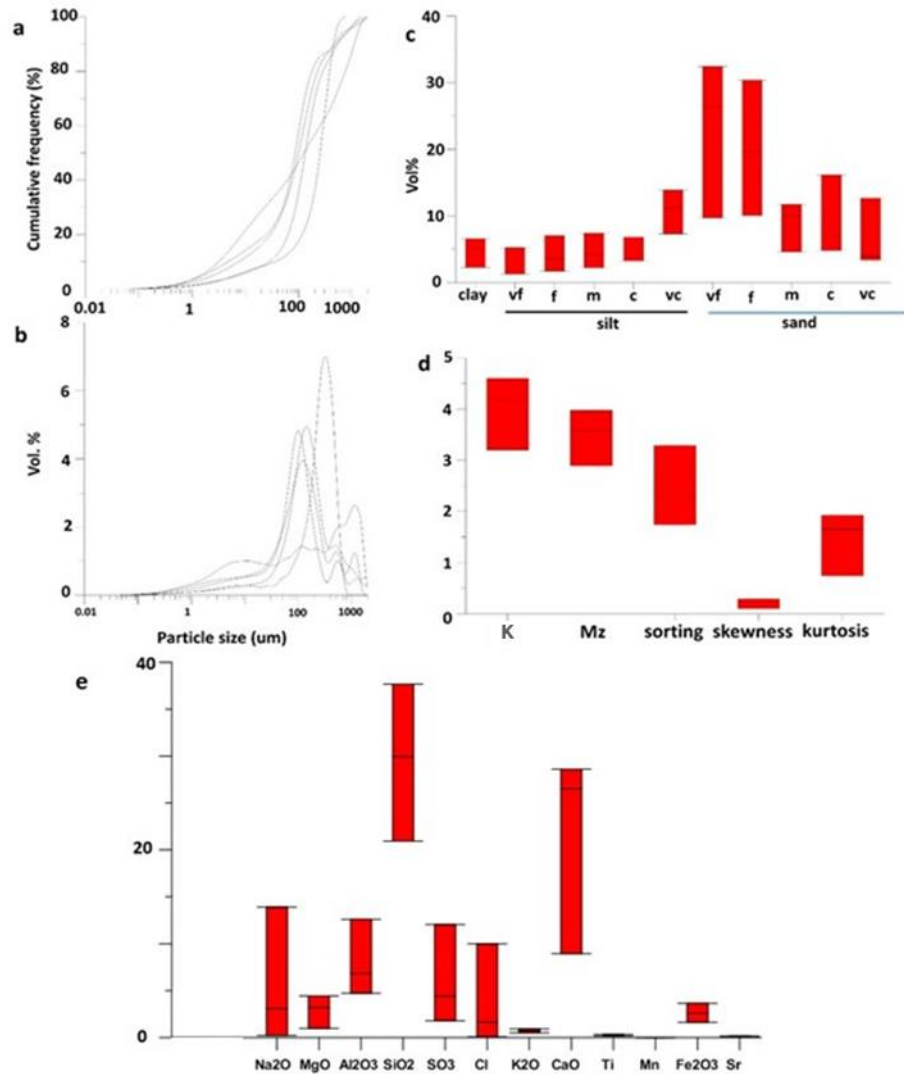
Figure 5.73 a) Particle size distribution curves of the GH5 section sediments. b) Cumulative frequency curves. c) Box plots of the Granulometric composition of the sediments. d) Granulometric statistical parameters (in phi units) and (κ) values. e) Elemental composition. Elements in wt.%.

5.4.4 Depositional and environmental history of the GH3, GH4 and GH5 sedimentary sequences

The sedimentological and geochemical analyses of the GH3/4 and GH5 sediments indicate variable hydrodynamics persisted during their deposition. The highest silica content is in the fluvio-aeolian sediments, and the highest allogenic element concentrations in the fluvial sediments, the positive covariance between silica content and Ti, and the negative covariance between CaO and Ti in the wetland sediments are all indicators of the variable hydrodynamics.

In the GH3/4 section, the variation in the granulometric parameters indicates variable fluvial hydrodynamics where the GH4 sediments, in the top of the section, shows higher values of sorting and skewness with coarser mean particle size (Mz)

(2.2 to 1.7 phi- fine to medium sand), compared to the GH3 fluvial sediments, the lower part of the section where the Mz ranges from 2.3 to 3.2 phi- very fine to fine sand. This suggests higher in-wash events probably deposited the GH4 sediments. The association of silica with Al_2O_3 and its weak positive correlation with allogenic markers probably suggest lower wind energy conditions and higher moisture availability during the deposition of the fluvial sediments. The weak correlation of CaO with allogenic markers suggest some of the CaO might be of endogenic deposition which is reflected in the lithology of the beds as carbonate concretions, probably deposited following sand in-wash under the influence of the groundwater table changes and periods of wetting and drying.

On the other hand, the fluvio-aeolian sediments record a decrease in moisture availability where a negative correlation is noted for silica with the other allogenic markers suggesting its deposition through aeolian processes associated by a decrease in (κ) values and dominance of wind processes. The positive correlations of K with most of the elements and its negative correlations with the silica suggest its validity as an indicator of catchment in-wash (higher) and aeolian deposition (lower).

During the wetland conditions, the dominance of fine-grained particles and the geochemistry in these beds suggests deposition under low energy conditions or in shallow water ponds associated with elevated (κ) values. However, unlike the wetland beds in the GH1 and GH2 sections, the wetland beds here are thin (few cm). The weak positive correlation of CaO with allogenic markers suggest that some of the CaO is of detrital origin.

The GH5 section records different hydrodynamics compared to the GH3/4 section. Here, the deposition of fine-grained (wetland) sediments shows a transition in the valley hydrodynamics from the base gravelly bed to the massive sand bed and then into the fine-dominated sediments suggesting deposition in shallow water or low energy conditions. The association of silica with catchment erosion probably suggest higher moisture availability. The CaO correlation with allogenic markers suggests that its deposition was influenced by catchment in-wash. Thus, this section probably records periods of valley hydrodynamic change from a fluvial-dominated system to shallow water low energy deposition in response to enhanced moisture availability and changes in groundwater level.

In addition, using a CM diagram (Figure 5.74) (Passega and Byramjee, 1969; Mycielska-DowgiaŁŁo and Ludwikowska-Kedzia, 2011), the fluvial sediments of

the GH3/4 section plot in the high turbulence saltation and low turbulence transportation processes. The observed variability between the GH3 and GH4 fluvial sediments characteristics (see above) is also observed here where samples from the GH4 section plot in the high turbulence saltation area suggesting higher energy compared to the GH3 fluvial sediments that plot in the low turbulence deposition segment (red diamonds). The wetland sediments, however, show primarily low turbulence, graded and uniform suspension as main transport processes (gold diamonds).

On the other hand, the GH5 sediments plot showing two different dominant processes; the Sm sample plots in the rolling and high turbulence deposition indicating the basin in-wash of the sand, while the Fm samples plot in the low turbulence suspension segment indicating their low energy deposition.
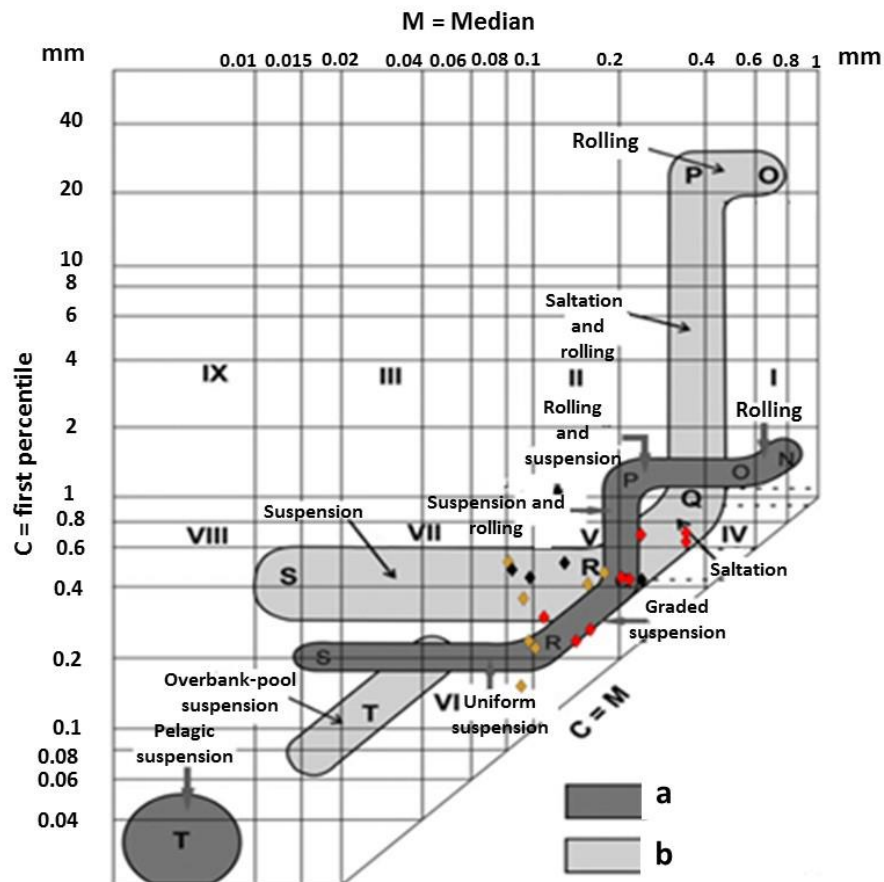
Figure 5.74 Complete CM pattern of tractive current deposits for GH5 sediments (gold) and GH3/GH4 sediments (fluvial sediments: red, wetland sediments (Fm): black). a) based on Passega (1964) and Passega & Byramjee (1969); b) based on Ludwikowska Kędzia (2000). I, II, III, IX: rolled grains; IV: High turbulence deposit; V: Low turbulence deposit; VI: Graded suspension; VII: Uniform suspension; VIII: Finest uniform suspension (after Passega and Byramjee, 1969) (Modified from Malgorzata and Ludwikowska-Kedzia, 2011.

In conclusion, the GH3/GH4 section records a mostly fluvial/fluvio-aeolian dominant depositional system at (115±8 ka to 69±6 ka) (Al-Saqarat et al., 2020). The uppermost part, the GH4 section, is primarily comprised of basin in-wash fluvial sand beds reflected by increased Ti and magnetic susceptibility, trending towards poor sorting and reduced wind energy. In the GH3/GH4 section, wetland conditions only developed following changes in the groundwater level indicating a system primarily driven by freshwater influxes where stream-fed shallow marsh environments probably prevailed.

The GH5 section is comprised of generally fine sediments (minimum Mz of 2.3 phi), compared to the GH3/GH4 section (minimum Mz of 1.4 phi). The lower SiO_2/Al_2O_3 content (<5 % compared to >10 % in GH3 section) also support deposition under higher moisture availability with less dominance of wind processes. The age estimate recovered from this section overlaps with the age estimate recovered from the GH4 section (74±7 ka and 69±6 ka, respectively (Al-Saqarat et al., 2020). Nonetheless, the results of this study indicate different environmental conditions for the deposition of the two sections that vary significantly, from the GH4 fluvial in-wash deposition transporting high amounts of sand, primarily medium and coarse, to the GH5 low energy (possible shallow water) conditions where fine grained sediments (silt, very fine, and fine sand) dominate (see Figures 5.68 and 5.72). This variability is also observed in the magnetic susceptibility where the GH4 sediments show a maximum value of 2.2, while the GH5 sediments show a maximum value of 4.6. In addition, the silica and LOI_{550} contents vary from a min. of 48 % in GH4 to a min of 21 % in GH5 and a maximum of 1.8 % in GH4 to a maximum of 5.3 % in GH5, respectively. These observations suggest that the two sections do not record compatible environments. The two sections are located at similar altitudes at both sides of the basin, thus further dating to confirm the age estimates is required in order to draw a complete assessment of the wetter/drier conditions and the wetland development in the valley.

5.5 Chapter conclusions

The detailed sedimentological and geochemical analyses of the Gharandal Valley (GH1, GH2, GH3/4 and GH5) sedimentary sequences have established the variability in the valley depositional hydrodynamics and environmental conditions.

The two sections (GH1 and GH2) located near the valley outlet record alternating periods of wetter and drier (enhanced/reduced moisture availability) conditions.

Through the lower parts of the sections, the environmental proxies record periods of aggradation and wetland development driven by water fluxes and groundwater level changes where thin wetland beds developed following the activation of the fluvial system and basin in-wash. Towards the top of the sections, more consistent wetland conditions prevailed where thick, up to 2 m, wetland beds were deposited suggesting signifficantly wetter conditions in the valley, compared to the present-day. During the deposition of these thick wetland beds, the proxies indicate reduction (or shutdown) in the aeolian processes probably as a response to higher mositure availability and possible standing water bodies fed by precipitation rather than stream influxes. The age estimates of the deposits in the GH1 and GH2 sections suggest deposition during different time periods (MIS5 and MIS6, respectively), however, probable dosimetry miscalculations are present and this needs further dating to confirm.

On the other hand, the GH3/4 section (ca. 130ka-70ka) records primarily fluvial/fluvio-aeolian deposition with occasional thin wetland beds probably in response to changes in groundwater levels recorded as carbonate concretions that suggest periods of wetting and drying. While, the GH5 section record, of similar age, indicates deposition in shallow standing water where finer sediments and higher contents of LOI_{550} and K are recorded, compared to the GH3/4 section.

The broader interpretation of these sequences is developed in Chapter 6.

Chapter 6. The Gharandal Valley depositional and environmental history

6.1   Introduction

This chapter presents the combined conclusions of the Gharandal Valley sedimentary sequences (GH1-GH5) (see Figure 4.11) to draw a more comprehensive understanding of the depositional and environmental history of the Valley. It also discusses the contribution of this project in relation to the previous work in the Gharandal Valley and the MIS6 records of the southern Levant and the surroundings.

6.2   The Gharandal GH1 and GH2 sections lateral continuity

The Gharandal GH1 and GH2 sections represent the main sedimentary sequences in the Gharandal Valley (see Chapter 5). Previous studies considered the two sections to represent one continuous sedimentary sequence (see section 4.3.6) where the GH1 section overlaps with the outcrop located south of the road (Mischke et al., 2017; Al-Saqarat et al., 2020), but no detailed sedimentological and/or geochemical analyses have been reported in order to confirm this hypothesis. Accordingly, the previous studies only investigated the lower ca. 6 m of the GH1 section and parts of the outcrop where the GH2 section of this project was selected.

The detailed sedimentological and geochemical investigations of this project indicate that, generally, both sections record periods of fluvial, fluvio-aeolian and wetland deposition (Figure 6.1). Both sections show in-wash events up to 13.4m above the base of the GH1 section and 10.8m above the GH2 section base (Figure 6.1). In addition, the GH1 section records extreme flood events in the lower 3 m represented by beds of clast supported gravel.

Overall, the GH2 section records less variable valley hydrodynamics and more stable proxy records. For example in terms of allogenic markers, the pebbly sand (Ss) beds record (κ)values of (0.3 to 2.1 $*10^{-6}$ SI), while the GH1 Ss beds show values up to 7 $*10^{-6}$ SI (see 5.3.4.1). The GH1 section massive sand associated with fluvio-aeolian deposition (Sma) beds show (κ) values of (-2.4 to 0.8 $*10^{-6}$ SI), while the Sma beds of the GH2 section are within the range from -0.3 to 1 $*10^{-6}$ SI (see 5.3.5). Also, the GH1 section wetland beds (Fm) show higher contents of silt (up to 79 vol. %) and clay (up to 30 wt. %) compared to the Fm beds of the GH2 section where the silt content is up to 66 wt.% and the clay content is up to 18 wt.% (see 5.3.6). However, these differences can be attributed to the sections

location within the valley where the GH1 section is a mid-valley section and the GH2 section is closer to the valley side. The location of the GH1 section may suggest that it is more affected by the incoming water influxes and probably the flow composition and axial distribution downstream.

Furthermore, these changes are also observed in the stratigraphy and lithological variability between the two sections (Figure 6.1), where the GH1 section is dominated by medium and coarser sands through the lower ca. 14 m that change into finer sands towards the top. The GH2 section is dominated by medium and coarser sand in the lower ca. 4 m of the section while starting from ca. 5 m above the section base, the section shows dominance of fine and very fine sands corresponding to more consistent wetland conditions. The silt and clay contents of the two sections also vary and are associated with the fine-dominated (wetland) beds.
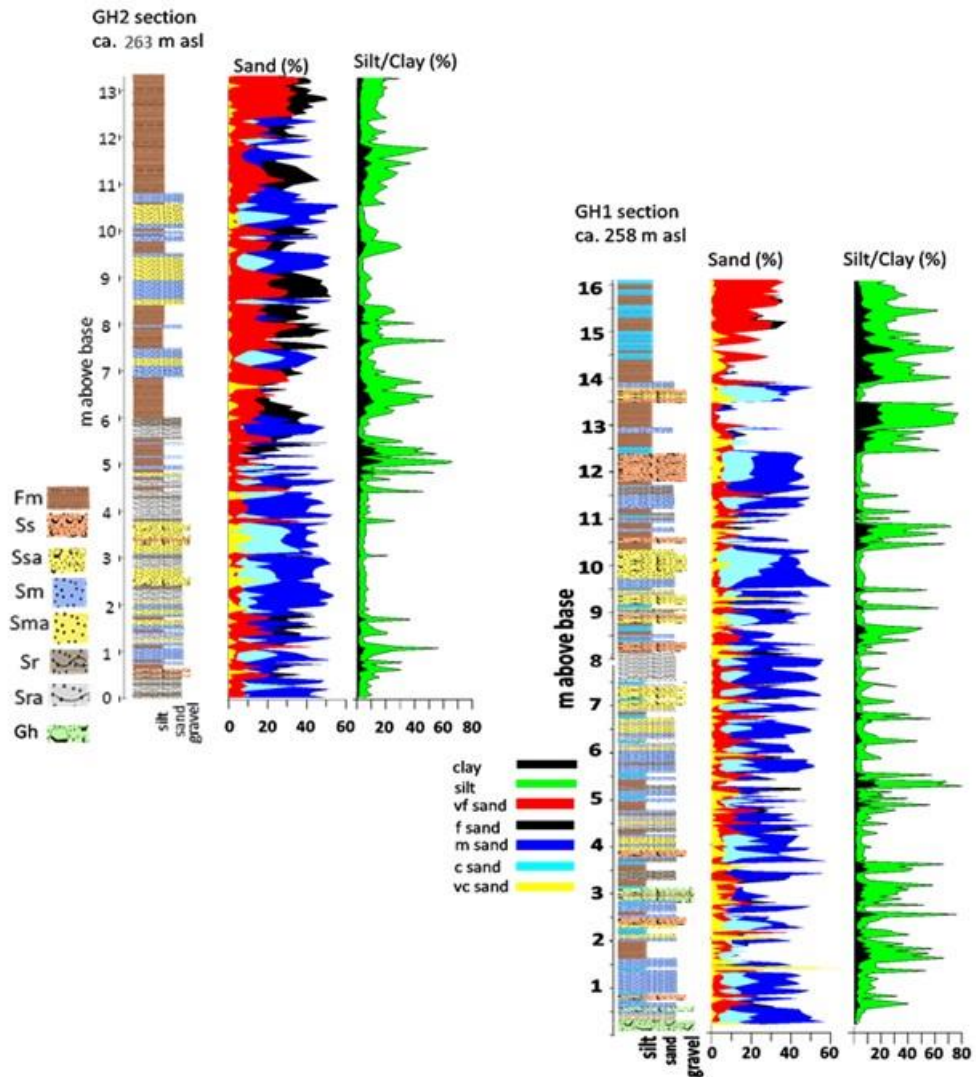
Figure 6.1 GH1 and GH2 sections stratigraphy showing the sand, silt and clay contents. Note the change in the dominance of finer grained sand starting from ca. 5m above the GH2 section base, compared to coarser sand through the GH1 section. Gh: gravel lithofacies, Ss: Pebbly sand lithofacies, Sm: massive sand lithofacies, Sr: sand lithofacies with sedimentary structures, Fl, Fm: wetland lithofacies, Ssa, Sma, Sra: fluvio-aeolian lithofacies.

Independent from the sediments' granulometric, elemental, organic and magnetic susceptibility contents, the upward lithofacies transitions also indicate different behaviours for the two sections. Even though using one section can limit the investigation of vertical lithofacies relationships (Markov Chain Analysis), it can still provide insights about their genetic relationships and the palaeoenvironemnt of the section (Beatriz Soto et al., 2014). Using the Strati-signal Software (Ndiaye, 2007), based on Walker Transition Matrix method (see Chapter 3, 3.5),

stratigraphic depositional models for the GH1 and GH2 sections were developed based on the field-based lithofacies upward transitions.

A first step is testing the input data for randomness. This is done based on chi-square (x^2) analysis with a null hypothesis that the data is random. For the GH1 section, the chi-square analysis indicated that the data are random (x^2= 17.8, degree of freedom= 11, critical x^2 at 95% confidence level= 19.675). Even though it is presumed that the facies relationships might not be reliable for random data (Ndiaye, 2007), the analysis was performed and a facies relationship diagram (FRD) was generated in order to show the system cyclicity. Tables 6.1 lists the statistical matrices used in the Markov chain analysis and Figure 6.2 a shows the FRD for the GH1 section. The analysis indicated that the fine-grained beds make up 40% of the section, the Sm beds 30%, the Sr beds 15%, the Ss beds 8% and the GH beds 7%. The GH1 FRD (Figure 6.2) shows the complexity and randomness in the GH1 section depositional model. As discussed previously (see Chapter 5, 5.2), the fining upward cyclicity is also indicated here where all the cycles terminate in the fine-grained lithofacies. Significant transiitons can be observed from Gh-Sr-F, Gh-Sm-F and Ss-F. These transitions agree with the discussed depositional environment of the GH1 section (see Chapter 5, 5.2), where the fining upward cycles start with a mass flow event that transitions into lower energy deposition and ending with the fine-grained beds. The transition from the Ss beds into the Fm beds suggests rapid decline in the depositional energy. The FRD also shows that the transitions between Gh-Sm and Sm-F can be cyclical.

For the GH2 section, the chi-square (x^2) analysis indicated that the data are not random (x^2= 15.3, degree of freedom= 5, critical x^2 at 95% confidence level= 11.29). The matrices used for the analysis are listed in Table 6.2 and the GH2 section FRD is shown in Figure 6.2 b. The results showed that the F lithofacies comrises 36% of the section, the Sm 39%, the Sr 15% and the Ss 9%. The FRD shows less complex depositional transitions compared to the GH1 section. The transitions show two main cycles: Ss-Sr and Ss-Sm-F. In addition, the Ss-Sr and the Sm-F can be cyclical. These transitions agree with the previously discussed hydrodynamics of the GH2 section (see Chapter 5, 5.3). The transition from the Ss lithofacies into Sr suggests lowering in the depositional energy. The GH2 section Sr lithofacies indicated that most of the CaO in the beds is possibly endogenic (see 5.3.4.2). This suggests possible wetland conditions where the transition is terminated. The Ss-Sm-F transition also shows the gradual reduction

of deposition energy and the development of wetland conditions following an in-wash event.

Table 6.1 GH1 section matrices used in the Markov chain analysis

Transition Matrix					
	F	Sr	Sm	Ss	Gh
F	0	7	14	4	0
Sr	8	0	1	0	1
Sm	13	1	0	1	3
Ss	4	0	1	0	0
Gh	1	2	2	0	0
Probability Matrix					
	F	Sr	Sm	Ss	Gh
F	0	0.28	0.56	0.16	0
Sr	0.8	0	0.1	0	0.1
Sm	0.72	0.056	0	0.056	0.167
Ss	0.8	0	0.2	0	0
Gh	0.2	0.4	0.4	0	0
Random Matrix					
	F	Sr	Sm	Ss	Gh
F	0	0.26	0.47	0.13	0.105
Sr	0.490	0	0.34	0.094	0.075
Sm	0.57	0.22	0	0.111	0.088
Ss	0.448	0.172	0.31	0	0.068
Gh	0.448	0.172	0.31	0.086	0
Walker Matrix					
	F	Sr	Sm	Ss	Gh
F	0	0.016	0.086	0.028	-0.105
Sr	0.309	0	-0.239	-0.094	0.024
Sm	0.14	-0.16	0	-0.055	0.077
Ss	0.351	-0.172	-0.110	0	-0.068
Gh	-0.248	0.227	0.089	-0.086	0
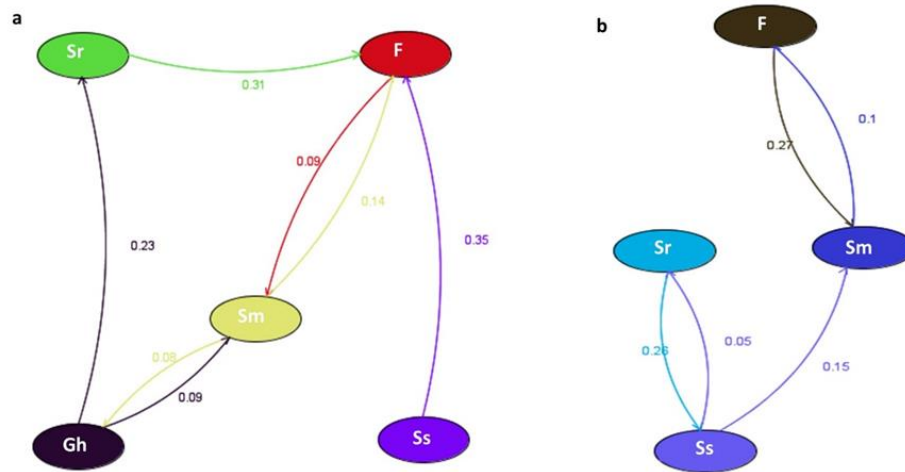
Figure 6.2 Markov Chain analysis (Walker method) facies relationship diagrams (FRD) for the GH1 (a) and GH2 section (b).

The Markov Chain analysis results also support the above discussion suggesting that the GH1 and GH2 sections probably do not record one continuous sequence from bottom to top where the GH2 deposition is not random, cyclical and more stable.

Furthermore, the OSL age estimates of this project indicate that the investigated GH2 section, located south of the road, spans 161±12 ka to 154±13 ka (mean depositional age of 158±7) (see Chapter 5; 5.3.2), while the age estimate of the lower part of the GH1 section is estimated to MIS5 (Al-Saqarat et al., 2020). Moreover, the ages recovered by Al-Saqarat et al. (2020) from the GH1 and close to the GH2 sections were not stratigraphically consistent. Alongside several factors (see 5.3.2), these age estimate discrepancies can be possibly affected by the fact that the two sections do not record one continuous sequence probably in response to the tectonic processes and the balance between tectonic-driven and climate-driven incisions and deposition in the valley, similar to what is observed for alluvial fans located to the south of the Gharandal Valley, where tectonic uplift has been suggested to have influenced the formation, surface area and slope of alluvial fans (Saqqa and Atallah, 2013).

These lateral and vertical variations can be expected in wetland settings fed by incoming water of variable energy conditions. In these settings, standing water ponds, springs and possibly terristrial habitats can occur at close proximity (Pigati et al., 2014). This is also supported by a previous suggestion that the deposition in the Gharandal Valley was intermittent and the sediments accumulated during different periods of valley blocking (Henry et al., 2001).

Table 6.2 GH2 section matrices used in the Markov chain analysis

Transition Matrix				
	Fm	Sm	Sr	Ss
Fm	0	16	2	0
Sm	15	0	4	2
Sr	3	2	0	3
Ss	1	3	1	0
Probability Matrix				
	Fm	Sm	Sr	Ss
Fm	0	0.88	0.11	0
Sm	0.71	0	0.19	0.095
Sr	0.375	0.25	0	0.375
Ss	0.2	0.6	0.2	0
Random Matrix				
	Fm	Sm	Sr	Ss
Fm	0	0.617	0.205	0.147
Sm	0.612	0	0.225	0.161
Sr	0.431	0.477	0	0.113
Ss	0.404	0.446	0.148	0
Walker Matrix				
	Fm	Sm	Sr	Ss
Fm	0	0.271	-0.094	-0.147
Sm	0.101	0	-0.035	-0.066
Sr	-0.056	-0.227	0	0.261
Ss	-0.20	0.153	0.051	0

Similar vertical and lateral lithological incontinuity was observed in two sections from the Jurf Ed Darawish area to the north of the Gharandal Valley (Mischke et al., 2021) (see Chapter 2, 2.4.1). The authors investigated two sections of fluvial/wetland deposits located at close proximity from one another and at similar altitudes that are presently separated by a channel and reported lithological and biofacies variability at both vertical and lateral scales and this was attributed to the assumption that different sub-environments may from close to each other in in-stream wetland settings. In addition, the authors also reported inconsistent OSL age estimates from the two sections where the top of one section (at higher altitude) showed an age estimate older than the top of the other section (at lower

altitude) which was attributed to the lateral and vertical changes (Mischke et al., 2021).

Accordingly, until further dating is obtained based on the criteria discussed in this work, the previous sampling strategies and considerations (e.g. Mischke et al., 2017; Al-Saqarat et al., 2020) need to be re-evaluated.

6.3   The Gharandal Valley outlet blocking

An important factor in establishing the understanding of the Gharandal Valley wetland hydrodynamics and significance as a palaeohydrological and palaeoclimate archive is the understanding of the blocking of the valley outlet, its process, timing and role (Henry et al., 2001; Al-Saqarat et al., 2020). Given the tectonic activity in the Gharandal Valley and its surroundings and proximity to the Dead Sea Transform Fault and the activity of the Aqaba Gharandal Fault (Ibrahim and Rashdan, 1988; Ibrahim, 1993) (see Chapter 4, Section 4.3), tectonic processes may have had a role in the valley outlet blocking, similar to other observed wadi dammings in Wadi Araba (Galli, 1999). It has been suggested that the Gharandal sediments were deposited as a result of the valley outlet episodic blocking (Henry et al., 2001). Following this, Ginat et al. (2017) suggested that the blocking was related to tectonic damming as observed in detached rock blocks near the valley outlet. This hypothesis was also supported by Al-Saqarat et al. (2020) who reported that the valley damming was the result of a landslide dam that left remnants of large detached rock blocks near the present day valley outlet (Figure 6.3). However, no analysis to support this hypothesis was provided. The detailed investigation of the sediments from the GH1 section base showed that the basal gravel bed is probably associated with a short-lived event possibly associated with tectonic processes. This outcome agrees with the previously suggested tectonic-related mechanism of the outlet blocking and the initiation of the wetland sediments deposition. Nonetheless, this still needs further trace elements analysis to confirm. Trace elements (e.g. Th, HF, Zr, Cr) and Rare Earth (REE) elements (e.g. Nd and Yb) can be used as indicators to discriminate the provenance and tectonic processes of sediments. These elements possess low mobility through the sedimentary cycle and are believed to preserve the parent rock signature. Using these elements and discrimination diagrams based on them, can inform about probable changes in tectonic settings in a basin (e.g. Bhatia and Crook, 1986; Amireh, 2020; Yan et al., 2021).

In terms of the timing of damming, it has been assumed it occurred prior to MIS5 (Al-Saqarat et al., 2020), but the OSL age estimates of this study indicate that the Gharandal wetland existed during MIS6 (ca.190-130 ka) which amends the timing of the initial damming that formed the wetland at least to older than 161±12 ka. Thus, this still needs further dating to confirm.

Figure 6.3 Remnants of the landslide damming near the present day valley outlet (modified after Al-Saqarat et al., 2020)

6.4   Environmental and depositional history of the Gharandal Valley

Compared to the present day deposition of primarily coarse sediments and clasts (>2 mm) in the Gharandal Valley (Ibrahim, 1993; Mischke et al., 2017), the Quaternary deposits record periods of different hydrodynamics that allowed the deposition of wetland and organic-rich beds at elevations where no similar deposition is occurring today.

Presently, the hydrodynamics in the Gharandal Valley are similar to those across the whole of Wadi Araba, that primarily depend on occasional intense rainfall events during the wet season that trigger flood events and drain the eastern highlands through the Gharandal Valley into Wadi Araba resulting in groundwater recharge of the shallow aquifer (Saqqa and Atallah, 2004; LeBéon et al., 2012).

The Quaternary outcrops in the valley are presently incised, probably as a result of a long period of flood events that breached the outlet dam and eroded the valley fill to the level of the present day valley floor (Mischke et al., 2017; Al-Saqarat et al., 2020). This erosion is an ongoing process today as noted just ca.100 m to the west of the valley outlet where sediments were observed in the field filling a Roman fort site (Darby and Darby, 2015), however, the elevation of the sediments near the outlet and along the valley slopes is topographically higher than the present day floods which maintained the thick outcrops.

Following the damming of the valley outlet during MIS6, the in-washed sediments were trapped in the lower parts of the valley near the dam. This in turn elevated the base flow and allowed the deposition of ground-water fed wetland deposits, such as shallow marshes, black mat and thick wetland beds primarily at the valley outlet. The nature of the sedimentary sequences in the valley, where thick and more frequent wetland beds are deposited near the valley outlet, but absent in the GH3/GH4 sections, located at higher elevations compared to GH1 and GH2 sections, indicates the significant role of the groundwater in maintaining these wetland beds.

The results of this project suggest that for the most part, the deposition in the Gharandal Valley was cyclical, where, a fluvial in-wash event is followed by transport energy lowering and probably groundwater recharge and spring discharge increase, resulting in thin (<0.5 m) wetland bed deposition. These depositional cycles are usually followed or interrupted by periods of fluvio-aeolian deposition, where, aeolian processes are active, indicating more aridity and less moisture availability. This cyclicity is supported by the presence of carbonate concretions indicative of episodic wetting and drying events that persisted during the deposition of the lower ca. 13 m and ca. 5 m of the GH1 and GH2 sections deposition, respectively. During the deposition of these parts of the sections, the deposition resembles the complex interaction between several geomorphic events; i.e. the valley damming, fluvial in-wash (climate-driven), sediment trap, the subsequent elevated base flow and enhanced spring discharge representing a stream-fed shallow wetland environment.

However, a change in the valley hydrodynamics and hydroclimate is recorded from ca. 5 m to 11.8 m above the section base of the GH2 section and at ca. 13 m to the top of the GH1 section, where thick (>0.5 m) wetland beds are deposited. Based on the GH2 section wetland conditions and age estimates, the deposition

of these wetland beds probably persisted during the glacial MIS6 when glacial conditions (e.g. reduced evaporation) may have contributed to the formation of these wetlands. Similarly, during the glacial MIS6, the lake levels of Lake Amora, the precursor of the Dead Sea, were higher than the lake levels during the following interglacial MIS5 indicating that a more positive water balance prevailed during MIS6 in the Dead Sea Basin (Waldmann et al., 2010).

Indeed, in the GH2 section, more persistent, and thick, wetland beds are constrained to the glacial MIS6, at a mean depositional age estimate of 158±7 ka. This indicates the Gharandal Valley response to regional hydroclimatic changes; i.e. positive water balance conditions as a result of the suggested enhanced moisture availability in southern Jordan (Petit-Maire et al., 2010; Waldmann et al., 2010) (see section 6.5). This enhanced moisture period is recorded in the GH2 section where the wetland bed at 10.7 to 11.5 m above the section base multi-proxy records suggest wetland conditions probably prevailed during more stable wet periods and reduced catchment erosion (see Chapter 5; 5.3.6). This positive water balance period is then followed by a fluvial-dominated system, from ca. 11.5 m to the top of the GH2 section, and catchment erosion, also possibly corresponding to a drying period in southern Jordan (see section 6.5). The progressive lowering of the dam (e.g. Al-Saqarat et al., 2020) and the frequent fluvial in-wash events may have initiated the dam incision and washed coarser sediments into the wetland as can be observed at high levels in the GH2 section.

Deposition of the GH3/GH4 sections primarily records fluvial in-wash with thin marshy beds and periods of wetting and drying where the wetland conditions are most probably driven by stream influxes and groundwater level variations (e.g. Al-Saqarat et al., 2020). Based on current dating control, this process of in-stream wetland is thought to have prevailed during MIS5, with episodic marshy wetlands and ending at ca. 69±6 ka as recovered from the youngest age from section GH4 (Site 2 in Al-Saqarat et al., 2020). On the other hand, the GH5 section multi-proxy records suggest periods of possible shallow water environment dominated by fine-grained sediments, unlike the GH3/4 section. The two overlapping ages recovered from the GH5 and GH4 sections, at 74±7 ka and 69±6 ka, respectively, may need to be revised and further dating control is required to estimate the timing the wetland conditions of these sections.

Regarding the damming incision and the start of the present day depositional processes, an OSL age estimate of 36.3 ka was recovered from a fluvial bed

capping the wetland sediments near the valley outlet (Al-Saqarat et al., 2020) and has been suggested to represent the damming incision timing.

6.5   Palaeoenvironmental context of the GH2 sedimentary sequence

This section presents the integration of the new OSL age estimates from the GH2 section within the local (southern Jordan), southern Levant, and regional climate and environmental records of the glacial MIS6 period (~191-130 ka) (Lisiecki and Raymo, 2005).

The glacial MIS6 records are sparse globally, and in the Levant in particular (Guillemot et al., 2019). The following discussion presents local and regional MIS6 records in the Levant and the surrounding areas (see Chapter 2, 2.4), and it is based on two considerations: 1) the spatial distribution of the records, relative to the Gharandal Valley, starting from the southernmost records of Oman to the northernmost records of Iran and Turkey, and 2) the reach of present day moisture bearing cyclones, where the Eastern Mediterranean cyclones reach as far south as the northern parts of the Negev desert, while the southern sources (e.g. ARSTs) reach into Wadi Araba (Kahana et al., 2002) (Figures 6.4 and 6.5 and see Chapter 2, 2.2).

Starting from the southernmost Hoti cave (Hoti in Figure 6.4) records of Oman, pluvial conditions are recorded at 200-180 kyr BP (H in Figure 6.5), as reflected by depleted speleothem calcite ($\delta^{18}O_c$) values of -8 ‰ and -5 ‰ compared to the early Holocene values of -6.5 ‰ to -4 ‰, and the present-day precipitation $\delta^{18}O_p$ values of -4.5 to +1‰ and -10 to -2‰, from the northern and southern-driven precipitation over northern Oman and the present-day monsoon precipitation $\delta^{18}O_p$ values of -1 and +1‰ over southern Oman. This depletion in the isotopic values was attributed to a northward migration of the ITCZ and increase in summer monsoon precipitation during peak interglacials (Fleitmann and Matter, 2009). To the north of Oman, in the United Arab Emirates (Sibetah in Figure 6.4), Parton et al. (2015a) reported wetter conditions and activation of the drainage system based on alluvial fan deposits from Al Sibetah. The deposits, clasts and fine siliciclastic sediments, from the site indicate periods of drainage activation and clast deposition that fines upward into silt-rich beds. The presence of palaeosols, roots and bioturbation suggest that vegetation was present at times. Through multi-proxy analyses of the sediments' granulometric, magnetic and geochemical composition, the authors reported several phases of stream activation and aggradation and the development of vegetated landscapes. These phases

persisted during different times in the past, particularly at 158.7±12.9 ka (mean depositional age) (MIS 6), 130 to 88 ka (MIS 5) and during early MIS3 (S in Figure 6.5). The records indicated that during the MIS 6 phases, a mix of C3 and C4 vegetation was present (based on phytolith data) associated with a depletion in $\delta^{18}O$ values, finer sediments particle sizes, and decrease in salinization during periods of vegetation landscape development. The authors reported that these wet phases were driven by monsoon precipitation coinciding with the intensification of monsoon activity during an interstadial at ca. 160 to 150 ka. The authors emphasized the heterogeneity and the importance of such terrestrial archives in interpreting palaeoenvironmental and palaeoclimate records from Arabia as some changes are not recorded in other records, such as speleothems (Parton et al., 2015a). To the northeast, in the Egyptian Eastern Sahara, one of the presently driest regions on earth with ca. 10 mm.yr^{-1} precipitation, fluvial deposition and streams dominated in the hyper-arid region as evidenced by extensive travertines at the Kurkur Oasis (Kurkur in Figure 6.4) suggesting more humid conditions at ~191 ka (K in Figure 6.5) that activated the drainage system and recharged the groundwater (Crombie et al., 1997). Additionally, Miller et al. (1991) suggested a humid lacustrine episode in Bir Tarfawi (Tarfawi in Figure 6.4) at 200±25 ka (T in Figure 6.5) based on U-series dating of the African Ostrich eggshells. While, Smith et al. (2004) suggested a humid mid-late glacial MIS6 (at ca. 140-120 ka, 100 ka and 50 ka) based on U-series ages of fossil spring deposits in the Kharga Oasis (Kharga in Figure 6.4). The authors reported stratigraphic, microfaunal, geochemical and mineralogical data obtained from a ca. 500 km^2 area where no stream tufa are being presently deposited and suggested that wetter conditions prevailed in the Sahara during times between 100 to 300 ka (KH in Figure 6.5) (Smith et al., 2004).

In the Jordanian southern desert (see section 2.4.1), Petit-Maire et al (2010) reported a large (ca. 200 km^2), deep (>40 m) palaeolake in the Mudawwara depression (Mud. in Figure 6.4) corresponding to MIS6 (at ~170 ka and150 ka) (Mud in Figure 6.6), while, in Wadi Araba, Le Béon et al. (2012), at a location ca. 15km north of the Gharandal Valley, suggested a humid alluviation and hydrological activation period at 163±19 ka (WA in Figure 6.5) (see Chapter 2; 2.4.1). In addition, in northern Negev, major humid intervals reflected by speleothem growth prevailed during the glacial MIS6 at 190-150 ka near Tzavoa Cave (see section 2.4), driven by the EM cyclones where precipitation was >300 mm.yr^{-1} (Tzav. in Figure 6.4) (Vaks et al., 2006). Nonetheless, arid conditions,

similar to present, prevailed from 150-144 ka and from 141 to 140 ka (TZ in Figure 6.5) (Vaks et al., 2006). In addition, Frumkin et al. (2011) suggested a generally wetter MIS6 period, compared to MIS7 and MIS5, in the northern Negev as evident by speleothem deposition, and argued that this wet period experienced increased rainfall, during which, the rainy season lasted longer. However, the exact amount of palaeorainfall cannot be identified (Frumkin et al., 2011).
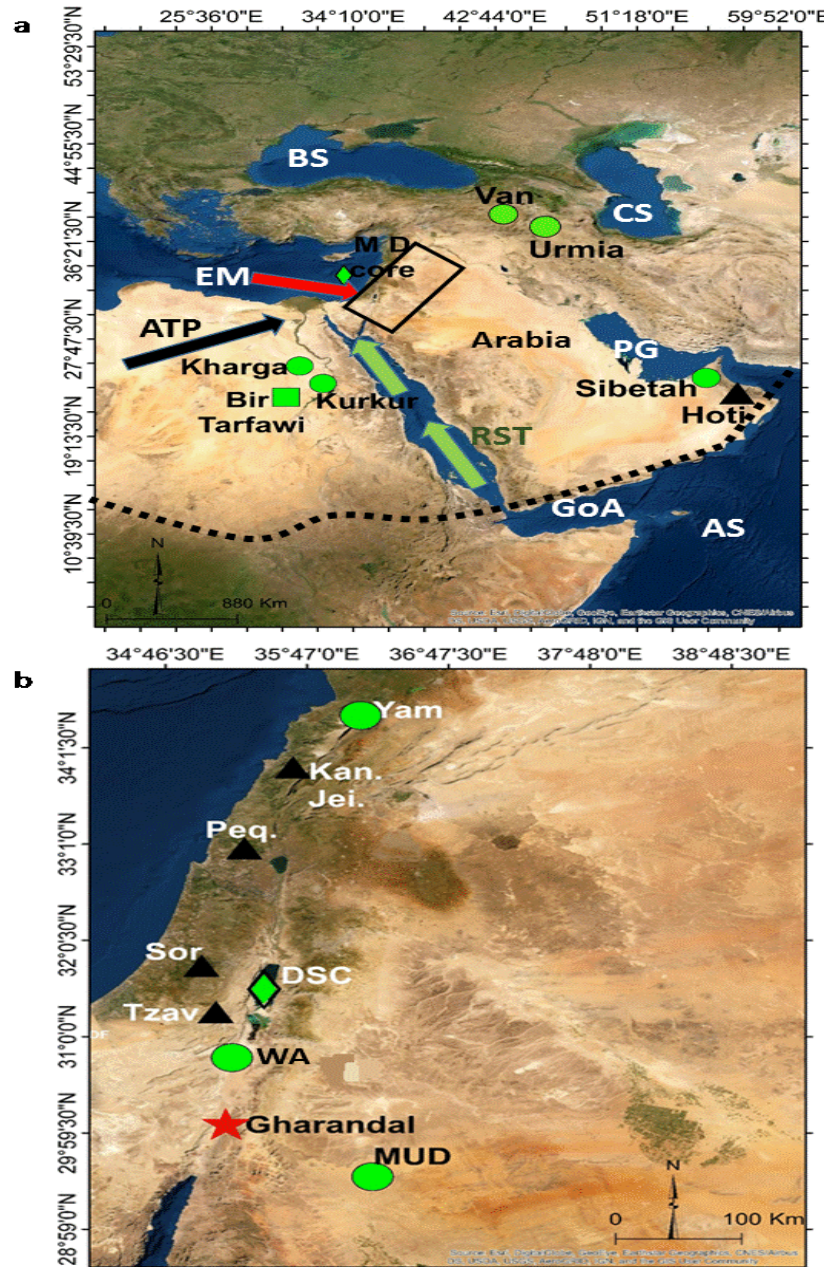
Figure 6.4 Maps showing the Gharandal Valley study area (**GH**) and locations of selected key palaeoclimate records of MIS6 discussed in section 6.5. a) Regional records. Black inset box shows the location of b. b) Local records of the Levant. **Hoti:** Hoti Cave, Oman, **Sibetah**: Al Sibetah, United Arab Emirates, **Kurkur:** Kurkur Oasis, Egypt, **Bir Tarfaw:i** Bir Tarfawi, Egypt, **Kharga**: Kharga Oasis, Egypt, **Mud**: Al Mudawwara, Jordan, **WA**: Wadi Araba, **Tzav**: Tzavoa Cave, Israel, **DSC**: The Dead Sea records, **Sor**: Soreq Cave, Israel, **Peq**: Peqiin Cave, **Kan, Jei**: Kanaan Cave, Lebanon,**Yam**: Yammouneh Basin, Lebanon, **Urmia**: Lake Urmia, Iran, **Van**: Lake Van, Turkey, **MD core**: MD 84-64 core. **Speleothems** (Black triangles), **Lacustrine records** (Green circles), **Marine Core** (Green Diamond). **EM**: Eastern Mediterranean Sea. **BS**: Black Sea. **CS**: Caspian Sea. **RS**: Red Sea. **GoA:** Gulf of Aden. **AS**: Arabian Sea. **PG**: Persian Gulf. **Red arrow**: EM cyclones. **Black arrow**: African Tropical Plumes. **Green arrow**: Red Sea Trough. **Black dashed line**: the approximate modern northern limit of the summer monsoon precipitation (synoptic systems data from Catlett et al. (2017); Torfstein et al. (2015)).
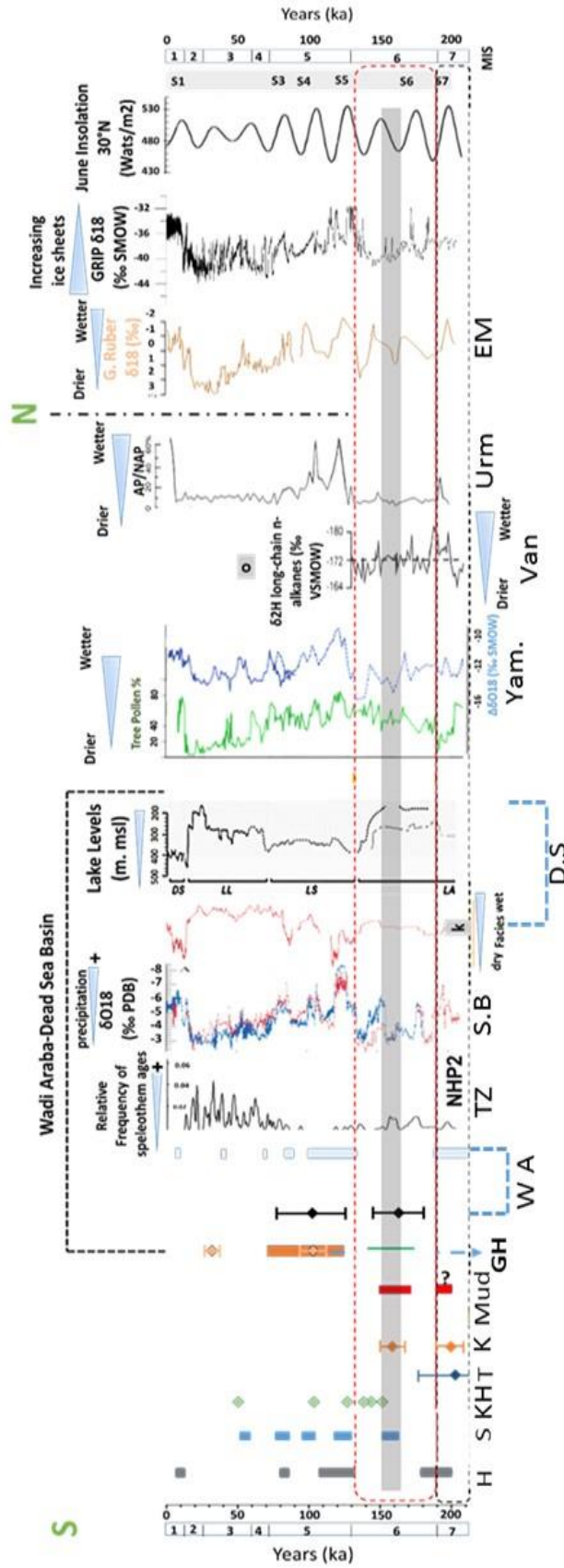
Figure 6.5 Comparison of the selected key palaeoclimate records mentioned in the text. **Grey bar** highlights the wet period suggested in this study based on the mean depositional age estimate. **(H)** Hoti Cave wet periods (Fleitmann & Matter., 2009). **(S)** Al Sibetah site (Parton et al., 2015a). **(KH)** Kharja Oasis (Smith et al., 2004). **(T)** Bir Tarfawi, (Miller et al., 1991). **(K)** Kurkur, (Crombie et al., 1997). **(e)** Jubbah Basin (Parton et al., 2018). **(MUD)** Mudawwara, (Petit-Maire et al., 2010). **(GH)** the Gharandal Valley (orange diamonds: Mischke et al., 2017; orange bar: Al-Saqarat et al., 2020). **(W A)** Wadi Araba alluviation (Le Béon et al., 2012) and Wadi Araba Travertines (Livnat and Kronfeld, 1985). **(TZ)** Tzavoa Cave speleothem growth (Vaks et al., 2006). **(S.B)** Soreq (blue) and Peqiin (red) δ18O records, (Bar-Matthews et al., 2003). **(D.S)** DSDDP 5017-1 Dead Sea core facies analysis, (Torfstein et al., 2015) and DSB lakes levels, DS: Dead Sea, LL: Lake Lisan, LA: Lake Amora, (Waldmann et al, 2010). **(Yam)** Yammouneh Basin, (Gasse et al., 2011). **(Van)** Lake Van, (Guillemot et al., 2019). **(Urm)** Lake Urmia (Djamali et al., 2008). **(EM)** East Mediterranean Sea, (Kallel et al., 2000). **(GRIP)** Greenland Ice Core Project (GRIP) ice core (in ‰) (Johnsen et al., 1997). **(Insolation)** June Insolation 30ºN (Wm⁻²). MISs: (Lisiecki and Raymo, 2005). **NHP2**: Neqev Humid Period 2 (Vaks et al., 2006).

In the Dead Sea Basin (DSC in Figure 6.4), to the north of Wadi Araba, relatively high stands of Lake Amora (LA), a precursor of the Dead Sea (see 2.4), indicate a generally humid MIS6, compared to the present day environment (DS in Figure 6.5) (Waldmann et al., 2010; Torfstein et al., 2015). In fact, the MIS6 period represents the longest wet stage in the documented LA sediments (~740 ka to 140 ka), during which, enhanced supply of freshwater was sustained for a long time (Torfstein, 2017). Facies analysis of a deep core from the Dead Sea also shows more wet facies (high lake levels) during MIS6, compared to the extreme hyper arid halite facies during MIS7 and MIS5 (Torfstein et al., 2015). In addition, based on pollen records from the same deep core, the late MIS6, specifically at 147.3 ka to 130.9 ka, is suggested to have been relatively semi-arid to arid in the low altitudes with dominant desert vegetation, while, the relative frequency of pistachio, Amaranthaceae and non-Artemisia Asteraceae plants slightly increased suggesting that the air temperature over the DSB had not declined significantly and that the dominant climate over the central and northern DSB highlands was sub-humid ($\geq$400 mm.yr^{-1} precipitation) (Chen and Litt, 2018).

This suggestion of wet intervals during MIS6 in the DSB, southern Jordan, the Sahara and Arabia is also reflected in the Soreq Cave and Peqiin Cave δ^{18}O records (Sor. And Peq. in Figure 6.4, respectively), where lighter δ^{18}O values, compared to interglacials, are recorded. Two significant low δ^{18}O values of ca. -5.6 ‰ and -6.2 ‰ in the Soreq record, occur at 180 ka to 178 ka and at 155 ka to 152 ka, respectively, and are attributed to increased rainfall. The excursion at 155 to 152 ka show a change of about 3‰ from ca. -3 ‰ to ca. -6.2 ‰ (S.B in Figure 6.5) (Bar-Matthews et al., 2003).

To the north of the DSB, in the central Levant, the speleothem record of the Kanaan Cave in Lebanon (Kan Jei. in Figure 6.4 and see section 2.4) provides a continuous record of climate variability of the Levant during mid MIS6 (ca. 163 ka to 154 ka) (Nehme et al., 2018). Nehme et al. (2018) observed a change into more humid conditions near the Kanaan Cave based on lower δ^{18}O values, mean -5.18 ‰, compared to the early MIS6 δ^{18}O values, mean -3.69 ‰. The generally low δ^{18}O values, speleothem growth rates and relatively low δ^{13}C values lead Nehme et al. (2018) to suggest a wet mid MIS6 with increased seasonal rainfall compared to the early MIS6. Four wet phases were recorded at 155.3 ka, 155.8 ka, 159.7 ka, and 162.7 ka, corresponding to interstadials. North of Kanaan Cave, the Yammouneh palaeolake (Yam. in Figure 6.4 and see section 2.4) sedimentary record points toward variably arid conditions that favour physical erosion through

MIS6 and conditions of efficient moisture at the late MIS6, compared to the other glacial periods. At 175-165 ka, the authors recorded a peak in carbonates and subaquatic plant pollen indicating high local water availability (Yam. In Figure 6.5) (Gasse et al., 2011).

To the north of the Levant, the MIS6 records from Lake Van and Lake Urmia in Turkey and Iran, respectively (Van and Urmia in Figure 6.4), suggest a general dry glacial prevailed over the Iran and Turkey (Van and Urm in Figure 6.5), compared to the interglacials MIS7 and MIS5. Guillemot et al. (2019) suggested a generally cold and dry MIS6 with relatively wet episodes reflected in elevated TOC and δ^2H values only at the onset of MIS6 around Lake Van (Van in Figure 6.4). However, two wetter periods synchronous with interstadials are noted. Likewise, the pollen record from Lake Urmia in Iran (Urmia in Figure 6.4) suggests general dry semi-desertic conditions through MIS6 dominated by a steppe, mainly Artemisia and grasses, vegetation through the entire glacial period (Djamali et al., 2008).

The new OSL age estimates from the GH2 section in the Gharandal Valley (Grey bar in Figure 6.5) fit well with the MIS6 humidity (effective moisture and water balance) records from the Levant, the Sahara and Arabia. Based on the GH2 section sediments' proxy records, the transition into more persistent wetland conditions, probably driven by precipitation at times, at ca. 158±7 ka (mean depositional age) is consistent with the humid conditions in Arabia (at ca. 158.7±12.9 ka) and the formation of a large lake/wetland in southern Jordan (ca. 170 and 150 ka) (Petit-Maire et al., 2010). It is also consistent with the hydrological activation in Wadi Araba, speleothem growth in the Negev and the Dead Sea (Lake Amora) high lake levels. In addition, this enhanced wetness is also recorded in the Soreq Cave and Peqiin Cave δ^{18}O records (Bar-Matthews et al., 2003) and records from the northern Levant (Nehme et al., 2018; Gasse et al., 2011).

Three possible "black mat" beds, recognized in the field by their dark to black colour in the GH2 section, are stratigraphically within the OSL age estimate limits. In addition, the aridification trend reported in the records (e.g. Chen & Litt, 2018) towards the end of MIS6 might be recorded in the upper ca.1.5 m of the GH2 section, where the proxies indicate the transition into more fluvial in-wash and catchment disturbance conditions. However, this requires additional dating control from the uppermost part of the section to constrain its age estimate.

Furthermore, the Gharandal Valley is located along the MIS6 migration route linking Africa with the Levant and Arabia (Frumkin et al., 2011; Breeze et al., 2016), particularly in the central parts of the Mudawwara/Tabuk Corridor (Breeze et al., 2016). The timing and routes of modern human migration out of Africa (OoA) are still debated (Breeze et al., 2016; Groucutt et al., 2021). Until recently, fossil dates from Skhul (at ca.130-100ka) and Qafzeh (at ca.100-90ka) caves have been considered the oldest later Levantine *H.sapiens* fossils outside Africa (Grun et al., 2005). However, a recent study reported ages of a maxilla and associated dentition (at 177 ka to 194 ka), discovered at Misliya Cave (Hershkovitz et al., 2018), ca. 200 km to the northwest of the Gharandal Valley. Thus far, these dates represent the earliest modern human fossils located outside Africa and suggests that the dispersal of the *Homo sapiens* out of Africa started earlier than previously documented. Accordingly, and considering the poor MIS6 records of southern Jordan, the MIS6 wetland of Gharandal (158±7 ka mean depositional age) along with the lake/wetland of Mudawwara (~170 ka to 150 ka) may have been significant sources of water during MIS6 and the early modern human dispersal out of Africa. This also supported by the presence of lithic artefacts in the valley indicating that the Gharandal Valley was visited by early AMH during different periods in the past (Henry et al., 2001; Al-Nahar and Clark, 2009; Al-Saqarat et al., 2020).

6.5.1 Moisture sources

As discussed earlier, the Levant climate records spanning the glacial MIS6 are scarce, sporadic and to some extent contradictory. Inconsistencies in the records seem to reflect site-specific conditions and the physiography controlling the degree of impact of synoptic scale systems in terms of precipitation, evaporation and temperature (e.g. Jones et al., 2017; Chen and Litt, 2018). High lake stands in the DSB, Negev speleothems growth, Wadi Araba alluviation and wetlands and lacustrine sediments in southern Jordan, the Sahara and Arabia during the glacial MIS6 correspond to dry conditions in Turkey and Iran. The MIS6 humid intervals correspond to interstadials, decreased ice sheets and the formation of the glacial sapropel S6 (at 180-170 ka), that was formed under relatively wet conditions regardless of the glacial conditions in Europe (Kallel et al., 2000). The southern Levant presently receives moisture from three main sources: (1) Eastern Mediterranean (EM) cyclones, (2) storms entering the region from the south through the Red Sea Trough (RST), and (3) tropical plumes originating from northeast Africa (ATPs) (see Chapter 2, 2.2). These systems largely contributed

to changes in hydrodynamics during the Pleistocene (Enzel et al., 2008; Waldmann et al., 2010; Parton et al., 2015; Catlett et al., 2017; Abed and Yaghan, 2000), however, resolving the timing and the extent of moisture from these systems is still debated (Parton et al., 2018). The main source of rainfall to the Levant today are the EM (winter) cyclones, which presently reach as far south as the northern Negev (Kahana et al., 2002). Enzel et al. (2008) argued that the EM cyclones were responsible for the high Lake Lisan stands during the last glacial, while the northern Negev Highlands would not have allowed these Lows to reach farther south into Wadi Araba and southern Jordan. Similarly, as suggested for the last glacial period (Enzel et al., 2008), during the glacial MIS6, the high stands of Lake Amora may be explained by the effect of the Northern Hemisphere ice sheet that triggered a southward migration of the mid-latitude westerlies allowing them to enter the Levant and provide moisture over the DSB, this coupled with decreased air temperature might have reduced evaporation and enhanced air humidity over the Lake (Enzel et al., 2008). This southward migration of the moisture bearing system might have reduced precipitation to the north of the Levant during glacials, and thus resulting in arid records in Turkey and Iran. Nevertheless, another assumption is presented to explain the humid intervals of the Negev, Wadi Araba, the Sahara and Arabia, where it could be attributed to a southerly (monsoon related) source of moisture (e.g Livnat and Kronfeld, 1985; Petit-Maire et al., 2010; Frumkin et al., 2011; Vaks et al., 2013; Parton et al., 2015a). In addition, the ATPs were suggested to have contributed in bringing moisture into southern Levant during the Quaternary (Enzel et al., 2008; Armon et al., 2018). The extent of ATPs is not studied yet in Jordan, however, at present, they reach into the southern Negev (Kahana et al., 2002), and they generate intense rainfall that causes geomorphological changes. The importance of the groundwater in the Gharandal Valley wetland deposition and the broad alluvial aquifer feeding the spring may suggest that the EM cyclones delivering precipitation over the DSB, and recharging the groundwater aquifer, associated with a decrease in temperature may have contributed to maintaining the Gharandal wetland during the glacial MIS6.

The Gharandal Valley location between the southern (Arabia) and northern (DSB) wet conditions, probably suggest an intensification of one or both of the winter and summer precipitation during glacial times. This positive moisture balance, during the intensification of both the southern summer monsoon precipitation and the EM cyclones, may have maintained standing water bodies in the Gharandal Valley,

alternating with fluvial deposition and basin in-wash during periods of reduced moisture availability reflected by the dominance of fluvial deposition (sand-dominated) lithofacies. These events may have fed the wetland and, together with the elevated groundwater level, maintained the water bodies. This moisture availability is also recorded in the GH2 sediments' proxy records as a possible shutdown of the aeolian system during the deposition of the wetland beds. Even though some authors argue against monsoon intensification during glacials (e.g. Catlett 2017), other studies indicated that during peak monsoon intensification the monsoon precipitation penetrated northward into Arabia (Parton et al., 2015a). The presence of the individual Mudawwara palaeolake at ca. 170-150 ka in southern Jordan, the evidence of enhanced monsoon in Al Sibetah in Arabia (Parton et al., 2015a), together with the new record from the Gharandal Valley, probably sugget that a northward migration of the monsoon precipitation may be more supported to explain the presence of significantly wetter conditions in southern Jordan during MIS6 (ca. 150 to 160 ka) as also recorded in the Arabian Sea core records represented by elevated monsoon factor values (Clemens and Prell, 2003). Thus, probably a combined intensification of the northeastern (winter) and southern (summer) precipitation, during stadials and interstadials, respectvely, was responsible for the formation of the Gharandal wetland.

6.6   Chapter conclusions

This study of the Gharandal Valley sedimentary sequences has provided the first detailed sedimentological and geochemical analyses of more than 30 m of combined sedimentary sequences and the first MIS6 record (spanning 161±12ka to 154±13ka) from the Gharandal Valley in southern Jordan.

The results indicated that the deposition of thick wetland beds is primarily located near the present day valley outlet. The deposition in the valley was cyclical. For most of the main sections (GH1 and GH2), the deposition was mainly the result of the valley outlet damming and fluvial in-wash events resulting in thin wetland beds.

The results of this project agree with the conclusions of Mischke et al. (2017) and Al-Saqarat et al. (2020), that the Gharandal sedimentary sequences represent a spring-fed wetland settings, particularly in the lower 7m of the GH1 section. but suggests that it aggraded into a possible precipitation-fed wetland towards the top of the sections near the valley outlet. The new age estimates amend the wetland age into MIS6. This also amends the previously reported timing of the valley damming (Al-Saqarat et al., 2020) to at least older than 161±12ka, thus indicating

the need for a better dating control of the damming timing. The new age estimates amend the wetland age into MIS6. The change in the valley hydrodynamics and more persistent spring discharge is noted during the period spanning ca. 161±12ka to 154±13ka and corresponds to periods of suggested positive moisture balance in the southern Levant and Arabia suggesting probable intensification of both southern and northeastern precipitation sources. Further microfossils analysis and age estimates, while considering the present understanding of the OSL dosimetry calculations and the valley sedimentological variability and hydrodynamics, are needed to support the previously published ostracod assemblages and to further constrain the lateral and vertical evolution of the wetland and to constrain its exact spatial and temporal extents within the valley. Nonetheless, the Gharandal Valley wetland represents an example of site-specific response to hydrodynamic and morphological conditions (e.g. Jones et al., 2017; Chen and Litt, 2018). The presence of a wetland spanning the glacial MIS6 and possibly MIS5 is significant in the southern Levant and contributes to our understanding of the Quaternary environmental records in an important region. This wetland is also of importance in understanding the AMH routes during their earliest migration out of Africa, together with the Mudawwara lake/wetland, they represent important sources of water during these early periods.

Chapter 7. Lake Lisan DS1 section

7.1   Introduction

This chapter presents the Lake Lisan DS1 section lithology and lithostratigraphic units with the sediments' sedimentological and geochemical characteristics including a brief discussion about the DS1 diatoms. Then, the DS1 laminae thicknesses and the carbonate laminae composition is presented. Following this, the DS1 chronology and corrections for tectonic processes are presented. Finally, a discussion of the DS1 sediments as relative lake level indicators and as short-term hydroclimatic variability indicators is discussed, followed by the hydroclimatic implications of the DS1 sediments with an initial assessment of the changing importance of the synoptic scale systems and moisture sources.

7.2   DS1 section

As suggested by Kaufman et al. (1992), and later confirmed by several authors (e.g. Bartov et al., 2002; Torfstein et al., 2013a), the most representative Lake Lisan exposed sections to be investigated along the western side of the Dead Sea Basin (DSB) are located in the central to southern DSB, e.g. Perazim (PZ) and Massada (MS) (Figure 7.1a), where continuous, ca. 40 m sequences, undisturbed by high fresh water input and erosion, can be obtained. This was emphasized on the eastern side of the DSB by Abed and Yaghan (2000), Landmann et al. (2002) where continuous well preserved Lake Lisan laminated sequences were recovered near the Lisan Peninsula (LSM2 in Figure 7.1 a). The DS1 section (Figure 7.1) is located in close proximity to the Lisan Peninsula, within an area of extensive Lisan Formation sedimentary exposures. This section was chosen based on several factors. The section is easily accessible and located at close proximity to the main road which was necessary considering that the author was alone in the field. In addition, the section sedimentological variability and lithology shows that it records the lake conditions during different periods as reflected by alternations between white and pale laminae sequences and primarily detrital sections. The presence of a gypsum bed was also considered as it can be used as a stratigraphic anchor point to correlate with sections from the western side of the basin.

The DS1 section (Figures 7.1 b) is a ca. 4.6 m lacustrine laminated sedimentary sequence, at a basal elevation of -338 m asl. The DS1 section was sampled in 16 (35*5*5cm) box samples as explained in the Methodology Chapter (Chapter 3; 3.3.2). From this section, 55 (c. 1 cm^3) bulk sediment samples were collected, at

an interval of c. 5-10 cm, and analysed for chemical composition (through conventional XRF), magnetic susceptibility (K) and particle size distribution, while 95 samples at an interval of c. 5 cm were analysed by Loss On Ignition (LOI) to estimate carbonate content. The samples were collected at equal intervals and based on lithological changes if present.
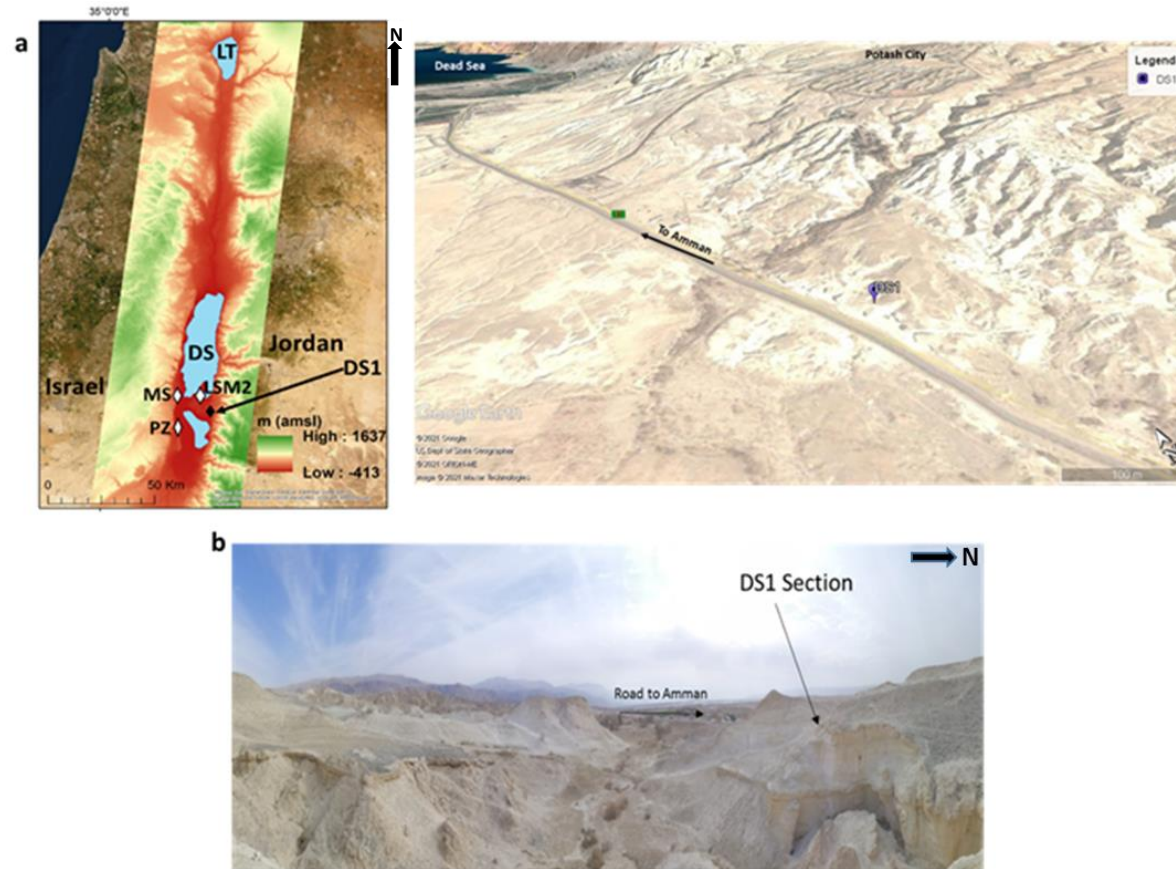
Figure 7.1 a) Map showing the DSB and the present-day Dead Sea (DS) with locations of main sites discussed in the text (left), and a close up view of the DS1 section location relative to the Potash city and the DS. **MS**: Massada, **PZ:** Perazim. **LT**: Lake Tiberius. **DS1**: DS1 section of this project. b) Westward view photograph showing the DS1 section and the lacustrine sedimentary exposures in the vicinity.

7.2.1 DS1 Lithology

The DS1 section was investigated and lithological and colour variations described in the field. Accordingly, the DS1 section comprises three distinct facies as follows:

7.2.1.1 Alternating pale and dark laminae packages

This facies is primarily comprised of alternating pale and dark laminae. These packages are referred to as alternating aragonite and detrital laminae (*aad*) facies in the literature (Figure 7.2 a) (see Chapter 4; 4.4.2.3) (e.g. Abed and Yaghan, 2000; Bartov et al., 2002; Ben Dor et al., 2019). This facies is mainly comprised of ca. 1 mm couplets of pale and dark laminae, however, at some locations ca. 4 mm pale laminae alternate with ca. 1-2 mm dark laminae.

7.2.1.2 Alternating dark laminae packages

This facies is primarily composed of grey to dark detrital (silt to clay sized) laminae forming one thick detrital bed with minor pale laminae (Figure 7.2 b). In the literature, this facies is referred to as laminated detrital (*ld*) facies. The detrital laminae vary in colour from grey to dark. The laminae thicknesses range from ca. 0.5 mm to cm scales. These packages are at some locations intercalated by mm-scale pale laminae.

7.2.1.3 Massive gypsum-dominated facies

Within the Lisan Formation, thick (tens of cm) gypsum-dominated beds are found (see also Chapter 4, 4.4.2.4) (Stein, 2001; Torfstein et al., 2013a). In the DS1 section, a thick, ca. 30cm, gypsum dominated bed is found at ca. 2 to 2.3 m above the section base.
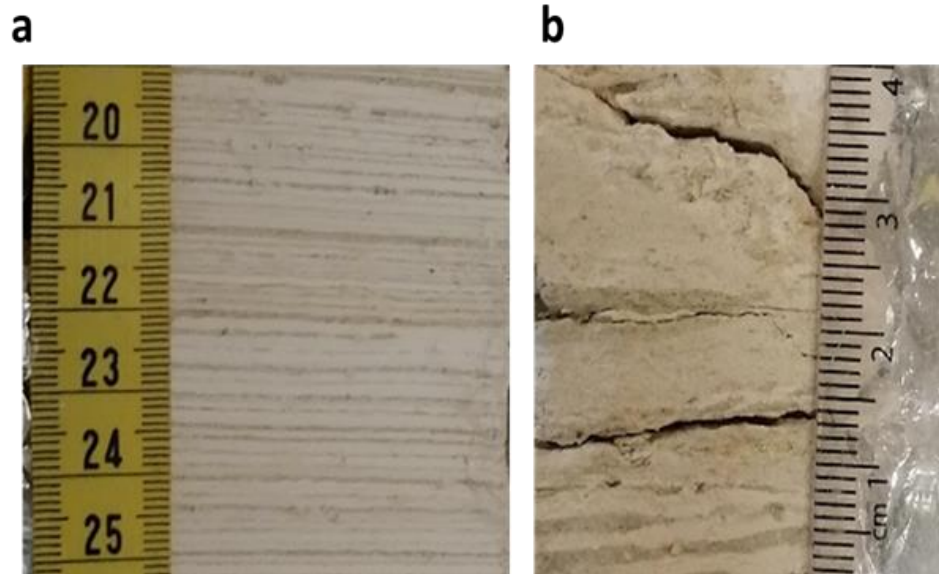
Figure 7.2 a) Representative sample of *aad* facies at ca. 1 to 1.05 m above the section base. b) Representative sample of *ld* facies at ca. 1.7 to 1.74 m above the section base

7.2.2   Sedimentary facies analysis

Following the first order field-based assignment of the facies, the PAleontological Statistics Software (PAST, v. 4.03; Hammer and Harper, 2006) was used to run the sedimentary facies PCA-LDA analyses (See Chapter 3, 3.4) for the 55 DS1 bulk sediment samples granulometric and geochemical compositions.

Based on the PCA analysis results (Figure 7.3), the first three eigenvectors explain 67% of the total variance. PCA1 (39%) correlates positively with fine sand (r^2= 0.4; $P<0.05$), very fine sand (r^2= 0.72; $P<0.05$), very coarse silt (r^2= 0.7; $P<0.05$), SiO_2 (r^2= 0.9; $P<0.05$), Fe_2O_3 (r^2= 0.8; $P<0.05$) and Ti (r^2= 0.86; $P<0.05$) and negatively with clay (r^2= -0.5; $P<0.05$), CaO (r^2= -0.67; $P<0.05$) and Sr (r^2= -0.6; $P<0.05$).

The second eigenvector PCA2 (19%) correlates positively with clay (r^2= 0.6; $P<0.05$), CaO (r^2= 0.4; $P<0.05$), Sr (r^2= 0.4; $P<0.05$), Ti (r^2= 0.4; $P<0.05$), Fe_2O_3 (r^2= 0.5; $P<0.05$) and negatively with SO_3 (r^2= -0.76; $P<0.05$) and the very coarse, coarse, medium and fine sand contents. While, the third eigenvector PCA3 (9%) correlates positively with SO_3 (r^2= 0.5; $P<0.05$) and negatively with CaO (r^2= -0.5; $P<0.05$) and Sr (r^2= -0.5; $P<0.05$). Accordingly, the fine sand, very fine sand, very coarse silt, fine silt and very fine silt contents with SiO_2, CaO, Ti, Fe_2O_3, Sr and SO_3 contents, were the dataset used for the LDA analysis (Figure 7.4).

The results of the LDA indicated that 96% of the samples are classified correctly, where the *aad* samples are characterized by silt, clay, CaO and Sr contents, the

ld samples are characterized by the allochthonous elements SiO_2, Ti, Fe_2O_3 and fine sand contents, and the GU samples are characterized by SO_3 content. Only three samples, at the section base, at 72 and 118 cm above the section base, were reclassified from *aad* to *ld* facies based on their composition. Table 7.1 lists the distinction between the three sedimentary facies based on the LDA results.
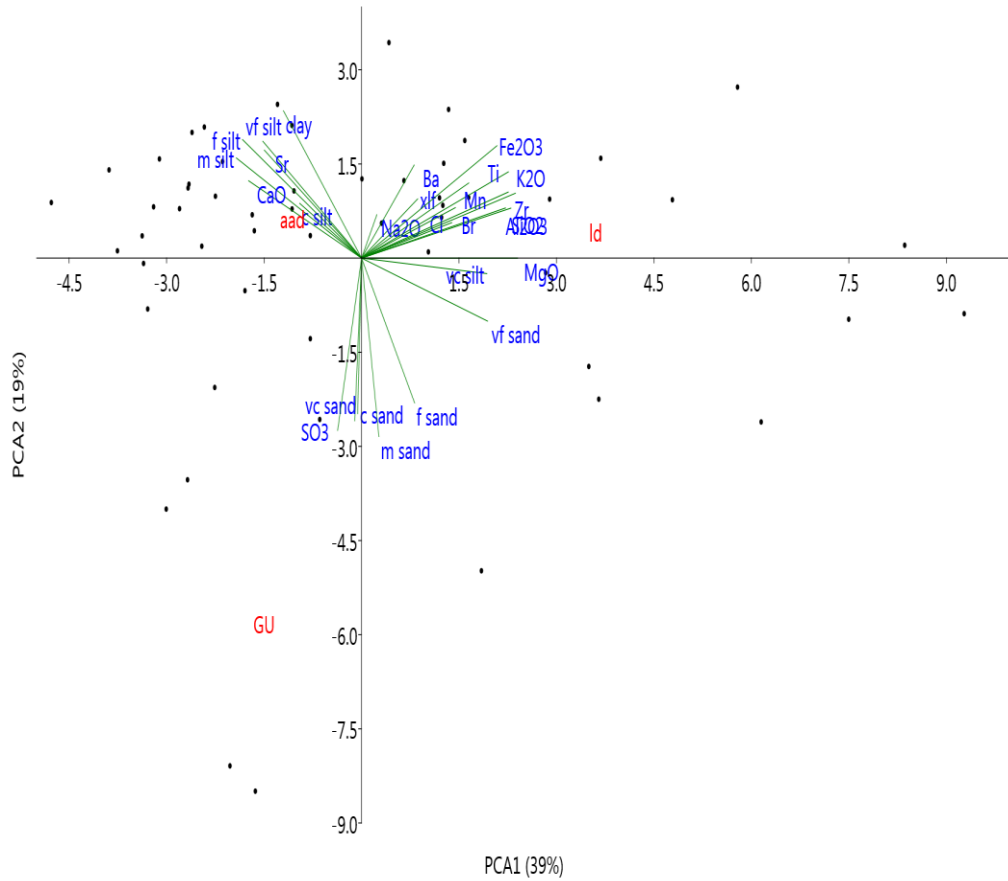
Figure 7.3 PCA analysis of the sedimentological and geochemical contents of the DS1 sediments, showing the first and second eigenvectors and the typical parameters of the three sedimentary facies *aad*, *ld* and GU.
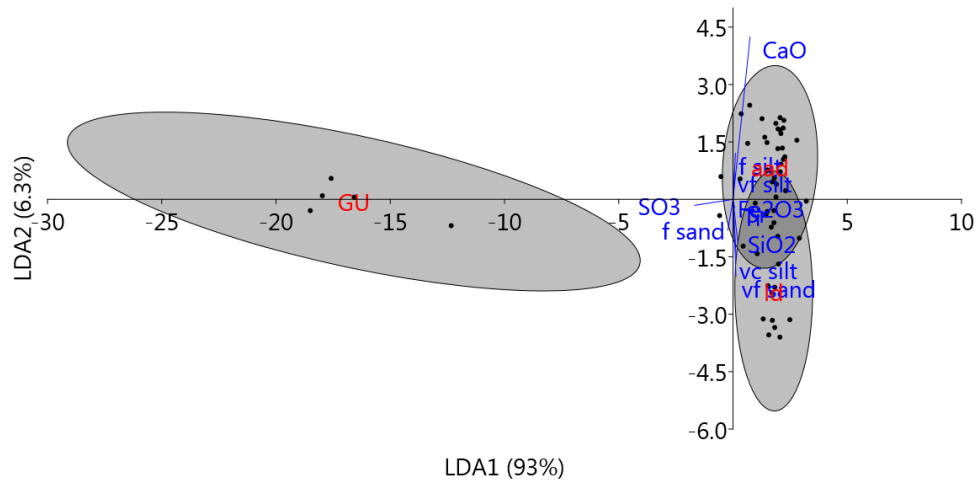
Figure 7.4 DS1 section sediments' LDA analysis of the PCA derived parameters showing the typical contents of the three different sedimentary facies *aad*, *ld* and GU.

Table 7.1 The characteristic compositions of the *aad*, *ld* and GU facies based on the LDA analysis

	f sand vol. %	vf sand vol. %	vc silt vol. %	f silt vol. %	vf silt vol. %	SiO$_2$ %	CaO %	Ti %	Fe$_2$O$_3$ %	Sr %	SO$_3$ %
aad											
Avg.	2.6	8.7	11.6	17.2	12.7	6.7	55.1	0.14	1.7	0.55	1.2
Min.	0	0.88	5	7.4	5.6	2.1	44.17	0.046	0.7	0.313	0.25
Max.	10.7	39.3	20.4	23.8	18.68	14.8	69.24	0.25	2.8	0.78	6.8
ld											
Avg.	5.8	16.9	18	12.4	10	10.5	40	0.22	2.5	0.3	1.8
Min.	1.5	5.6	11	5.05	3.80	3	29.5	0.1	1.24	0.12	0.28
Max.	24.76	42.78	34	18.4	15.6	18.8	54.5	0.34	3.5	0.57	5.04
GU											
Avg.	8.33	8.53	10.6	13.54	10.31	3.4	34.7	0.05	0.5	0.09	36.7
Min.	3.67	7.0	9	9.80	6.74	1	33.2	0.013	0.164	0.05	23.9
Max.	11.4	11.75	11.7	17.70	14.98	10.3	35.9	0.16	1.5	0.15	42.05

7.2.3   DS1 lithostratigraphic units

Sedimentary processes in the DSB are affected by the catchment-wide hydrological conditions (Bani Sakhir, 1996; Stein et al., 1997; Abed and Yaghan, 2000). Lake Lisan water levels are thus considered as a regional "hydro-climatic gauge" (Enzel et al., 2003; 2008). In the DS1 section, alternations of the three facies reflect the lake response to the hydrological conditions in the catchment. These alternations record different episodes of lake limnological conditions, and accordingly the DS1 section can be subdivided into different lithostratigraphic units reflecting the corresponding hydrological and hydroclimatic changes based on the granulometric and geochemical composition of the sediments.

7.2.3.1   Particle size distribution

The results of the particle size distribution analysis show that the different DS1 sedimentary facies have distinct granulometric characteristics (Figure 7.5). The *aad* facies are dominated by silt and clay-sized particles with a main particle mode of 4.7 to 111 μm (mean Mz 25 μm), while the *ld* facies show higher contents of sand-sized particles with a main mode of 6 to 177 μm (mean Mz 114 μm), and the GU facies also show higher sand contents, compared to *aad* with a main mode of 5 to 213 μm (mean Mz 275 μm) and one sample shows a main mode of 1144 μm (Figures 7.5). Coarse sand is present primarily in the gypsum unit samples, however, this could be the effect of gypsum crystals as the gypsum was not completely removed during sample preparation.

Plotting the particle size distributions with the DS1 stratigraphy (Figure 7.6) shows that alternations between sand, silt and clay peaks correspond to changing facies from *aad* to *ld* and GU.
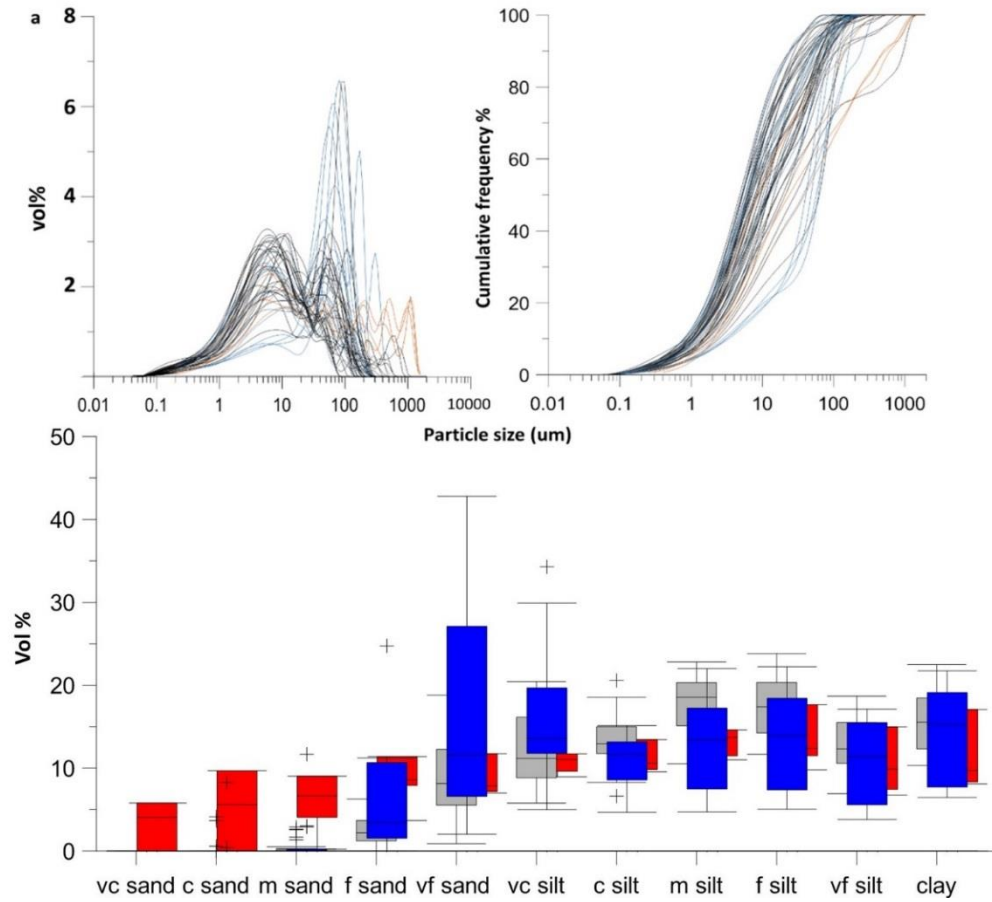
Figure 7.5 a) Particle size distribution frequency curves (left) and Cumulative frequency curves (right) of the DS1 sediments. b) Box plots of the Granulometric composition of the DS1 sediments. Outliers are data located at 1.5 times the interquartile range. **Grey**: *aad* facies, **blue**: *ld* facies, **red**: GU facies
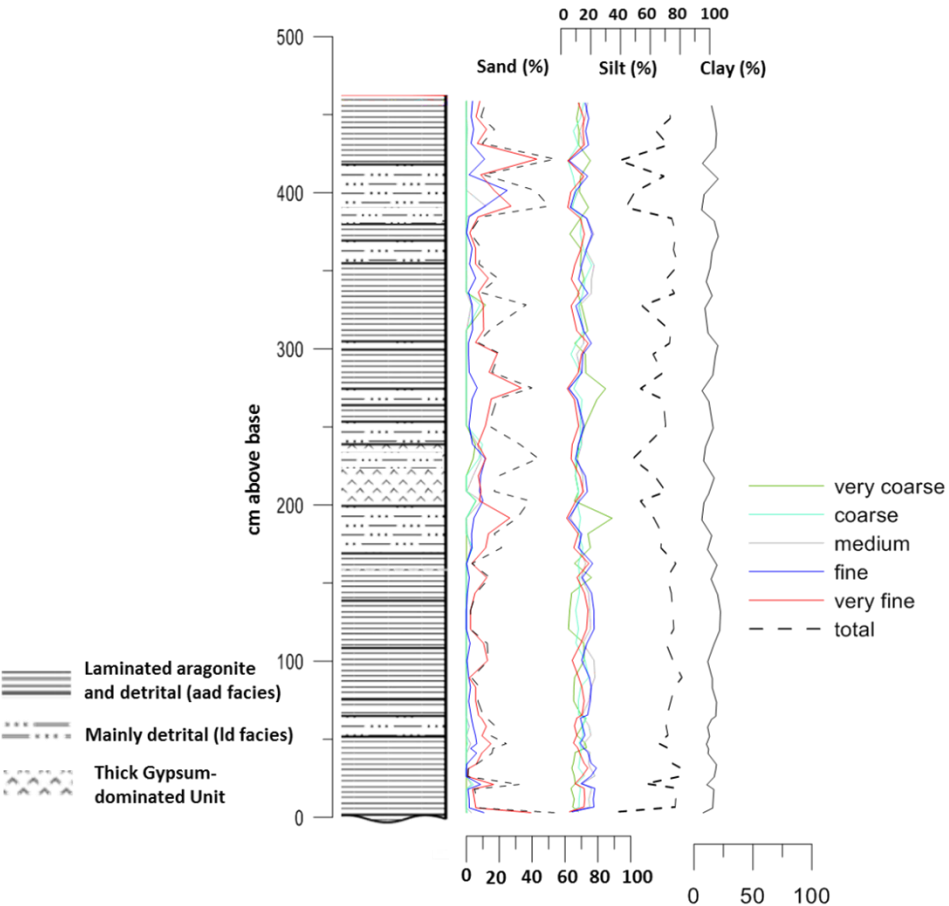
Figure 7.6 DS1 section stratigraphy with the particle size distributions showing the sand peaks corresponding to *ld* facies and the GU, while the silt and clay peaks correspond to *aad* facies.

Based on PCA analysis (Figure 7.7), PCA1 (70%) correlates positively with the silt and clay contents ($r^2>0.7$; $P<0.05$) and negatively with the sand contents. In addition it correlates positively with the mean particle size (Mz) ($r^2=0.87$; $P<0.05$). Accordingly, Mz can be considered as a valid indicator of the particle size distribution variability in the DS1 section.

To further characterize the facies and their dominant transportation processes, the CM diagram (Figure 7.8) (Passega and Byramjee, 1969; Mycielska-DowgiałŁo and Ludwikowska-Kedzia, 2011) shows that the *aad* facies primarily plot as standing water deposition, while the *ld* facies show more graded and uniform suspension transportation processes. These processes probably reflect the location of the DS1 section and the amount of detrital material reaching the site during enhanced and/or reduced catchment in-wash.
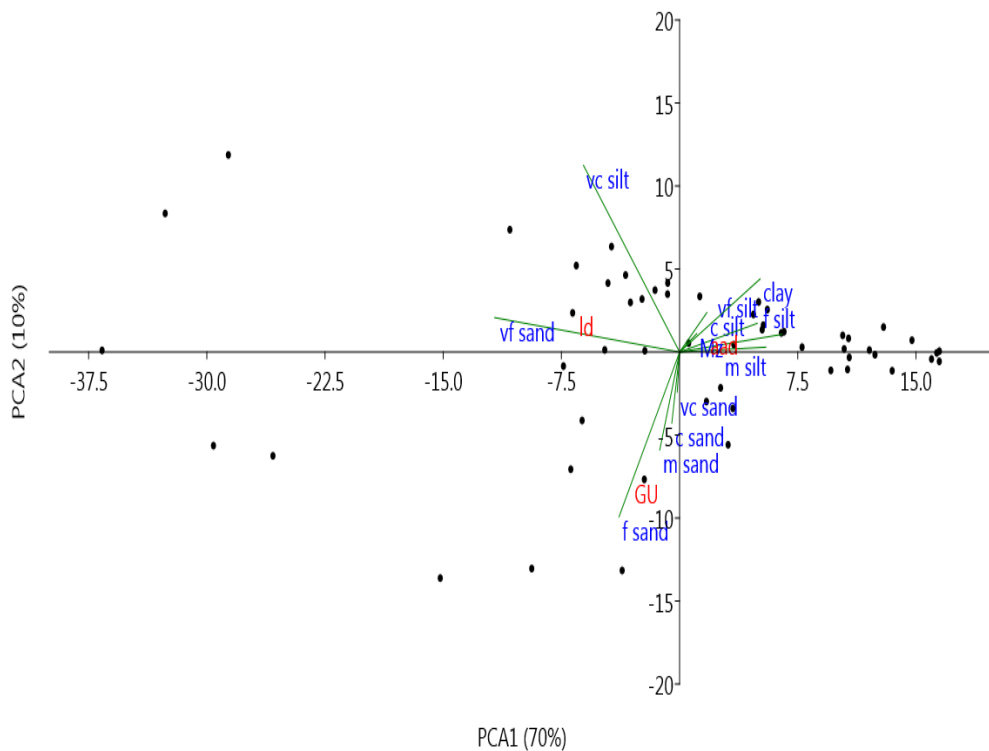
Figure 7.7 PCA analysis results of the granulometric composition of the DS1 section showing the first and second eigenvectors and the typical parameters of the three sedimentary facies *aad*, *ld* and GU.
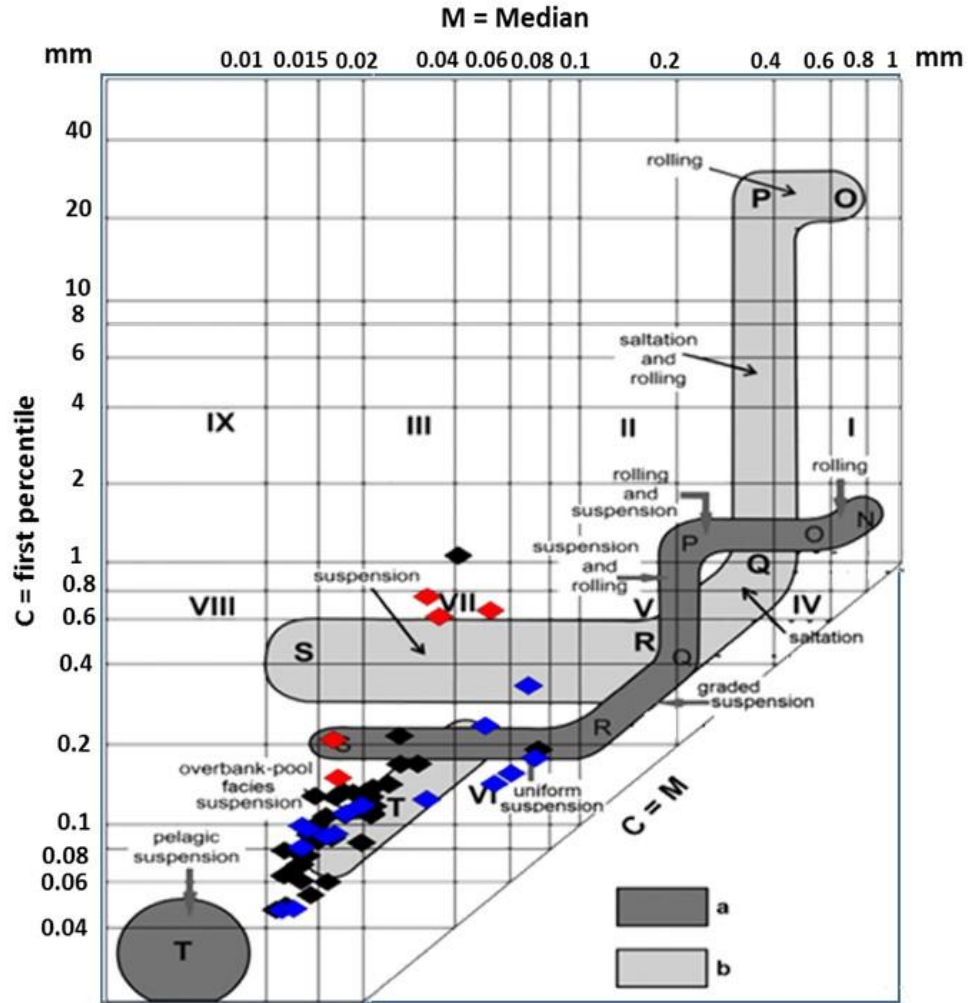
Figure 7.8 10 Complete CM pattern of tractive current deposits for DS1 sediments. **Black: aad facies, Blue: ld facies and Red: GU facies**. a) Dark shade-based on Passega (1964) and Passega & Byramjee (1969); b) Light shaded- based on Ludwikowska Kędzia (2000). I, II, III, IX: rolled grains; IV: High turbulence deposit; V: Low turbulence deposit; VI: Graded suspension; VII: Uniform suspension; VIII: Finest uniform suspension (after Passega and Byramjee, 1969) (Modified from Malgorzata and Ludwikowska-Kedzia, 2011).

7.2.3.2 Bulk geochemistry and magnetic susceptibility

The results of the bulk geochemistry of the DS1 sediments indicate that the three facies are characterized by different element contents, primarily of CaO, SO_3 and SiO_2 (Table 7.2). A high correlation is noted between CaO and Sr with (r^2=0.97, P<0.001). This is in agreement with the results of Landmann et al. (2002), who reported a highly linear relationship between Sr/Ca from HCl-extracts of pure aragonite from the eastern side of the DSB. In addition, CaO correlates negatively with Ti (r^2=-0.5; P<0.001) suggesting its endogenic deposition and Ti correlates positively with Fe_2O_3 (r^2=0.96; P<0.001). Furthermore, K correlates positively with the allochthonous elements (e.g. SiO_2, Fe_2O_3 and Ti) and negatively with CaO, Sr and SO_3 indicating its validity as an indicator of catchment disturbance and in-

wash, which is also indicated by the K variable range values for the three facies: -0.1 to 2.37 (Std. 0.63) for the *aad* facies, -0.2 to 3.4 (Std. 0.96) for the *ld* facies and 0 to 1.1 (Std. 0.43) for the GU facies, which shows that the highest values are for the *ld* facies associated with catchment in-wash.

Generally, the variability in elemental composition and K reflect the lithological variations in the section, where higher values of Ca, Sr correspond to fine-grained sediments and the presence of lighter colour (aragonite) laminae in parts of the section and higher contents of Fe_2O_3 and Ti correspond to elevated sand contents in more detrital sections. The results also highlight the gypsum-dominated unit, marked by higher values of SO_3 and a decrease in CaO and other key elements. Furthermore, an increase in Fe_2O_3, Ti and (κ) occurs following the gypsum-dominated unit probably reflecting a period of enhanced catchment erosion and water input into the lake (lake filling up), which then decreases, marked by an increase in Ca and Sr. Generally, the variations in key chemical elements and K through the DS1 section indicate alternating periods of enhanced and reduced catchment erosion corresponding to the alternation between the different facies.

In order to investigate this variability further and to attempt to combine the environmental proxies, PCA was applied to the sediment's complete elemental composition dataset (Figure 7.9 a). The results indicate that the first and second eigenvectors explain 97% of the total variance. PCA1 (73%) correlates positively with SO_3 (r^2=0.9; P<0.05), and negatively with CaO (r^2=-0.87; P<0.05) and Sr (r^2=-0.9; P<0.05). While, PCA2 (24%) correlates positively with CaO, Sr and SO_3 (r^2=0.5, 0.38 and 0.4, respectively; P<0.05) and negatively with Ti, Fe_2O_3, and SiO_2 (r^2= -0.92, -0.9 and -0.87, respectively, P<0.05).

Since the high SO_3 content in the gypsum bed (5 samples) shows a high effect on driving the PCA results, the analysis was conducted on the datatset after removing these 5 samples in order to show whether the results vary (Figure 7.9 b).

The results showed that the first two eigenvectors explain 97% of the total variance. PCA1 (91%) correlates positively with CaO and Sr (r^2= 0.99 and 0.97, respectively, P<0.05). PCA2 (6%) correlates positively with Al_2O_3 and SiO_2 (r^2= 0.4 and 0.5, respectively, P<0.05). PCA 3 (2%) correlates positively with the SO_3 content (r^2= 0.9, P<0.05). The two PCA analyses indicate that the variance is dirven by similar characteristics. The PCA of the complete dataset is thus used henceforth.

Table 7.2 Elemental and magnetic composition of the DS1 facies. Elements in %, (κ) *10^{-6}SI.

	aad				*ld*				GU			
	Min	Max	avg.	Std.	min	max	avg.	Std.	min	max	avg.	Std.
CaO	44.2	69.2	55.1	6.8	29.5	54.5	39	6.5	33.2	35.8	34	0.9
SiO$_2$	2.1	14.80	6.7	3.4	3	18	10	1.8	1.06	10.3	3.4	38
SO$_3$	0.25	6.8	1.1	1.3	0.28	5	1.8	1.5	23.9	42.05	36.7	7.3
Al$_2$O$_3$	0	3.8	1.4	1.1	0	5.2	2.6	1.8	0	2.9	0.6	1.3
Fe$_2$O$_3$	0.7	2.8	1.72	0.6	1.3	3.5	2.5	0.6	0.16	1.4	0.5	0.5
Na$_2$O	0.00	0.96	0.19	0.18	0	3.8	0.3	1	0.00	0.00	0.00	0.00
MgO	0	2	0.76	0.4	0.25	2.7	1.6	0.8	0.7	1.6	0.9	0.4
K2O	0.005	0.6	0.24	0.15	0.14	0.8	0.5	0.2	0	0.37	0.07	0.16
Ti	0.05	0.25	0.14	0.05	0.1	0.34	0.2	0.07	0.013	0.16	0.05	0.06
Mn	0	0.05	0.02	0.01	0.01	0.05	0.03	0.01	0.006	0.031	0.01	0.01
Sr	0.30	0.78	0.56	0.1	0.13	0.5	0.3	0.1	0.05	0.15	0.09	0.03
Zr	0.00	0.07	0.01	0.01	0.006	0.028	0.01	0.00	0.00	0.01	0.003	0.003
Ba	0.007	0.07	0.01	0.01	0.009	0.03	0.01	0.003	0.002	0.012	0.004	0.004
Br	0	0.03	0.01	0.01	0.008	0.05	0.02	0.01	0.002	0.02	0.005	0.008
Cl	0.02	1.2	0.4	0.3	0.7	4.7	1.7	1	0	0.8	0.16	0.3
(κ)	-0.1	2.3	0.86	0.6	-0.2	3.30	1.2	1	0.00	1.10	0.45	0.4

Since the deposition of gypsum in Lake Lisan is representative of low lake levels and mixing between the upper freshwater layer and the brine (Stein et al., 1997; Torfstein et al., 2013a), PCA1 could be representative of deposition during low lake levels and decreased input of freshwater into the lake, while, with enhanced freshwater input (lower PCA1 values), carbonates (aragonite) are deposited and thus reflect relatively higher lake levels.

While, PCA2 is probably representative of alternations between in-lake deposition (higher values) and catchment erosion (lower values). Figure 7.10 shows the proxies based on the PCA and the elemental ratios and their correspondence to the lithological variations and laminae thicknesses measured in the DS1 section. PCA1 values (higher/lower) agree with the Sr/CaO and SO_3/CaO representing aragonite/gypsum deposition (stable/low lake levels). PCA2 results (higher/lower) correspond to Ti/CaO ratios (lower/higher) reflecting (reduced/enhanced) catchment in-wash processes.

The geochemical composition of the DS1 sediments can also be used to calculate the water balance based on the elements normalized concentartions. The aragonite deposition is represented by the ratio that increases with increased freshwater input (see Chapter 4; 4.4.2.3), while the total detrital input, which is dependent on catchment erosion and aeolian processes, can be estimated by summing the ratios of CaO/(SO_3+Sr), for the detrital carbonate, and Ti/Ca for the siliciclastic input, while the gypsum deposition, representing the reduced freshwater input and aridity, is estimated by SO_3/CaO ratio. Summing the normalized ratios that record freshwater input (Sr/CaO+ CaO/(SO_3+Sr)+ Ti/Ca) and subtracting the gypsum (SO_3/CaO), results in a curve that may reflect the water balance of the lake, in which positive values represent aragonite and detrital deposition and negative values mainly represent gypsum deposition (e.g. Neugebauer et al., 2016). The results of the water balance estimation roughly agree with the previously discussed proxies of catchment erosion/in-lake deposition (wet and dry periods) extracted from the elemental composition PCA analysis (Figure 7.10) where the gypsum deposition is marked by negative water balance and the other parts of the section show alternations between positive and negative water balance conditions.
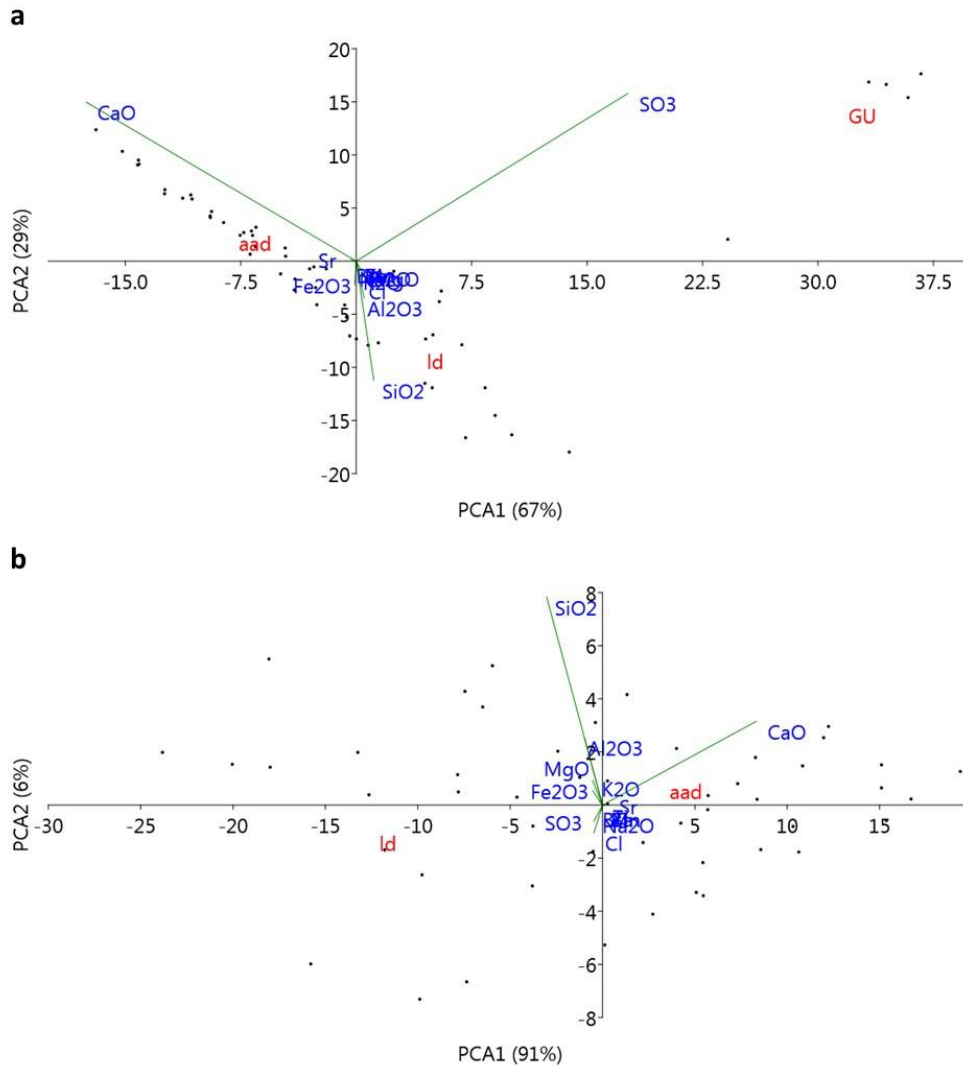
Figure 7.9 PCA analysis results of the elemental composition of the DS1 sediments showing the first and second eigenvectors and the typical parameters of the three sedimentary facies *aad*, *ld* and GU. a) The complete dataset. b) The dataset excluding the GU samples.

Based on the sediments lithology and environmental proxies reflecting particle size variability (Mz), catchment in-wash (Ti/CaO), gypsum deposition (SO_3/CaO) and aragonite deposition (Sr/CaO), four primary lithostratigraphic units (SU1 to SU4) can be distinguished, representing the different periods of limnological and hydroclimatic processes of the DS1 record (Figure 7.10). These units reflect relatively stable lake levels, during which *aad* deposition is dominant, low lake levels during which catchment in-wash and/or gypsum deposition are dominant and lake filling-up stages following low lake levels. These units are discussed in the next section.
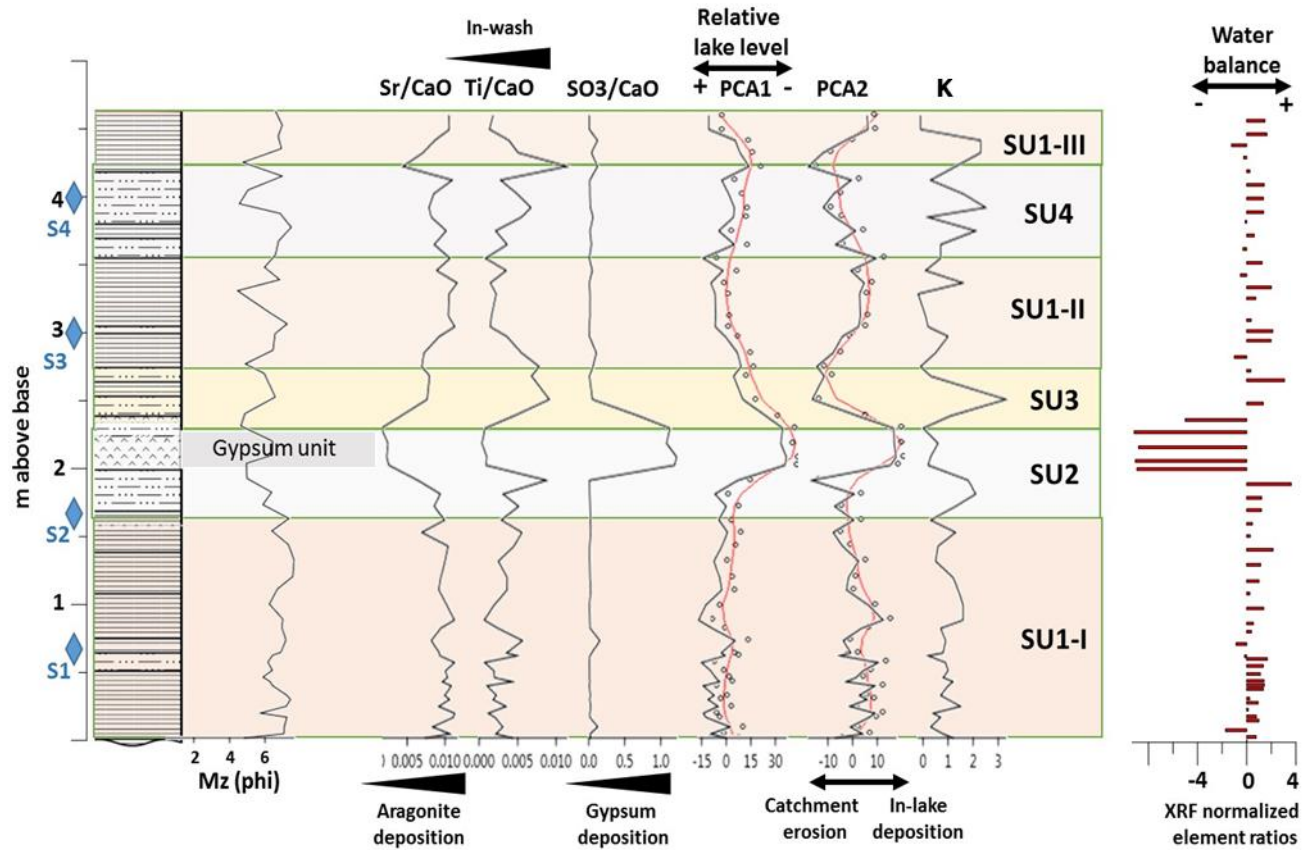
Figure 7.10 The DS1 section stratigraphy with key environmental proxies. **SU**: lithostratigraphic unit. Smooth lines for PCA1 and PCA2 were calculated using "smooth.spline" function in R software with 0.5 smoothing step. **S1-4**: locations of Blocks S1 to S4 discussed in the text (see 7.2.5). For stratigraphy legend refer to Figure 7.6.

7.2.3.3 Lithostratigraphic units

Based on the field-observations and the sediments' composition, four lithostratigraphic units were identified (SU1 to SU4).

7.2.3.3.1 Lithostratigraphic Unit (SU1)

The lithostratigraphic unit (SU1) represents periods of relatively high lake levels as reflected by primarily *aad* deposition in the record lithology. This unit is found in three different parts of the DS1 section (SU1-I to III in Figure 7.10). The SU1 sub-units all comprise fine particle sizes compared to the other lithostratigraphic units.

SU1-I

Lithostratigraphic unit SU1-I represents the lower part of the DS1 section (section base to ca. 1.6 m above base) preceding the dominance of *ld* deposition and the Gypsum Unit deposition. This unit is indicated by primarily *aad* deposition with detrital laminae at some locations corresponding to catchment in-wash. It is characterized by low variability in environmental proxies near its base and a trend towards decreasing in-lake deposition and Sr/CaO ratios and increased catchment in-wash and Ti/CaO. The (κ) and Mz show relatively stable values. SU1-I ends with a change in catchment hydrology and lake limnology towards lake level lowering.

SU1-II

Lithostratigraphic unit SU1-II occurs at ca. 2.75 m to 3.5 m above base following the lake filling up stage (SU3). This unit is marked by a decrease in (κ) values, decreased in-wash processes (Ti/CaO) and elevated aragonite deposition ratios (Sr/CaO).

SU1-III

Lithostratigraphic unit SU1-II occurs in the upper ca. 0.5 m of the section following a period of generally *ld* deposition and enhanced catchment erosion. Similar to SU1-I and SU1-II, this unit is marked by decreased in-wash (Ti/CaO) and elevated aragonite deposition (Sr/CaO) (in-lake deposition). The (κ) values also show a decrease towards the top of the unit.

7.2.3.3.2 Lithostratigraphic Unit (SU2)

The lithostratigraphic unit (SU2) records the driest episode of the DS1 history. This unit starts with high peaks of (κ), compared to SU1, enhanced in-wash processes

and catchment erosion (Ti/CaO), reduced aragonite deposition (Sr/CaO) and *ld* deposition indicating a change in the lake limnological and hydroclimatic conditions. This unit is then dominated by in-lake gypsum deposition of the thick GU, at ca. 2 to 2.3m above the section base, reflecting the lake overturn and lower Sr/CaO and Ti/CaO.

7.2.3.3.3 Lithostratigraphic Unit (SU3)

The lithostratigraphic unit (SU3), at ca. 2.3 to 2.75m above the base, records the lake level rise following the dry SU2 unit. This unit is marked by the highest (κ) peak (3.3 $*10^{-6}$ SI) in the record, enhanced in-wash and catchment erosion processes (Ti/CaO), and increased aragonite deposition (Sr/CaO). This unit comprises mainly *ld* facies deposition and peaks in detrital laminae thicknesses with minor *aad* deposition and a fluctuating Mz values from fine to coarse corresponding to the prominent depositional pattern; i.e. either *ld* or *aad*.

7.2.3.3.4 Lithostratigraphic Unit (SU4)

The lithostratigraphic unit (SU4), at ca. 3.5 to 4.1m above the section base records a change in the lake limnological conditions, where primarily *ld* facies occur. This unit is marked by peaks of thick detrital laminae and in-wash processes (Ti/CaO) with a trend towards lower aragonite deposition near its top with a trend towards coarser Mz values.

7.2.4 DS1 section diatom flora

Diatoms, single-celled benthic siliceous algae, occurrences and variability have been used in different regions around the world to provide significant palaeoenvironmental and palaeolimnological data, considering that each species thrives in its specific ecological conditions (e.g. Metcalfe, 1995; Begin et al., 2004; Swann and Leng, 2009). However, the implementation of this proxy is still limited in the Levant in general and in the DSB in particular (Hartung et al., 2020). Lake Lisan records span ca.70 ka to 14 ka and thus provide an excellent opportunity to investigate the presence, and preservation, of diatoms and the possibility of integrating this proxy with the other sedimentological and geochemical proxies of Lake Lisan.

Begin et al. (2004) investigated the diatoms of Lake Lisan as part of biological indicators to model the palaeosalinity of the Lake Lisan upper layer trends in the DSB. They concluded that, in the Lisan sediments, diatoms are only present in the northern DSB and near its southern end, due to the presence of enhanced freshwater inputs, primarily from the north and to a lesser extent in the south,

which dilutes the upper water layer and reduces its salinity. However, the central area, where the present Dead Sea is located has been considered an area with no diatoms, attributed to the effects of the salt diapir of the Lisan Peninsula (Begin et al., 2004). A recent study, Hartung et al. (2020), aiming to investigate diatom preservation in the evaporitic facies of Lake Lisan ICDP core, reported that, contrary to the above, there is excellent preservation of diatoms in all the facies with high abundance in samples during high lake levels (>300 m bsl) at 62ka and 24ka, and low lake levels (<300m bsl) at 47ka and 11ka. The authors reported diatoms of *Lindavia ocellata species complex, Navicula spp., Nitzschia lembiformis, Achnanthidium sp.,* and *Amphora pediculus* (Hartung et al., 2020). This indicates that further investigation of the diatom contents of the Lisan sediments may provide a new proxy to aid in the understanding of Lake Lisan limnological and environmental history.

Even though a detailed diatom investigation is out of the scope of this thesis, it is intriguing to mention that, in contrast to earlier publications (e.g. Begin et al., 2004), and in agreement with the recent study of Hartung et al. (2020), two aragonite laminae from the DS1 section, at ca.1.6 m above the section base (Block S2, Section 7.2.5), showed contents of well-preserved diatoms (Figure 7.11).

This observation is significant since this is the first time diatoms have been reported from Lisan sediments collected from exposures in the area surrounding the present-day DS and the Lisan Peninsula. Even though the diatoms observed in the DS1 laminae were not identified, this may provide an opportunity for a comprehensive diatom investigation and taxonomical identification, to provide significant data about Lake Lisan diatom flora and the upper water layer dilution events, at close-to-annual to decadal scales, despite previous suggestions that the Lake Lisan area surrounding the present DS was particularly more saline compared to the lake's northern and southern ends (Begin et al., 2004). This understanding of the Lake Lisan diatoms is promising in order to test whether the diatom content is applicable as a lake level reconstruction proxy to support the previously published lake level curves (Hartung et al., 2020).
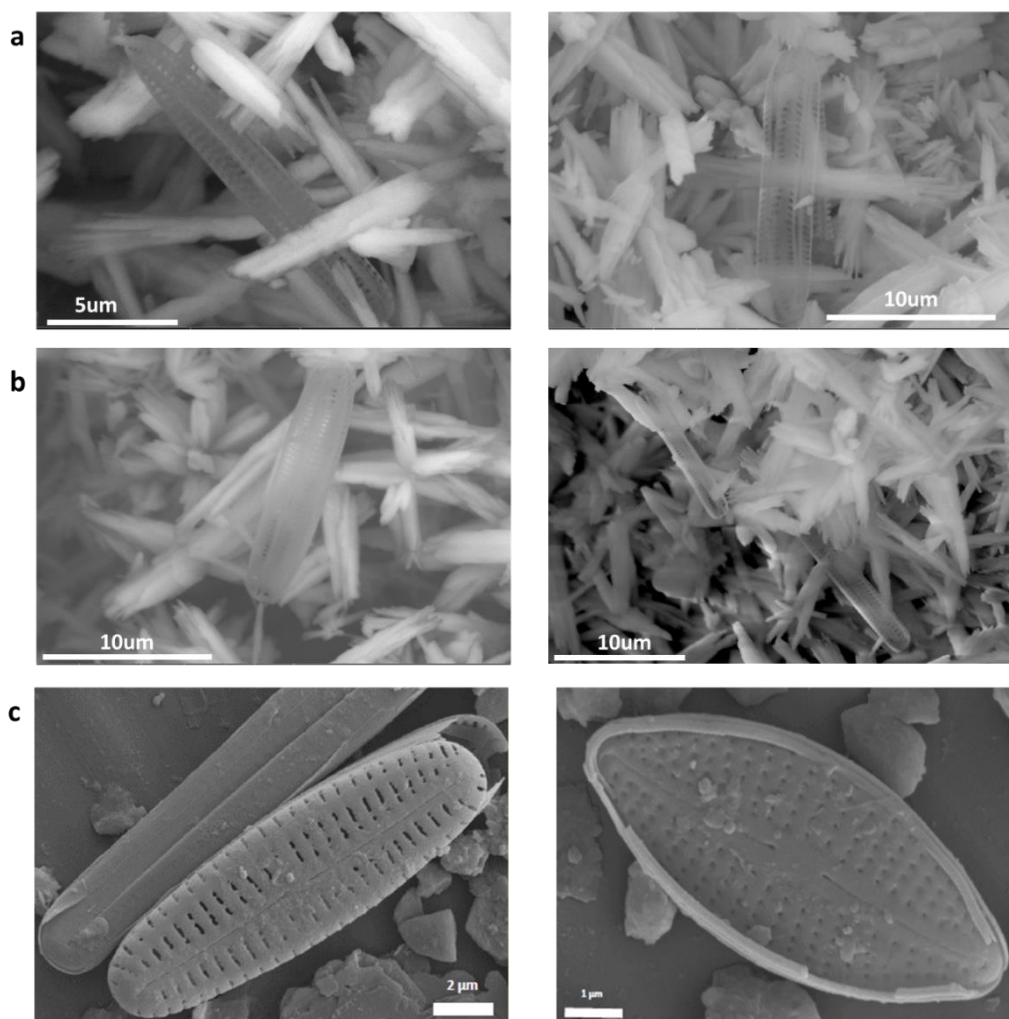
Figure 7.11 SEM images of the Lake Lisan diatom flora. a and b) from two aragonite laminae (ca. 4mm thick) at 1.6m above the DS1 section base. Sampled 2cm above a U/Th age estimate of 39.45±1.09ka (Sample 156-1 in Table 7.5). c) *Navicula spp*. recovered at 48ka (right) and at 11ka from aragonite laminae in the ICDP DS core (from Hartung et al. (2020)).

7.2.5   DS1 section laminae

This section presents the specific characteristics of the DS1 section laminae. It provides the variability in the pale and dark laminae thicknesses through the section. This is followed by presenting the carbonate laminae mineralogical and isotopic composition at different levels through the section.

7.2.5.1   Laminae thicknesses

The DS1 laminae thicknesses were measured directly from the samples, considering that no thin sections have been prepared. The thicknesses were measured visually using the mobile application (Prime Ruler) which provides a ruler scale to 0.25 mm. Each lamina was measured directly from the sample and the thickness was recorded in an excel spreadsheet for both the dark and pale laminae. All laminae <0.25 mm were considered as minimum scale value. The

thickness measurements were undertaken to show the relative variability through the section, as these variations, particularly of the pale laminae, can be indicative of changing environmental conditions (Stein, 2001).

The detrital and pale (aragonite) laminae thickness variability is shown in Figure 7.12 and Table 7.3 and it indicates that the aragonite laminae varies from <1 mm up to >5 mm, while, the detrital beds show thicknesses >30 mm at some locations.

The aragonite and detrital laminae thickness variations are consistent with the section lithology where thick (>1 cm) detrital laminae primarily represent the *ld* facies. The detrital laminae do not essentially reflect periods of enhanced freshwater input, they are rather representative of catchment in-wash bringing the detrital material that is eroded during low lake levels (Prasad et al., 2009; Ben Dor et al., 2019). This also seems to apply in the DS1 section where more frequent detrital laminae are observed at different locations during relatively low lake levels, for example, just prior to the Gypsum Unit (GU) deposition (believed to reflect low lake level and overturn) (see 7.2.2). Following the GU deposition, detrital laminae peaks are still relatively high during the lake filling up stage, compared to the *aad* deposition periods. These peaks are also recorded at around 4 m above the section base.

On the other hand, the thickness of the aragonite laminae is representative of periods of enhanced freshwater input (e.g. Stein et al., 1997; Stein, 2001). Aragonite deposition requires the addition of bicarbonates from the freshwater entering the low-bicarbonate lake (see Chapter 4; 4.4.2.3), thus, the thick aragonite laminae indicate enhanced freshwater input. In the DS1 section, the thickness peaks of the aragonite laminae are higher in the lower parts, below the GU, and during the lake filling-up stage up to ca. 3.5 m above the section base. From 3.5 m to ca. 4.25 m above the section base, alternating *aad* and *ld* facies are recorded with high peaks of detrital layers, probably representing lake level fluctuations and an unstable period. From ca. 4.25 m to the top of the section, a return to *aad* deposition, hence relatively high lake levels, is recorded by high peaks of aragonite laminae thicknesses and lower detrital thicknesses.
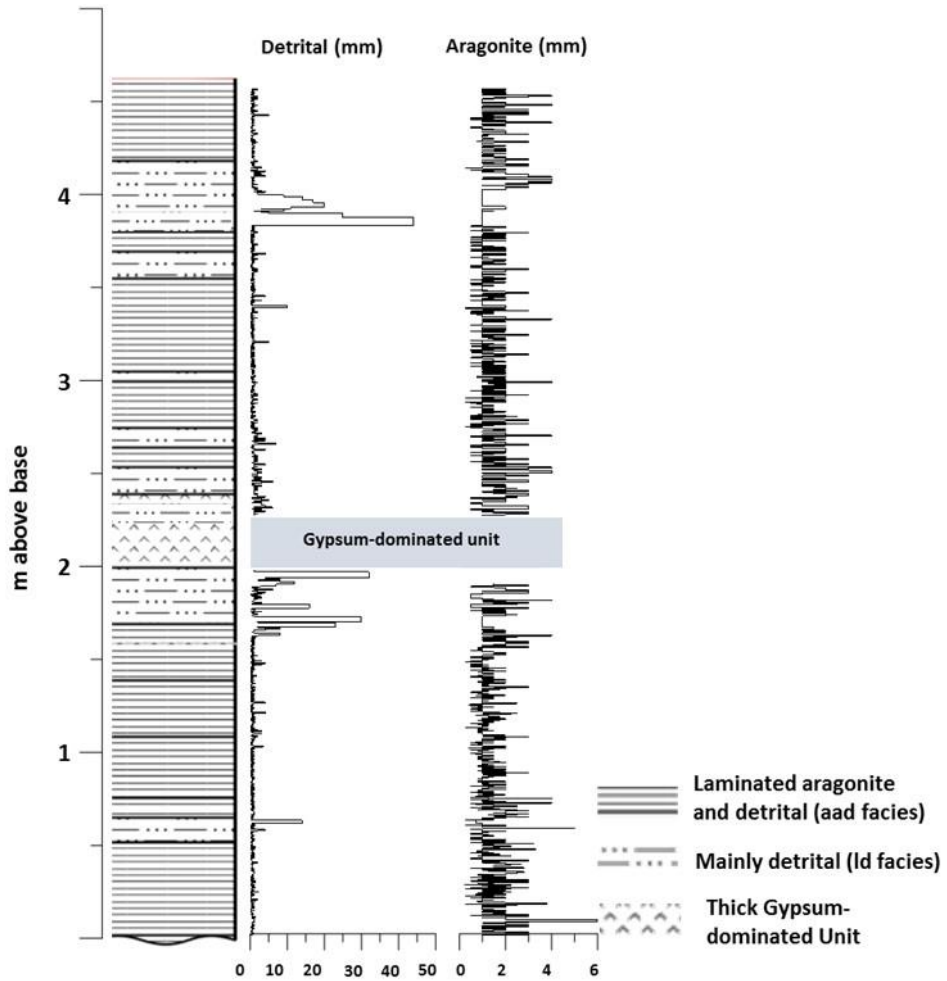
Figure 7.12 DS1 section stratigraphy and the detrital and aragonite (pale) laminae thicknesses.

Table 7.3 Laminae thicknesses through the DS1 section with the U/Th age estimates (see 7.2.6).

Elevation above base (m)	U/Th age estimate (ka) / elevation (m)	Detrital laminae avg. thickness (mm)	Aragonite laminae avg. thickness (mm)
0 - 0.765	39.2± 0.2 / 0.765	0.5 (std. 0.8)	1.4 (std. 0.6)
0.765 - 1.58	39.45± 1.09 / 1.58	0.7 (std.0.5)	1.2 (std. 0.45)
2.00-2.35	--	--	--
1.58 - 2.632	37.88± 1.53 / 2.632	1.9 (std. 2.9)	1.5 (std. 0.8)
2.632 - 4.60	--	0.9 (std. 2.08)	1.3 (std. 0.6)

7.2.5.2 DS1 section carbonate laminae mineralogical and isotopic composition

At different levels through the DS1 section, continuous laminated blocks were samples and analysed for their minerological and isotopic composition in order to show the nature of the DS1 carbonates and their response to lithological variations.

Two blocks of continuous aragonite laminae (15 laminae each) were analysed for their mineralogical composition through XRD analysis and their mineralogical phases were identified using Profex v.4.2.3 Software (Figure 7.13). The two blocks represent laminae collected from an *aad* sequence in the middle of SU1-I (Block S1) and at the end of SU1-I and the onset of the lake limnological changes and primary *ld* deposition (Block S2) (Figure 7.13). The changes in the Lisan sediments mineralogical phases are directly related to the changing climatic conditions in the catchment (Landmann et al., 2002).

The results from Block S1, at ca. 0.63 to 0.68 m above the section base, show that the main mineralogical phase for these laminae is aragonite (96 to 99.8%), while other phases are all present in percentages <4 %. This block generally indicates deposition under stable hydroclimatic conditions and steady freshwater input into the lake to maintain the dominance of the aragonite phase in all 15 laminae. This is also observed by the multi-proxy results of a relatively stable Sr/CaO ratio suggesting periods of water input and aragonite deposition.

On the other hand, Block S2, at ca. 159 to 163 cm above the section base, mineralogy shows that the aragonite mineralogical phase is less dominant (ca. 53 to 95%), while calcite and halite phases show higher percentages, compared to S1, of ca. 6 to 35% and 0.8 to 22.6%, respectively. This is consistent with deposition in variable lake conditions (e.g. Stein et al., 1997; Landmann et al., 2002; Neugebauer et al., 2016). The elevated percentages of calcite and the high negative correlation between aragonite and calcite (r^2= -0.88; P<0.05) are indicative of aragonite flushing by flood freshwater input, as the Lisan aragonites are rapidly diagenetically transformed to calcite when flushed with freshwater which reduces the Mg ratio in the lake water (Katz and Kolodny, 1989; Landmann et al., 2002). Block S2 was sampled from a sequnce where *aad* and *ld* deposition alternate reflecting variable catchment hydrological conditions and thus the enhanced calcite formation probably records the effect of such flooding events, which is followed by a return to higher aragonite percentages. In addition, the

presence of a halite phase is indicative of negative water balance (Neugebauer et al., 2016) supported by the high negative correlation between aragonite and halite (r^2= -0.74; P<0.05) indicating their varying depositional conditions. This enhanced evaporative concentration of halite indicates a shift to NaCl lake chemistry driven by drier conditions in the catchment. These variations in the minerological composition of the laminae probably suggest short-term variability in the DSB catchment hydrological conditions and P/E ratio. Similar observation has been reported for the Dead Sea where halite deposition occurs under the present-day conditions (e.g. Sirota et al., 2021). Similarly, in Balikun Lake, China, Zhao et al. (2021) suggested a trend towards more aridity, reduced vegetation and lower lake volume during the late MIS3 based on multi-proxy analyses and halite deposition in a lake core (Zhao et al., 2021).

Furthermore, to confirm the XRD results, the lamina with the highest halite phase was analysed using SEM EDS, and showed that high peaks of Na and Cl are present in the sample, thus confirming the mineralogical phase analysis suggesting deposition under increasingly negative water balance (Figure 7.14). Nonetheless, the absence of thick halite laminae in the DS1 section rules out lake levels lowering to similar levels as today's DS levels (ca. -400 m asl) or lower as observed in other Lisan sections (e.g. Neugebauer et al., 2016).
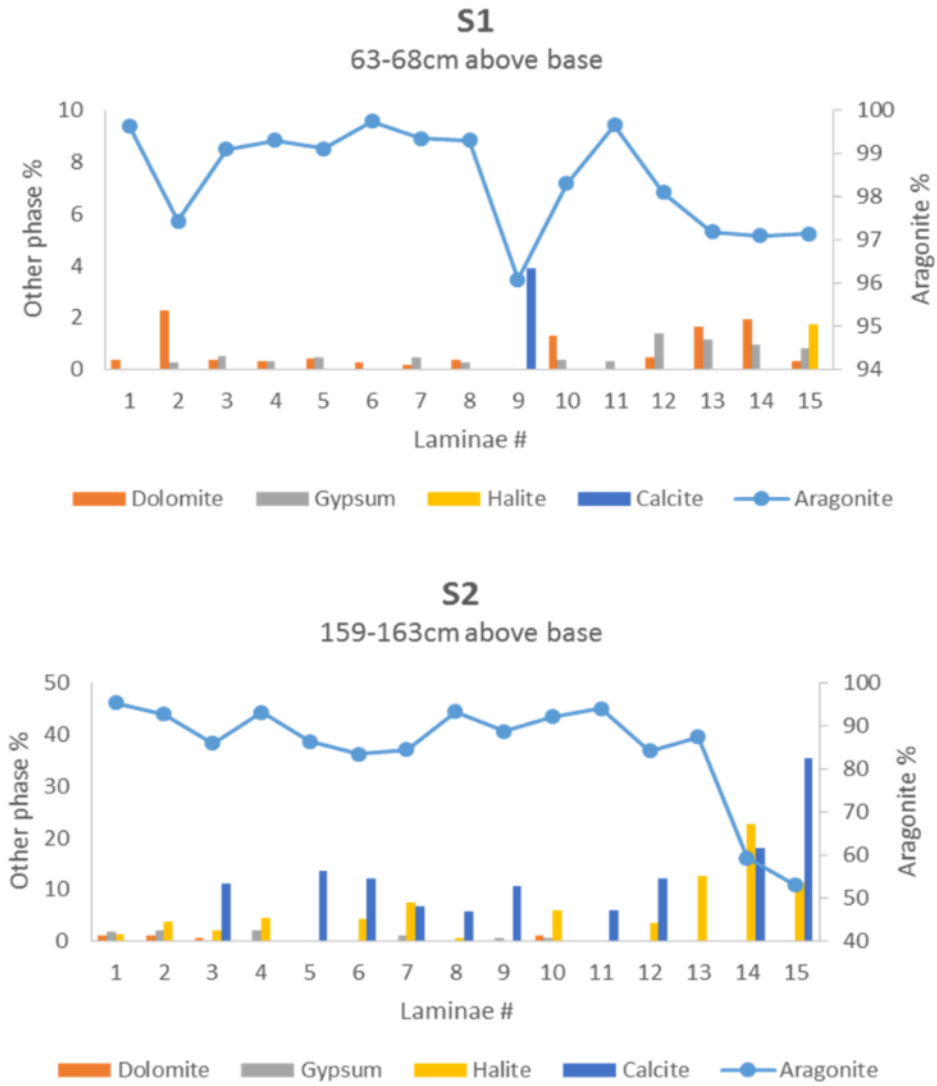
Figure 7.13 Mineralogical composition of Blocks S1 (top) and S2 (bottom) aragonite laminae. For locations refer to Figure 7.10.
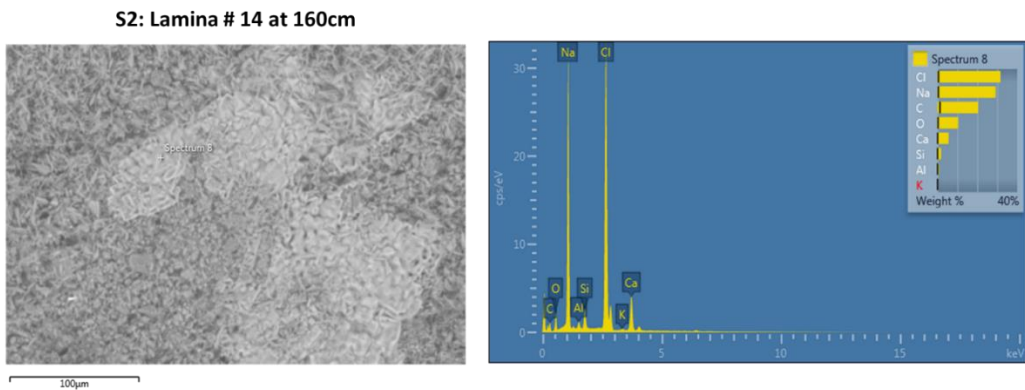
Figure 7.14 SEM EDS image and spectra of aragonite laminae number 14 from Block S2 showing the Na and Cl peaks.

An interesting observation for both Blocks is the presence of a dolomite phase, generally <2.5%, in several samples. The dolomite phase was detected by the Profex v.4.2.3 software refinement based on a poorly defined peak with a maximum at 30.37 to 30.96° 2-theta. This peak was observed in other Lisan sediments from the Lisan Peninsula and was considered as dolomite-like material that is synthetically produced at low temperatures and thus represents unordered Mg-calcite (Landmann et al., 2002). Nonetheless, the presence of dolomite in the catchment (see Chapter 4; 4.4) may suggest some influence on the mineralogy.

The next section presents the DS1 aragonites isotopic composition and discusses its relation to the mineralogy and implications for the wider DSB hydroclimate.

DS1 laminae isotopic composition

As previously discussed (see Chapter 4; Section 4.4.2.7), the isotope composition of Lisan aragonites can be used to investigate short-term climate variability. Four laminated Blocks (S1, S2, S3 and S4) (for locations see Figure 7.10) were analysed for their $\delta^{13}C$ and $\delta^{18}O$ isotope composition. In Lake Lisan, the short-term $\delta^{18}O$ values are representative of precipitation amount rather than source effect (Kolodny et al., 2005), thus, the results of the stable isotope analyses are compared with the isotope values for the Lisan aragonites recovered from the western side of the DSB (e.g. for the Middle Member, ranging from +1.6 to +6.8‰ (long-term avg. +4.6±1‰) for $\delta^{18}O$ and -2.1 to +3.7‰ (long-term avg. +1.3±1‰) for $\delta^{13}C$, where excursions from these values, especially in the $\delta^{18}O$, indicate either wet (lighter values) or drought (enriched values) conditions in the DSB, and a change in the P/E ratio in the catchment (Kolodny et al., 2005).

Since the sediment blocks record the lake system composition during relatively stable and unstable hydroclimatic condition; e.g. as recovered from XRD results of Blocks S1 and S2, stable isotope ratios were measured in order to understand the lake isotopic system response to short-term, changing hydroclimatic conditions; i.e. P/E ratio.

From each Block, 15 individual laminae and 5 mixed laminae (3 laminae each) were used for the analysis. This sampling method is aimed to show how the single sample and mixed samples reflect the system behaviour and whether the mixed laminae could mask significant single laminae variability.

Oxygen isotope composition of the DS1 aragonites

A total of 80 aragonite laminae were analysed for their $\delta^{18}O$ composition. The complete dataset values range from +0.19 to +5.67 ‰ with an average of +3.24 ‰ (Std. 0.98 ‰). These values are in agreement with previous work on Lake Lisan aragonites (Kolodny et al., 2005).

Block S1, sampled following a clastic (ca. 2 cm) lamina, shows $\delta^{18}O$ values for the 15 individual laminae in the range from +4.4 to +2.2‰ with an average value of +3.3‰ (std. 0.7‰). While, the range for the mixed laminae samples is +3.52 to +2.52 ‰ (avg. +3.16‰; std. 0.39‰) (Figure 7.15).

The results show that the lighter $\delta^{18}O$ values for the lower 4 laminae, #15 (+2.52‰) to #12 (+2.21 ‰), from bottom to top, show variations of ca. <1 ‰ from the long-term average Lisan Middle Member values, however, they fall within the DS1 complete dataset average values. These laminae probably record short-lived enhanced freshwater input events into the lake where lighter $\delta^{18}O$ values are achieved. From laminae #11 (+3.39 ‰) to 5 (+3.22 ‰), the $\delta^{18}O$ values are all within the long-term average of the Lisan Middle Member and the average of the DS1 dataset indicating that the lake returned to more stable conditions without intense water input or drought events. Laminae #4 (+2.62 ‰) then shows an excursion of ca. 1 ‰ from the long-term Lisan average, nonetheless, the next two laminae, #3 (+3.6 ‰) and 2 (+3.98 ‰), show a return to long-term average values followed by a ca. 0.6 ‰ excursion in laminae #1 (+2.94 ‰). Similar to the short-term laminae $\delta^{18}O$ record from Massada (Kolodny et al., 2005), Block S1 generally indicates deposition under stable hydroclimatic conditions. This is also supported by the mineralogical and elemental analyses, where this block is primarily dominated by aragonite (96 to 99.8%) suggesting deposition under sufficient input of freshwater that maintained the aragonite deposition and a relatively stable Sr/CaO ratio.
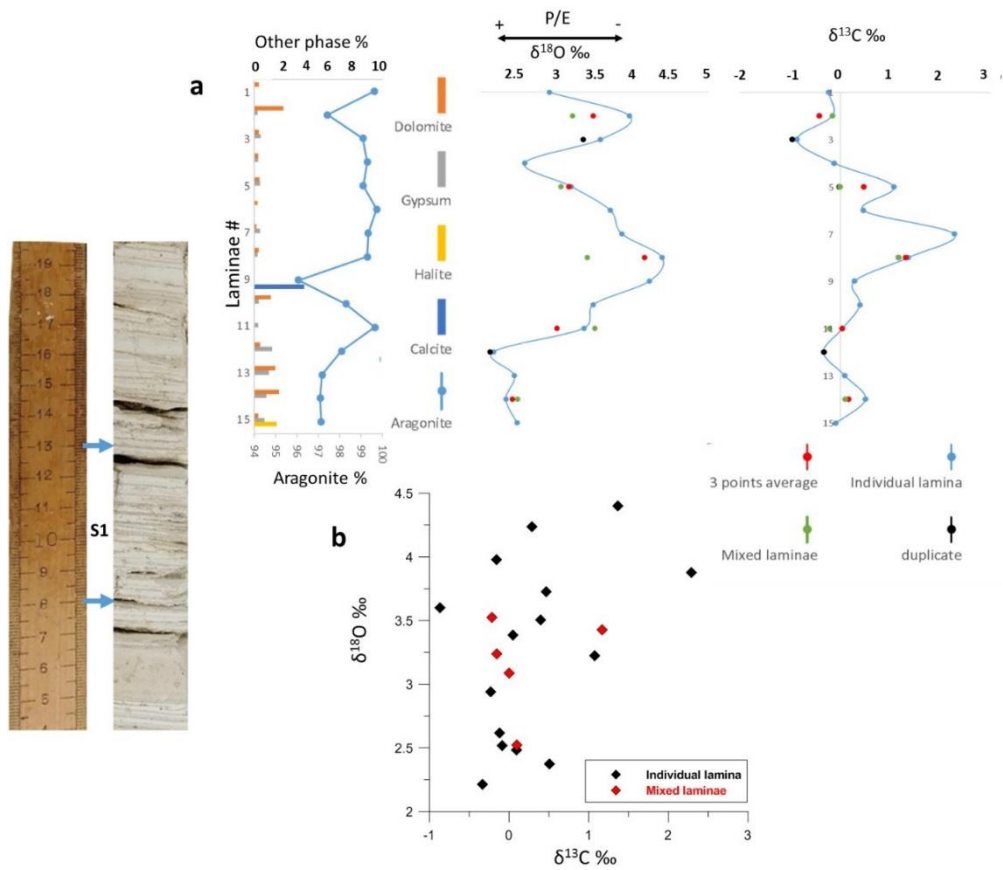
Figure 7.15 a) Block S1 mineralogical and isotopic composition. b) $\delta^{13}C/\delta^{18}O$ covariance. Individual laminae r^2= 0.4; P=0.14. Mixed laminae r^2= 0.18; P=0.78. The complete datatset r^2= 0.38; P=0.098.

Block S2 $\delta^{18}O$ values (Figure 7.16) for the 15 individual laminae range from +3.6 to +0.19‰ with an average value of +2.46‰ (std. 0.99‰), while, the range for the mixed laminae is +3.04 to +2.44‰ (avg. 2.7‰; std. 0.25‰). The individual lamina values are generally lower than the average long-term Lisan Middle Member $\delta^{18}O$ values (e.g. Kolodny et al., 2005) but within the DS1 complete dataset average values. The lower 2 laminae, #15 and #14, +0.19 ‰ and +0.7 ‰, repsectively, from the bottom to top, indicate extreme excursions of ca. 3‰ suggesting short-lived intense flooding events, more extreme than the excursions in Block S1. In addition, the mineralogical content of these two laminae show lower contents of aragonite and elevated calcite phases (Figure 7.16) which could have affected the $\delta^{18}O$ composition considering that, when formed at similar temperatures, $\delta^{18}O_{aragonite}$ is ca. +0.7 ‰ higher than $\delta^{18}O_{calcite}$ (Kim et al., 2007). These observations also agree with the previously discussed multi-proxy analysis and the hydroclimatic conditions of the transition from SU1 to SU2 deposition. However, these excursions, similar to those observed by Kolodny et al. (2005) of ca. 3‰ at ca. 35 ka, indicate a short-lived event of enhanced floocding into the

lake, and hence increased precipitation in the catchment. This suggests a short-lived substantial increase in freshwater input, and the dilution of the upper water layer which is also reflected by the presence of well-preserved diatoms in Block S2 (see section 7.2.3) (Begin et al., 2004), even if only for a short-lived period. From laminae #13 (+1.65 ‰) to #10 (+3.42 ‰) an increase in the $\delta^{18}O$ is recorded and the long-term average value is achieved in lamina #10. From lamina #9 (+2.48 ‰) to #1 (+2.84), the $\delta^{18}O$ does not show extreme excursions probably suggesting deposition under stable Lisan conditions with minor flooding events, compared to laminae #15 and #14.
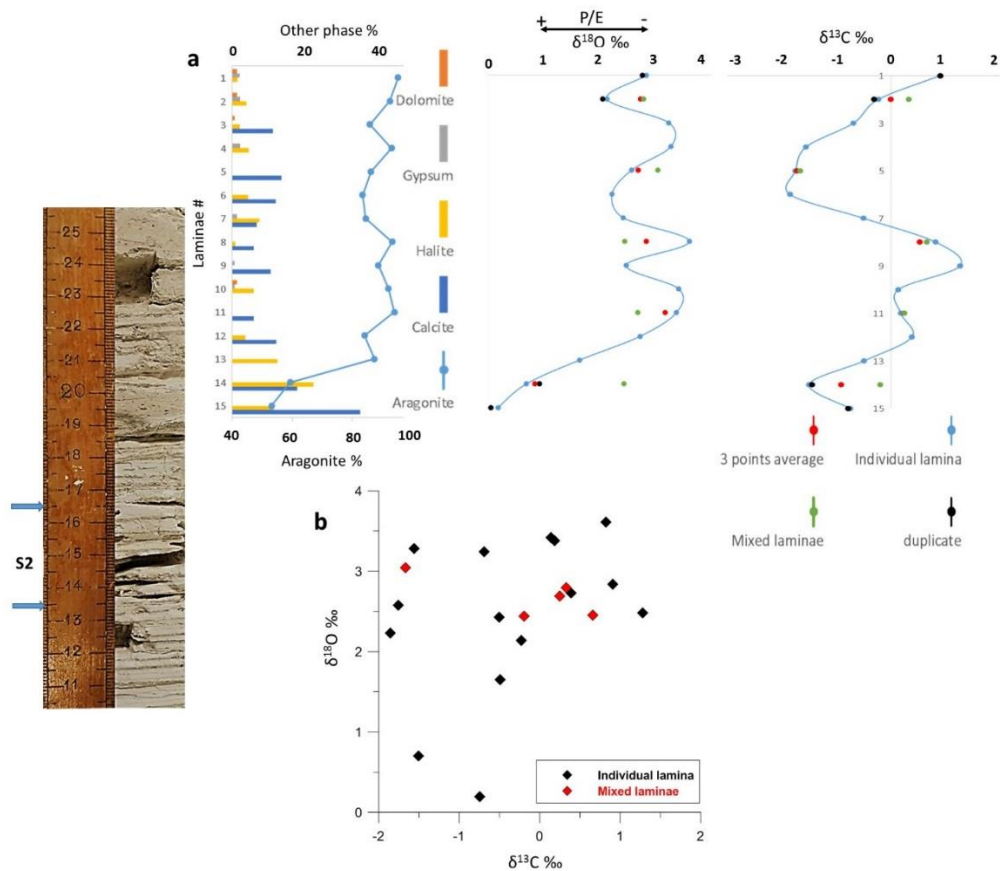
Figure 7.16 a) Block S2 mineralogical and isotopic composition. b) $\delta^{13}C/\delta^{18}O$ covariance. Individual laminae r^2= 0.36; P=0.19. Mixed laminae r^2= -0.72; P=0.17. The complete datatset r^2= 0.29; P=0.22.

In Block S3, collected at ca. 3 m above the section base from a thick *aad* sequence (Figure 7.17), results indicate that the individual lamina $\delta^{18}O$ values range from +4.6 to +1.4‰ with an average value of +3.3‰ (std. 0.92‰), while, the range for the mixed laminae is +4.4 to +1.35‰ (avg. +3‰; std. 1.1‰). The results indicate that the $\delta^{18}O$ values are generally within the long-term Lisan Middle Member and the DS1 aragonite averages with excursion of ca. 1‰, similar to Block S1,

indicating deposition in a rather stable lake hydroclimatic settings. Lamina #9 shows an excursion of ca. 2 ‰ from the average ratios to +1.43 ‰ probably indicating an intense short-lived flood event followed by an increase in $\delta^{18}O$. These results are also supported by the multi-proxy results that show an increase in the Sr/CaO ratio, and a decrease in Ti/CaO.
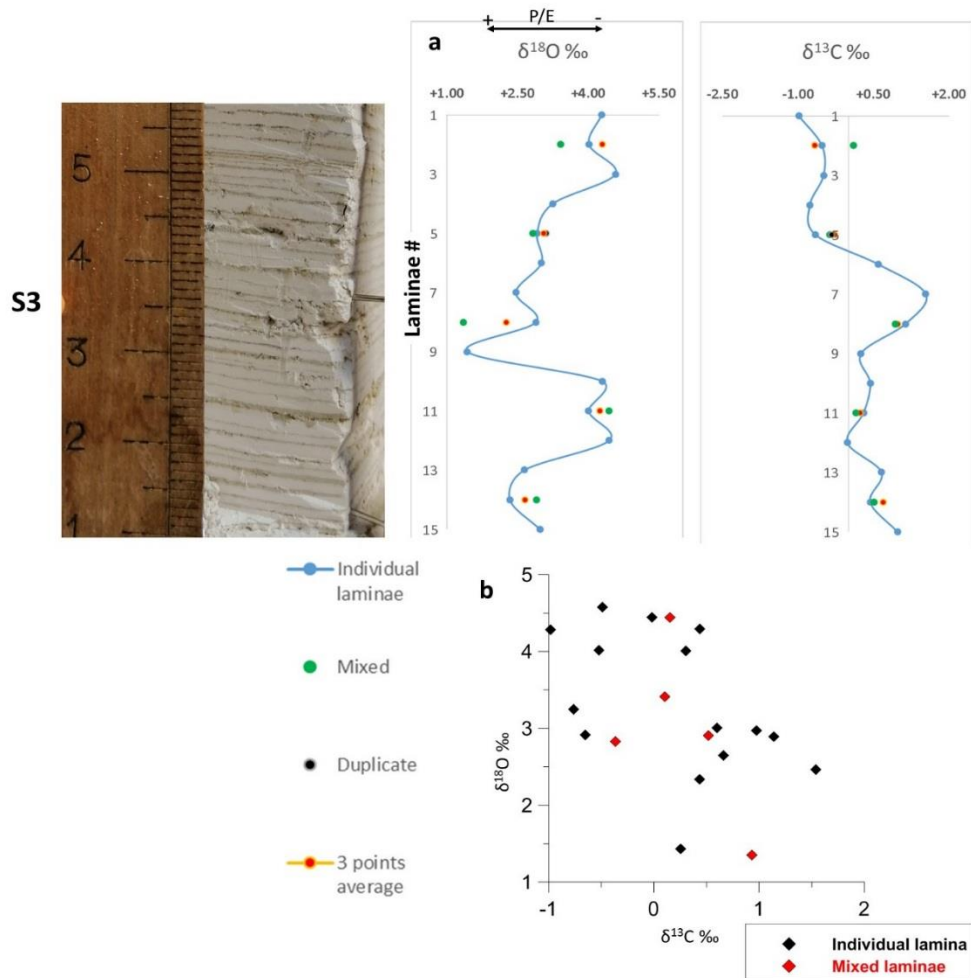
Figure 7.17 a) Block S3 isotopic composition. b) $\delta^{13}C/\delta^{18}O$ covariance. Individual laminae r^2= -0.48; P=0.073. Mixed laminae r^2= -0.57; P=0.31. The complete datatset r^2= -0.48; P=0.032.

Block S4, collected at ca. 4m above the section base was sampled from a primarily *ld* and thick (ca. 0.5 cm) detrital laminae sequence and records the isotopic system response during low lake levels (e.g. Machlus et al., 2000; Neugebauer et al., 2014) (Figure 7.18). The results show that the individual lamina $\delta^{18}O$ values range from +5.7 to +2.8‰ with an average value of +3.8‰ (std. 0.8‰). While, the range for the mixed laminae is +4.93 to +2.2‰ (avg. +3.8‰; std. 1.1‰). The ratios indicate that the $\delta^{18}O$ composition is generally within the range of the Lisan long-term values of the Lisan sediments but higher than the average of the DS1

aragonites. Few laminae show more enriched values not observed in the previous 3 blocks. Enrichment of ca. 1‰ in δ^{18}O ratios from the Lisan long-term and the DS1 average values is recorded in several laminae, e.g. laminae #15 (+5.67‰), #14 (+4.99 ‰), #12 (+5.49 ‰) and #10 (+4.86‰). This enrichment suggests drought events, hence lower lake levels and reduced freshwater input into the lake. This observation is also supported by the lithology of the DS1 section where thick detrital laminae are found in this part of the section indicating lower lake levels (e.g. Machlus et al., 2000; Neugebauer et al., 2014). This is also supported by decreased Sr/CaO ratios, compared to Block S3, increased particle size (Mz) compared to the other blocks, and minor peaks in SO$_3$/CaO.

Table 7.4 lists the statistical parameters of the aragonite isotopic composition where the most enriched δ^{18}O values are recorded during low lake levels (Block S4) and the lightest values are recorded at the transition from SU1 to SU2 (Block S2). The results show that excursions in δ^{18}O values occurred at short-term scales during the deposition of the DS1 section. These observations agree with previous results from the Lisan aragonites (Kolodny et al., 2005) and the general short-term MIS3 climatic variability at decadal scales (Huber et al., 2006).
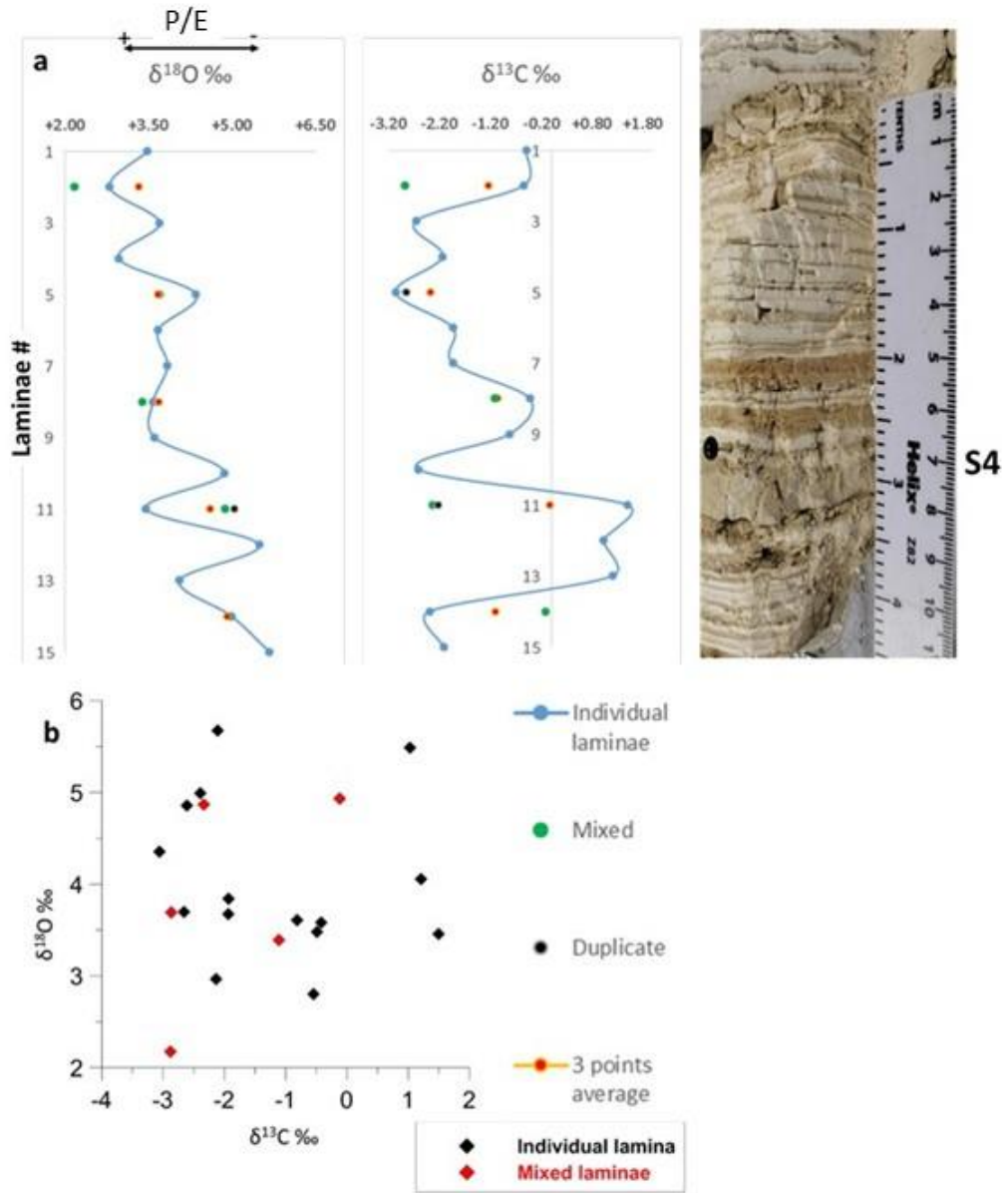
Figure 7.18 a) Block S4 isotopic composition. b) $\delta^{13}C/\delta^{18}O$ covariance. Individual laminae r^2= -0.13; P=0.63. Mixed laminae r^2= 0.53; P=0.36. The complete datatset r^2= 0.043; P=0.86.

Table 7.4 Statistical parameters of the $\delta^{18}O$ and $\delta^{13}C$ composition for Blocks S1 to S4.

	$\delta^{18}O$ ‰ VPDB			
	S1	S2	S3	S4
Min.	2.2	0.19	1.43	2.80
Max.	4.4	3.6	4.58	5.67
Avg.	3.3	2.46	3.3	4.04
Std.	0.7	0.99	0.92	0.86
	$\delta^{13}C$ ‰ VPDB			
	S1	S2	S3	S4
Min.	-0.87	-1.85	-0.98	-3.06
Max.	2.28	1.28	1.54	1.49
Avg.	0.31	-0.37	0.19	-1.16
Std.	0.77	1	0.75	1.50

Carbon isotope composition of the DS1 aragonites

It is presumed that the $\delta^{13}C$ composition of lake waters is recorded in the precipitated carbonates, where $\delta^{13}C$ can be an indicator of past changes in $\delta^{13}C_{TDIC}$, that can be affected by the incoming water isotope composition and the carbon cycle (Leng and Marshall, 2004). $\delta^{13}C_{TDIC}$ sourced from C3 soil is assumed to have $\delta^{13}C$ of -10 to -22‰, while it varies from -7 to +1‰ if derived from C4 soil (Lacey et al., 2016). In addition, since the Lake Lisan water inflow is primarily delivered through the northern and western carbonate outcrops and aquifers, the ^{13}C-enriched HCO_3^- most probably originates from carbonate dissolution which generally yields values of -3 ‰ to +3‰ $\delta^{13}C$. Thus, excursions in lake carbonates $\delta^{13}C$ can be attributed to enhanced/reduced delivery of ^{12}C, where lighter values can be associated with soil development and increase in, isotopically light carbon, terrestrial C3 vegetation in the catchment during warmer conditions, while the enhanced desert C4 vegetation would yield more enriched values (e.g. Abu Ghazleh, 2011; Lacey et al., 2016; Rogerson et al., 2019).

Lake Lisan Middle Member long-term $\delta^{13}C$ values vary from -2.1 to +3.7‰ (avg. +1.3±1‰) (Kolodny et al., 2005). During MIS3, an increase in *Artemisia* pollen associated with a reduction in herbs and shrubs is recorded in the DSB suggesting an increase of moisture availability, while pollen ratios indicate variations in the vegetation assemblages probably corresponding to D-O events. Generally, the pollen assemblages indicate that mixtures of desert and woodland vegetation prevailed during MIS3 in the DSB (Miebach et al., 2017).

The association of $\delta^{13}C$ variability with soil development and vegetation type does not, however, seem to explain the variability of $\delta^{13}C$ composition in the DS1 sediments. The most extreme $\delta^{13}C$ excursion of -3.06 ‰ is recorded in Block S4 associated with the most enriched $\delta^{18}O$ values (up to +5.7‰) (Table 7.6), of all samples analysed, indicating drought and low lake levels, while during the deposition of the S1 and S3 blocks, under more stable lake conditions with lighter $\delta^{18}O$ (reaching +1.43‰), the $\delta^{18}C$ values range from -0.98‰ to +1.54‰. This is probably the result of the observed different behaviour of $\delta^{13}C$ and $\delta^{18}O$ and the fact that $\delta^{13}C$ variability in Lake Lisan act at a different time constant compared to the $\delta^{18}O$ (e.g. Kolodny et al., 2005). Thus, further understanding of Lake Lisan productivity and $\delta^{13}C$ system is required for better interpretation of the lake aragonite $\delta^{13}C$ (Oren and Gurevich, 1995; Kolodny et al., 2005) (see Chapter 4, 4.4.2.7).

DS1 aragonites Carbon and Oxygen isotopes relationship

It has been reported that in terminal, closed, lakes such as the DS and its precursors, carbonate $\delta^{13}C$ and $\delta^{18}O$ covariance is an indicator of hydrological closure (Talbot, 1990). Nonetheless, no covariance in Lake Lisan aragonites $\delta^{13}C$ and $\delta^{18}O$ was observed except during low lake levels (Kolodny et al., 2005), which was attributed to the short-life of the upper water layer and the sediment's limited isotopic 'memory' (Talbot, 1990). Similarly, in their investigation of 24 Mediterranean lake basins biogenic and endogenic carbonate $\delta^{13}C$ and $\delta^{18}O$ compositions, Roberts et al. (2008) showed that controls over the isotope compositions have not been consistent through space or time during the Late Quaternary and that the $\delta^{13}C$ and $\delta^{18}O$ covariance is not a reliable palaeohydrological closure indicator (Roberts et al., 2008). This observation was also reported for hyper alkaline closed lakes as their $\delta^{13}C$ composition is insensitive to changes in lake volume (Li and Ku, 1997). However, Li and Ku (1997) reported that the presence of this covariance is fundamentally a function of two factors: (1) when the input water and lake water ΣCO_2 concentration is approximately similar, with different $\delta^{13}C$ compositions, and (2) when the lake level declines, as a result of decreased water input and/or increased evaporation, then the $\delta^{13}C$ and $\delta^{18}O$ will co-vary (Li and Ku, 1997). Considering that the ΣCO_2 of Lake Lisan was relatively low and the freshwater input was the main source of ΣCO_2, the suggested conditions of Li and Ku (1997) could only be achieved when the freshwater input significantly decreased and the water input was balanced by evaporation, i.e. during periods of lake mixing (Kolodny et al., 2005). Thus, for

most of the Lake Lisan period, no covariance is expected for the sediments $\delta^{13}C$ and $\delta^{18}O$ composition. For the DS1 sediments' isotopic composition, the complete dataset (80 samples) plot shows an r^2 value of -0.13 (P=0.23) indicating that no covariance is present for the four blocks combined (Figure 7.19).
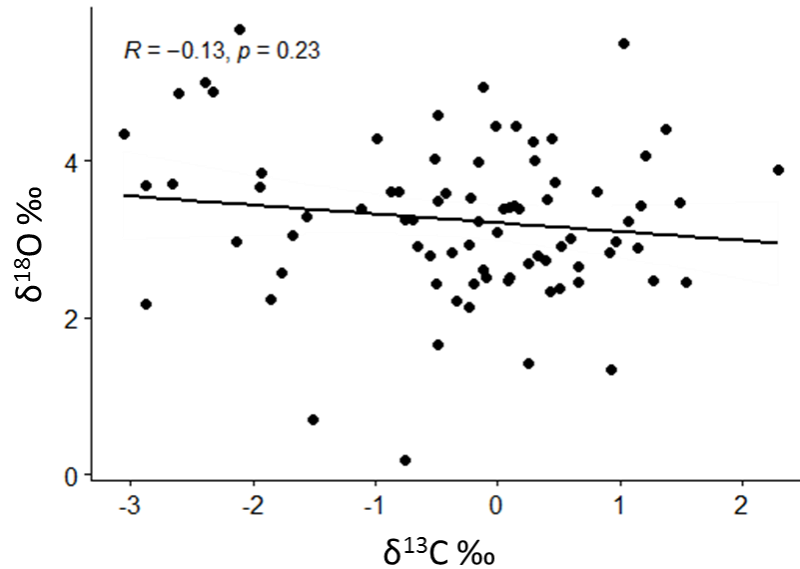
Figure 7.19 $\delta^{18}O$ ‰/$\delta^{13}C$ ‰ covariance for the complete dataset of the DS1 aragonites showing the general negative covariance.

However, when looking at the individual blocks, positive and negative covariance is noted at different levels through the DS1 section. As shown in Figures 7.15 to 7.18, Block S1 results show weak positive correlation for both individual and mixed laminae datasets, r^2= 0.4 and 0.18, respectively. Block S2 results indicate that positive correlation is present for the individual laminae (r^2=0.36), while the mixed laminae shows a negative covariance (r^2= -0.72). Block S3 results show negative correlation for both individual and mixed laminae (r^2= -0.48 and -0.57, respectively). Block S4 indicate that the individual laminae results are negatively correlated (r^2= -0.13), while the mixed laminae are positively correlated (r^2=0.53). All the previously mentioned correlations are insignifcant (P>0.05), however, only in Block S3 a significant correlation is noted when plotting the individual and mixed laminae together (r^2= -0.48; P=0.032). The results indicate that the relationship between $\delta^{13}C$ and $\delta^{18}O$ in the DS1 section varies through the section probably in response to changing environmental conditions at both short and long-term scales.

7.2.6   DS1 chronology

This section explains the identification of the clean DS1 aragonites using SEM EDS analysis. Then, the U/Th dating results of the DS1 aragonites is presented.

7.2.6.1   The DS1 aragonites

In the published *aad* sequences, the pale laminae are considered as authigenic aragonite (Stein et al., 1997; Stein, 2001; Haase-Schramm et al., 2004). However, in order to use the DS1 sediments for U/Th dating, the pale laminae were investigated in order to confirm their authigenic aragonite nature. Accordingly, thick (ca, 2-4 mm) laminae through the 4.6 m section were located visually and based on LOI_{925} contents and then examined using the SEM EDS analysis to locate the cleanest aragonite, identifiable in the SEM by its acicular crystal habit. Laminae with EDS spectra indicating an absence of detrital contamination (i.e. lacking Fe and Ti) were then chosen for analysis, while samples that showed contamination with detrital material were excluded, even if the contamination is minimal (e.g. Figure 7.20).
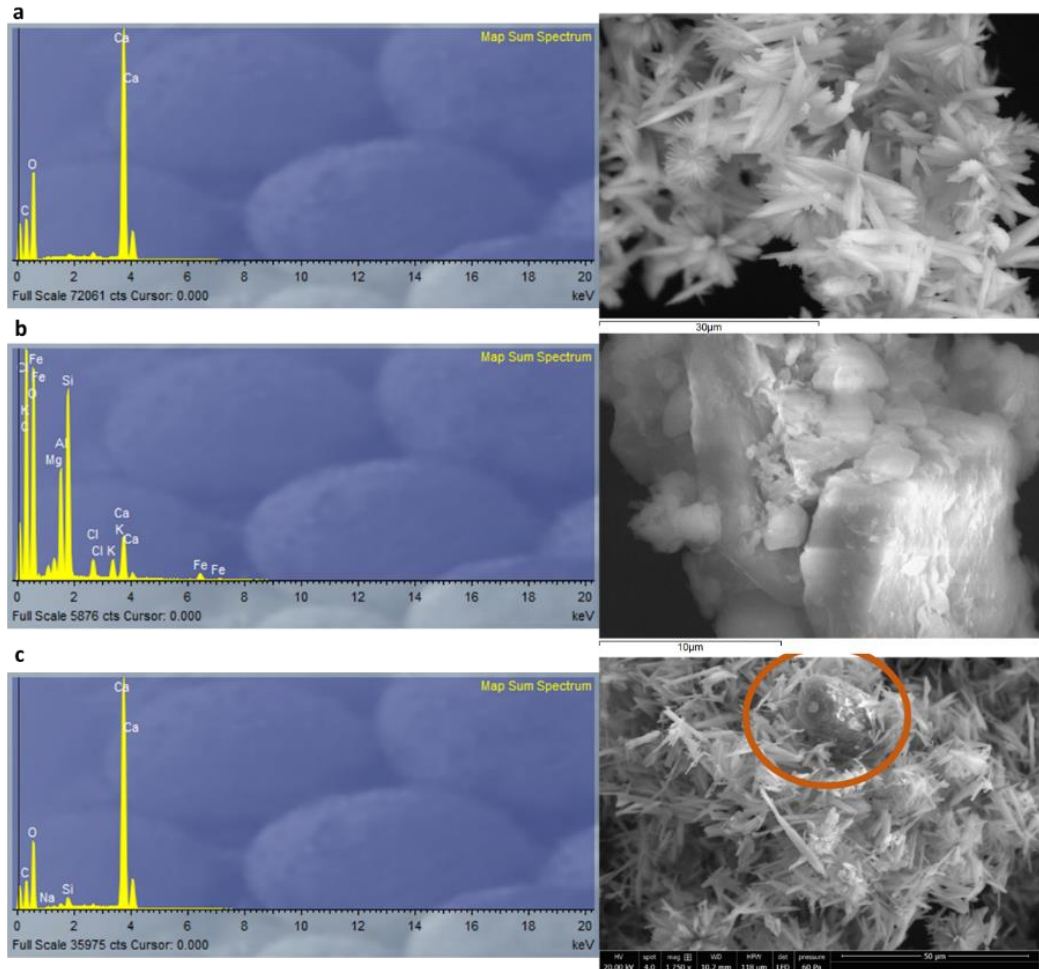
Figure 7.20 a) SEM image of a clean aragonite lamina at 2.65 m above the DS1 base with EDS spectra showing the high Ca value and absence of contaminants. b, c) SEM images of contaminated aragonite laminae at ca. 2.97 m and 0.68 m from base, respectively, with EDS spectra showing proportions of clastic markers.

7.2.6.2 U/Th dating

The U/Th data presented in this section is part of an ongoing work on DS1 aragonite, clastic and gypsum samples.

Prior to the U/Th dating, the DS1 section laminae were counted based on visual identification, the pale and the dark laminae are distinguishable (e.g. Figure 7.2 a), while the micro detrital sub-laminae (Ben Dor et al., 2019) cannot be distinguished. The counting was done twice, primarily based directly on the samples and at some locations, where the samples were broken due to shipping (accounting for ca. 20 cm of the total section), the laminae were counted based on photographs taken after sample collection. Pins were used at 5 cm intervals along the complete section and laminae couplets were counted accordingly. Where there is *ld* facies, the detrital laminae were counted as distinguishable by

their distinct colours (grey to dark) but were excluded from the total couplets count as they could reflect several in-wash events in one year, or several years, during low lake levels and reduced precipitation in the catchment that did not facilitate aragonite deposition (see section 4.4.2.3) (Neugebauer et al., 2014; Ben Dor et al., 2019). The counting results indicated that the DS1 section comprises ca. 1927±67 laminae couplets.

For optimal conditions, where the carbonates are free of initial ^{230}Th, and the U is completely considered as derived from the precipitating solution, i.e. lake water, the U/Th ages can be calculated with no further need for corrections (Kaufman and Broecker, 1965). However, in natural systems, this could be valid to certain limits for speleothems (e.g. Nehme et al., 2018; Rowe et al., 2020) and corals (e.g. Stein et al., 2017) that usually comprise negligible contents of detrital U and Th and hydrogenous Th, while lake carbonates are more likely to contain Th and U from detrital and hydrogenous sources (Haase-Schramm et al., 2004; Torfstein et al., 2013a; Dean et al., 2015).

Dating the Lisan sediments using U/Th ratios is thus problematic. Haase-Schramm et al. (2004), based on one sedimentary sequence from the Perazim Valley (PZ in Figure 7.1a), conducted a detailed study of U/Th dating and estimated values for the detrital and hydrogenous corrections. In their study, the detrital U and Th correction was based on a detrital end member (DEM) of Th/U$_{(atomic)}$=0.85±10%, U=4.26ppm and ^{234}U/^{238}U=1. In terms of correcting for the hydrogenous Th, they considered the values of Th=0.08ppm and ^{232}Th/^{230}Th$_{(atomic)}$= 44,000 for the single sample correction, based on U/Th dating of an authigenic modern aragonite sample (with negligible detrital content) (Haase-Schramm et al., 2004). These values have since been since considered in the correction of U/Th dated sediments from the DSB (e.g. Lisker et al., 2009; Torfstein et al., 2009; Abu Ghazleh, 2021).

For a preliminary study of the DS1 aragonites and to test their validity for U/Th dating, four clean aragonite samples, with high Ca content and absence of detrital contaminants based on the EDS spectra (see above), were chosen and analysed for U/Th dating at the British Geological Survey (BGS). In order to minimize the detrital contamination in the samples, ca. 10 to 20 mg of sample were used for the analysis (pers. comm. with Dr. Diana Sahy). The pilot study results are in the range of accepted U/Th isotopic composition from the DSB (e.g. Haase-Schramm et al.,

2004; Torfstein et al., 2009) where the measured $^{230}U/^{232}U$ ratios are all >10 and Th values <0.5 (Table 7.5).

The Th isotope ratios of the DS1 aragonites (Table 7.5) consistently show only minor detrital contamination, but this is still significant. Independent of the detrital and hydrogenous Th corrections used in this pilot, based on the Haase-Schramm et al. (2004) correction, ages were not always in stratigraphic order (Figure 7.21). Generally, lacustrine aragonites from the DSB basin having Th content of >0.5 are considered to include high detrital contamination (Torfstein et al., 2009). This tendency, closer to 0.5 Th content, is observed in the DS1 aragonites, where Sample 156-3 showed the lowest Th content and resulted with a more constrained age estimate compared to the other samples, while Sample 156-4 which contained the highest Th content of 0.35 resulted with a corrected age with high uncertainty (±2s) (Table 7.5 and Figure 7.21).

Table 7.5 DS1 sediments pilot study U/Th age estimates results.

Lab ID	m above base	U ppb	232Th ppb	230/232 AR	Measured, Tracer-Corrected						Detrital-Corrected					Date uncorr (ka)	±2s (abs)	Date corr (ka)	±2s (abs)	Initial 234U/238U AR	±2s (abs)
					232/238 AR	±2s (%)	230/238 AR	±2s (%)	234/238 AR	±2s (%)	230Th/238U AR	±2s (%)	234U/238U AR	±2s (%)	Corr. Coef 08-48						
156-2	2.632	3.12	0.185	25.6	0.01944	0.35	0.497	0.45	1.46	0.15	0.489	1.29	1.47	0.69	0.35	44.20	0.25	43.03	0.63	1.53	0.01
156-1	1.58	3.44	0.161	32.3	0.01541	0.35	0.497	0.46	1.45	0.12	0.491	1.06	1.46	0.54	0.34	44.64	0.26	43.71	0.53	1.52	0.01
156-3	0.765	4.45	0.058	110.2	0.00425	0.36	0.468	0.44	1.45	0.15	0.466	0.52	1.46	0.21	0.13	41.52	0.23	41.26	0.26	1.51	0.00
156-4	0.748	5.63	0.349	23.4	0.02035	0.35	0.477	0.43	1.44	0.12	0.468	1.40	1.45	0.71	0.34	42.86	0.23	41.62	0.66	1.51	0.01
Recalculated following Haase-Schramm et al., 2004																					
156-2	2.632	3.12	0.11	42.16	0.011	0.354189	0.47	0.45	1.47	0.153	0.44	3.554	1.49	1.754	0.32	40.84	0.24	37.87	1.52	1.54	0.028
156-1	1.58	3.44	0.08	60.21	0.007	0.352718	0.47	0.46	1.45	0.124	0.45	2.431	1.47	1.219	0.33	41.55	0.24	39.44	1.09	1.52	0.019
156-3	0.765	4.45	0.00	26057	0.000	0.355945	0.45	0.44	1.45	0.145	0.45	0.441	1.45	0.145	0.00	39.19	0.21	39.18	0.21	1.50	0.002
156-4	0.748	5.63	0.27	29.27	0.016	0.352147	0.46	0.43	1.44	0.118	0.43	5.348	1.47	2.537	0.30	40.98	0.22	36.65	2.22	1.52	0.040
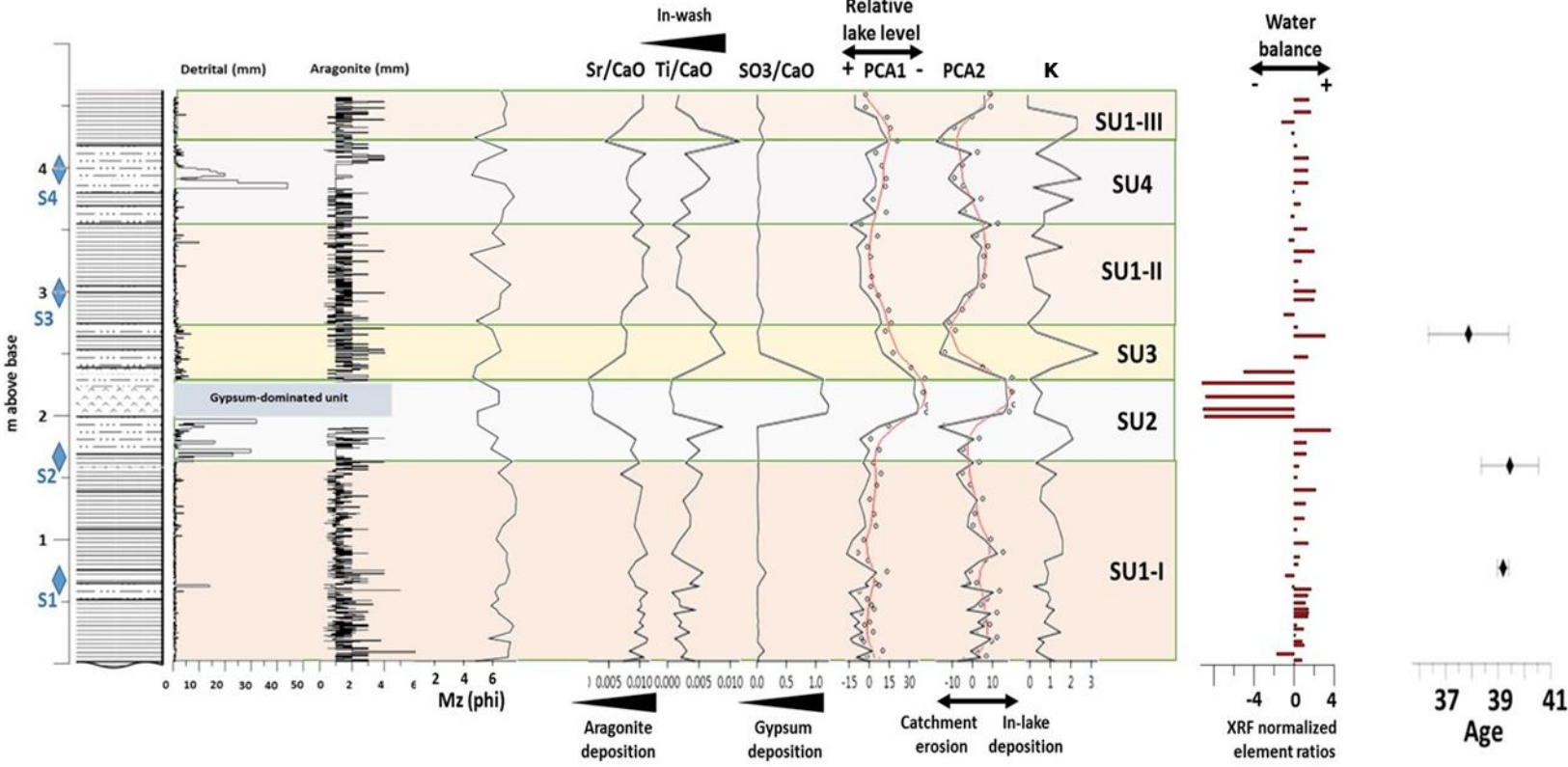
Figure 7.21 The DS1 section stratigraphy with key environmental proxies and U/Th age estimates. SU: lithostratigraphic unit. Smooth lines for PCA1 and PCA2 were calculated using "smooth.spline" function in R software with 0.5 smoothing step. S1-4: locations of Blocks S1 to S4 discussed in the text. For stratigraphy legend refer to Figure 7.6.

Initial $^{234}U/^{238}U$ activity ratios

The Lake Lisan sediments have estimated common initial $^{234}U/^{238}U$ activity ratio ranges of 1.47 to 1.54 (Haase-Schramm et al., 2004) and 1.521±0.03 (Torfstein et al., 2013a) as measured by samples along the western DSB. In addition, a recent Dead Sea aragonite showed an initial ($^{234}U/^{238}U$) ratio of 1.497±0.001 (Haase-Schramm et al., 2004).

This ratio varies for Lake Lisan sediments between different sections, for example, Torfstein et al. (2013a) reported initial $^{234}U/^{238}U$ ratios of 1.525±0.032 and 1.508±0.019 for two sections in Massada and Perazim valley, respectively. Generally, this ratio decreases during lower lake level periods, i.e. negative water balance, which is explained by the fact that freshwater input contributes high $^{234}U/^{238}U$ to the DSB, while the brines in the basin contribute low $^{234}U/^{238}U$ (Haase-Schramm et al., 2004; Kiro et al., 2020). In their study, Haase-Schramm et al. (2004) reported present-day $^{234}U/^{238}U$ values of ca. 1.7, 1.75 for the freshwater input from the Jordan River and the freshwater springs, respectively. In addition, they reported values of ca. 1.1 and ca. 1.4 for the saline springs in the DSB. Accordingly, it has been suggested that Lake Lisan probably sustained a stable $^{234}U/^{238}U$ system and any deviation from the Lake Lisan aragonites reported ranges could reflect the effects of detrital contamination or diagenetic alterations (Haase-Schramm et al., 2004) or freshwater sources (Kiro et al., 2020), thus these values represent a base to evaluate the validity of any measured U/Th ages of Lisan aragonite samples (Haase-Schramm et al., 2004; Torfstein et al., 2013a). Following this approach, the DS1 aragonites initial $^{234}U/^{238}U$ ratios of 1.52±0.04, 1.50±0.002, 1.54±0.028 and 1.52±0.019 (Table 7.5) are within the accepted range of Lake Lisan $^{234}U/^{238}U$ ratios, indicating the validity of the results. However, the significance of the need for a correct, section-specific, DEM can be best demonstrated by the ages of samples 156-3 and 156-4 (Table 7.5). The two samples are only ca. 1.5 cm apart, however, the age estimates show high variation, where sample 156-3 at 76.5 cm from base is the cleanest sample in terms of detrital contamination.

So although the pilot data are promising, further analysis is needed to finalise the chronology for the DS1 section, not least in better constraining the local impact of detrital Th. The DS1 pilot study results agree with other studies in the DSB that have suggested that it is difficult to determine a single time-constant and basin-wide detrital end member (DEM) and hydrogenous correction procedure in the

DSB and that the estimation of specific DEM for individual sets of coeval samples in different sedimentary sequences might be required (e.g. Torfstein et al., 2013a). For example, even though Haase-Schramm et al. (2004) applied the detrital and hydrogenous corrections on the PZ sediments and obtained good agreement with radiocarbon ages, few sets of aragonite coeval samples showed scatter higher than analytical errors suggesting an additional variability in the U/Th systematics. This variability could be the result of variable DEM compositions and/or hydrogenous components (Torfstein et al., 2013a). In their study, Torfstein et al. (2013a) showed that variable DEMs can be calculated for different sets of coeval samples, within the same section and in different sections.

Accordingly, 19 additional samples from the DS1 section are currently being analysed at the BGS under a NERC NEIF Grant (2314.0920). The samples include:

- three samples from clastic laminae with the coarsest grainsize and highest Fe and Ti content in the DS1 section, which will be used to constrain the U/Th systematics of the detrital fraction and allow comparison to the detrital corrections used by Haase-Schramm et al. (2004) and Torfstein et al. (2013a).

- 15 aragonite samples, distributed over five levels through the section, with three subsamples per level. This procedure is undertaken to help account for the contribution of any initial hydrogenous Th in the samples. Following an approach similar to that advocated for stalagmites with high initial Th (Hellstrom, 2006). Starting from the published correction values of Haase-Schramm et al. (2004), we will use an iterative approach to constrain a range of possible hydrogenous Th isotope compositions that result in the best agreement between dates from samples from the same level, and then between the age and stratigraphic position of samples from different levels. The approach of Hellstrom (2006) is based on the assumption that all samples behave as a closed system with respect to U and Th, and therefore any dates that fall out of order within a sedimentary succession are the result of variations in initial Th composition. This assumption is difficult to justify for speleothems, and is almost certainly not valid for aragonite lacustrine sediments that may have been subject to weathering. However, the use of three aragonite subsamples per level should allow us to identify any outliers due to potential open

> system behaviour with respect to either U or Th, thus reducing the number of initial assumptions within our age models.
>
> • one gypsum sample. Considering that the capability of U/Th dating of gypsum has recently been developed at the BGS, the accuracy of this date will be evaluated based on ages from surrounding aragonite-layers.

7.2.6.3 DS1 section within the Lisan Formation

Considering the above discussion about the U/Th pilot study, the current age estimates of the DS1 section do not provide a well-stratigraphically constrained age model that allows for high resolution reconstructions, however, the results are significant and provide insights regarding the location of the DS1 section within the Lisan Formation.

The age estimates, excluding the age at 74.8 cm above base with the high uncertainty, place the DS1 section at ca. 39.45±1.09 ka to 37.87±1.5 ka (Figure 7.21). Considering that the Lisan Formation has been subdivided into three distinct members corresponding to MISs 4, 3 and 2 (Stein, 2001; Bartov et al., 2003; Haase-Schramm et al., 2004), the DS1 section is chronologically placed within the Lisan Middle Member (ca. 58-31ka).

The Lisan Middle Member is distinguished from the Upper and Lower Members by its high content of clastic (detrital) laminae and the presence of *ld* facies reflecting catchment in-wash during low lake levels (Abed and Yaghan, 2000; Torfstein et al., 2013b). Based on sedimentary exposures along the western DSB, this member is subdivided into two sub-sections separated by a hiatus from 47 to 43 ka (Machlus et al., 2000). The placement of the DS1 section as part of the Lisan Middle member is also supported by the lithological variations and the facies of the DS1 section, where *ld* facies are present in different parts and the presence of the GU indicating alternating high and low lake levels (section 7.2.1).

7.2.7 Correction for tectonic activity

As discussed in Chapter 4 (section 4.4.2.2), the DSB tectonic settings have affected the Lisan sediments on both sides of the basin (Bartov et al., 2006; Torfstein et al., 2013b; Jara-Muñoz et al., 2020) resulting in different subsidence and uplift rates across the DSB. Thus, due to these pronounced tectonic processes, a tectonic correction is required prior to discussing the DS1 section in relation to other Lake Lisan records (e.g. Bartov et al., 2006; Torfstein et al., 2013b). One method of stratigraphic correlation is the use of dated marker beds

(e.g. Bartov et al., 2002; Neugebauer et al., 2014). Within the Lisan, the assumed ages of the gypsum beds reported by Torfstein et al. (2013a) (see Chapter 4, 4.4.2.4) and their corrected altitudes reported in Torfstein et al. (2013b) can be thus implemented in evaluating the relative tectonic displacement of the DS1 section Gypsum Unit (GU).

In the DS1 section, the thick, ca. 30cm, Gypsum Unit (GU) at ca. 2m (-336m asl) above the section base can be traced laterally for meters (Figure 7.22). This bed reflects a significant lake level drop, as indicated by the multi-proxy records and lithostratigraphic units, and could be chronologically and topographically correlated with the Gypsum Units of Torfstein et al. (2013a). Based on the preliminary U/Th age estimates (section 7.2.6), the DS1 GU is located between two age estimates of 39.4±1.09 ka and 37.8±1.53 ka. Thus, the DS1 GU can be chronologically correlated with the Broken Gypsum Unit of Torfstein et al. (2013a) (Table 7.6).

The subsidence or uplift is determined by the sediments location, for example, in Massada (MS) and Nahal Meshmar (MSH) (Figure 7.23) (Bartov et al., 2006; Torfstein et al., 2013b), a subsidence rate of 0.3 m/ka for the last 50 ka was calculated and applied to correct the Lisan sediments altitudes. On the other hand, in the Lisan Peninsula, the estimated uplift rate was 2.3 m/ka for the last 34ka (Bartov et al., 2006).

The Broken GU was initially measured at -356.96 m asl (Torfstein et al., 2013a), however, following the application of a subsidence rate of 0.3 m/ka, Torfstein et al. (2013b) modified the altitude of the Broken Gypsum Unit to -345 m asl. This latter correction indicates a stratigraphic difference of ca. 9m between the DS1 GU and the Broken Gypsum Unit.

This stratigraphic discrepancy can be resolved when applying the uplift rate calculated by Jara-Muñoz et al. (2020). The authors calculated an uplift rate of 0.19 m/ka for the last 50ka at the Potash Site (Figure 7.23) located less than 1km to the south of the DS1 section. By applying this uplift rate to the DS1 section, the DS1 GU can be topographically adjusted to -343.4±0.3m asl (Figure 7.24). This suggests a good correlation between the eastern and western DSB Lisan exposures and thus adjusts the DS1 section altitude to ca. -345 to -340.5 m asl, however, considering that the U/Th age estimates of the DS1 section are still under development, this correlation is preliminary and could be refined accordingly.

Figure 7.22 Westward view photograph showing the DS1 section and the lacustrine sedimentary exposures in the vicinity. Dashed white line denotes the DS1 Gypsum Unit.
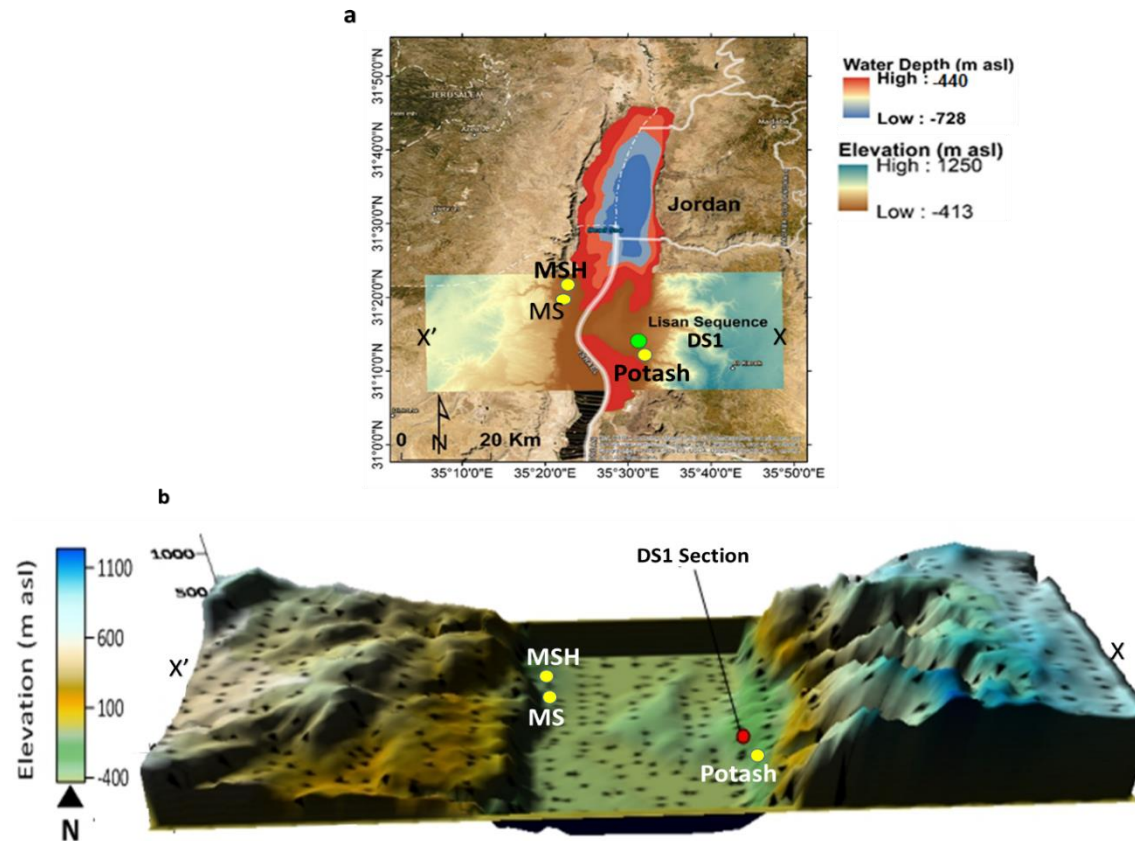
Figure 7.23 a) Schematic map showing the present-day Dead Sea and locations of key sites discussed in the text. b) E-W 3D topographic representation of the X-X' profile marked on (a) and illustrating the difference in the uplift rates between the two sides of the DSB where higher summits are located along the eastern side of the basin. Created using Surfer8 software based on SRTM v3 (30m pixel) Digital Elevation Model (DEM). **MSH**: Nahal Meshmar, **MS**: Massada. Dead Sea bathymetry data from Neugebauer et al. (2014).

Table 7.6 Correlation between the DS1 Gypsum Unit and the Broken Gypsum Unit of Torfstein et al. (2013b) (after the application of 0.3m/ka). The applied tectonic correction for the DS1 GU is 0.19m/ka uplift based on Jara-Muñoz et al. (2020).

	Torfstein et al. (2013b) Broken GU					DS1 GU			
	Top	Bottom	Elev. m a.s.l	Correc. Elev.		Above	Below	Elev. m a.s.l.	Correc. Elev.
Tuned age (ka)	38.3	39.7	-357	-345	U/Th age (ka)	37.8	39.4	-336	-343.4 ±0.3
±	0.5	0.5			±2s	1.53	1.09		
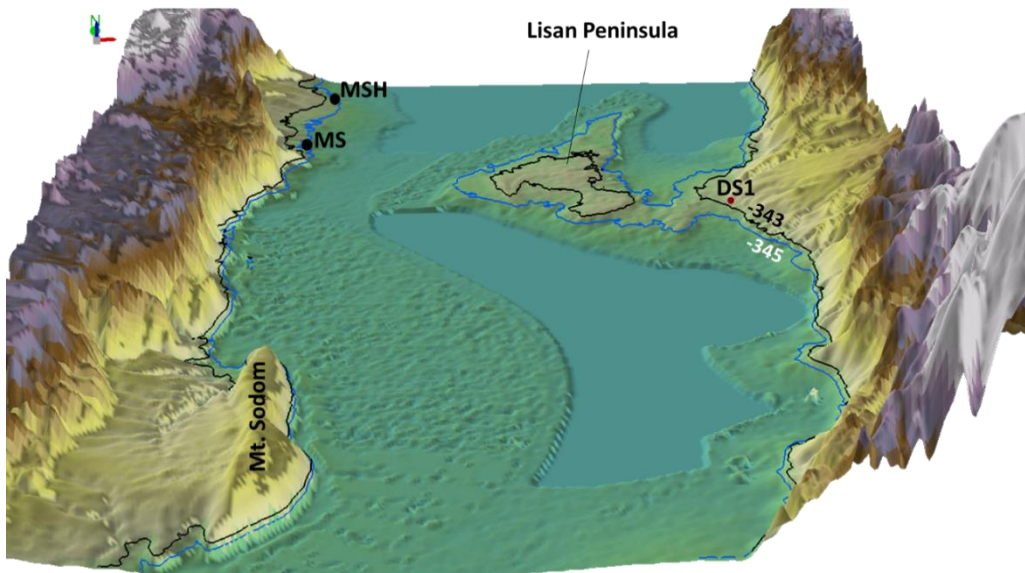
Figure 7.24 3D representation of the southern DSB showing the location of DS1 section relative to MSH and MS. Contour lines indicate the assumed altitudes of the Broken Gypsum Unit of Torfstein et al (2013b) and the DS1 GU at -345 and -343m asl, respectively. Vertical scale exaggerated for better delineation. **MSH**: Nahal Meshmar, **MS**: Massada.

7.2.8   Discussion

7.2.8.1   DS1 sediments as relative lake level indicators

During the Lisan Middle Member period, Lake Lisan levels fluctuated over millennial timescales by up to 100m, at lower levels compared to MIS4 and MIS2 (Machlus et al., 2000; Stein and Goldstein, 2017; Torfstein and Enzel, 2017). From 55 to 50 kyr the lake level was relatively low indicating a shallow water environment and the lake level stood at ca. -290 m asl. Following this, at ca. 47 kyr, the lake level dropped to ca. -320 to -330 m asl and an erosional channel was developed in the Perazim Valley. Then, at ca. 42 kyr, the lake level rose to ca. -280 m asl depositing *aad* sequences in the Perazim Valley and Massada off-shore sections. Following this lake level rise, at ca. 39 to 38 kyr the lake levels fluctuated depositing *aad* and gypsum in the lake and sand and gravel at the shore near Perazim, during which the gypsum unit at ca. 39 ka was deposited corresponding to low lake levels approaching ca. -330 m asl (Stein and Goldstein, 2017). This fluctuation was then followed by a lake level of ca. -285 m asl from 37 to 35 kyr (Machlus et al., 2000). Accordingly, the DS1 section, spanning ca. 40 to 37 ka, at an altitude of ca. -345 to -340.5m asl, after applying the tectonic uplift correction, records Lake Lisan limnological and hydroclimatic changes during an important period of the Lake, when it fluctuated between ca. -330 to -280m asl (Machlus et al., 2000) (Figure 7.25).

The generally low lake levels during MIS3 generated a lake sedimentation system that was sensitive to small lake level changes causing rapid and short-term, centennial to millennial, transitions from one facies to another (Machlus et al., 2000; Kolodny et al., 2005; Torfstein and Enzel, 2017).
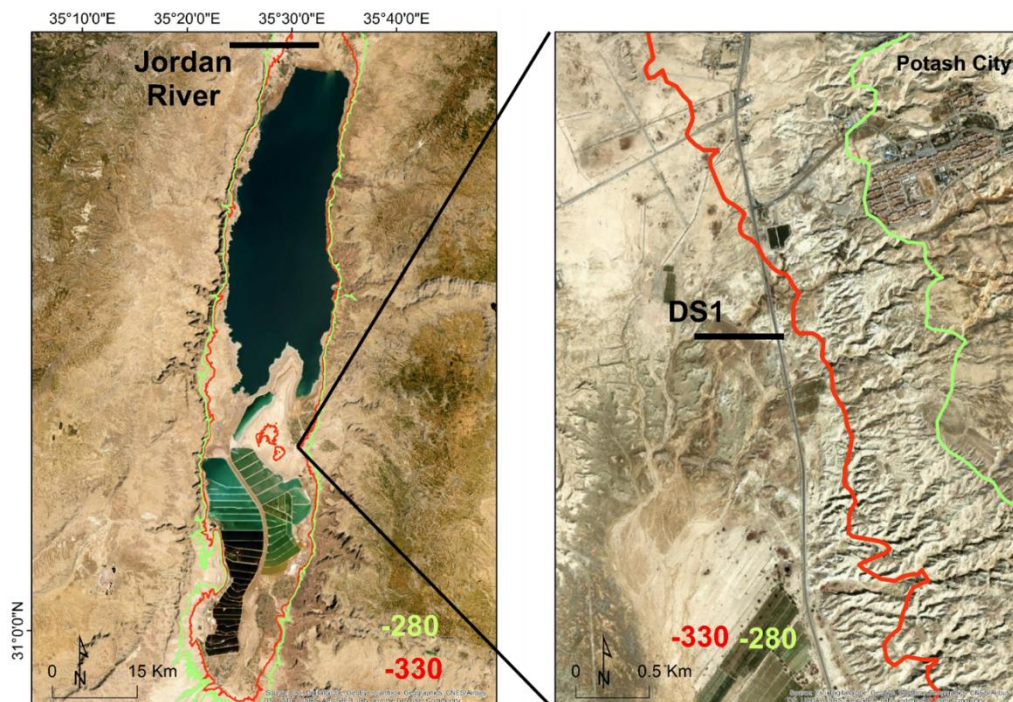
Figure 7.25 Present-day Dead Sea with Lake Lisan extension during the high (-280m asl) and low (-330m asl) levels of the Lisan Middle Member (left). Blow-up of the DS1 section location relative to the Lisan Middle Member high and low lake extensions (right). Based on SRTM v3 (30m pixel) Digital Elevation Model (DEM).

These limnological changes are recorded in the DS1 section lithostratigraphic units indicating the long-term variability and in the DS1 aragonite laminae reflecting the short-term, close to annual, changes.

Based on the current dating control, the DS1 SU1-I corresponds to an age of ca. 39.18±0.21 ka to 39.44±1.09 ka (Figure 7.21). During the deposition of this unit, the record indicates rather stable hydroclimatic conditions with small variations in the in-lake deposition and catchment in-wash in the DSB, where the deposition is dominated by *aad* sequences and rare *ld* periods. Near the middle of this unit, Block S1 (see 7.2.5) was collected. The mineralogical and isotopic composition of this block also indicates that the short-term climate variability was minimal and stable hydroclimatic conditions dominated.

Towards the end of SU1-I, the environemntal proxies indicate a gradual change in the lake conditions and the catchment hydrology. SU2, at ca. 39.44±1.09 ka, starts with a decrease in lake levels and catchment in-wash suggesting variable climatic conditions with increased aridity leading to the deposition of the GU (Figure 7.21). Indeed, this long term climate variability is also recorded in the laminae composition. Block S2 sediments (see 7.2.5) indicate that during the transition

from SU1-I to SU2 high, short-term, climate variability is recorded as reflected by periods of intense flooding ($\delta^{18}O$ excursions) and periods of increased aridity. This climate instability ends with a pronouced arid period and lake mixing depositing the DS1 GU.

Following the DS1 GU, the DS1 proxies indicate lake transgression and increased levels, during which the catchment in-wash and the aragonite deposition were both enhanced (SU3). The lake filling stage ends at ca. 37.87± 1.52 ka. Following this stage, the lake returned to more stable conditions dominated by *aad* deposition and minor *ld* deposition, marking SU1-II. During this period, the lake levels progressively increased with a reduction in the detrital components suggesting consistently wetter conditions. This long-term trend is also recorded at short-term scales in the carbonate laminae. Block S3 (see 7.2.5) indicates that at close to annual scales, the aragonite $\delta^{18}O$ composition was within the DS1 average values with minor excursions suggesting hydroclimate stability (Figure 7.26). The top of SU1-II is not constrained with an age estimate, however, the proxies show a change in the DSB hydroclimate with lake regression and increased detrital components and dominance of *ld* deposition suggesting a period of decreased freshwater input and dryness in the wider-catchment (SU4). Indeed, at short-term scales, the aragonite $\delta^{18}O$ values of Block S4 (see 7.2.5) record the most enriched values suggesting a pronounced drought period not recorded in any other sedimentary block. This period records the lake's history during increasingly evaporative conditions and low lake levels (Figure 7.26).

This dry period is followed by SU1-III marking a period of lake transgression and reduced detrital components suggesting consistent wet climate and freshwater input. This unit persists towards the top of the DS1 section.

The previous discussion indicates that the DS1 sediments represent an important archive for Lake Lisan hydroclimate variability and records both long-term and short-term climate variability during a significant period through MIS3 (Figure 7.26).
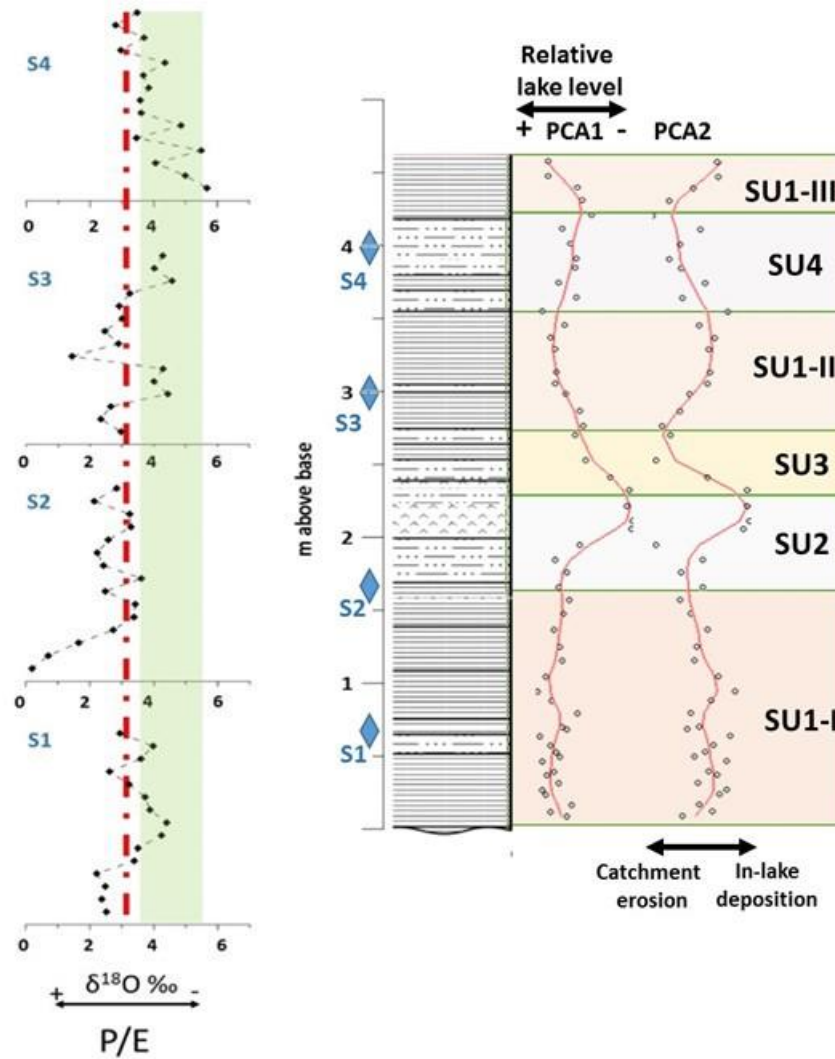
Figure 7.26 DS1 section stratigraphy with the PCA-derived proxies (smoothed lines). Also showing the δ¹⁸O isotopic response to short-term variability during different lake conditions. **SU**: lithostratigraphic unit, **S**: Block S. **Green shaded bar**: Lisan Middle Member long-term δ¹⁸O average (Kolodny et al., 2005). **Red dashed line**: Mean δ¹⁸O value of the DS1 aragonites.

7.2.8.2 Hydroclimatic implications of the DS1 section

The current U/Th dating control of the DS1 section, at ca. 40 to 37 ka, indicates that the section records the Lake Lisan hydroclimatic history during periods of the MIS3 Lisan Middle Member (ca. 58 to 31ka) (Machlus et al., 2000; Bartov et al., 2002; Torfstein et al., 2013b) (see 7.2.6).

MIS3 was characterized by abrupt millennial-scale climatic changes as recorded in ice cores from the Northern hemisphere (Rasmussen et al., 2014), in cores from the Arabian Sea (AL-Tabet et al., 2002), the Andaman Sea (Liu et al., 2021) and in the Indian Ocean (Mohtadi et al., 2014). These changes are represented by

recurrent short-term (millennial scale) warming periods (known as Dansgaard-Oeschger (D-O) events) (Dansgaard et al., 1993). These events comprise the warm Greenland Interstadials (GI) (Huber et al., 2006), that are interspersed by cold periods (known as Greenland Stadials (GS)), during which ice rafting took place in the North Atlantic Ocean, where the most extreme stadials are known as Heinrich Events (HEs) (Dansgaard et al., 1993; Hemming, 2004; Tzedakis et al., 2004; Siddall et al., 2008; Fleitmann et al., 2009; Rasmussen et al., 2014). Based on climate simulations and 3D modelling, Van Meerbeeck et al. (2009) reported that MIS3 global mean annual temperatures were +1.7°C and +2°C higher than the LGM temperatures, for the MIS3 Stadials and Interstadials, respectively, which is associated with increased NH summer insolation and enhanced seasonality (Van Meerbeeck et al., 2009). This was also observed in the Arabian Sea records where Clemens and Prell (2003) reported stronger monsoon events for the MIS3 period reflected by higher summer monsoon factor compared to MIS2.

Even though the Greenland core records suggest that GSs and HEs were dominated by equally cold conditions, records obtained from the western and eastern Mediterranean suggest that the HEs cold conditions were more extreme in these localities compared to the intervening GSs (e.g. Bartov et al., 2003; Tzedakis et al., 2004; Torfstein et al., 2013b). For example, the sea surface temperature (SST) reconstructed from the Alboran Sea core MD95-2043 (3 in Figure 7.27 and Figure 7.28) indicates that the temperature declines are more extreme during HEs, compared to the other GSs, probably reflecting the polar water delivered to the core site through the Strait of Gibraltar (Cacho et al., 1999). Additionally, the HEs in the Alboran Sea records, are marked by a decrease in temperatures where the percentage of *Neogloboquadrina pachyderma* (s) was significantly higher during HE4, compared to HE5 and HE3, indicating that HE4 was more extreme (Tzedakis et al., 2004). These extreme events entering through the Strait of Gibraltar would be disseminated eastward through the Mediterranean resulting in lower SSTs and evaporation which would result in lower moisture content of the Mediterranean climatic circulation, and drier conditions. Following the HEs, the EM cyclones recovered as recorded in the marine and terrestrial archives from Europe, Turkey and the Levant (e.g. Cheddadi and Rossignol-Strick, 1995; Cacho et al., 1999; Tzedakis et al., 2004; Fleitmann et al., 2009; Torfstein et al., 2013b; Rasmussen et al., 2014; Ntinou and Kyparissi-Apostolika, 2016; Torfstein and Enzel, 2017). These short-term climate variations were observed in a lake record from Turkey (Dean et al., 2015). The authors reported,

using carbonate isotopic and mineralogical composition, that short term climate variability in Turkey, through the last glacial and into the Holocene, was related to cold events in the North Atlantic indicating the control of the NA over the EM climate. The understanding of these short-term abrupt climatic events and their drivers is significant as it could further our understanding of the recent rapid climatic changes (Siddall et al., 2008). The following discussion focuses on selected records spanning MIS3 (ca. 47 to 34 ka) in a W-E direction from southern Europe to the DSB (Figures 7.27 and 7.28).
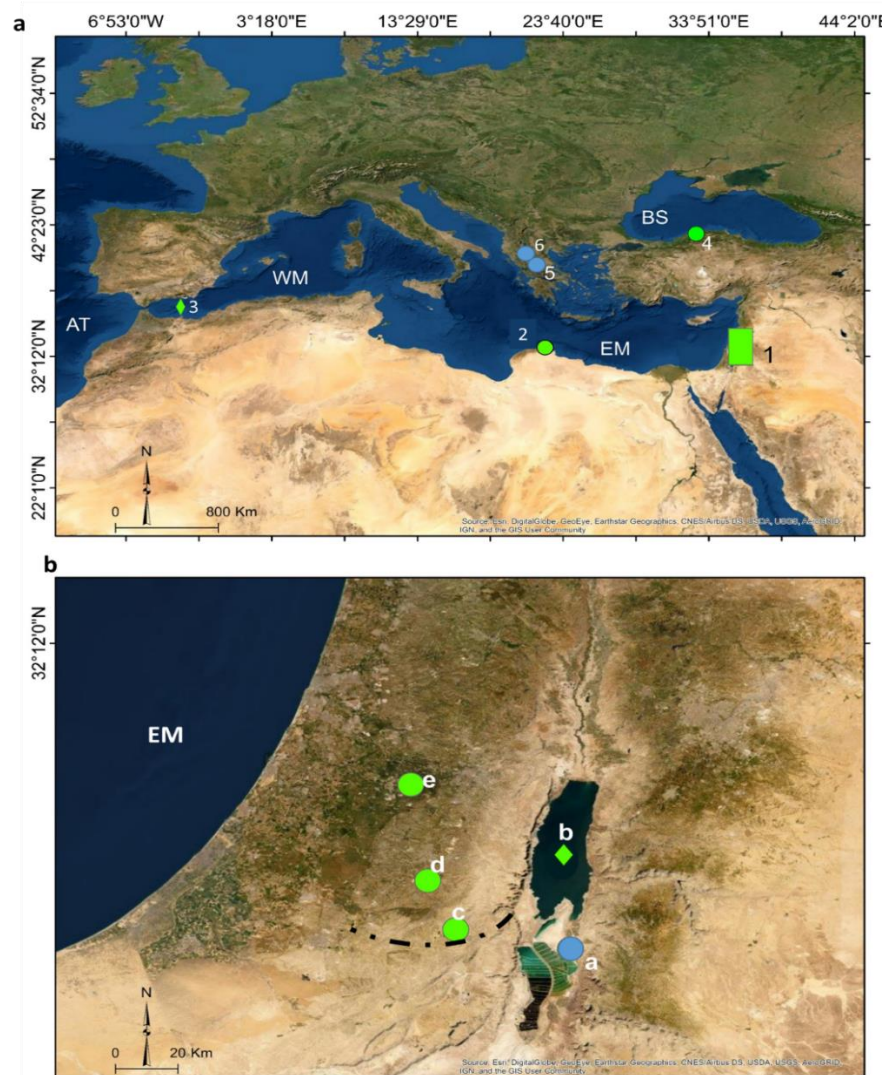
Figure 7.27 Maps showing the DSB (Green Box) and locations of selected key palaeoclimate records of MIS3 discussed in text. (a) Regional records. (b) Local records of the DSB. **Speleothems** (Green circles): 2. Susah Cave, 4. Sofular Cave, 5. Theopetra Cave, d. Ma'ale–Deragot Cave, c. Tzavoa Cave, e: Soreq Cave. **Lacustrine records** (Blue circles): 6: Ioaniina Basin, a: DS1 section. **Cores (Green diamond)**: 3. Core MD95-2043 Alboran Sea, b: DSDDP 5017-1 core. **AT**: Atlantic Ocean. **WM**: Western Mediterranean Sea. **EM**: Eastern Mediterranean Sea. **BS**: Black Sea. Dashed black line: Southern limit of EM moisture penetration at ca. 85-25ka.
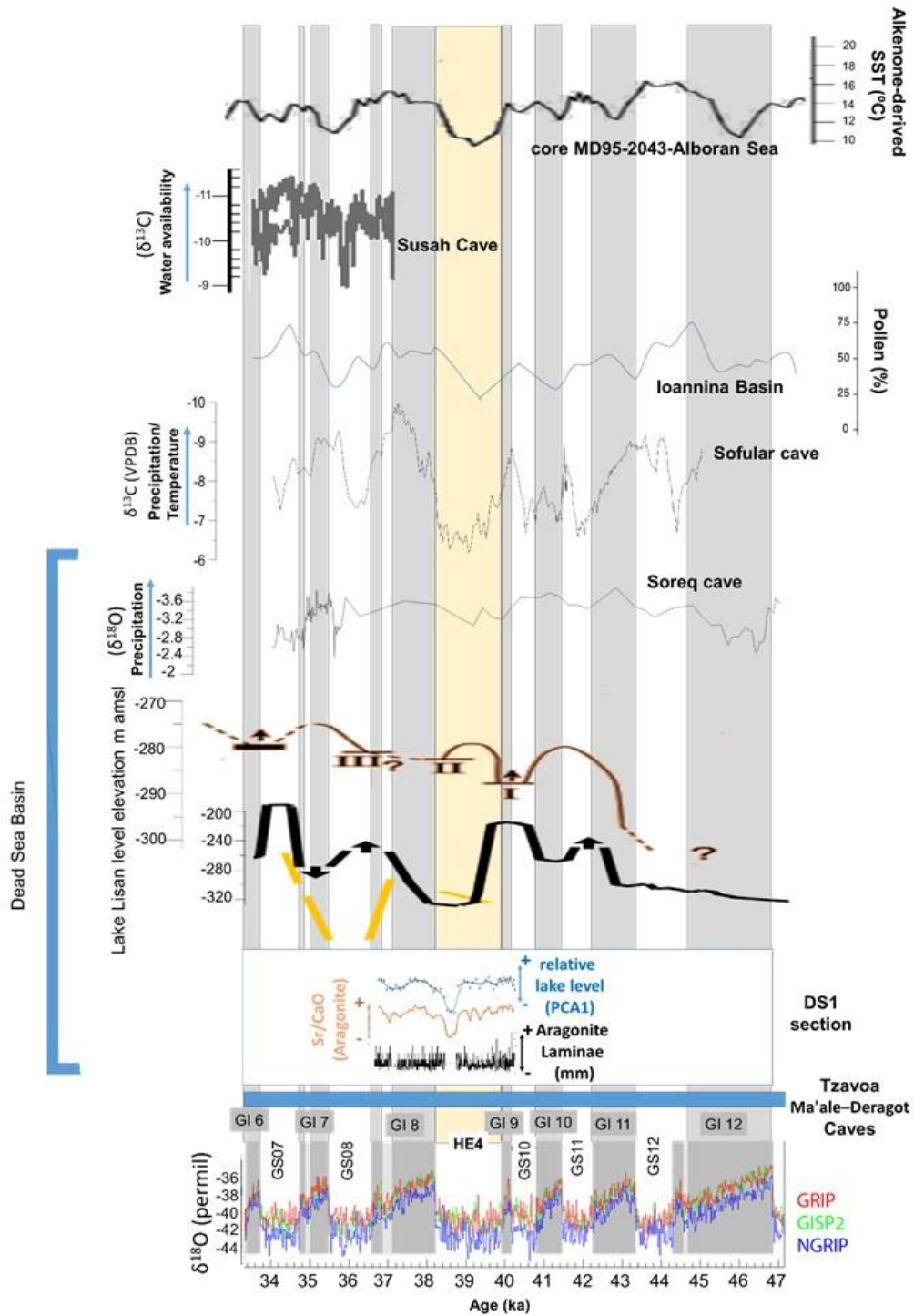
Figure 7.28 Reconstructed records from sites illustrated on Figure 7.27. From bottom to top, data sources: GRIP, GISP and NGRIP records (Rasmussen et al., 2014), Tzavoa and Ma'ale-dragot caves (Vaks et al., 2006), DS1 section: This study, Lake Lisan Levels: black (Torfstein and Enzel, 2017), orange (Landmann et al., 2002), brown (Machlus et al., 2000), Soreq Cave (Bar-Matthews et al., 2003), Sofular Cave (Fleitmann et al., 2009), Ioannina Basin (Tzedakis et al., 2004), Susah Cave (Rogerson et al., 2019), Core MD95-2043-Alboran Sea (Cacho et al., 1999).

Wood charcoal records from Theopetra cave in Greece (5 in Figure 7.27 a) (Ntinou and Kyparissi-Apostolika, 2016) and the pollen record from the Ioannina Basin (6 in Figures 7.27 a and 7.28) (Tzedakis et al., 2004) indicate that the MIS3 period was characterized by abrupt and variable climatic changes. In the Ioannina Basin, the variability in temperate tree pollen records indicates that the effect of the HEs and the GSs are a function of the geographic and orographic location of the record (Tzedakis et al., 2004). The authors reported that in locations receiving high present-day precipitation (ca. 1200 mm.yr^{-1}) at an altitude of 470m asl, even the extreme HEs were not as severe as in locations receiving ca. 470 mm.yr^{-1} located at ca. 40 to 100 m asl. Based on the tree populations' tolerance threshold with regards to climatic oscillations, the pollen record from the localities at lower altitudes showed an almost complete absence of temperate tree populations during HEs, intermediate decline during GSs and increase during the wetter GISs (Tzedakis et al., 2004). This MIS3 abrupt and high climate variability is also reported for lacustrine sediments $\delta^{18}O_{calcite}$, $\delta^{13}C_{calcite}$ and diatom records from the western Mediterranean, including Lake Banyoles in Spain, where the MIS3 period records significant $\delta^{18}O_{calcite}$ and $\delta^{13}C_{calcite}$ excursions, changes in TOC and preserved benthic diatoms suggestung large lake level changes. These fluctuations were attributed to changes in the North Atlantic atmospheric circulation and temperature variability (Lacey et al., 2016).

In Libya, northeastern Africa, the speleothem δ^2H_{excess}, $\delta^{18}O$ and $\delta^{13}C$ records from Susah Cave in Cyrenaica (2 in Figure 7.27) indicated that most of the rainfall reaching this region during MIS3 was primarily sourced from the Mediterranean Basin. Nonetheless, even though the North Atlantic was not a main source of moisture of the MIS3 precipitation over Cyrenaica, the resultant momentum of the Atlantic storm tracks was an important factor in supplying moisture over North Africa (Rogerson et al., 2019). In addition, a moisture source from the eastern Mediterranean is also recorded. Changes of water availability (precipitation amount) in the catchment were estimated using the $\delta^{13}C_{cc}$ record (Figure 7.28) where the lighter values correspond to rapid speleothem growth, and probably reflect changes in vegetation and soil respiration in the catchment. Their results also showed $\delta^{18}O_{cc}$ excursions, from -3.5 to -5.5 ‰ at 40 to 30 kyr BP, corresponding to high δ^2H_{excess} values suggesting an eastern Mediterranean source of moisture (Rogerson et al., 2019).

In Turkey, the Sofular Cave (4 in Figure 7.27) speleothem $\delta^{18}O$ and $\delta^{13}C$ records (Fleitmann et al., 2009) showed that during GIs, the isotopic values vary, at

decadal- to centennial-scales. The $\delta^{13}C$ records, representative of climate-driven variability in the ecosystem, indicate shifts of ca. 1-3 ‰ at few decades-scales during GIs (3 to 13) indicative of increased C3 vegetation and enhanced moisture availability (Figure 7.28), while a shift towards enriched values occur during GSs (Fleitmann et al., 2009).

In the DSB, the Soreq cave $\delta^{18}O$ record (e in Figure 7.27), located ca. 35 km to the east of the EM shore and ca. 40 km to the west of the present-day Dead Sea, reflects amount effects resulting from enhanced EM winter cyclones (Bar-Matthews et al., 1997; Bar-Matthews et al., 2003), showing more enriched $\delta^{18}O$ values corresponding to the GSs and lighter values corresponding to GIs (Bar-Matthews et al., 2003). However, similar to other localities discussed earlier, the Soreq Cave isotope record response to GSs varies, while the values are generally lighter during GIs with variations of ca. 1.2 ‰ (Figure 7.28). To the south of Soreq Cave, in the Tzavoa and Ma'ale–Deragot Caves (c and d in Figure 7.27) speleothem growth records generally wetter conditions, compared to the present, during the period from 47 to 34 ka (Vaks et al., 2006). Tzavoa Cave is presently located in a desert environment (<300 mm.yr^{-1} precipitation) and no Holocene speleothem deposition has been recovered from the cave. To the north of Tzavoa Cave, Ma'ale–Deragot Cave, presently receives ca. 300 mm.yr^{-1} precipitation, with minor Holocene speleothem deposition. Vaks et al. (2006) suggested that Tzavoa cave represents the southernmost extent of thick speleothem deposition in the DSB for the last 200 ka with EM cyclones as the main moisture source (dashed line in Figure 7.27 b) with no significant contribution from southern tropical moisture sources (Vaks et al., 2006).

The Lake Lisan records from exposures in the DSB (Machlus et al., 2000; Bartov et al., 2002; 2003; Landmann et al., 2002; Torfstein et al., 2013a) and from the DSDDP core (b in Figure 7.27) (Torfstein et al., 2015; Neugebauer et al., 2016) provided data on long-term (e.g. glacial/interglacial) lake level fluctuations and indicated the control of the North Atlantic Ocean and EM climatic conditions over the lake level changes. Few studies attempted to recover short-term, millennial to decadal, lake level variations in order to identify short-term changes in P/E ratios and flood events and to assess the changing moisture sources (e.g. Prasad et al., 2004; Ben Dor et al., 2018; Lu et al., 2020).

Generally, the Lake Lisan integrated level curve (Torfstein et al., 2013a) (Figure 7.28) shows the close relationship between the DSB, the EM and North Atlantic

climatic variability. The GIs are represented by higher lake levels (wetter conditions), while the GSs are reflected by generally lower lake levels (drier conditions) (Abu Ghazleh, 2021). The most significant lake level drops observed in the Lisan exposures along the western DSB, reflected by gypsum deposition, coincide with HEs in the North Atlantic (Bartov et al., 2003). This relationship indicates the dominance of the EM cyclones in driving the DSB hydroclimatology during the period from 47 to 34 ka. Similar to other localities, the DSB hydroclimate shows varying responses to the different GSs with the most extreme lake level drop synchronous to HE4, depositing a thick gypsum unit (Torfstein et al., 2013b). Short-term high Lake Lisan levels are recorded at 42.4, 40.5, 36.7 and 34.5 ka corresponding to the warm GIs following the cold HEs or GSs (Figure 7.28), indicating a close relationship between the DSB hydrology and the North Atlantic climate (Torfstein et al., 2013b), which was also observed at decadal to centennial time scales during MIS2 (Prasad et al., 2004).

In addition to the main moisture from the EM cyclones, a southern source of moisture has also been suggested to have contributed to Lake Lisan level fluctuations during MIS3 (Waldmann et al., 2010; Torfstein et al., 2015) based on the presence of travertine deposits in Wadi Araba to the south of the present Dead Sea which suggests a northern migration of the ITCZ and a tropical moisture source reaching the DSB (Waldmann et al., 2010), but whether the source was the Red Sea Trough (ARSTs) or the African Tropical Plumes (ATPs) is still a debate. Further south, the formation of lakes and wetlands in Arabia (Jubbah and Al Marrat Basins) during MIS3 at ca. 60 ka also suggest northward intrusion of the southern monsoon precipitation during periods through MIS3 (Parton 2018; Jennings; 2016).

The DS1 section (a in Figure 7.27), at ca. 40 to 37 ka, comprises four different lithostratigraphic units reflecting variable lake limnological and hydroclimatic conditions. From ca. 0.70 m (at 39.187±0.216 ka) to 1.6 m (at 39.446±1.09 ka) above the section base, the lithostratigraphic unit SU1-1 represents relatively high lake levels, *aad* deposition and a positive water balance as recorded in the environmental proxies (see section 7.2.8.1). This unit is probably synchronous to GI9 indicating higher water input into the lake reflecting increased runoff consistent with what is observed in other local and regional records. Excursions to lighter $\delta^{18}O$ values, changes from 3.6 to 0.19 ‰, are recorded close to the end of this unit at ca. 1.59 to 1.62 m above the section base indicating that short-term, close to seasonal, changes in water input into the lake took place towards the end of

this period and the transition into HE4. Following this period, the SU2 unit records a change in the basin hydroclimate, relatively lower lake levels and dominance of *ld* deposition, probably reflecting the response to lower precipitation reaching the DSB during early HE4 and followed by the deposition of the Gypsum bed indicating a significant lake level drop during the HE4 peak. This period records the lowest lake level in the section, and even though the age estimates are still to be confirmed, the negative water balance conditions and aridity caused by HE4 in the DSB for a sustained period would cause a shift in the lake chemistry and salt concentrations leading to the gypsum bed deposition.

After this arid period, from ca. 2.3 m to 2.65 m above the section base (at 37.872±1.529 ka), the lake filling stage is indicated by the deposition of the SU3 (see section 7.2.8.1) with a gradual return to positive water balance conditions and enhanced freshwater input into the lake probably synchronous to GI8 and the positive water balance recorded in the local and regional records. The upper ca. 2 m of the section are not yet constrained by age estimates, however, the lithological nature of the sediments and the multi-proxy results show two limnological and hydroclimatic periods. The deposition of SU4, which primarily reflects fluctuations of catchment in-wash and decrease in lake levels, could also be synchronous to GI8 fluctuations, while the deposition of SU1-III reflects a return to positive water balance conditions and could be synchronous to the reconstructed Lake Lisan level rise prior to GS8 peak. However, this needs further dating control to constrain and correlate, with high resolution local and regional records. In addition to the millennial-scale hydroclimatic variability, the DS1 aragonites record close-to-annual environmental variability and indicate that the DSB experienced short-lived events, of intensified precipitation, and possible seasonality variations, where enhanced precipitation is recorded at times and severe droughts, probably more arid than the present, are recorded during the low lake levels and most likely corresponding to HEs and GSs.

Further constraining of the DS1 section age estimates and reconstructing its complete environmental history will add significant information on the short-term response of the DSB to local, and regional, climatic fluctuations and the changing frequency and intensity of the moisture bearing systems.

7.2.8.3 Synoptic-scale and moisture sources inferred from the DS1 sediments

The present-day precipitation over the Levant, and the DSB, is primarily of EM origin, namely the winter EM cyclones, while the effect of these cyclones is a function of their characteristic depth, intensity and frequency (Enzel et al., 2003; 2008; Kushnir et al., 2017). Other, less effective moisture sources, reach the Levant from the south during transitional seasons, namely the ARSTs and the ATPs (Saqqa and Atallah, 2004; Dayan et al., 2008; Kushnir et al., 2017) (see Chapter 2, 2.2). It has been suggested that similar climatic controls prevailed over the Levant through times during the Late Quaternary (Enzel et al., 2008).

Lake Lisan endogenic precipitates, such as aragonites, record changes in moisture sources driving their deposition, over time and space, making them valuable archives to assess the changing importance of these sources (e.g. Kolodny et al., 2005; Kiro et al., 2020).

Variations in the endogenic aragonite initial ($^{234}U/^{238}U$) activity ratios are discussed here in relation to assessing changing water sources, hence moisture sources (Kiro et al., 2020), that prevailed during the deposition of the DS1 sediments.

The uranium is primarily sourced from the fresh water that enters the lakes in the DSB, from the north, south and groundwater sources, where its residence time is ca. 300 years and its steady state is achieved in ca. 1500 years. Due to its solubility and short residence time, U has been reported to be suitable to investigate temporal changes of water sources (e.g. Haase-Schramm et al., 2004; Kiro et al., 2020). Nonetheless, implementing the $^{234}U/^{238}U$ ratios as water source indicators requires careful consideration of the local geological and hydroclimatic conditions of the record (Robinson et al., 2004).

Lakes in the DSB have fluctuated in magnitudes of hundreds of meters, but the range of long-term $^{234}U/^{238}U$ initial ratios remained in a steady range. For example, the Holocene Dead Sea aragonites have $^{234}U/^{238}U$ initial ratio of 1.45 and the aragonites from the last glacial, when Lake Lisan reached high levels, show a ratio of 1.51±0.01. This is attributed to the dominance of the northern and western tributaries as main water sources, where the $^{234}U/^{238}U$ ratios from these tributaries range from 1.4-1.7 (Figure 7.29) (Haase-Schramm et al., 2004; Torfstein et al., 2015; Kiro et al., 2020).

Since the lakes in the DSB are low in uranium, Kiro et al. (2020) reported that changes in the DSB aragonites initial $^{234}U/^{238}U$ ratios primarily reflect changing sources of moisture over time. Figure 7.29 shows the present-day $^{234}U/^{238}U$ ratios of the water entering the DSB from the northern, western, southern and eastern sources (Kiro et al., 2020). The variability in the ratios primarily depends on the lithology and the water-rock interaction period, where the water coming from the north and west is discharged through carbonate rocks with longer rock-water interactions and shows higher ratios compared to the eastern and southern water, primarily with shorter rock-water interaction intervals. In addition, the water from the southern and eastern floods, mainly associated with southern sources of moisture, have generally low $^{234}U/^{238}U$ ratios (ca. 1.08 to 1.3) (Kiro et al., 2020). Thus, changes in the aragonite initial $^{234}U/^{238}U$ ratios reflect the variability in the dominant moisture source where the southern and eastern sources, associated with tropical moisture show relatively lower values.

However, the DSB aragonites are contaminated with detrital U (see section 7.2.6) which could result in lower $^{234}U/^{238}U$ ratios and thus a correction is needed prior to implementing these ratios in any further analysis (Haase-Schramm et al., 2004; Torfstein et al., 2013b; Kiro et al., 2020).

Figure 7.29 ^{234}U/^{238}U activity ratios in the present-day Dead Sea water sources (from Kiro et al., 2020). Also shown is location of DS1 section.

The DS1 aragonites $^{234}U/^{238}U$ ratios were corrected for the detrital contamination following the approach of Haase-Schramm et al. (2004) and the results (Table 7.7) show that the corrected ratios are not significantly altered compared to the uncorrected ratios, indicating that the detrital contamination does not have a significant effect on the initial $^{234}U/^{238}U$ ratios, and probably record the change in water sources, similar to the observations of Kiro et al. (2020). Nonethelss, sample 156-4, the sample with the highest detrital contamination, shows the highest change in the $^{234}U/^{238}U$ ratios of ca. 0.014 units.

Table 7.7 Initial $^{234}U/^{238}U$ ratios for the DS1 aragonites showing the change after applying the - Haase-Schramm et al. (2004) detrital correction.

Sample	Bulk earth corrected		Corrected- Haase-Schramm et al., 2004	
	Initial $^{234}U/ ^{238}U$	±2σ	Initial $^{234}U/ ^{238}U$	±2σ
156-1	1.520	0.009	1.522	0.020
156-2	1.534	0.011	1.540	0.029
156-3	1.512	0.003	1.507	0.002
156-4	1.506	0.011	1.520	0.041

Based on the present-day calculated ratios and the U isotope budget calculations, Kiro et al. (2020) classified the changing moisture sources based on $^{234}U/^{238}U$ initial ratios of the endogenic precipitates of the DSB (Figure 7.30). The four aragonite samples of the DS1 section suggest that the northern (Jordan River) and western catchment were the primary source of water input and thus the dominance of the EM winter cyclones in providing the moisture during the deposition of the DS1 section.

These observations agree with the calculated water budget for the last glacial Lake Lisan (Kiro et al., 2020) where the southern and eastern catchment floods contributed ca. 12% of the total water reaching the DSB. In addition, even though there was a northward intrusion of the monsoon precipitation into the Arabian peninsula at ca. 55 ka (Jennings et al., 2016; Parton 2018), these initial results suggest that this southern precipitation did not reach the DSB at ca. 40 ka to 37 ka which further distinguishes MIS3 in the DSB from the interglacials, e.g. MIS5e (Waldmann et al., 2010), when a significant contribution of tropical moisture, of ca. 55% of the total water reaching the DSB, is recorded (Kiro et al., 2020). This also agrees with the local records from Soreq cave and the Negev Caves suggesting the dominance of the EM cyclones in supplying water through the northern and western tributaries to the DSB during this period and the southern migration of the

desert belt to the south of Tzavoa Cave (Figure 7.28 b) (Bar-Matthews et al., 2003; Vaks et al., 2006) and the observed intensification of the EM cyclogenesis reaching coastal Libya between 40 to 30 kyr BP (Rogerson et al., 2019). This is also significant as it indicates that the short-lived, intense precipitation/severe drought events observed through the DS1 aragonite $\delta^{18}O$ records were probably the result of intensified/reduced EM cyclones reaching the southern DSB and not the result of localized ARSTs as observed today (e.g. Kahana et al., 2002).
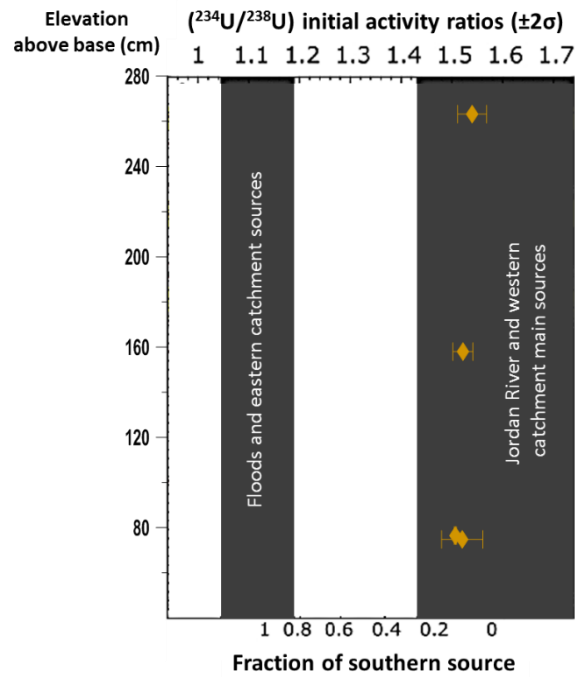
Figure 7.30 Initial $^{234}U/^{238}U$ ratios in DS1 aragonite vs. elevation above base in section (left axis), showing that the DS1 samples are within the typical value for both interglacials and glacials in the DSB (ca. 1.4-1.5).Also showing that sample 156-4 uncertainty is higher than the other samples due to its content of detrital contamination (modified after Kiro et al., 2020).

The ongoing work on the DS1 aragonites, gypsum and clastic samples will add significant data to assessing this changing importance of the EM cyclones at a higher resolution. This is significant in the DSB and the Levant, as assessing the changing sources of water during the abrupt climatic conditions of the MIS3 could provide important insights into the recent and future climatic changes.

7.3   Chapter Conclusions

Representative Lake Lisan exposures are located in the central to southern Dead Sea Basin (DSB). The DS1 section, ca. 4.6 m, lies in the southern DSB close to the Lisan Peninsula and it is comprised of three main facies: the alternating aragonite and detrital (*aad*) facies, the laminated detrital (*ld*) facies and the gypsum unit (GU).

Based on previously reported correction factors, the DS1 aragonites yielded U/Th age estimates of ca. 40 to 37 ka which place the DS1 section as part of the Lisan Middle Member (ca. 58 to 31ka) that prevailed during MIS3, and based on laminae couplets count, a total *aad* laminae couplets of 1927±67 was estimated. All samples are within the range of accepted U/Th isotopic composition from the DSB aragonites and the initial $^{234}U/^{238}U$ activity ratio range.

The DS1 section is subdivided into 4 main lithostratigraphic units (SU1 to 4) based on the sedimentological and geochemical composition of the bulk sediments. SU1 generally record periods of lake stability and aad deposition, SU2 records the lake regressive phase that ends with the deposition of the thick gypsum unit, SU3 records the lake filling-up stage and primarily catchment in-wash and SU4 records periods of lake regression and low lake levels where primarily *ld* deposition is present. Well-preserved diatoms were located in two laminae from the DS1 section and these represent the first reported diatoms from the southern DSB indicating the potentiality of the DS1 section for a high resolution diatom investigation.

Based on chronological correlation of the DS1 gypsum unit and the marker gypsum units on the western side of the basin, a correction of 0.19 m/yr was used to account for the tectonic uplift of the DS1 section.

The sedimentological and geochemical characteristics of the DS1 sediments record millennial scale, relative lake limnological changes (in-lake deposition/catchment in-wash) reflecting the wider catchment hydrodynamics and are in agreement with the previously reported lake levels for the Lisan Middle Member. Furthermore, based on 80 aragonite laminae isotopic ratios, the DS1 aragonites provided high resolution, close to annual, changes in the lake limnology as a response to changes in the wider catchment.

These results, in agreement with previous studies, indicated that the MIS3 period was characterized by rapid environmental and climatic changes in the DSB

corresponding to the GSs and GIs, at both millennial and close to annual scales, recording changes in the synoptic scale moisture bearing system, the EM cyclones in the case of the DS1 section.

Further U/Th dating will add significant data in order to constrain the DS1 section age estimates and provide means to test whether the *aad* facies do represent varves or not, which will also allow for a more detailed reconstruction of the, close to annual, hydroclimatic changes in the DSB during MIS3. This is significant in the DSB and the Levant, as assessing the changing sources of water during the abrupt climatic conditions of the MIS3 could provide important insights into the recent and future climatic changes, and the modelled future aridity in the region where more arid condition are expected over the next decades (e.g Alraggad et al., 2017). These changes are critical for water availability in the Levant which is a critical factor in the region's socio-economic and political stability (Kelley et al., 2015).

Chapter 8. Conclusions

This study aimed to contribute new data and understanding regarding the Quaternary sedimentology of Jordan, through undertaking multi-proxy analyses on sediments from two study areas in arid southern Jordan, presently receiving ca. 50 mm.yr^{-1} precipitation: the fluvial/wetland Gharandal Valley system and the eastern Dead Sea Basin (DSB) lacustrine system (DS1 section).

Using detailed (high resolution) sedimentological and geochemical records from two sedimentary sections (ca. 30 m of sediments) and lower resolution sampling from three other sections, from the presently arid Gharandal Valley, this research emphasized the importance of detailed investigation and analyses of sediments in better understanding the depositional environments and hydrodynamics of palaeo fluvial/wetland systems in arid regions.

In addition, through high resolution analyses of a 4.6 m section of finely laminated lacustrine sediments from the Jordanian side of the DSB, this research provided new insights regarding the DSB past relative lake levels, the lacustrine sediments' nature, composition and the tectonic settings in the basin. Laminae by laminae analysis, from some parts of the DSB section, provided data about the lake system sensitivity to short-term (close to annual) local and regional changes in P/E ratio.

This Chapter presents the key findings from the two study sites before outlining the contribution of this research to the Quaternary of Jordan and recommendations for future work.

8.1   Sediments as palaeoenvironmental archives

Through detailed analyses of the sediments from the two study sites, the depositional environments, environmental conditions, and how these changed, and to some extent their timing were reconstructed.

8.1.1   The Gharandal Valley

The five sections from the valley were found to be characterized by four primary sedimentary lithofacies representing distinct depositional processes and cycles. The lithofacies include: the flood lithofacies (*Gh*) characterized by its content of significant amounts of gravel-sized clasts (>2 mm); mass flow deposits (pebbly sand *Ss* lithofacies) that is mainly composed of coarse sand fractions and <15 wt. % small granules; the sand lithofacies of primary sand contents (*Sm*, and *Sr* lithofacies) that are distinguished by the presence of sedimentary structures (*Sr*) and the massive nature of the sediments (*Sm*), and the fine sediments (wetland)

lithofacies (*Fm* and *Fl*) distinguished based on the presence of faint lamination (*Fl*) and the massive nature (*Fm*) and their elevated organic (LOI$_{550}$) content.

The GH1 section is the only section where all lithofacies are present indicating the complexity of the depositional history recorded in its sediments (Chapter 5; 5.2). The GH2 section comprises the *Ss, Sm, Sr* and *Fm* lithofacies, while the flood lithofacies (*Gh*) is absent (Chapter 5; 5.3). The GH3/GH4 sections are primarily dominated by the sand lithofacies, while the GH5 section is primarily *Fm* lithofacies (Chapter 5; 5.4).

The GH1 and GH2 sections have been previously considered as one continuous sequence (Mischke et al., 2017; Al-Saqarat et al., 2020). Although the two sections record alternating periods of fluvio-aeolian, fluvial and wetland conditions and in-wash events up to 13.4 m above the base of the GH1 section and 10.8m above the GH2 section base, the outcomes of this study indicated stratigraphical, sedimentological and geochemical variability within the two sections.

Stratigraphically, the two sections do not show vertical and lateral continuity from the base of the GH1 section to the top of the GH2 section (see Figure 6.1), particularly starting from ca. 5m above the GH2 section base where the granulometric composition indicates dominance of fine and very fine sand contents compared to the general dominance of medium and coarser sand through the GH1 section. This combined with the absence of the flood *Gh* lithofacies in the GH2 section suggests the dominance of lower energy valley hydrodynamics during its deposition, compared to the GH1 section. This variability is also indicated when applying the vertical facies Markov Chain analysis model (see Chapter 6, 6.2). The two sections indicate that the fining upward deposition is typical, however, the results indicate that the deposition through the GH1 section is random while the GH2 deposition follows a non-random cyclicity.

In terms of the elemental composition, the SiO$_2$ content shows significantly higher values in the GH2 sediments reaching up to 96 %, compared to ca. 70 % in the GH1 sediments. In addition, the GH2 section environmental proxies show a more stable depositional environment where the allogenic markers show narrower ranges and variability. For example, the K values range from -1.1 to 13.5 (mean 2.6, std. 2.6) and Ti (from 0.05 to 0.57 wt. %, mean 0.2 wt. %, std. 0.1 wt. %) compared to the values of the GH1 sediments of K (from -6.3 to 16.6, mean 3.2, std. 3.9) and Ti (from 0.07 to 0.7 wt. %, mean 0.3 wt. %, std. 0.15 wt. %) (see Chapter 5). These variations can be attributed to several reasons; for example,

the location of the section in the valley where the GH1 section is a mid-valley section, while the GH2 section is located closer to the valley side, valley hydrodynamics, the flow characteristics, composition and axial distribution and the fill and cut of fluvial deposition.

Overall, the GH1 and GH2 sections record the valley sediments aggradation from stream-fed wetland depositional conditions where thin wetland beds developed following in-wash events, in the lower parts, into more consistent wetland (wetter) conditions towards the top of the sections. These cycles were identified in 16 fining upward primary associations in the GH1 section and 8 fining upward primary associations in the GH2 section.

The GH3/4 sections primarily record sand lithofacies with only few thin wetland beds. This is probably due to the sections' location upstream and the reduced influence of the groundwater table at these altitudes, compared to the downstream near the valley outlet, while the GH5 section records wetland beds overlying a gravel dominated bed indicating the change in valley hydrodynamics.

The demise of the Gharandal wetland probably occurred as a result of fluvial in-wash events as recorded in the upper part of the GH2 section that eventually breached the outlet dam and did not permit the formation of wetland conditions.

Regarding the dating of the Gharandal sediments, the results of this study and the re-evaluation of previously published OSL age estimates indicated that they are sensitive to depth, long-term average water content and sediments' overburden density. This sensitivity increases with the sediment age, where the understanding of the sediments' composition and associated valley hydro (aero) dynamics is required in order to achieve better constrained age estimates. The stratigraphically inconsistent age estimates recovered from the two sections may also be affected by the lack of continuity between the GH1 and GH2 sections and the probable effect and balance between tectonic-driven and climatic-driven incisions and deposition.

8.1.2 The lacustrine Dead Sea Basin DS1 section

The environmental history of the DS1 section was reconstructed as recorded in the multi-proxy records of four lithostratigraphic units (Chapter 7, 7.2.3). The DS1 section records periods of enhanced/reduced freshwater input into the lake (P/E ratio) at millennial, centennial and close to annual scales (see below), reflected in relative changes in lake levels and the carbonates mineralogical and isotopic

composition. Within the DS1 section, a thick (ca. 30cm) gypsum bed is present indicating a significant lake level drop.

This study also reported the presence of diatoms in the DS1 section providing potential for further detailed investigations of this environmental proxy.

Regarding the dating of the Lisan aragonites, the results of this study indicated the importance of examining the laminae for detrital contamination through SEM EDS and mineralogical analyses in order to reduce its effect on the age estimates (Chapter 7; 7.2.5). In addition, it emphasized the previously reported suggestion that, for each distinct sedimentary section in the DSB, specific detrital end member (DEM) and hydrogenous correction should be estimated. This study also showed that ca. 10 mg of clean aragonite can provide reliable age estimates, less than previously used amounts of ca. 100 mg of carbonates (Torfstein et al., 2013a).

Based on the preliminary U/Th age estimates, the DS1 aragonites yielded an age of ca. 40 ka to 37 ka (MIS3), consistent with the counted laminae couplets of 1927±67 (Chapter 7, 7.2.5) and the presence of a thick gypsum bed, placing the DS1 section as part of the Lisan Middle Member (ca. 58 ka to 31ka) (Machlus et al., 2000; Torfstein and Enzel, 2017).

In terms of the debated tectonic effects on the Lisan sediments, the chronostratigraphic correlation of the DS1 gypsum bed with gypsum anchor points from the western DSB indicated a significant effect of tectonics on the altitude of the DS1 section, where ca. 7.5 m uplift for the sediments was calculated.

Regarding the environmental implications of the DS1 section, and bearing in mind the current age control and uncertainties, the environmental proxies suggest that during Greenland Interstadials (GIs), the lake level was relatively higher than during Stadials (GSs) where the lowest relative lake level in the record (deposition of the gypsum bed) probably coincides with Heinrich Event 4 (HE4) peak. At centennial scales, the environmental proxies record lake level changes corresponding to the GIs fluctuations indicating variable amounts of freshwater reaching the DSB (Chapter 7).

8.2   High resolution environmental records

High resolution, centennial to decadal and close to annual, environmental reconstruction can be achieved through detailed, lamina by lamina, analysis. Based on the hydroclimatic changes inferred from the environmental proxies across the whole section, four sediment blocks (ca. 5 cm) representing different Lake Lisan conditions were analysed, at high resolution, for their mineralogical and isotopic contents (Chapter 7).

The analyses indicated that the isotopic and mineralogical composition of the Lisan authigenic precipitates is primarily dependent on the P/E ratio, where during relatively high lake levels, dominance of aragonite precipitation is recorded corresponding to stable $\delta^{18}O$ values.

Bearing in mind the age uncertainties, a possible interpretation is that during GI-9 (Block S1) the results indicate lake levels were relatively high with dominance of aragonite precipitation, while the transition into GS-9 is marked by a change in the P/E ratio (Block S2). The unstable climatic conditions of this period are also reflected by excursions to lighter $\delta^{18}O$ values and in the mineralogy of the aragonites, where calcite and halite phases are present with a decrease in the aragonite precipitation indicating periods of intense flooding and droughts, respectively. During GI-8c (Block S3), the $\delta^{18}O$ values indicate consistent freshwater input into the lake during relatively high lake levels. In contrast, during GI8-b (Block S4) enriched $\delta^{18}O$ values are indicative of drought events and reduced freshwater input into the lake. These results indicate the control of the Northern Hemisphere climate over the DSB hydroclimatology, probably at decadal timescales.

Further constraining of the DS1 age estimates and the confirmation of the laminae *varved* nature could add significant information about the short-term changes in moisture availability, their specific timing, drivers and the DSB hydrological and limnological response to these changes.

8.3 Changing importance of synoptic scale systems and moisture sources

The present-day precipitation over the Levant, and Jordan, is primarily of Eastern Mediterranean (EM) origin, namely the winter EM cyclones reaching as far south as the northern Negev Desert. Other, less effective moisture sources, reach the Levant from the south during transitional seasons, namely the Active Red Sea Trough (ARSTs) and the African Tropical Plumes (ATPs). However, the role of these synoptic-scale systems in driving the Levant climate during past times is still not yet resolved (Chapter 2; 2.4.2).

The age estimates from the Gharandal Valley have high uncertainties making it harder to correlate the environmental proxies with specific periods of changing climate conditions. However, when considering the variance-weighted mean and standard error of the age estimates, of 158±7 ka (Chapter 5; 5.3.2), which suggest that the significant wetland conditions of the GH2 section probably persisted during this period (MIS6), a rough correlation of the environmental proxies with local records of enhanced precipitation (Soreq Cave records) suggests that the Gharandal wet periods during MIS6 are to some extent synchronous to enhanced Eastern Mediterranean precipitation in the DSB (Chapter 7). In addition, the mean depositional age corresponds to periods of enhanced monsoon precipitation in Arabia at 158.7±12.9 ka (Parton et al., 2015a) probably suggesting that during the period from ca. 150 to 160 ka, the suggested intensification of both EM cyclones and southern monsoon precipitation may have maintained the wetland and wet conditions in the Gharandal valley.

On the other hand, the DS1 section laminated sediments provide the potential for higher resolution assessment of the changing importance of moisture sources. The DS1 endogenic precipitates record changes in moisture sources driving their deposition. Based on variations in the DS1 endogenic aragonite initial $^{234}U/^{238}U$ ratios (Chapter 7; 7.2.5), an initial assessment of the moisture sources was done. Based on other studies, the higher lake levels in the DS1 section may be driven by enhanced (and more southerly) EM cyclones, providing precipitation through the northern (Jordan River) and western catchment. This also suggests that the short-term droughts/floods events observed in the high resolution environmental reconstruction were primarily driven by changes in the EM cyclones. Higher resolution analysis of the DS1 laminae will add significant information to resolving the cyclicity and intensity of the EM cyclones during MIS3 in the southern Levant.

8.4   Contribution to Quaternary records of Jordan

This research has contributed new data and understanding to the Quaternary of Jordan and the Levant.

The long, high resolution, sedimentary records recovered from the Gharandal Valley have emphasized the importance of understanding the detailed sedimentological composition and associated hydrodynamics of a given study area, particularly in arid regions, prior to establishing palaeoenvironmental reconstructions and periods of wet/dry conditions, and also its role in achieving better chronological age estimates as sediments from the valley are sensitive to depth, long-term water content and sediments overburden average density. Using the correct dosimetry calculations have shown that better constrained and stratigraphically consistent age estimates can be recovered (see Chapter 5, 5.3.2).

The results of this study indicated the presence of an MIS6 wetland in southern Jordan which adds important information for the understanding of the region's palaeoenvironmental conditions, since Quaternary records, particularly spanning MIS6, are scarce in Jordan and in the Levant (Chapter 2). Assigning these deposits to the MIS6 period is significant since only one other record in southern Jordan from the Qa' Mudawwara spans MIS6 (Petit-Maire et al., 2010) but with uncertain age estimates (Rech et al., 2017). Wetter conditions in southern Jordan during MIS6 synchronous to enhanced monsoon precipitation in Arabia and wet phases in the DSB and Lebanon (northern Levant) (see Chapter 2, 2.4) suggest more uniform climate, compared to the present-day conditions, may have prevailed.

Furthermore, considering the earliest modern human dispersal out of Africa (at 177 ka to 194 ka) (Hershkovitz et al., 2018) and the location of the Gharandal Valley along the MIS6 route linking Africa with the Levant and Arabia, particularly in the central parts of the Tabuk Corridor (Breeze et al., 2016), and considering the poor MIS6 records of southern Jordan, the MIS6 wetland of Gharandal may have been a significant source of water during this period. Which is also supported by the presence of lithic artefacts indicating that the Gharandal Valley was visited by early humans during different periods in the past.

In addition, this study provided the first high resolution sedimentological and environmental records, spanning MIS3, based on the current age estimates, for the Lisan sediments on the eastern side of the DSB, in particular the high

resolution lamina by lamina analyses. It also indicated the role of tectonics in influencing lake level reconstructions and that the previously published records that did not apply such corrections need to be revised. Also, the high resolution laminae analyses indicated relatively large excursions in the Lisan aragonite isotopic composition (ca. 3‰), at close to annual scales, indicating that the natural variability in the system may be masked or lost if sampled at low resolution.

Identifying higher lake levels corresponding to short-term variability during MIS3 in the DSB is significant as it is synchronous with enhanced EM cyclones in the DSB (Bar-Matthews et al., 2003) and monsoon precipitation in Arabia (e.g. Govil and Naidu, 2010; Parton et al., 2013) during GIs, thus providing an opportunity to assess the relationship between the two systems at short time scales. Further dating of the DS1 section sediments and further studies from the southern Jordanian desert will add significant information about these relationships.

8.5   Future work

The observed variability in the Gharandal sedimentological and environmental records indicates their significance as palaeoenvironmental archives for future studies. Further dating of the sediments on both vertical and lateral scales to constrain the spatio-temporal development of the wetland will add significant data to reconstruct the specific timing of arid/wet periods in southern Jordan. Further microfossil analysis of the thick wetland beds identified in this study towards the top of the sections may also add important information to the previously published ostracod data from the lower parts (Mischke et al., 2017) and to the assessment of the nature of the water bodies and their development.

The DS1 section sediments record the limnological and hydrological changes of Lake Lisan at high resolution and provides an opportunity for further palaeoenvironmental reconstruction studies. The observed relationship between the carbonates' mineralogy and isotopic composition can be further investigated through high resolution analyses of the carbonate laminae which may provide a proxy for environmental reconstruction and understanding of the lake system during different hydroclimatic conditions. Microfacies analyses (e.g. Ben Dor et al., 2018) of the laminated sediments can also provide means for statistical and spectral analyses to assess the influence of particular synoptic atmospheric systems on the lake system. In addition, the presence of diatoms accompanying excursions in the isotopic system can be also investigated further, providing another environmental proxy that can aid in understanding the lake chemistry and

salinity thresholds and the importance of the changing moisture sources in driving this variability. The ongoing work to date the DS1 gypsum bed, aragonites and clastic layers will add significant data to constrain the age of the DS1 section and to confirm the current age control.

In conclusion, bearing in mind the age estimates uncertainties and calculations, pushing the Gharandal Valley wetland age estimates back to the MIS6 period is significant and in keeping with records from Arabia (Parton et al., 2015a), suggest that wetter condition and enhanced moisture availability for these arid regions probably was not restricted to interglacial periods.

The outcomes of this study also added new data to the eastern DSB records of Lake Lisan. The outcomes of this study emphasized the need for well dated records from the eastern DSB in order to achieve basin-wide correlations. It also highlighted the importance of accounting for site specific corrections for U/Th dating, since correction factors implemented on the western side of the basin may not be appropriate due to the different catchment geology and the sites' specific location in the basin. Accordingly, future studies on the DSB lacustrine sediments from both sides of the basin should consider the outcomes of this study and should be based on a comprehensive approach that accounts for the different variables; tectonics, climate and the section location within the basin. In addition, future work on stable isotope composition of the Lisan sediments should be done with caution and consideration of the system changes in order not to mask the natural signal in the sediments, particularly during periods of known short-term abrupt climate variability (e.g. MIS3).

The outcomes of this study indicate the heterogeneity and the complexity of the past sedimentological and environmental records of southern Jordan, thus the need for continued investigations and dating control, based on more detailed comprehensive approaches.

References

Ababsa, M., 2013. Atlas of Jordan: History, Territories and Society. Web. <http://books.openedition.org/ifpo/4560>.

Abbas, M., Al-Saqarat, B., Al-Shdaifat, A., 2016. Paleoclimate reconstruction of the quaternary sediments near the Gulf of Aqaba (Southern Jordan). Arabian Journal of Geosciences 9, 1–13. doi:10.1007/s12517-016-2346-5

Abed, A.M., 1983. Paleoclimates of the Upper Pleistocene in the Jordan Rift. Proc. 2nd. Intern. Cong. Archeol. Jord 2, 81–95.

Abed, A.M., 1985a. Geology of the Damya Formation. Dirasat, Science and Geography 12, 99–108.

Abed, A.M., 1985b. The Geology of the Dead Sea (in Arabic). Dar Al-Urqam, Amman, Jordan. p. 209.

Abed, A.M., 2002. An overview of an inland sabkha in Jordan: the Taba Sabkha, southern Wadi Araba. In: Barth, H.-J., Bo¨er, B. (Eds.), *Sabkha Ecosystems*. pp. 83–97.

Abed, A.M., 2017. Geology of Jordan, its Environment and Water (in Arabic). Dar Wael, Amman, Jordan. p. 583.

Abed, A.M., Al-Hawari, Z., 1991. Geology and Sepiolite Formation in the Taba Continental Sabkha, Southern Dead Sea – Araba Rift, Jordan. Dirasat 18, 41–65.

Abed, A.M., Yaghan, R., 2000. On the paleoclimate of Jordan during the last glacial maximum. Palaeogeography, Palaeoclimatology, Palaeoecology 160, 23–33. doi:10.1016/S0031-0182(00)00042-0

Abed, A.M., Yasin, S., Sadaqa, R., Al-Hawari, Z., 2008. The paleoclimate of the eastern desert of Jordan during marine isotope stage 9. Quaternary Research 69, 458–468. doi:10.1016/j.yqres.2008.02.006

Abou Karaki, N., Closson, D., 2012. Field Guide. EAGE Workshop on the Dead Sea sinkholes: Amman, Jordan. p. 45.

Abu-Jaber, N., Khasawneh, S. Al, Alqudah, M., Hamarneh, C., Al-Rawabdeh, A., Murray, A., 2020. Lake Elji and a geological perspective on the evolution of Petra, Jordan. Palaeogeography, Palaeoclimatology, Palaeoecology 557, 109904. doi:10.1016/j.palaeo.2020.109904

Abu-Jaber, N.S., 1998. A new look at the chemical and hydrological evolution of the Dead Sea. Geochimica et Cosmochimica Acta 62, 1471–1479. doi:10.1016/S0016-7037(98)00083-0

Abu Ghazleh, S., 2011. Lake Lisan and the Dead Sea: Their Level Changes and the Geomorphology of their Terraces. Unpub. PhD. Thesis. Technischen Universität

References

Darmstadt. p. 137.

Abu Ghazleh, S., Kempe, S., 2021. Discovery of high-level terraces of Last Glacial Lake Lisan (Dead Sea) and Eastern Mediterranean paleoclimatic implications. Quaternary International. doi:10.1016/j.quaint.2021.04.037

Al-Karablieh, E., Salman, A., 2016. Water Resources, Use and Management in Jordan-A focus on Groundwater. Middle East Regional Platform. Amman, Jordan. p. 113.

Al-Masaeed, Q., 2014. Geological and paleoenvironmental investigation for Quaternary deposits in Gharandal area using GIS and Remote Sensing. Unpub. MSc. Thesis. p. 80.

Al-Nahar, M., Clark, G.A., 2009. The Lower Paleolithic in Jordan. Al-Majala al Ordoniyya Lltarekh w Al athar [Jordanian Journal of History and Archaeology] 3, 173–215.

Al-Saqarat, B.S., Abbas, M., Lai, Z., Gong, S., Alkuisi, M.M., Abu Hamad, A.M.B., Carling, P.A., Jansen, J.D., 2020. A wetland oasis at Wadi Gharandal spanning 125–70 ka on the human migration trail in southern Jordan. Quaternary Research 100, 154-169. doi:10.1017/qua.2020.82

Al-Shdaifat, A., 2015. A Geological and Paleoenvironmental study of the Pleistocene deposits in Hamra Faddan area – Jordan. Unpub. MSc. Thesis. Al Al-Bayt Univeristy. p. 128.

Al-Weshah, R.A., 2000. The water balance of the Dead Sea: an integrated approach. Hydrological Processes 14, 145–154.

Al-Zu'bi, Y., 2007. Effect of irrigation water on agricultural soil in Jordan valley: An example from arid area conditions. Journal of Arid Environments 70, 63–79. doi: 10.1016/j.jaridenv.2007.01.001

Alawabdeh, M., Pérez-Peña, J. V., Azañón, J.M., Booth-Rea, G., Abed, A.M., Atallah, M., Galve, J.P., 2016. Stress analysis of NW Jordan: New episode of tectonic rejuvenation related to the Dead Sea transform fault. Arabian Journal of Geosciences 9, 264. doi:10.1007/s12517-015-2239-z

Alçiçek, H., Varol, B., Özkul, M., 2007. Sedimentary facies, depositional environments and palaeogeographic evolution of the Neogene Denizli Basin, SW Anatolia, Turkey. Sedimentary Geology 202, 596–637. doi:10.1016/j.sedgeo.2007.06.002

Alraggad, M., Johnsen-Harris, B., Shdaifat, A., Abugazleh, M.K., Hamaideh, A., 2017. Groundwater resilience to climate change in the eastern Dead Sea basin Jordan. Scientific Research and Essays 12, 24–41. doi:10.5897/sre2016.6459

Ameur, M. Ben, Masmoudi, S., Abichou, A., Medhioub, M., Yaich, C., 2019. Use of the magnetic, geochemical, and sedimentary records in establishing paleoclimate change in the environment of Sebkha: Case of the Sebkha Mhabeul in southeastern

References

Tunisia. Comptes Rendus - Geoscience 351, 487–497. doi:10.1016/j.crte.2019.10.003

Amireh, B.S., 2015. Grain size analysis of the Lower Cambrian–Lower Cretaceous clastic sequence of Jordan: Sedimentological and paleo-hydrodynamical implications. Journal of Asian Earth Sciences 97, 67–88. doi:10.1016/j.jseaes.2014.09.029

Amireh, B.S., 2020. Weathering, recycling, hydraulic sorting and metamorphism/metasomatism implications of the NE Gondwana lower Cambrian-Lower Cretaceous siliciclastic succession of Jordan. Journal of Asian Earth Sciences 191, 104228. doi:10.1016/j.jseaes.2020.104228

Aristizábal, E., Roser, B., Yokota, S., 2005. Tropical chemical weathering of hillslope deposits and bedrock source in the Aburrá Valley, northern Colombian Andes. Engineering Geology 81, 389–406. doi:10.1016/j.enggeo.2005.08.001

Armon, M., Dente, E., Smith, J.A., Enzel, Y., Morin, E., 2018. Synoptic-scale control over modern rainfall and flood patterns in the Levant drylands with implications for past climates. Journal of Hydrometeorology 19, 1077–1096. doi:10.1175/JHM-D-18-0013.1

Atallah, M., 2002. Morphotectonic indices of the eastern Wadi Araba (Dead Sea Rift, Jordan). Geografia Fisica e Dinamica Quaternaria 25, 3–10.

Atallah, M., Al-Taj, M., 2004. Active surface ruptures of the Dead Sea Transform in Wadi Araba, Jordan. Dirasat 31, 59-80.

Atallah, M., Niemi, T., Mustafa, H., 2002. Deformation at a strike-slip, stepover zone along the southeastern margin of the Dead Sea pullapart basin, Jordan. EGU Stephan Mueller Special Publication Series 2, 49–62.

Avni, Y., 2017. Tectonic and Physiographic Settings of the Levant. In: Enzel, Y., Bar-Yosef, O. (Eds.), *Quaternary of the Levant: Environments, Climate Change, and Humans*. Cambridge University Press, pp. 3–16. doi:10.1017/9781316106754.002

Baiyegunhi, C., Liu, K., Gwavava, O., 2017. Grain size statistics and depositional pattern of the Ecca Group sandstones, Karoo Supergroup in the Eastern Cape Province, South Africa. Open Geosciences 9, 554–576. doi:10.1515/geo-2017-0042

Bani Sakhir, Z., 1996. Lithofacies, paleoenvironment and paleoclimatic changes of the Quaternary sediments (Lisan Formation) east of the southern Basin of The Dead Sea. Unpub. MSc. Thesis. Yarmouk University. p. 125.

Bar-Matthews, M., Ayalon, A., Kaufman, A., 1997. Late Quaternary Paleoclimate in the Eastern Mediterranean Region from Stable Isotope Analysis of Speleothems at Soreq Cave, Israel. Quaternary Research 47, 155–168.

Bar-Matthews, M., Ayalon, A., Gilmour, M., Matthews, A., Hawkesworth, C.J., 2003. Sea

References

- land oxygen isotopic relationships from planktonic foraminifera and speleothems in the Eastern Mediterranean region and their implication for paleorainfall during interglacial intervals. Geochimica et Cosmochimica Acta 67, 3181–3199. doi:10.1016/S0016-7037(02)01031-1

Bar-Matthews, M., Ayalon, A., Vaks, A., Frumkin, A., 2017. Climate and Environment Reconstructions Based on Speleothems from the Levant. In: Enzel, Y., Bar-Yosef, O. (Eds.), *Quaternary of the Levant: Environments, Climate Change, and Humans*. Cambridge University Press, pp. 151–164. doi:10.1017/9781316106754.017

Barkan, E., Luz, B., Lazar, B., 2001. Dynamics of the carbon dioxide system in the Dead Sea. Geochimica et Cosmochimica Acta 65, 355–368. doi: 10.1016/S0016-7037(00)00540-8

Bartov, Y., Stein, M., Enzel, Y., Agnon, A., Reches, Z., 2002. Lake Levels and Sequence Stratigraphy of Lake Lisan, the Late Pleistocene Precursor of the Dead Sea. Quaternary Research 57, 9–21. doi: 10.1006/qres.2001.2284

Bartov, Y., Goldstein, S.L., Stein, M., Enzel, Y., 2003. Catastrophic arid episodes in the Eastern Mediterranean linked with the North Atlantic Heinrich events. Geology 31, 439–442. doi: 10.1130/0091-7613(2003)031

Bartov, Y., Agnon, A., Enzel, Y., Steinc, M., 2006. Late Quaternary faulting and subsidence in the central Dead Sea basin. Israel Journal of Earth Sciences 55, 18–31. doi:10.1560/e3rk-0rdy-3cup-ln5a

Bartov, Y., Enzel, Y., Porat, N., Stein, M., 2007. Evolution of the Late Pleistocene-Holocene Dead Sea Basin from Sequence Statigraphy of Fan Deltas and Lake-Level Reconstruction. Journal of Sedimentary Research 77, 680–692. doi:10.2110/jsr.2007.070

Basanta K. Sahu, 1964. Depositional Mechanisms from the Size Analysis of Clastic Sediments. SEPM Journal of Sedimentary Research Vol. 34, 73–83. doi:10.1306/74d70fce-2b21-11d7-8648000102c1865d

Beatriz Soto, M., Leonardo Durán, E., Aldana, M., 2014. Stratigraphic Columns Modeling and Cyclicity Analysis of the Misoa Formation, Maracaibo Lake, Venezuela, using Markov Chains. Geofísica Internacional 53, 277–288. doi: 10.1016/S0016-7169(14)71505-3

Begin, Z.B., Stein, M., Katz, A., Machlus, M., Rosenfeld, A., Buchbinder, B., Bartov, Y., 2004. Southward migration of rain tracks during the last glacial, revealed by salinity gradient in Lake Lisan (Dead Sea rift). Quaternary Science Reviews 23, 1627–1636. doi:10.1016/j.quascirev.2004.01.002

Belnap, J., Munson, S.M., Field, J.P., 2011. Aeolian and fluvial processes in dryland regions: the need for integrated studies. Ecohydrology 4, 615–622. doi:

References

10.1002/eco.258

Bender, F., 1974. Geology of Jordan. Gebrüder Borntraeger. p. 196.

Béon, M. Le, Klinger, Y., Al-Qaryouti, M., Mériaux, A.S., Finkel, R.C., Elias, A., Mayyas, O., Ryerson, F.J., Tapponnier, P., 2010. Early holocene and late pleistocene slip rates of the southern dead sea fault determined from 10Be cosmogenic dating of offset alluvial deposits. Journal of Geophysical Research: Solid Earth 115, 1–24. doi:10.1029/2009JB007198

Bhatia, M.R., Crook, K.A.W., 1986. Trace element characteristics of graywackes and tectonic setting discrimination of sedimentary basins. Contributions to Mineralogy and Petrology 92, 181–193. doi:10.1007/BF00375292

Blott, S.J., Pye, K., 2001. Gradistat: A grain size distribution and statistics package for the analysis of unconsolidated sediments. Earth Surface Processes and Landforms 26, 1237–1248. doi:10.1002/esp.261

Brauer, A., Mangili, C., Moscariello, A., Witt, A., 2008. Palaeoclimatic implications from micro-facies data of a 5900 varve time series from the Piànico interglacial sediment record, southern Alps. Palaeogeography, Palaeoclimatology, Palaeoecology 259, 121–135. doi: 10.1016/j.palaeo.2007.10.003

Breeze, P.S., Groucutt, H.S., Drake, N.A., White, T.S., Jennings, R.P., Petraglia, M.D., 2016. Palaeohydrological corridors for hominin dispersals in the Middle East ~250-70,000 years ago. Quaternary Science Reviews 144, 155–185. doi:10.1016/j.quascirev.2016.05.012

Briant, R.M., Bates, M.R., Schwenninger, J.-L., Wenban-Smith, F., 2006. An optically stimulated luminescence dated Middle to Late Pleistocene fluvial sequence from the western Solent Basin, southern England. Journal of Quaternary Science 21, 507–523. doi:10.1002/jqs.1035

Broecker, W.S., 1995. Cooling the tropics. Nature 376, 212-213. doi: 10.1038/376212a0

Bullard, J.E., Livingstone, I., 2002. Interactions between aeolian and fluvial systems in dryland environments. Area 34, 8–16. doi:10.1111/1475-4762.00052

Büntgen, U., Myglan, V.S., Ljungqvist, F.C., McCormick, M., Cosmo, N. Di, Sigl, M., Jungclaus, J., Wagner, S., Krusic, P.J., Esper, J., Kaplan, J.O., Vaan, M.A.C. de, Luterbacher, J., Wacker, L., Tegel, W., Kirdyanov, A. V, 2016. Cooling and societal change during the Late Antique Little Ice Age from 536 to around 660 AD. Nature Geoscience 9, 231–236. doi:10.1038/ngeo2652

Cacho, I., Grimalt, J.O., Pelejero, C., Canals, M., Sierro, F.J., Flores, J.A., Shackleton, N., 1999. Dansgaard-Oeschger and Heinrich event imprints in Alboran Sea paleotemperatures. Paleoceanography 14, 698–705. doi: 10.1029/1999PA900044

References

Catlett, G.A., Rech, J.A., Pigati, J.S., Kuisi, M. Al, Li, S., Honke, J.S., 2017. Activation of a small ephemeral lake in southern Jordan during the last full glacial period and its paleoclimatic implications. Quaternary Research 88, 98–109. doi:10.1017/qua.2017.29

Cheddadi, R., Rossignol-Strick, M., 1995. Eastern Mediterranean Quaternary paleoclimates from pollen and isotope records of marine cores in the Nile Cone Area. Paleoceanography 10, 291–300. doi: 10.1029/94PA02672

Chen, C., Litt, T., 2018. Dead Sea pollen provides new insights into the paleoenvironment of the southern Levant during MIS 6–5. Quaternary Science Reviews 188, 15–27. doi:10.1016/j.quascirev.2018.03.029

Cheng, H., Lawrence Edwards, R., Shen, C.-C., Polyak, V.J., Asmerom, Y., Woodhead, J., Hellstrom, J., Wang, Y., Kong, X., Spötl, C., Wang, X., Calvin Alexander, E., 2013. Improvements in ^{230}Th dating, ^{230}Th and ^{234}U half-life values, and U–Th isotopic measurements by multi-collector inductively coupled plasma mass spectrometry. Earth and Planetary Science Letters 371–372, 82–91. doi: 10.1016/j.epsl.2013.04.006

Clark, G.A., 1984. The Negev Model for Paleoclimatic Change and Human Adaptation in the Levant and Its Relevance for the Paleolithic of the Wadi el Hasa (West-Central Jordan). Annual of the Department of Antiquities of Jordan 28, 225–48.

Clemens, S.C., Prell, W.L., 2003. A 350,000 year summer-monsoon multi-proxy stack from the Owen Ridge, Northern Arabian Sea. Marine Geology 201, 35–51. doi:10.1016/S0025-3227(03)00207-X

Cordova, C.E., Ames, C.J.H., 2017. Quaternary Sediments and Soils of Jordan: Palaeoclimatic and Geoarchaeological Implications. In: Enzel, Y., Bar-Yosef, O. (Eds.), *Quaternary of the Levant: Environments, Climate Change, and Humans*. Cambridge University Press, pp. 531–538. doi:10.1017/9781316106754.058

Cox, R., Lowe, D.R., Cullers, R.L., 1995. The influence of sediment recycling and basement composition on evolution of mudrock chemistry in the southwestern United States. Geochimica et Cosmochimica Acta 59, 2919–2940. doi: 10.1016/0016-7037(95)00185-9

Craig, H., 1957. Isotopic standards for carbon and oxygen and correction factors for mass-spectrometric analysis of carbon dioxide. Geochimica et Cosmochimica Acta 12, 133–149. doi: 10.1016/0016-7037(57)90024-8

Crémière, A., Lepland, A., Chand, S., Sahy, D., Kirsimäe, K., Bau, M., Whitehouse, M.J., Noble, S.R., Martma, T., Thorsnes, T., Brunstad, H., 2016. Fluid source and methane-related diagenetic processes recorded in cold seep carbonates from the Alvheim channel, central North Sea. Chemical Geology 432, 16–33. doi:

References

10.1016/j.chemgeo.2016.03.019

Crombie, M.K., Arvidson, R.E., Sturchio, N.C., Alfy, Z. El, Abu Zeid, K., 1997. Age and isotopic constraints on pleistocene pluvial episodes in the Western Desert, Egypt. Palaeogeography, Palaeoclimatology, Palaeoecology 130, 337–355. doi:10.1016/S0031-0182(96)00134-4

Dansgaard, W., Johnsen, S.J., Clausen, H.B., Dahl-Jensen, D., Gundestrup, N.S., Hammer, C.U., Hvidberg, C.S., Steffensen, J.P., Sveinbjörnsdottir, A.E., Jouzel, J., Bond, G., 1993. Evidence for general instability of past climate from a 250-kyr ice-core record. Nature 364, 218–220. doi:10.1038/364218a0

Darby, R., Darby, E., 2015. The Late Roman fort at 'Ayn Gharandal, Jordan: Interim report on the 2009-2014 field seasons. Journal of Roman Archaeology 28, 461–470. doi:10.1017/S1047759415002603

Davies, C.P., 2005. Quaternary paleoenviroments and potential for human exploitation of the Jordan Plateau desert interior. Geoarchaeology 20, 379–400. doi:10.1002/gea.20055

Davies, C.P., Fall, P.L., 2001. Modern pollen precipitation from an elevational transect in central Jordan and its relationship to vegetation. Journal of Biogeography 28, 1195–1210. doi:10.1046/j.1365-2699.2001.00630.x

Dayan, U., Ziv, B., Shoob, T., Enzel, Y., 2008. Suspended dust over southeastern Mediterranean and its relation to atmospheric circulations. International Journal of Climatology 28, 915–924. doi:10.1002/joc.1587

Dean, J.R., Jones, M.D., Leng, M.J., Noble, S.R., Metcalfe, S.E., Sloane, H.J., Sahy, D., Eastwood, W.J., Roberts, C.N., 2015. Eastern Mediterranean hydroclimate over the late glacial and Holocene, reconstructed from the sediments of Nar lake, central Turkey, using stable isotopes and carbonate mineralogy. Quaternary Science Reviews 124, 162–174. doi: 10.1016/j.quascirev.2015.07.023

Dean, W.E.J., 1974. Determination of carbonate and organic matter in calcareous sediments and sedimentary rocks by loss on ignition: Comparison with other methods. Journal of Sedimentary Petrology 44, 242–248. doi:10.1306/74D729D2-2B21-11D7-8648000102C1865D

Dearing, J., 1994. Environmental Magnetic Susceptibility, Using the Bartington MS2 System. Oxford. p. 43.

Dercourt, J., Paquet, J., 1985. Geology Principles & Methods, Graham & Trotman Limited. Springer Netherlands, Dordrecht. doi:10.1007/978-94-009-4956-0

Diabat, A., Masri, A., 2005. Orientation of the principal stresses along Zerqa-Ma'in Fault. Mu'tah Lil-Buhuth wad-Dirasat 20, 57–71.

References

Diabat, A.A., 2013. Fracture systems of granites and Quaternary deposits of the area east of Aqaba: indicators of reactivation and neotectonic activity. Arabian Journal of Geosciences 6, 679–695. doi:10.1007/s12517-011-0389-1

Diabat, A.A., Atallah, M., Salih, M.R., 2004. Paleostress analysis of the Cretaceous rocks in the eastern margin of the Dead Sea transform, Jordan. Journal of African Earth Sciences 38, 449–460. doi:10.1016/j.jafrearsci.2004.04.002

Djamali, M., Beaulieu, J.L. de, Shah-hosseini, M., Andrieu-Ponel, V., Ponel, P., Amini, A., Akhani, H., Leroy, S.A.G., Stevens, L., Lahijani, H., Brewer, S., 2008. A late Pleistocene long pollen record from Lake Urmia, NW Iran. Quaternary Research 69, 413–420. doi:10.1016/j.yqres.2008.03.004

Doebelin, N., Kleeberg, R., 2015. Profex: a graphical user interface for the Rietveld refinement program BGMN. Journal of Applied Crystallography 48, 1573–1580. doi:10.1107/S1600576715014685

Dor, Y. Ben, Armon, M., Ahlborn, M., Morin, E., Erel, Y., Brauer, A., Schwab, M.J., Tjallingii, R., Enzel, Y., 2018. Changing flood frequencies under opposing late Pleistocene eastern Mediterranean climates. Scientific Reports 8, 8445. doi:10.1038/s41598-018-25969-6

Dor, Y. Ben, Neugebauer, I., Enzel, Y., Schwab, M.J., Tjallingii, R., Erel, Y., Brauer, A., 2019. Varves of the Dead Sea sedimentary record. Quaternary Science Reviews 215, 173–184. doi: 10.1016/j.quascirev.2019.04.011

Duller, G.A.T., 2008. Luminescence Dating Guidelines on using luminescence dating in archaeology, Swindin: English Heritage. doi:10.1002/jqs.1328

Duzgoren-Aydin, N.S., Aydin, A., Malpas, J., 2002. Re-assessment of chemical weathering indices: case study on pyroclastic rocks of Hong Kong. Engineering Geology 63, 99–119. doi:10.1016/S0013-7952(01)00073-4

Edwards, R., Chen, J.H., Wasserburg, G.J., 1987. 238U234U230Th232Th systematics and the precise measurement of time over the past 500,000 years. Earth and Planetary Science Letters 81, 175–192. doi:10.1016/0012-821X(87)90154-3

Engel, M., Matter, A., Parker, A.G., Parton, A., Petraglia, M.D., Preston, G.W., Preusser, F., 2017. Lakes or wetlands? A comment on 'The middle Holocene climatic records from Arabia: Reassessing lacustrine environments, shift of ITCZ in Arabian Sea, and impacts of the southwest Indian and African monsoons' by Enzel et al. Global and Planetary Change. doi:10.1016/j.gloplacha.2016.11.001

Enzel, Y., Bookman, R., Sharon, D., Gvirtzman, H., Dayan, U., Ziv, B., Stein, M., 2003. Late Holocene climates of the Near East deduced from Dead Sea level variations and modern regional winter rainfall. Quaternary Research 60, 263–273. doi:10.1016/j.yqres.2003.07.011

References

Enzel, Y., Amit, R., Dayan, U., Crouvi, O., Kahana, R., Ziv, B., Sharon, D., 2008. The climatic and physiographic controls of the eastern Mediterranean over the late Pleistocene climates in the southern Levant and its neighboring deserts. Global and Planetary Change 60, 165–192. doi:10.1016/j.gloplacha.2007.02.003

Fedo, C.M., Nesbitt, H.W., Young, G.M., 1995. Unravelling the effects of potassium metasomatism in sedimentary rocks and paleosols, with implications for paleoweathering conditions and provenance. Geology 23, 921–924. doi:10.1130/0091-7613(1995)023<0921:UTEOPM>2.3.CO

Ferry, M., Meghraoui, M., Karaki, N.A., Al-Taj, M., Amoush, H., Al-Dhaisat, S., Barjous, M., 2007. A 48-kyr-long slip rate history for the Jordan Valley segment of the Dead Sea Fault. Earth and Planetary Science Letters 260, 394–406. doi:10.1016/j.epsl.2007.05.049

Fiebig, M., Preusser, F., Steffen, D., Thamó-Bozsó, E., Grabner, M., Lair, G.J., Gerzabek, M.H., 2009. Luminescence dating of historical fluvial deposits from the Danube and Ebro. Geoarchaeology 24, 224–241. doi:10.1002/gea.20264

Fleitmann, D., Matter, A., 2009. The speleothem record of climate variability in Southern Arabia. Comptes Rendus Geoscience 341, 633–642. doi:10.1016/j.crte.2009.01.006

Fleitmann, D., Cheng, H., Badertscher, S., Edwards, R.L., Mudelsee, M., Göktürk, O.M., Fankhauser, A., Pickering, R., Raible, C.C., Matter, A., Kramers, J., Tüysüz, O., 2009. Timing and climatic impact of Greenland interstadials recorded in stalagmites from northern Turkey. Geophysical Research Letters 36. doi: 10.1029/2009GL040050

Folk, R.L., Ward, W.C., 1957. Brazos River bar; a study in the significance of grain size parameters. Journal of Sedimentary Research 27, 3–26. doi:10.1306/74d70646-2b21-11d7-8648000102c1865d

Francke, A., Wennrich, V., Sauerbrey, M., Juschus, O., Melles, M., Brigham-Grette, J., 2013. Multivariate statistic and time series analyses of grain-size data in quaternary sediments of Lake El'gygytgyn, NE Russia. Climate of the Past 9, 2459–2470. doi:10.5194/cp-9-2459-2013

Freund, R., 1965. A Model of the Structural Development of Israel and Adjacent Areas Since Upper Cretaceous Times. Geological Magazine 102, 189–205. doi:10.1017/S0016756800053218

Freund, R., Zak, I., Garfunkel, Z., 1968. Age and Rate of the Sinistral Movement along the Dead Sea Rift. Nature 220, 253–255. doi:10.1038/220253a0

Frumkin, A., Bar-Yosef, O., Schwarcz, H.P., 2011. Possible paleohydrologic and paleoclimatic effects on hominin migration and occupation of the Levantine Middle Paleolithic. Journal of Human Evolution 60, 437–451.

References

doi:10.1016/j.jhevol.2010.03.010

Galli, P., 1999. Active tectonics along the Wadi Araba-Jordan Valley transform fault. Journal of Geophysical Research: Solid Earth 104, 2777–2796. doi:10.1029/1998JB900013

Garfunkel, Z., Zak, I., Freund, R., 1981. Active faulting in the dead sea rift. Tectonophysics 80, 1–26. doi:https://doi.org/10.1016/0040-1951(81)90139-6

Garzanti, E., Resentini, A., 2016. Provenance control on chemical indices of weathering (Taiwan river sands). Sedimentary Geology 336, 81–95. doi:10.1016/j.sedgeo.2015.06.013

Garzanti, E., Andò, S., France-Lanord, C., Vezzoli, G., Censi, P., Galy, V., Najman, Y., 2010. Mineralogical and chemical variability of fluvial sediments1. Bedload sand (Ganga–Brahmaputra, Bangladesh). Earth and Planetary Science Letters 299, 368–381. doi:10.1016/j.epsl.2010.09.017

Gasse, F., Vidal, L., Develle, A.L., Campo, E. Van, 2011. Hydrological variability in the Northern Levant: A 250 ka multiproxy record from the Yammoûneh (Lebanon) sedimentary sequence. Climate of the Past 7, 1261–1284. doi:10.5194/cp-7-1261-2011

Gasse, F., Vidal, L., Campo, E. Van, Demory, F., Develle, A.L., Tachikawa, K., Elias, A., Bard, E., Garcia, M., Sonzogni, C., Thouveny, N., 2015. Hydroclimatic changes in northern Levant over the past 400,000 years. Quaternary Science Reviews. doi:10.1016/j.quascirev.2014.12.019

Gasse, F., Campo, E. Van, Benedetti, L., Demory, F., Develle, A.L., Kaniewski, D., Tachikawa, K., Thouveny, N., Vidal, L., 2017. Late Quaternary Palaeoenvironments in Northern Levant (Lebanon and Syria). In: Bar-Yosef, O., Enzel, Y. (Eds.), *Quaternary of the Levant: Environments, Climate Change, and Humans*. Cambridge University Press, Cambridge, pp. 173–178. doi:DOI: 10.1017/9781316106754.019

Gat, J.R., 1984. The stable isotope composition of Dead Sea waters. Earth and Planetary Science Letters 71, 361–376. doi:10.1016/0012-821X(84)90103-1

Gertman, I., Hecht, A., 2002. The Dead Sea hydrography from 1992 to 2000. Journal of Marine Systems 35, 169–181. doi:10.1016/S0924-7963(02)00079-9

Ginat, H., Enzel, Y., Avni, Y., 1998. Translocated Plio-Pleistocene drainage systems along the Arava fault of the Dead Sea transform. Tectonophysics 284, 151–160. doi:10.1016/S0040-1951(97)00165-0

Ginat, H., Opitz, S., Ababneh, L., Faershtein, G., Lazar, M., Porat, N., Mischke, S., 2018. Pliocene-Pleistocene waterbodies and associated deposits in southern Israel and southern Jordan. Journal of Arid Environments 148, 14–33.

References

doi:10.1016/j.jaridenv.2017.09.007

Girdler, R.W., 1990. The Dead Sea transform fault system. Tectonophysics 180, 1–13. doi:10.1016/0040-1951(90)90367-H

Govil, P., Naidu, P.D., 2010. Evaporation-precipitation changes in the eastern Arabian Sea for the last 68 ka: Implications on monsoon variability. Paleoceanography 25. doi:10.1029/2008PA001687

Groucutt, H.S., White, T.S., Scerri, E.M.L., Andrieux, E., Clark-Wilson, R., Breeze, P.S., Armitage, S.J., Stewart, M., Drake, N., Louys, J., Price, G.J., Duval, M., Parton, A., Candy, I., Carleton, W.C., Shipton, C., Jennings, R.P., Zahir, M., Blinkhorn, J., Blockley, S., Al-Omari, A., Alsharekh, A.M., Petraglia, M.D., 2021. Multiple hominin dispersals into Southwest Asia over the past 400,000 years. Nature 597, 376–380. doi:10.1038/s41586-021-03863-y

Guillemot, T., Stockhecke, M., Bechtel, A., Ladd, S.N., Nelson, D.B., Schubert, C.J., 2019. Paleoenvironmental and paleoclimatic variations around Lake Van (Eastern Turkey) recorded by sedimentary source specific biomarkers 250–130 ka (MIS7 and MIS6). Quaternary Science Reviews 225, 105997. doi:10.1016/j.quascirev.2019.105997

Haase-Schramm, A., Goldstein, S.L., Stein, M., 2004. U-Th dating of Lake Lisan (late Pleistocene dead sea) aragonite and implications for glacial east Mediterranean climate change. Geochimica et Cosmochimica Acta 68, 985–1005. doi:10.1016/j.gca.2003.07.016

Hammer, Ø., Harper, D., Ryan, P., 2001. PAST-palaeontological statistics. Palaeontologia electronica 4, 1–15.

Hanamgond, P., Chavadi, V.C., 1998. Sedimentological Study of Kwada and Belekeri Bay Beaches, Uttara Kannada, West Coast, India. Journal of Geological Society of India 51, 193–200.

Hartung, H., Reed, J.M., Litt, T., 2020. The diatom flora of Lake Lisan (Israel): a preliminary investigation. EGU General Assembly EGU2020-84, 4–8.

Hazan, N., Stein, M., Agnon, A., Marco, S., Nadel, D., Negendank, J.F.W., Schwab, M.J., Neev, D., 2005. The Late Quaternary limnological history of Lake Kinneret (Sea of Galilee), Israel. Quaternary Research 63, 60–77. doi:10.1016/j.yqres.2004.09.004

Hazermoshar, A., Lak, R., Espahbood, M.R., Ghadimvand, N.K., Farajzadeh, R., 2016. Geochemical, Sedimentological and Mineralogical Characterization of Surficial Sediments in Eynak Marsh (North of Iran). Open Journal of Geology 06, 640–659. doi:10.4236/ojg.2016.67050

He, J., Croix, A.D. La, Wang, J., Ding, W., Underschultz, J.R., 2019. Using neural networks and the Markov Chain approach for facies analysis and prediction from well logs in

the Precipice Sandstone and Evergreen Formation, Surat Basin, Australia. Marine and Petroleum Geology 101, 410–427. doi:10.1016/j.marpetgeo.2018.12.022

Hect, A., Isaac, G., 2003. Dead Sea Meteorological Climate. In: Nevo, E., Oren, A., Wasser, S.P. (Eds.), *Biodiversity of Cyanoprocaryotes, Algae and Fungi of Israel. Fungal Life in the Dead Sea.* International Center for Cryptogamic Plants and Fungi, Institute of Evolution, University of Haifa, Israel, p. 361.

Heiri, O., Lotter, A.F., Lemcke, G., 2001. Loss on ignition as a method for estimating organic and carbonate content in sediments: Reproducibility and comparability of results. Journal of Paleolimnology 25, 101–110. doi:10.1023/A:1008119611481

Hellstrom, J., 2006. U–Th dating of speleothems with high initial 230Th using stratigraphical constraint. Quaternary Geochronology 1, 289–295. doi:https://doi.org/10.1016/j.quageo.2007.01.004

Hemming, S.R., 2004. Heinrich events: Massive late Pleistocene detritus layers of the North Atlantic and their global climate imprint. Reviews of Geophysics 42, RG1005. doi:10.1029/2003RG000128

Henry, D., Bauer, H., Kerry, K., Beaver, J., White, J., 2001. Survey of prehistoric sites, Wadi Araba, southern Jordan. Bulletin of the American Schools of Oriental Research 323, 1–19.

Hershkovitz, I., Weber, G.W., Quam, R., Duval, M., Grün, R., Kinsley, L., Ayalon, A., Bar-Matthews, M., Valladas, H., Mercier, N., Arsuaga, J.L., Martinón-Torres, M., Castro, J.M. de, Fornai, C., Mart\'\in-Francés, L., Sarig, R., May, H., Krenn, V.A., Slon, V., Rodr\'\iguez, L., Garc\'\ia, R., Lorenzo, C., Carretero, J.M., Frumkin, A., Shahack-Gross, R., Bar-Yosef Mayer, D.E., Cui, Y., Wu, X., Peled, N., Groman-Yaroslavski, I., Weissbrod, L., Yeshurun, R., Tsatskin, A., Zaidner, Y., Weinstein-Evron, M., 2018. The earliest modern humans outside Africa. Science 359, 456–459. doi:10.1126/science.aap8369

Hossain, H.M.Z., Kawahata, H., Roser, B.P., Sampei, Y., Manaka, T., Otani, S., 2017. Geochemical characteristics of modern river sediments in Myanmar and Thailand: Implications for provenance and weathering. Geochemistry 77, 443–458. doi:10.1016/j.chemer.2017.07.005

Hseinat, M. Al, Al-Rawabdeh, A., Al-Zidaneen, M., Ghanem, H., Al-Taj, M., Diabat, A., Jarrar, G., Atallah, M., 2020. New Insights for Understanding the Structural Deformation Style of the Strike-Slip Regime along the Wadi Shueib and Amman-Hallabat Structures in Jordan Based on Remote Sensing Data Analysis. Geosciences 10, 253. doi:10.3390/geosciences10070253

Huber, C., Leuenberger, M., Spahni, R., Flückiger, J., Schwander, J., Stocker, T.F., Johnsen, S., Landais, A., Jouzel, J., 2006. Isotope calibrated Greenland temperature

record over Marine Isotope Stage 3 and its relation to CH4. Earth and Planetary Science Letters 243, 504–519. doi:10.1016/j.epsl.2006.01.002

Ibrahim, K., 1993. The Geology of the Wadi Gharandal Area. Bulletin No. 24. Ministry of Energy and Mineral Resources, Amman, Jordan.

Ibrahim, K., Rashdan, M., 1988. Wadi Gharandal Map (sheet 3050III). 1:50,000. Geological Map Series. Ministry of Energy and Mineral Resources, Amman, Jordan.

Ibrahim, K.M., El-Naqa, A.R., 2018. Inverse geochemical modeling of groundwater salinization in Azraq Basin, Jordan. Arabian Journal of Geosciences 11, 237. doi:10.1007/s12517-018-3557-8

IPCC, 2012. Managing the Risks of Extreme Events and Disasters to Advance Climate Change Adaptation. In: Field, C.B., Barros, V., Stocker, T.F., Qin, D., Dokken, D.J., Ebi, K.L., Mastrandrea, M.D., Mach, K.J., Plattner, G.-K., Allen, S.K., Tignor, M., Midgley, P.M. (Eds.), A Special Report of Working Groups I and II of the Intergovernmental Panel on Climate Change. Cambridge University Press, p. 582.

IPPC, 2014. Climate change 2014: Synthesis report. Contribution of working groups I, II and III to the fifth assessment report of the Intergovernmental panel on climate change [Core Writing Team, R.K. Pachauri and L.A. Meyer (eds.)], IPCC. Geneva.

Itambi, A.C., Dobeneck, T. von, Mulitza, S., Bickert, T., Heslop, D., 2009. Millennial-scale northwest African droughts related to Heinrich events and Dansgaard-Oeschger cycles: Evidence in marine sediments from offshore Senegal. Paleoceanography 24. doi:10.1029/2007PA001570

Jara-Muñoz, J., Agnon, A., Fohlmeister, J., Mey, J., Frank, N., Plessen, B., Schroeder-Ritzrau, A., Garcin, Y., Darvasi, Y., Melnick, D., Strecker, M., 2020. Lake level changes in the Dead Sea during the late Pleistocene recorded by fossil lake shorelines. EGU General Assembly. https://presentations.copernicus.org/EGU2020/EGU2020-5669_presentation.pdf

Joffe, S., Garfunkel, Z., 1987. Plate kinematics of the circum Red Sea—a re-evaluation. Tectonophysics 141, 5–22. doi: 10.1016/0040-1951(87)90171-5

Jones, M.D., Imbers, J., 2010. Modeling Mediterranean lake isotope variability. Global and Planetary Change 71, 193–200. doi: 10.1016/j.gloplacha.2009.10.001

Jones, M.D., Richter, T., 2011. Paleoclimatic and archeological implications of Pleistocene and Holocene environments in Azraq, Jordan. Quaternary Research 76, 363–372. doi:10.1016/j.yqres.2011.07.005

Jones, M.D., Roberts, C.N., Leng, M.J., 2007. Quantifying climatic change through the last glacial-interglacial transition based on lake isotope palaeohydrology from central Turkey. Quaternary Research 67, 463–473. doi:10.1016/j.yqres.2007.01.004

References

Jones, M.D., Metcalfe, S.E., Davies, S.J., Noren, A., 2015. Late Holocene climate reorganisation and the North American Monsoon. Quaternary Science Reviews 124, 290–295. doi: 0.1016/j.quascirev.2015.07.004

Jones, M.D., Maher, L.A., Richter, T., Macdonald, D., Martin, L., 2017. Human-environment interactions through the epipalaeolithic of eastern Jordan. In: *The Archaeology of Human-Environment Interactions: Strategies for Investigating Anthropogenic Landscapes, Dynamic Environments, and Climate Change in the Human Past*. pp. 121–140. doi:10.4324/9781315697697

Jones, M.D., Abu-Jaber, N., AlShdaifat, A., Baird, D., Cook, B.I., Cuthbert, M.O., Dean, J.R., Djamali, M., Eastwood, W., Fleitmann, D., Haywood, A., Kwiecien, O., Larsen, J., Maher, L.A., Metcalfe, S.E., Parker, A., Petrie, C.A., Primmer, N., Richter, T., Roberts, N., Roe, J., Tindall, J.C., Ünal-İmer, E., Weeks, L., 2019. 20,000 years of societal vulnerability and adaptation to climate change in southwest Asia. Wiley Interdisciplinary Reviews: Water 6, e1330. doi:10.1002/wat2.1330

Jones, M.D., Richter, T., Rollefson, G., Rowan, Y., Roe, J., Toms, P., Wood, J., Wasse, A., Ikram, H., Williams, M., AlShdaifat, A., Pedersen, P.N., Esaid, W., 2021. The palaeoenvironmental potential of the eastern Jordanian desert basins (Qe'an). Quaternary International. doi: 10.1016/j.quaint.2021.06.023

Jungmann, M., Kopal, M., Clauser, C., Berlage, T., 2011. Multi-class supervised classification of electrical borehole wall images using texture features. Computers and Geosciences 37, 541–553. doi:10.1016/j.cageo.2010.08.008

Kahana, R., Ziv, B., Enzel, Y., Dayan, U., 2002. Synoptic climatology of major floods in the Negev Desert, Israel. International Journal of Climatology 22, 867–882. doi:10.1002/joc.766

Kallel, N., Duplessy, J.C., Labeyrie, L., Fontugne, M., Paterne, M., Montacer, M., 2000. Mediterranean pluvial periods and sapropel formation over the last 200 000 years. Palaeogeography, Palaeoclimatology, Palaeoecology 157, 45–58. doi:10.1016/S0031-0182(99)00149-2

Kaniewski, D., Campo, E. Van, Weiss, H., 2012. Drought is a recurring challenge in the Middle East. Proceedings of the National Academy of Sciences 109, 3862–3867. doi:10.1073/pnas.1116304109

Katz, A., 1973. The interaction of magnesium with calcite during crystal growth at 25–90°C and one atmosphere. Geochimica et Cosmochimica Acta 37, 1563–1586. doi: 10.1016/0016-7037(73)90091-4

Katz, A., Kolodny, N., 1989. Hypersaline brine diagenesis and evolution in the Dead Sea-Lake Lisan system (Israel). Geochimica et Cosmochimica Acta 53, 59–67. doi:10.1016/0016-7037(89)90272-X

References

Kaufman, A., Broecker, W., 1965. Comparison of Th 230 and C 14 ages for carbonate materials from lakes Lahontan and Bonneville. Journal of Geophysical Research 70, 4039–4054. doi:10.1029/JZ070i016p04039

Kaufman, A., Yechieli, Y., Gardosh, M., 1992. Reevaluation of the Lake-Sediment Chronology in the Dead Sea Basin, Israel, Based on New 230Th/U dates. Quaternary Research 38, 292–304. doi:10.1016/0033-5894(92)90039-L

Kelley, C.P., Mohtadi, S., Cane, M.A., Seager, R., Kushnir, Y., 2015. Climate change in the Fertile Crescent and implications of the recent Syrian drought. Proceedings of the National Academy of Sciences 112, 3241–3246. doi:10.1073/pnas.1421533112

Kelts, K., Hsü, K.J., 1978. Freshwater Carbonate Sedimentation. In: Lakes. Springer New York, New York, NY, pp. 295–323. doi:10.1007/978-1-4757-1152-3_9

Khalifa, M.A., 2005. Lithofacies, diagenesis and cyclicity of the "Lower Member" of the Khuff Formation (Late Permian), Al Qasim Province, Saudi Arabia. Journal of Asian Earth Sciences 25, 719–734. doi:10.1016/j.jseaes.2004.05.008

Kim, S.-T., O'Neil, J.R., Hillaire-Marcel, C., Mucci, A., 2007. Oxygen isotope fractionation between synthetic aragonite and water: Influence of temperature and Mg2+ concentration. Geochimica et Cosmochimica Acta 71, 4704–4715. doi: 10.1016/j.gca.2007.04.019

Kiro, Y., Goldstein, S.L., Kushnir, Y., Olson, J.M., Bolge, L., Lazar, B., Stein, M., 2020. Droughts, flooding events, and shifts in water sources and seasonality characterize last interglacial Levant climate. Quaternary Science Reviews 248, 106546. doi:10.1016/j.quascirev.2020.106546

Kittel, P., 2014. Slope deposits as an indicator of anthropopressure in the light of research in Central Poland. Quaternary International 324, 34–55. doi:10.1016/j.quaint.2013.07.021

Klinger, Y., Avouac, J.P., Dorbath, L., Karaki, N.A., Tisnerat, N., 2000. Seismic behaviour of the Dead Sea fault along Araba valley, Jordan. Geophysical Journal International 142, 769–782. doi:10.1046/j.1365-246x.2000.00166.x

Kolodny, Y., Stein, M., Machlus, M., 2005. Sea-rain-lake relation in the Last Glacial East Mediterranean revealed by δ18O-δ13C in Lake Lisan aragonites. Geochimica et Cosmochimica Acta 69, 4045–4060. doi:10.1016/j.gca.2004.11.022

Kushnir, Y., Dayan, U., Ziv, B., Morin, E., Enzel, Y., 2017. Climate of the Levant. In: Quaternary of the Levant: Environments, Climate Change, and Humans. Cambridge: Cambridge University Press, pp. 31–44. doi:10.1017/9781316106754.004

Lacey, J.H., Leng, M.J., Höbig, N., Reed, J.M., Valero-Garcés, B., Reicherter, K., 2016. Western Mediterranean climate and environment since Marine Isotope Stage 3: a

References

50,000-year record from Lake Banyoles, Spain. Journal of Paleolimnology 55, 113–128. doi:10.1007/s10933-015-9868-9

Lai, Z.P., 2006. Testing the use of an OSL standardized growth curve (SGC) for De determination on quartz from the Chinese Loess Plateau. Radiation Measurements 41, 9–16. doi: 10.1016/j.radmeas.2005.06.031

Lai, Z.P., Wintle, A.G., 2006. Locating the boundary between the Pleistocene and the Holocene in Chinese loess using luminescence. The Holocene 16, 893–899. doi: 10.1191/0959683606hol980rr

Lai, Z.P., Kaiser, K., Brückner, H., 2009. Luminescence dated aeolian deposits of late Quaternary age in the southern Tibetan Plateau and their implications for landscape history. Quaternary Research 72, 421–430. doi: 10.1016/j.yqres.2009.07.005

Lai, Z.P., Mischke, S., Madsen, D., 2013. aleoenvironmental implications of new OSL dates on the formation of the "Shell Bar" in the Qaidam basin, northeastern of Qinghai–Tibetan Plateau. Journal Paleoliminology 51, 197–210. doi: 10.1007/s10933-013-9710-1

Lamine Malick, B.M., Ishiga, H., 2016. Geochemical Classification and Determination of Maturity Source Weathering in Beach Sands of Eastern San' in Coast, Tango Peninsula, and Wakasa Bay, Japan. Earth Science Research 5, 44–55. doi:10.5539/esr.v5n1p44

Landmann, G., Abu Qudaira, G.M., Shawabkeh, K., Wrede, V., Kempe, S., 2002. Geochemistry of the Lisan and Damya Formations in Jordan, and implications for palaeoclimate. Quaternary International 89, 45–57. doi: 10.1016/S1040-6182(01)00080-5

Lazar, B., Stein, M., 2011. Freshwater on the route of hominids out of Africa revealed by U-Th in Red Sea corals. Geology 39, 1067–1070. doi:10.1130/G32257.1

Lazar, B., Sivan, O., Yechieli, Y., Levy, E.J., Antler, G., Gavrieli, I., Stein, M., 2014. Long-term freshening of the Dead Sea brine revealed by porewater Cl-and δO18 in ICDP Dead Sea deep-drill. Earth and Planetary Science Letters 400, 94–101. doi:10.1016/j.epsl.2014.03.019

LeBéon, M., Klinger, Y., Mériaux, A.S., Al-Qaryouti, M., Finkel, R.C., Mayyas, O., Tapponnier, P., 2012. Quaternary morphotectonic mapping of the Wadi Araba and implications for the tectonic activity of the southern Dead Sea fault. Tectonics 31. doi:10.1029/2012TC003112

Leng, M.J., Marshall, J.D., 2004. Palaeoclimate interpretation of stable isotope data from lake sediment archives. Quaternary Science Reviews 23, 811–831. doi:10.1016/j.quascirev.2003.06.012

References

Li, H.-C., Ku, T.-L., 1997. $\delta^{13}C$–$\delta^{18}C$ covariance as a paleohydrological indicator for closed-basin lakes. Palaeogeography, Palaeoclimatology, Palaeoecology 133, 69–80. doi: 10.1016/S0031-0182(96)00153-8

Liang, L., Sun, Y., Beets, C.J., Prins, M.A., Wu, F., Vandenberghe, J., 2013. Impacts of grain size sorting and chemical weathering on the geochemistry of Jingyuan loess in the northwestern Chinese Loess Plateau. Journal of Asian Earth Sciences 69, 177–184. doi:10.1016/j.jseaes.2012.12.015

Lindsay, W.L., 1979. Chemical equilibria in soils. John Wiley and Sons Ltd., Chichester, Sussex. p. 449.

Lionello, P., Malanotte-Rizzoli, P., Boscolo, R., Alpert, P., Artale, V., Li, L., Luterbacher, J., May, W., Trigo, R., Tsimplis, M., Ulbrich, U., Xoplaki, E., 2006. The Mediterranean climate: An overview of the main characteristics and issues. In: Lionello, P., Malanotte-Rizzoli, P., Boscolo, R. (Eds.), *Mediterranean, Developments in Earth and Environmental Sciences.* Elsevier, pp. 1–26. doi: 10.1016/S1571-9197(06)80003-0

Lisiecki, L.E., Raymo, M.E., 2005. A Pliocene-Pleistocene stack of 57 globally distributed benthic $\delta^{18}O$ records. Paleoceanography 20. doi: 10.1029/2004PA001071

Lisker, S., Vaks, A., Bar-Matthews, M., Porat, R., Frumkin, A., 2009. Stromatolites in caves of the Dead Sea Fault Escarpment: implications to latest Pleistocene lake levels and tectonic subsidence. Quaternary Science Reviews 28, 80–92. doi:10.1016/j.quascirev.2008.10.015

Litt, T., Ohlwein, C., Neumann, F., Hense, A., Stein, M., 2012. Holocene climate variability in the Levant from the Dead Sea pollen record. Quaternary Science Reviews 49, 95–105.

Liu, B., Jin, H., Sun, Z., Zhao, S., 2016. Geochemical weathering of aeolian sand and its palaeoclimatic implications in the Mu Us Desert, northern China, since the Late Holocene. Journal of Arid Land 8, 647–659. doi:10.1007/s40333-016-0014-y

Livnat, A., Kronfeld, J., 1985. Paleoclimatic implications of U-series dates for lake sediments and travertines in the Arava Rift Valley, Israel. Quaternary Research 24, 164–172. doi:10.1016/0033-5894(85)90003-1

López-Merino, L., Leroy, S.A.G., Eshel, A., Epshtein, V., Belmaker, R., Bookman, R., 2016. Using palynology to re-assess the Dead Sea laminated sediments - Indeed varves? Quaternary Science Reviews 140, 49–66. doi:10.1016/j.quascirev.2016.03.024

Lu, Y., Bookman, R., Waldmann, N., Marco, S., 2020. A 45 kyr laminae record from the Dead Sea: Implications for basin erosion and floods recurrence. Quaternary Science Reviews 229, 106143. doi: 10.1016/j.quascirev.2019.106143

References

Lucke, B., Roskin, J., Vanselow, K.A., Bruins, H.J., Abu-Jaber, N., Deckers, K., Lindauer, S., Porat, N., Reimer, P.J., Bäumler, R., Erickson-Gini, T., Kouki, P., 2019a. Character, Rates, and Environmental Significance of Holocene Dust Accumulation in Archaeological Hilltop Ruins in the Southern Levant. Geosciences 9, 190. doi:10.3390/geosciences9040190

Lucke, B., Sandler, A., Vanselow, K.A., Bruins, H.J., Abu-Jaber, N., Bäumler, R., Porat, N., Kouki, P., 2019b. Composition of Modern Dust and Holocene Aeolian Sediments in Archaeological Structures of the Southern Levant. Atmosphere 10, 762. doi:10.3390/atmos10120762

Machlus, M., Enzel, Y., Goldstein, S.L., Marco, S., Stein, M., 2000. Reconstructing low levels of Lake Lisan by correlating fan-delta and lacustrine deposits. Quaternary International 73–74, 137–144. doi:10.1016/S1040-6182(00)00070-7

Madukwe, H.Y., 2016. Granulometric Analysis Of The Sandstone Facies Of The Ise Formation , Southwestern Nigeria. Journal of Multidisciplinary Engineering Science and Technology 3, 3909–3919.

Makhlouf, I., Amireh, B., Abed, A., 2010. Sedimentology and Morphology of Quaternary Alluvial Fans in Wadi Araba, Southwest Jordan. Jordan Journal of Earth and Environmental Sciences 3, 79–98.

Makhlouf, I.M., Abed, A.M., 1991. Depositional facies and environments in the Umm Ishrin Sandstone Formation, Dead Sea area, Jordan. Sedimentary Geology 71, 177–187. doi:10.1016/0037-0738(91)90100-R

Makhlouf, I.M., El-Haddad, A.A., 2006. Depositional environments and facies of the Late Triassic Abu Ruweis Formation, Jordan. Journal of Asian Earth Sciences 28, 372–384. doi:10.1016/j.jseaes.2005.10.017

McCrea, J.M., 1950. On the Isotopic Chemistry of Carbonates and a Paleotemperature Scale. The Journal of Chemical Physics 18, 849–857. doi:10.1063/1.1747785

McLaren, S.J., Gilbertson, D.D., Grattan, J.P., Hunt, C.O., Duller, G.A.T., Barker, G.A., 2004. Quaternary palaeogeomorphologic evolution of the Wadi Faynan area, southern Jordan. Palaeogeography, Palaeoclimatology, Palaeoecology 205, 131–154. doi:10.1016/j.palaeo.2003.12.006

Meerbeeck, C.J. Van, Renssen, H., Roche, D.M., 2009. How did Marine Isotope Stage 3 and Last Glacial Maximum climates differ? – Perspectives from equilibrium simulations. Climate of the Past 5, 33–51. doi:10.5194/cp-5-33-2009

Metcalfe, S., Davies, S., 2007. Deciphering recent climate change in central Mexican lake records. Climatic Change 83, 169–186. doi:10.1007/s10584-006-9152-0

Metcalfe, S., Say, A., Black, S., McCulloch, R., O'Hara, S., 2002. Wet conditions during

the last glaciation in the Chihuahuan Desert, Alta Babicora Basin, Mexico. Quaternary Research 57, 91–101. doi:10.1006/qres.2001.2292

Metcalfe, S.E., 1995. Holocene environmental change in the Zacapu Basin, Mexico: a diatom-based record. The Holocene 5, 196–208. doi:10.1177/095968369500500207

Metcalfe, S.E., O'Hara, S.L., Caballero, M., Davies, S.J., 2000. Records of Late Pleistocene–Holocene climatic change in Mexico — a review. Quaternary Science Reviews 19, 699–721. doi: 10.1016/S0277-3791(99)00022-0

Metcalfe, S.E., Jones, M.D., Davies, S.J., Noren, A., MacKenzie, A., 2010. Climate variability over the last two millennia in the North American Monsoon region, recorded in laminated lake sediments from Laguna de Juanacatlán, Mexico. Holocene 20, 1195–1206. doi:10.1177/0959683610371994

Meunier, A., Caner, L., Hubert, F., Albani, A. El, Pret, D., 2013. The weathering intensity scale (WIS): An alternative approach of the chemical index of alteration (CIA). American Journal of Science 313, 113–143. doi:10.2475/02.2013.03

Miall, A.D., 1977. A review of the braided-river depositional environment. Earth Science Reviews 13, 1–62. doi:10.1016/0012-8252(77)90055-1

Miall, A.D., 1996. The Geology of Fluvial Deposits (Sedimentrary Facies. Basin Analysis, and Petroleum Geology). Springer. p. 565.

Miebach, A., Chen, C., Schwab, M.J., Stein, M., Litt, T., 2017. Vegetation and climate during the Last Glacial high stand (ca. 28–22 ka BP) of the Sea of Galilee, northern Israel. Quaternary Science Reviews 156, 47–56. doi: 10.1016/j.quascirev.2016.11.013

Migowski, C., Stein, M., Prasad, S., Negendank, J.F.W., Agnon, A., 2006. Holocene climate variability and cultural evolution in the Near East from the Dead Sea sedimentary record. Quaternary Research 66, 421–431. doi:10.1016/j.yqres.2006.06.010

Miller, G.H., Wendorf, F., Ernst, R., Schild, R., Close, A.E., Friedman, I., Schwarcz, H.P., 1991. Dating lacustrine episodes in the eastern Sahara by the epimerization of isoleucine in ostrich eggshells. Palaeogeography, Palaeoclimatology, Palaeoecology 84, 175–189. doi:10.1016/0031-0182(91)90043-Q

Mischke, S., Almogi-Labin, A., Al-Saqarat, B., Rosenfeld, A., Elyashiv, H., Boomer, I., Stein, M., Lev, L., Ito, E., 2014. An expanded ostracod-based conductivity transfer function for climate reconstruction in the Levant. Quaternary Science Reviews 93, 91–105. doi: 10.1016/j.quascirev.2014.04.004

Mischke, S., Opitz, S., Kalbe, J., Ginat, H., Al-Saqarat, B., 2015. Palaeoenvironmental inferences from late Quaternary sediments of the Al Jafr Basin, Jordan. Quaternary

References

International 382, 154–167. doi:10.1016/j.quaint.2014.12.041

Mischke, S., Ginat, H., Al-Saqarat, B.S., Faershtein, G., Porat, N., Braun, P., Rech, J.A., 2017. Fossil-Based Reconstructions of Ancient Water Bodies in the Levantine Deserts. In: Enzel, Y., Bar-Yosef, O. (Eds.), *Quaternary of the Levant: Environments, Climate Change, and Humans.* Cambridge University Press, pp. 381–390. doi:10.1017/9781316106754.045

Mischke, S., Lai, Z., Faershtein, G., Porat, N., Röhl, M., Braun, P., Kalbe, J., Ginat, H., 2021. A Late Pleistocene Wetland Setting in the Arid Jurf ed Darawish Region in Central Jordan. Frontiers in Earth Science 9, 785. doi:10.3389/feart.2021.722435

Moumani, K., Alexander, J., Bateman, M.D., 2003. Sedimentology of the Late Quaternary Wadi Hasa Marl Formation of central Jordan: A record of climate variability. Palaeogeography, Palaeoclimatology, Palaeoecology 191, 221–242. doi: 10.1016/s0031-0182(02)00715-0

Moustafa, Y. a, Pätzold, J., Loya, Y., Wefer, G., 2000. Mid-Holocene stable isotope record of corals from the northern Red Sea. International Journal of Earth Sciences 88, 742–751. doi: 10.1007/s005310050302

Murray, A.S., Wintle, A.G., 2000. Luminescence dating of quartz using an improved single-aliquot regenerative-dose protocol. Radiation Measurements 32, 57–73. doi: 10.1016/S1350-4487(99)00253-X

Mycielska-DowgiaŁŁo, E., Ludwikowska-Kedzia, M., 2011. Alternative interpretations of grain-size data from quaternary deposits. Geologos 17, 189–203. doi:10.2478/v10118-011-0010-9

Ndiaye, M., 2007. A multipurpose software for stratigraphic signal analysis. Université de Genève. Unpub. PhD. Thesis. Université de Genève. doi:10.13097/archive-ouverte/unige:717

Neev, D., Emery, K.O., 1967. The Dead Sea: Depositional Processes and Environments of Evaporites, (Ministry of Development, Geological Survey. Bulletin). Monson Press. p. 147.

Nehme, C., Verheyden, S., Breitenbach, S.F.M., Gillikin, D.P., Verheyden, A., Cheng, H., Lawrence Edwards, R., Hellstrom, J., Noble, S.R., Farrant, A.R., Sahy, D., Goovaerts, T., Salem, G., Claeys, P., 2018. Climate dynamics during the penultimate glacial period recorded in a speleothem from Kanaan Cave, Lebanon (central Levant). Quaternary Research 90, 10–25. doi:10.1017/qua.2018.18

Nesbitt, H.W., Young, G.M., 1982. Early proterozoic climates and plate motions inferred from major element chemistry of lutites. Nature 299, 715–717. doi:10.1038/299715a0

References

Neugebauer, I., Brauer, A., Schwab, M.J., Waldmann, N.D., Enzel, Y., Kitagawa, H., Torfstein, A., Frank, U., Dulski, P., Agnon, A., Ariztegui, D., Ben-Avraham, Z., Goldstein, S.L., Stein, M., 2014. Lithology of the long sediment record recovered by the ICDP Dead Sea Deep Drilling Project (DSDDP). Quaternary Science Reviews 102, 149–165. doi:10.1016/j.quascirev.2014.08.013

Neugebauer, I., Schwab, M.J., Waldmann, N.D., Tjallingii, R., Frank, U., Hadzhiivanova, E., Naumann, R., Taha, N., Agnon, A., Enzel, Y., Brauer, A., 2016. Hydroclimatic variability in the Levant during the early last glacial (~117–75 ka) derived from micro-facies analyses of deep Dead Sea sediments. Climate of the Past 12, 75–90. doi:10.5194/cp-12-75-2016

Niemi, T.M., Smith, A.M., 1999. Initial results of the southeastern Wadi Araba, Jordan Geoarchaeological Study: Implications for shifts in late quaternary aridity. Geoarchaeology 14, 791–820. doi:10.1002/(SICI)1520-6548(199912)14:8<791::AID-GEA6>3.0.CO;2-C

Ntinou, M., Kyparissi-Apostolika, N., 2016. Local vegetation dynamics and human habitation from the last interglacial to the early Holocene at Theopetra cave, central Greece: the evidence from wood charcoal analysis. Vegetation History and Archaeobotany 25, 191–206. doi:10.1007/s00334-015-0538-7

Odeh, O., 2019. Water Shortage in Jordan. International Journal of Engineering and Management Sciences 4, 277–286.

Oren, A., Gurevich, P., 1995. Dynamics of a bloom of halophilic archaea in the Dead Sea. Hydrobiologia 315, 149–158. doi:10.1007/BF00033627

Oyedotun, T.D.T., 2018. X-ray fluorescence (XRF) in the investigation of the composition of earth materials: a review and an overview. Geology, Ecology, and Landscapes 2, 148–154. doi:10.1080/24749508.2018.1452459

Oyedotun, T.D.T., 2020. Compositional and multivariate statistical analyses for grain-size characterisation of intertidal sedimentary facies in an estuarine environment. Geology, Ecology, and Landscapes 1–7. doi:10.1080/24749508.2020.1814186

Palmer, C., 2013. Biogeography. In: Ababsa, M. (Ed.), Atlas of Jordan. Presses de l'Ifpo, pp. 77–87. doi:10.4000/books.ifpo.4871

Pandey, S., Parcha, S.K., 2017. Provenance, tectonic setting and source-area weathering of the lower Cambrian sediments of the Parahio valley in the Spiti basin, India. Journal of Earth System Science 126, 27. doi:10.1007/s12040-017-0803-5

Parker, A.G., Morley, M.W., Armitage, S.J., Engel, M., Parton, A., Preston, G.W., Russ, H., Drechsler, P., 2020. Palaeoenvironmental and sea level changes during the Holocene in eastern Saudi Arabia and their implications for Neolithic populations. Quaternary Science Reviews 249, 106618. doi:10.1016/j.quascirev.2020.106618

References

Parton, A., Farrant, A.R., Leng, M.J., Schwenninger, J.-L., Rose, J.I., Uerpmann, H.-P., Parker, A.G., 2013. An early MIS 3 pluvial phase in Southeast Arabia: Climatic and archaeological implications. Quaternary International 300, 62–74. doi:10.1016/j.quaint.2013.02.016

Parton, A., Farrant, A.R., Leng, M.J., Telfer, M.W., Groucutt, H.S., Petraglia, M.D., Parker, A.G., 2015a. Alluvial fan records from southeast Arabia reveal multiple windows for human dispersal. Geology 43, 295–298. doi:10.1130/G36401.1

Parton, A., White, T.S., Parker, A.G., Breeze, P.S., Jennings, R., Groucutt, H.S., Petraglia, M.D., 2015b. Orbital-scale climate variability in Arabia as a potential motor for human dispersals. Quaternary International 382, 82–97. doi:10.1016/j.quaint.2015.01.005

Parton, A., Clark-Balzan, L., Parker, A.G., Preston, G.W., Sung, W.W., Breeze, P.S., Leng, M.J., Groucutt, H.S., White, T.S., Alsharekh, A., Petraglia, M.D., 2018. Middle-late Quaternary palaeoclimate variability from lake and wetland deposits in the Nefud Desert, Northern Arabia. Quaternary Science Reviews 202, 78–97. doi:10.1016/j.quascirev.2018.10.010

Passega, R., 1964. Grain size representation by CM patterns as a geologic tool. Journal of Sedimentary Research 34, 830–847. doi:10.1306/74d711a4-2b21-11d7-8648000102c1865d

Passega, R., Byramjee, R., 1969. Grain-Size Image of Clastic Deposits. Sedimentology 13, 233–252. doi:10.1111/j.1365-3091.1969.tb00171.x

Petit-Maire, N., Carbonel, P., Reyss, J.L., Sanlaville, P., Abed, A., Bourrouilh, R., Fontugne, M., Yasin, S., 2010. A vast Eemian palaeolake in Southern Jordan (29°N). Global and Planetary Change 72, 368–373. doi:10.1016/j.gloplacha.2010.01.012

Pettijohn, f. j., Potter, P.E., SieverR., 1972. Sand and Sandstone, 1st ed. Springer-Verlag New York. p.631.

Pigati, J.S., Miller, D.M., Bright, J.E., Mahan, S.A., Nekola, J.C., Paces, J.B., 2011. Chronology, sedimentology, and microfauna of groundwater discharge deposits in the central Mojave Desert, Valley Wells, California. Bulletin of the Geological Society of America 123, 2224–2239. doi:10.1130/B30357.1

Pigati, J.S., Rech, J.A., Quade, J., Bright, J., 2014. Desert wetlands in the geologic record. Earth Science Reviews 132, 67–81. doi:10.1016/j.earscirev.2014.02.001

Powers, D.W., Easterling, R.G., 1982. Improved methodology for using embedded Markov chains to describe cyclical sediments. Journal of Sedimentary Petrology 52, 913–923. doi: 10.1306/212F808F-2B24-11D7-8648000102C1865D

Prasad, S., Vos, H., Negendank, J.F.W., Waldmann, N., Goldstein, S.L., Stein, M., 2004. Evidence from Lake Lisan of solar influence on decadal- To centennial-scale climate

variability during marine oxygen isotope stage 2. Geology 32, 581–584. doi:10.1130/G20553.1

Prasad, S., Negendank, J.F.W., Stein, M., 2009. Varve counting reveals high resolution radiocarbon reservoir age variations in palaeolake Lisan. Journal of Quaternary Science 24, 690–696. doi:10.1002/jqs.1289

Preusser, F., Degering, D., Fuchs, M., Hilgers, A., Kadereit, A., Klasen, N., Krbetschek, M., Richter, D., Spencer, J.Q.G., 2008. Luminescence dating: basics, methods and applications. E&G Quaternary Science Journal 57, 95–149. doi:10.3285/eg.57.1-2.5

Qdais, H.A.A., Batayneh, F., 2002. The role of desalination in bridging the water gap in Jordan. Desalination 150, 99–106. doi: 10.1016/S0011-9164(02)00934-7

Radaideh, O.M.A., Melichar, R., 2015. Tectonic paleostress fields in the southwestern part of Jordan: New insights from the fault slip data in the southeastern flank of the Dead Sea Fault Zone. Tectonics 34, 1863–1891. doi:10.1002/2015TC003919

Rasmussen, S.O., Bigler, M., Blockley, S.P., Blunier, T., Buchardt, S.L., Clausen, H.B., Cvijanovic, I., Dahl-Jensen, D., Johnsen, S.J., Fischer, H., Gkinis, V., Guillevic, M., Hoek, W.Z., Lowe, J.J., Pedro, J.B., Popp, T., Seierstad, I.K., Steffensen, J.P., Svensson, A.M., Vallelonga, P., Vinther, B.M., Walker, M.J.C., Wheatley, J.J., Winstrup, M., 2014. A stratigraphic framework for abrupt climatic changes during the Last Glacial period based on three synchronized Greenland ice-core records: refining and extending the INTIMATE event stratigraphy. Quaternary Science Reviews 106, 14–28. doi: 10.1016/j.quascirev.2014.09.007

Rech, J.A., Ginat, H., Catlett, G.A., Mischke, S., Tully, E.W., Pigati, J.S., 2017. Pliocene–Pleistocene Water Bodies and Associated Deposits in Southern Israel and Southern Jordan. In: Enzel, Y., Bar-Yosef, O. (Eds.), *Quaternary of the Levant: Environments, Climate Change, and Humans*. Cambridge University Press, pp. 127–134. doi:10.1017/9781316106754.014

Roberts, C.N., Zanchetta, G., Jones, M.D., 2010. Oxygen isotopes as tracers of Mediterranean climate variability: An introduction. Global and Planetary Change 71, 135–140. doi:10.1016/j.gloplacha.2010.01.024

Roberts, N., Jones, M.D., Benkaddour, A., Eastwood, W.J., Filippi, M.L., Frogley, M.R., Lamb, H.F., Leng, M.J., Reed, J.M., Stein, M., Stevens, L., Valero-Garcés, B., Zanchetta, G., 2008. Stable isotope records of Late Quaternary climate and hydrology from Mediterranean lakes: the ISOMED synthesis. Quaternary Science Reviews 27, 2426–2441. doi:10.1016/j.quascirev.2008.09.005

Roberts, N., Allcock, S.L., Arnaud, F., Dean, J.R., Eastwood, W.J., Jones, M.D., Leng, M.J., Metcalfe, S.E., Malet, E., Woodbridge, J., Yiğitbaşıoğlu, H., 2016. A tale of two lakes: a multi-proxy comparison of Lateglacial and Holocene environmental change

References

in Cappadocia, Turkey. Journal of Quaternary Science 31, 348–362. doi: 10.1002/jqs.2852

Robinson, L.F., Henderson, G.M., Hall, L., Matthews, I., 2004. Climatic Control of Riverine and Seawater Uranium-Isotope Ratios. Science 305, 851–854. doi:10.1126/science.1099673

Rogerson, M., Dublyansky, Y., Hoffmann, D.L., Luetscher, M., Töchterle, P., Spötl, C., 2019. Enhanced Mediterranean water cycle explains increased humidity during MIS~3 in North Africa. Climate of the Past 15, 1757–1769. doi:10.5194/cp-15-1757-2019

Röhl, M., 2015. Rekonstruktion pleistozäner Ablagerungsräume im südlichen Israel und Jordanien anhand von Korngrößendaten. Unpub. MSc. Thesis. Freie Universität Berlin. p. 74.

Romanski, J., Romanou, A., Bauer, M., Tselioudis, G., 2012. Atmospheric forcing of the Eastern Mediterranean Transient by midlatitude cyclones. Geophysical Research Letters 39. doi: 10.1029/2011GL050298

Roser, B.P., Korsch, R.J., 1988. Provenance signatures of sandstone-mudstone suites determined using discriminant function analysis of major-element data. Chemical Geology 67, 119–139. doi:10.1016/0009-2541(88)90010-1

Rowe, P.J., Wickens, L.B., Sahy, D., Marca, A.D., Peckover, E., Noble, S., Özkul, M., Baykara, M.O., Millar, I.L., Andrews, J.E., 2020. Multi-proxy speleothem record of climate instability during the early last interglacial in southern Turkey. Palaeogeography, Palaeoclimatology, Palaeoecology 538, 109422. doi:10.1016/j.palaeo.2019.109422

Royse, C.F., 1970. A sedimentologic analysis of the Tongue River – Sentinel Butte Interval (Paleocene) of the Williston Basin, western North Dakota. Sedimentary Geology 4, 19–80.

Rubin, S., Ziv, B., Paldor, N., 2007. Tropical Plumes over Eastern North Africa as a Source of Rain in the Middle East. Monthly Weather Review 135, 4135–4148. doi:10.1175/2007MWR1919.1

Ryan, K.M., Williams, D.M., 2007. Testing the reliability of discrimination diagrams for determining the tectonic depositional environment of ancient sedimentary basins. Chemical Geology 242, 103–125. doi:10.1016/j.chemgeo.2007.03.013

Saaroni, H., Halfon, N., Ziv, B., Alpert, P., Kutiel, H., 2010. Links between the rainfall regime in Israel and location and intensity of Cyprus lows. International Journal of Climatology 30, 1014–1025. doi: 10.1002/joc.1912

Saffarini, G.A., Amireh, B.S., 2016. Distinguishing depositional environments of the Lower

References

Cambrian–Lower Cretaceous siliciclastic sequence of Jordan using geostatistical techniques: A proposal. Arabian Journal of Geosciences 9, 370. doi:10.1007/s12517-016-2365-2

Sagy, A., Reches, Z., Agnon, A., 2003. Hierarchic three-dimensional structure and slip partitioning in the western Dead Sea pull-apart. Tectonics. doi:10.1029/2001TC001323

Salameh, E., 1996. Water Quality Degradation in Jordan. Friedrich Ebert Stiftung and the Jordan Royal Society for the Conservation of Nature, Amman, Jordan. p. 178.

Salameh, E., 2008. Over-exploitation of groundwater resources and their environmental and socio-economic implications: the case of Jordan. Water International 33, 55–68. doi:10.1080/02508060801927663

Salameh, E., Farajat, M. Al, 2007. The role of volcanic eruptions in blocking the drainage leading to the Dead Sea formation. Environmental Geology 52, 519–527. doi:10.1007/s00254-006-0484-x

Santisteban, J.I., Mediavilla, R., López-Pamo, E., Dabrio, C.J., Zapata, M.B.R., García, M.J.G., Castaño, S., Martínez-Alfaro, P.E., 2004. Loss on ignition: a qualitative or quantitative method for organic matter and carbonate mineral content in sediments? Journal of Paleolimnology 32, 287–299. doi:10.1023/B:JOPL.0000042999.30131.5b

Saqqa, W., Atallah, M., 2004. Characterization of the aeolian terrain facies in Wadi Araba Desert, southwestern Jordan. Geomorphology 62, 63–87. doi:10.1016/j.geomorph.2004.02.002

Saqqa, W., Atallah, M., 2013. Tectonic Geomorphology of Alluvial Fans east of the Wadi Araba Fault (Dead Sea Transform), Jordan. Jordan Journal of Earth and Environmental Sciences 5, 79–86.

Schuldenrein, J., Clark, G.A., 2001. Prehistoric Landscapes and Settlement Geography along the Wadi Hasa, West-Central Jordan. Part I: Geoarchaeology , Human Palaeoecology and Ethnographic Modelling. Environmental Archaaeology 6, 23–38.

Seager, R., Liu, H., Henderson, N., Simpson, I., Kelley, C., Shaw, T., Kushnir, Y., Ting, M., 2014. Causes of Increasing Aridification of the Mediterranean Region in Response to Rising Greenhouse Gases. Journal of Climate 27, 4655–4676. doi:10.1175/JCLI-D-13-00446.1

Shaukat, S.S., Rao, T.A., Khan, M.A., 2016. Impact of sample size on principal component analysis ordination of an environmental data set: Effects on eigenstructure. Ekologia Bratislava 35, 173–190. doi:10.1515/eko-2016-0014

Siddall, M., Rohling, E.J., Thompson, W.G., Waelbroeck, C., 2008. Marine isotope stage 3 sea level fluctuations: Data synthesis and new outlook. Reviews of Geophysics 46,

References

RG4003. doi:10.1029/2007RG000226

Sirota, I., Enzel, Y., Mor, Z., Moshe, L. Ben, Eyal, H., Lowenstein, T.K., Lensky, N.G., 2021. Sedimentology and stratigraphy of a modern halite sequence formed under Dead Sea level fall. Sedimentology 68, 1069–1090. doi: 0.1111/sed.12814

Sivan, D., Greenbaum, N., 2017. Middle–Late Quaternary Wetlands along the Coastal Plain of Israel. In: Enzel, Y., Bar-Yosef, O. (Eds.), *Quaternary of the Levant: Environments, Climate Change, and Humans.* Cambridge University Press, pp. 447–456. doi:10.1017/9781316106754.051

Sivan, D., Greenbaum, N., Cohen-Seffer, R., Sisma-Ventura, G., Almogi-Labin, A., Porat, N., Melamed, Y., Boaretto, E., Avnaim-Katav, S., 2016. Palaeo-environmental archive of groundwater–surface water interaction zone, the Kebara wetlands, Carmel coast, Israel. Quaternary International 396, 138–149. doi:10.1016/j.quaint.2015.03.036

Skaberne, D., 1996. Interpretation of Depositional Environment Based on Grain Size Distribution of Sandstones of the Val Gardena Formation in the Area Between Cerkno and Smrečje, Slovenia. Geologija 39, 193–214. doi:10.5474/geologija.1996.008

Smith, J.R., Giegengack, R., Schwarcz, H.P., McDonald, M.M.A., Kleindienst, M.R., Hawkins, A.L., Churcher, C.S., 2004. A reconstruction of Quaternary pluvial environments and human occupations using stratigraphy and geochronology of fossil-spring tufas, Kharga Oasis, Egypt. Geoarchaeology 19, 407–439. doi:10.1002/gea.20004

Staňová, S., Soták, J., Hudec, N., 2009. Markov Chain analysis of turbiditic facies and flow dynamics (Magura Zone, Outer Western Carpathians, NW Slovakia). Geologica Carpathica 60, 295–305. doi:10.2478/v10096-009-0021-4

Stein, M., 2001. The sedimentary and geochemical record of Neogene-Quaternary water bodies in the Dead Sea Basin - inferences for the regional paleoclimatic history. Journal of Paleolimnology 26, 271–282. doi:10.1023/A:1017529228186

Stein, M., Goldstein, S.L., 2017. Lake Lisan: The Archive of the Last Glacial Levant's Hydroclimatology. In: Enzel, Y., Bar-Yosef, O. (Eds.), Quaternary of the Levant: Environments, Climate Change, and Humans. Cambridge University Press, pp. 107–114. doi:10.1017/9781316106754.012

Stein, M., Starinsky, A., Katz, A., Goldstein, S.L., Machlus, M., Schramm, A., 1997. Strontium isotopic, chemical, and sedimentological evidence for the evolution of Lake Lisan and the Dead Sea. Geochimica et Cosmochimica Acta 61, 3975–3992. doi: 10.1016/S0016-7037(97)00191-9

Stein, M., Lazar, B., Torfstein, A., Goldstein, S.L., 2017. Chronologies of Late Quaternary

Coral Reefs and Lake Sediments from the Red Sea and Dead Sea Rift Valley. In: Enzel, Y., Bar-Yosef, O. (Eds.), *Quaternary of the Levant: Environments, Climate Change, and Humans.* Cambridge University Press, pp. 75–82. doi:10.1017/9781316106754.008

Swann, G.E.A., Leng, M.J., 2009. A review of diatom δ18O in palaeoceanography. Quaternary Science Reviews 28, 384–398. doi:10.1016/j.quascirev.2008.11.002

Swann, G.E.A., Mackay, A.W., Leng, M.J., Demory, F., 2005. Climatic change in Central Asia during MIS 3/2: a case study using biological responses from Lake Baikal. Global and Planetary Change 46, 235–253. doi: 0.1016/j.gloplacha.2004.09.019

Talbot, M.R., 1990. A review of the palaeohydrological interpretation of carbon and oxygen isotopic ratios in primary lacustrine carbonates. Chemical Geology: Isotope Geoscience section 80, 261–279. doi: 10.1016/0168-9622(90)90009-2

Talbot, M.R., 2005. Sedimentary Environments | Lake Processes and Deposits. In: Selley, R.C., Cocks, L.R.M., Plimer, I.R. (Eds.), Encyclopedia of Geology. Elsevier, Oxford, pp. 550–561. doi: 10.1016/B0-12-369396-9/00493-7

Tewari, R.C., Singh, D.P., Khan, Z.A., 2009. Application of Markov chain and entropy analysis to lithologic succession - an example from the early Permian Barakar Formation, Bellampalli coalfield, Andhra Pradesh, India. Journal of Earth System Science 118, 583–596. doi:10.1007/s12040-009-0037-2

Thompson, R., Oldfield, F., 1986. Environmental Magnetism. Springer Netherlands, Dordrecht. doi:10.1007/978-94-011-8036-8

Toms, P., Hosfield, R.T., Chambers, J.C., Green, C.P., Marshall, P., 2005. Optical dating of the Broom Palaeolithic sites, Devon & Dorset. London.

Torfstein, A., 2017. The Amora Formation, Dead Sea Basin. In: Enzel, Y., Bar-Yosef, O. (Eds.), Quaternary of the Levant: Environments, Climate Change, and Humans. Cambridge University Press, pp. 91–98. doi:10.1017/9781316106754.010

Torfstein, A., Enzel, Y., 2017. Dead Sea Lake Level Changes and Levant Palaeoclimate. In: Enzel, Y., Bar-Yosef, O. (Eds.), *Quaternary of the Levant: Environments, Climate Change, and Humans.* Cambridge University Press, pp. 115–126.

Torfstein, A., Haase-Schramm, A., Waldmann, N., Kolodny, Y., Stein, M., 2009. U-series and oxygen isotope chronology of the mid-Pleistocene Lake Amora (Dead Sea basin). Geochimica et Cosmochimica Acta 73, 2603–2630. doi:10.1016/j.gca.2009.02.010

Torfstein, A., Goldstein, S.L., Stein, M., Enzel, Y., 2013a. Impacts of abrupt climate changes in the Levant from Last Glacial Dead Sea levels. Quaternary Science Reviews 69, 1–7. doi: /10.1016/j.quascirev.2013.02.015

References

Torfstein, A., Goldstein, S.L., Kagan, E.J., Stein, M., 2013b. Integrated multi-site U-Th chronology of the last glacial Lake Lisan. Geochimica et Cosmochimica Acta 104, 210–231. doi:10.1016/j.gca.2012.11.003

Torfstein, A., Goldstein, S.L., Kushnir, Y., Enzel, Y., Haug, G., Stein, M., 2015. Dead Sea drawdown and monsoonal impacts in the Levant during the last interglacial. Earth and Planetary Science Letters 412, 235–244. doi:10.1016/j.epsl.2014.12.013

Tucker, M.E., 2001. Sedimentary petrology : an introduction to the origin of sedimentary rocks, Third edit. ed. Malden, MA : Blackwell Science., Oxford. p. 272.

Tzedakis, P.C., Frogley, M.R., Lawson, I.T., Preece, R.C., Cacho, I., Abreu, L. de, 2004. Ecological thresholds and patterns of millennial-scale climate variability: The response of vegetation in Greece during the last glacial period. Geology 32, 109–112. doi:10.1130/G20118.1

Vaks, A., Bar-Matthews, M., Ayalon, A., Schilman, B., Gilmour, M., Hawkesworth, C.J., Frumkin, A., Kaufman, A., Matthews, A., 2003. Paleoclimate reconstruction based on the timing of speleothem growth and oxygen and carbon isotope composition in a cave located in the rain shadow in Israel. Quaternary Research 59, 182–193. doi:10.1016/S0033-5894(03)00013-9

Vaks, A., Bar-Matthews, M., Ayalon, A., Matthews, A., Frumkin, A., Dayan, U., Halicz, L., Almogi-Labin, A., Schilman, B., 2006. Paleoclimate and location of the border between Mediterranean climate region and the Saharo–Arabian Desert as revealed by speleothems from the northern Negev Desert, Israel. Earth and Planetary Science Letters 249, 384–399. doi:10.1016/j.epsl.2006.07.009

Vaks, A., Bar-Matthews, M., Matthews, A., Ayalon, A., Frumkin, A., 2013. Corrigendum to "Middle-Late Quaternary paleoclimate of northern margins of the Saharan-Arabian Desert: reconstruction from speleothems of Negev Desert, Israel". Quaternary Science Reviews 65, 144. doi:10.1016/j.quascirev.2013.01.006

Venkatesan, S., Singarasubramanian, S.R., Suganraj, K., 2017. Depositional mechanism of sediments through size analysis from the core of Arasalar river near Karaikkal, east coast of India. Indian Journal of Geo-Marine Sciences 46, 2122–2131.

Verheyden, S., Nader, F.H., Cheng, H.J., Edwards, L.R., Swennen, R., 2008. Paleoclimate reconstruction in the Levant region from the geochemistry of a Holocene stalagmite from the Jeita cave, Lebanon. Quaternary Research 70, 368–381. doi:10.1016/j.yqres.2008.05.004

Verheyden, S., Nehme, C., Nader, F.H., Farrant, A.R., Cheng, H., Noble, S.R., Sahy, D., Edwards, R.L., Swennen, R., Claeys, P., Delannoy, J.J., 2017. Speleothems from Lebanon. In: Bar-Yosef, O., Enzel, Y. (Eds.), *Quaternary of the Levant: Environments, Climate Change, and Humans.* Cambridge University Press,

References

Cambridge, pp. 165–172. doi:10.1017/9781316106754.018

Visher, G.S., 1969. Grain size distribution and depositional processes. Journal of Sedimentary Petrology 39, 1074–1106.

Waldmann, N., 2017. The Stratigraphy and Chronology of the Samra Formation. In: Bar-Yosef, O., Enzel, Y. (Eds.), *Quaternary of the Levant: Environments, Climate Change, and Humans.* Cambridge University Press, Cambridge, pp. 99–106. doi: 10.1017/9781316106754.011

Waldmann, N., Starinsky, A., Stein, M., 2007. Primary carbonates and Ca-chloride brines as monitors of a paleo-hydrological regime in the Dead Sea basin. Quaternary Science Reviews 26, 2219–2228. doi:10.1016/j.quascirev.2007.04.019

Waldmann, N., Torfstein, A., Stein, M., 2010. Northward intrusions of low- and mid-latitude storms across the Saharo-Arabian belt during past interglacials. Geology 38, 567–570. doi:10.1130/G30654.1

Wang, L., Mackay, A.W., Leng, M.J., Rioual, P., Panizzo, V.N., Lu, H., Gu, Z., Chu, G., Han, J., Kendrick, C.P., 2013. Influence of the ratio of planktonic to benthic diatoms on lacustrine organic matter $\delta 13C$ from Erlongwan maar lake, northeast China. Organic Geochemistry 54, 62–68. doi: 10.1016/j.orggeochem.2012.09.010

Weltje, G.J., Tjallingii, R., 2008. Calibration of XRF core scanners for quantitative geochemical logging of sediment cores: Theory and application. Earth and Planetary Science Letters 274, 423–438. doi: 10.1016/j.epsl.2008.07.054

Williams, M., Nitschke, N., Chor, C., 2006. Complex geomorphic response to late Pleistocene climatic changes in the arid Flinders Ranges of South Australia. Géomorphologie : relief, processus, environnement 12. doi:10.4000/geomorphologie.47

Winer, E.R., 2010. Interpretation and climatic significance of late Quaternary valley-fill deposits in Wadi Hasa, West-Central Jordan. Unpub. MSc. Thesis. Miami University, United States of America. p. 97.

Worne, S., Kender, S., Swann, G.E.A., Leng, M.J., Ravelo, A.C., 2019. Coupled climate and subarctic Pacific nutrient upwelling over the last 850,000 years. Earth and Planetary Science Letters 522, 87–97. doi: 10.1016/j.epsl.2019.06.028

Xiao, K., Griffis, T.J., Baker, J.M., Bolstad, P. V, Erickson, M.D., Lee, X., Wood, J.D., Hu, C., Nieber, J.L., 2018. Evaporation from a temperate closed-basin lake and its impact on present, past, and future water level. Journal of Hydrology 561, 59–75. doi: 10.1016/j.jhydrol.2018.03.059

Yan, K., Wang, C., Mischke, S., Wang, J., Shen, L., Yu, X., Meng, L., 2021. Major and trace-element geochemistry of Late Cretaceous clastic rocks in the Jitai Basin,

southeast China. Scientific Reports 11, 13846. doi:10.1038/s41598-021-93125-8

Yang, J.H., Du, Y.S., 2017. Weathering geochemistry and palaeoclimate implication of the Early Permian mudstones from eastern Henan Province, North China. Journal of Palaeogeography 6, 370–380. doi:10.1016/j.jop.2017.08.003

Yang, S., Ding, F., Ding, Z., 2006. Pleistocene chemical weathering history of Asian arid and semi-arid regions recorded in loess deposits of China and Tajikistan. Geochimica et Cosmochimica Acta 70, 1695–1709. doi:10.1016/j.gca.2005.12.012

Yu, L., Lai, Z., 2014. Holocene climate change inferred from stratigraphy and OSL chronology of aeolian sediments in the Qaidam Basin, northeastern Qinghai–Tibetan Plateau. Quaternary Research 81, 488–499.

Zhang, Y., Zhang, J., McGowan, S., Metcalfe, S., Jones, M., Leng, M.J., Hou, J., 2021. Climatic and environmental change in the western Tibetan Plateau during the Holocene, recorded by lake sediments from Aweng Co. Quaternary Science Reviews 259, 106889. doi: 10.1016/j.quascirev.2021.106889

Zhao, Y., An, C.-B., Zhou, A., Zhang, X., Zhao, J., Dong, W., Miao, Y., 2021. Late Pleistocene hydroclimatic variabilities in arid north-west China: geochemical evidence from Balikun Lake, eastern Tienshan, China. Journal of Quaternary Science 36, 415–425. doi: 10.1002/jqs.3288

Zieliński, T., Goździk, J., 2001. Palaeoenvironmental interpretation of a Pleistocene alluvial succession in central Poland: Sedimentary facies analysis as a tool for palaeoclimatic inferences. Boreas 30, 240–253. doi:10.1111/j.1502-3885.2001.tb01225.x

Žigovečki Gobac, Ž., Posilović, H., Bermanec, V., 2009. Identification of biogenetic calcite and aragonite using SEM. Geologia Croatica 62, 201–206. doi:10.4154/GC.2009.14